Sedimentological and tectonostratigraphic models for synrift to post-rift transitions : the case of the Upper Jurassic to Lower Cretaceous of the Norwegian Sea

Romain Grime

N°d'ordre NNT : 2021LYSE1225

THESE de DOCTORAT DE L'UNIVERSITE DE LYON

opérée au sein de
l'Université Claude Bernard Lyon 1

Ecole Doctorale E2M2
(Evolution Ecosystèmes Microbiologie Modélisation)

Spécialité de doctorat : Sciences de la Terre
Discipline : Géologie

Soutenue publiquement le 25/10/2021, par :
GRIME Romain

Modèles sédimentologiques et tectonostratigraphiques durant la période de transition syn-rift - post-rift : le cas du Jurassique Supérieur et du Crétacé Inférieur de la Mer de Norvège

---

Devant le jury composé de :

Présidente :	
MATTIOLI Emanuela	Professeure des Universités, Université Claude Bernard Lyon 1
Rapporteurs :	
BOURQUIN Sylvie	Directrice de recherche, CNRS Rennes
HODGSON David	Professeur, Université de Leeds
MULDER Thierry	Professeur des Universités, Université de Bordeaux
Examinateurs :	
HUYGHE Pascale	Maître de conférences, Université Grenoble Alpes
SORREL Philippe	Maître de conférences, Université Claude Bernard Lyon 1
Directeur :	
PITTET Bernard	Maître de conférences, Université Claude Bernard Lyon 1
Co-directeur :	
RASMUSSEN Sten	Ingénieur, Edison Norge AS
Invités :	
BORRACCINI Francesco	Géologue, Energean
D. M. L. VELOSO Fernanda	Chercheure, BRGM

“As geology is essentially a historical science, the working method of the geologist resembles that of the historian. This makes the personality of the geologist of essential importance in the way he analyzes the past”

Reinout Willem van Bemmelen in "The Scientific Character of Geology" (1961)

In memory of my PhD supervisor and friend Bernard Pittet
(26/01/1966 – 08/10/2021)

Acknowledgments

Some people will find this acknowledgement inappropriate; others will find it funny. The COVID-19 pandemic has however impacted the formulation and delivery of this PhD study and the people that I met and collaborated with. During this study I observed effects of the different phases of the COVID-19 restrictions that we all had to endure. Without judging the quality of the decisions and implementation of the international response to the "crisis", there have been very real consequences for the people that I would like to acknowledge. With this in mind I have synthesised a correlation between rifting and the COVID-19 pandemic (Fig. 0.1). Before acknowledging all those that have contributed to the successful completion of this PhD work. Contributions have included both technical and methodological support, as well as physical, emotional, gastronomic and mental stimulation. I understand that some people will only look at *Fig. 0.1A*, and will say that the post-* period has not yet started, and that the entire curve should be interpreted as a syn-* period… to this I reply: "just imagine the Halten Terrace during the Jurassic and Cretaceous times, and everything will become clearer after that 😉" (Fig. 0.1B).

During the Pre-* period (Fig. 0.1) that began on the 28th of March 2017, I compiled the first draft of the PhD proposal. I would first, like to thank my wife, Lisa Grime who continually supported and encouraged me in my endeavours towards completing my PhD. I would like to thank Alexandre Bouche, Sébastien Landru and Jonathan Furic for taking the time to review this first draft. My PhD supervisor, Bernard Pittet, who kindly provided feedback and suggestions to improve this 1st version of the PhD proposal. The final version of the PhD proposal was completed by mid-September 2017, having from a single page to 27 fully developed pages. Thanks to Bernard, at this stage, for trusting my ambitious project. On the 20th of September 2017, Alexandre gave me very good news regarding Emerson's sponsorship of the PhD project, which provided me the full access to Paradigm software solution. I would once again like to thank Alexandre and his company, Paradigm (now called Emerson), for investing in my PhD project. I made a technical flyer that was sent to all Oil & Gas companies in Norway telling them that I would be in Oslo from 10th to 11th October 2017, and in Stavanger from 12th to 17th October 2017, to seek sponsorship for the project. I would like to thank Alexandre and Gina for hosting me in Oslo as well as Sébastien, Nataliya and Chloé for providing me with board and lodgings (and more) in Stavanger. I got positive feedback from most of the companies I contacted. During my time in Norway promoting my PhD, seven companies booked a time slot to hear my presentation. I would like to thank my LinkedIn network for making this happen, and I would like to thank all the companies that replied to me, for considering this project. Less than a month after my trip in Norway, the 2nd of November 2017, Edison Norge AS (now Sval Energi AS) offered to fully sponsor this PhD project. I would like to sincerely thanks Milly Tornaghi, Andrea Sitta and Sten Rasmussen from Edison Norge AS for trusting me and my project and giving me the chance to start this incredible adventure. On the 6th of April 2018, I made a presentation to the doctoral school (E2M2) who officially accepted my candidacy for this PhD project.

On the 1st of June 2018, I officially started my project as a PhD student at the University of Lyon 1. Between the 1st of June 2018 to the beginning of March 2020, I had the chance to conduct, several core sessions in Norway, with Bernard. Thanks to Bernard for the good times, we had to describing this huge collection of sedimentary rocks! A special thank you for his technical advice that will be valuable throughout my career. Thanks also to Edison Norge AS, and all G&G colleagues for the good time we shared in the Troll office (Jåttåvågen, Stavanger). Thanks also to all my Norwegian friends for hosting me when I was in Norway. Again, thanks to the Landru family, thanks to Kåre and Ely Maristad for hosting me in Sandnes in their P2 basement. Thanks to Elisa and Sammy for their hospitality. Thanks also to Benjamin Kyle Bowlin, Bartosz Goledowski, Davide Duranti, Stefano Carruba, Michele Marco Comisso, Benjamin Bonnier, Raja Ouerghi, Simon and Pauline Fillacier and Qaiser Shakeel for the good times we had whilst travelling in Norway around a morning coffee or an evening Tau beer. I also would like to thanks all my colleagues in Géode (University of Lyon 1) for the fruitful discussion we had, and the good atmosphere that prevailed in the lab. A particular thanks to Amir Kalifi, Farid Saleh, Hicham Baghli, Céline Salaviale, Emanuela Mattioli, Victoire Lucas, Frédéric Quillévéré, Guillaume Suan and Claude Colombié. A huge thanks to the two students, Laure Aillaud and Lucas Goyard, who conducted their internships under my supervision to assist me in my research. I sincerely thank all the members of the follow-up committee that guided me in my Research. Thanks to Gilles Escarguel for his dedicated time, thanks to Philippe-Hervé Leloup and Philippe Sorrel for their contribution to the smooth running of the PhD. Thanks to Francesco Borraccini for mentoring me regarding structural geology (I learned a lot from the 3 days we spent in Milan about structural geology). Thanks once more to Sten and Bernard for their effective supervision throughout the full PhD. Thanks to the Emerson office in Paris for providing me a full training week that helped me to substantiate my findings. Thanks to Fleur Grime, Marie Fleuroux and Jonathan Furic for hosting me in Paris when I had meetings in the capital. I want to also thank with all my heart my grand-mother Noëlle Pascal who passed away the 3rd of May 2019. She was always there for me, and she was sure that my PhD project would be successfully completed. Thank you to all my friends and family for those special moments we shared. I would also thank my wife, Lisa Grime, for everything and for giving birth to our little baby Hugo Grime, on the 19th of November 2019 that given us so much happiness.

During the *-initiation period (Fig. 0.1), I entered myself in pre-confined mode as I saw that the situation across the world worsening. Between 17th of March and 11th of May 2020, which corresponded approximately to the *-climax, we were all locked down. This was a complicated period to work from home for my wife and I, with a newly born baby. Following the cancellation of my last planned core session in Stavanger in April 2020, I would like to thank Bernard, one more time, for his encouragement and for advising me to “try to work if you can (with Hugo), but to not forget to enjoy this good weather”. I managed some work, and I especially enjoyed spending time with my son Hugo, my wife, Lisa, and the rest of the family, my two cats Souris and New-pi, and the three hens, Grisette, Blanchette and Noirette. Thanks to all my neighbours (Marie, Roger, Roland, Brigitte, Laurie, Ronan, Martin, Sophie, May, Philippe, Patou and Val.) for their kindness which made the “Rue Berthelot” a good place to be. I found a good rhythm of work during the final-* stage as Hugo started to spending time with his nanny Delphine on the 11th May 2020. During *-sag, I solely worked from home during the

preparation of my first article. I would sincerely thank all my co-authors, Bernard, Sébastien, Alexandre, Amir, Francesco and Sten for their feedback, suggestions and contributions. I would also thank Tim Rice and Benjamin Kyle Bowlin who contributed to improving the manuscript in many ways. I would like to also thank Zoom our dog, born the 30th April 2020. It was lovely to see Hugo and Zoom playing together during the summer 2020.

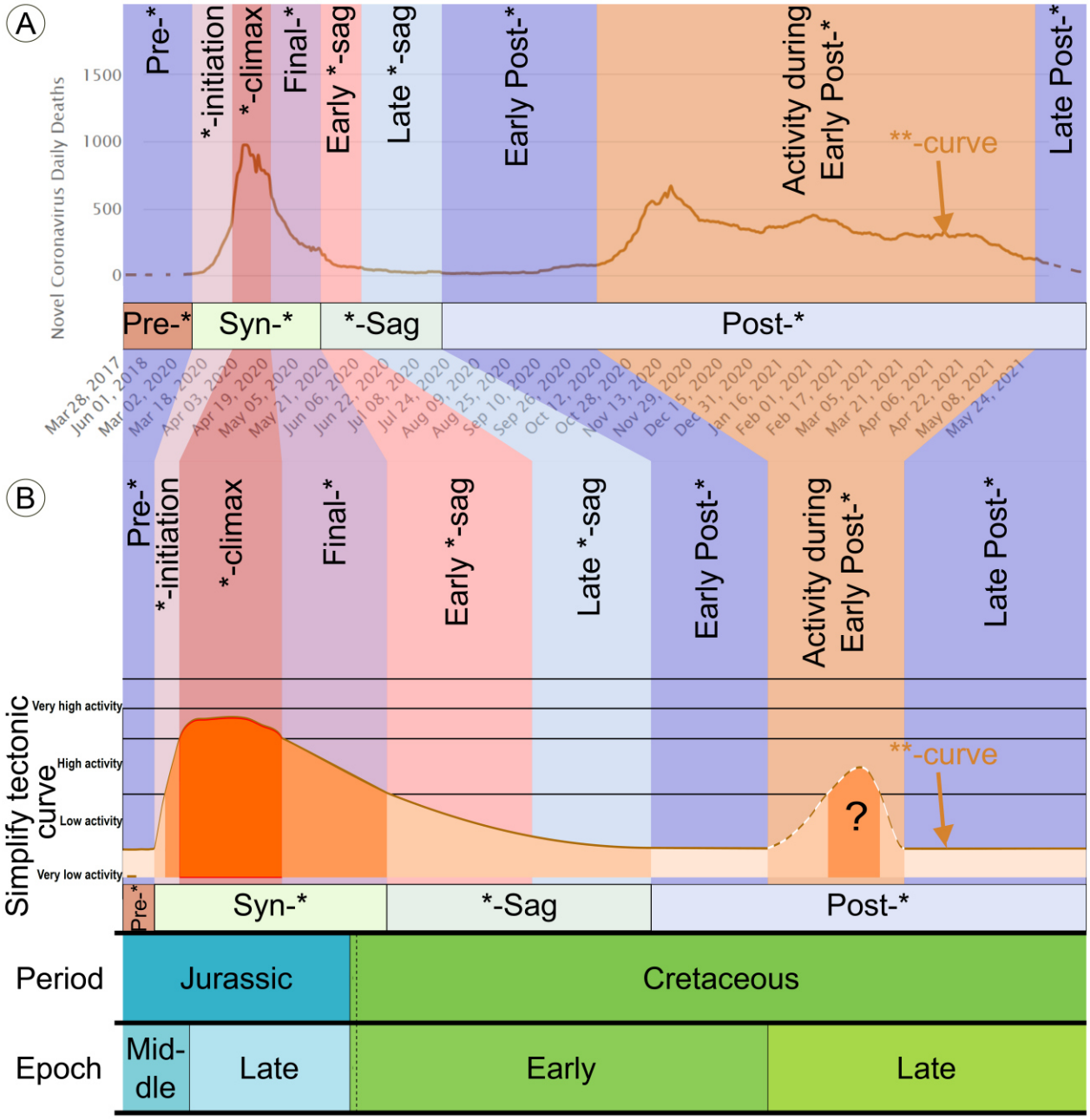

Fig. 0.1: Correlation between (A) COVID-19 pandemic in France, and (B) rifting in the Norwegian Sea. One asterisk can be replaced by "rift" or "COVID-19 pandemic", two asterisks can be replaced by "tectonic activity" or "daily deaths"

The Early Post-* period was almost identical to the syn-* and *-sag period during which I worked from home with only rare interactions with the outside world (Fig. 0.1). Between 30th October and 15th December 2020, the second lockdown impacted me severally since only virtual interactions were permitted. At this point I decided to shake up my daily routine by making daily trips to my gastronomic sponsor, “Le Séchoir du Bugey” where I was once again able to speak with real people (Nelly, Marion and Eugénie). Thanks to this beautiful place and wonderful people. With my wife, son and dog in tow, we started hiking 2 or 3 times per week with the club “Randos et Balades Canine 01” where we met new friends, such as Denis, Margorie, Peggy, Christophe, Cyril, Fred… and their lovely dogs. This provided me with a breath of fresh air and the impetus to start the final stretch, “the production of the manuscript”. The second paper was quickly written with the collaboration and contribution of all the co-authors. Once more, thanks to Bernard, Philippe, Sébastien, Alexandre, Tim, Benjamin and Jonathan (who I consider as the perfect technical dream team) for the fruitful e-discussions we had. Thanks to Kévin Boulesteix for his excellent contribution on the second paper. During the Late Post-* period, I want to sincerely thanks my wife, Lisa Grime, who planned all the weekends with Hugo and Zoom, providing me with additional free time to work on my manuscript. Moreover, thanks to my wife for helping in formatting my PhD manuscript. Thanks once again to the perfect technical dream team. Thanks to Sval Energi AS for providing me access to their Geocloud that permit me to finish some figures with Petrel (Schlumberger). Sincerely thanks to Sylvie Bourquin, Thierry Mulder and David Hodgson who accepted to review this manuscript. A huge thanks to the rest of the PhD committee members composed of Pascal Huyghe, Emmanuela Mattioli, Sten Rasmussen, Bernard Pittet, Francesco Borraccini and Fernanda M. L. Veloso for accepting to be part of my PhD committee. Thank you to my physiotherapist, Marc Pelluet that cured my back pain when I was mainly sited to write my PhD manuscript. I would also like to thank my friends, Ju, Laurine, Lorette, Amélie, Bastien, Perrine, Fabien, Matthieu, Laurine Logan, Steph, Nico., Virginie, Kev., Chris, Elo., Hugo, Amir, Kåre, Ely, Juliette, Sylvain, Nataliya, Chloé, Marc, le petit Seb., Flo., Mel., Julie, Jérem, Myriam, Pierre, Ombeline, Dub., Hughes, Wes, Axel, Carl and Leticia for sharing good times with me, and always supporting me in my work. I would like to sincerely thank, my grand-Pa, Gilles Pascal, my mum, Caroline Grime, my father, Nobert Grime, my two sisters and brother, Julie, Fleur and Tanguy but also Marie, Pierre-Olivier, Stéphanie, Adrien, Léo, Jean-loup, Chantal, Manon, Mathieu, Amaury, Laura and my rooster Wrouch best morning singer ever, for always be there for me.

Résumé et mots clés

Les successions stratigraphiques de bassins de type rift ont fait l'objet d'un nombre considérable d'études tectonostratigraphiques au cours des dernières décennies. Cependant, la transition entre la période syn-rift et la période post-rift constitue toujours actuellement un sujet de débat au sein de la communauté scientifique. Cette thèse de doctorat présente le cas de la marge continentale de la Mer de Norvège afin de reconstituer l'évolution des environnements de dépôt au cours des périodes syn-rift et post-rift. Ce site a été choisi pour la largeur atypique de son domaine de terrasse, sur lequel une énorme quantité de données est disponible mais n'a jamais analysée de manière intégrée.

Dans cette étude, l'identification de quinze séquences stratigraphiques (S1 à S15), combinée à une zonation des kystes de dinoflagellés revue et corrigée, permet de diviser l'intervalle stratigraphique étudié en trois périodes majeures avec (i) la période syn-rift (S1 à S7, datée du Bathonien moyen au Berriasien moyen/final), (ii) la période transitoire rift-sag (S8, datée du Berriasien moyen/final à la limite Aptien/Albien) et (iii) la période post-rift (S9 à S15, datée de la limite Aptien/Albien au Coniacien précoce). Ces trois périodes majeures s'inscrivent bien dans l'évolution multiphasée du rift Atlantique.

Le stade syn-rift est marquée par une activité tectonique intense où de larges systèmes deltaïques se sont développés conjointement à des environnements côtiers dominés houle. Le stade rift-sag est une période de transition où l'activité tectonique se raréfie entre le domaine de la terrasse et de la plate-forme, générant néanmoins quelques complexes de lobes turbiditiques d'eau profonde. La phase rift-sag correspond très probablement à une période de migration de la déformation du domaine de la terrasse vers le domaine profond. Le stade post-rift est défini par une phase de quiescence tectonique contemporaine aux dépôts d'épaisses successions d'argiles offshore.

Mots clés : Norvège centrale; Terrasse de l'Halten; Terrasse de Dønna; Séquence stratigraphique; Autocyclique et allocyclique; Environnements côtiers; Dépôts marins peu profonds silicoclastiques; Flux de densité sédimentaire subaquatique

Sedimentological and tectonostratigraphic models for syn-rift to post-rift transitions: the case of the Upper Jurassic to Lower Cretaceous of the Norwegian Sea

Abstract and keywords

Stratigraphic rift-basin successions have promoted a tremendous amount of tectonostratigraphic studies during the last decades. However, the syn-rift to post-rift transition is still a matter of debate. This PhD thesis presents the case of the Norwegian Sea continental margin, intending to reconstruct the evolution of depositional environments during the syn-rift and post-rift stages. The Norwegian Sea has been chosen for its atypically wide terrace domain across which a tremendous amount of data has been acquired, but never comprehensively integrated.

In this study, the identification of fifteen stratigraphic sequences (S1 to S15), combined with a reappraised dinoflagellate cyst zonation, enables the studied stratigraphic interval to be divided into three major periods with (i) the syn-rift period (S1 to S7, dated from the Middle Bathonian to the Middle/Late Berriasian), (ii) the transitional rift-sag period (S8, dated from the Middle/Late Berriasian to the Aptian/Albian boundary) and (iii) the post-rift period (S9 to S15, dated between the Aptian/Albian boundary and the Early Coniacian). Those three major periods fit well into the Atlantic multiphased rift evolution.

The syn-rift period is marked by an intense tectonic activity during which coarse-grained deltas have conjointly developed with wave-dominated coasts. The rift-sag stage is a transitional period during which tectonic activity waned between the terrace and the platform domains while fostered the development of deep-water turbidite lobe complexes. The rift-sag phase most probably corresponds to a period of migration of the deformation from the terrace domain to the deep domain. The post-rift stage is defined by a phase of tectonic quiescence coevally with the deposition of thick offshore marine mudstone successions.

Keywords: Mid-Norway; Halten Terrace; Dønna Terrace; Sequence stratigraphy; Autocyclic and allocyclic; Coastal environments; Siliciclastic shallow-marine deposits; Subaqueous sedimentary density flow

Résumé étendu

La théorie de la dérive des continents (Wegener, 1920) est essentielle pour comprendre le mouvement des plaques tectoniques et donc indirectement l'évolution des rifts continentaux. Cependant, ce n'est que depuis les années 1960 que l'hypothèse proposée par Alfred Wegener a été confirmée par des campagnes océanographiques de grande envergure, ainsi que sur le domaine terrestre avec le développement du GPS. Dès lors, la compréhension des mécanismes liés à l'extension de la lithosphère a considérablement évolué. Les progrès technologiques combinés aux données recueillies sur le terrain ont ainsi permis de modéliser les processus inhérents au contexte de rifting. Dans le but de comprendre l'évolution des anciens bassins de type rift, l'élaboration de modèles sédimentologiques et tectonostratigraphiques s'avère donc essentielle, sinon cruciale.

Afin de reconstituer l'évolution sédimentologique et tectonostratigraphique au cours des périodes syn-rift et post-rift, cette thèse présente le cas de la marge continentale de la Mer de Norvège. Ce lieu a été choisi pour son domaine de terrasse atypiquement large où une importante quantité de données a été acquise durant ces 40 dernières années mais jamais intégrée de manière exhaustive. En outre, la marge conjuguée du Groenland oriental a révélé des dépôts syn-rift et post-rift dans des affleurements terrestres fournissant des informations sédimentologiques et tectonostratigraphiques complémentaires à l'ensemble des données de sub-surface (offshore) disponibles en Mer de Norvège.

Au cours de ce travail de recherche, l'interprétation de quinze séquences stratigraphiques (S1 à S15) sur la base de l'analyse intégrée de diagraphies, de carottes sédimentaires et de données sismiques, combinée à une réévaluation du cadre biostratigraphique, permet de subdiviser l'intervalle stratigraphique étudié en trois périodes majeures. Ces subdivisions comprennent (i) la période syn-rift (S1 à S7, datée du Bathonien moyen au Berriasien moyen/final), (ii) la période transitoire rift-sag (S8, datée du Berriasien moyen/final à la limite Aptien/Albien) et (iii) la période post-rift (S9 à S15, datée de la limite Aptien/Albien au Coniacien précoce). Ces trois périodes majeures s'inscrivent bien dans l'évolution multiphasée du rift Atlantique.

L'évolution sédimentologique et tectonostratigraphique de la période syn-rift de la Mer de Norvège s'est déroulée en trois étapes majeures : (i) le stade d'initiation du rift marqué par une initiation de l'activité tectonique ; (ii) le stade de climax du rift caractérisé par une intense activité tectonique ; (iii) le stade final du rift, marqué par un arrêt progressif de l'activité des failles. Afin de mettre en évidence les caractéristiques propres à ces trois étapes majeures, une investigation architecturale des dépôts siliciclastiques d'environnement marin peu profond en Mer de Norvège en contexte syn-rift a été réalisée au sein de la terrasse de l'Halten (i.e., Viking Group), datée du Jurassique tardif au Crétacé Inférieur. Cette étude est basée sur une base de données sismiques 3D réévaluée, des diagraphies de puits pétroliers, des carottes de sédiments ainsi que des données biostratigraphiques. Dix puits d'exploration forés dans la zone d'étude ont fourni près d'un demi-kilomètre de carottes sédimentaires, à partir desquelles deux environnements de dépôt ont été identifiés sur la base d'une analyse

détaillée des faciès sédimentaires (i.e., environnements deltaïques subaquatiques et environnements côtiers dominés par la houle). La description des dépôts deltaïques et la reconnaissance de différents dépôts sédimentaires densitaires gravitaires subaquatiques ont permis de caractériser des variations latérales des faciès au sein des cônes deltaïques, principalement liées à l'activité tectonique. Sept séquences (S1 à S7) de 3ème ordre ont été reconnues pour les dépôts syn-rift jurassiques sur la base d'un schéma biostratigraphique réévalué. L'évolution stratigraphique des environnements de dépôts identifiés durant la période syn-rift de la terrasse de l'Halten s'est déroulée en trois étapes successives: (i) la phase d'initiation du rift au cours de laquelle l'activité tectonique, l'eustatisme et les changements climatiques ont été les principaux moteurs de l'évolution des environnements deltaïques et des milieux côtiers dominés par les vagues ; (ii) le stade de climax du rift, principalement caractérisé par une intense activité des failles favorisant le développement de multiples systèmes deltaïques; (iii) la phase finale du rift, marquée par d'importantes fluctuations à court terme du niveau de la mer et à un déclin de l'activité tectonique ayant favorisé le développement à grande échelle de sables littoraux dominés par la houle (grès) et d'argiles offshore riches en matière organique. Un modèle 4D reliant l'évolution de l'architecture tectonostratigraphique aux changements de processus sédimentaires dominants (et les environnements de dépôt associés) ouvre de nouvelles perspectives d'exploration en améliorant les capacités de prédiction des réservoirs pétroliers siliciclastiques marin peu profonds en contexte syn-rift.

Le stade rift-sag est une période de transition entre le stade syn-rift caractérisé par une forte activité tectonique et le stade post-rift marqué par une quiescence tectonique. En Mer de Norvège, la période rift-sag est caractérisée par une diminution progressive de l'activité tectonique, dès lors confinée aux failles maîtresses séparant la plate-forme et le domaine de la terrasse. Un nouveau jeu de failles semble s'initier le long de failles préexistantes d'âge Calédonien séparant le domaine profond du domaine de la terrasse. La phase rift-sag correspond très probablement à une période de migration de la déformation du domaine de la terrasse vers le domaine profond. Au cours de cette période, des argiles marines se sont principalement déposées contemporainement à de rares complexes de lobes turbiditiques d'eau profonde adossés à l'activité des failles. L'évolution sédimentologique et tectonostratigraphique du rift-sag de la Mer de Norvège s'est déroulée en deux étapes : (i) le rift-sag précoce dominé par une faible activité tectonique le long des failles maîtresses entre le domaine de la terrasse et de la plate-forme à l'opposé du (ii) rift-sag tardif dominé par de rares mouvements tectoniques, entre ces 2 domaines, conduisant au développement d'unités turbiditiques d'eau profonde isolées telles que les "sables aptiens".

Le stade post-rift est caractérisé par une longue période de quiescence tectonique. Les dépôts sédimentaires sont essentiellement composés d'argiles marines profondes avec de rares complexes de lobes turbiditiques d'eau profonde. L'évolution sédimentologique et tectonostratigraphique post-rift de la Mer de Norvège s'est déroulée en deux étapes : (i) le post-rift précoce caractérisé par une phase de quiescence tectonique et une subsidence différentielle entre les hauts structuraux et les bas structuraux ayant conduit à la mise en place de dépôts turbiditiques d'eau profonde ; (ii) le post-rift tardif caractérisé par une période de

quiescence tectonique et le développement d'argiles marines profondes à large échelle en Mer de Norvège ainsi que de rares lobes turbiditiques.

L'étude sédimentologique multi-échelle des complexes de lobes turbiditiques d'eaux profondes datés du Turonien au Coniacien dans la grande région de Marulk (Terrasse de Dønna, Mer de Norvège) a été entreprise sur la base de données sismiques et de carottes sédimentaires. L'analyse sédimentologique a établi quatre associations de faciès qui définissent trois sous-environnements du lobe axial : le chenal et/ou le lobe proximal (CPL), le lobe moyen à distal (MDL) et la frange frontale du lobe (FLF), ainsi qu'un sous-environnement du lobe localisé hors axe et décrit comme une frange latérale du lobe (LLF) définissant un interlobe. Sur la base d'un nouveau modèle d'empilement des lobes turbiditiques d'eau profonde, cette étude propose une méthode inédite pour la discrimination des facteurs de contrôle autocycliques ou allocycliques dominants. Les processus autocycliques sont couramment observés à partir de carottes sédimentaires, tandis que les processus allocycliques s'expriment davantage dans les données diagraphiques. Dans un environnement de lobe turbiditique, les processus autocycliques contrôlent l'autorégulation de la dispersion des sédiments en évoluant d'un sous-environnement à un autre soit par (i) une migration latérale du lobe, (ii) une migration axiale du lobe c'est-à-dire par progradation ou rétrogradation ou enfin (iii) une migration verticale impliquant une aggradation des lobes turbiditiques successifs. A l'inverse, les facteurs de contrôle allocycliques provoquent une migration axiale rapide et abrupte entraînant souvent une discontinuité dans l'évolution des sous-environnements de dépôt au sein de la succession sédimentaire turbiditique. Dans cette étude, 4 facteurs de contrôle autocycliques ont été identifiés. Le contrôle autocyclique n°1 s'exprime à l'échelle du lit de lobe, dans lequel la dispersion des sédiments est auto-répartie dans l'espace et le temps. Ce système auto-organisé définit le type de lit et le nombre de lits dans l'élément du lobe. Le facteur de contrôle autocyclique #2 implique un déplacement latéral du lobe permettant une régulation spatiale et temporelle de la dispersion des sédiments. Le facteur de contrôle autocyclique n°3 concerne le centre de gravité du lobe, situé au centre du lobe turbiditique (sous-environnement MDL). La probabilité qu'un sous-environnement MDL soit précédé, ou succédé, par tout autre sous-environnement de dépôt est égale. Le facteur de contrôle autocyclique n°4 permet à un lobe de migrer le long de son axe longitudinal par progradation, rétrogradation, ou le long de son axe vertical par aggradation. En outre, trois facteurs de contrôle allocycliques ont été identifiés. Les facteurs de contrôle #5 et #6 sont attribués à des impulsions allocycliques, qui impliquent une rétrogradation ou une progradation rapide à l'échelle extra-lobe ou intra-lobe, respectivement, tandis que le facteur de contrôle allocyclique #7 exerce un contrôle primaire sur la tendance évolutive générale du lobe turbiditique. La compréhension des facteurs autocycliques et allocycliques est un élément clé de prédiction de l'évolution sédimentaire au sein d'un complexe de lobe turbiditique.

Extended abstract

The theory of continental drift (Wegener, 1920) is crucial in understanding plate motion and, therefore, continental rift evolution. However, it is only since the 1960s that the proposed hypothesis of Alfred Wegener has been confirmed by large-scale oceanographic campaigns, and on land owing to the development of GPS. By then, our understanding of the mechanisms related to the extension of the lithosphere has evolved significantly. Technological advances combined with fieldwork data have encouraged the scientific community to better model rifting dynamics and processes. Hence the elaboration of sedimentological and tectonostratigraphic models is mandatory for reconstructing the evolution of ancient rift-basins.

This PhD thesis handles a sedimentological and tectonostratigraphic reconstruction of Mesozoic depositional environments during the syn-rift and post-rift periods from the Norwegian Sea continental margin. This location was chosen for its atypically wide terrace domain where a tremendous amount of data has been acquired over the past 40 years but never comprehensively integrated. In addition, the East Greenland conjugate margin revealed onshore syn-rift and post-rift deposits that provide complementary sedimentological and tectonostratigraphic information to the offshore subsurface dataset available within the Norwegian Sea.

In this study, the interpretation of 15 stratigraphic sequences (S1 to S15) using well-log, sediment core and seismic data, combined with a refined proposed dinoflagellate cyst zonation allows the subdivision of the studied stratigraphic interval into three major periods. These subdivisions include (i) the syn-rift period (S1 to S7, dated from the Middle Bathonian to the Middle/Late Berriasian), (ii) the transitional rift-sag period (S8, dated from the Middle/Late Berriasian to the Aptian/Albian boundary) and (iii) the post-rift period (S9 to S15, dated between the Aptian/Albian boundary and the Early Coniacian). Those three major periods fit well into the Atlantic multiphased rift evolution.

The syn-rift sedimentological and tectonostratigraphic evolution of the Norwegian Sea occurred in three stages: (i) the rift initiation stage, during which tectonic activity steadily increased allowing the coeval evolution of delta fans and wave-dominated coastal environments; (ii) the rift-climax stage, which was mainly controlled by tectonic activity leading to the development of multiple coarse-grained deltas; (iii) the final rift stage, as marked by a progressive cessation of fault activity and the development of widespread wave-dominated shoreface to foreshore environments and the deposition of organic-rich offshore mudstones. This syn-rift model improves the prediction of siliciclastic shallow-marine petroleum reservoirs.

The rift-sag stage is a transitional period between the syn-rift stage characterised by high tectonic activity, and the post-rift stage defined by a tectonic quiescence. In the Norwegian Sea, the rift-sag period is characterised by a progressive decrease in tectonic activity, which was then only confined to master faults separating the platform and the terrace domains. A new set of faults seems to initiate along pre-existing Caledonian faults separating the terrace domain from the deep domain. The rift-sag phase most probably corresponds to a period of

migration of the deformation from the terrace domain to the deep domain. Deep-marine offshore mudstones were primarily deposited along with rare deep-water turbidite lobe complexes associated with (rare) fault motions. The rift-sag sedimentological and tectonostratigraphic evolution of the Norwegian Sea took place in two stages: (i) the early rift-sag, characterised by a weak tectonic activity along master faults separating the terrace and the platform domains and, (ii) the late rift-sag, which is dominated by rare tectonic activity between those 2 domains and the development of isolated deep-water turbidite deposits, such as the “Aptian sands”.

The post-rift stage is characterised by a long period of tectonic quiescence, and the deposition of offshore marine mudstones along with rare deep-water turbidite lobe complexes. The post-rift sedimentological and tectonostratigraphic evolution of the Norwegian Sea occurred in two stages: (i) the early post-rift, characterised by a tectonic quiescence and differential subsidence between intraterrace highs and intraterrace lows, which led to the formation of the Breiflabb and Lysing deep-water turbidite members; (ii) the late post-rift substage, which is characterised by a period of tectonic quiescence and the development of offshore mudstones across the entire Norwegian Sea.

Table of content

Table of supplementary data

List of abbreviations

Abbreviation	Explanation
^{232}Th	Thorium 232
^{238}U	Uranium 238
2D	two-dimensional
2U3	Unconformity between sequence 2 and 3
3D	three-dimensional
^{40}K	Potassium 40
4D	four-dimensional
AD	All Data
Ajp	Axial jump pattern group
Ap	Axial pattern group
API	American Petroleum Institute units
Asp	Axial straight pattern group
avg.	average
AVO	Amplitude Versus Offset
BCU	Base Cretaceous Unconformity
btw.	between
C1	Coastal facies 1 - Lower shoreface
C2	Coastal facies 2 - Middle shoreface
C3	Coastal facies 3 - Upper shoreface
C4	Coastal facies 4 - Foreshore
C5	Coastal facies 5 - Backshore
CD	Conical Deltas
cm	centimetre
Co1	Gravity-driven facies - Concentrated density flow
CoG	Centre of Gravity
CP	Compound pattern family
CPL/C	Channel and/or Proximal Lobe
CPX	Complex pattern family
D	Germany
DCZ	Dinoflagellate Cyst Zone
De1	Gravity-driven facies - Debris flow of type 1
Df1	Gravity-driven facies - Debris flow of type 2
DK	Denmark

DLF	Distal Lobe Fringe
dm	decimetre
DT	Dønna Terrace
EO	Exclusion of Outliers
FC	Fault Complex
FLF/F	Frontal Lobe Fringe
Fm./Fms.	Formation/Formations
Fp	Frontal pattern group
FS	Fault Segment
ft/h	foot per hour
GD	Gilbert-type Deltas
Gp./Gps.	Group/Groups
GR	Gammay-Ray
GTS	Geologic Time Scale
HCS	Hummocky Cross-Stratification
HEB/HEBs	Hybrid Event Bed/Hybrid Event Beds
HT	Halten Terrace
Hy1	Gravity-driven facies - Hyperconcentrated density flow *sensu stricto*
Hy1/2	Gravity-driven facies - Hyperconcentrated density flow *sensu lato*
Hy2	Gravity-driven facies - Grain-flow
IMU	Intra-Melke Unconformity
JLM	Jameson, Liverpool Land Margin
Ka/kyr	thousands of years
km	kilometre
KU	Kimmeridgian Unconformity
Ljp	Lateral jump pattern group
LLF/L	Lateral Lobe Fringe
Lp	Lateral pattern group
Lsp	Lateral shift pattern group
m	metre
m/h	metre per hour
Ma/Myr	Millions of years
max.	maximum
MD	Measured Depth
MDL/M	Mid to Distal Lobe
MFS	Maximum Flooding Surface
min.	minimum

MLW	Mean Low Water
mm	millimetre
Mp	Mid pattern group
NL	Netherland
NPD	Norwegian Petroleum Directorate
NR	Nordland Ridge
NTF	Near Top Fangst
O1	Offshore facies 1 - Distal offshore
O2	Offshore facies 2 - Proximal offshore
OE	Outliers Excluded
OM	Organic Matter
PhD	Doctor of Philosophy
Pp	Proximal pattern group
RG	Romain Grime
S	Simple pattern family
S/Sq./Seq.	Stratigraphic Sequence
SB/SBs	Sequence Boundary/Sequence Boundaries
SCS	Swaley Cross-Stratification
SF	Subbasin Flank
SH	Structural High
SL	Structural Low
Sl1	Gravity-driven facies - Slurry flow
Sp	Stacked pattern group
SSDF/ SSDFs	Subaqueous Sedimentary Density Flow/ Subaqueous Sedimentary Density Flows
stk.	stacked
SU/SUs	Seismic Unconformity/ Seismic Unconformities
thk.	thickness
TOC	Total Organic Carbon
T-R	Transgressive-Regressive
Tu1	Gravity-driven facies - Turbidity flow of type 1
Tu2	Gravity-driven facies - Turbidity flow of type 2
Un1	Gravity-driven facies - Undefined flow
VFC	Vingleia Fault Complex
WD	Wave-dominated coasts

CHAPTER I: Introduction

It has been a century since the theory of continental drift (Wegener, 1920) was proposed by the scientist Alfred Wegener. The term “rift” is however *circa* two hundred years old and was first defined as a “major elongate tectonic depression bounded by normal faults” (de Beaumont, 1827, 1830; Gregory, 1896; Olsen, 1995). This definition however, did not venture to provide clarification as the mechanisms for forming these depressions or an explanation for the genesis of continental rifts. Olsen (1995) proposed a new definition for “continental rift”, simply termed “rift”. A continental rift is “an elongate tectonic depression associated in which the entire lithosphere has been modified in extension” (Olsen, 1995). This new definition described the geometry of rifts similarly to the original definition; however, this also defines their mode and the mechanisms for the development of continental rift. It is only since the sixties that the majority of the scientific community has accepted continental drift theory and continental rift mechanisms.

Depositional environments generated during rifting are mainly influenced by allocyclic parameters such as the tectonic activity, however sea-level fluctuations and climate changes also play a role (Gawthorpe et al., 1990). Rift or syn-rift period is defined by intense tectonic activity whereas the post-rift is characterised as a period of tectonic quiescence commonly marked by thermal subsidence (Olsen, 1995). However, both periods are commonly studied separately. To better understand syn-rift to post-rift transition, a multi-disciplinary study that includes sedimentological, biostratigraphy and geophysical analyses has been undertaken, incorporating a significant amount of well, sediment core, biostratigraphic and seismic datasets. This chapter will begin by introducing the conceptual evolution of passive margins through their associated depositional records and the scientific interrogations. The chapter will then take these concepts to focus on the North Atlantic rift with a particular emphasis on the Greenland-Norwegian conjugate margins. The final part of the introduction will present the research objectives, the scope of the study and the methodology employed to achieve its objectives.

1. Overview, from continental margins to rift-related sedimentation

1.1. « Active » vs « Passive » continental margins

Continental margins can be categorised into two types. The “active” continental margins, also known as “Pacific-type” margins, are characterised by a coastal zone within which volcanoes, earthquakes and tectonic displacement are caused by tectonic plate motion (Burk and Drake, 2013). “Active” continental margins are frequently located along convergent plate boundaries. The “Pacific-type” margins are commonly delineated by deep oceanic trenches such as the Peru-Chili trench, (also known as the Atacama trench), on the west side of the South American plate (Fig. 1.1). The Atacama trench reaches depths of up to 8 km, and extends for almost 6.000 km. Coastal depositional environments associated with “Pacific-type” margins are commonly narrow and restricted because the subduction zone implies the presence of trenches where water column increases very rapidly from the coast.

“Passive” continental margins, also known as “Atlantic-type” margins are coastal zones located at the transition of continental crust and oceanic crust which are not located in an active tectonic plate boundary setting (Burk and Drake, 2013). Coastal depositional environments are commonly widely developed in a passive continental margin setting. The “Atlantic-type” margins, as opposed to the “Pacific-type” margins, are generally not associated with intense tectonic activity, volcanism and hot spots (Fig. 1.1). There are however two types of continental passive margins, the “magma-rich” and the “magma-poor” margins.

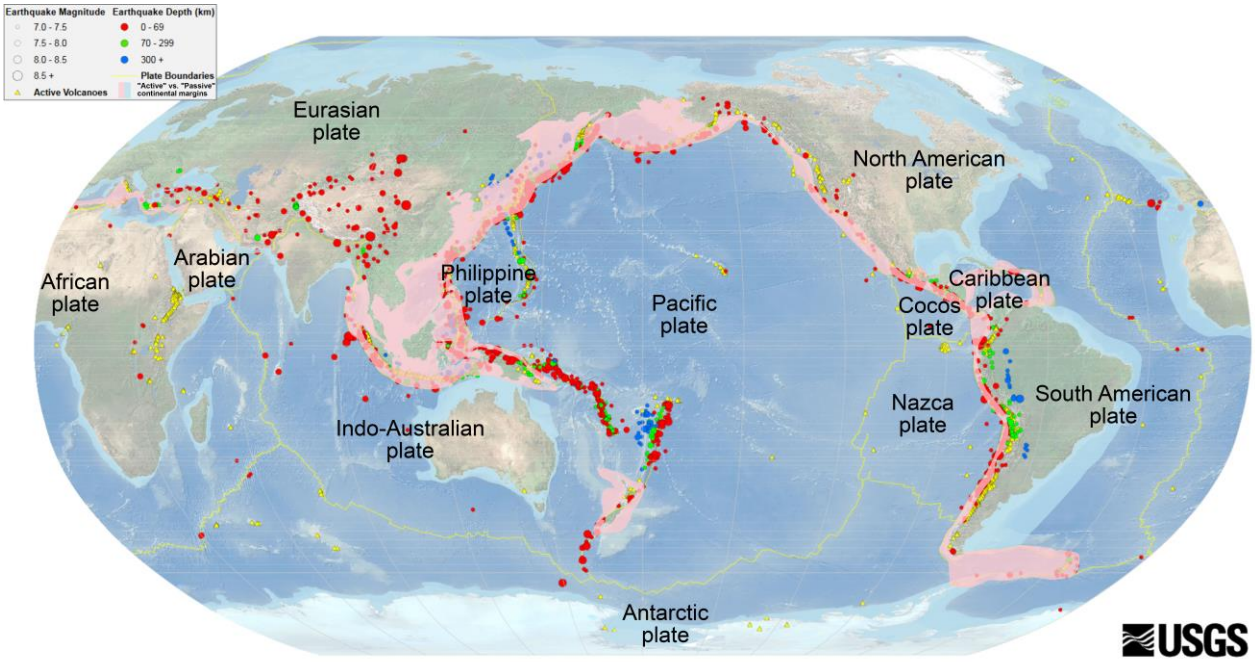

Fig. 1.1: Map showing major tectonic plates, earthquakes (between 1900 and 2013), volcanoes and “active” vs. “passive” continental margins, based on USGS world map (USGS, 2013)

1.1.1. Magma-rich versus magma-poor rifted margins

"Magma-rich" and "magma-poor" margins represent two end-members, leaving a full range of scenarios between those two extremities (Franke, 2013; Peron-Pinvidic and Manatschal, 2019). In "magma-poor" margins, the entire crust spreads before the break-up of the lithospheric mantle, which is a prerequisite for mantle exhumation in such margins (Lister et al., 1991; Franke, 2013). Conversely, in "magma-rich" margins, the breakup of the lithospheric mantle occurs coevally to the crust spreading, or eventually before, thereby producing large volumes of syn-rift volcanic rocks (Planke and Eldholm, 1994; Franke, 2013). In recent years thanks to improvements in modelling techniques and offshore imaging, new observations and a new vocabulary have allowed rifted margins to be analysed in the light of the progressive evolution of the processes at work (Peron-Pinvidic and Manatschal, 2019) (Fig. 1.2).

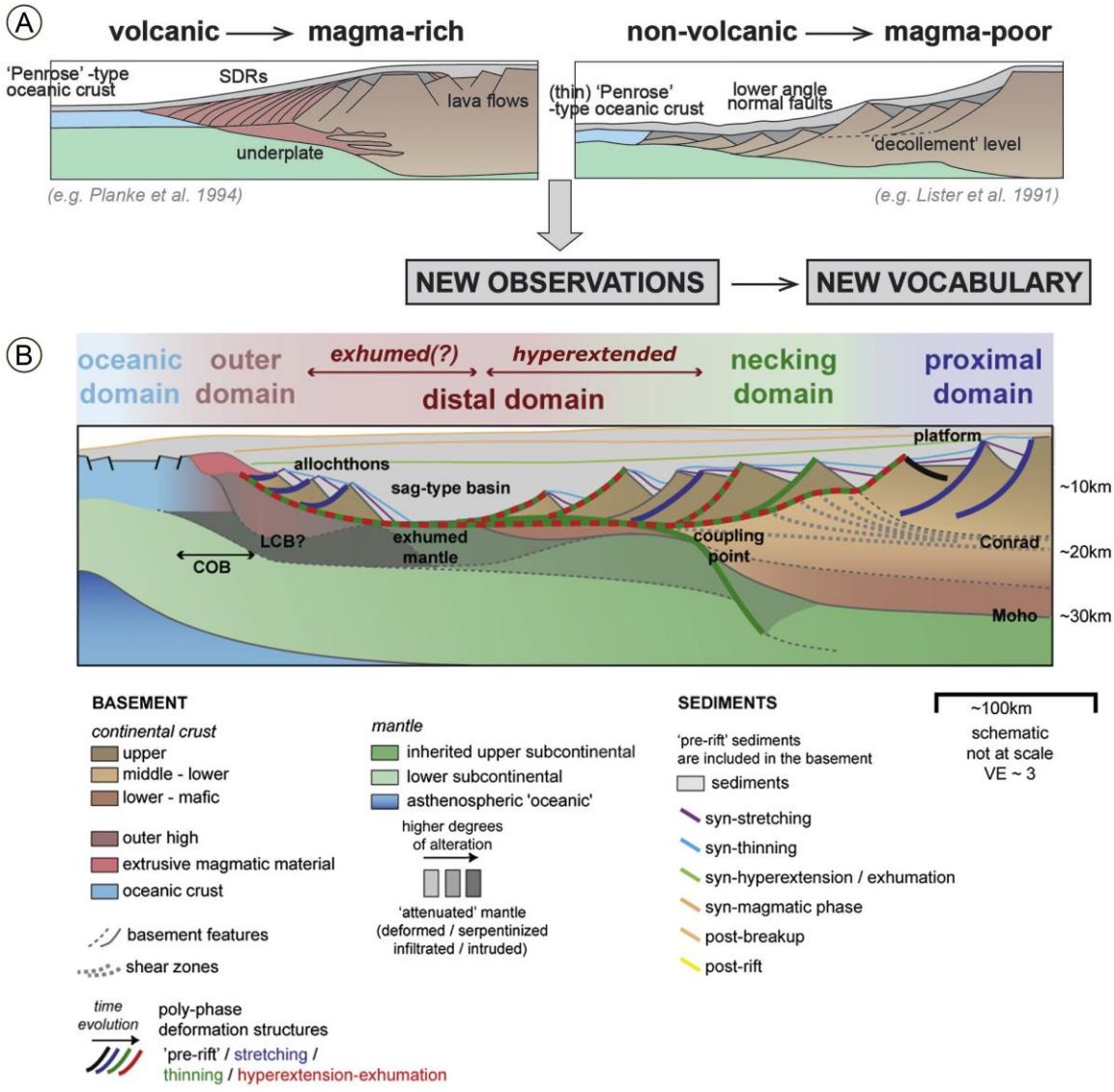

Fig. 1.2: Evolution of concepts regarding rifted margins thanks to the improvement of technology revealing new observations which involved an adjustment of the vocabulary; (A) magma-rich vs magma-poor margins (after Peron-Pinvidic and Manatschal (2019)); (B) Schematic section of a rifted margin with the new terminology (after Peron-Pinvidic et al. (2013))

1.1.2. Rift-induced processes – The case of the "Atlantic-type" rifted margins

The Atlantic rift has been extensively studied with the goal of evaluating rift-induced processes. In the early 1990s, multiphase rifting history was investigated in the North Sea and Norwegian Sea (Bartholomew et al., 1993; Dauteuil and Brun, 1993; Oudmayer and de Jager, 1993). A multiphase rifting is a polyphase deformation of the mantle lithosphere and the crust which lead to the architectural set up of the rift domains (e.g., proximal, necking, distal) during the entire rift history (Naliboff et al., 2017). Multiphase rift systems were then modelled in the late nineties. Laboratory experiments concluded that the first extensional phase significantly controls subsequent rifting phases. Pre-existing structures generated during the first rifting phase will strongly impact later extensional phases (Keep and McClay, 1997). Since the end of the nineties, several "Atlantic-type" rifted margins have been investigated showing polyphase rifting, such as in the Eastern China margin (Lin et al., 2002), the Gulf of Aden margin (Bellahsen et al., 2006), the Iberia-Newfoundland conjugate margins (Péron-Pinvidic and Manatschal, 2009), Angola-Brazil conjugate margins (Unternehr et al., 2010). Since the beginning of the 2010s, the observed multiphase rift history associated with polyphase deformation indicates that "rifting is a localisation process" (Peron-Pinvidic et al., 2013). In other words, the oldest rifting phase configurates the proximal rift domain, whereas the youngest rifting phase is involved in the formation of the distal rift domain (Fig. 1.2B).

As a consensus, rifting has a polyphase history and results from the interaction of mantle and crustal dynamics. Rift-induced processes affect different locations through time (Peron-Pinvidic et al., 2013; Peron-Pinvidic and Manatschal, 2019). According to Peron-Pinvidic and Manatschal (2019), the newly established terminology makes it possible to link geomorphological domains (e.g., platform, terrace, deep) with rift domains (e.g., proximal, necking, distal) and rift-induced processes (e.g., stretching, thinning, hyperextension/exhumation). The platform domain that constitutes the proximal rift domain forms during the stretching phase (Fig. 1.3A). This phase occurs at a regional-scale and develops significant topography (Peron-Pinvidic et al., 2013). The terrace domain that equates to the necking rift domain forms during the thinning phase (Fig. 1.3B). This phase occurs at a local-scale and implies a rise of the mantle and major crustal thinning deformation migrates without the formation of significant topography (Peron-Pinvidic et al., 2013). The deep domain that constitutes the distal rift domain forms during the hyperextension/exhumation phase (Fig. 1.3C). This phase produces progressive basinward migration of the deformation during which sag-type basins develop over the exhumed mantle and/or the hyper-extended crust (Peron-Pinvidic et al., 2013).

The terrace domain is a site of intense rifting activity during the thinning phase. During this phase, the deformation is localised in the necking rift domain where syn-extensional sediments are deposited. In other words, with in the terrace domain, syn-thinning sediments are regarded as syn-rift deposits situated on the hanging wall of extensional faults (Fig. 1.3D). Half-grabens and rotated fault blocks are well-developed in the terrace domain during the syn-rift (syn-thinning) phase. These syn-rift deposits have wedge shape geometries. The syn-stretching deposits, in the terrace domain, can be considered as the pre-rift deposits. In turn, the deformation during the hyperextension/exhumation phase is localised in the deep domain. This last rifting phase can be viewed as post-rift deposits in the terrace domain (Fig. 1.3D). Pre-, syn- and post-rift deposits are commonly separated by major unconformities (Fig. 1.3D).

To summarise the new terminology for the terrace domain:

- the syn-stretching sediments (main deformation localised in the platform domain) are equivalent to pre-rift sediments in the terrace domain;
- the syn-thinning deposits (main deformation localised in the terrace domain) are by consequence identified as syn-rift deposits in the terrace domain;
- the syn-hyperextension/exhumation sedimentation (main deformation localised in the deep domain) are regarded as post-rift sediments in the terrace domain.

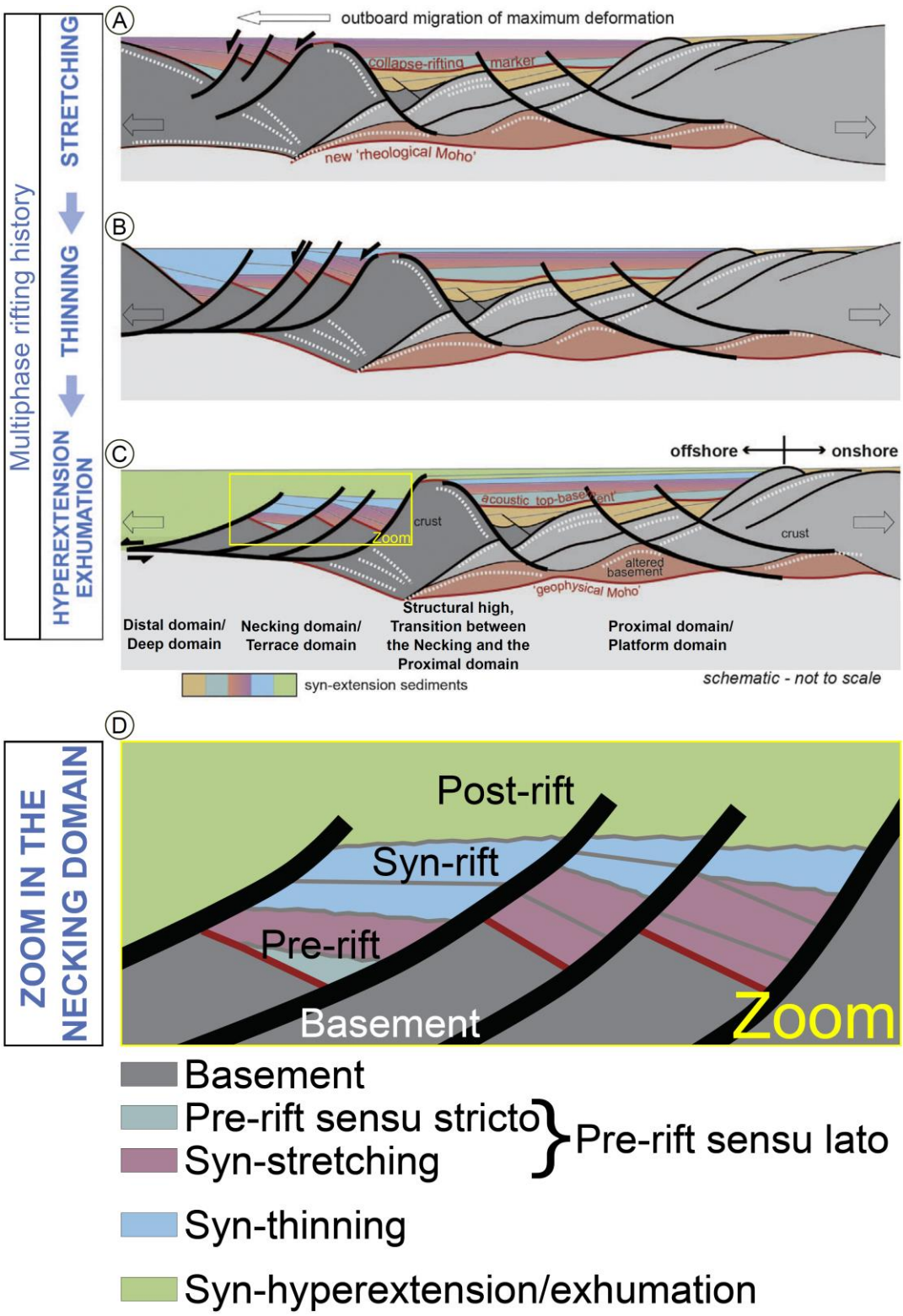

Fig. 1.3: Schematic multiphase rifting history evolution after Peron-Pinvidic et al. (2020); (A) Syn-stretching; (B) Syn-thinning; (C) Syn-hyperextension/exhumation; and (D) Zoom in the necking rift domain using a simplified terminology

The conceptual model of Ravnås and Steel (1998), enables the subdivision of the syn-rift period into three sub-stages based on fault related processes. The rift initiation stage, also known as the “early” or “initial” rift stage corresponds to an increased rate of fault-related subsidence and the initiation of fault propagation and fault linkage (Folkestad et al., 2014). The rift-climax stage, also known as the “main” or “peak” rift stage, corresponds to a high rate of fault-related subsidence. The degree of fault linkage is at its peak during this stage. The climax-rift stage is marked by the development of rotated fault blocks. The final rift-stage, also named the “late” or “transition to post-rift” is characterised by a waning in the rate of fault related subsidence and a decrease in tilt-rates (Ravnås and Steel, 1998; Folkestad et al., 2014). This final stage is also marked by a progressive cessation of fault activity; hence the post-rift corresponds to a period of tectonic quiescence. This conceptual model that permits the subdivision of the syn-rift phase into three sub-stages (rift initiation, rift-climax and final rift) is being commonly used in recent researches (Jones et al., 2020; Salomon et al., 2021; Würtzen et al., 2021).

1.2. Sedimentary successions in rift basins

1.2.1. Depositional environments

Sedimentary environments developed during the rifting period exhibit a large diversity, ranging between continental, lacustrine to marine settings. Marine sediments can be subdivided into shallow-marine and deep-marine rift deposits. These deposits can be further divided into three sub-categories based on the type of sedimentation. Rift-related deposits are usually dominated by siliciclastic (Fig. 1.4A), carbonate deposits (Fig. 1.4B) or both in mixed carbonate-siliciclastic deposits (Fig. 1.4C). However, whether they are siliciclastic, carbonate or mixed deposits in essence, gravity-driven deposits are generated by the intense tectonic activity typical of the rifting phase. Coevally with gravity-driven deposits, coastal depositional environments develop along more stabilised marginal highs (Fig. 1.4).

The conjoint development of coastal and gravity-driven deposits is characteristic of the shallow-marine rift setting (Jones et al., 2020; Cumberpatch et al., 2021; Masiero et al., 2021). Conversely, during the post-rift period, in the terrace domain, extensional motions have mostly ceased, and basins are filled and largely controlled by thermal subsidence (Copestake et al., 2003; Lohr and Underhill, 2015). Tectonic quiescence, thermal subsidence, which in some cases are combined with sea-level rise can lead to the drowning of rift basins which are finally filled with thick offshore marine mudstone deposits and potentially associated with deep-water turbidites (Dam and Sønderholm, 2021; Privat et al., 2021).

During the syn-rift period when fault displacement is maximum, fault-related gravity-driven deposits are commonly associated with coarse-grained deltaic environments. Such deltas are commonly of Gilbert-type along steep fault scarps (Gilbert, 1885; Gawthorpe et al., 1990). Gilbert type deltas are in a steady state meaning that if the deltas are properly fed, it can last through time and space. Conversely, and in an unsteady state, coarse-grained deltas correspond to conical deltas (Nemec, 1990a). Those two subaqueous coarse-grained deltas (conical and Gilbert-type) are conjointly formed with wave-dominated coastal environments (Longhitano and Steel, 2016; Martinius, 2017; Rees et al., 2017). Commonly, conical deltas

(CD), may evolve into wave-dominated (WD) coastal deposits or into Gilbert-type deltas (GD) (Fig. 1.5). In particular, the evolution from conical deltas to Gilbert-type deltas generally occurs if fault scarps become steepened and generate significant volumes of gravity-driven deposits (Chiarella et al., 2021).

Coarse-grained deltas can be further subdivided into two main sub-environments, the delta front (foreset) referring to the proximal sloping portion of the delta, whereas the prodelta (bottomset) corresponding to the more gentler sloping distal part of the delta. With regard to wave-dominated coastal deposits, the coasts are commonly narrow during the syn-rift period and progressively pass from distal to proximal deposits or vice-versa. The post-rift thermal subsidence, which is linked to the cooling of the crust, and associated with the cessation of fault activity, leads to the development, in some rift-basins, of thick offshore marine mudstone deposits (McKenzie, 1978; Privat et al., 2021) developed coevally with deep-water turbidite lobe complexes (Prélat et al., 2009; Mulder and Etienne, 2010). The lobe environment can be subdivided along its axial axis, with the proximal, medial and distal part and along its lateral axis with axial, off-axial and fringe settings (Hodgson, 2009).

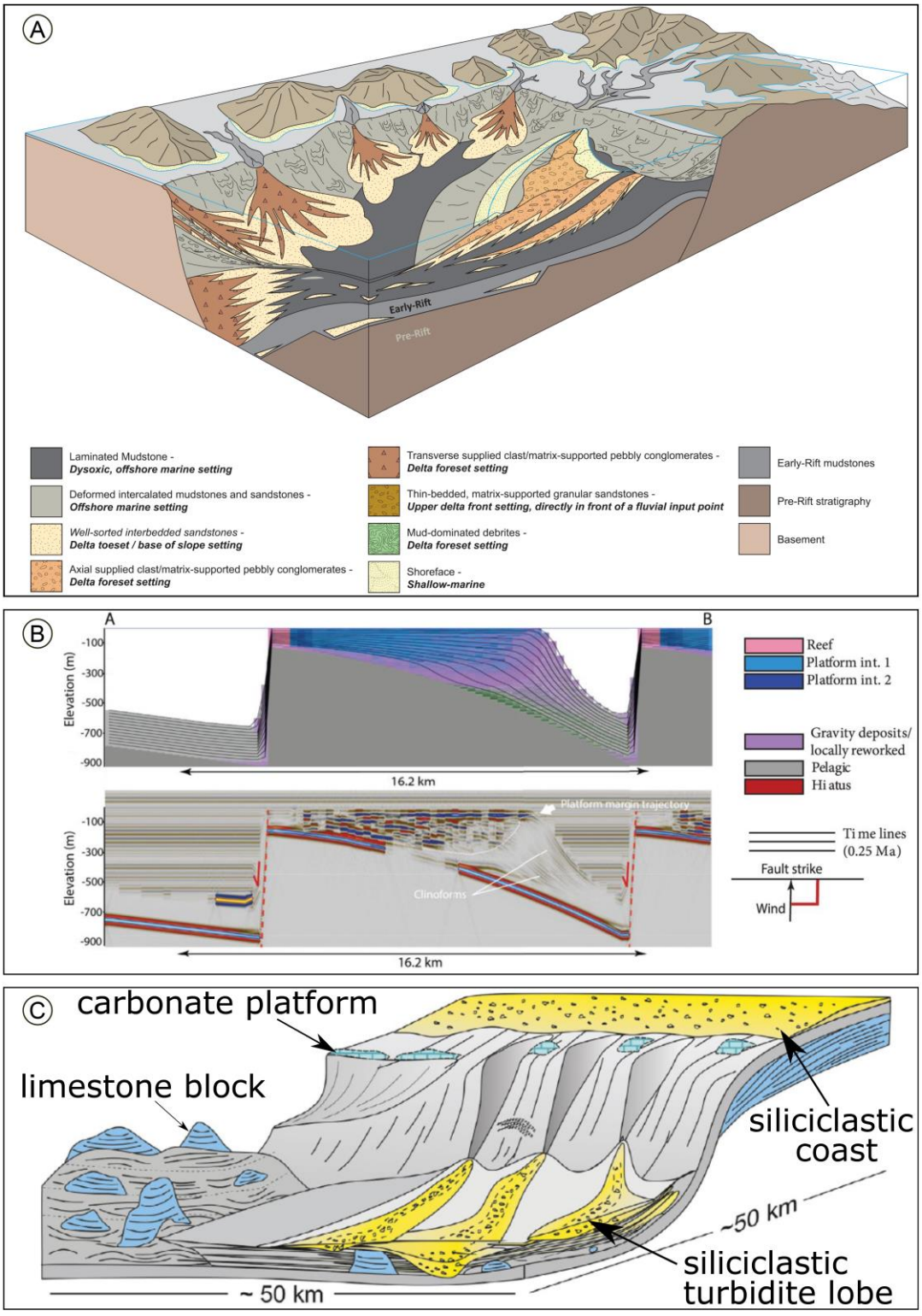

Fig. 1.4: Marine rift-related depositional environments; (A) dominated by siliciclastic sedimentation (after Jones et al. (2020)); (B) dominated by carbonate sedimentation (after Masiero et al. (2021)); and (C) mixed carbonate-siliciclastic sedimentation (after (Cumberpatch et al., 2021)).

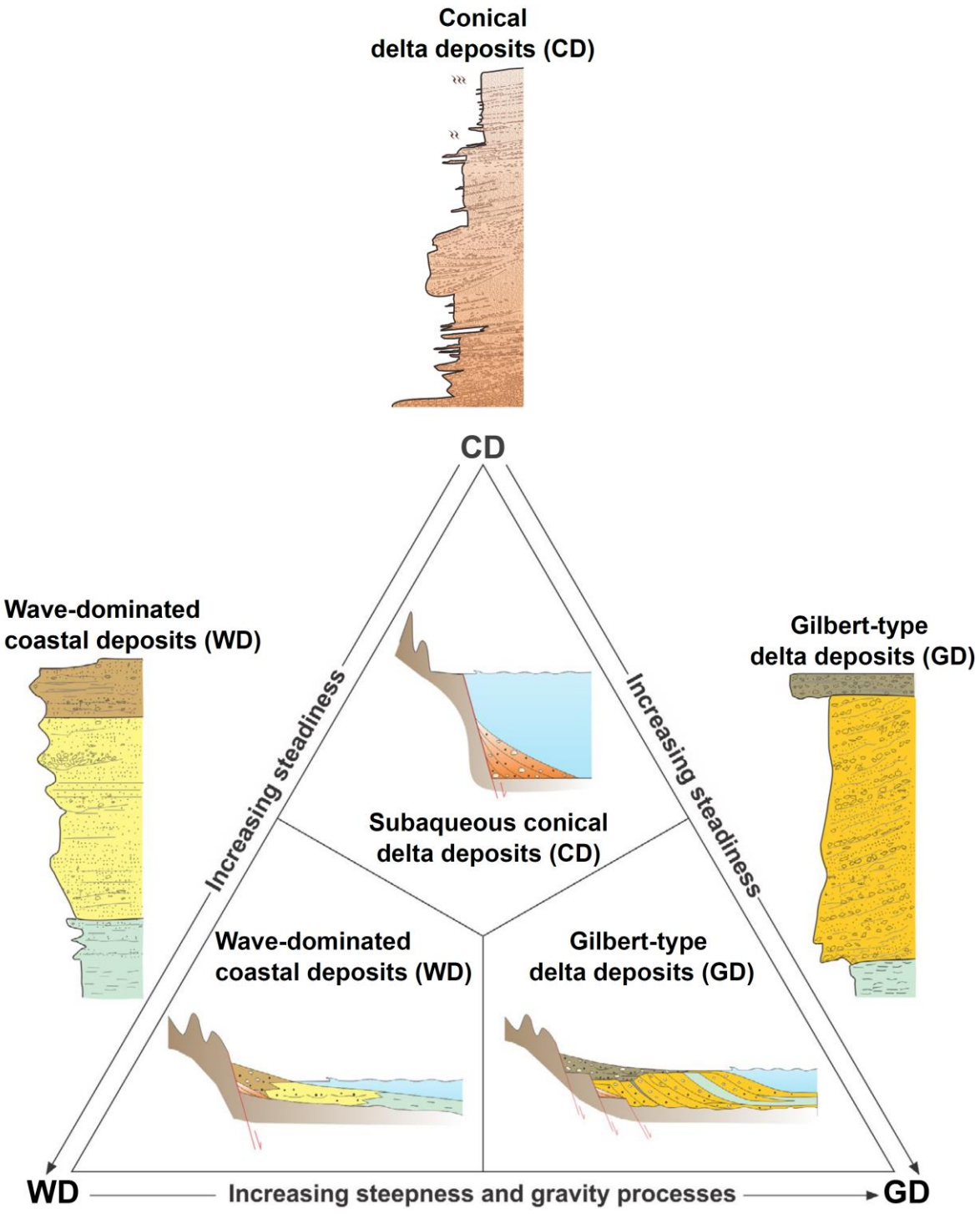

Fig. 1.5: Schematic diagram of siliciclastic shallow-marine environments which are fault-controlled and related to scarp steepness and system steadiness (modified after Chiarella et al. (2021))

1.2.2. Sedimentary successions

1.2.2.1. Wave-dominated coastal deposits

Coarse-grained deltas are conjointly deposited with coarse-grained beaches (Fig. 1.6). Beaches are commonly influenced by wave action (Bardaji et al., 1990; Reading, 2009). Sub-coastal depositional environments are characterised by a combination of sedimentary structures, type and degree of bioturbation and grain-size, sorting etc. The most distal environment corresponds to a structureless highly bioturbated marine offshore mudstone. This distal to intermediate mudstone, with the occurrence of the Zoophycos or Nereites ichnofacies (Fig. 1.7) (Walker, 1992; Pemberton et al., 2012).

The proximal offshore, also named “offshore transition” is composed of the same distal mudstone but includes sand- to silt-rich laminae interpreted as wave-generated structures (de Raaf et al., 1977). This zone is interpreted to be located between the storm- and the fair-weather wave bases (Bardaji et al., 1990; Reading, 2009). The proximal offshore is characterised by the Cruziana ichnofacies (Fig. 1.7), such as in the lower part of the lower shoreface (Pemberton et al., 2012).

The lower shoreface is characterised by fine to very fine-grained sandstone (Fig. 1.6) angular to planar laminations, small-scale cross-laminations and curved to undulating laminations (de Raaf et al., 1977). The lower shoreface is interpreted to be deposited above the fair-weather wave base (FWWB) and is characterised at the base by the Cruziana ichnofacies and at the top by Skolithos ichnofacies (Dashtgard et al., 2021) (Figs. 1.6, 1.7).

The middle shoreface consists of fine- to medium-grained sandstone with the presence of swaley cross-stratification (SCS) and hummocky cross-stratification (HCS) at a larger scale than the lower shoreface. The middle shoreface is interpreted to be located between the fair-weather wave base and the mean low water (MLW) corresponding to the breaker zone (Fig. 1.6). The middle shoreface is characterised by Skolithos ichnofacies (Fig. 1.7).

The upper shoreface typified by the Skolithos ichnofacies exhibits a decrease in the degree of bioturbation (Fig. 1.7). The upper shoreface consists of medium- to coarse-grained sandstone with horizontal to sub-horizontal plane-parallel laminations and large-scale SCS. Erosional surfaces or sharp contact can be observed (Fig. 1.6). The upper shoreface is located in the surf zone (Reading, 2009; Dashtgard et al., 2021) (Fig. 1.6).

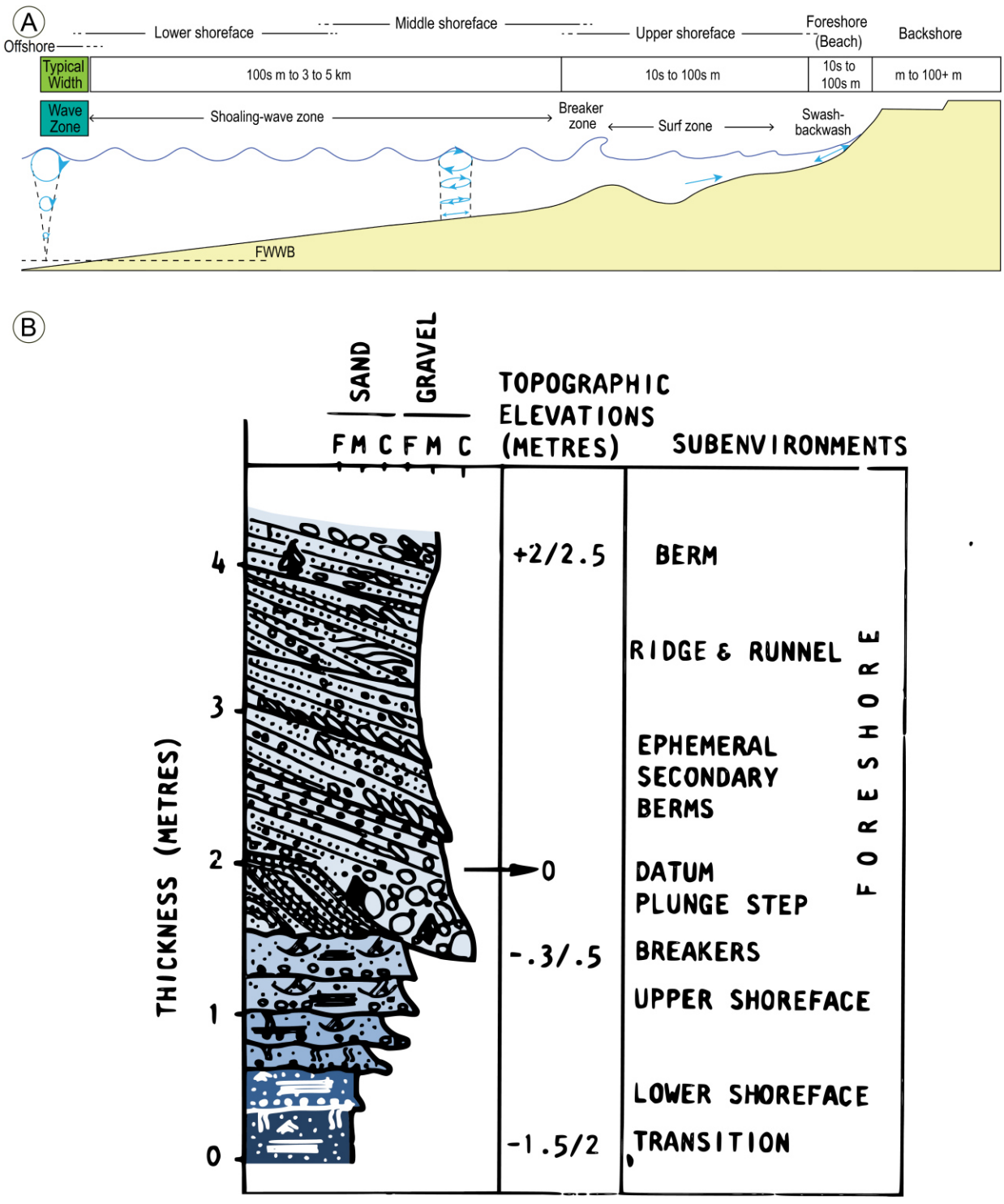

Fig. 1.6: Wave-dominated coastal environments with (A) idealised profile (after Dashtgard et al. (2021)), and (B) synthetic sedimentary logs (recolorised after Bardaji et al. (1990))

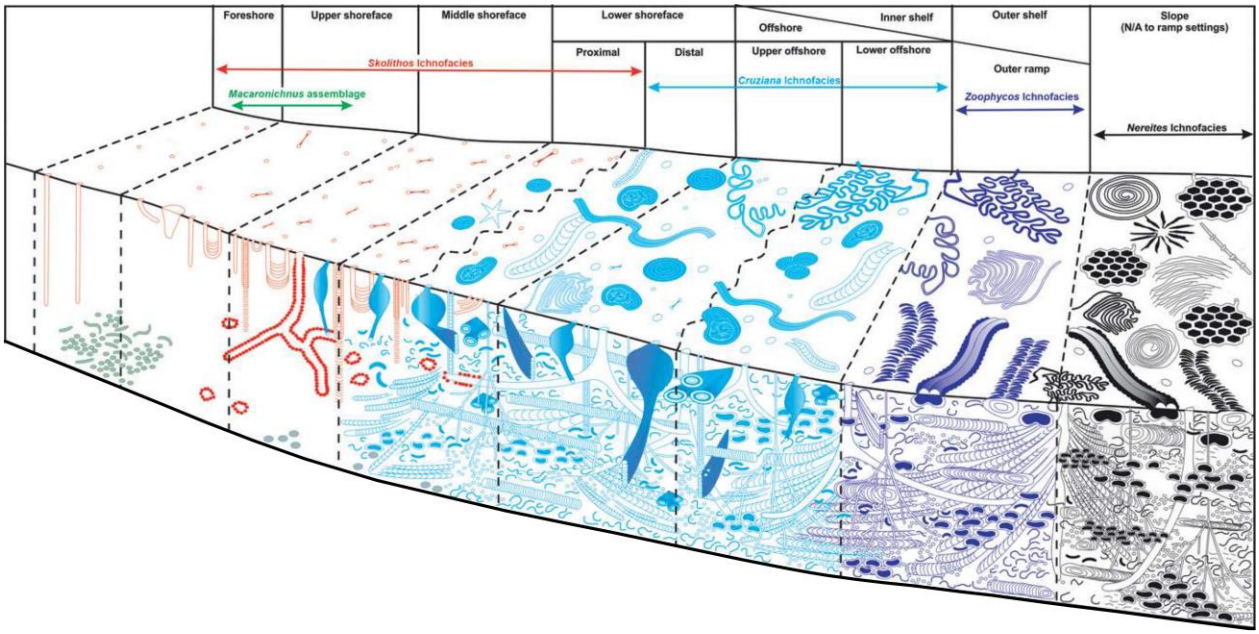

Fig. 1.7: Schematic diagram of marine ichnofacies (Diagram adapted from Seilacher (1967), modified after (MacEachern et al., 2008) and Pemberton et al. (2012))

The foreshore environment is located between the mean low water (MLW) and the wave-built storm ridge corresponding to the swash-backwash zone (Bardaji et al., 1990; Otvos, 2000; Reading, 2009; Hayes et al., 2010) (Fig. 1.6). Commonly the foreshore consists of coarse-grained sandstone with the presence of granule- and pebble-rich layers and seaward-inclined parallel laminations (Fig. 1.6). The degree of bioturbation is very low and, if burrows are observed, they most often correspond to the Skolithos ichnotaxon (Fig. 1.7).

The backshore is located above the berm up to the aeolian dunes and consists of a medium- to coarse-grained sandstone with the presence of plane parallel laminations, steep dipping foreset beds, and commonly composed of roots and plant debris, with no bioturbation (Brenninkmeyer, 1982).

The succession of the coastal sub-environments exhibits a progressive evolution of the type and degree of bioturbation, grain-size and sedimentary structures between distal offshore marine mudstones and wave-induced coarse-grained berm ridges (Reading, 2009).

1.2.2.2. Coarse-grained deltaic deposits

The proximal part of the delta front of coarse-grained deltas is conglomeratic, whereas the distal part of the prodelta consists of well-sorted fine-grained sandstones to siltstones. Flow transformations operate in the foresets and the bottomsets of deltas and highlight a continuum between density flows. Based on Mulder and Alexander (2001)'s classification, the gravity-driven deposits, also termed subaqueous sedimentary density flow (SSDF) deposits are classified based on grain-support mechanisms, sediment concentration and physical flow properties (Fig. 1.8). Two main families of flow can be identified: cohesive flows (Fisher, 1971; Hampton, 1972) and non-cohesive flows (Kuenen, 1966; Middleton, 1967).

Cohesive flows have a pseudoplastic rheology due to a significant amount of mud that is acting as a cohesive material. Debris flow is a type of cohesive flow that has a low friction number and a laminar flow regime (Mulder and Alexander, 2001). The main grain-support mechanism of the debris flow is the “matrix strength” that provides cohesion between the muddy matrix and the sedimentary particles (Fig. 1.8) However, pore pressure and buoyancy are also important, whereas grain-to-grain interaction and liquefaction may be locally significant (Major and Iverson, 1999).

Non-cohesive flows do not have sufficient cohesive material to have “matrix strength” as the dominant grain-support mechanism. According to the Mulder and Alexander (2001)’s classification, non-cohesive density flows can be divided into three flow types: hyperconcentrated density flows, concentrated density flows and turbidity flows. The main grain-support mechanism for hyperconcentrated density flows is the grain-to-grain interaction (Fig. 1.8). The deposition of the hyperconcentrated density flows is caused by frictional freezing. Two subclasses of hyperconcentrated density flows can be identified, the hyperconcentrated density flow *sensu stricto* and the grain-flow. The latter occurs when fluids play a minor role, while major interactions correspond to grain-to-bed collisions and grain-to-grain interactions (Jaeger et al., 1996; Mulder and Alexander, 2001).

The concentrated density flow deposits corresponding to Lowe sequences (Lowe, 1982), and are mainly dominated by grain-to-grain support mechanisms (Fig. 1.8). Grain collision interaction and water entrainment of these more diluted flows (compared to hyperconcentrated density flows), make the flows behave as Newtonian fluids (Lowe, 1982). Commonly, the upper part of the concentrated density flow is entirely turbulent (Mulder and Alexander, 2001).

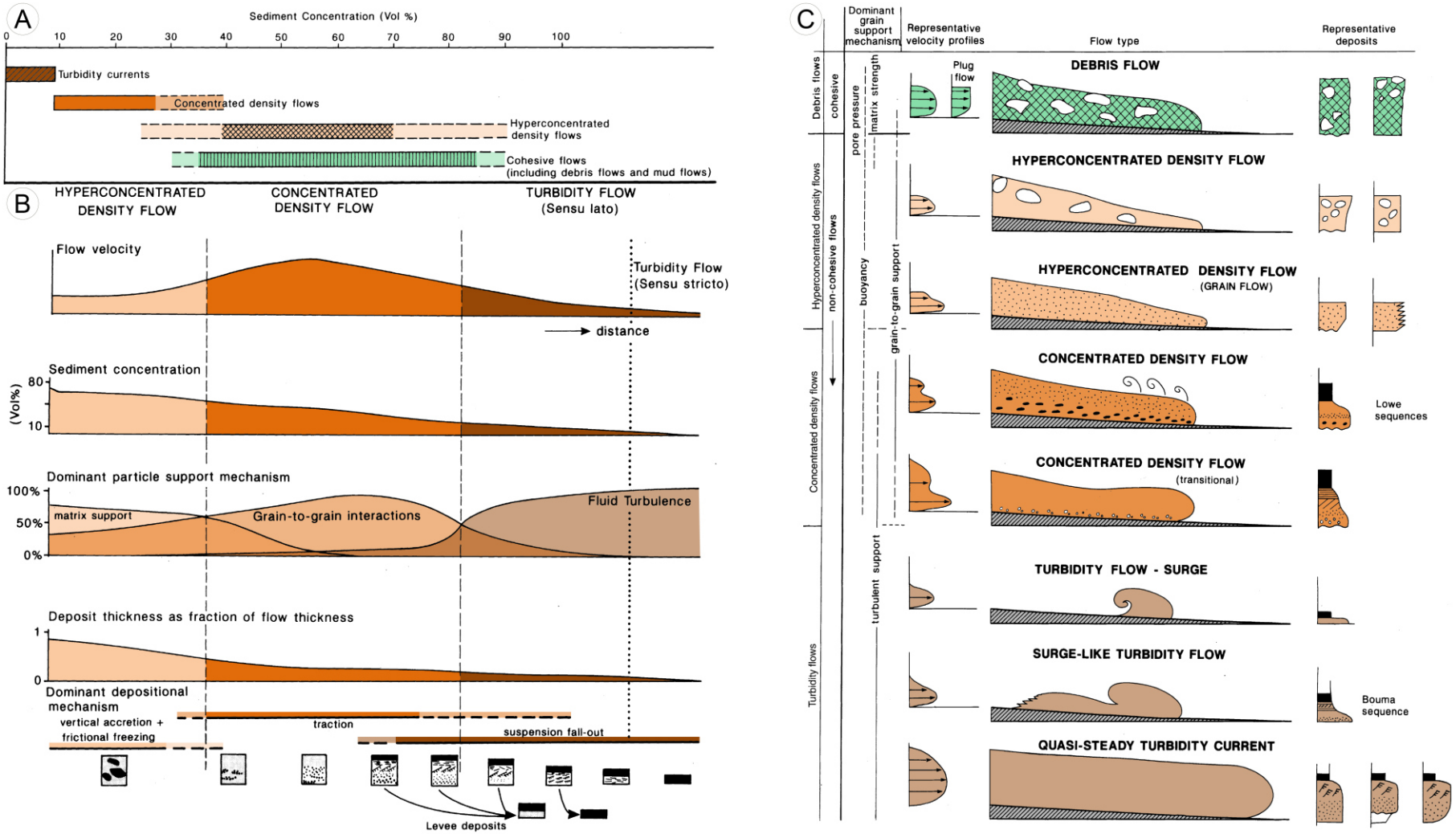

Fig. 1.8: Subaqueous sedimentary density flow (SSDF); with (A) flow type terminology based on sediment concentration; (B) schematic definition diagram; and (C) transformation diagram (recolorised after Mulder and Alexander (2001))

The turbidity flows are mainly controlled by turbulent grain-support mechanisms (Fig. 1.8). Turbidity flow deposits consist of the terms described by (Bouma, 1962). According to the Mulder and Alexander (2001)'s classification, most turbidity currents are not able to transport clasts larger than coarse sands, which therefore marks the threshold separating turbidity flows from concentrated density flows.

In coarse-grained deltas, foresets with high angle slope are mainly formed by hyperconcentrated density flow and concentrated density flow deposits, whereas the gentle slope gradient of the bottomsets is mainly composed of concentrated density flow and turbidity flow deposits. Based on the mud content delivered by the sediment source, debris flow deposits may be deposited both in the delta front and prodelta (Longhitano et al., 2021).

According to the Mulder and Alexander (2001)'s classification, there is a continuum between SSDFs. Hyperconcentrated density flows (*sensu lato*) evolve into concentrated density flows which evolve themselves into turbidity flows (Fig. 1.8). A continuum from non-cohesive flows and cohesive flows is also frequently observable. Hyperconcentrated, concentrated density, and turbidity flows are all subjected evolve into debris flows depending on mixing and dilution (Hampton, 1972), entrainment at the top of the SSDF sediment body (Fisher, 1983), hydraulic jumps (Weirich, 1988), or a combination of those mechanisms (Fisher, 1983).

1.2.2.3. Deep-water turbidite deposits

In deep-water turbidite lobe complexes, turbidity flow deposits commonly progress into debris flows (Lowe and Guy, 2000; Haughton et al., 2003, 2009). This sedimentary succession is composed at the base of turbidity flow deposits and at the top of debris flow deposits, and is commonly termed "linked debrites" (*sensu* Haughton et al. (2003)) or hybrid event beds (HEBs) (*sensu* Haughton et al. (2009)). HEBs are characterised at the base by signatures of turbulent flows evolving to transitional flows termed slurry-flows (*sensu* Lowe and Guy (2000)), then to debris flows (Fig. 1.9A), and then in some cases back to fine- to very fine-grained turbidity flows (Fig. 1.9B).

The deep-water turbidite lobe environment can be further subdivided into axial and off-axial sub-environments. The most proximal lobe sub-environment, the inner-fan (*sensu* Fonnesu et al. (2018)), is located near the lobe apex, on the slope break (Fugelli and Olsen, 2007). According to Fonnesu et al. (2018), the sedimentary succession in the inner-fans is mainly composed of hyperconcentrated to concentrated density flow deposits (*sensu* Mulder and Alexander (2001)). No HEBs are present in the inner fan.

The mid-fan is composed of HEBs with thick turbidity flow and slurry flow deposits (Fig. 1.9A), whereas the fan fringe (*sensu* Haughton et al. (2003)) also termed frontal lobe fringe (*sensu* Spychala et al. (2017b)) is composed of HEBs dominated by debris flow deposits, which are capped by fine- to very fine-grained turbidity flow deposits (Fig. 1.9B).

The continuum between flows between the mid-fan and the fan fringe (Fig. 1.9C) highlights several processes such as water injection, overpressure implying typical sedimentary structures (dish structures, flame structures, etc.) in the HEBs (Fig. 1.9D). According to Spychala et al. (2017b), the axial frontal lobe fringe can be distinguished from the off-axial lateral lobe fringe. Off-axial lateral lobe fringes are mainly composed of turbidity flow deposits having a thickness less than 2 cm, with very rare HEBs (Spychala et al., 2017b).

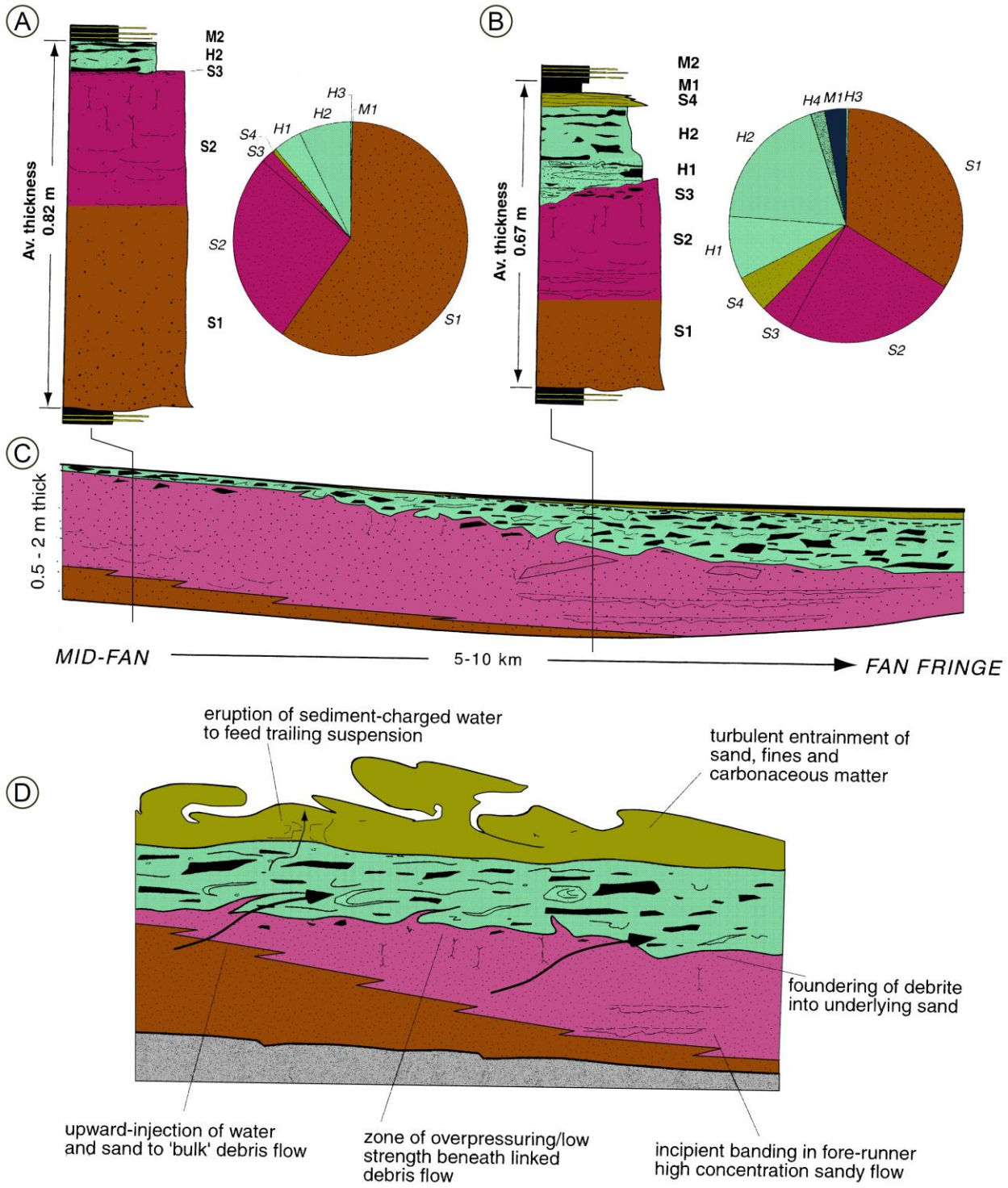

Fig. 1.9: Hybrid event beds (HEBs); with (A) synthetic sedimentary log located in mid-fan; (B) synthetic sedimentary log located in fan fringe; (C) geological cartoon illustrating facies evolution from mid-fan to fan fringe; and (D) processes and mechanisms showing the formation of HEBs (recolorised after Haughton et al. (2003))

1.3. Rift-related scientific interrogations

Rift basins and more precisely siliciclastic rift basins such as in Greenland, North Sea, Corinth, Suez, East Africa, etc. have been studied intensively since the 1990s (Gawthorpe et al., 1990; Scholz et al., 1990; Gupta et al., 1999; Colella and Prior, 2009; Turner and Cronin, 2018; Barrett et al., 2020). Most of existing siliciclastic rift basins studies have highlighted the link between tectonic and sedimentary architecture (Gawthorpe et al., 1990; Gupta et al., 1999). Other works focus on well log data and biostratigraphic analysis to precisely dated syn-rift stratigraphic successions (Verreussel et al., 2018; Higgs et al., 2020). Post-rift stratigraphic intervals are commonly of second interest because mainly composed of deep-marine mudstones (Vergara et al., 2001; Privat et al., 2021). The drowning of the syn-rift stratigraphic succession is commonly due to differential subsidence between syn-rift and post-rift phases. However, mudstone-dominated post-rift successions enclose some sand-dominated deep-water turbidites (Shanmugam et al., 1994; Vergara et al., 2001; Privat et al., 2021).

Syn-rift and post-rift stratigraphic successions are commonly studied independently. However, the syn-rift to post-rift transition is key in understanding multiphase rift history. Syn- to post-rift transition in the terrace domain provides pieces of evidence of the migration of the deformation from the necking domain (terrace domain) to the distal domain (deep domain) (Peron-Pinvidic et al., 2013; Peron-Pinvidic and Manatschal, 2019). However, (i) how do the depositional records reflect the syn-rift to post-rift transition? (ii) Is this transition abrupt, meaning a sudden cessation of fault activity? (iii) How precisely syn-rift coarse-grained successions can be dated when stratigraphic intervals are hindrance by reworked fossils? (iv) How do we explain the development of deep-water turbidites during the post-rift period? (v) the tectonic seems to be the main driver during syn- to post-rift transition, however, how are the impact of climate change and sea-level fluctuation?

In the goal to provide some pieces of evidence and replies to these rift-related fundamental questions, we have decided to choose the Norwegian Sea as a study case. The Norwegian Sea is a good candidate for several reasons: (i) the zone is rich in data (well-log, sediment core, biostratigraphic, and seismic data); (ii) the multiphase rift history of the Norwegian Sea continental margin is linked to the Atlantic rift, this latter one is well documented; (iii) the conjugate rift margin of the Norwegian Sea, the NE Greenland presents outcrops and time equivalent depositions. To reply to the previously mentioned interrogations, the database needs to be treated from a very local scale and integrated at a basin scale. For this, multi-disciplinary approaches (e.g., sedimentology, sequence stratigraphy, biostratigraphy) such as multi-scale analyses (e.g., local, semi-regional, basin) will be performed to find evidence throughout detailed core analysis, reappraised biostratigraphic charts, local to basin-scale well correlations and seismic interpretations.

2. From the Atlantic rifting to the Greenland-Norwegian conjugate margins

2.1. The Atlantic rift

The Atlantic Ocean has been subdivided into segments based on the timing of the continental breakup and onset of seafloor spreading that is directly linked to its multiphase rift history. The continental breakup of the Atlantic was diachronous. The first breakup occurred in the Central Atlantic segment during the Early Jurassic, followed by the breakup of South Atlantic segment, then the breakup of the Southern North Atlantic, followed by the Equatorial Atlantic segment (Fig. 1.10). These last three segments had their continental breakup during the Early Cretaceous (Müller et al., 2008; Mercier de Lépinay et al., 2016). The Southern South Atlantic segment breakup took place during the Late Cretaceous, and the Northern North Atlantic segment breakup occurred during the Palaeocene (Fig. 1.10) (Müller et al., 2008; Mercier de Lépinay et al., 2016).

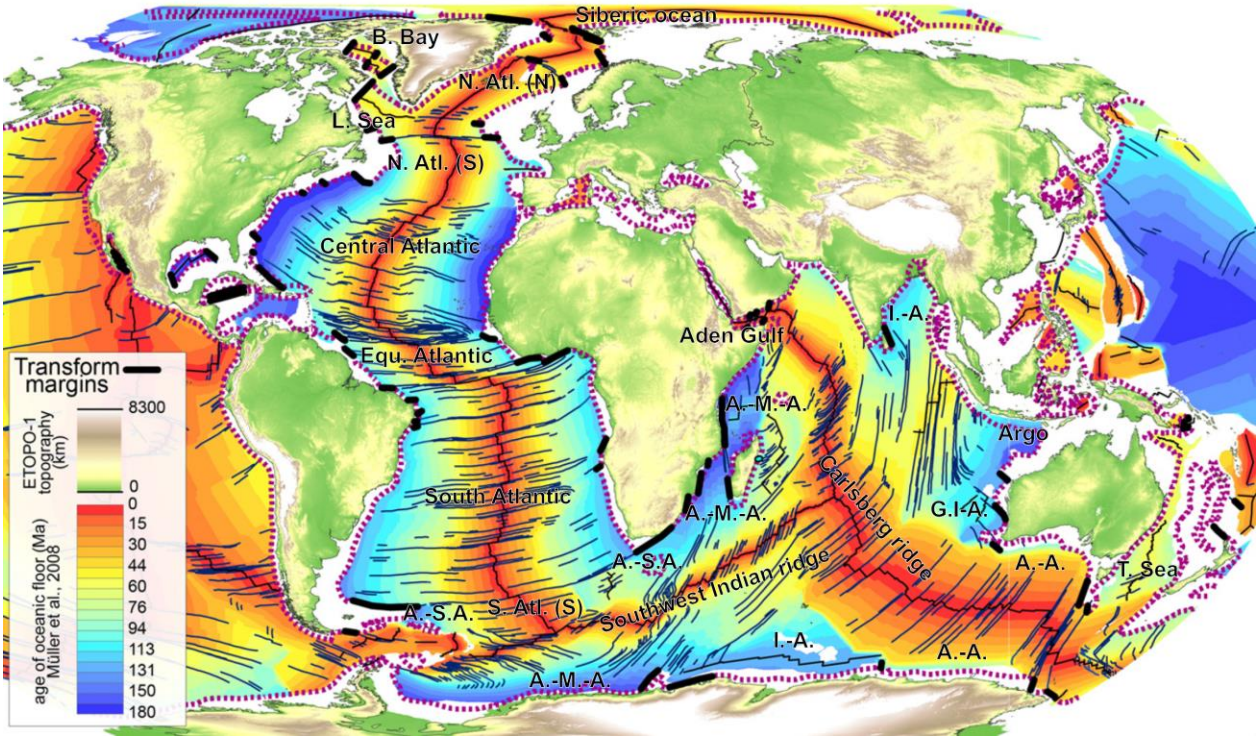

Fig. 1.10: Transform margin locations over the world with the ocean floor age (after Müller et al. (2008)), oceanic fracture zones (after Matthews et al. (2011)) and the major oceanic domains/segments (after Mercier de Lépinay et al. (2016) and Exxon World Mapping Project (1985)). Abbreviations for the oceanic domains: B. Bay = Baffin Bay; L. Sea = Labrador Sea; N. Atl. (N) = Northern North Atlantic; N. Atl. (S)=Southern North Atlantic; Equ. Atlantic = Equatorial Atlantic; A.-S.-A. = Africa-South America; A.-M.-A. = Africa-Madagascar-Antarctic; I.-A. = India-Antarctic; A.-A. = Australia-Antarctic; G.I.-A. = Greater India-Australia; Argo = Argo abyssal plain; T. Sea = Tasman Sea.

The drifting that chronologically succeeds the rifting is the period of oceanisation and seafloor spreading (Pollitz, 1999). According to Peron-Pinvidic et al. (2013), the South Atlantic

segment may have started its initial rifting phase (stretching phase) during the Upper Triassic and most probably ended at the Jurassic-Cretaceous boundary (Fig. 1.11). The 2nd rifting phase corresponding to the thinning phase probably started during the earliest Cretaceous and ended during the Early Cretaceous, followed by the 3rd rift phase, the hyperextension/exhumation phase followed the thinning phase and ended during the Early Cretaceous. In the South Atlantic segment, drifting started during the Early Cretaceous (Müller et al., 2008; Peron-Pinvidic et al., 2013; Mercier de Lépinay et al., 2016).

In the Equatorial Atlantic segment, the first rifting phase (stretching) started during the Late Triassic and ended during the Early Jurassic (Crawford et al., 1984; Loparev et al., 2021). The second rifting phase (thinning) occurred during the Middle Jurassic to the earliest Cretaceous (Crawford et al., 1984), and the third phase (hyperextension/exhumation) most probably happened during the earliest Cretaceous and ended during the Early Cretaceous (Fig. 1.11). In this segment, the drifting (oceanisation and seafloor spreading) started after the last rift phase, during the Early Cretaceous (Müller et al., 2008; Mercier de Lépinay et al., 2016; Loparev et al., 2021).

In the Central Atlantic, the polyphase rift history is difficult to analyse due to the short duration of the rift period, which complicates the subdivision of the three rift phases (Fig. 1.11). However, the stretching phase (1st rifting phase) started during the Earliest Triassic and the hyperextension/exhumation (3rd rifting phase) ended during the Early Jurassic (Piqué and Laville, 1996; le Roy and Piqué, 2001). The drifting (oceanisation and seafloor spreading) started during the EarlyJurassic in the Central Atlantic segment (Müller et al., 2008; Mercier de Lépinay et al., 2016).

In the Southern North Atlantic segment, at the boundary between the Central Atlantic segment and the Southern North Atlantic segment, the Iberia-Newfoundland conjugate margins reveal an initial rifting phase (stretching) started during the Early Triassic and ended during the Middle Jurassic (Fig. 1.11). The second rifting phase (thinning) started during Middle Jurassic and ended during the Early Cretaceous. In the Southern North Atlantic segment, the 3rd rifting phase (hyperextension/exhumation) and the drifting phase (oceanisation and seafloor spreading) occurred consecutively during the Early Cretaceous (Müller et al., 2008; Peron-Pinvidic et al., 2013; Mercier de Lépinay et al., 2016).

In the Northern North Atlantic segment, the mid-Norwegian, Jan Mayen and mid-East Greenland conjugate system, stretching (first rifting phase) was initiated during the Carboniferous-Permian and lasted until the Middle Jurassic (Jongepier et al., 1996; Brekke, 2000). The thinning phase (second rifting phase) started during the Middle Jurassic and ended during the earliest Cretaceous (Osmundsen et al., 2002; Faleide et al., 2008; Tsikalas et al., 2012). The hyperextension/exhumation phase (3rd rifting phase) started during the earliest Cretaceous (Osmundsen and Ebbing, 2008; Peron-Pinvidic and Osmundsen, 2018) with the development of sag-type basins (Fig. 1.11). The oceanisation and seafloor spreading (drifting phase) started during the latest Cretaceous/earliest Palaeocene (Müller et al., 2008; Peron-Pinvidic et al., 2013; Mercier de Lépinay et al., 2016).

From all these observations, the first rifting phase seems to be initiated in the Northern North Atlantic segment and then was propagated toward the South Atlantic segment (Blue arrow on

Fig. 1.11). The Central Atlantic segment where it is difficult to separate the 3 rifting phases, appears to be where the thinning first took place and then propagated towards the South and North (Green arrow on Fig. 1.11). The Hyperextension/exhumation also started from the Central Atlantic segment and propagated concurrently southward and northward (Red arrow on Fig. 1.11). Drifting started again from the Central Atlantic segment and propagated toward the South and North at different times. Note that the duration of the rift and drift phases varies from one segment to another. The duration of the different tectonic phases appears to increase outwards away from the Central Atlantic segment. The duration of the thinning phase however, was similar for each of the segments except the Central Atlantic segment.

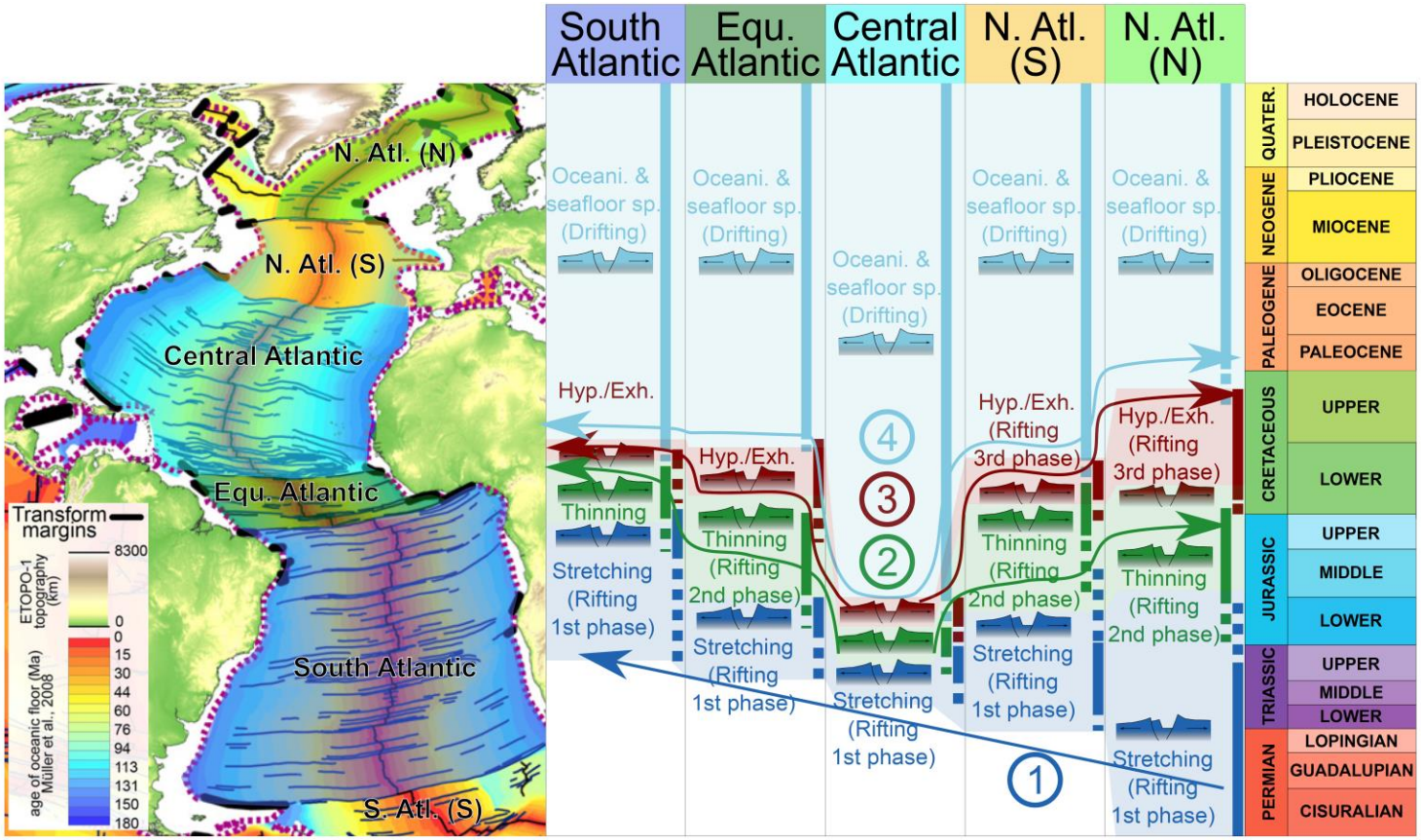

Fig. 1.11: Atlantic rifting and Drifting. From left to right: map of the Atlantic Ocean (reframed after Mercier de Lépinay et al. (2016)); the first column corresponds to the South Atlantic segment with the different rifting and drifting phases after Müller et al. (2008); Peron-Pinvidic et al. (2013); Mercier de Lépinay et al. (2016); the second column corresponds to the Equatorial Atlantic segment, the described phases are after Crawford et al. (1984); Müller et al. (2008); Mercier de Lépinay et al. (2016); Loparev et al. (2021). The third column is the Central Atlantic segment, observations are from Piqué and Laville (1996); le Roy and Piqué (2001); Müller et al. (2008); Mercier de Lépinay et al. (2016). The fourth column corresponds to the Southern North Atlantic segment, the observed rifting and drifting phases are after Müller et al. (2008); Peron-Pinvidic et al. (2013); Mercier de Lépinay et al. (2016). The fifth and last column is the Northern North Atlantic segment, observation are coming from Jongepier et al. (1996); Brekke (2000); Osmundsen et al. (2002); Faleide et al. (2008); Müller et al. (2008); Osmundsen and Ebbing (2008); Tsikalas et al. (2012); Peron-Pinvidic et al. (2013); Mercier de Lépinay et al. (2016); Peron-Pinvidic and Osmundsen (2018). Abbreviations are "Oceani." for oceanisation, "seafloor sp." for seafloor spreading and "Hyp./Exh." for hyperextension/exhumation.

2.2. The Northern North Atlantic segment

The Northern North Atlantic segment can be subdivided based on its major fracture zones (Schiffer et al., 2020). The Northern North Atlantic segment consists, from the South to the North, of the Irminger-Iceland Basin, this is the Iceland hotspot where high volcanic activity has been recorded since 55 Ma, the Norwegian-Greenland conjugate margins, the Fram Strait and the Eurasia Basin (Fig. 1.12). Within the North Sea the Viking Graben is considered to be an aborted rift arm (Beniest, 2017), and similarly in the South West Barents Sea includes the Hammerfest Basin which is considered to be a failed rift (Gabrielsen et al., 1990; Ahmed, 2012).

The Mid-Atlantic Ridge is a largely underwater geological feature, with the exception of the Iceland hotspot which constitutes an emerged volcanic island along the ridge (Fig. 1.12). In the Southern part of the Norwegian-Greenland Sea, the Jan Mayen microcontinent, which is associated with the Icelandic plume (Peron-Pinvidic and Osmundsen, 2018), is located between the active Mid-Atlantic Ridge named in this area Kolbeinsey Ridge located to the West, and the extinct Aegir Ridge located to the East (Fig. 1.12). The Aegir Ridge was active for approximately 22 Myr (Fig. 1.13, between 55 Ma to 33 Ma [Palaeogene]). After this period of activity, the Aegir Ridge sea floor spreading ceased and was replace by the Kolbeinsey Ridge (current Mid-Atlantic Ridge) (Gaina et al., 2009; Faleide et al., 2015). The Norwegian-Greenland Sea is composed of several active marine transform faults and their associated fracture zones (Mosar et al., 2002; Hensen et al., 2019; Gernigon et al., 2020).

2.3. The Mid Norwegian – NE Greenland conjugate margins

2.3.1. Rifting domains

The Norwegian-Greenland Sea segment can be subdivided into two subsegments based on major marine transform faults and associated fracture zones. The southern part of this segment is composed of the Jan Mayen microcontinent bounded to the South by the Iceland segment and to the North by the Jan Mayen fracture zone. The Northern part of the Norwegian-Greenland Sea segment is located between the Jan Mayen fracture zone to the South, and the Senja and Greenland fracture zones to the North. At the time of breakup (Fig. 1.13A), the Mid Norwegian / NE Greenland conjugate margins provide a good example of the 3 rifting phases.

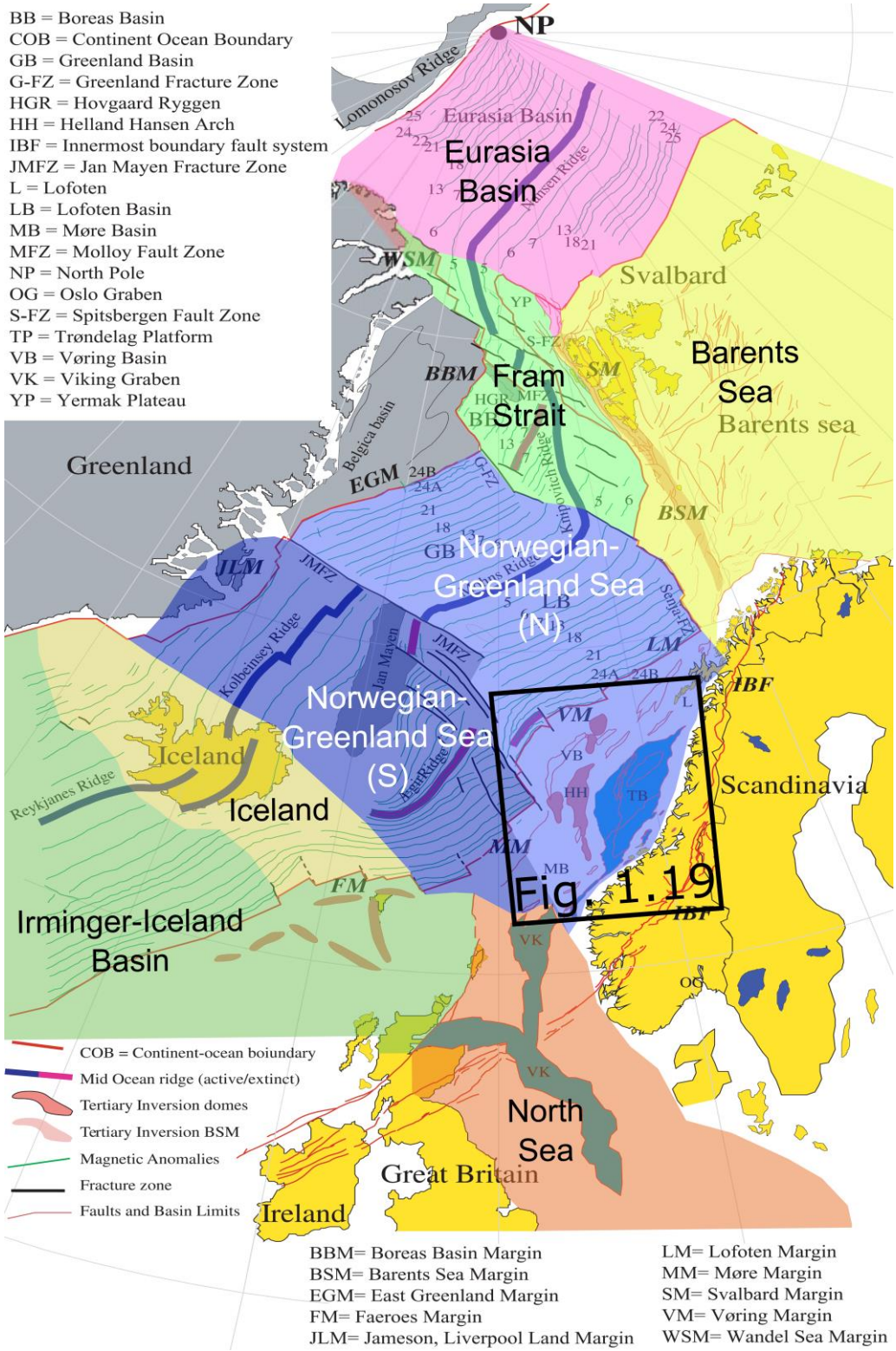

Fig. 1.12: Map of the Northern North Atlantic segment highlighting the Greenland-Norwegian conjugate margins (map after Mosar et al. (2002)). Observed sub-segments are mainly after Schiffer et al. (2020). Abbreviations of the sub-segments are Norwegian Greenland Sea (S): Southern Norwegian Greenland Sea sub-segment; and Norwegian Greenland Sea (N): Northern Norwegian Greenland Sea sub-segment. The location of Fig. 1.19 is shown on the map.

Late Palaeozoic deposits were deposited during the stretching phase (1st rift phase) in the proximal domain that forms the present platform domain (Fig. 1.13A). The Late Jurassic – Early Cretaceous sediments were deposited predominately during the thinning phase in the necking domain that forms the terrace domain. The distal domain, composed mainly of Late Cretaceous – Palaeocene deposits, forms the present-day deep domain (Fig. 1.13A).

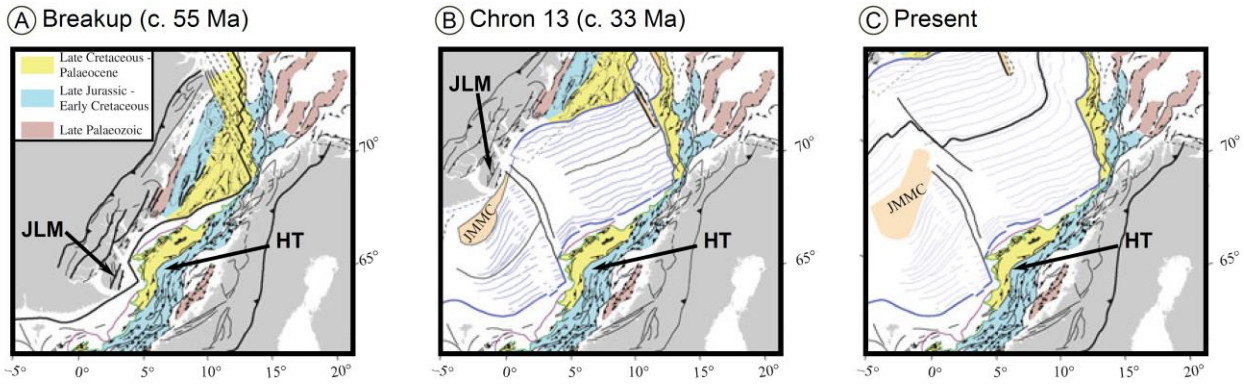

Fig. 1.13: Plate tectonic reconstructions of the Greenland-Norwegian conjugate margins (reframed maps after Faleide et al. (2015)); (A) reconstruction at breakup time (circa 55 Ma); (B) reconstruction at circa 33 Ma (Chron 13); (C) present day map. Jameson, Liverpool Land Margin (JLM) in East Greenland and the Halten Terrace (HT) in Mid-Norway were connected before the breakup. JLM and HT are key locations for Chapter 2.

The geological illistration (Fig. 1.14) proposed by Peron-Pinvidic and Osmundsen (2018) accurately describes the different rift domains accross the Koldewey Platform in East Greenland and the Trøndelag Platform, Nordland Ridge, Frøya Highs, etc. Within the Mid Norway conjugate margin which forms the proximal rift domain. The necking domain in East Greenland comprises the Trail Ø, Jameson Land, Liverpool Land, etc. and along the Mid Norway conjugate margin by the Dønna Terrace, Halten Terrace, etc. (Peron-Pinvidic and Osmundsen, 2018). The distal domain in East Greenland is formed by the Tethis basin, Jan Mayen basin, and by the Lofoten, Vøring and Møre Basins across the Mid Norway conjugate margin (Fig. 1.14).

2.3.2. Focus on the Necking domain

2.3.2.1. Syn-rift (thinning phase)

The necking domain forms during the 2nd rift phase (thinning phase) started during the Upper Bajocian (Middle Jurassic) in East Greenland (Surlyk, 2003; Surlyk and Ineson, 2003) and ended during the Berriasian (lowermost Cretaceous). According to Elliott et al. (2015), similar time constraints for the thinning phase are proposed in the Halten Terrace (Norwegian margin). However, a recent study (Jones et al., 2020), proposed a later initiation of the thinning phase in the Halten Terrace during the Late Callovian. Jameson Land (onshore Greenland) is located at the same palaeolatitude of the Halten and Dønna Terraces (Fig. 1.15), here rifting initiated during the Middle Jurassic. At that time siliciclastic shallow-marine deposits (deltas, beach environments) were deposited above 40° N, whereas below this palaeolatitude, the depositional environments were dominated by marine carbonates principally due to climate more favourable for carbonate factories (Fig. 1.15) (Surlyk and Ineson, 2003).

The majority of the Greenland necking domain is located onshore; this has allowed very detailed sedimentological fieldwork data to have been collected (Fig. 1.16) for the Middle and Upper Jurassic deposits (Kelly et al., 2015). Conversely, the necking domain in the Norwegian conjugate margin, is located offshore and only very rare relics are located onshore. One such example is on Andøy (50 km north of the Lofoten Islands) where Middle and Upper Jurassic are exposed (Fig. 1.16) (Dalland, 1981; Bøe et al., 2010). The Middle Jurassic lithology in the Mid Norwegian – NE Greenland conjugate margins, is dominated by shallow-marine sandstone to mudstone deposits. In offshore Mid-Norway, these Middle Jurassic formations are represented by the Ile Formation, the Not Formation, the Garn Formation, the Melke Formation and the Intra-Melke Formation sandstones (Fig. 1.16). The Upper Jurassic is characterised in both margins by the development of organic rich mudstone, namely the Spekk Formation in the Norwegian margin, which is associated with sandy shallow-marine deposits of the Rogn Formation (Fig. 1.16). The Viking Group which has been deposited during the syn-rift period in the Norwegian Sea, corresponds to the Melke, Intra-Melke, Spekk and Rogn formations (Elliott et al., 2015).

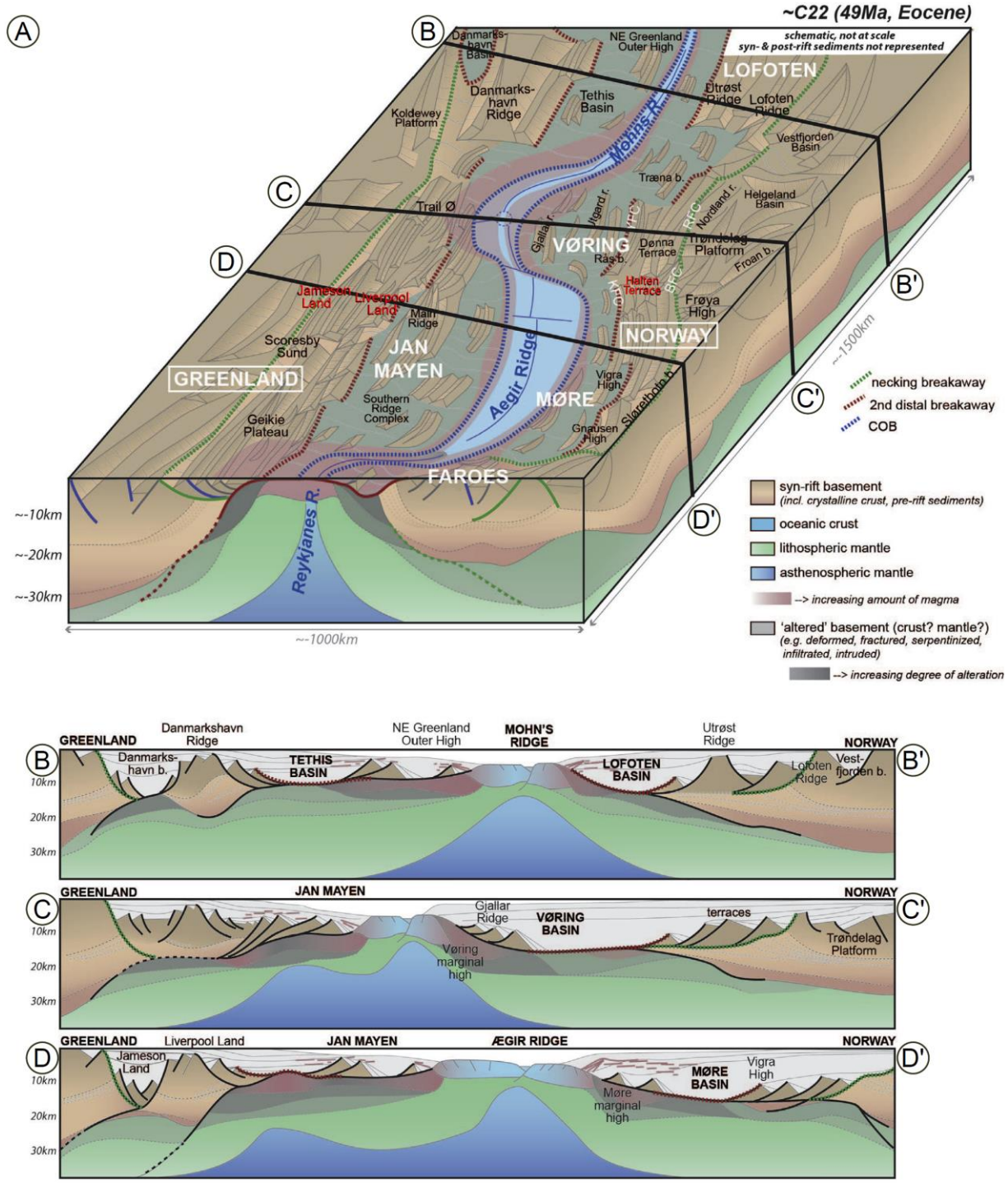

Fig. 1.14: (A) Schematic cartoon reconstruction of the Greenland-Norwegian conjugate margins at circa 49 Ma (Chron 22) with 3 schematic cross sections crossing in the Norwegian margin (B) the Lofoten Basin; (C) the Vøring Basin; and (D) the Møre Basin (Cartoon and cross sections after Peron-Pinvidic and Osmundsen (2018)). Jameson, Liverpool Land Margin (JLM) in East Greenland and the Halten Terrace (HT) in Mid-Norway were connected before the breakup. JLM and HT are key locations for Chapter 2.

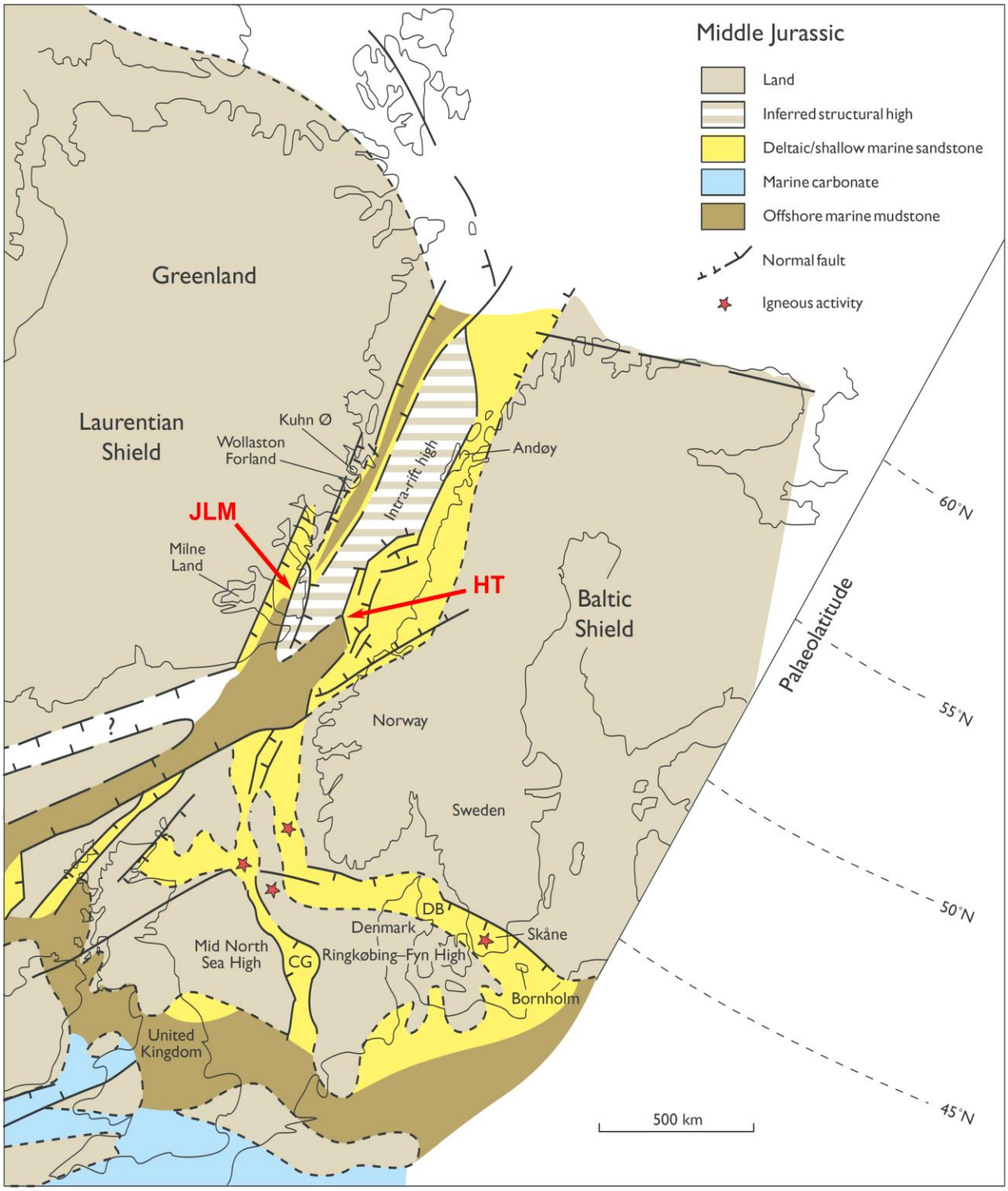

Fig. 1.15: Schematic reconstruction during the Middle Jurassic of the Greenland-Norwegian conjugate margins (map after Surlyk and Ineson (2003)). This palaeo-reconstruction corresponds to the initiation of the thinning phase (second rift phase) where the necking domain has been developed. Abbreviations are CG for Central Graben and DB for Danish Basin. Jameson, Liverpool Land Margin (JLM) in East Greenland and the Halten Terrace (HT) in Mid-Norway are key locations for Chapter 2.

2.3.2.2. Post-rift (hyperextension/exhumation)

During hyperextension/exhumation phase, rift activity was localised in the distal domain (deep domain); whereas during this phase, the sediment deposited in the necking domain (terrace domain) are identified as post-rift sediments. The deep domain was composed of the Tethis basin, Jan Mayen basin in East Greenland, and of the Lofoten, Vøring and Møre Basins in Mid Norway, all of which acted as depocenters (Fig. 1.14). In East Greenland, from the Berriasian to the Hauterivian, the rift waned (Surlyk and Ineson, 2003). This phase can be characterised as a transitional phase separating the syn-rift period and the post-rift period. Commonly this phase cannot be separated from the post-rift phase. According to Jones et al. (2019), the transitional/sag phase is defined by the decline in fault movement across the remaining active faults, during this time the sag-type basins developed. In other words, the rift-sag period corresponds to a transitional period between a high tectonic activity period (syn-rift) and a tectonic quiescence period (post-rift) where master faults are progressively sealed (Jones et al., 2019). Sag-type basins will generally smooth pre-existing topography by thinning on elevated structural highs and thicken on structural lows. According to Kingston et al. (1983), a sag basin is located on continental crust in a divergent zone, and are formed by simple sagging. Middleton (1989) proposed a simple model for the formation of the sag basins; which is driven by weakly-coupled convective downwelling of the asthenosphere underneath the lithosphere. The Møre, Lofoten, Vøring, Jan Mayen and Tethis basins are considered to be sag-type basins (Peron-Pinvidic et al., 2012; Peron-Pinvidic and Osmundsen, 2018).

Post-rift *sensu lato* (including transitional/sag-rift phase), during the Cretaceous in the Greenland-Norwegian conjugate margins, is characterised by the development of thick offshore marine mudstone successions concentrated in depocentres within the deep domains. According to Swiecicki et al. (1998), during Aptian-Albian times, both conjugate margins were dominated by mudstone-prone successions with the rare development of shallow to deep-water turbidite deposits along structural highs (Fig. 1.17).

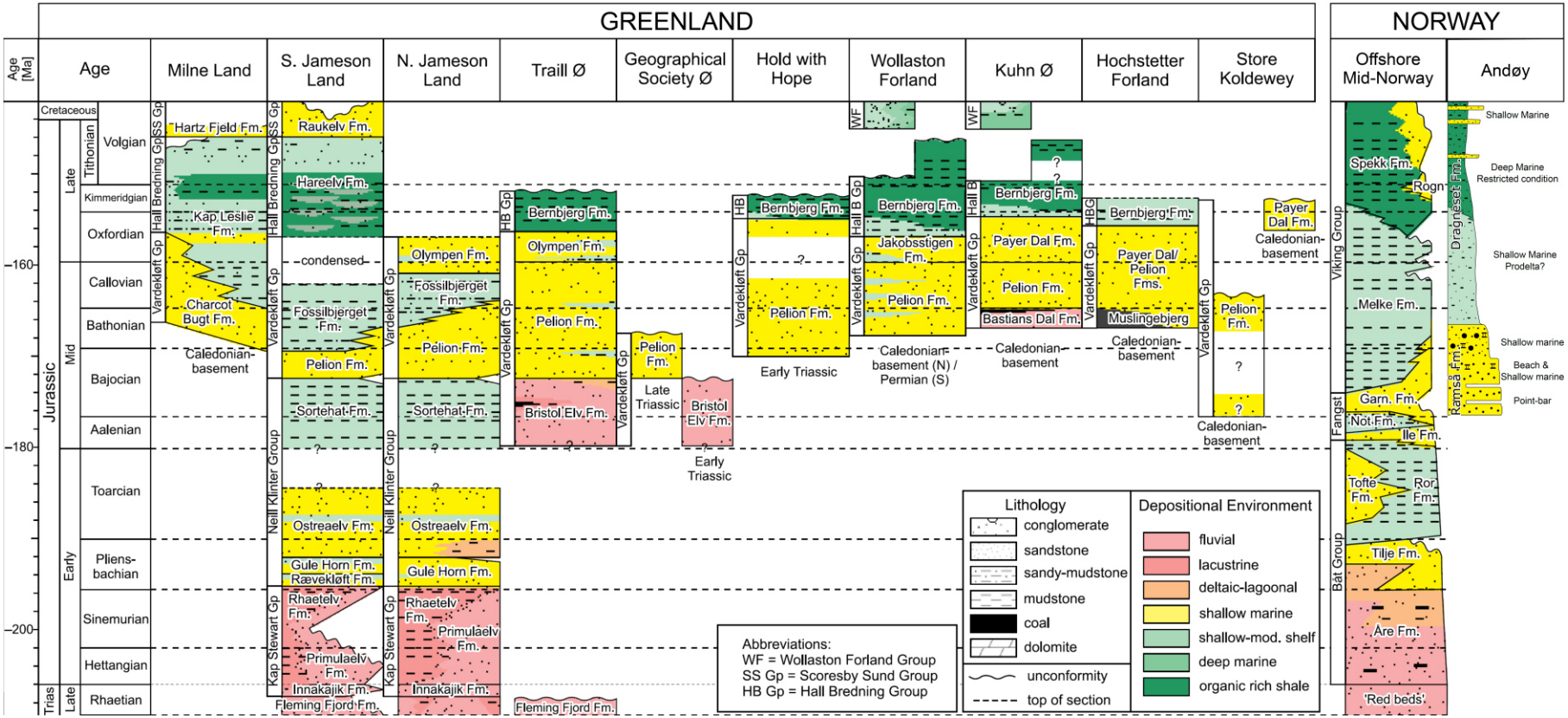

Fig. 1.16: Jurassic stratigraphic correlation of the Greenland-Norwegian conjugate margins (Modified after Kelly et al. (2015), Andøy synthetic stratigraphic column are modified after Bøe et al. (2010) which has been redrawn from Dalland (1981)).

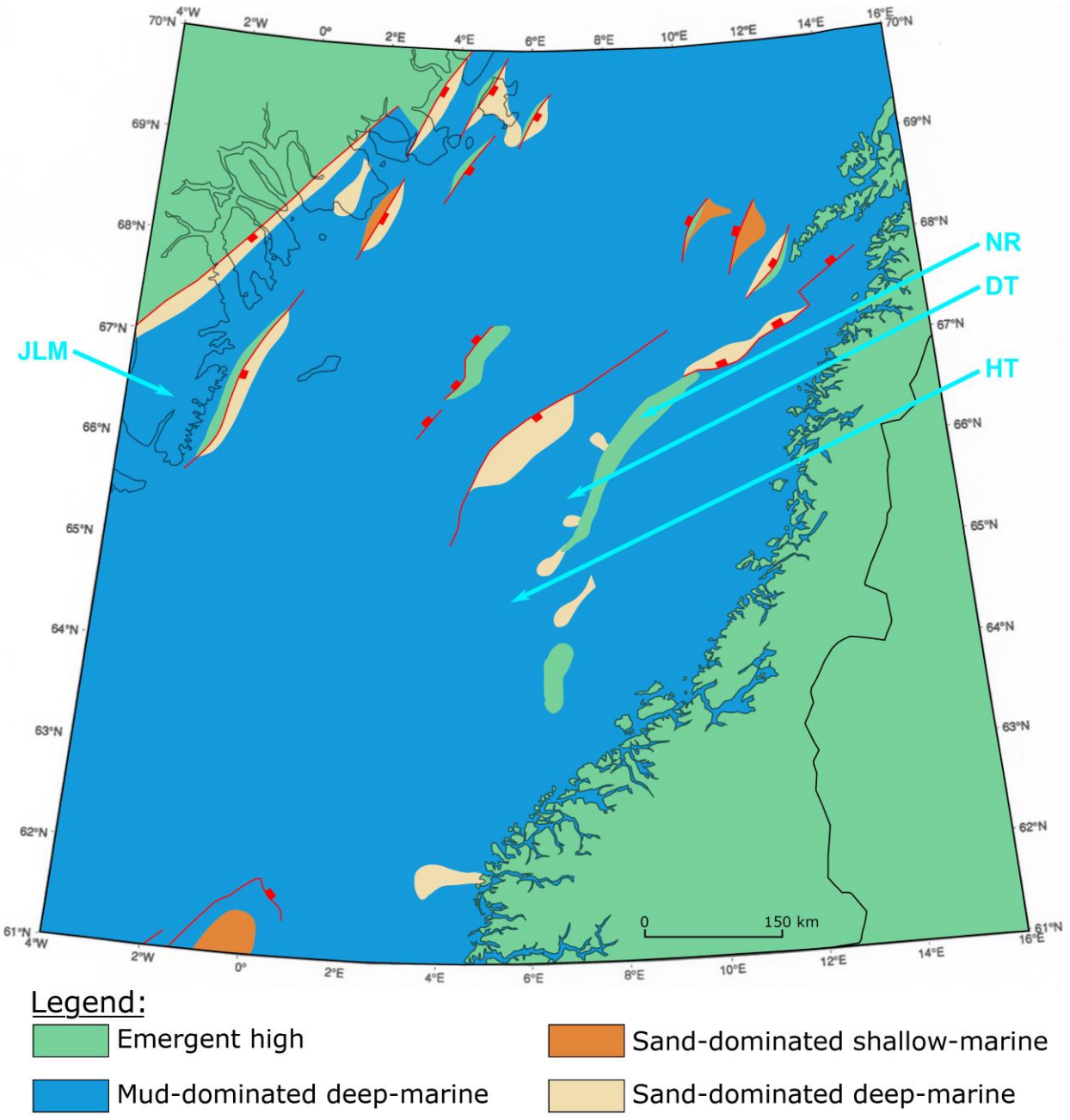

Fig. 1.17: Aptian-Albian palaeogeographic reconstruction of the Greenland-Norwegian conjugate margins (recolorised after Swiecicki et al. (1998)). This interval is characterised by the deposition of thick offshore marine mudstones. Jameson, Liverpool Land Margin (JLM) in East Greenland and the Halten Terrace (HT) in Mid-Norway are key locations for Chapter 2. However, the key post-rift locations mentioned in Chapter 3 are the Nordland Ridge (NR) which is the main sediment source of the deep-water turbidites deposited over the Dønna Terrace (DT).

The entire Cretaceous period is considered to correspond to the post rift (*sensu lato*) mudstone-prone successions (Fig. 1.18). Onshore fieldwork observations in East Greenland and offshore drilling campaigns in the Norwegian Sea, have identified shallow to deep-water turbidite deposits on both conjugate margins. In the offshore Mid-Norway, the “Aptian sands” (Gradstein and Waters, 2016) are time equivalent to the Rold Bjerge Formation in East Greenland (Fig. 1.18) (Bjerager et al., 2020). The Coniacian sandstone corresponds to the Lysing Formation (Dalland et al., 1988; Vergara et al., 2001), this has been recently reclassified as the Lysing Member (Gradstein and Waters, 2016) and is time equivalent to the Månedal Formation in East Greenland (Fig. 1.18) (Bjerager et al., 2020). In the Norwegian Sea, the mudstone-prone unit is subdivided into two formations. The calcareous mudstone grading up to marlstone is named Lyr Formation; the mudstone formation is the Lange Formation which are interbedded by sandstone intervals (Aptian sands, Lysing Members, etc.) form the Cromer Knoll Group.

3. Research objectives

3.1. The Norwegian Sea continental margin

3.1.1. Structural map

The Norwegian Sea is composed from east to west of the platform, terrace and deep domains, respectively. The platform domain consists, from north to south of the Lofoten-Vesterålen Margin, the Trøndelag Platform and the Møre Platform.

The Trøndelag platform is bounded to the north by the Nordland Ridge and to the south by the Frøya High (Fig. 1.19). The Froan and Helgeland basins are located on the Trøndelag Platform (Blystad et al., 1995; Zastrozhnov et al., 2020). The terraces and intra-basinal elevations are from north to south, the Lofoten-Vesterålen marginal highs, the Dønna and the Halten terraces and the Møre Marginal Plateau. These terraces are mainly composed of rotated fault blocks, horsts and grabens forming intraterrace highs and lows (Koch and Heum, 1995). The deep domain is composed of two main basins, to the north the Vøring Basin and to the south the Møre Basin. Both basins contain several subbasins (Fig. 1.19).

The Halten and Dønna terraces are adjacent to each other and together extend approximately 200 km and have an average width of 80 km. Travelling northward, the Halten terrace is bounded to the east, by the Frøya High, the Froan Basin, the Trøndelag Platform and the Norland Ridge. The Dønna Terrace is bounded to the east, by the Nordland Ridge (Fig. 1.19). On the west side, both the Halten and Dønna terraces are mainly bounded by subbasins or marginal Cretaceous highs which are part of the Vøring Basin (Fig. 1.19). The Dønna and Halten Terraces are bounded by major detachment faults that belong to larger fault complexes (FC). Four major fault complexes (FC) have been identified, progressing northward these are the Klakk FC, the Vingleia FC, the Bremstein FC and the Revfallet FC (Fig. 1.19). Syn-rift (thinning phase) generated structures formed the palaeotopography during the post-rift period (hyperextension/exhumation phase).

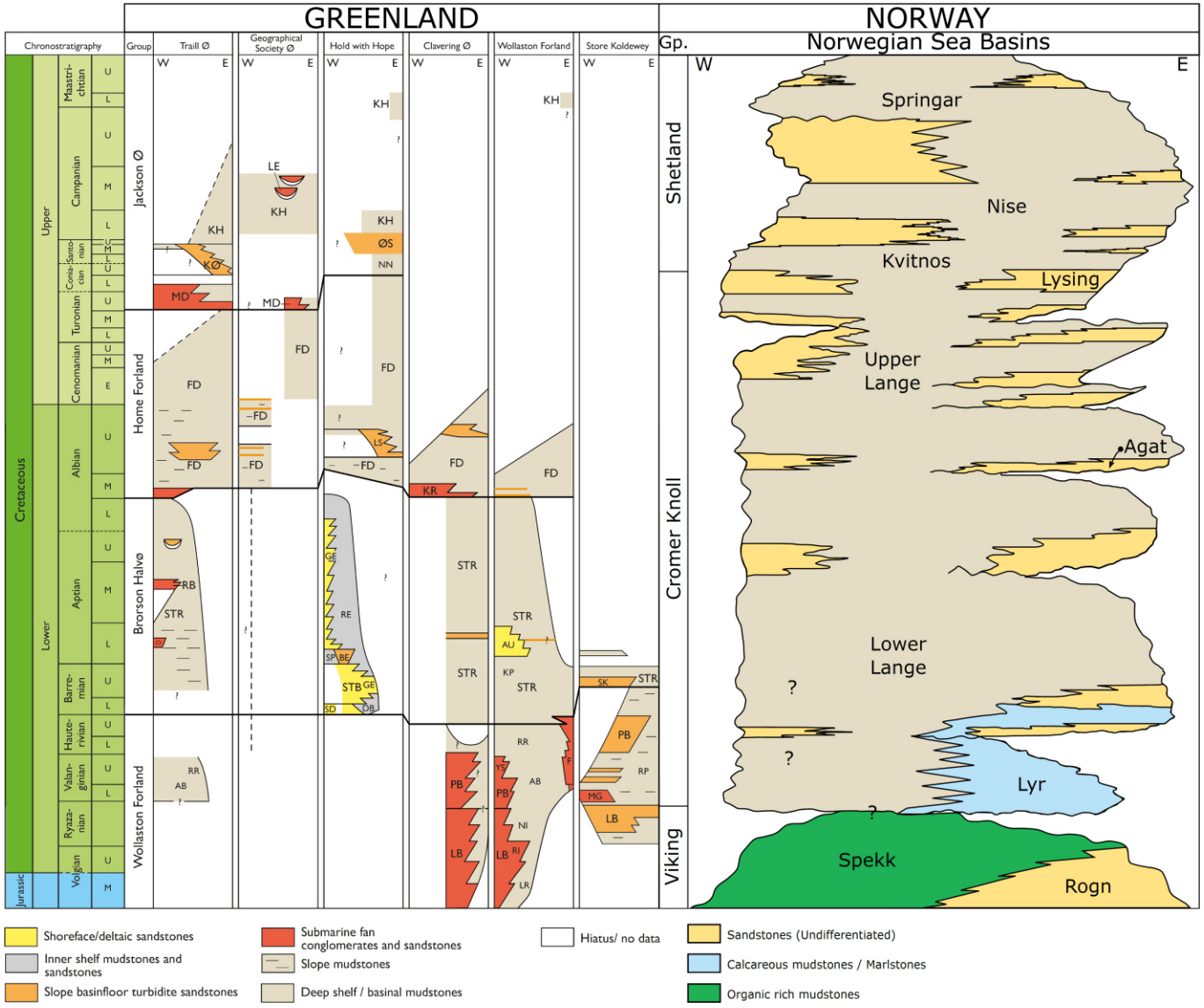

Fig. 1.18: Cretaceous stratigraphic schemes for onshore East Greenland and offshore Mid-Norway. East Greenland after Bjerager et al. (2020), and Mid-Norway recolorised after Vergara et al. (2001), this latter one is based on Dalland et al. (1988) and Brekke et al. (1999). Abbreviations for the Formations (Fm) and Members (Mb): AB = Albrechts Bugt Mb, AU = Aucellabjerg Mb, BE = Blåelv Mb, DB = Diener Bjerg Mb, F = Falskebugt Mb, FD = Fosdalen Fm, GE = Gulelv Mb, KH = Knudshoved Fm, KR = Kontaktravine Fm, KØ = Kista Ø Fm, LR = Laugeites Ravine Mb, LB = Lindemans Bugt Fm, LE = Leitch Bjerg Fm, LS = Langsiden Mb, MD = Månedal Fm, MG = Midter Gneisnæs Mb, NI = Niesen Mb, NN = Nanok Mb, PB = Palnatokes Bjerg Fm, RB = Rold Bjerge Fm, RE = Rødelv Mb, RI = Rigi Mb, RP = Ravn Pynt Mb, RR = Rødryggen Mb, SD = Stribedal Mb, SK = Sorte Kløft Mb, SP = Stensiö Plateau Mb, STB = Steensby Bjerg Fm, STR = Stratumbjerg Fm, YS = Young Sund Mb, ØS = Østersletten Fm.

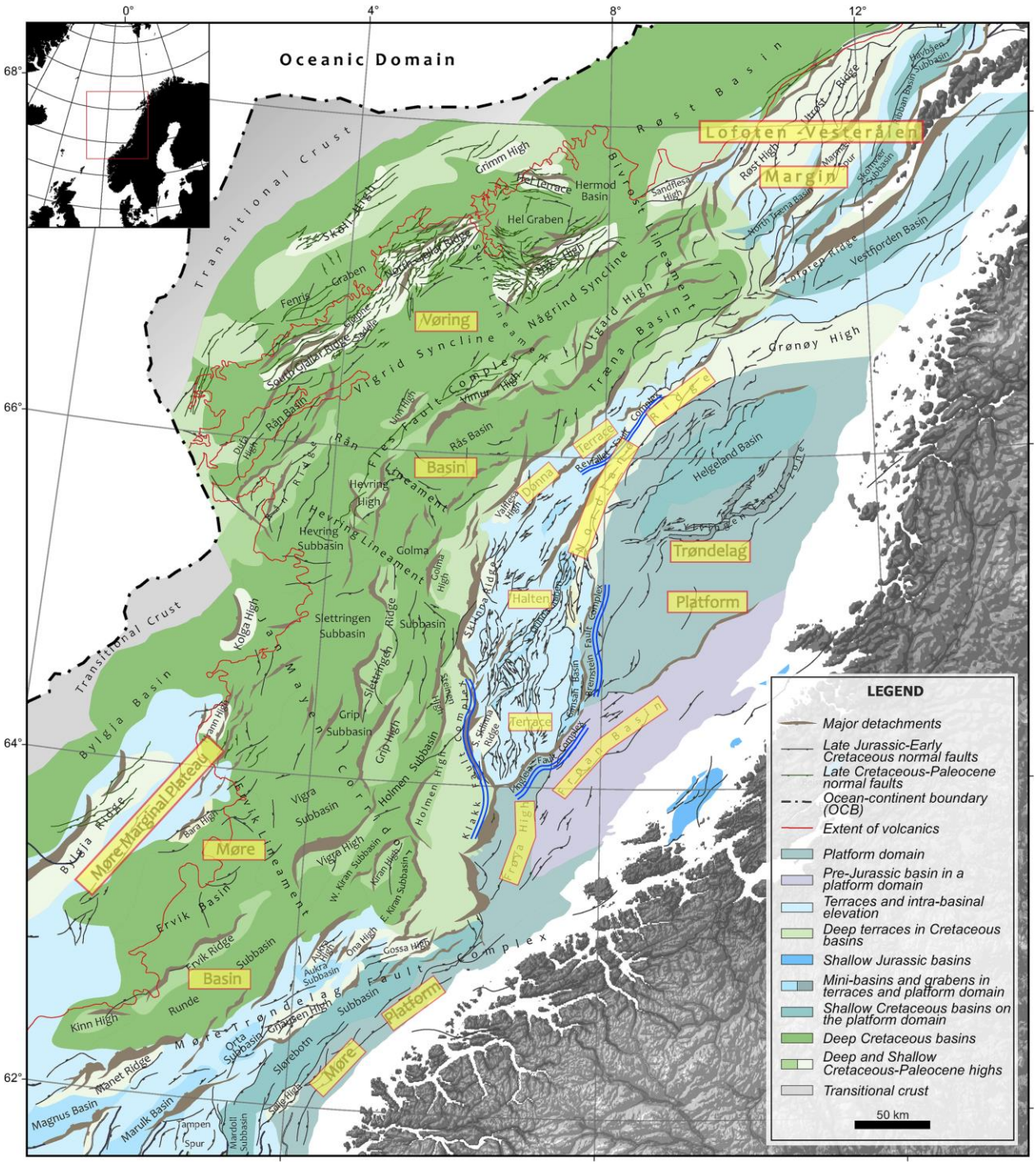

Fig. 1.19: Structural map of the mid-Norwegian margin. This map is from Zastrozhnov et al. (2020) and based on Blystad et al. (1995) and Brekke (2000).

3.1.2. Rich subsurface laboratory

The Norwegian Sea continental margin is an incredibly rich subsurface laboratory for the study of the thinning and hyperextension/exhumation phases (2nd and 3rd rifting phases) of a rifted continental margin. Unlike the majority of continental margins, the Halten and Dønna terraces are in average two times wider than other terraces (Table 1.1).

Conjugate system	Passive continental margin	Average width of the terraces (km)
Iberia - Newfoundland	Iberia Margin	40
	Newfoundland Margin	30
Angola - Brasil	Angola Margin	45
	Brasil Margin	45
East Greenland - Norwegian Sea	East Greenland Margin	35
	Norwegian Sea Margin	40

Norwegian Sea terraces	Maximum width of the terraces (km)	Average width of the terraces (km)
Halten Terrace	110	80
Dønna Terrace	90	70

Table 1.1: Table summarising the width of the terrace domain (necking domain) of some conjugate continental margins over the Atlantic rift system with a focus on the Norwegian Sea terraces (after Peron-Pinvidic et al. (2013)).

The Halten and Dønna terraces are submerged beneath water depths ranging from 200 to 500 m, which facilitates seismic and drilling campaigns. Since the eighties, 395 petroleum exploration wells have been drilled in the Norwegian Sea, with approximately 80% of them drilled on the Dønna and Halten terraces (NPD, 2021). These wells were targeting pre- (*sensu lato*, including syn-stretching sediments), syn- (syn-thinning) and post-rift (syn-hyperextension/exhumation) deposits (Fig. 1.20). Well data frequently includes well-log data (Gamma Ray log, Density log, Resistivity log, etc.), biostratigraphic data (Macro-, micro-, nanno-fossils) and some targeted core data (approximately 3000 m of core for the 395 wells). These well data are commonly only integrated at a local scale (field scale). In addition to the well data, significant 2D and 3D reflection seismic data have been acquired over the platform, terrace and deep domains providing good imaging of the subsurface (Fig. 1.20). The seismic dataset combined and calibrated to the well dataset allows the elaboration of a robust tectonostratigraphic model.

In the goal to provide answers to scientific interrogations (cf. section *1.3 Rift-related scientific interrogations*), the Halten and Dønna terraces of the Norwegian Sea have been chosen to build regional tectonostratigraphic models for the syn-thinning (syn-rift) and the syn-hyperextension/exhumation (post-rift) phases, for the following reasons:

- The Dønna and Halten terraces have a wide necking domain (Table 1.1), allowing us to investigate in detail the link between tectonic activity and sedimentation in detail.
- Significant data (well log, core, biostratigraphic, seismic) covering the Norwegian Sea has been acquired but never fully integrated for the entire region. Constructing an integrated dataset for the region will enhance our understanding of the

tectonostratigraphic evolution of the entire Norwegian Sea continental margin (Fig. 1.20).

- As complementary data, the existing fieldwork studies on the East Greenland conjugate margin provide a good onshore analogue for comparison with subsurface data on the Norwegian Sea (Figs. 1.15, 1.16, 1.17, 1.18).

3.2. Scope of the study

The aborted North Sea rift, adjacent to the Norwegian Sea continental margin has been intensively drilled since the fifties (Stauble and Milius, 1968). Approximately 30 years later, the Norwegian Sea started to be drilled (NPD, 2021). The Norwegian Sea remains understudied and underexplored and poses other questions at different scales (e.g. very local scale to basin-scale), in addition to the main scientific interrogations previously evocated (cf. section *1.3 Rift-related scientific interrogations*).

The Norwegian Sea continental margin is part of the Northern Atlantic segment. As previously discussed, with the exception of the Central Atlantic segment, the thinning phase has along the North Atlantic segment had a similar duration (25 to 30 Ma). At the scale of the Atlantic rifting, it is therefore fundamental to verify if the Norwegian Sea continental margin had a similar duration for the thinning phase. If not, what does this imply at the scale of the Atlantic rift?

The Norwegian Sea continental margin evolved from the thinning phase to the hyperextension/exhumation phase at *circa* Jurassic-Cretaceous boundary (Elliott et al., 2015; Jones et al., 2020). However, some questions still remain at the scale of the continental margin. For instance, can the proposed model of Ravnås and Steel (1998) be used to subdivide the syn-rift phase (thinning phase) into sub-phases (Rift initiation, rift-climax and final rift phase)? Did fault activity cease abruptly at the end of the thinning phase on the Dønna and Halten terraces? Do we observe, as proposed by Jones et al. (2019), a transitional/sag rift phase?

According to some authors, at the terrace scale, the post-rift phase in the Norwegian Sea is characterised by tectonic quiescence (Færseth and Lien, 2002; Lien, 2005; Lien et al., 2006), others have interpreted tectonic activity during this phase (Doré et al., 1997b, 1999; Lundin and Doré, 1997). Deep-water turbidite lobe complexes have been generated during the post-rift period in the Halten and Dønna terraces. According to Picot (2015), sea level fall, climate alternating humid and arid periods or intense tectonic activity will lead to the development of turbidite systems. Is tectonic activity responsible for generating these turbidite lobe complexes? What was the impact of climate and eustatism at that time? Which allocyclic parameters are dominant during the post-rift phase? How did the palaeotopography influence these turbidite systems?

Allocyclic parameters such as tectonic activity during syn-rift phase are keys at the scale of the Dønna and Halten terraces. However, climate and eustatic changes have fluctuated during the Cretaceous and the Jurassic in the Norwegian Sea terraces. Allocyclic parameters such as tectonic activity, eustatic and climate change may be dominant or dominated which

will be recorded in the depositional environments (Beerbower, 1964; Cecil et al., 2011). At the scale of the Norwegian Sea terraces, which allocyclic parameters are dominant during the syn-rift and post-rift periods, and when and how did the depositional environments evolve as a function of these parameters?

Autocyclic parameters allow to self-regulation sediment dispersal at the scale of a turbidite lobe (Hamilton et al., 2015, 2017; Ferguson et al., 2020). Sedimentary deposits during the syn-rift (thinning) and post-rift (hyperextension/exhumation) periods need to be investigated in terms of self-regulation of sediment dispersal. How can we decipher between the different autocyclic mechanisms? Are autocyclic parameters uniquely observable at bed scale? Are allocyclic parameters observable at bed scale?

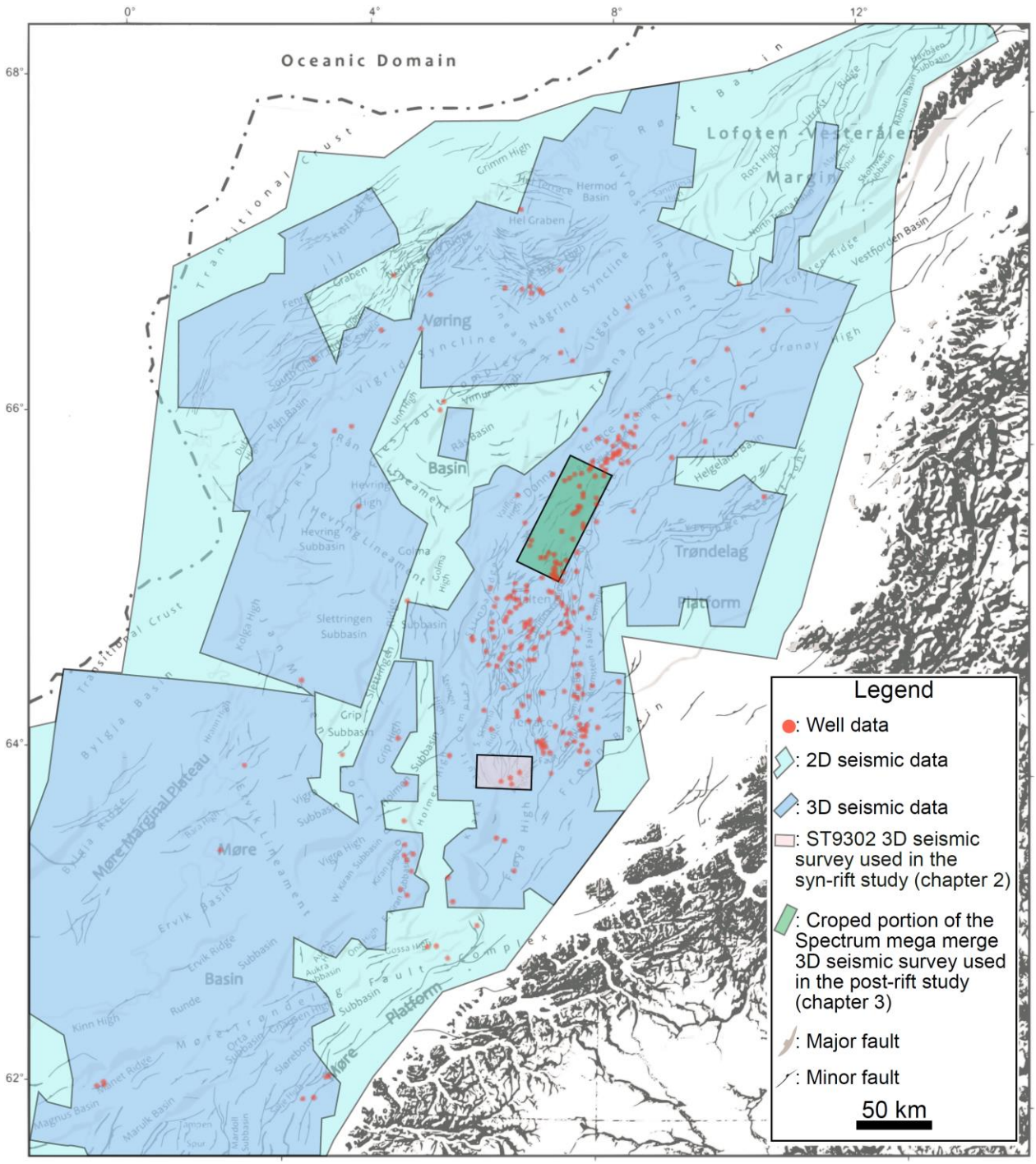

Fig. 1.20: Available well data and seismic data (2D and 3D seismic surveys). The pink rectangle represents the 3D seismic survey used for the syn-rift study (Chapter 2); and the green polygon corresponds to the post rift study (Chapter 3). Background map after Zastrozhnov et al. (2020).

3.3. Research plan and methodology

The main objective of this PhD study consists of building tectonostratigraphic models for the entire Norwegian Sea continental margin during the thinning and hyperextension/exhumation phases. The construction of these models required multi-disciplinary and multi-scale approaches to understand the detailed evolution of the depositional environments related mainly to varying allocyclic parameters.

In order to investigate the sedimentological and tectonostratigraphic evolution during the syn-rift and post-rift periods of the Norwegian Sea, this PhD manuscript is organised as follow:

- The second chapter focused on the syn-rift (syn-thinning) period in the Halten Terrace (Fig. 1.20). The syn-rift chapter is a local study where (Chapter 2) 10 wells have been described at 1:100 scale from well-logs and core data (approximately 500 m of core data). In this chapter, we elaborated a dinoflagellate cyst zonation to refine the chronostratigraphic dating of the sub-thinning stages. Checkshot which is a method providing the rough time to depth conversion for a well, has been used to calibrate well and seismic data. When calibrated, the 3D seismic data was used to interpret horizons and faults with the goal of understanding the tectonostratigraphic evolution during the thinning phase (Table 1.2).
- The third chapter focused on the post-rift (syn- hyperextension/exhumation) period in the Dønna Terrace. In the post-rift chapter, we examined just under 250 m of sediment core described at 1:100 to 1:1000 scale (Table 1.2). In addition to the sediment core description, we have interpreted well-log and seismic data (Chapter 3). This chapter focused on the impact of allocyclic and autocyclic controlling factors on sediment dispersal within turbidite lobe complexes.
- The two last chapters (Chapter 4 and Chapter 5) discusses and concludes regarding the proposed sedimentological and tectonostratigraphic evolutionary model of the Norwegian Sea continental margin during the syn-rift (syn-thinning) and the post-rift (syn- hyperextension/exhumation) periods. These two chapters treat with emphasis the role of the autocyclic and allocyclic parameters on sedimentary architecture. Subaqueous sedimentary density flow (SSDF) deposits have been intensively described on sediment cores allowing to make a focus on flow transformation. Petroleum exploration targets associated to the interpreted syn-rift and post-rift depositional environments are also briefly evocated.

WELL DATA	Core data	Described at Weatherford core store	Used in chapters #2 & #4	1	6406/12-3 A	[92.2 m]	11	6406/3-9	[50.5 m]	21	6407/6-7 S	[22.3 m]	31	6204/10-2 R	[10.1 m]				
				2	6406/12-3 S	[209.8 m]	12	6407/10-1	[28.0 m]	22	6407/7-1 S	[13.1 m]	32	6204/11-1	[100.3 m]				
				3	6406/12-4 S	[42.0 m]	13	6407/1-7	[8.5 m]	23	6407/7-5	[8.7 m]	33	6201/11-2	[13.9 m]				
				4	6405/7-1	[31.1 m]	14	6407/1-7 A	[18.4 m]	24	6408/4-1	[1.4 m]	34	6205/3-1	[7.3 m]				
				5	6406/12-1 S	[36.6 m]	15	6407/2-5 S	[44.5 m]	25	6407/9-1	[39.5 m]	35	6205/3-1 R	[47.5 m]				
				6	6406/12-2	[61.3 m]	16	6407/4-1	[7.0 m]	26	6407/9-2	[40.7 m]	36	6305/1-1	[20.0 m]				
				7	6406/2-3	[45.0 m]	17	6407/5-1	[9.1 m]	27	6407/9-3	[46.4 m]	37	6305/12-1	[7.0 m]				
				8	6406/3-3	[14.5 m]	18	6407/5-2 S	[27.8 m]	28	6407/9-5	[42.4 m]	38	6305/12-2	[33.9 m]				
				9	6406/3-4	[10.0 m]	19	6407/6-1	[17.4 m]	29	6407/9-6	[16.8 m]	39	6306/10-1	[11.3 m]				
				10	6406/3-5	[10.0 m]	20	6407/6-6	[9.0 m]	30	6407/9-8	[82.7 m]	40	6306/6-1	[18.8 m]				
														Total (core store)	[1356.8 m]				
		Described on core photos	Used in chapters #3 & #4	41	6507/2-2	[59.6 m]	43	6507/2-4	[27.8 m]	45	6507/3-9 S	[43.7 m]	47	6507/7-1	[8.7 m]				
				42	6507/2-3	[50.7 m]	44	6507/3-3	[26.7 m]	46	6507/5-3	[14.8 m]							
														Total (picture)	[232.0 m]				
		Total												TOTAL of core described at 1:100 scale	[1588.8 m]				
	Well log data		Used in chapters #2, #3 & #4	When well-log data were available, this type of data has been used															
	Biostrati-graphic data		Used in chapters #2, #3 & #4	When biostratigraphic reports were in the public the domain, or when we got approval from the operator, we used this type of data															
SEISMIC DATA	2D seismic data		Used in chapter #4	When 2D seismic lines were in the public the domain, we used them															
	3D seismic data		Used in chapters #2, #3 & #4	When 3D seismic survey were in the public the domain, this type of data has been used in the synthesis study (chapter 4) 3D seismic survey used in the syn-rift study (chapter 2) was the ST9302 seismic survey 3D seismic survey used in the post-rift study (chapter 3) was a croped portion of the public seismic survey named the Spectrum mega merge														

Table 1.2: Table of data used in this PhD research study highlighting well data (core data, well-log data and biostratigraphic data) and seismic data (2D and 3D seismic surveys) interpreted.

In the Introduction chapter (Chapter 1), a first section deals with the conceptual evolution of passive continental margins and rift-related sedimentation characteristics; secondly, the geological evolution of the Atlantic rift with a focus on the Mid Norwegian – NE Greenland conjugate margins is presented, before the research objectives undertaken within the following chapters are provided (Chapter 2, Chapter 3, Chapter 4 and Chapter 5). The Introduction chapter (Chapter 1) outlines the state-of-the-art of rift evolution using "deep" subsurface data (e.g., gravity and magnetic data, deep crustal reflection seismic data…) at broad regional scale (e.g., Atlantic rift). In the next chapter (Chapter 2), a detailed syn-rift sedimentological and stratigraphic study is conducted in the Greater Fenja area (located in the South Halten Terrace) based on "shallow" subsurface data (e.g., sediment core, well-log, biostratigraphy) and 3D seismic reflection data covering approximately 600 km². As raised in the Introduction chapter (Chapter 1): (i) Is the syn-rift stage can be subdivided into sub-stages? (ii) If so, what are the controlling mechanisms during the different sub-stages? –

In the syn-rift study (Chapter 2), the main objective is to identify the main controlling mechanisms (e.g., tectonic/climatic/eustatic) that govern syn-rift stratigraphic successions. Based on a tremendous amount of "shallow" subsurface data (composed of a 3D seismic survey and 10 exploration logged wells), the analysis of the sedimentological and stratigraphic syn-rift evolution of the greater Fenja area is undertaken in the syn-rift study (Chapter 2). Chapter 2 documents the identification of two depositional environments (subaqueous delta-scale clinoforms and wave-dominated coastal environments) by the identification of 11 sedimentary facies helping to decipher the depositional environment evolution during the different syn-rift sub-stages. These sub-stages are composed of seven 3rd order sequences that have been dated biostratigraphically using a reappraised dinoflagellate cyst zonation. The syn-rift study (Chapter 2) is crucial to discriminate the controlling mechanisms at work during the syn-rift evolution. The evolution of depositional environments during syn-rift sub-stages, as documented in the syn-rift study (Chapter 2), highlights major syn-rift controlling mechanisms observed at crustal scale (Chapter 1).

CHAPTER 2: Syn-rift study

Article submitted to Basin Research

Title:

Depositional environments and process change during the Mesozoic syn-rift siliciclastic shallow-marine evolution of the Norwegian Sea

Authors: Romain GRIME[1,5,@], Bernard PITTET[1], Philippe SORREL[1], Sébastien LANDRU[2], Alexandre BOUCHE[3], Amir KALIFI[1], Francesco BORRACCINI[4], Sten RASMUSSEN[5]

[1] Univ Lyon, Univ Lyon 1, ENSL, CNRS, LGL-TPE, F-69622, Villeurbanne, France.

[2] Stavanger, Norway.

[3] Emerson E&P Software, 1 rue Gramont, 75002 Paris, France.

[4] Edison International SpA – Foro Buonaparte 31, 20121 Milan, Italy.

[5] Edison Norge AS, Jattavagveien 18 – Troll Building, 4065 Stavanger, Norway.

[@] grime.romain@gmail.com

CRediT author statement:

Romain GRIME: Conceptualization, Methodology, Software, Writing – Original Draft, Formal analysis, Investigation, Data Curation, Writing – Review & Editing, Visualization

Bernard PITTET: Supervision, Project Administration, Resources, Validation, Formal analysis, Writing – Review & Editing, Visualization

Philippe SORREL: Supervision, Project Administration, Resources, Validation, Formal analysis, Writing – Review & Editing, Visualization

Sébastien LANDRU: Validation, Formal analysis, Writing – Review & Editing, Visualization

Alexandre BOUCHE: Software, Validation, Writing – Review & Editing, Visualization

Amir KALIFI: Writing – Review & Editing, Visualization

Francesco BORRACCINI: Validation, Writing – Review & Editing

Sten RASMUSSEN: Resources, Funding acquisition, Validation, Writing – Review & Editing

Keywords: Rift initiation; Rift-climax; Final rift stage; Coarse-grained deltas; Coastal depositional environments; Mesozoic; Fenja field; Mid-Norway

1. Abstract

This study presents an integrated sedimentological and stratigraphic architectural investigation of the Late Jurassic to Early Cretaceous syn-rift siliciclastic shallow-marine deposits of the Viking Group (Halten Terrace, Norwegian Sea), based on reappraised 3D seismic, well logs, sediment core, and biostratigraphic data. Ten exploration wells drilled within the study area provide almost half a kilometre of sediment cores, from which two depositional environments were identified based on a detailed sedimentary facies analysis (subaqueous delta-scale clinoforms and wave-dominated coastal environments). The description of deltaic deposits and the recognition of various subaqueous sedimentary density flow deposits supported the identification of lateral facies variation across the delta fans primarily linked to tectonic activity. Seven third-order sequences are recognised for the Jurassic syn-rift deposits based on a reappraised Middle Jurassic to Early Cretaceous biostratigraphic scheme relying on dinoflagellate cyst assemblages.

The syn-rift sedimentological and stratigraphic evolution of the Halten Terrace occurred in three successive stages: (i) the rift initiation stage during which tectonic activity, eustatism and climate change were the main drivers of delta fan and wave-dominated coastal settings evolution; (ii) the rift-climax stage mainly controlled by fault activity, leading to the development of multiple coarse-grained deltas; (iii) the final rift stage marked by a notable aridification of the climate combined with important short-term sea-level fluctuations and a waning of fault activity, which favoured the wide development of wave-dominated shoreface to foreshore sandstones and organic-rich offshore mudstones. A 4D model linking the evolution of the tectonostratigraphic architecture with process changes (and the associated depositional environments) opens new exploration perspectives by improving prediction capacities of syn-rift siliciclastic shallow-marine petroleum reservoirs.

2. Introduction

Coarse-grained rift margin systems have been observed in most rift basins during syn-rift periods, which are commonly formed of coarse-grained deltas developed coevally with tectonic activity, as a first-order control (Gawthorpe et al., 1990; Scholz et al., 1990; Gupta et al., 1999; Colella & Prior, 2009; Turner & Cronin, 2018; Barrett et al., 2020). In shallow-marine and coastal environments, sediment sources and transport are dominantly controlled by the growth and linkage of extensional faults, as well as antecedent drainage cuts (Gupta et al., 1999; Cowie et al., 2000; Elliott et al., 2015). Conceptual models dealing with the stratigraphic architecture of siliciclastic shallow-marine rift deposits revealed that the syn-rift stage can be subdivided into three sub-stages: (1) the rift initiation stage, characterized by the development of fault segments and the initiation of the primary sediment routes; (2) the rift-climax stage, marked by enhanced vertical offsets and well-established sedimentary entry points, and (3) the final rift stage, which records a decrease in tectonic activity (i.e., fault motion), is marked by a progressive closure of the latest sediment routes (Ravnås & Steel, 1998; Folkestad et al., 2014; Jones et al., 2020).

Coarse-grained deltas having steep slopes are classified into two categories: subaqueous conical deltas with poorly developed (or no) topsets, and Gilbert-type deltas characterised by a tripartite subdivision: topsets, foresets and bottomsets (Gilbert, 1885; Nemec, 1990a; Surlyk et al., 2017). Subaqueous conical deltas are not in an equilibrium state due to the excessive height of the delta-slope corresponding to the sediment transfer zone. If the system reaches a stable state, the conical delta evolves into a Gilbert-type delta (Nemec, 1990a). In this case, coarse-grained deltas correspond in general to Gilbert-types, or will evolve into Gilbert-type deltas (Nemec, 1990b). Gilbert deltas fans are usually limited in size (ca. 10 km²), with a maximum fan extension of 20 km² for the wider deltas (Gawthorpe et al., 1990) and are commonly associated with wave-dominated coastal environments (Longhitano, 2008; Longhitano & Steel, 2016; Martinius, 2017; Rees et al., 2017).

The Norwegian Sea corresponds to the eastern rift margin of the North Atlantic Ocean, whereas East Greenland forms the western conjugate rift margin (Lundin & Doré, 2002; Surlyk & Ineson, 2003; Peron-Pinvidic et al., 2013). The Jurassic syn-rift deposits of the Norwegian Sea are located offshore from mid-Norway whereas, in Greenland, Jurassic deposits are subaerially exposed (Fig. 2.1A). Fieldwork campaigns were conducted along the eastern coast of Greenland with the view to better understand the chronostratigraphy of siliciclastic shallow-marine syn-rift environments (Surlyk, 2003; Vosgerau et al., 2004). Coastal sedimentary environments, such as deltaic systems, could be recognized in outcrops and accurately dated using established biostratigraphic schemes (Kelly et al., 2015). Such detailed analyses are, however, very difficult to conduct at the basin scale in 3D tectonostratigraphic models. In contrast, the Norwegian Continental Shelf is covered by a large existing dataset enabling the development of basin-scale sedimentological and stratigraphic models. Well data including well logs and sedimentary cores provide high vertical resolution (1:100 scale), while 3D seismic data help to constrain 3D geometries at different scales (basin to local scale). Hence, fieldwork in the East Greenland margin combined with subsurface data from offshore mid-Norway are highly complementary and allow to build a robust sedimentological and stratigraphic model.

The Norwegian Sea continental margin located in the Northern North Atlantic segment is therefore an ideal setting to investigate the sedimentological and stratigraphic evolution of syn-rift deposits, where a tremendous amount of data is available but not integrated yet. The study area is well constrained by 3D seismic data covering more than 600 square kilometres, as well as ten exploration wells drilled within the seismic survey area. Seven wells drilled after 2014 include high-quality well logs acquired with the latest generation petrophysical tools. In this study, around half a kilometre of sedimentary cores was described focusing on the Viking Group dated between the Middle Jurassic and the Early Cretaceous, which contains the Intra-Melke Formation and the Rogn Formation (NPD, 2021) recognized as two prolific petroleum reservoirs.

Rifting period is defined as a period of intense tectonic activity; however, the proposed detailed sedimentary core analysis provides the possibility to identify depositional environments and their evolution which are directly linked to the dominant external forces (tectonic, eustatism and climate changes). Sedimentologically-based, the identification of process changes during the different rifting phases (rift initiation, rift-climax and final rift stages) should left footprints in the depositional environment record which suggest a change in the dominant external processes. Based on a multi-disciplinary and multi-scale approaches, the aim of the study is to improve sedimentological and stratigraphic models. The propose model will highlight a link between syn-rift depositional environments' evolution to the dominant external forces' evolution.

3. Geological setting

3.1. Structural geology

The Northeast Greenland and Mid-Norwegian conjugate margins (Fig. 2.1) were affected by a complex geological history with three main rifting phases (Peron-Pinvidic & Osmundsen, 2018). The first main rifting phase corresponds to the Carboniferous – Triassic rift phase (Brekke, 2000; Peron-Pinvidic & Osmundsen, 2018; Phillips et al., 2019; Schiffer et al., 2019); the second major phase occurred between the Middle Jurassic and the Early Cretaceous (Koch and Heum, 1995; Phillips et al., 2019; Schiffer et al., 2019); and the last rifting episode started during the Late Cretaceous and ended during the Early Eocene (Brekke, 2000). The oldest rifting phase, corresponding to the stretching phase, was localised in the platform domain; in turn, the second rifting phase defined as the thinning phase (Peron-Pinvidic & Osmundsen, 2018) was strongly influenced by pre-existing structural trends, even though syn-rift normal faults are commonly newly-generated faults (Fossen et al., 2017). The last rifting phase, preceding the seafloor spreading, corresponds to the hyperextension/exhumation phase localised in the deep domain.

The Halten Terrace, located between the Vøring Basin and the Trøndelag Platform (Fig. 2.1B), was mainly affected by the second rifting phase (thinning phase). The Halten Terrace is 130 km long and 80 km wide, and has a surface area of approximately 10,000 km² (Blystad et al., 1995; Marsh et al., 2010; Elliott et al., 2015). The study area is located in the central south segment of the Halten Terrace (Koch and Heum, 1995; Zastrozhnov et al., 2020), north of the "Vingleia branching point" (Fig. 2.1C). This branching point corresponds to a complex tectonic configuration, identified across the proximal, necking and distal domains referred to as the platform, terrace and deep domains, respectively (Peron-Pinvidic et al., 2013; Peron-Pinvidic & Osmundsen, 2016, 2018). The syn-rift period in the terrace domain mainly corresponds to the thinning phase.

The Frøya High (Fig. 2.1B) is part of the platform domain, and was eroded during the syn-rift stage, thereby providing sedimentary inputs to the terrace and deep domains through several entry points (Elliott et al., 2015). The Møre and Vøring Basins (Fig. 2.1B) correspond to the deep domain, which are filled up with Cretaceous post-rift sediments. Between the platform and the deep domains, the Halten Terrace is forming the terrace domain. Here thick syn-rift successions have accumulated along the hanging walls of extensional faults (Blystad et al., 1995). The "Vingleia Fault Complex" (Fig. 2.1C) (Ehrlich & Gabrielsen, 2004; Elliott et al., 2015), newly-formed extensional faults commonly linked to pre-existing structures were generated during the Middle to Late Jurassic syn-rift episode (Brekke, 2000; Ehrlich & Gabrielsen, 2004; Fossen et al., 2017).

In the study area (Figs. 2.1C, 2.1D), a series of syn-rift west-dipping normal faults forms the "Vingleia Fault Complex" (VFC). The VFC separates the Frøya High from the Halten Terrace with an observed footwall uplift of *circa* 3 km occurring mainly during the Late Jurassic (Roberts & Yielding, 1991). Footwall uplift favoured the erosion of the Frøya High that locally fed the coarse-grained deposits observed in the Halten Terrace (Elliott et al., 2020; Jones et al., 2020). Moreover, footwall collapse driven by Triassic salt detachment was observed (Elliott et al., 2012, 2020). The narrow rift of the Halten Terrace is the site across which coastal depositional environments of the Melke, Intra-Melke, Rogn and Spekk formations are encountered (Fig. 2.2).

In a recent study, Jones et al. (2020) advocated the use of the syn-rift model in three sub-stages to described the syn-rift stratal architecture observed in the Halten Terrace. They described a first phase named "early-rift phase" and dated Late Callovian to Early Oxfordian. This phase corresponding to the rift initiation stage is characterised by small offsets associated with the initiation of isolated normal faults. The most active rifting phase is the rift-climax stage, attributed in Jones et al. (2020) to the "peak-rift phase" and dated Middle to Late Oxfordian. This second stage is characterised by the greatest fault offsets, as well as large sediment supplies. Subsidence associated with fault activity across the hanging wall provided accommodation for hundreds of metres of coarse-grained deposits. The final rift stage entitled in Jones et al. (2020) the "late-rift stage" is dated Kimmeridgian to Ryazanian. This final stage is marked by a considerable decrease in fault activity (or even waning), with the conjoint acceleration of thermal subsidence leading to the drowning of the entire system (Ravnås & Steel, 1998; Folkestad et al., 2014; Jones et al., 2020).

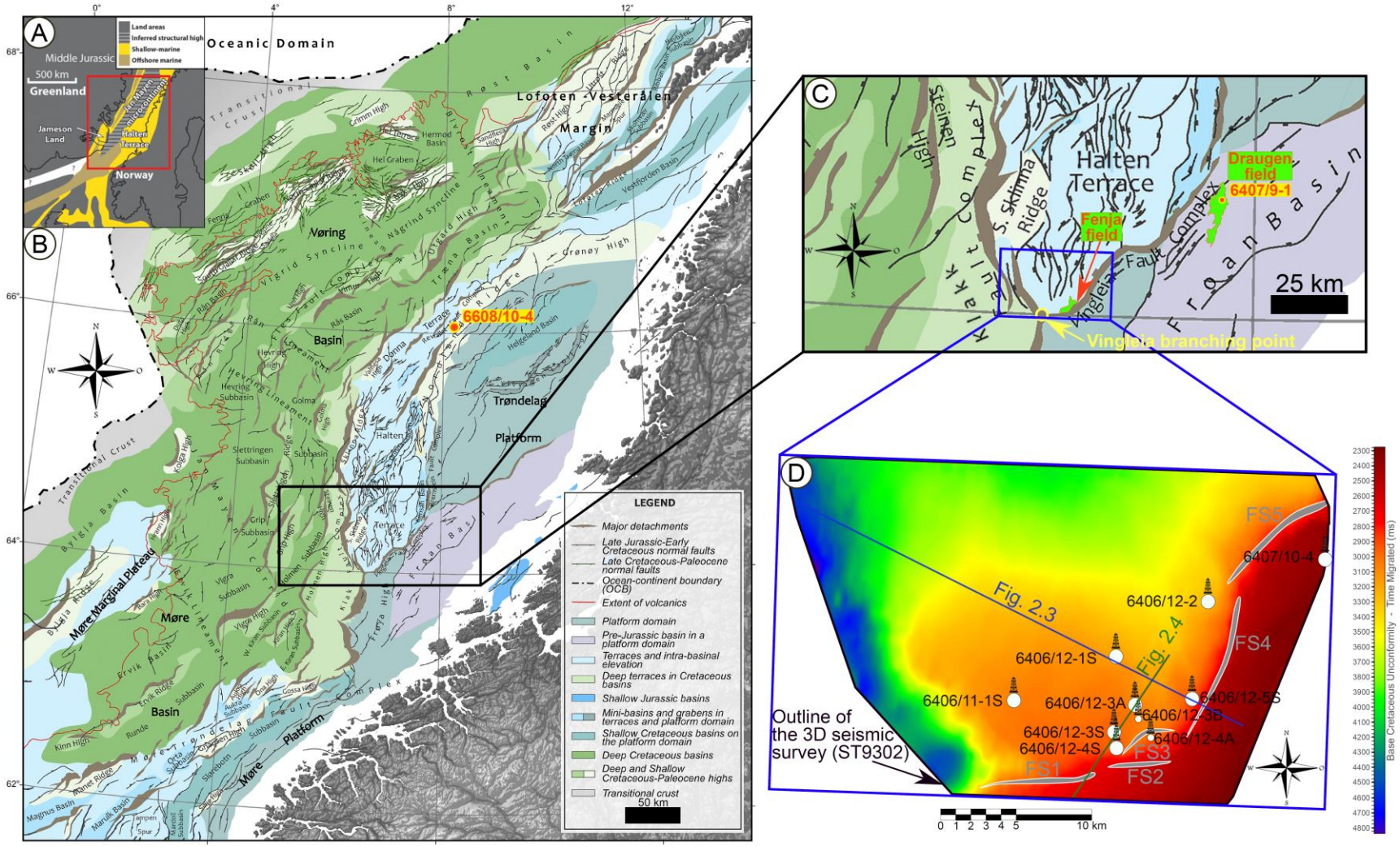

Fig. 2.1: (A) Middle Jurassic sedimentary reconstruction of the Norwegian-Greenland Seaway. Based on Ziegler (1988), Doré (1992) and Eide et al. (2017). (B) Structural map of the mid-Norwegian margin. Based on Blystad et al. (1995), Brekke (2000) and Zastrozhnov et al. (2020). (C) Detailed map of the study area (blue rectangle) highlighting the "Vingleia branching point". Based on Zastrozhnov et al. (2020). (D) Base Cretaceous Unconformity (BCU) map in time (ms) interpreted on the 3D seismic survey ST9302, which shows the location of the 10 exploration wells and of the 5 fault segments (FS). The location of the seismic lines of Figs. 2.3 and 2.4 are displayed on this BCU surface.

3.2. Stratigraphy

On the mid-Norwegian continental shelf, syn-rift Middle Jurassic to lowermost Cretaceous sandstones, which correspond to the Intra-Melke Formation (informal) sandstones and Rogn Formation (NPD, 2021), were encountered during various drilling campaigns on the Dønna and Halten terraces (Figs. 2.1, 2.2). the Intra-Melke Formation (Fig. 2.2), which consists of coarse-grained sandstones and conglomerates, corresponds to coarse-grained deltaic sediments deposited in shallow- to deep-marine environments during the Middle to Late Jurassic (Dalland et al., 1988; Elliott et al., 2015). Occasionally, these coarse-grained deltas are described as Gilbert-type deltas (Elliott et al., 2015) fed from the nearby Frøya High (Figs. 2.1B, 2.1C). The Intra-Melke Formation often includes reworked assemblages which complexify the dating of this unit. In the Halten Terrace, the Intra-Melke sandstones are dated between the Middle and the Late Oxfordian (Jones et al., 2020), or are even potentially older (i.e., from the Late Callovian to the Early Tithonian). The Intra-Melke sandstone reservoir was encountered for the first time in well 6608/10-4 in 1994 (NPD, 2021) on the Nordland Ridge (Fig. 2.1B).

In turn, The Rogn Formation (Fig. 2.2), dominated by medium to coarse-grained sandstones, is made of wave-dominated shallow-marine deposits (Koch and Heum, 1995; Jongepier et al., 1996; Poprawski et al., 2010; Elliott et al., 2015), which develop between the Tithonian and the Berriasian (Jones et al., 2020), or potentially during the Early to Late Tithonian (Dalland et al., 1988; Provan, 1992; Elliott et al., 2015; Chiarella et al., 2020). The Rogn Formation was first encountered in 1984 in the Draugen field in well 6407/9-1 (Fig. 2.1C). Since 1984, more than 25 new exploration wells have penetrated the Rogn Formation, some of which being located several hundred kilometres away from the Draugen field (Fig. 2.1D). The greater Fenja field (Fig. 2.1C) which comprised the Pil, Bue and Boomerang discoveries, contains 4 wells (6406/12-3A, 6406/12-3B, 6406/12-3S and 6406/12-4S) that encountered oil and/or gas in the Intra-Melke and Rogn sandstone reservoirs (Figs. 2.1C, 2.1D). Since 2014, coring and well-logging campaigns have generated a tremendous amount of data that had not previously been integrated and interpreted.

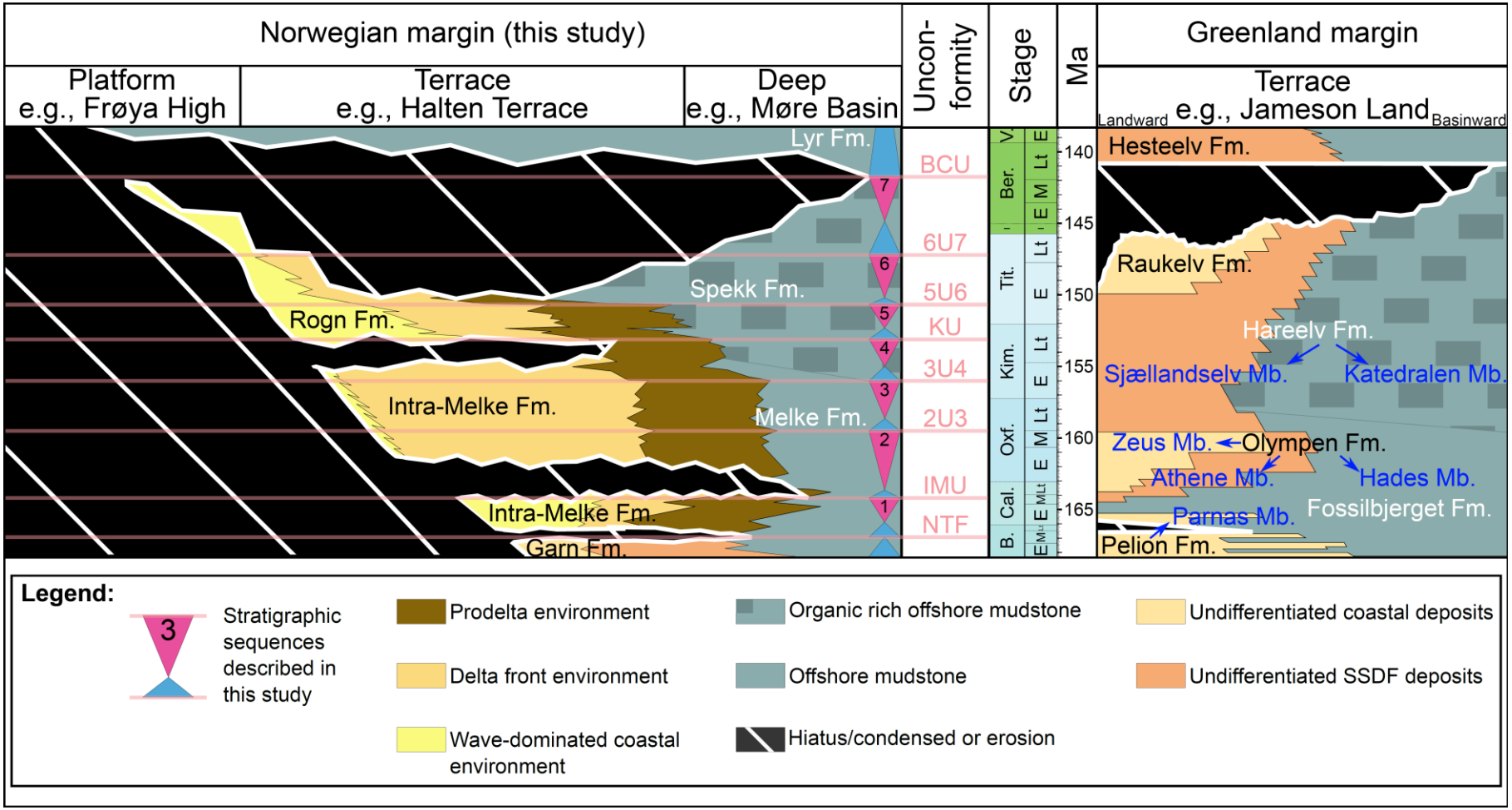

Fig. 2.2: From left to right: the first column corresponds to the proposed lithostratigraphic chart for the Viking group in the Norwegian Sea. The second column highlights the 8 identified unconformities. The third and fourth columns correspond to stage and absolute age after Ogg et al. (2016), respectively. The last column highlights the stratigraphic development on the Greenland conjugate margin (Jameson Land) after Surlyk (2003). Observed unconformities are: Near Top Fangst (NTF), Intra-Melke Unconformity (IMU), Kimmeridgian Unconformity (KU), Base Cretaceous Unconformity (BCU), 2U3 (Unconformity between sequence 2 and 3), 3U4, 5U6 and 6U7.

The distinction between the Intra-Melke Formation (informal) sandstones and the Rogn Formation sandstones relies on their genuine distal sedimentary facies successions (Dalland et al., 1988; Koch and Heum, 1995; Jongepier et al., 1996; Poprawski et al., 2010; Elliott et al., 2015). When distal deposits are very rich in organic matter (OM), formed under anoxic conditions, they are attributed to the Spekk Formation (Dalland et al., 1988; Karlsen et al., 2004; Mann & Zweigel, 2008; Alsen & Piasecki, 2018). The Rogn Formation corresponds to proximal sandy deposits within the offshore muddy Spekk Formation (Dalland et al., 1988; Elliott et al., 2015). Alternatively, the distal Melke mudstones are poor in OM and were formed under more oxic environmental conditions (Dalland et al., 1988). The associated proximal sandy deposits of the Melke Formation are assigned to the Intra-Melke Formation (informal) sandstones (Fig. 2.2). This new stratigraphic scheme will be presented in detail in the results and interpretations section (cf. section *5. Results and interpretations*), where major unconformities subdivide the main geological formations (Fig. 2.2).

The Greenland-Norwegian conjugate margins have delivered similar (and coeval) depositional environment successions during the rifting phase (Fig. 2.2). The two conjoint lithostratigraphic charts of the Norwegian Sea and the Greenland basins presented in *Fig. 2.2* are described in details in *Supplementary data 2.A*.

4. Material and Methods

In this study, the sedimentological and stratigraphic evolution of the greater Fenja field located in the south Halten Terrace is presented. This study focuses on well data (biostratigraphy, core and well log data) and uses 3D seismic data as background data (due to their overall low resolution). Based on biostratigraphy, core description and well log correlation, 3rd order stratigraphic sequences are interpreted using the conceptual model proposed by Ravnås and Steel (1998). 3rd order sequences are further used to sub-divide the syn-rift stage into three sub-stages: rift initiation stage, rift-climax stage and final rift stage. Depositional environments generated during each sub-stage will be interpreted in the light of the dominant allocyclic parameters (tectonic activity, eustatism and climate change). Subaqueous sedimentary density flow (SSDF) deposits have been described relying on Mulder and Alexander (2001)'s classification. Well-log correlations provide the basis for identifying seven stratigraphic sequences that are chronostratigraphically constrained. Palaeoenvironmental reconstruction maps and 3D-block diagrams have been elaborated to illustrate syn-rift shallow-marine depositional environments and the stratigraphic evolution of the Viking Group on the Halten Terrace.

The dataset used in this study includes a 3D seismic reflection data and 10 exploration wells, which have been logged and dated biostratigraphically using dinoflagellate cyst assemblages. The 3D seismic cube ST9302 (Fig. 2.1D) covers an area of 635 km^2 with a vertical resolution of *circa* 30 metres within the stratigraphic interval of interest (i.e., the Viking Group). This seismic survey was acquired in 1993; hence the data quality is not optimal, but the 10 calibrated wells have been accurately tied to seismic data using checkshots, thus avoiding major seismic pitfalls. Each of the 10 exploration wells includes wireline logs within their datasets. In this study, only presenting gamma ray log data (GR logs) are presented; however,

other well log data like neutron, density, resistivity data have been used to discriminate facies similarities, such as coal beds or calcite stringers. A total of 442 metres of cores was described at 1:100 scale.

Eight existing biostratigraphic reports were used in this study, mainly based on dinoflagellate cysts (Stratlab AS, 1991a; b; Biostrat, 1995; Ichron Limited, 2014a; b, 2015a; b; RPS Ichron, 2016).

In order to integrate all data altogether, a routine method was developed to establish a robust sedimentological and stratigraphic model. It consists of a workflow that is composed of three main steps: sequence stratigraphy, chronostratigraphy, and finally, a sedimentological and stratigraphic evolution analysis. Seismic data coupled with sediment core analysis enabled 3D reconstructions of the targeted geological units. The vertical resolution is defined by well-log data and sediment core data if available (centimetres to tens of centimetre scale), whereas the lateral resolution is defined by seismic data (metres to tens of metre scale). This method supports multi-disciplinary and multi-scale approaches helping to improve sedimentological and stratigraphic models through an iterative process between horizontal and vertical directions. The three main steps can be further subdivided into sub-steps (Supplementary data 2.B), which are based on sequence stratigraphy concepts as defined by Embry (1993, 1995).

4.1. Sequence stratigraphy

Seismic data allow the recognition of the main unconformities and fault segments. Nevertheless, due to the low resolution of the ST9302 seismic survey, sequence stratigraphy analyses were mainly focused on sediment core and well-log data. Facies interpretation was initially performed based on a detailed core description. Subsequently, facies identification for well-log data was conducted by using GR cut-off values calibrated on core description (Supplementary data 2.B). Finally, well-log data associated with core data allow the identification of well-log signatures, sequence boundaries (SBs) and maximum flooding surfaces (MFS) *sensu* Embry (1993, 1995). SB as defined by Embry (1993, 1995) corresponds to a transgressive surface, which is an ideal SB for the following reasons: (i) SB are characterized by an obvious lithological change on both sides of the boundary, which is easily identifiable by using any kind of data (well-log, core and seismic data), (ii) in most cases, the diachroneity is minor, (iii) SBs are expressed basinward as well and frequently merged with the subaerial unconformity (SU) landwards. This approach enables the correlation of transgressive-regressive sequences (T-R sequences). The identification of forced regressions (*sensu* Posamentier et al., 1992) on well-logs are illustrated by a sharp contact between proximal coastal facies and distal offshore facies, and imply an abrupt decrease in GR values. Finally, a validation step is undertaken, which links all interpretations for each single dataset. It may be conducted as an iterative process, starting from the major sequences easily recognisable to the smaller sequences identifiable (i.e., parasequences).

4.2. Chronostratigraphy

Based on existing biostratigraphic reports (Stratlab AS, 1991a; b; Biostrat, 1995; Ichron Limited, 2014a; b, 2015a; b; RPS Ichron, 2016), dinoflagellate cyst assemblages identified in the studied stratigraphic interval were grouped into a biostratigraphic scheme combining several dinoflagellate cyst zones in order to obtain a dinoflagellate cyst zonation. Such a scheme provides a chronostratigraphic age (with stages and sub-stages) to the studied stratigraphic sequences. Those sequences are then compared to existing sequences from the North Sea, such as the J sequences (Partington et al., 1993). Time range uncertainty at the boundary between two dinoflagellate cyst zones was considered based on the time duration of the common assemblages occurring in two juxtaposed biozones.

The identification of reworked fossils was a challenging but necessary task in order to avoid a misdating of stratigraphic sequences. The syn-rift period (and more precisely the rift-climax stage) was a period during which sediments originated from the erosion of local palaeohighs (i.e. the Frøya High). The utilisation of a biostratigraphic scheme, which combine several dinoflagellate cyst zones, facilitated the identification of reworked fossil assemblages.

4.3. Sedimentological and stratigraphic evolution analysis

The conjoint use of chronostratigraphic data and sequence stratigraphic interpretations allows to set up the 4D sedimentological and stratigraphic evolution of the study area. The first step deals with the construction of 2D palaeoenvironmental maps based on 3rd order stratigraphic sequences from core and well log data. The attributed chronostratigraphic age for each single map is based on the proposed dinoflagellate cyst zonation. The localization of fault segments, as well as major seismic markers, was constrained based on seismic data and further tied to well-log and core data. Due to the low seismic resolution, seismic interpretation (i.e., fault segments and reflectors) was only used to establish the background part of 2D palaeoenvironmental maps. The fault segments which have been interpreted on seismic data and apparent on the background of 2D palaeoenvironmental maps are highlighting broad published rift concepts such as fault initiation, maximum fault displacement and the final fault cessation phase (Ravnås & Steel, 1998; Folkestad et al., 2014; Jones et al., 2020). The last step aims at creating 3D sedimentological and stratigraphic block-diagrams based on the previously constructed 2D maps.

5. Results and interpretations

5.1. Sedimentology and stratigraphy of the Viking Group

5.1.1. Seismic interpretation

The 3D seismic cube interpretation contains 14 major seismic horizons for the entire stratigraphic succession (from the Caledonian basement to the seabed). The identified pre-, and post-rift intervals highlight with precision the highly faulted syn-rift stratigraphic interval (Fig. 2.3). Focusing on the syn-rift stage, major unconformities are identified from seismic reflection terminations (erosional truncation, downlaps, onlaps and toplaps).

The Viking Group is bounded at its base by the “top Fangst”, interpreted on seismic data as a “near” top Fangst (NTF) that is considered by Stoker et al. (2016) to be unconformable to conformable with the Middle Jurassic Fangst Group. The upper boundary of the Viking Group is the regional unconformity named “Base Cretaceous Unconformity” (BCU). The NTF is identified by several downlap terminations above the NTF surface; it corresponds to the pre- to syn-rift transition easily identified by erosional truncations at the base (thus below the NTF) (Figs. 2.3, 2.4). In contrast, the BCU corresponds to the transition between the syn- and the post-rift stages. This unconformity is diachronous during the Cretaceous, thereby merging several Cretaceous erosional surfaces. According to Kyrkjebø et al. (2004), the BCU exhibits a high-angle unconformity landwards, whereas the BCU is more conformable basinwards. As mentioned by Kyrkjebø et al. (2004), the polychronous character and complex configuration of this remarkable surface make the term “BCU” (Base Cretaceous Unconformity) inadequate. The authors proposed to name this unconformity “Northern North Sea Unconformity Complex”; however, the “BCU” is interpreted in the same way up to the Norwegian Eastern Barents Sea (NPD, 2021). Hence this complex polychronous unconformity is referred here as the “Northern North Atlantic Segment Unconformity Complex” thus reflecting its wide extension. Nevertheless, as “BCU” is the standard naming convention for the entire Norwegian continental shelf (NCS), we have decided to stick with the term “Base Cretaceous Unconformity” (BCU), for comparison purposes.

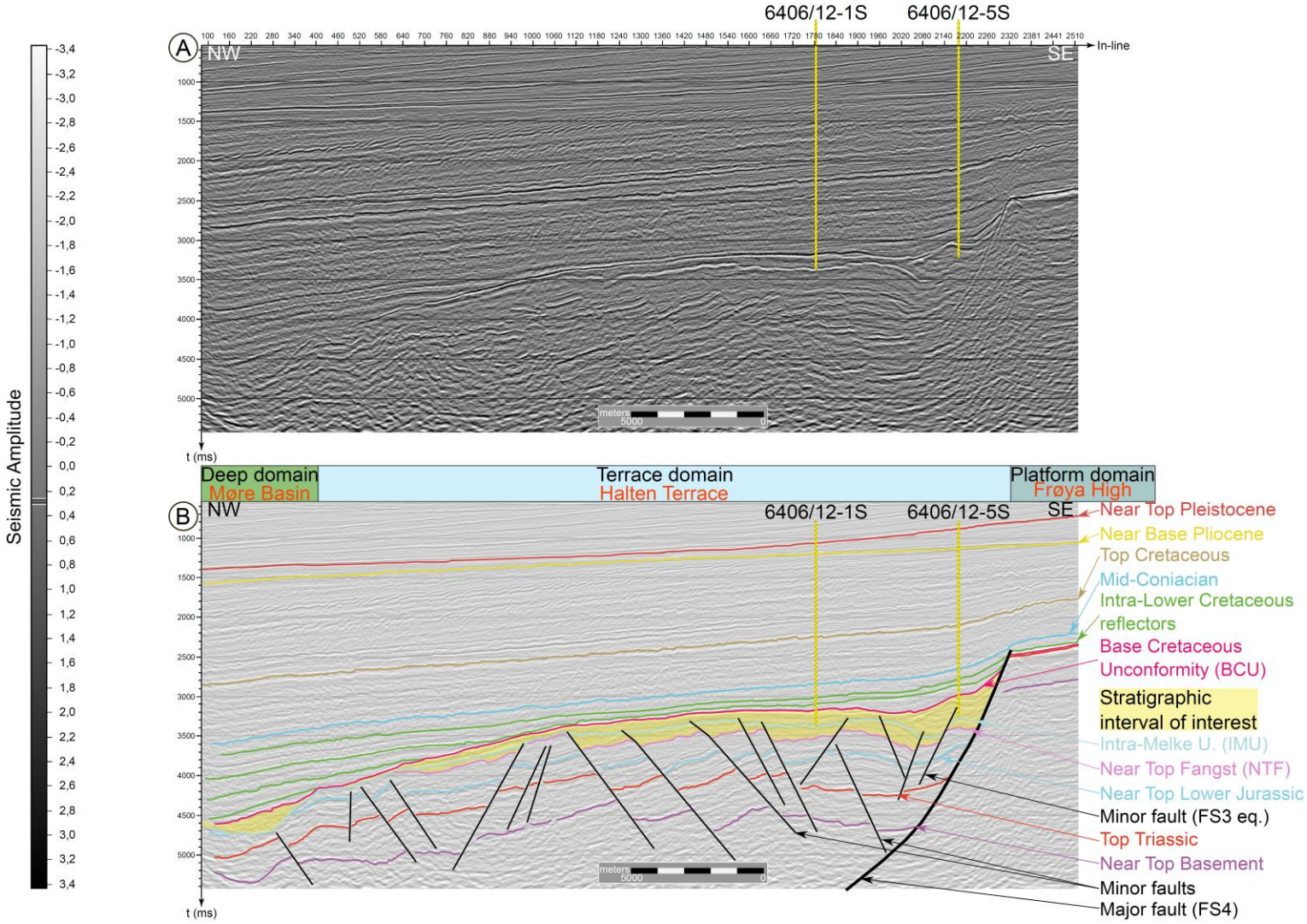

Fig. 2.3: Semi-regional seismic line taken from the 3D seismic survey ST9302 (A) Uninterpreted; (B) Interpreted highlighting the major structural domains. Wells 6406/12-1S and 6406/12-5S are very slightly projected and have been accurately tied to the seismic using checkshots. See Fig. 2.1D for location.

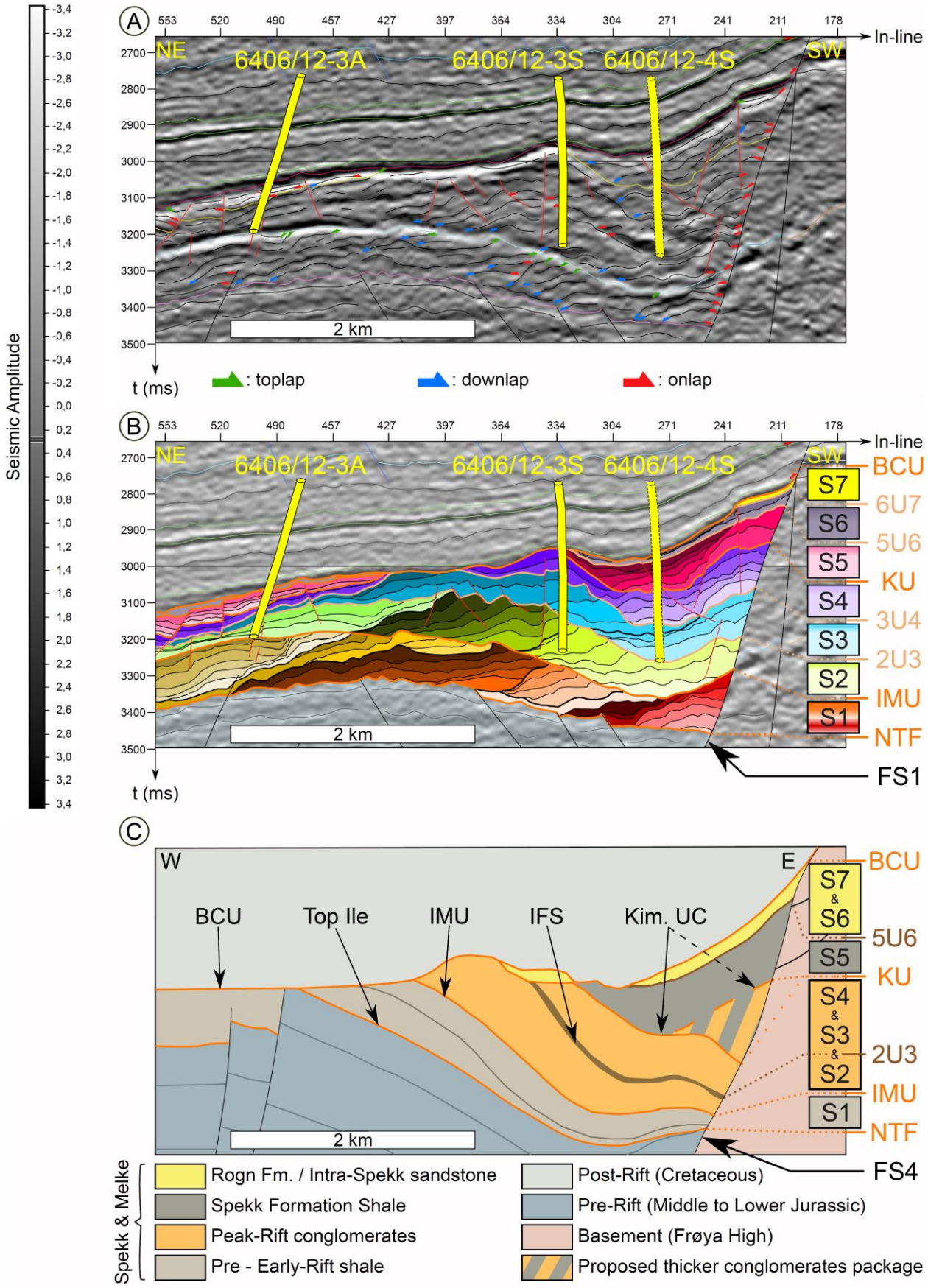
Seismic Amplitude
-3,4
-3,2
-3,0
-2,8
-2,6
-2,4
-2,2
-2,0
-1,8
-1,6
-1,4
-1,2
-1,0
-0,8
-0,6
-0,4
-0,2
0,0
0,2
0,4
0,6
0,8
1,0
1,2
1,4
1,6
1,8
2,0
2,2
2,4
2,6
2,8
3,0
3,2
3,4
A
553 520 490 457 427 397 364 334 304 271 241 211 178
In-line
NE
6406/12-3A
6406/12-3S
6406/12-4S
SW
2700 2800 2900 3000 3100 3200 3300 3400 3500
2 km
t (ms)
: toplap
: downlap
: onlap
B
553 520 490 457 427 397 364 334 304 271 241 211 178
In-line
NE
6406/12-3A
6406/12-3S
6406/12-4S
SW
BCU
S7
6U7
S6
5U6
S5
KU
S4
3U4
S3
2U3
S2
IMU
S1
NTF
FS1
2700 2800 2900 3000 3100 3200 3300 3400 3500
2 km
t (ms)
C
W
E
BCU
Top Ile
IMU
IFS
Kim. UC
BCU
S7 & S6
5U6
S5
KU
S4 & S3 & S2
2U3
IMU
S1
NTF
FS4
2 km
Spekk & Melke
Rogn Fm. / Intra-Spekk sandstone
Spekk Formation Shale
Peak-Rift conglomerates
Pre - Early-Rift shale
Post-Rift (Cretaceous)
Pre-Rift (Middle to Lower Jurassic)
Basement (Frøya High)
Proposed thicker conglomerates package

Fig. 2.4: Detailed seismic interpretation of the greater Fenja area. (A) Local seismic line of the 3D seismic survey ST9302 passing through syn-rift wedge-shaped sedimentary layers crossing wells 6406/12-3A, 6406/12-3S, with one projected well (6406/12-4S) highlighting seismic reflector terminations (toplap, downlap, onlap). (B) Same seismic line as Fig. 2.4A where the 8 interpreted seismic unconformities are highlighted: Near Top Fangst (NTF), Intra-Melke Unconformity (IMU), Kimmeridgian Unconformity (KU), Base Cretaceous Unconformity (BCU), 2U3 (Unconformity between sequence 2 and 3), 3U4, 5U6 and 6U7 bringing to light the 7 seismic sequences (S1, S2, S3, S4, S5, S6 and S7). Wells 6406/12-3A, 6406/12-3S and 6406/12-4S have been accurately tied to the seismic using checkshots, thus avoiding major seismic pitfalls. Fault segment 1 (FS1) is highlighted. See Fig. 2.1D for location. (C) Redrawn geoseismic cross-section orientated west-east exhibiting the main stratigraphic divisions after Jones et al. (2020), with proposed thicker peak-rift conglomerate package along the Vingleia Fault Complex. Exact location of the line is not indicated but it is located in the greater Fenja area. Note that the erosion of the BCU is significant towards the west. In black the unconformities/markers observed after Jones et al. (2020): BCU (Base Cretaceous Unconformity), Top Ile, IMU (Intra-Melke Unconformity), IFS (intra-fan shale), Kim. UC (Kimmeridgian Unconformity) and their equivalent in this study on the right side. IFS corresponds exactly in this study to the J54A MFS (Partington et al., 1993) that is almost merged with the 2U3 unconformity.

Two other major internal syn-rift unconformities were observed and named after Jones et al. (2020): the “Intra-Melke Unconformity” (IMU) and the “Kimmeridgian Unconformity” (KU), respectively. Detailed seismic interpretations exhibit synthetic and antithetic faults with regards to the main growth fault, as well as secondary seismic unconformities named 2U3 (Unconformity between sequence 2 and 3), 3U4, 5U6 and 6U7 (Figs. 2.1D, 2.4). Five fault segments (FS1 to FS5) were used to build the 2D palaeoenvironmental maps. The interpretation of seismic horizons along the Vingleia Fault Complex (VFC) is challenging due to chaotic seismic reflection near the footwall scarp where landslide complexes are found on the immediate hanging wall (Fig. 2.4). On seismic data, the rift-climax (or peak-rift) exhibits a thick wedge-shaped sedimentary package along the main faults. In accordance to Prosser (1993), data reveal that the peak-rift conglomerate sediment package has a well-defined wedge-shape (Fig. 2.4B), in contrast to the proposed interpretation of Jones et al. (2020) (Fig. 2.4C).

5.1.2. Sedimentary facies and their associations

Five cored wells (6406/12-1S, 6406/12-2, 6406/12-3A, 6406/12-3S, 6406/12-4S; Fig. 2.1D) located in the central-south segment of the Halten Terrace were described at 1:100 scale. The description of 442 metres of sediment cores confirmed the identification of eleven facies based on sedimentary structures, grain size, grain sorting, average bed thickness, degree of bioturbation, clast type and matrix composition. Based on those 11 facies, facies associations are established, allowing to discriminate two major depositional environments (section *5.1.3. Depositional models*).

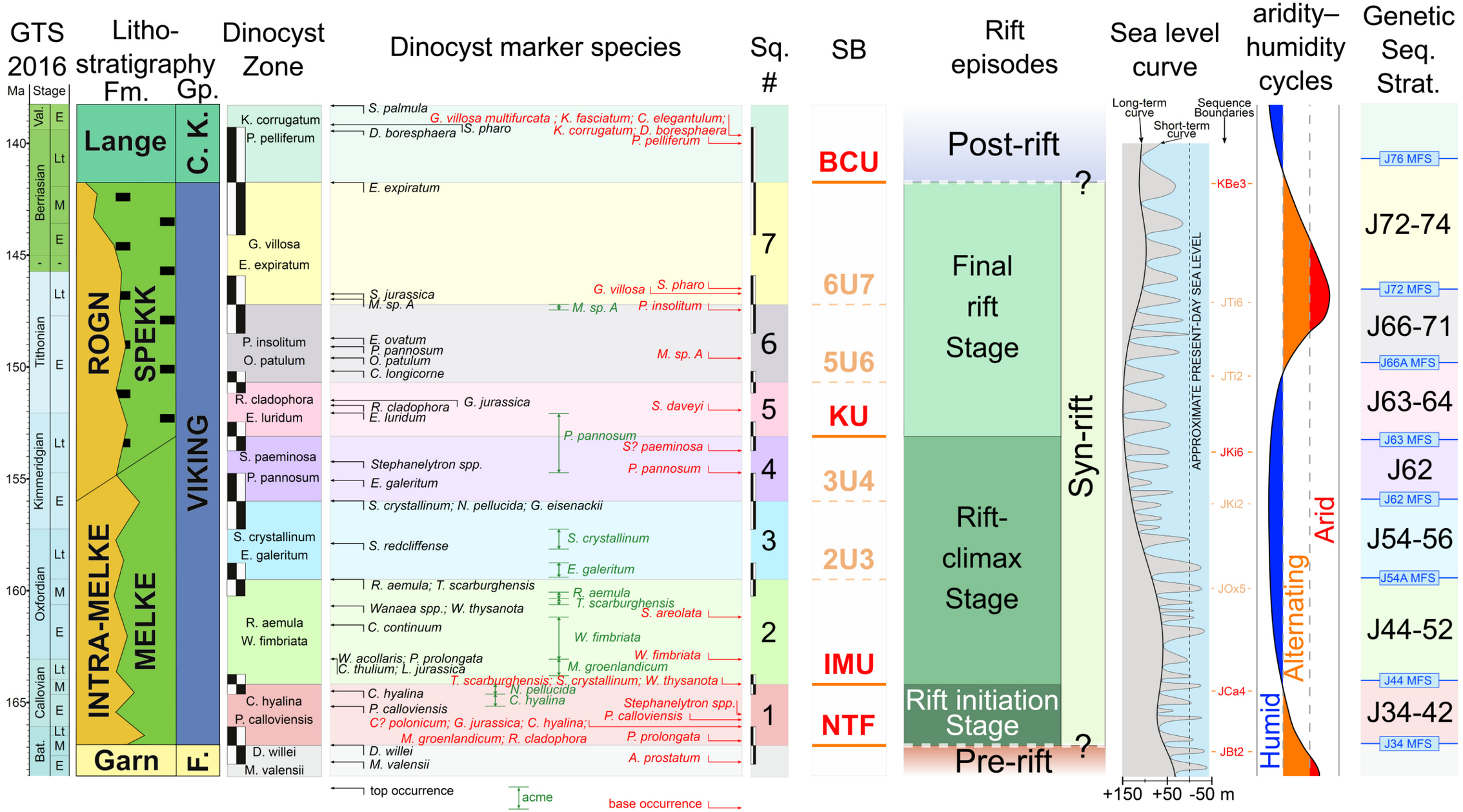

Fig. 2.5: Biostratigraphic chart, seismic markers, rift episodes, sea-level fluctuations, aridity-humidity cycles and genetic sequence stratigraphy. From left to right: the first column corresponds to the chronostratigraphic chart imported from TS Creator and based on Ogg et al. (2016). The second column show the lithostratigraphy (the Garn Fm., when not eroded, is the youngest geological formation of the Fangst Gp. (F.) and corresponds to the lower boundary of the Viking Gp.; its upper boundary is the Lange Fm. which is part of the Cromer Knoll Gp. (C. K.)). The lower part of the Viking Gp. is characterised by the Intra-Melke informal Formation sandstones and Melke Fm. mudstones whereas the upper Viking Gp. is characterised by the Rogn Formation sandstones and the Spekk Fm. mudstones rich in organic matter (OM). The third column corresponds to dinoflagellate cyst zones based on 8 internal biostratigraphic reports (Stratlab AS, 1991a, 1991b; Biostrat, 1995; Ichron Limited, 2014a, 2014b, 2015a, 2015b; RPS Ichron, 2016); Details for dinoflagellate cyst (species) markers are specified in the fourth column. The fifth column displays the sequences associated to the seismic markers in the sixth column. Column seven corresponds to the different rift phases, column height presents the short- and long-term sea-level curve of Haq (2017) and their associated sequence boundaries based on Hardenbol et al. (1998) and Snedden and Liu (2010). The ninth column corresponds to the aridity-humidity cycles of Price (1999) and the last (10th) column, by way of comparison, corresponds to the genetic stratigraphic sequences and their associated MFS after Partington et al. (1993).

5.1.2.1. Coastal sedimentary facies

Facies O1 consists of highly bioturbated mudstones to siltstones (Table 2.1, Figs. 2.6A, 2.6B, 2.6C, 2.6D, and Fig. 2.Ca in *Supplementary data 2.C*). Pyritised J-shaped burrows are usually observed in O1 (Fig. 2.6A), unless sediments are deposited under anoxic conditions (Fig. 2.6D). O1 is structureless and is composed of cm-thick intervals enriched in bivalve shells (Figs. 2.6B, 2.6C), provisionally attributed to the extinct genus *Inoceramus* (Fig. 2.6C). Dinoflagellate cysts are common in O1.

Facies O2 is composed of an alternation of mudstones/siltstones with mm-thick siltstone to very fine-grained sandstone laminae (Table 2.1, Fig. 2.6E, and Fig. 2.Cb in *Supplementary data 2.C*). Those silty to sandy laminae have sharp bases exhibiting cross-bedded laminations and plane-parallel laminations. Dinoflagellate cysts are common in O2. The ichnotaxon *Chondrites* is commonly observed in O2 (Fig. 2.6E).

Facies C1 is formed of very fine- to fine-grained sandstones (Table 2.1, Fig. 2.6E, and Fig. 2.Cb in *Supplementary data 2.C*). The sporadic presence of sub-angular to very angular coarse sand clasts is noteworthy (Fig. 2.6E). The dominant sedimentary structures include small-scale cross-laminations, angular planar to horizontal planar laminations and curved to undulated laminations. Thin silty to muddy layers occur locally along with sandy lenses (Fig. 2.6E). C1 is marked by an intense bioturbation judging from the presence of the ichnotaxa, *Phycosiphon, Palaeophycus* and *Skolithos*.

Facies C2 is made of fine- to medium-grained sandstones (Table 2.1, Figs. 2.6F, 2.6G, and Fig. 2.Cb *Supplementary data 2.C*), with the sporadic presence of sub-angular to very angular coarse sand clasts (Figs. 2.6F, 2.6G, and Fig. 2.Cb in *Supplementary data 2.C*). Horizontal to sub-horizontal plane-parallel laminations are observed, with local occurrences of small-scale to large-scale hummocky cross-stratification (HCS) and swaley cross-stratification (SCS) structures (Figs. 2.6F, 2.6G). Rare bioclasts are found in C2 (Fig. 2.6F). The degree of bioturbation is moderate compared to C1, as only the ichnotaxon *Skolithos* was identified (Figs. 2.6F, 2.6G). Long vertical burrows (> 30 cm) are observed and were attributed to the ichnotaxon *Ophiomorpha* (Fig. 2.6G).

Facies C3 consists of medium-grained sandstones (Table 2.1, Figs. 2.6H, 2.6I, 2.6J, 2.6K, and Fig. 2.Cb in *Supplementary data 2.C*), with the rare presence of granules having a sub-angular to very angular shape (Figs. 2.6I, 2.6K). Horizontal to sub-horizontal plane-parallel laminations with common occurrences of large-scale SCS (but rare HCS) are observed (Figs. 2.6H, 2.6I, 2.6J, 2.6K). Rare erosional bases (or sharp contacts) are also found, as a few coal fragments. The degree of bioturbation is relatively low, as only the ichnotaxon *Skolithos* was recognised in C3 (Fig. 2.6J).

Table 2.1: Facies description summary. Columns from left to right: facies number, lithology, texture and average bed thickness, sedimentary structures, depositional mechanism, main environment and sub-environment.

Facies #	Lithology	Texture and average bed thickness	Sedimentary structures	Depositional mechanism	Main depositional environment	Sub-environment
O1	Mudstone to siltstone	Mud-supported and well sorted.	Structureless and highly bioturbated (J-shaped burrows); In anoxic conditions, the O1 facies is barren of bioturbation. Centimetric intervals rich in bivalve shells (provisionally attributed to the extinct genus *Inoceramus*).	Relatively calm zone (absence of wave energy) Transport by suspension below the storm wave-base.	**Offshore**	Intermediate to distal offshore
O2	Mudtstone/siltstone with millimetric siltstone to very fine-grained sandstone laminae	Mud-supported and badly sorted due to the presence of millimetric siltstone to very fine-grained sandstone laminae which are grain-supported.	Muddy to silty, highly bioturbated, background sedimentation: see O1. Millimetric siltstone to sandstone beds are characterized by sharp bases exhibiting cross-laminations and parallel-laminations. Highly bioturbated (*Chondrites* ichnotaxon).	Shoaling process: Low energy condition impacted by storm events. Suspension cloud during the waning stage of a storm; This zone is located between the storm wave-base and the fair-weather wave-base.		Proximal offshore
C1	Very fine- to fine-grained sandstone	Grain-supported, well-sorted, rounded grains. Sporadic presence of sub-angular to very angular coarse sand clasts. Thin silty to muddy layers locally occur along with sandy lenses.	Small-scale cross-laminations, angular planar to horizontal planar laminations and curved to undulated laminations. Highly bioturbated (*Phycosiphon* , *Palaeophycus* and *Skolithos* ichnotaxa).	Shoaling process: Low energy conditions with occurrences of storm events. This zone is located in the distal part of the shoaling zone directly above the fair-weather wave base.	**Shoreface to foreshore**	Lower shoreface
C2	Fine- to medium-grained sandstone	Grain-supported, well-sorted, rounded grains. Sporadic presence of sub-angular to very angular coarse sand clasts.	Horizontal to sub-horizontal plane parallel laminations are present with local occurrences of small-scale to large-scale HCS and SCS structures. Moderately bioturbated (*Skolithos* and *Ophiomorpha* ichnotaxa).	Breaking process: Wave action is the principal depositional mechanism. This zone is located between the fair-weather wave base and the mean low water (MLW).		Middle shoreface
C3	Medium-grained sandstone	Grain-supported, well-sorted, rounded grains. Sporadic presence of granules with a sub-angular to very angular shape.	Horizontal to sub-horizontal plane parallel laminations with common occurrence of SCS and rare HCS structures. Rarely to moderately bioturbated (*Skolithos* ichnotaxon).	Surfing process: Wave action predominates in this zone. This zone is located in the surf-zone just below the mean low water (MLW).		Upper shoreface
C4	Medium- to coarse-grained sandstone	Grain-supported, well to badly sorted, well-rounded to highly-angular grains. Common presence of granule- and pebble-rich laminae (layers from 1 to 8 cm).	High-angle cross beddings formed of parallel laminations to inclined parallel laminations. Absence to rare trace of bioturbation.	Swash process: Swash and backswash motion (wave energy). This zone is located between the mean low water (MLW) and the beach berm.		Foreshore
Tu1	Very fine- to medium-grained sandstone at the base, and the top is dominated by siltstone to mudstone	Passing progressively from grain-supported to mud-supported. The entire sequence is well sorted. Clasts (mudstone clasts, coal or wood fragments) are poorly rounded to very well rounded. Bed thickness: few millimetres up to 30 cm.	Bouma sequence (ideal succession rarely observed entirely); Terms (T) from bottom to top: - erosional base; - Ta: massive to normally graded sands; - Tb: plane parallel laminations; - Tc: trough cross-beddings and ripples; - Td: parallel laminated; - Te: suspension fallout.	Turbidity flow is a non-cohesive flow (turbidity currents).	**Prodelta**	Distal prodelta
Co1	Coarse to very coarse-grained sandstone at the base, whereas the top is dominated by fine grained-sandstone or siltstone	Passing progressively from grain-supported to mud-supported. The entire sequence is moderately to well sorted. Clasts (mudstone clasts, coal or shell fragments) are angular to rounded. Presence of armored mudstone clasts. Bed thickness: few centimetres up to 90 cm.	Lowe sequence (ideal succession rarely observed entirely), - strong erosional base; - massive sand composed of gravels, mudclasts, shell and wood fragments; inverse grading can be observed (Ta term); - Ta thickness is much greater than Tb, Tc, Td & Te; - Tb, Tc, Td & Te show normal grading.	Concentrated density flow is a non-cohesive flow. (the base of the event bed is mostly controlled by frictional freezing, whereas the top is controlled by partially turbulent flows).		Proximal prodelta
De1	Conglomeratic mudstone	Mud-supported, can be well sorted to extremely badly sorted (chaotical arrangement of the clasts). Clasts (polygenic origin) are rounded to very angular. Bed thickness: a few centimetres for well sorted conglomeratic mudstone up to 70 cm for badly sorted conglomeratic mudstone.	Slightly erosional base. Clasts in the muddy-matrix are well sorted (normal grading).	Debris flow is a cohesive flow. Well sorted debris flow are observed in distal settings, hydroplaning process allow to travel long distances and sort clasts.		Proximal to distal prodelta
			Slightly erosional base. Chaotical arrangement of the clasts (structureless).	Debris flow is a cohesive flow. Chaotical debris flow are observed in proximal settings, The two major depositional processes for debris flow deposits are en-masse, and freezing.	**Delta front**	Proximal to distal delta front
Hy1	Grain-supported conglomerate	Grain-supported, poorly to very poorly sorted. Clasts (mudstone clasts, coal, shell and carbonate fragments) are angular to very angular. Presence of armored mudstone clasts. Bed thickness: 20 cm up to 3.00 m.	Erosional base with some traction structures. Structureless. Common presence of inverse grading.	Hyperconcentrated density flow *sensu stricto* is a non-cohesive flow. Frictional freezing process due to grain-to-grain interaction, and hydroplaning process.		Proximal delta front
Hy2	Massive coarse- to very coarse-grained sandstone	Grain-supported, well to poorly sorted. Clasts (polygenic origin, mudstone clasts and carbonate fragments) are sub-rounded to very angular. Rare presence of armored mudstone clasts. Bed thickness: 10 cm up to 1.05 m.	Erosional base with some traction structures and sand injectites. Structureless. Common presence of inverse grading.	Grain-flow is a non-cohesive flow. Grain-flow belongs to hyperconcentrated density flow *sensu lato* . Frictional freezing process due to grain-to-grain interaction, and hydroplaning process.		Distal delta front

Facies C4 corresponds to medium- to coarse-grained sandstones (Table 2.1, Figs. 2.6L, 2.6M, 2.6N, and Figs. 2.Cb, 2.Cc in *Supplementary data 2.C*). The predominant sedimentary structures are NW-oriented (inclined) parallel laminations, which are well marked as soon as granules to fine-grained pebble layers (1 to 8 cm) dominate over sands (Figs. 2.6L, 2.6N, and Fig. 2.Cb in *Supplementary data 2.C*). Such laminations are composed of angular to very angular polygenic granules (to fine pebbles) within a sandy matrix. High-angle cross beddings formed of parallel laminations are commonly observed when those laminae are present. Plant remains occur in C4 (Fig. 2.6M). Bioturbation is absent, or very rare, in this facies.

5.1.2.2. Gravity-driven sedimentary facies

Facies Tu1 consists of very fine- to medium-grained sandstones at the base, whereas the top is dominated by siltstones and mudstones (Table 2.1, Figs. 2.7A, 2.7B, 2.7C, 2.7D, 2.7E, and Fig. 2.Cc in *Supplementary data 2.C*). Tu1 has an erosional base and is characterised by normal grading. Facies Tu1 is currently deposited over mudstones and siltstones of facies O1. Bed thicknesses in Tu1 range from a few millimetres up to 30 centimetres. The mm-thick deposits are commonly characterised by very fine- to fine-grained sandstones with a sharp base (Figs. 2.7A, 2.7B, 2.7C). In most cases, no visible structure but few plane-parallel laminations can be found in Tu1. Folding due to slumping, as well as syn-tectonic structures such as small-scale normal faults or small-scale boudinage (Figs. 2.7B, 2.7C), are also observed. If Tu1 deposits are a few cm up to a few dm-thick, erosional bases are well pronounced and characterised by medium-grained sandstones (Fig. 2.7D) exhibiting several sedimentary structures such as parallel laminations, trough cross-beddings and/or current ripples. Cm-thick deposits of Tu1 consist of fine- to medium-grained sandstones thinning upward to siltstones or mudstones with either planar parallel laminations or current ripples (Fig. 2.7E). Cm-thick deposits are often deformed due to normal faulting, boudinage and folding (Fig. 2.7D). Alternatively, dm-thick deposits exhibit a well-defined erosional base and massive medium-grained sandstones, overlain by fine-grained sandstones with parallel laminations and, less commonly, by trough cross-beddings and current ripples in very fine-grained sandstones that finally evolve into siltstones or mudstones (Fig. 2.7E). Such dm-thick deposits are affected by folding due to slumping. Clasts are poorly rounded to very well rounded. Mudstone clasts, coal or wood fragments can be observed in Tu1.

Fig. 2.6: Facies description summary related to wave-dominated coastal environments. (A-C) Facies O1 is characterised by J-shaped burrows (j) in a structureless mudstone to siltstone commonly composed of centimetric intervals rich in bioclasts (b) that are provisionally attributed to the extinct genus Inoceramus. (D) Facies O1 can be barren of bioturbation. (E) From the bottom to the top, the three first centimetres corresponds to Facies O2 that is characterised by an alternation of mudstone/siltstone with millimetric siltstone to very fine-grained sandstone laminae having sharp bases exhibiting cross-laminations and parallel-laminations (white dashed lines) and marked by an intense bioturbation composed of Chondrites (c) ichnotaxon; above it, Facies C1 predominates; it is a very fine- to fine-grained sandstone characterised by an intense bioturbation with the following preserved ichnotaxa: Phycosiphon (p), Palaeophycus (pa) and Skolithos (s), along with the presence of small-scale cross-laminations (black dashed lines). (F) Facies C2 is a fine- to medium-grained sandstone characterised by the presence of bioclasts (b); it is moderately bioturbated with the presence of Skolithos (s) and Ophiomorpha? (o?) ichnotaxa (G). (F, G)

Facies C2 is marked by small-scale to large-scale cross-stratifications (dashed lines). Facies C3 (H, I, J, K) consists of medium-grained sandstones composed of horizontal to sub-horizontal plane-parallel laminations with common occurrence of SCS and rare HCS (dashed lines) having a relatively low degree of bioturbation (J), mainly Skolithos (s) ichnotaxon. Facies C4 (L, M, N) corresponds to medium- to coarse-grained sandstones containing bioclasts (b) and occurrences of granule- and pebble-rich laminae highlighting inclined parallel laminations (dashed line). Black and white rectangles represent the vertical scale in centimetres.

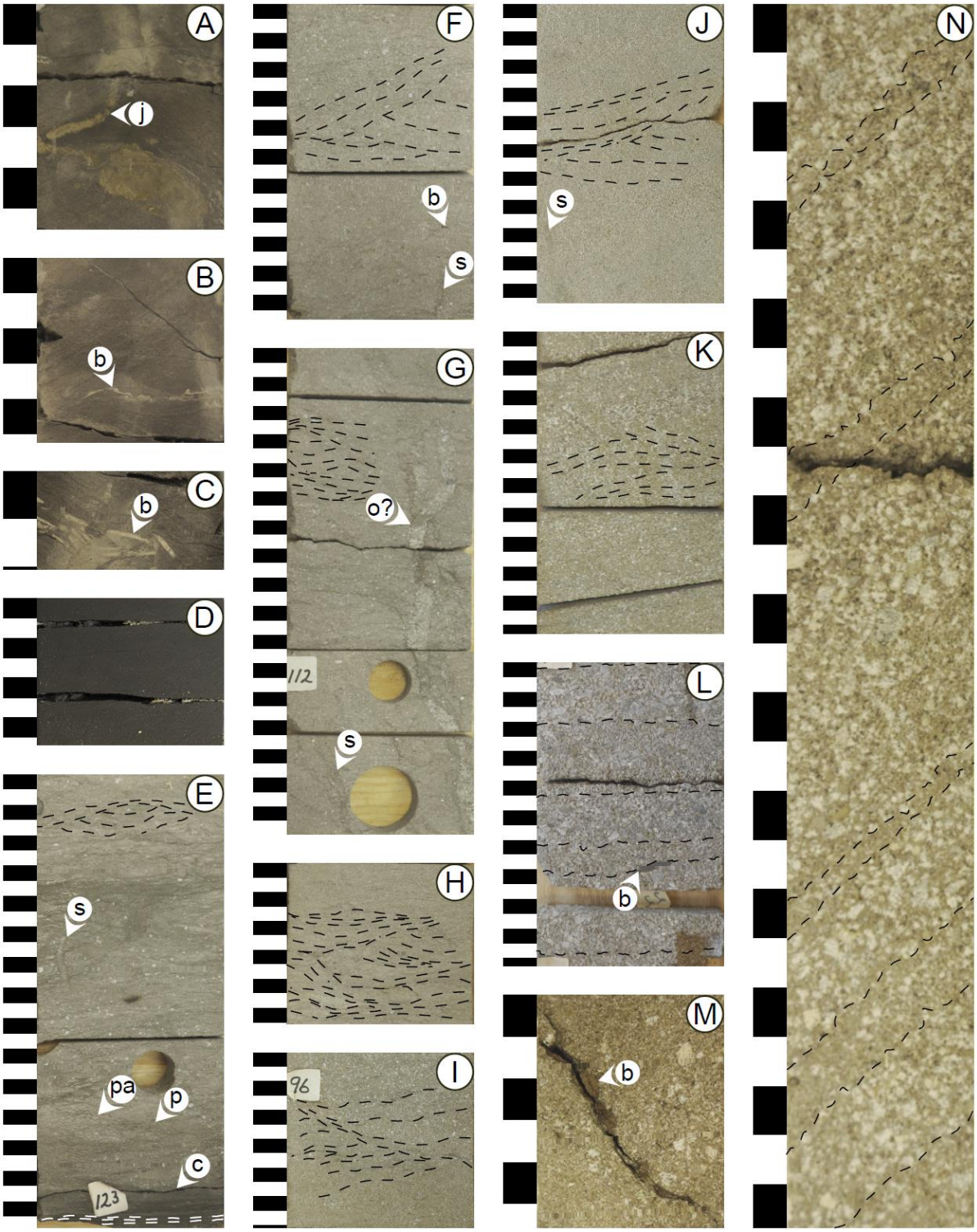

Facies Co1 consists of coarse- to very coarse-grained sandstones at the base, whereas the top is dominated by fine-grained sandstones or siltstones (Table 2.1, Figs. 2.7F, 2.7G, 2.7H, 2.7I, and Figs. 2.Cc, 2.Cd in *Supplementary data 2.C*). Co1 is characterised by normal grading, with less commonly inversely-graded deposits at the base (Figs. 2.7F, 2.7G). Co1 is currently deposited over mudstones and siltstones of facies O1. Co1 usually includes gravels and mudstone clasts at its base. Commonly, Co1 is commonly composed of armored mudstone clasts (i.e., a mudstone clast surrounded by gravels/pebbles at its periphery; Figs. 2.7H, 2.7I). The base of Co1 can be strongly erosional and is often capped by massive sandstones. Bed thickness of Co1 range from a few centimetres up to 90 centimetres. Cm-thick deposits are characterised by coarse-grained sandstones with a well-defined erosional base (Fig. 2.7F); in such deposits, the lower part corresponds to structureless massive coarse-grained sandstones, while the upper part is fining upward to fine-grained sandstones exhibiting plane parallel laminations. Such Co1 deposits can, in some cases, be difficult to discriminate from cm-thick deposits of Tu1. Deposits including clasts larger than coarse sand grains are attributed to Co1 (Fig. 2.7F), whereas deposits containing finer clasts are attributed to Tu1 (Fig. 2.7D). The cm-thick deposits of Co1 can be folded due to slumping and/or warped due to small-scale boudinage (syn-tectonic deposition). Dm-thick deposits of Co1 are strongly erosional at their base and overlain by thick and massive coarse-grained sandstones deprived of any sedimentary structure. Less commonly, the base of these deposits can be marked by flame structures (e.g., in well 6406/12-3A at -4160.40 m, Fig. 2.Cc in *Supplementary data 2.C*). The massive and structureless sandstones are commonly capped by thinner fine-grained sandstones or siltstones exhibiting planar parallel laminations (Fig. 2.7G), or less frequently by ripple-cross laminations (e.g., in well 6406/12-3A at -4151.50 m, Fig. 2.Cc in *Supplementary data 2.C*). Such dm-thick deposits of Co1 can be folded due to slumping. Clasts are angular to rounded. Mudstone clasts, coal or shell fragments are also usually observed in Co1 (Figs. 2.7H, 2.7I).

Facies De1 is made of conglomeratic mudstones including silt- to boulder-size clasts, with the rare presence of mudstone clasts, shell fragments and plant remains (Table 2.1, Figs. 2.7J, 2.7K, and Figs. 2.Cd, 2.Ce in *Supplementary data 2.C*). De1 is mud-supported; the clasts are rounded to very angular and commonly have a polygenic origin. The base of De1 is generally slightly erosional (Fig. 2.7K). Two types of conglomeratic mudstones were observed: (i) the first type is structureless with a chaotic arrangement of the clasts and rare occurrences of mudstone clasts (Fig. 2.7J). The thickness of such deposits ranges from a few centimetres up to seven decimetres and are often associated with coarse or very coarse-grained sandstones (e.g., in well 6406/12-3S from -3530.10 to -3529.10 m, Fig. 2.Cd in *Supplementary data 2.C*); (ii) the second type of De1 exhibits an internal organisation of the clasts. Clasts are normally graded in a mud-supported matrix (Fig. 2.7K). The thickness of these deposits range between a few centimetres up to about ten centimetres. Such deposits are often associated with O1 and with mm-thick Tu1 deposits (Fig. 2.7K).

Fig. 2.7: Facies description summary related to ***subaqueous coarse-grained delta environments****. (A) Millimetric Tu1 deposits characterised by very-fine to fine-grained sandstones with a sharp base (red dashed line) and a normal grading (yellow triangle). (B, C) Folded mm-scale Tu1 deposits due to slumping (f: fold axis): Tu1 deposits also exhibit other syn-sedimentary structures such as small-scale boudinage (bo). (D) Centimetric Tu1 deposits have a well pronounced erosional base (red dashed line) and a normal grading (yellow triangle); they are made up of a medium-grained sandstone that can be affected by*

small-scale normal faults (white dashed lines). (E) Decimetric Tu1 deposits are composed of a well-defined erosional base (red dashed line) overlain by a massive medium-grained sandstone, followed by parallel laminations in a fine-grained sandstone evolving upwards to trough cross-beddings and current ripples (r) in a very fine-grained sandstone. Thin siltstones to mudstone finally cap the succession. (F) Centimetric Co1 deposits are characterised by coarse-grained sandstones with a well-defined erosional base (red dashed line); the lower part corresponds to a structureless massive coarse-grained sandstone including gravel grains, while the upper part is fining upward (yellow triangle) to fine-grained sandstones commonly displaying plane parallel laminations. (G) Decimetric Co1 deposit has a sharp base (red dashed line), followed by a thick and massive coarse-grained sandstone often deprived of any sedimentary structure. The base of the deposit shows inverse grading (orange triangle followed by a normal grading (yellow triangle) up to fine-grained sandstones or siltstones showing planar parallel laminations. (H) Decimetric Co1 deposits exhibiting armored mudstone clasts (am)...

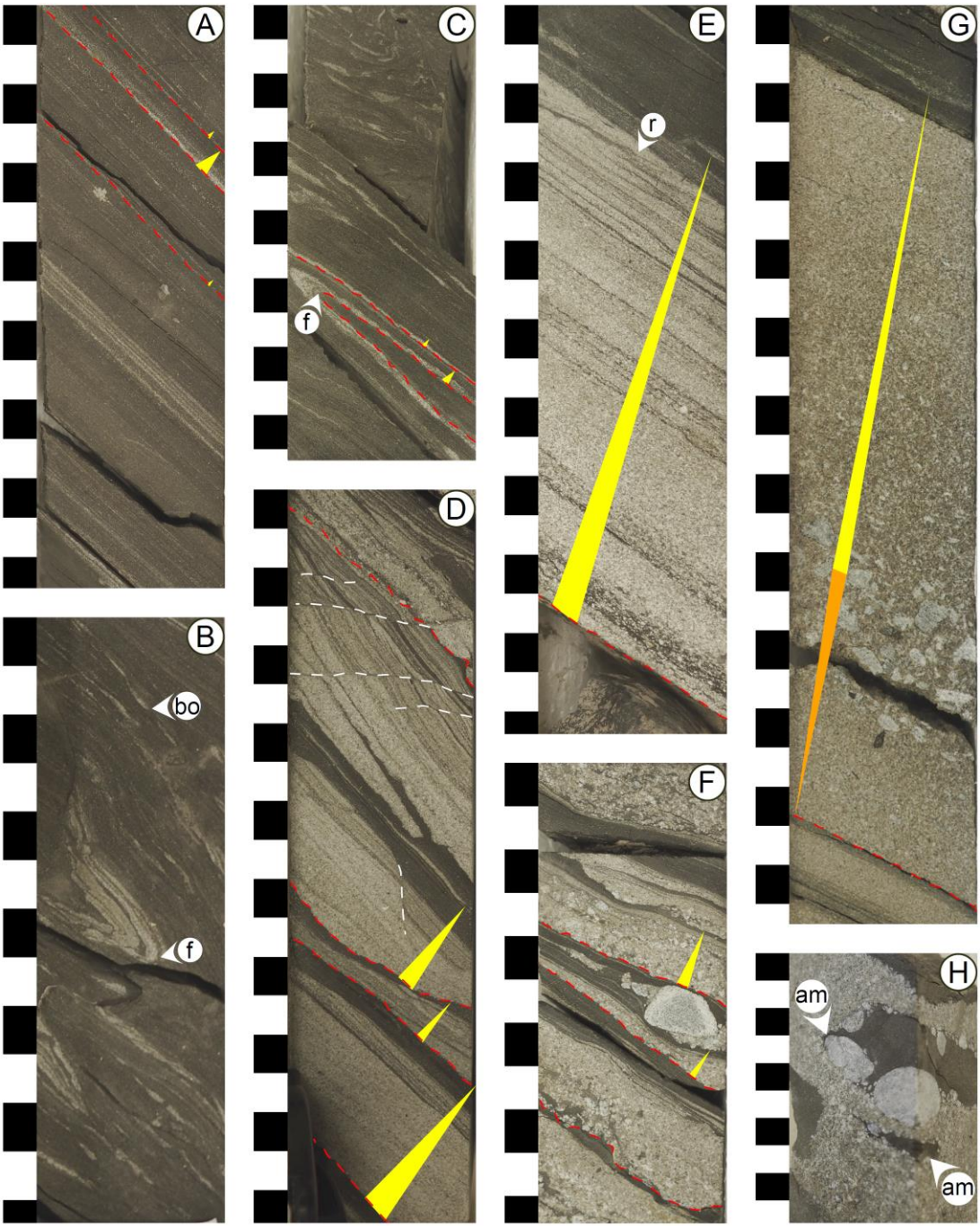

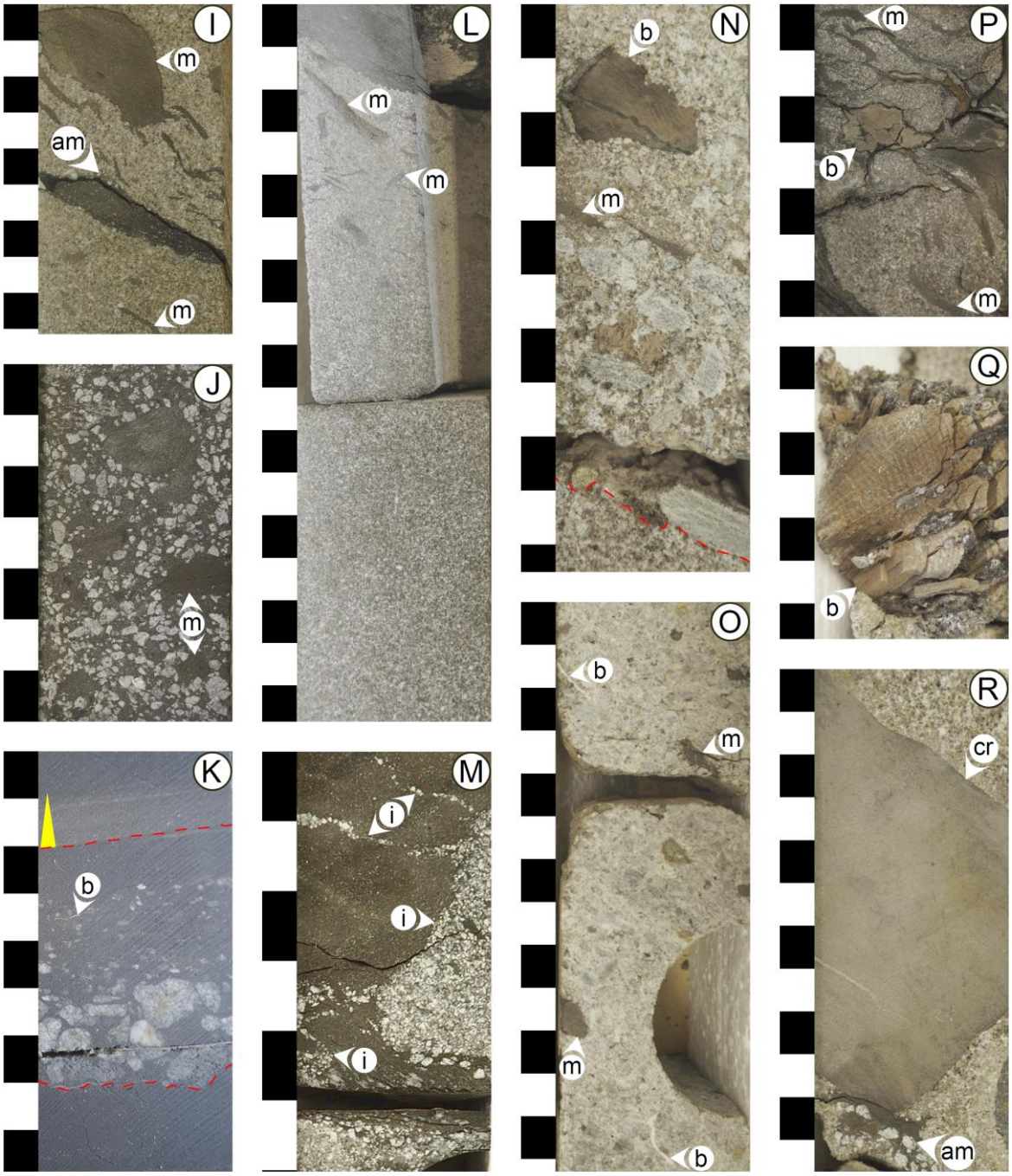

Fig. 2.7 (continued): ... (I) Decimetric Co1 deposits having elongated mudstone clasts (m). (J) Decimetric De1 conglomeratic mudstone deposits composed of mudstone clasts (m) showing a chaotic arrangement of the clasts. (K) Centimetric De1 conglomeratic mudstone deposits characterised by an internal organisation of the clasts including bioclasts (b) and a slightly erosional base (red dashed line); De1 deposits are often associated with O1 as well as with millimetric Tu1 deposits showing a sharp base and a normal grading (yellow triangle). (L) Facies Hy2 consists of massive coarse- to very coarse-grained sandstones with a common presence of mudstone clasts (m). (M) Hy2 is characterised by sand injectites (i) commonly observed in the above layers, principally when they are mudstones. (N, O, P, Q, R) Hy1 consists of grain-supported conglomerates composed of a large panel of clasts varying in size between boulders to silts with occurrences of mudstone clasts (m), armored mudstone clasts (am), bioclasts (b) such as shell fragments, plant materials and fragments of carbonate rocks (cr). Black and white rectangles represent the vertical scale in centimetres.

Facies Hy1 is made of grain-supported conglomerates; Hy1 is therefore poorly to very poorly sorted (Table 2.1, Figs. 2.7N, 2.7O, 2.7P, 2.7Q, 2.7R, and Figs. 2.Cd, 2.Ce in *Supplementary data 2.C*). Hy1 is composed of a large panel of clasts varying in size between silts and boulders. Clasts are often angular to very angular. Mudstone clasts are commonly found with elongated to rounded shapes (Figs. 2.7N, 2.7O, 2.7P). Armored mudstone clasts are also frequently observed (Fig. 2.7R). Hy1 is structureless, and very often exhibits an inverse grading (e.g., in well 6406/12-2 from -4003.20 to -4002.80 m, Fig. 2.Ce in *Supplementary data 2.C*). The base of Hy1 is slightly erosional (Fig. 2.7N). In addition to mudstone clasts, coal, shell fragments, plant materials and fragments of carbonate rocks are also observed in Hy1 (Figs. 2.7N, 2.7O, 2.7P, 2.7Q, 2.7R). Bed thickness of Hy1 ranges from 20 cm up to 3 m.

Facies Hy2 consists of well to poorly sorted massive coarse- to very coarse-grained sandstones, with common occurrences of mudstone clasts (Table 2.1, Figs. 2.7L, 2.7M, and Figs. 2.Cd, 2.Ce in *Supplementary data 2.C*) whose size range between coarse sands up to cobbles (Fig. 2.7L). Very rare armored mudstone clasts are observed (e.g., in well 6406/12-2 at -4000.50 m, Fig. 2.Ce in *Supplementary data 2.C*). Hy2 is commonly composed of clasts up to granule size, which are commonly sub-rounded to very angular, and having a polygenic origin. Hy2 is structureless, but however commonly exhibit an inverse grading (e.g., in well 6406/12-3S from -3716.10 to -3713.00 m, Fig. 2.Cd in *Supplementary data 2.C*). The base of Hy2 is often erosional. Elongated mudstone clasts (Fig. 2.7L) and sand injectites in the above mudstone layers are commonly observed (Fig. 2.7M). Bed thickness of Hy2 ranges from 10 cm up to 1.05 m.

5.1.3. Depositional models

Two main depositional environments are reconstructed for the Middle to Late Jurassic syn-rift successions of the study area. These two depositional environments can occur subsequently, passing from a wave-dominated shoreface to foreshore environment (Fig. 2.8A) to a coarse-grained deltaic environment (Fig. 2.8B) or, conversely, from a subaqueous deltaic environment to a wave-dominated coastal environment.

5.1.3.1. Wave-dominated coastal environment

A progressive evolution in the degree of bioturbation is inferred between O1 and C4, with a highly bioturbated (O1) to non-bioturbated sedimentary environment (C4) (Fig. 2.8A). Moreover, the grain size evolves from mudstones (O1) to coarse-grained sandstones (C4). Wave-generated structures such as HCS and SCS, along with wave ripples, imply shallow water and wave action (de Raaf et al., 1977). In addition, the presence of the *Chondrites* ichnotaxon in O2, compared to the presence of *Skolithos* ichnotaxon in C1 to C3, reveals that O2 corresponds to a deeper depositional environment than C1, C2, and C3 (Walker, 1992; Pemberton et al., 2012). All these observations support the interpretation of O1 to C4 as belonging to a wave-dominated coastal environment.

Alternatively, O1 was deposited in a deep and quiet environment. The presence of the bivalve genus *Inoceramus* indeed implies a significant water column (from several hundred to several thousand metres) and therefore, below the storm wave base. The epibenthic species of *Inoceramus* thrived on the substratum, confined to the continental shelves and slopes. *Inoceramus* is commonly found in anoxic to sub-oxic bottom-water conditions (Thiede & Dinkelman, 1977; Ludvigsen & Beard, 1997). In contrast, O2 is interpreted as belonging to the zone between the storm and the fair-weather wave bases. This zone is described as a proximal offshore environment, also known as the offshore transition (Bardaji et al., 1990; Reading, 2009). The proximal offshore zone refers to a quiet environment (mudstones and siltstones), in which high-energy events (i.e., storms) are inferred based on the occurrence of silty to sandy laminae exhibiting wave action (de Raaf et al., 1977; Bardaji et al., 1990; Reading, 2009).

In turn, C1 deposited above the fair-weather wave base, thereby suggesting a lower shoreface environment where small-scale wave-generated structures are common (de Raaf et al., 1977; Bardaji et al., 1990; Reading, 2009; Dashtgard et al., 2021). C2 likely deposited within the breaker zone between the fair-weather wave base and the mean low water (MLW), where wave action predominated as inferred from the presence of small-scale to large-scale HCS and SCS (Reading, 2009). C2 is described as belonging to the middle shoreface. Deposition of C3 is interpreted to be located just below mean low water (MLW), where large-scale SCS and HCS are dominant; C3 is thus attributed to the upper shoreface (Reading, 2009). The sporadic presence of coarser grains (i.e., granules, pebbles) in the shoreface (facies C1, C2 & C3) suggests a proximity to the foot of the upstream beach, from which bigger clasts are reworked by wave energy (Bardaji et al., 1990; Roberts et al., 2013; Gallagher et al., 2016). Moreover, the angularity of the granules and pebbles implies a short transport distance and thus, a high proximity to the sediment source (Fitzgerald et al., 1992).

Finally, the C4 depositional environment most probably correspond to the foreshore, located in the swash-backwash zone between the mean low water (MLW) up to the seaward-inclined wave-built beach ridge or beach berm (Bardaji et al., 1990; Otvos, 2000; Reading, 2009; Hayes et al., 2010). The alternation of well-sorted sandstones with granule- and pebble-rich layers in C4 likely reflects the progradation of wave-built beach ridges. Beach ridges built under wave action are known in the literature as “storm ridges”, “storm berms” or simply “berms” (Bardaji et al., 1990; Fitzgerald et al., 1992; Otvos, 2000; Reading, 2009; Hayes et al., 2010). The angularity of the granules and pebbles within the berm deposits suggests a proximity to the sediment source (Fitzgerald et al., 1992). Recent provenance and petrophysical studies (within the greater Fenja area) revealed the presence of detrital kaolinite likely originating from the local Frøya High, reworked by the weathering of the granitic basement (Jones et al., 2020).

This facies succession (Fig. 2.8A) between offshore mudstones (O1) and the foreshore (C4) corresponds to a typical coastal environment dominated by wave energy (De Raaf et al., 1977; Wright et al., 1979, 1985; Short, 1984; Wright & Short, 1984; Walker, 1992; Clifton, 2005; Reading, 2009; Reineck & Singh, 2012; Yu et al., 2018; Dashtgard et al., 2021).

5.1.3.2. Coarse-grained deltaic environment

For the Tu1 sequence, the sedimentary succession (including the normal grading) is interpreted as a typical Bouma sequence (Bouma, 1962), which is however rarely complete (Fig. 2.7E). Such gravity-driven deposits correspond to turbidites generated by a turbidity flow. Mm-thick deposits are commonly composed of Td and Te terms, whereas cm-thick deposits are commonly composed of Tb and/or Tc capped by Te characteristic of the final suspension fallout. Dm-thick deposits are commonly composed of Ta, Tb with less commonly Tc, Td and Te.

In turn, Co1 was differentiated in two categories based on sediment thickness. Dm-thick Co1 deposits include a strong erosional base and the frequent presence of inverse grading above it, passing to massive and structureless coarse-grained sandstones capped with fine-grained sandstones. Such deposits are characteristic of the Lowe sequence (Lowe, 1982) and are generated by concentrated density flows. Deposition at the base of the eventite is controlled by frictional freezing due to grain-to-grain interaction, whereas deposition at the top of the layer is governed by partially turbulent flows. Inversely graded beds represent deposition as traction carpets (Fig. 2.7G). Concentrated density flow can transport clasts larger than coarse grains, in contrast to turbidity currents. The threshold of coarse sand-grade clasts differentiates the cm-thick deposits of Tu1 and Co1 (Mulder & Alexander, 2001).

In contrast, De1 is a conglomeratic mudstone interpreted to be deposited as a result of subaqueous debris flows. The mud acts as a cohesive material imparting a pseudoplastic rheology to the deposits. The two major depositional processes for debris flow deposits are en-masse or freezing (Mulder & Alexander, 2001). Hy2 corresponds to a structureless, well-sorted, massive coarse- to very coarse-grained sandstone. Based on the Mulder and Alexander (2001) classification, Hy2 is generated during hyperconcentrated density flow *sensu lato* (grain-flow). Major observed processes are grain-to-bed and grain-to-grain collisions with potential fluidisation, liquefaction and injection mechanisms (Fig. 2.7M). Localised inverse grading is observed and expressed by the development of traction carpets.

In turn, Hy1 is a structureless and poorly to very poorly sorted grain-supported conglomerate, containing clasts up to boulder size with frequent inverse grading. Hy1 is interpreted to be generated during hyperconcentrated density flow *sensu stricto* implying the development of traction carpets. The difference between Hy1 and Hy2 deposits is the size of the clasts, since Hy2 is dominated by coarse- to very coarse-grained sandstones (deposited during grain-flow) whereas Hy1 is a grain-supported conglomerate deposited during hyperconcentrated density flow *sensu stricto* (Mulder & Alexander, 2001).

Tu1, Co1, De1, Hy1 and Hy2 are thus generated by different types of subaqueous sedimentary density flow (SSDF). In reference to the classification of Mulder and Alexander (2001), the SSDF deposits are named based on their dominant flow types. Tu1 corresponds to turbidity flow deposits, Co1 to concentrated flow deposits, De1 to debris-flow deposits, Hy2 to grain-flow deposits and Hy1 to hyperconcentrated flow deposits. Excluding cohesive flow deposits (De1), and based on the previous observations and interpretations, it is noteworthy that there is a continuum between each non-cohesive flow deposit (Tu1, Co1, Hy1 and Hy2).

Each SSDF facies is characterised by a relatively well-defined erosional base, which denotes the beginning of a new subaqueous gravity flow event. Such SSDF deposits are related to palaeo-slopes on which regularly occurred soft-sediment deformation linked with slumping and/or syn-sedimentary tectonic activity (Figs. 2.Ca, 2.Cc in *Supplementary data 2.C*).

The recognition of SSDF deposits supports the distinction of different sub-environments within coarse-grained syn-rift deltaic systems (Gilbert, 1885; Falk and Dorsey, 1998; Longhitano, 2008; Gobo et al., 2014; Elliott et al., 2015; Gobo et al., 2015; Henstra et al., 2016b). However, the absence of deltaic topsets (Fig. 2.4B) in this study can be caused either by an intense erosion, or a non-deposition caused by the development of unsteady subaqueous conical deltas. This prevents the attribution of subaqueous delta-scale clinoforms to conical deltas, or to Gilbert-type deltas (Patruno & Helland-Hansen, 2018; Surlyk & Bruhn, 2020). For this reason, the depositional environment corresponding to facies Tu1, De1, Co1 Hy1 and Hy2 is referred to a “coarse-grained delta”. Note that the co-occurrence of conical and Gilbert-type deltas was recently reported from the Viking Group (Jones et al., 2020). This study also revealed, based on a provenance study, that local sediment sources likely originated from the Frøya High (Jones et al., 2020).

The subaqueous (coarse-grained) deltaic environment (Fig. 2.8B) can be subdivided into two sub-environments: (i) the delta front, corresponding to the proximal delta (foresets) where deltaic deposits are thick, unsorted and structureless with the frequent occurrence of inverse grading (Hy1 and Hy2) due to the steep slope and (ii) the prodelta to distal toe of the delta (bottomsets) that exhibits a more gentle slope, where deltaic deposits are thinner, better sorted and composed of several internal structures along with the presence of normal grading (Co1 and Tu1). Cohesive flows (De1) can be observed both in the proximal and more distal parts of the deltaic environment. Debris flow (De1) transformation is not well understood yet, and may evolve into concentrated density flow (Co1), hyperconcentrated density flows (Hy1 and Hy2) (Hampton, 1972, 1975; Mulder & Alexander, 2001) or turbidity flow (Tu1) (Haughton et al., 2009) due to either potential dilution and mixing (Hampton, 1972), hydraulic jumps (Weirich, 1988), entrainment at the top of the SSDF sediment body (Fisher, 1983), or a combination of those three mechanisms (Fisher, 1983).

Debris flow deposits (De1) mainly occur in the delta front environment depending on the size of available particles and mud proportion (Hampton, 1972, 1975; Mulder & Alexander, 2001). Within debris flow deposits, chaotical facies are mainly observed in the delta front, whereas well-sorted deposits travelling longer distances are commonly found in the prodelta. The coarse-grained deltaic succession (Fig. 2.8B) evolves from distal offshore mudstones (O1) to the distal prodelta sub-environment with the presence of numerous turbidity flow deposits (Tu1), then passing to the proximal prodelta sub-environment with the dominance of concentrated flow deposits (Co1). These are followed by a distal delta front sub-environment including stacked grain-flow deposits (Hy2) and, finally, to proximal delta front succession dominated by hyperconcentrated density flow deposits *sensu stricto* (Hy1). Debris flow deposits (De1) are commonly found within the delta front and the proximal prodelta, but may travel long distances to reach deeper offshore environments (O1) in the basin plain.

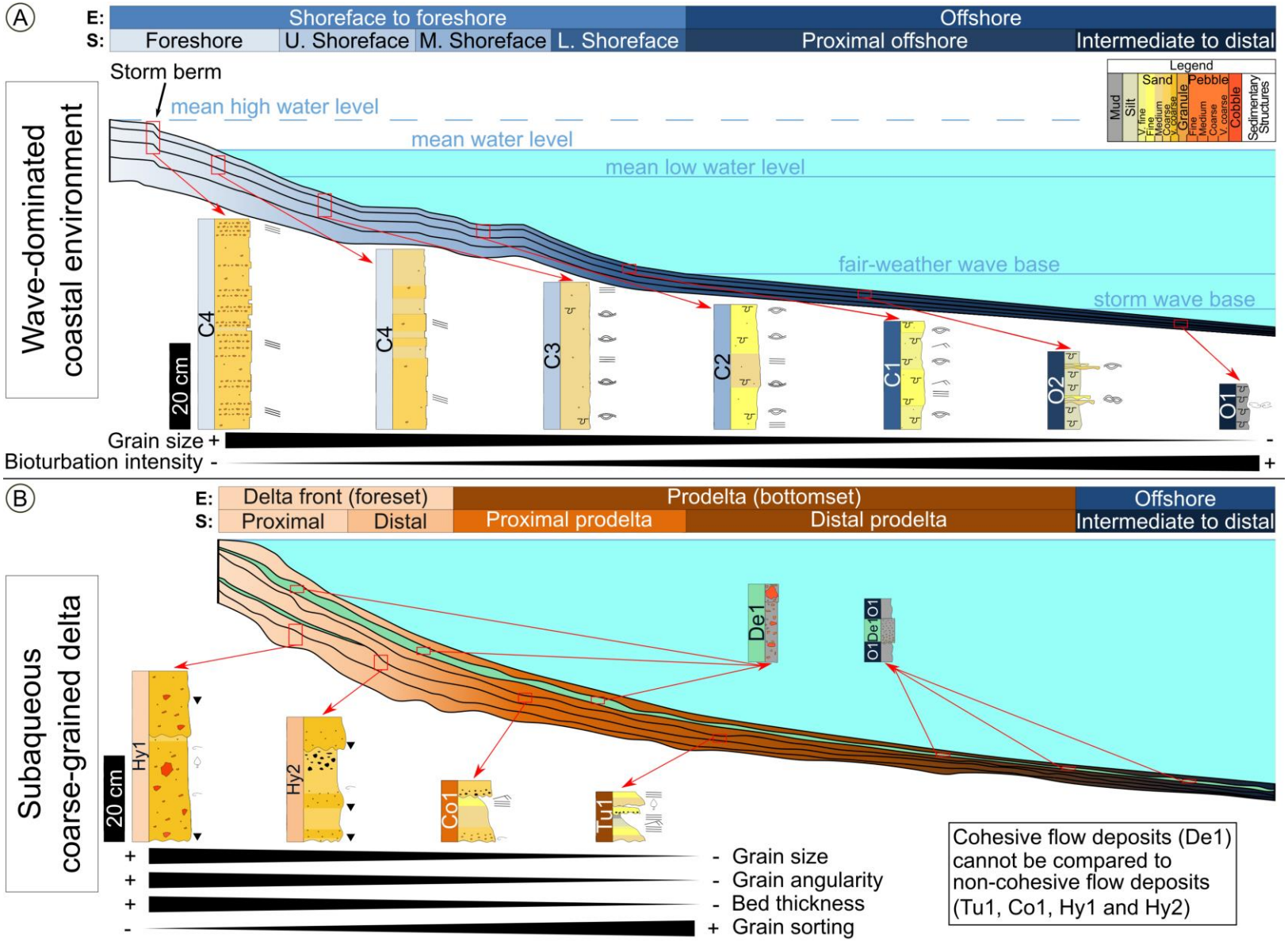

Fig. 2.8: Depositional models and synthetic sedimentary logs for (A) the wave-dominated coastal environment, and (B) the coarse-grained deltaic environment; with E.: main environment and S.: sub-environment. Legend including clast composition and sedimentary structures of the synthetic sedimentary logs are shown on Fig. 2.Ca in Supplementary data 2.C.

5.2. Stratigraphic sequences and gamma-ray log signatures

Seismic unconformities (SUs) identified in *Fig. 2.4* were also described from sediment cores and gamma-ray logs (Fig. 2.9). The use of checkshot data allows the SUs to be calibrated on the sequence boundaries (SBs) *sensu* Embry (1993, 1995). The Walther's law is commonly not observed just above the SB *sensu* Embry (1993, 1995), since the basinward shift of coastal environments exhibit a transgressive gap of one or two sub-environments. In a wave-dominated shoreline including coarse-grained deltas and shoreface to foreshore environments, the parasequence boundary displays an abrupt shift to finer-grained facies (McLaughlin, 2005). Such a shift is observed in our core data and is marked by an abrupt increase in gamma-ray values (Fig. 2.9).

Two SBs *sensu* Embry (1993, 1995) were observed based on core and log data, the KU (Figs. 2.9A, 2.9B, 2.9C) and the 3U4 (Figs. 2.9A, 2.9D, 2.9E). Those two SBs are merged with the subaerial unconformity. The other SBs (NTF, IMU, 2U3, 5U6, 6U7, and BCU) were identified on gamma-ray (GR) logs. GR logs associated with facies description therefore offers the possibility to define gamma-ray log signatures (Fig. 2.10). Note that most SBs for the 10 studied wells are located close to the land and are, therefore, often merged with the subaerial unconformity.

Well log signatures can be used to decipher depositional environments using mainly GR log data (Fig. 2.8). In addition to the GR logs, neutron and density logs help to discriminate facies similarities such as calcite stringers or coal beds. In a wave-dominated coastal environment, two sedimentary successions can be identified (Fig. 2.10). A coarsening-upward sequence exhibits a transition from high GR values to low GR values corresponding to the transition between offshore and shoreface to foreshore environments. Conversely, a fining-upward succession highlights a smoothed evolution from low GR values (i.e., foreshore to shoreface environments) to high GR values (offshore facies). Coarsening-upward and fining-upward sequences in a wave-dominated coastal environment are continuous and smooth (Fig. 2.10).

Forced regression (*sensu* Posamentier et al., 1992) on well-logs is illustrated by a sharp contact between shoreface/foreshore facies and offshore mudstones, and imply an abrupt decrease in GR values of at least 50 API (Fig. 2.10). Alternatively, the GR-log signature within a coarse-grained deltaic environment reveals two different coarsening-upward and fining-upward successions, as compared to the wave-dominated coastal system. The coarsening-upward sequence exhibits a transition from high GR values (prodelta) to low GR values (delta front), whereas, in turn, the fining-upward sequence is characterised by the rapid transition between low GR values (delta front) and high GR values (prodelta to offshore) (Fig. 2.10). Sandy shoreface/foreshore and delta front environments, which are both characterised by spiky and low GR log values, can be further discriminated based on well log signatures. Whereas a smoothed and progressive evolution of the GR log curve often reflects a foreshore to shoreface environment, a drastic change in GR values (plus or minus 50 API in a few metres) most likely corresponds to a coarse-grained deltaic environment.

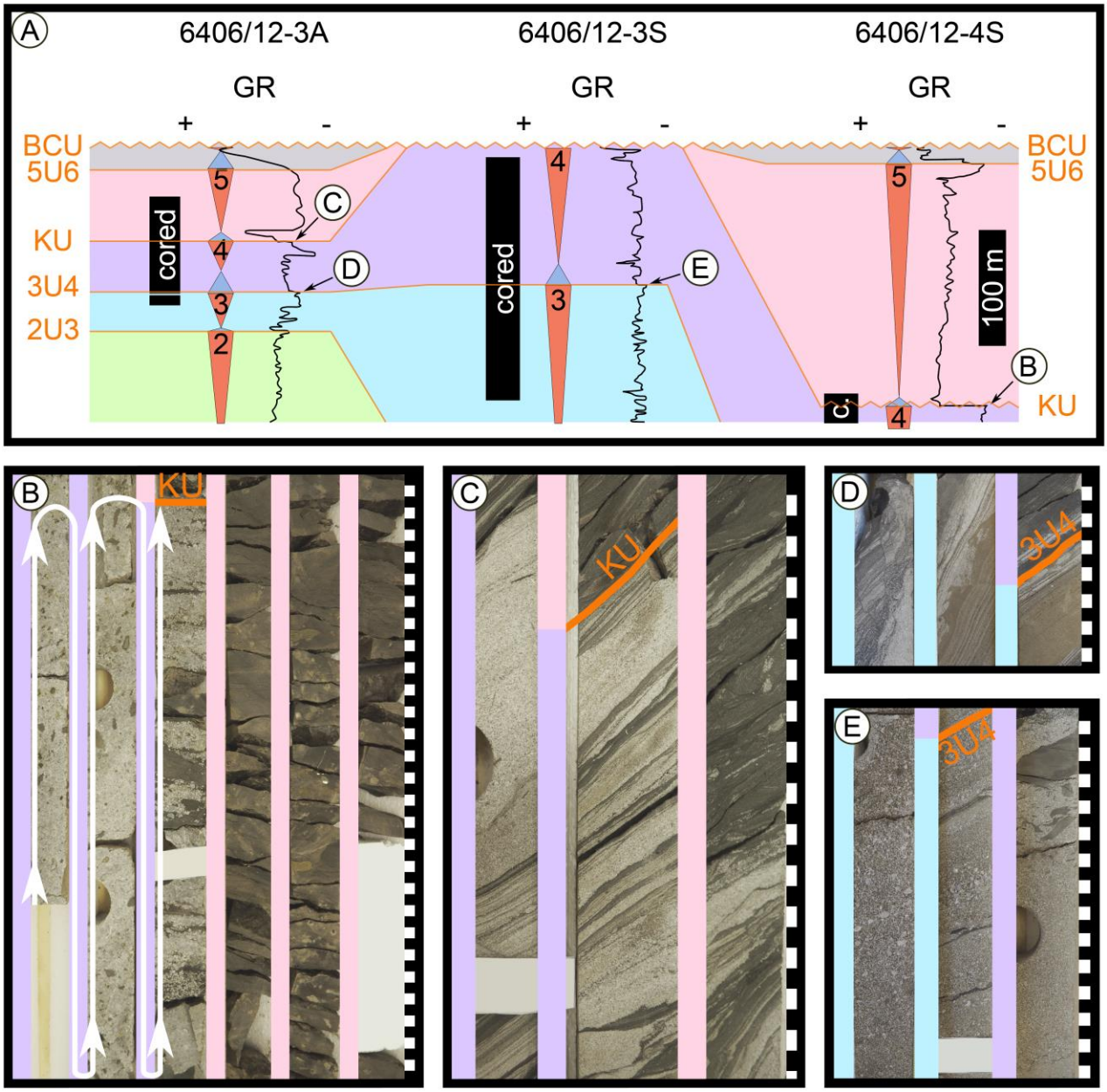

Fig. 2.9: Observation of the sequence boundaries (SBs) sensu Embry (1993, 1995) in sedimentary cores. (A) Well correlation highlighting the cored SBs and the location of the core pictures. (B) Core picture of well 6406/12-4S showing the KU location with grain-supported conglomerates (Hy1) in Sequence 4 (purple) evolving to a bioturbated mudstone (O1) after the SB in Sequence 5 (pink). (C) Core picture of well 6406/12-3A showing the KU location with a stacked succession of decimetric Co1 deposits in Sequence 4 (purple) passing rapidly after the SB to a mudstone (O1) with millimetric Tu1 deposits in Sequence 5 (pink). (D) Core picture of well 6406/12-3A showing the 3U4 location with an amalgamated succession of decimetric Tu1 and Co1 deposits in Sequence 3 (blue) passing rapidly after the SB to a succession dominated by offshore mudstones (O1) in Sequence 4 (purple). (E) Core picture of well 6406/12-3S showing the 3U4 location with an amalgamated succession of grain-supported conglomerate deposits (Hy1) in Sequence 3 (blue) evolving after the SB to a succession dominated by massive coarse- to very coarse-grained sandstones rich in mudstone clasts (Hy2) in Sequence 4 (purple). Black and white rectangles in core pictures represent the vertical scale in centimetres. Well location is shown on Fig. 2.1D and colour of the sequences is shown on Fig. 2.Ca in Supplementary data 2.C.

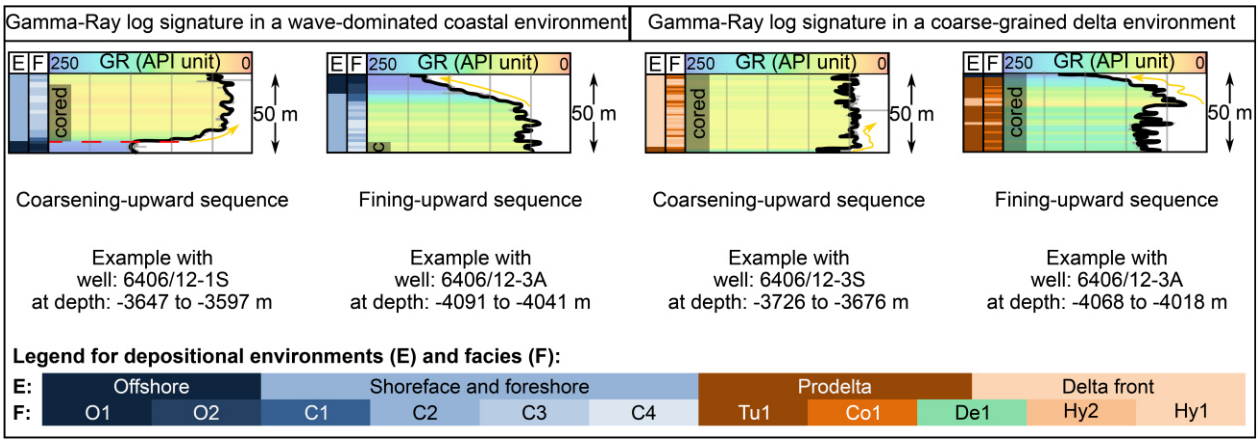

Fig. 2.10: Gamma-Ray (GR) log signatures highlighting coarsening- and fining-upward sequences in a wave-dominated coastal environment (the two GR logs on the left side) and coarse-grained deltaic environment (the two GR logs on the right side). GR-log signatures have been built based on facies description (F) and depositional environment identification (E). The orange arrows indicate the coarsening- or fining-upward trend, and the red dashed line outlines the sharp base of a forced regression.

5.3. Chronostratigraphy

Based on the reappraised chronostratigraphic framework, nine dinoflagellate cyst zones have been established, thus assigning a chronostratigraphic age to the identified stratigraphic sequences S1 to S7: the pre-rift assemblage is identified within the "*D. willei & M. valensii*" dinoflagellate cyst zone, and dated to the pre-Middle Bathonian. S1 started during the Middle Bathonian and ended during the Middle Callovian; it is identified within the zone "*C. hyalina & P. calloviensis*". S2 corresponds to the "*R. aemula & W. fimbriata*" dinoflagellate cyst assemblage, ranging between the Middle Callovian and the beginning of the Late Oxfordian. S3 corresponds to the zone "*S. crystallinum & E. galeritum*" dated from the Late Oxfordian to the Early Kimmeridgian.

In turn, S4 corresponding to the assemblage "*S. paeminosa & P. pannosum*", started during the Early Kimmeridgian and terminated during the Late Kimmeridgian. S5 is identified by the dinoflagellate cyst assemblage "*R. cladophora & E. luridum*", starting during the Late Kimmeridgian and ending during the Early Tithonian. S6 is defined by the assemblage "*P. insolitum & O. patulum*", which started during the Early Tithonian and ended during the Late Tithonian. S7 commenced during the Late Tithonian and terminated approximately at the end of the Middle Berriasian, and corresponds to the "*G. villosa & E. expiratum*" zone. The post-rift assemblage is dated to the post-Middle Berriasian, as revealed from the "*K. corrugatum & P. pelliferum*" dinoflagellate cyst zone (Fig. 2.5). A detailed composition of the nine dinoflagellate cyst zones is provided in the *Supplementary data 2.D*.

6. Discussion

6.1. Sedimentological and stratigraphic evolution

Seven stratigraphic sequences, ranging in age between the Middle Jurassic and the Early Cretaceous, were identified within the Viking Group from the southern Halten Terrace (Fig. 2.2). According to Catuneanu (2019) the seven identified sequences are 3rd order stratigraphic sequences based on their average thicknesses and temporal scales. From these sequences, the sedimentological and stratigraphic evolution of the study area was analysed for the syn-rift period of the Intra-Melke and Rogn formations, and their respective distal equivalents, the Melke and the Spekk formations, based on the entire database available (well-logs, cores, biostratigraphy and seismic data).

The tectonostratigraphic scheme is then compared to other studies tackling the rifting phase within the Central Graben area (e.g., Verreussel et al. (2018) (Fig. 2.11A). 2D palaeoenvironmental maps based on published rift concepts (Ravnås & Steel, 1998; Folkestad et al., 2014; Jones et al., 2020) are also presented here and will be discussed for each rifting stage (Fig 2.12). Finally, 3D sedimentological and stratigraphic block-diagrams based on the 2D maps are provided and discussed (Fig. 2.13).

6.1.1. Rift initiation stage (S1 - Middle Bathonian to Middle Callovian)

The rift initiation stage is composed of S1 dated between the Middle Bathonian and the Middle Callovian. S1 (Figs. 2.4, 2.5, 2.11) is bounded by two SBs: at the base, the “Near Top Fangst” (NTF), and, at the top, the Intra-Melke Unconformity (IMU). From well log data, a clear log signature in wells 6406/11-1S, 6406/12-1S and 6406/12-3A exhibits an environmental shift from offshore (O1) to prodelta (Tu1) environments. S1 is a mudstone-dominated sequence characterised by the deposition of prodeltaic and offshore deposits. Locally, 6406/12-3B exhibits coarser delta front deposits on the hanging wall of the Vingleia Fault Complex (Halten Terrace) (Fig. 2.12).

The top of S1 is marked by a strong erosional event (IMU), correlated to a global sea-level drop (Haq, 2017), while climate conditions alternated between arid and more humid periods (Price, 1999) (Fig. 2.5). S1 corresponds to the rift initiation stage (early-rift phase), during which isolated faults (with small offsets) initiated the formation of coarse-grained deltas within offshore environments (Jones et al., 2020) (Figs. 2.11B, 2.12). Our results are consistent with the conclusions of Verreussel et al. (2018), which documents a rift initiation stage starting during the Early Bathonian and ending in the Early Callovian for the North Sea (Fig. 2.11A). The rift initiation stage reported here appears to commence and terminate slightly earlier in the Central Graben compared to in the Norwegian Sea (Fig. 2.11).

6.1.2. Rift-climax stage (S2, S3 and S4 - Middle Callovian to Late Kimmeridgian)

The rift-climax stage is composed of S2, S3 and S4, dated between the Middle Callovian and the Late Kimmeridgian. S2, S3 and S4 (Figs. 2.4, 2.5, 2.11) are bounded by two SBs: at the base, the Intra-Melke Unconformity (IMU) and, at the top, the Kimmeridgian Unconformity (KU). From well log data, S2 to S4 are conglomerate-dominated sequences indicating deposition within (coarse-grained) delta front and prodelta environments. Locally, at well location 6406/12-1S (remote from the main faults), offshore mudstones are observed (Fig. 2.12). The top of S4 is marked by a strong erosional event (KU) that corresponds to a well-defined transgressive surface (SB *sensu* Embry (1993, 1995)) merged with a subaerial unconformity, therefore highlighting a transgressive pattern between S4 (rift-climax stage) and S5 (final rift stage) (Figs. 2.11, 2.12). The Top of S4 highlights a clear tectonic transition which may also be interpreted as a decrease in subsidence/accommodation, and is favourable for the development of the Kimmeridgian Unconformity (KU).

S2, S3 and S4 occur coevally with a global sea-level rise (Haq, 2017), and a relatively humid climate (Price, 1999) (Fig. 2.5). This conglomerate-dominated succession, bounded by the IMU and the KU, characterises the rift-climax stage (peak-rift phase), during which asymmetric wedge-shaped geometries increases in thickness towards the VFC (Figs. 2.4, 2.11B, 2.12). Jones et al. (2020) reported that the peak-rift episode, in the greater Fenja area, is marked by an increase in fault linkage strain in the basin depocentre resulting in significant footwall uplift and a considerable erosion of the Frøya High. Our results are consistent with the conclusions of Verreussel et al. (2018) that highlight an increase in tectonic activity and a rift-climax stage occurring during the Early Callovian and ending at the Early/Late Kimmeridgian boundary (Fig. 2.11A). The rift-climax stage appears to commence and terminate slightly earlier in the Central Graben compared to in the Norwegian Sea (Fig. 2.11).

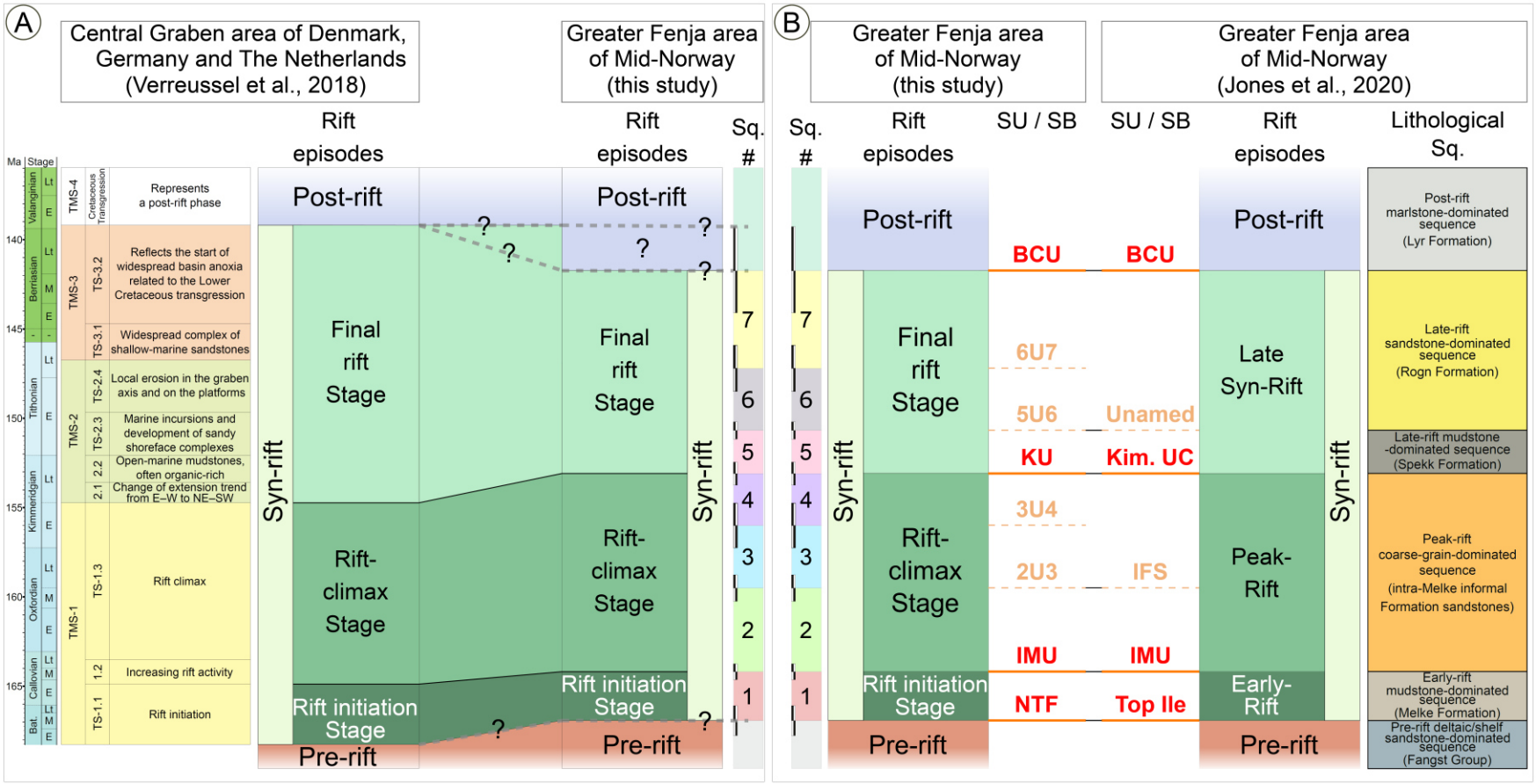

Fig. 2.11: Comparison to other tectonostratigraphic studies: (A) Comparison of the stratigraphic framework (this study) to the tectonostratigraphic mega-sequences (TMS) of Verreussel et al. (2018) focusing in the Central Graben area of Denmark, Germany and the Netherlands with on the left the chronostratigraphic chart imported from TS Creator and based on Ogg et al. (2016) (B) Comparison of the stratigraphic framework (this study) to the tectonostratigraphic sequences of Jones et al. (2020) located in the greater Fenja area, with the observed seismic unconformities (SU) and their equivalence observed on well logs and cores defined as sequence boundaries (SB). The abbreviations of the SU/SB are: Near Top Fangst (NTF), Intra-Melke Unconformity (IMU), Kimmeridgian Unconformity (KU), Base Cretaceous Unconformity (BCU), 2U3 (Unconformity between sequence 2 and 3), 3U4, 5U6 and 6U7 bringing to light the 7 seismic sequences (S1, S2, S3, S4, S5, S6 and S7). The abbreviations in Jones et al. (2020) of the SU/SB are: BCU (Base Cretaceous Unconformity), Top Ile, IMU (Intra-Melke Unconformity), IFS (intra-fan shale), Kim. UC (Kimmeridgian Unconformity) and the "Unamed" SB has been observed but not precisely named.

6.1.3. Final rift stage (S5, S6 and S7 - Late Kimmeridgian to Middle Berriasian)

The final rift stage is composed of S5, S6 and S7. The final rift phase started in the Late Kimmeridgian and ended up approximately at the end of the Middle Berriasian (Fig. 2.5). S5, S6 and S7 (Figs. 2.4, 2.5, 2.11) are bounded by two SBs: at the base, the Kimmeridgian Unconformity (KU), and, at the top, the Base Cretaceous Unconformity (BCU). From well log data, S5, S6 and S7 correspond to shoreface and foreshore environments, instead of coarse-grained deltas (Fig. 2.12). S5, S6 and S7 are mudstone to sandstone-dominated successions that are characterised by the deposition of shoreface/foreshore to offshore mudstones. Locally, at well location 6406/12-2, coarse-grained deltas still thrived (Figs. 2.12, 2.13).

From well log data, conspicuous evidence for forced regressions are observed in S5, S6 and possibly S7. S5 (bounded at the base by KU, and at the top by 5U6) exhibits a conspicuous forced regression (*sensu* Posamentier et al., 1992) in two wells (6406/12-3A and 6406/12-4S). Well 6406/12-3A (Fig. 2.Cc in *Supplementary data 2.C*, and Fig. 2.Ea in *Supplementary data 2.E*) is dominated by offshore mudstones at its base and a sharp evolution to coarse-grained shoreface and foreshore sandstone deposits. Furthermore, in well 6406/12-4S, S5 reveals the occurrence of isolated coarse-grained shoreface to foreshore sandstones encased in deep offshore mudstones, which confirms the hypothesis of a forced regression. Alternatively, S6 was highly eroded by the BCU in most wells. In well 6406/12-1S, S6 exhibits a sharp evolution between shoreface to foreshore sandstones deposited on top of offshore mudstones, thus also confirming the occurrence of a forced regression (Figs. 2.Ea, 2.Eb in *Supplementary data 2.E*). It is, however, not possible to confirm the presence of a forced regression during S7 due to strong Cretaceous erosional events (BCU).

Fig. 2.12: 2D palaeomaps and the associated summary diagrams: (A) 12 palaeomaps from late S1 (map #1) to late S7 (map #12) taking into account both well logs and cores and using seismic interpretations as background data, as well as published rift concepts (Ravnås and Steel, 1998; Folkestad et al., 2014; Jones et al., 2020). Approximated absolute ages of each map are displayed on the chronostratigraphic chart imported from TS Creator and based on Ogg et al. (2016)…

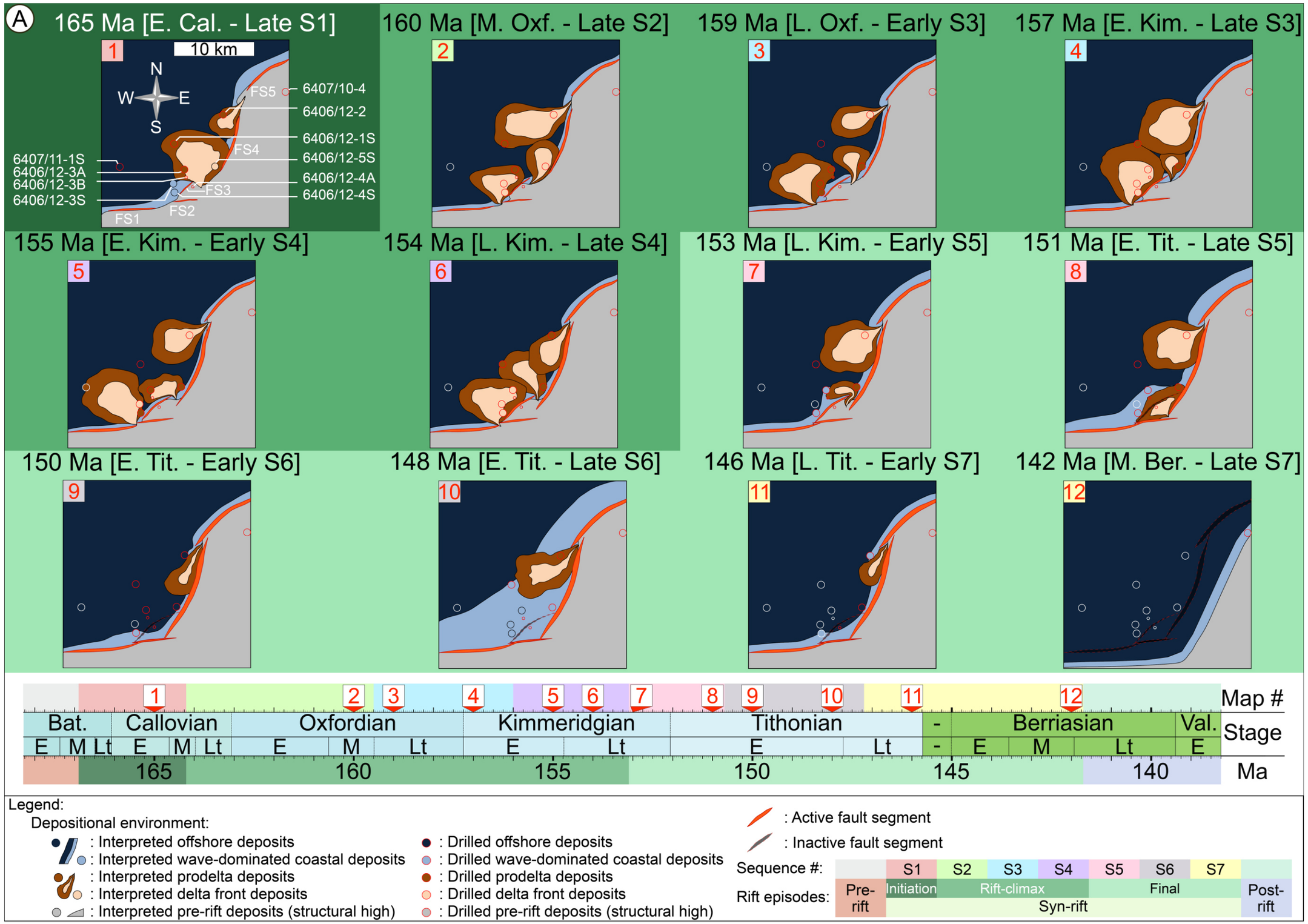
A
165 Ma [E. Cal. - Late S1]
1
10 km
N
W
E
S
FS5
FS4
FS3
FS2
FS1
6407/10-4
6406/12-2
6406/12-1S
6406/12-5S
6406/12-4A
6406/12-4S
6407/11-1S
6406/12-3A
6406/12-3B
6406/12-3S
160 Ma [M. Oxf. - Late S2]
2
159 Ma [L. Oxf. - Early S3]
3
157 Ma [E. Kim. - Late S3]
4
155 Ma [E. Kim. - Early S4]
5
154 Ma [L. Kim. - Late S4]
6
153 Ma [L. Kim. - Early S5]
7
151 Ma [E. Tit. - Late S5]
8
150 Ma [E. Tit. - Early S6]
9
148 Ma [E. Tit. - Late S6]
10
146 Ma [L. Tit. - Early S7]
11
142 Ma [M. Ber. - Late S7]
12
Bat.
Callovian
Oxfordian
Kimmeridgian
Tithonian
Berriasian
Val.
E M Lt E M Lt E M Lt E Lt E Lt - E M Lt E
165 160 155 150 145 140
Map #
Stage
Ma
Legend:
Depositional environment:
: Interpreted offshore deposits
: Interpreted wave-dominated coastal deposits
: Interpreted prodelta deposits
: Interpreted delta front deposits
: Interpreted pre-rift deposits (structural high)
: Drilled offshore deposits
: Drilled wave-dominated coastal deposits
: Drilled prodelta deposits
: Drilled delta front deposits
: Drilled pre-rift deposits (structural high)
: Active fault segment
: Inactive fault segment
Sequence #:
S1 S2 S3 S4 S5 S6 S7
Rift episodes:
Pre-rift
Initiation
Rift-climax
Final
Post-rift
Syn-rift

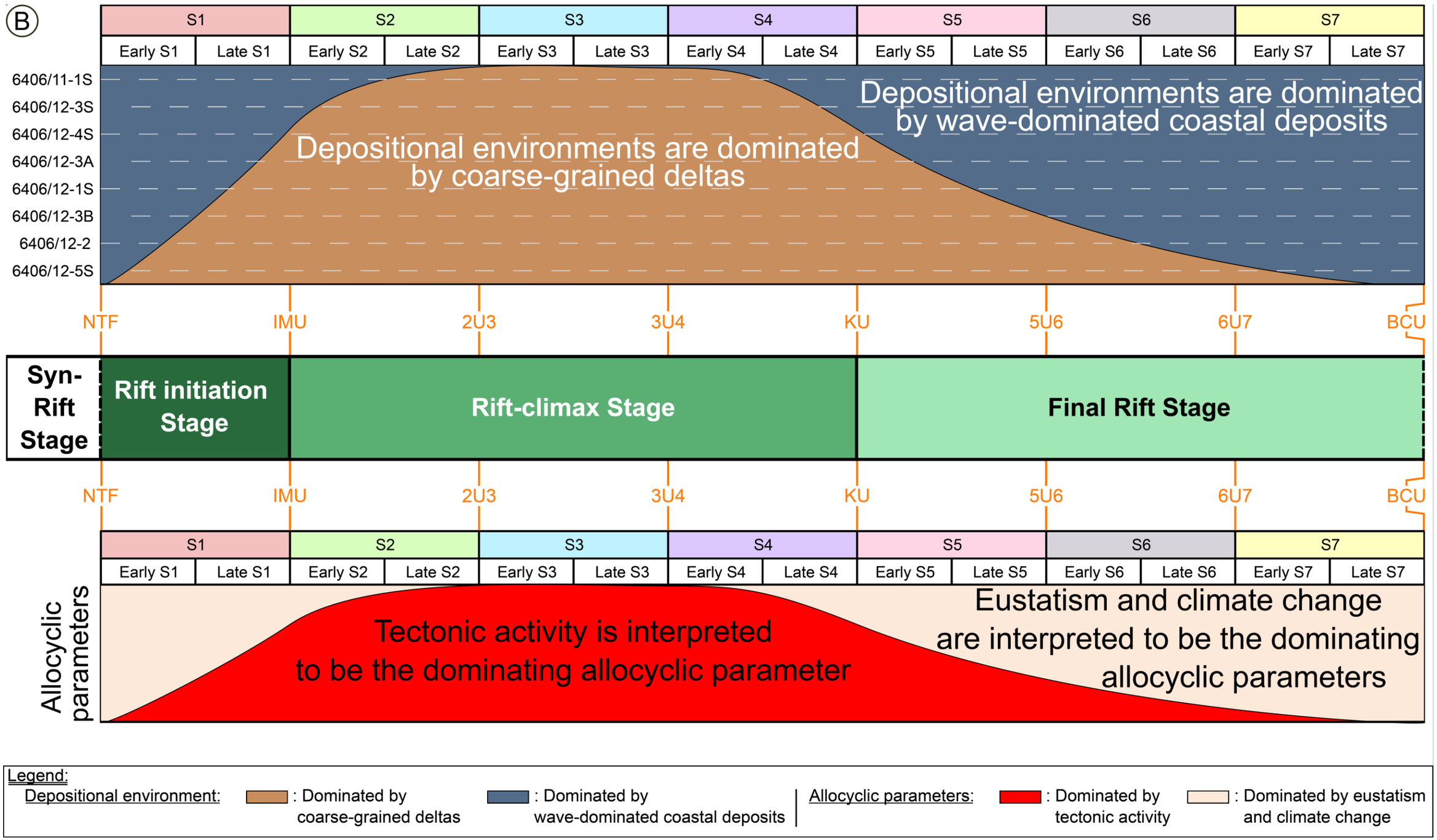

Fig. 2.12 (continued): ... (B) Upper diagram shows the depositional environments for each well and each sequence, the second diagram corresponds to the syn-rift stages with the associated sequence boundaries (SBs: Near Top Fangst (NTF), Intra-Melke Unconformity (IMU), Kimmeridgian Unconformity (KU), Base Cretaceous Unconformity (BCU), 2U3 (Unconformity between sequence 2 and 3), 3U4, 5U6 and 6U7), the last diagram presents the dominating allocyclic parameters (tectonic vs. eustatism and climate change) that are directly linked to the observed depositional environments (upper diagram).

S5 to S7 are marked by rapid (about 400 ka) and short-term sea-level fluctuations of circa 100 metres (Haq, 2017) (Fig. 2.5). During S5, the climate switched from a purely humid climate to more alternating periods of aridity and humidity (Price, 1999). In turn, the climate evolved towards more arid conditions at the termination of S6, while climate conditions turned out to more alternating periods of aridity and humidity during S7 (Fig. 2.5). In contrast, the Cretaceous post-rift period is characterised by the return of a more humid climate (Price, 1999). S5, S6 and S7, bounded by the KU and the BCU, correspond to the final rifting episode (late rift phase) in the greater Fenja area; this phase is characterised by a decrease in fault activity along with an increase in thermal subsidence rates, which favoured the drowning of structural highs and a reduction in coarse-grained sediment supply (Jones et al., 2020) (Figs. 2.11B, 2.12). Our results are consistent with the conclusions of Verreussel et al. (2018), which highlight fault activity and salt motion coevally with a period of organic-rich shale deposition and sand starvation starting at the Early/Late Kimmeridgian boundary and ending towards the Berriasian/Valanginian boundary (Fig. 2.11A). The final rift stage appears to start slightly earlier, and end later, in the Central Graben compared to in the Norwegian Sea (Fig. 2.11), as further developed in the discussion.

Recent studies focusing on the Kimmeridge Clay Formation throughout northwest Europe (which is coeval to the Spekk Formation) have attributed the increase in TOC widely observed during this period to orbitally-controlled climatic changes mainly triggered by eccentricity changes (Atar et al., 2019). Moreover, rapid (about 400 ka) and significant (100 m) sea-level falls that induce a suite of forced regressions during the deposition of the Rogn Formation has been outlined in this study (Fig. 2.5). Our results therefore strengthen the hypothesis of a significant impact of the long eccentricity cycle on the development of black shales widely deposited during the Late Jurassic in the Boreal Seaway (Armstrong et al., 2016). The transition between the Melke and the Spekk mudstones (enriched in TOC) occurred coevally during S4, as observed throughout the whole North Sea area (Partington et al., 1993; Fraser et al., 2002; Armstrong et al., 2016; Verreussel et al., 2018; Atar et al., 2019).

6.2. Dating uncertainty

The syn-rift sub-stages (Fig. 2.11A) identified within the greater Fenja area (Mid-Norway) occur slightly later (between 0.7 and 1.6 Ma) than in the sequences described by Verreussel et al. (2018) for the Central Graben (DK, NL, D). This time shift of +0.7 to +1.6 Ma observed in the Halten Terrace (Norwegian Sea) compared to the Central Graben (North Sea) most probably reflects the northward migration of the rifting activity (Alves et al., 2009; Nirrengarten et al., 2017). This time shift is, however, within the range of uncertainty for the defined sequences leading to difficulties in validating this hypothesis.

The main discrepancy between this study and the study of Verreussel et al. (2018) is the time shift of 2.5 Ma at the end of the final rift stage, since the final rift stage ended 2.5 Ma earlier in the Norwegian Sea compared to in the North Sea. It is noteworthy, however, that the study of Verreussel et al. (2018) relies on 230 studied wells that allowed the establishment of a refined dinoflagellate cyst zonation. In contrast, in the present study, only 10 wells have been used to establish biozones, while only 4 of these wells (6406/12-2, 6406/12-4A, 6406/12-5S and 6407/10-4) encountered the last sequence of the final rift stage (i.e., S7). From these wells, only 2 of them contained available biostratigraphic reports (6406/12-2 and 6406/12-4A).

Moreover, the upper part of S7 was largely eroded in the 4 wells mentioned above. Based on these considerations, we propose that the end of the final rift stage most likely corresponds to the Berriasian/Valanginian boundary, instead of the Middle to Late Berriasian boundary.

6.3. Sediment sources and physiognomy of depositional systems

Former studies dealing with sediment provenances reported the identification of distinct garnet types, and thus different possible sources (Jones et al., 2020). The abundance of detrital kaolinite in marine sediments has been interpreted as weathering products from the local granitic basement of the Frøya High. In addition, the occurrence of landslide blocks linked to earthquakes was mainly associated to the rift-climax stage due to slope instability and collapse along exposed fault scarps (Jones et al., 2020). Hence the sediment sources of coarse-grained deltaic environments are predominantly local due to erosion of adjacent palaeo-highs (Frøya High), even if more distal sources likely also entered the depositional area from the footwall drainage system (Fig. 2.13).

Coarse-grained deltas developing along steep basin margins commonly form wedge-shaped to isolated fan bodies that cover an area <10 km² (Gawthorpe et al., 1990). During the syn-rift stage, the smallest coarse-grained deltas reconstructed within this study have an approximate length of 6 km and a width of 3 km, whereas the largest subaqueous deltas have an approximate length of 9 km and a width of 7 km and likely occur as isolated fan bodies (Fig. 2.12A). Based on recent studies focusing on seismic data within the Central South segment of the Halten Terrace, schematic palaeogeographic maps were proposed for the Viking Group (Elliott et al., 2015; Jones et al., 2020). Elliott et al. (2015) reported the occurrence of coarse-grained deltas with a minimum dimension of 3.5 km × 2.5 km, and a maximum dimension of 8.5 km × 6.5 km. Alternatively, Jones et al. (2020) documented the co-existence of both small coarse-grained deltas (4 km × 3 km) and big subaqueous deltas (7 km × 9 km).

The shoreline-shelf system is commonly continuous over several hundred to thousands of square kilometres. The width of the shelf in a wave-dominated setting is narrower compared to tidal- or fluvial-dominated shelves (Nyberg & Howell, 2016). Modern wave-dominated shelf profiles are commonly steeper compared to tide-dominated shelf profiles (Ainsworth et al., 2011). On average, wave-dominated coastal systems reach a 20 m water column after 2 km distance from the shore, whereas tide-dominated coasts reach a 20 m water column at approximately 100 km from the shore (Ainsworth et al., 2011). Hence steepened shelf profiles are observed for wave-dominated coasts compared to the flattened shelf profiles of the tide-dominated coasts (Ainsworth et al., 2011). Modern wave-dominated shoreface to foreshore environments have an average width of 2 km with an oscillation from 200 m (narrowest) to 20 km (widest) (Ainsworth et al., 2011). In this study, the narrowest wave-dominated shoreface to foreshore systems reconstructed from well data are estimated to be around 400 m, whilst the widest shelf is estimated at circa 8 km. For comparison purposes, Elliott et al. (2015) proposed palaeogeographic maps with shoreface environments ranging between 800 m and 8 km in width, whereas Jones et al. (2020) reported shoreface settings having a width ranging from 400 m to 4 km.

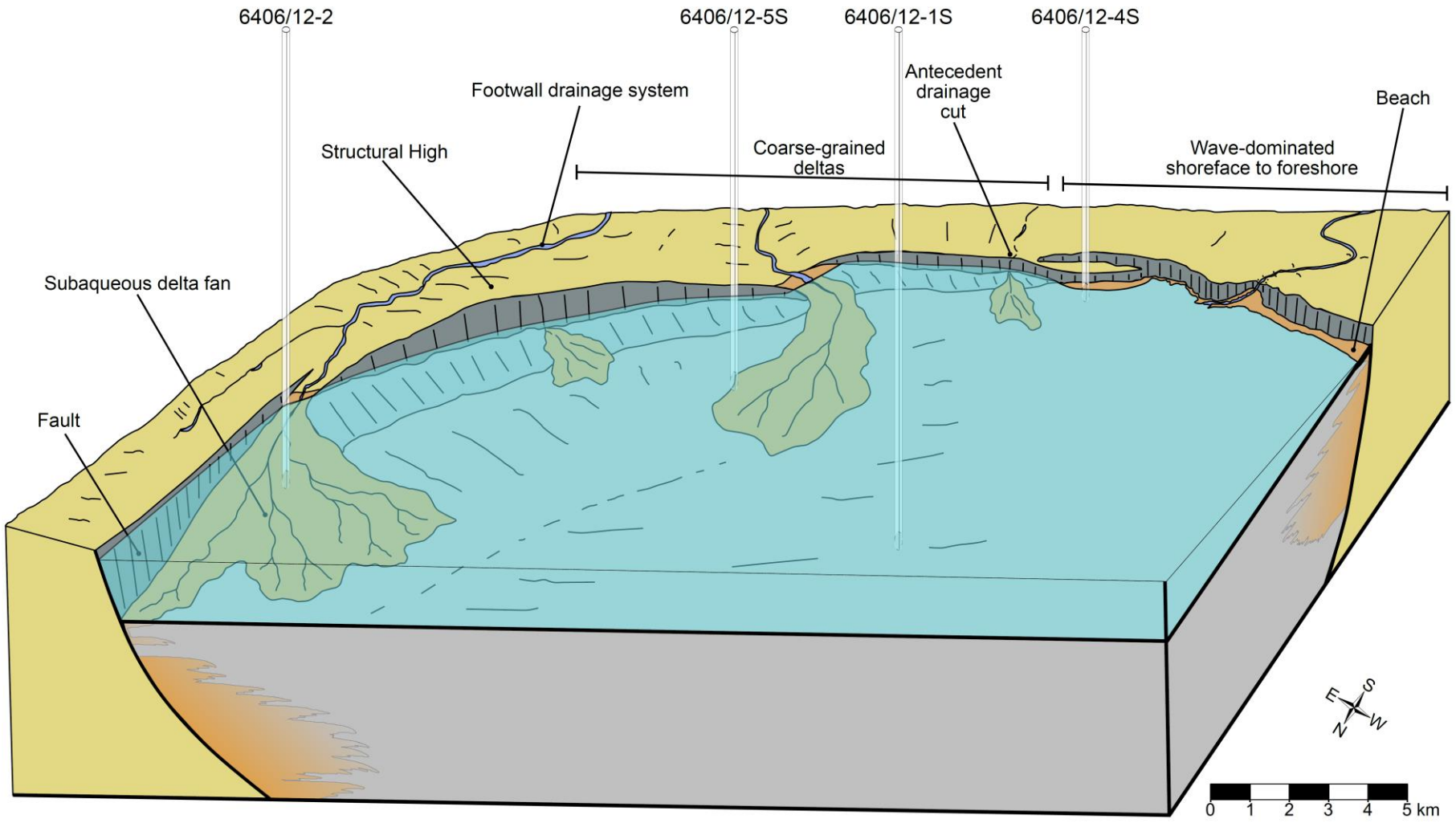

Fig. 2.13: 3D-block diagram illustrating the palaeo-environments of the Viking Group during the beginning of the final rift stage in the Halten Terrace (Late Sequence 5 - Early Tithonian, map #8 in Fig. 2.12A). Approximate well locations outline the penetrated depositional environments. Well 6406/12-2, 6406/12-5S, 6406/12-4S and 6406/12-1S encountered delta front, prodelta, shoreface to foreshore and offshore environments, respectively.

6.4. Coarse-grained sediments and their significance in sequence stratigraphy

The boundaries between each subaqueous sedimentary density flow (SSDF) are, in some cases, difficult to establish because a continuum exists between flow types (Mulder & Alexander, 2001; Mulder & Hüneke, 2014; Talling et al., 2012). Sediment distribution and accumulation within coarse-grained deltas are controlled by multiple factors such as delta location and physiognomy, internal geometry, basin-fill architecture but also by climate, sea-level changes and sediment supply (Gawthorpe et al., 1990; Postma, 1995). Syn-rift coarse-grained deltas commonly have a wedge-shaped geometry as they bound a master fault, thereby implying higher sedimentation rates in the foresets and lower accumulation in the bottomsets.

Fining-upward sequences within a coarse-grained delta system characterise transgressive cycles, whereas regressive cycles are inferred from coarsening-upward sequences. The description (and interpretation) of fining- and coarsening-upward successions within coarse-grained deltaic systems have been thus improved with the use of flow transformation classification, as documented in this study. For instance, a thinning and fining-up succession evolving from hyperconcentrated density flow to turbidity flow deposits (e.g., in well 6406/12-3A from -4138.07 to -4134.25 m, Fig. 2.Cc in *Supplementary data 2.C*) is characterised, at the base, by flow transformation between hyperconcentrated density flows *sensu lato* and concentrated density flows, whereas the top of the sequence exhibits flow transformation between concentrated density flows and turbidity flows. Conversely, a coarsening-upward succession as characterised by turbidity flow deposits evolving into hyperconcentrated density flow deposits (e.g., in well 6406/12-3S from -3560.56 to -3559.52 m, Fig. 2.Cd in *Supplementary data 2.C*) outlines a succession towards thicker and coarser SSDF deposits.

Flow transformation is, however, most often observed in fining-up successions compared to coarsening-up successions that usually have embedded a suite of thicker and coarser SSDF deposits with erosional bases. Fourth-order thinning and fining-up sequences (3 to 10 m thick after Catuneanu, 2019) that evolve from hyperconcentrated density flow to turbidity flow deposits (e.g., in well 6406/12-3A from -4138.07 to -4134.25 m, Fig. 2.Cc in *Supplementary data 2.C*) may stem from a waning of fault motion. In turn, the identification of fifth-order fining-up sequences (1 to 3 m thick after Catuneanu, 2019) passing rapidly from hyperconcentrated density flow to turbidity flow deposits (e.g., in well 6406/12-3S from -3558.47 to -3557.25 m and from -3557.25 to -3556.28 m, Fig. 2.Cd in *Supplementary data 2.C*) probably result from a lateral migration of the delta fan deposits (thus auto-regulating sediment budgets). Each sequence order can therefore be undertaken by tackling flow transformation and facies succession within syn-rift coarse-grained deltaic systems.

7. Conclusions and perspectives

The syn-rift evolution of the Viking Group in offshore mid-Norway exhibits the relationships between process change, tectonic activity and allocyclic mechanisms during the Middle Jurassic and the lowermost Cretaceous. The description of 11 sedimentary facies (and their association) allows the reconstruction of two main depositional environments in the Viking Group: wave-dominated coastal environments and subaqueous coarse-grained deltaic systems. Based on the description of 442 metres of sediment cores combined with well log and seismic data, seven 3rd stratigraphic sequences were established and chronostratigraphically constrained using a reappraised dinoflagellate cyst zonation. This updated biostratigraphic zonation can thus be used as a complementary dataset to calcareous nannofossils or benthic foraminifera for dating other locations within the Norwegian Sea.

The sedimentological and stratigraphic evolution of siliciclastic shallow-marine syn-rift deposits can be summarised in three main stages. The rift initiation stage, in the Halten Terrace, is marked by the predominance of coarse-grained deltas and the less development of wave-dominated shoreface to foreshore environments. This stage is most probably controlled in equal proportion by tectonic activity, eustatism and climatic change. Subsequently, the rift-climax stage, during which tectonic activity climaxed, was a period favouring the development of coarse-grained delta systems judging from the dominance of wedge-shaped geometries and intensified sediment erosion and supply. The final rift stage was marked by an aridification of the climate coupled with important short-term sea-level fluctuations and a waning of fault activity. Such rapid (about 400 ka) and significant (approximately 100 m) short-term sea-level drops triggered a succession of forced regressions during the deposition of the Rogn Formation. Finally, the description of coarse-grained deltaic facies using SSDF classifications revealed lateral variations of the delta fans and a direct impact of fault activity on sediment supply.

Sedimentological and stratigraphic data were used concurrently to build a 4D picture of the rift basin evolution and highlights the prevailing depositional environments develop during the rift initiation, the rift-climax and the final rift stages. Near-field exploration using such an integrated approach is therefore highly promising, as it further allows the prediction of lateral facies variations and heterogeneity of reservoirs. This should in turn help to quantify the risks for potential appraisal wells. In new venture explorations, the detection of wedge-shaped sedimentary bodies related to growth faults within a syn-rift siliciclastic shallow-marine system appears as a robust approach for tracking deposits with good primary reservoir properties.

8. Acknowledgements

This work forms one chapter of Romain Grime's PhD thesis. The authors thank Edison Norge AS for financing RG's PhD and Neptune Energy Norge AS for providing the database. We would like to sincerely thank Emerson E&P Software for providing high-quality support and software solutions (https://www.pdgm.com/). We thank Jonathan Furic for his critical and constructive feedback. Thanks to Tim Rice and Benjamin Kyle Bowlin for their sedimentological and stratigraphic feedbacks in addition to their contribution for English spell-checking. We thank Gabriela Mangano for her contribution for the identification of ichnotaxa. Thanks to Ian Sharp, Claudio Nicola Di Celma and David Iacopini for their valuable comments that improved the manuscript in many ways. Thanks to my three PhD reviewers, Sylvie Bourquin, David Hodgson and Thierry Mulder, and to the rest of my PhD committee members composed of Emanuela Mattioli, Pascale Huyghe and Fernanda De Mesquita Lobo Veloso who contributed to propose the final version of this manuscript.

In the syn-rift study (Chapter 2), the main conclusion highlights the relationships between process change, the prevailing depositional environments and the controlling mechanisms during the syn-rift stage. As to summarize, the rift initiation stage is marked by the development of deltaic and coastal environments and outlines the initiation of rift-related normal faults coevally with sea-level fluctuations and climatic changes. In turn, the rift climax stage corresponds to the period during which tectonic activity climaxed and favoured the development of coarse-grained delta systems. Finally, the final rift stage is typified by the development of wave-dominated coastal environments and a cessation of tectonic activity. The next chapter, entitled post-rift study (Chapter 3), focuses on the post-rift period characterised by a period of tectonic quiescence. The post-rift study (Chapter 3) is undertaken in the Dønna Terrace area, where almost 250 m of sediment cores were analysed. Chapter 3 tackles how autocyclic and allocyclic mechanisms regulate the organisation of turbidite lobe complexes.

In the post-rift study (Chapter 3), the main objective is to establish turbidite lobe stacking patterns. Based on sediment cores and well-log data, detailed sedimentological and statistical analyses have been performed to decipher the main controlling mechanisms (autocyclic vs allocyclic) on lobe architecture and geometry. Two main depositional environments (deep-marine offshore environment and deep-water turbidite lobe deposits) are reconstructed based on the identification of 10 sedimentary facies, allowing the recognition of 4 facies associations or lobe sub-environments. Three axial lobe sub-environments (channel and/or proximal lobe (CPL), mid to distal lobe (MDL), frontal lobe fringe (FLF)) and one off-axial lobe sub-environment (lateral lobe fringe (LLF)) were identified. A fifth facies association, corresponding to the distal lobe fringe (DLF), should be considered; however, based on low core picture resolution, it was not possible to discriminate between offshore marine mudstones of the LLF facies association and distal lobe fringe deposits (DLF deposits). Those 4 lobe sub-environments (CPL, MDL, FLF and LLF excluding the DLF) enable the reconstruction of lobe sedimentary dynamics (axial *vs* lateral motion). Based on a new deep-water turbidite lobe stacking pattern analysis, the post-rift study (Chapter 3) presents a novel way to identify whether autocyclic or allocyclic controlling factors predominated. Four autocyclic and three allocyclic controlling factors governing lobe architecture were discriminated. The reconstruction of both syn-rift (Chapter 2) and post-rift (Chapter 3) stratigraphic evolutions helps to decipher the controlling factors at work between syn-rift and post-rift periods.

CHAPTER 3: Post-rift study

Article submitted to Sedimentology

Title:

Autocyclic and allocyclic controls on turbidite lobe stacking pattern: the case of the Turonian to Coniacian deep-water turbidite lobe complexes (Dønna Terrace, offshore Mid-Norway)

Authors: Romain GRIME[1,2,@], Bernard PITTET[1], Philippe SORREL[1], Kévin BOULESTEIX[3], Sébastien LANDRU[4], Alexandre BOUCHE[5], Tim RICE[6], Benjamin Kyle BOWLIN[4]

[1] Univ Lyon, UCBL, ENSL, UJM, CNRS, LGL-TPE, F-69622, Villeurbanne, France.

[2] Edison Norge AS, Jattavagveien 18 – Troll Building, 4065 Stavanger, Norway.

[3] Department of Earth and Environmental Sciences, University of Manchester, Oxford Road, Manchester M13 9PL, United Kingdom.

[4] Stavanger, Norway.

[5] Emerson E&P Software, 1 rue Gramont, 75002 Paris, France.

[6] Glasgow, United Kingdom.

[@] grime.romain@gmail.com

CRediT author statement:

Romain GRIME: Conceptualization, Methodology, Software, Writing – Original Draft, Formal analysis, Investigation, Data Curation, Writing – Review & Editing, Visualization

Bernard PITTET: Supervision, Project Administration, Resources, Validation, Formal analysis, Writing – Review & Editing, Visualization

Philippe SORREL: Supervision, Project Administration, Resources, Validation, Formal analysis, Writing – Review & Editing, Visualization

Kévin BOULESTEIX: Validation, Formal analysis, Writing – Review & Editing, Visualization

Sébastien LANDRU: Validation, Formal analysis, Writing – Review & Editing, Visualization

Alexandre BOUCHE: Software, Validation, Writing – Review & Editing, Visualization

Tim RICE: Validation, Writing – Review & Editing, Visualization

Benjamin Kyle BOWLIN: Validation, Writing – Review & Editing, Visualization

Keywords: Frontal lobe fringe; Lateral lobe fringe; Post-rift; Norwegian Sea; Marulk field; Intra-Lange sandstones; Turbidite lobes; Cretaceous

1. Abstract

The mechanisms controlling the stacking patterns of deep-water lobes (autocyclic and allocyclic) are currently open to a wide range of interpretations. A study of Turonian to Coniacian deep-water lobe complexes in the greater Marulk area (Dønna Terrace, Norwegian Sea) has been undertaken to examine the balance and influences of various controlling factors based on core, well, and seismic data. As a result, both autocyclic and allocyclic forcings could be identified based on the stacking patterns of the lobe sediments. Autocyclic processes (best observed in core data) control the self-regulation of sediment dispersal and the broad evolution of lobe sub-environments. Conversely, allocyclic controls (best observed in well data) regulate axial migration within the turbidite lobe succession. While these controlling mechanisms can be difficult to discriminate, we have identified four autocyclic factors. At the bed scale, control #1 governs the self-organising system defining the bed type and number of beds within the lobe element. Lateral displacement of the lobe is a function of control #2, which regulates the spatial and temporal dispersal of sediment. Control #3 deals with the centre of gravity of the lobe. Migration of the lobe along its longitudinal or vertical axes (progradation, retrogradation, or aggradation) is determined by control #4. In addition, three allocyclic factors (#5, #6, and #7) control various sediment pulses and ultimately the general evolutionary trend of the turbidite lobe complex.

2. Introduction

“Lobe” was used for the first time to describe the “bulge” morphology of the distal part of a deep-water turbiditic system (Normark, 1970). The lobe region is bounded proximally by the submarine erosional conduit, and distally by the basin plain region (Mutti et al., 2003). The lobe has a convex-up ovoid morphology, creating a positive relief above the basin-floor (Mulder & Etienne, 2010). A recent experimental study highlights that when a turbidity current encounters a significant decrease in slope angle (slope-break), sediment deposition is favoured (Pohl et al., 2020). The architectural elements that form a lobe are hierarchical depending on the scale of observation. Lobe beds form the building blocks of a lobe. Their sedimentary structures are determined by their depositional processes varying both distally and laterally (Haughton et al., 2003; Spychala et al., 2017b). The lobe itself is one element, which may combine with others to form a lobe complex that is observable at the basin scale (Prélat et al., 2009).

During the last decade, lobe beds to lobe complexes have been intensively studied (Kane et al., 2017; Spychala et al., 2017a; Brooks et al., 2018a, 2018b; Hansen et al., 2019; Boulesteix et al., 2020a). Hodgson (2009) defines longitudinal (proximal, medial and distal) and lateral subdivisions (axis, off-axis and fringe) of turbiditic lobes. This subdivision was further improved by differentiating the frontal lobe fringe (FLF) from the lateral lobe fringe (LLF) based on lobe bed facies (Spychala et al., 2017b). A recent study by Boulesteix et al. (2020b) focusing on the muddy distal fringe of the lobe highlights that relatively thin sedimentary packages (< 70 cm) composed of marine background mudstone separating bedsets are mainly the result of autocyclic lobe mechanisms. In contrast, thicker basin-floor background

packages (> 70 cm) composed of massive marine mudstones are interpreted as being caused mainly by allocyclic processes resulting in a basin-wide decrease of sediment supply (Boulesteix et al., 2020b).

When describing geological features, factors affecting sediment supply can be difficult to discriminate. Tectonic, eustatic and climate changes are in some cases difficult to disentangle and can act conjointly during a specific period of sediment input, or starvation. Allocyclic controls are external processes that impact the sedimentary system by causing energy fluctuations, which themselves regulate sediment delivery (Beerbower, 1964; Cecil et al., 2011). Climate changes are commonly periodic and can be associated with Milankovitch cycles (Berger, 1988), whereas tectonic processes are aperiodic and can be superimposed over the effects of orbital forcing (Cecil et al., 2011). In turn, autocyclic processes can cause a redistribution of potential energy and sediment within a system where accommodation space is available (Beerbower, 1964). Autocyclic processes pervasively operate through time and may be considered as cyclic processes inherent to the system (Cecil et al., 2011). Their occurrence frequency is, however, not predetermined and is consequently aperiodic (Cecil et al., 2011). Autocyclic control on ancient deep-water turbidite lobes, such as lateral shift and compensational relief infill, have been reported in previous works (e.g., Postma and Kleverlaan, 2018; Piazza and Tinterri, 2020). Recent experimental studies also deciphered the internal processes of lateral lobe shifting and lobe compensation (Ferguson et al., 2020), while other laboratory experiments focused on the dynamics of axial lobe displacement by progradation or retrogradation combined with aggradation (Hamilton et al., 2015, 2017). Despite this, the study of allocyclic and autocyclic processes in deep-water lobes is still sketchy and appeals for further investigations from lobe beds to lobe complexes based on detailed sedimentological analyses.

This study focuses on discriminating autocyclic from allocyclic processes by analysing the stratigraphic succession of depositional sub-environments from Turonian to Coniacian deep-water turbidite lobe complexes in the Dønna Terrace, located offshore Mid-Norway. More specifically, the objectives of this study are to: (i) tackle facies sedimentology within deep-water turbidite lobes based on detailed core description analyses; (ii) define which controlling mechanism (autocyclic and allocyclic) predominate by focusing on turbidite lobe stacking patterns; (iii) modelise the depositional setting of the three studied sandstone members which are the Breiflabb, Skolest equivalent and Lysing members part of the Cromer Knoll Group.

3. Geological setting

Lobe complexes in the Norwegian Sea have been extensively studied and can contain very prolific petroleum reservoirs (Shanmugam et al., 1994). The Intra-Lange informal Formation sandstones (Doré et al., 1997a) and Lysing Formation (Dalland et al., 1988), respectively reclassified as Breiflabb Member and Lysing Member are Turonian to Coniacian deep-water turbidite lobe complexes (Gradstein and Waters, 2016). Since the early 1980s, the Lysing Member has been drilled by 136 exploration wells and is commonly defined as a primary to secondary exploration target (NPD, 2021). The study area is located in the greater Marulk area (Dønna Terrace, offshore Mid-Norway) where several turbidite lobe complexes have

been identified such as the “Snadd turbidite” complex or the “South turbidite lobe complex” (Fugelli and Olsen, 2007). A recent study using spectral decomposition reported lobate features in the Lysing Member that highlight the complexity and the spatial distribution of turbidite lobe complexes in the Norwegian Sea terraces (Hansen et al., 2021).

The Dønna Terrace is located offshore mid-Norway, north of the Halten Terrace and is bounded to the west by the Rås sub-basin part of the Cretaceous Vøring Basin, and to the east by the southern part of the Nordland Ridge (Fig. 3.1). The stratigraphy is based on Dalland et al. (1988) with some readjustments by Gradstein and Waters (2016) (Fig. 3.2). The stratigraphic interval of interest is dated between the Early Turonian and the Early Coniacian (Gradstein and Waters, 2016). This includes three sandstone members (Breiflabb, Skolest equivalent and Lysing) within the Lange Formation, composed largely of mudstones interpreted as relatively deep-water deposits (Dalland et al., 1988; Gradstein et al., 1999; Gradstein and Waters, 2016). The Breiflabb Member is generally dated to the Early Turonian. The minor sandstones observed between the Breiflabb and Lysing Members are time equivalent to the Skolest Member developed in the Møre Basin (Figs. 3.1A, 3.2). The Skolest Member is dated across the Middle/Late Turonian boundary (Gradstein and Waters, 2016), whereas the Lysing member is Late Turonian to Early Coniacian in age. The Breiflabb and Lysing Members are interpreted as deep-water fan lobe deposits accumulated on a slope or basin-floor setting (Hastings, 1987; Norsk Hydro AS, 1992; Vergara et al., 2001; Gradstein and Waters, 2016). The Lyr Fm. is a marlstone to calcareous mudstone preceding the Lange Fm. Both formations form the Cromer Knoll Gp., which was interpreted as a Cretaceous passive infill succession postdating the Jurassic rifting episode recorded in the Viking Gp (Fig. 3.2). The syn-rift phase left a structurally complex topography composed of pronounced intraterrace structural highs and lows that constrained Cretaceous confined slope to basin-floor turbidite systems (Lomas and Joseph, 2004; Smith, 2004; Fugelli and Olsen, 2007; Soutter et al., 2021).

The exact nature of the Cretaceous tectonic activity responsible for the development of the Breiflabb, Skolest equivalent and Lysing sandstones turbiditic members, is still intensively debated (Fig. 3.2). Some authors mentioned a period of tectonic quiescence (Færseth and Lien, 2002; Lien, 2005; Lien et al., 2006) combined with global sea-level rise and aridification of the climate (Price, 1999; Haq, 2014). This is at odds with other interpretations suggesting a period of high tectonic activity (Doré et al., 1997b, 1999; Lundin and Doré, 1997) coeval with the development of the sandstones turbidite members. However, such turbidite fan systems could have developed during a phase of tectonic quiescence and result from the combination of thermal subsidence and moderate uplift phases related to isostatic adjustments and elastic rebound (which were estimated at one to two kilometres for the Nordland ridge; Roberts and Yielding, 1991; Færseth and Lien, 2002). The Dønna and Halten terraces are transitional zones between, in the west, a deep Cretaceous basin (i.e., the Vøring Basin including the Rås sub-basin), and to the east, the Nordland Ridge that remained above sea-level during the entire Cretaceous period. During the Middle to Upper Jurassic syn-rift period, the intense tectonic rifting activity created inherited palaeotopographies that constrained the sedimentation during the post-rift period, with structural highs (horsts) guiding Cretaceous turbidite fan systems along the adjacent grabens or half-grabens.

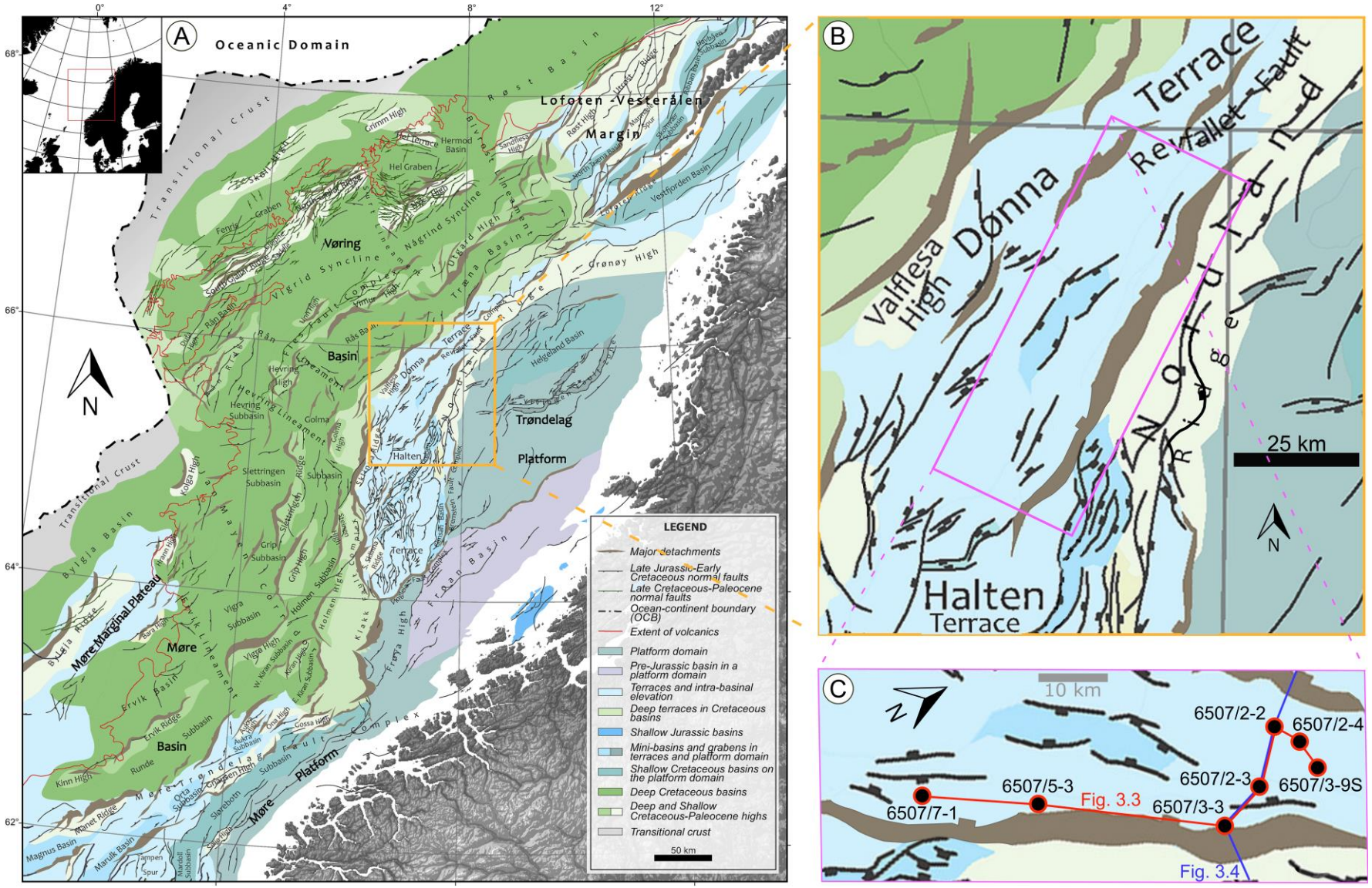

Fig. 3.1: (A) Structural map of the Norwegian Sea. Based on Blystad et al. (1995), Brekke (2000) and Zastrozhnov et al. (2020). (B) Detailed map of the study area identified as the greater Marulk area (orange rectangle), (C) Zoom on the the 3D seismic survey (purple polygon) highlighting well location, the well correlation (Fig. 3.3) and the seismic line (Fig. 3.4). Map are based on Zastrozhnov et al. (2020).

The persistence of a complex palaeotopography during the Jurassic and Cretaceous periods across the terraces shaped intraterrace lows and highs. New faults generated in response to uplift phases of the Nordland Ridge are likely inherited from earlier Jurassic syn-rift faults, and probably originate from a combination of differential compaction and/or footwall uplift (Shanmugam et al., 1994; Færseth and Lien, 2002; Lien, 2005; Lien et al., 2006; Faleide et al., 2010). Uplift phases commonly occurred during interglacial periods as a consequence of isostatic adjustments and elastic rebound of the lithosphere (Riis and Fjeldskaar, 1992; Doré et al., 1999). In contrast, the new generation of normal faults is interpreted by other authors to have spread during the Turonian extensional phase (Blystad et al., 1995), or even earlier during the Cenomanian (Doré et al., 1997a, 1999; Lundin and Doré, 1997). According to these studies, the Mid-Cretaceous extension was a key tectonic event delivering sand pulses during the Turonian (Breiflabb sandstone member). Doré et al. (1997a) suggested that the Breiflabb sandstone Member developed coevally to the Mid-Cretaceous extension, whereas the Coniacian-aged Lysing sandstone Member probably deposited during a significant short-term sea-level fall. Most recent sea level curves (Haq, 2014) have evaluated such a sea level change at ~100 m in 1 Ma. For Sømme and Jackson (2013), greenhouse conditions during the Cretaceous may have generated glacio-eustatic sea-level fluctuations in the range of around a few tens of meters superimposed over variations associated with Milankovitch cycles. However, it was suggested that lower sea levels cannot be the only and primary mechanism influencing the development of such turbidite fan systems. The Turonian-Coniacian sediment pulses responded to both eustatic sea-level changes and a regional uplift, which led to the expansion, steepening and rejuvenation of the onshore drainage along the emerged narrow and fault-controlled shelf (Sømme and Jackson, 2013).

It is a scientific consensus that the Nordland Ridge was subaerially exposed during the entire Cretaceous period. This exposed hinterland was subjected to erosion that locally supplied sediments to the Turonian-Coniacian deep-water fan systems (Fugelli and Olsen, 2007). Whole-rock geochemistry and petrology of deep-water fan systems indicate, in addition to the Nordland Ridge sediment source, potentially another more distal provenance from northern Greenland (Olsen, 2019). However, based on several provenance models, Turonian-Coniacian sandstones observed in the Dønna Terrace are either sourced from the northern part of the Nordland Ridge, or distally from northern Greenland, or even alternatively from a more local sediment source located east of the Nordland Ridge (Shanmugam et al., 1994; Koch and Heum, 1995; Vergara et al., 2001; Lien, 2005; Fugelli and Olsen, 2007; Olsen, 2019).

Fig. 3.2: Lithostratigraphic chart from Tithonian to Santonian. Chart is based on Dalland et al. (1988) and Gradstein and Waters (2016). From bottom to top, the Viking Group has been deposited during the syn-rift period. The Rogn Formation corresponds to shallow-marine sandstones deposited conjointly with organic-rich mudstones, the Spekk Formation. The Cromer Knoll Group is composed of calcareous mudstones to marlstones (the Lyr Formation) and mudstones (the Lange Formation). Deep-water turbidite sandstone members dated to the Turonian and Coniacian have been encountered and correspond to the stratigraphic interval of interest. From the oldest to the youngest, the well-developed Breiflabb sandstone Member, then the poorly developed Skolest sandstone Member equivalent, and finally the thick and well-developed Lysing sandstone Member. The Shetland Group (S. Gp.) is composed of deep-marine mudstones named Kvitnos Formation where minor deep-water turbidite sandstones developed. Cromer Knoll and Shetland groups evolved during the post-rift period.

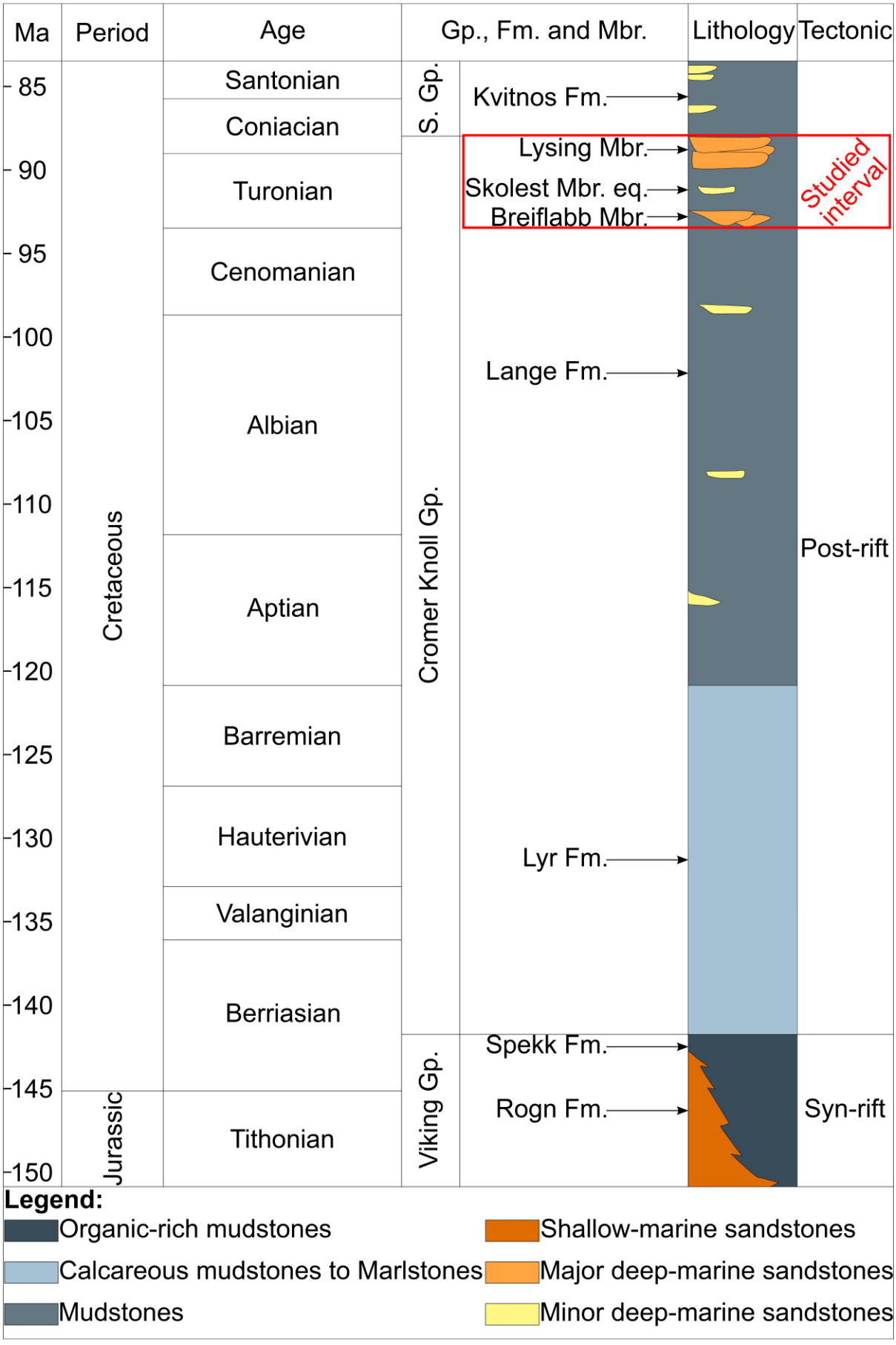
Ma
Period
Age
Gp., Fm. and Mbr.
Lithology
Tectonic
85
90
95
100
105
110
115
120
125
130
135
140
145
150
Cretaceous
Jurassic
Santonian
Coniacian
Turonian
Cenomanian
Albian
Aptian
Barremian
Hauterivian
Valanginian
Berriasian
Tithonian
S. Gp.
Cromer Knoll Gp.
Viking Gp.
Kvitnos Fm.
Lysing Mbr.
Skolest Mbr. eq.
Breiflabb Mbr.
Lange Fm.
Lyr Fm.
Spekk Fm.
Rogn Fm.
Studied interval
Post-rift
Syn-rift
Legend:
Organic-rich mudstones
Calcareous mudstones to Marlstones
Mudstones
Shallow-marine sandstones
Major deep-marine sandstones
Minor deep-marine sandstones

4. Material and methods

4.1. General database

The database is composed of a public 3D seismic survey named “Spectrum mega merge survey” (NPD, 2021), having a standard seismic resolution (approximately 25 metres) and seven exploration wells (6507/2-2, 6507/2-3, 6507/2-4, 6507/3-3, 6507/3-9S, 6507/5-3, 6507/7-1) (Table 3.1, Fig. 3.1). Biostratigraphy is based on Gradstein and Waters (2016) for the following wells: 6507/2-2, 6507/2-3, 6507/7-1, and from biostratigraphic reports for the other wells, when available (Palcon, 1985; Duxbury and Harpur, 1993; Stratlab AS, 1994; Geostrat, 1999; Costa, 2000). Biostratigraphy data and well-log data enable a precise correlation of the sandstone bodies embedded in Cretaceous marine mudstones. This study focuses on core photographs and well-log data to define sedimentary facies and Gamma-Ray (GR)-log trends. 3D seismic data were further used to constrain the structural setting at each well location, as well as to analyse sand body architecture and geometries. Checkshot data were further used to tie wells to seismic data in order to highlight the exact occurrence of sand bodies on the seismic lines.

4.2. Sediment core description

233 metres of cores from the seven studied wells have been described from core photographs available on the Norwegian Petroleum Directorate (NPD, 2021) website (NPD, 2021) (if part of the public domain), or directly from the drilling operator (if still confidential). The precision of sedimentological descriptions is highly dependent on core picture quality, as the vertical resolution can vary from 1:100 to 1:1000 scale. We thus estimate that for a core stick (i.e., 1 metre long), the uncertainty can be up to two centimetres depending on the position of the camera. The closer the camera is positioned to the centre of the stick, the lower the uncertainty.

Sediment grain size was evaluated from core pictures. Basically, the grain size uncertainty corresponds to plus or minus one class. For instance, medium-grained sandstones have an uncertainty ranging between fine- and coarse-grained sandstones. When possible, our grain-size estimates was compared to other core descriptions of the studied cores (Fjellanger et al., 2005; Martinsen et al., 2005; Tegle, 2017; Olsen, 2019).

Table 3.1: Table of the seven studied wells (6507/2-2, 6507/2-3, 6507/2-4, 6507/3-3, 6507/3-9S, 6507/5-3, 6507/7-1) highlighting core depth interval, drilling purpose, discovery, content, 1st and 2nd level with hydrocarbons, completed year of the drilling, primary and secondary target and structural setting (with SF: sub-basin flank; SL: structural low; and SH: structural high).

		6507/2-2	6507/2-3	6507/2-4	6507/3-3	6507/3-9S	6507/5-3	6507/7-1
Core depth in metre (m) with MD for Measured Depth	Lysing Member	Core #1 (2822,00 - 2849,50 m MD)	Core #1 (2850,00 - 2878,00 m MD) + Core #2 (2878,00 - 2890,90 m MD)	Core #1 (2835,00 - 2852,00 m MD)	/	Core #1 (2850,00 - 2866,10 m MD) + Core #2 (2868,00 - 2895,60 m MD)	Core #1 (2836,50 - 2840,00 m MD) + Core #2 (2843,00 - 2843,70 m MD) + Core #3 (2844,00 - 2851,60 m MD) + Core #4 (2852,00 - 2855,00 m MD)	/
	Skolest Member equivalent	/	/	/	Core #1 (2721,00 - 2747,70 m MD)	/	/	/
	Breiflabb Member	Core #2 (3273,00 - 3295,80 m MD) + Core #3 (3330,00 - 3339,30 m MD)	Core #3 (3254,00 - 3263,80 m MD)	Core #2 (3334,00 - 3342,30 m MD) + Core #3 (3342,30 - 3344,80 m MD)	/	/	/	Core #1 (3504,00 - 3512,70 m MD)
General information	Drilling purpose	Wildcat exploration well	Wildcat exploration well	Appraisal exploration well	Wildcat exploration well	Wildcat exploration well	Wildcat exploration well	Wildcat exploration well
	Discovery	Yes	No	No	Yes	Yes	Yes	No
	Content	Gas & Condensate	Oil shows	Gas & Condensate	Gas	Gas	Gas	Gas shows
	Member or Formation with 1st level containing hydrocarbons	Lysing Member	/	Lysing Member	Middle Jurassic Formation	Lysing Member	Lysing Member	/
	Member or Formation with 2nd level containing hydrocarbons	Breiflabb Member	/	/	Lower Jurassic Formation	/	/	/
	Completed year	1992	1994	2010	1999	2012	2000	1984
Exploration target	Main target	Jurassic sandstones	Lysing and Intra-Lange sst Fms.	Lysing Formation	Jurassic sandstones	Lysing Formation	Lysing Formation	Jurassic sandstones
	Secondary objective	Lysing and Intra-Lange sst Fms.	Lyr Formation	Intra-Lange sst Formation	Lysing and Intra-Lange sst Fms.	/	/	Jurassic sandstones
Structural setting	Structural High (SH) or Structural Low (SL) or Subbasin Flank (SF)	Subbasin Flank (SF)	Structural Low (SL)	Structural Low (SL)	Structural High (SH)	Structural Low (SL)	Structural Low (SL)	Subbasin Flank (SF)

4.3. Lobe analysis and nomenclature

Each lobe sub-environment was studied in terms of composition regarding the number and type of beds. Based on this observation we defined an average bed number and mean bed type for each depositional sub-environment. We then analysed the stratigraphic succession of lobe sub-environments as compiled in a depositional sub-environment pattern table (Table 3.3). Statistical analysis finally allows to define the internal organisation of the lobes and their relation to allocyclic and autocyclic forcings.

Sedimentary facies was described based on the Mulder and Alexander (2001)'s classification designed for gravity-driven deposits and subaqueous sedimentary density flow (SSDF). Bed types are composed of several "SSDF facies". A stacked sedimentary succession of similar bed types is then used to define a "lobe element" (Prélat et al., 2009).

Four lobe elements have been recognised in this study, three axial lobe elements and one lateral lobe element (Prélat et al., 2009; Spychala et al., 2017b). However, the identification of lobe sub-environments does not allow the interpretation of lobe dynamics (i.e., lateral motion *vs* axial motion) because the "axial", "off-axial" and "fringe" lobe sub-environments have an ovoid shape surrounding the lobe centroid (Hodgson, 2009; Prélat et al., 2009). In other words, if the succession passes from an off-axis to an axis lobe sub-environment, this could be interpreted either as progradation (axial migration) or as lateral migration (lateral left or lateral right motion). Therefore, in order to discriminate between lateral *vs* axial migration of the lobe, we have used the axial lobe sub-environment description of Prélat et al. (2009), and we have distinguished lateral lobe sub-environment after the descriptions of Spychala et al. (2017b). In the axial direction of the lobe, from the lobe apex to the distal lobe fringe, we have identified (i) the channel and/or proximal lobe (CPL) sub-environment which is equivalent to the lobe "axis" sub-environment described by Prélat et al. (2009), (ii) the mid to distal lobe (MDL) sub-environment, which is equivalent to the lobe "off-axis" sub-environment of Prélat et al. (2009) and the frontal lobe fringe (FLF) described by Spychala et al. (2017b), as opposed to the lateral lobe fringe (LLF) identified by Spychala et al. (2017b). This implies that any axial deposits (CPL, MDL and FLF) can evolve into a LLF sub-environment due to a lateral shift of the lobe. A fifth depositional sub-environment, named distal lobe fringe (DLF) after Boulesteix et al. (2020b), could not be deciphered in this study due to low core picture resolution. However, any FLF or LLF can evolve axially or laterally into a DLF.

We further used the hierarchical scheme of deep-water lobes of Prélat et al. (2009) that identifies the lobe bed as the smallest component, and the lobe complex as the largest one. At the lobe scale, a succession of several lobe elements defines a lobe. Each lobe is separated by interlobes. Lobe complexes were observed mainly from well-log data, whereas lobe beds, lobe elements and lobes were described based on sediment core pictures. Cores located in the greater Marulk area (Dønna Terrace, offshore Mid-Norway) allow the establishment of three depositional models for each of the geological members (Breiflabb, Skolest equivalent and Lysing).

4.4. Data exploitation

Each turbiditic lobe sub-environment (i.e., CPL, MDL, FLF and LLF) was individually analysed in order to evaluate the influence of allocyclic *vs* autocyclic factors on the stacking pattern, by investigating the type and number of lobe beds and the lobe succession probability (i.e., which lobe sub-environment may be succeeded or preceded by another lobe sub-environment).

For the 233 m of cores studied, a total of 96 lobe sub-environments were identified, including 12 CPL, 29 MDL, 22 FLF and 33 LLF. Lobe sub-environments were further used to establish depositional patterns. The occurrence frequency of observed depositional patterns was then used to decipher trends in lobe organisation under the influence of autocyclic and allocyclic forcings. The identification of lobe sub-environments within a lobe complex therefore helps to identify the balance between allogenic and autogenic processes on the stacking pattern. Recurrent depositional successions observed at the lobe scale (or at the lobe element scale) are mainly attributed to autocyclic processes, whereas unusual depositional successions are generally ascribed to dominant allocyclic processes that disturb the self-regulation of sediment dispersal.

As to determine whether autocyclic or allocyclic processes are involved, a cut-off occurrence frequency was determined. A single occurrence of a depositional sub-environment pattern is considered as being uncommon and most probably related to allocyclic processes; in contrast, 2 to 5 occurrences are regarded as common, whereas 6 or more occurrences are classified as very common and most probably related to autocyclic processes.

5. Results and interpretations

5.1. Structural setting

Cored sections have concentrated on the Breiflabb and Lysing sandstone members. Only one coring campaign was performed for the Skolest member equivalent for well 6507/3-3 (Table 3.1, Figs. 3.1, 3.3). Based on Gradstein and Waters (2016) and available biostratigraphic reports (Palcon, 1985; Duxbury and Harpur, 1993; Stratlab AS, 1994; Geostrat, 1999; Costa, 2000), the different sandstone members can be easily correlated. Wells 6507/2-2 and 6507/3-3, which both penetrated Jurassic horst structures, intend to evaluate the hydrocarbon potential of the Breiflabb, Skolest equivalent and Lysing sandstone members (Figs. 3.3, 3.4). During the Cretaceous, the inherited Jurassic horsts acted as a positive topography forming intraterrace highs (Fig. 3.4). 6507/2-2 found a well-developed Breiflabb Member (72 m thick) and a thinner Lysing sandstone Member (13 m), both containing hydrocarbons. In contrast, well 6507/3-3 only revealed sandstone stringers in the Skolest Member equivalent (Table 3.1, Fig. 3.3). Moreover, different tectonic settings are involved for these two exploration wells: 6507/3-3 is located on an intraterrace high, whereas well 6507/2-2 is located on the flank of a sub-basin (Figs. 3.1, 3.4). Well 6507/3-3 was drilled on the top of a Jurassic fault block, most probably located in a Cretaceous “sediment bypass and erosion area” (*sensu* Talling et al. (2007)). Well 6507/2-2, in turn, was drilled on the flank of the Jurassic fault block where Cretaceous turbidite fan systems, originating from N to NE of the Nordland Ridge, likely developed (Fig. 3.4). Well 6507/2-3 was drilled on an intraterrace structural low and yields 41

metres of Lysing sandstones and 28 meters of the Breiflabb Member (Figs. 3.3, 3.4). Other wells drilled on sub-basin flanks (6507/7-1) or in intraterrace lows (6507/2-4, 6507/3-9S, 6507/5-3 and 6507/7-1) revealed well-developed sand-rich turbidite systems (Fig. 3.3).

In a confined structural setting, intraterrace highs constrain the boundaries of turbidite fan depocenters. Each sub-basin consists of the following three structural elements (Table 3.1, Fig. 3.4):

- The intraterrace high, or structural high (SH) of a sub-basin, corresponds to a zone of erosion, by-pass or non-deposition. Wells drilled in SH areas display only minor sandstone stringers (well 6507/3-3; Fig. 3.1);
- The intraterrace low, or the structural low (SL) of the sub-basin, corresponds to the depocenter of turbidite fan systems. The narrower the SL, the more amalgamated the turbidite fan. SL areas contain well-developed turbidite sandstones (6507/2-3, 6507/2-4, 6507/3-9S and 6507/5-3; Fig. 3.1);
- The sub-basin flank zone (SF) lies in an intermediate position, between an intraterrace high (SH) and an intraterrace low (SL). The SF zone corresponds to the slope between the SH and SL settings. Well-developed turbidite sandstones (6507/2-2 and 6507/7-1; Fig. 3.1) were discovered in the SF.

These three structural elements (SH, SL and SF) define two types of sub-basins: symmetrical and asymmetrical sub-basins. Symmetric sub-basins have similar width and elevation between the sub-basin flanks. Conversely, asymmetric sub-basins have different widths and elevation between the sub-basin flanks (Fig. 3.4).

Fig. 3.3: Gamma-Ray (GR) log correlations show the different sandstone members in the greater Marulk area. Blue colour corresponds to Jurassic syn-rift faulted blocks (palaeo-highs), green shading corresponds to deep-marine mudstones (i.e., the Lange Formation), whereas the other colours refer to deep-water turbidite deposits. The Lysing and Breiflabb sandstone members can be easily identified and correlated because sandstones are well-developed, whereas the Skolest member equivalent is poorly developed. Studied core intervals correspond to the black boxes. Blue arrows correspond to retrograding to aggrading trends (type A), and yellow arrow to prograding to aggrading trends (type B). See Fig. 3.1B for location.

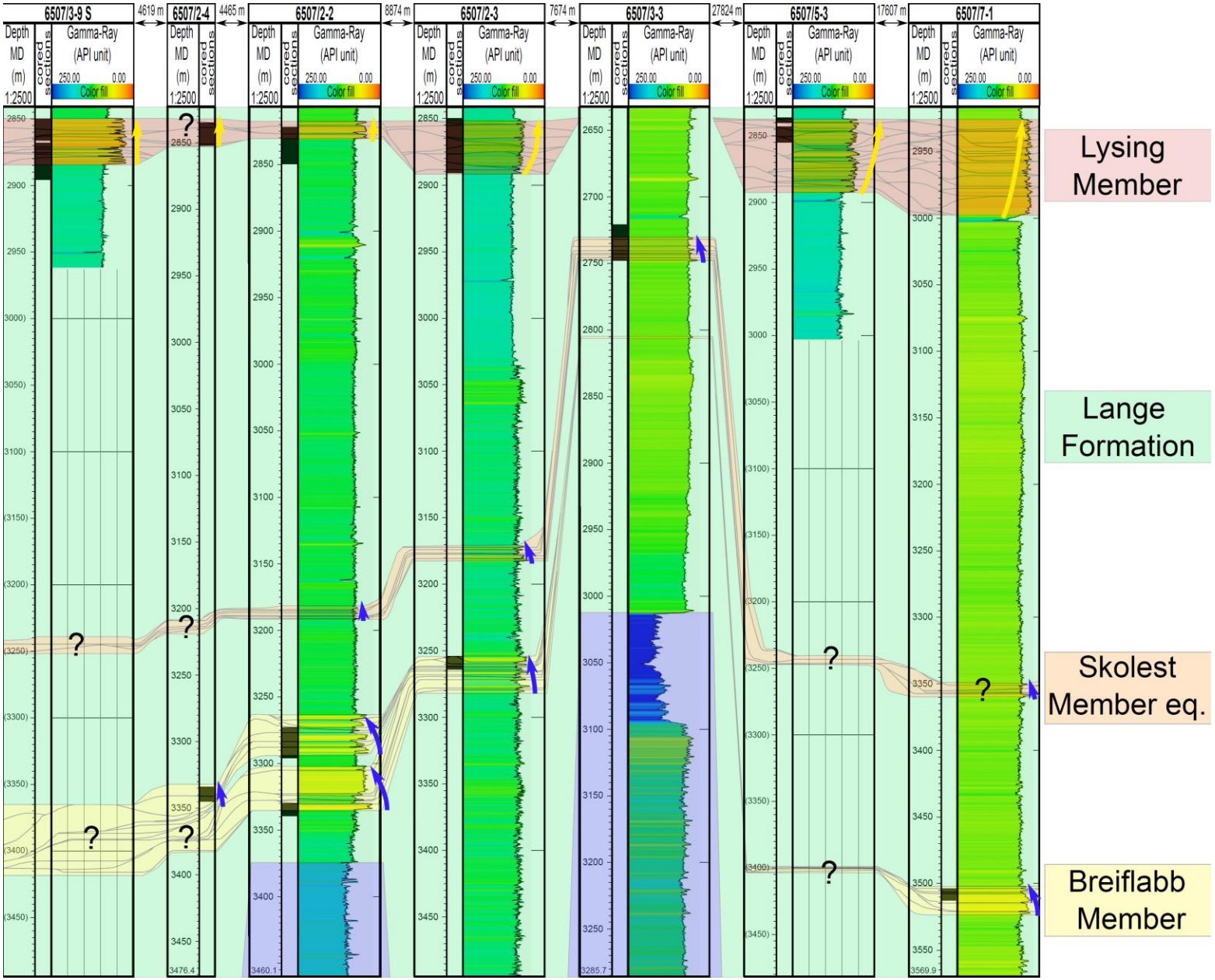
6507/3-9 S
4619 m
6507/2-4
4465 m
6507/2-2
8874 m
6507/2-3
7674 m
6507/3-3
27824 m
6507/5-3
17607 m
6507/7-1
Depth MD (m) 1:2500
cored sections
Gamma-Ray (API unit)
250.00
0.00
Color fill
Lysing Member
Lange Formation
Skolest Member eq.
Breiflabb Member

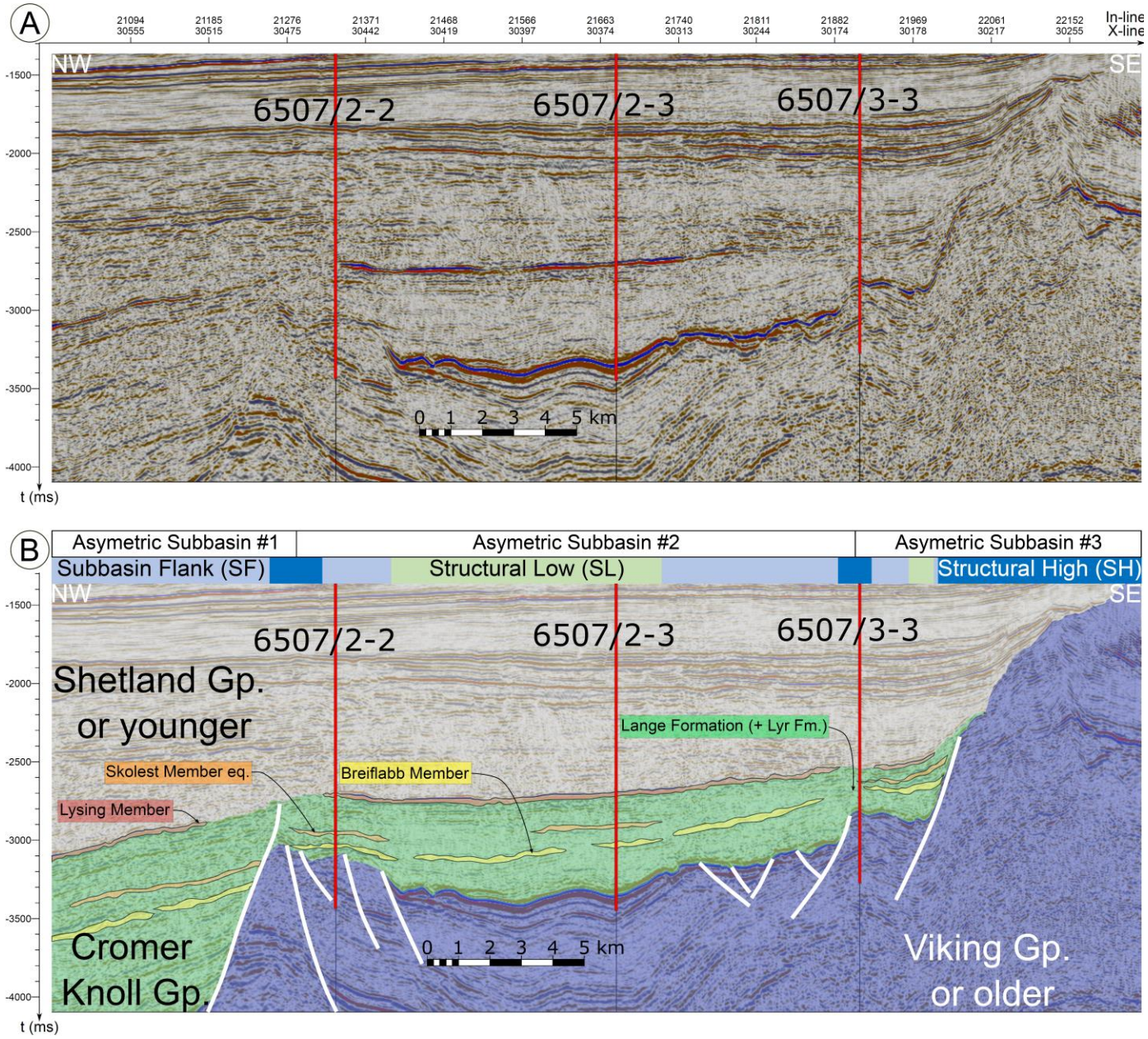

Fig. 3.4: Semi-regional seismic line taken from the 3D seismic "Spectrum mega merge" survey (A) Uninterpreted line; (B) Interpreted line, highlighting the different geological groups (in blue, the Viking Group or older; in green the Cromer Knoll Group with the studied sandstones; in light grey, the Sheltland and younger groups). The 3 wells (6507/2-2, 6507/2-3 and 6507/3-3) have been tied to seismics using checkshot data. Fault sticks are indicated in white. Structural elements (SF, SL and SH) defining a basin or sub-basin are highlighted. See Fig. 3.1B for location.

5.2. Sedimentary facies

From the description of 233 meters of core sections at 1:100 to 1:1000 scale, eight facies (Table 3.2) have been identified (O1, Hy1/2, Co1, Tu1, Tu2, Sl1, Df1 and Un1) and further grouped into four facies associations. Each facies association defines a deep-water turbidite lobe sub-environment (channel and/or proximal lobe (CPL), mid to distal lobe (MDL), frontal lobe fringe (FLF), and lateral lobe fringe (LLF)). In this study, 12 CPL, 29 MDL, 22 FLF and 33 LLF (a total of 96 lobe sub-environments) have been identified.

5.2.1. Facies description

Facies O1 is predominately composed of dark, bioturbated, grey mudstones (Table 3.2). No sedimentary structure was observed based on the core photographs (Fig. 3.5A). This facies is commonly observed, such as in well 6507/2-2 from -2847.00 to -2846.00 m (Fig. 3.6), or in well 6507/2-3 from -3259.00 to -3258.00 m (Fig. 3.7). This accounts for more than 25% (in thickness) out of the 233 m of studied cores.

Facies Hy1/2 is composed of two sub-facies (Table 3.2). Sub-facies Hy1 corresponds to grain-supported conglomerates, whereas sub-facies Hy2 consists of coarse- to very coarse-grained sandstones. Due to a low presence of each sub-facies (0.28% in thickness for Hy1 and Hy2 facies), these two sub-facies have been grouped into the facies Hy1/2. Facies Hy1/2 is structureless and consists of coarse- to very coarse-grained sandstones grading up to grain-supported conglomerates. Hy1/2 is commonly composed of a large range of clasts having a polygenic origin (Fig. 3.5B). Clasts are sub-rounded to sub-angular. Elongated mudstone clasts are common. Facies Hy1/2 can measure between 23 and 43 cm in thickness; it exhibits an erosional base but no other diagnostic sedimentary structure. Facies Hy1/2 is very rare and was observed only twice, in well 6507/2-2 from -3286.86 to -3286.43 m (Fig. 3.6) and in well 6507/2-3 from -2888.25 to -2888.02 m (Fig. 3.7).

Facies Co1 consists of very coarse-grained sandstones fining upwards to fine-grained sandstones (Table 3.2) exhibiting normal grading (Fig. 3.5C). Clasts are commonly sub-angular to rounded and can range up to the gravel size at the base of Co1. Mudstone clasts are commonly present. Facies Co1 exhibits a strong erosional base overlain by massive and structureless coarse to very coarse-grained sandstones fining upward to fine grained-sandstones, which are commonly composed of plane parallel laminations with occasional trough cross-bedding and ripples at top. This facies is rare (19 occurrences) and accounts for approximately 3% out of the 233 metres of studied cores. Co1 thickness ranges from 5 cm to 1.24 m. This facies was mainly observed in wells 6507/2-2 (Fig. 3.6), 6507/2-3 (Fig. 3.7) and 6507/5-3 (Fig. 3.8).

Facies Tu1 can be subdivided into two types based on bed thickness (Table 3.2). Tu1 of type 1 (Fig. 3.5D) consists of a massive medium-grained sandstones fining upward to siltstones commonly exhibiting parallel laminations and, less commonly, ripples and trough cross-beddings. Clasts are sub-rounded to rounded. The base of Tu1 of type 1 is commonly erosive (and less commonly sharp). Bed thickness of Tu1 of type 1 can vary from 2 cm up to 70 cm.

Tu1 of type 1 was observed throughout the seven cored wells. Tu1 of type 2 will be presented shortly after, because this facies is only deposited with mudstone of facies O1.

Facies Sl1 (Table 3.2) consists of very fine- to medium-grained sandstones (Figs. 3.5E, 3.5F, 3.5G, 3.5H, 3.5I, 3.5J, 3.5K, 3.5L). It exhibits normal grading with, at the base medium-grained sandstones, and, at the top, very fine-grained sandstones and less commonly siltstones. Clasts are commonly sub-rounded to rounded. Elongated mudstone clasts are commonly observed at the top of Sl1 (Fig. 3.5K). Sl1 exhibits syn-depositional sedimentary structures and/or post-depositional water escape and soft-sediment features. Identified primary structures are banded sandstones, dish structures and wispy laminations (*sensu* Lowe and Guy (2000)). Post-depositional structures, such as convolute laminations and vertical escape features can be observed. Banded sandstones correspond to alternating light and dark bands (Figs. 3.5H, 3.5J). Dark bands are enriched in mud content (including mudstone clasts). Dish structures occur as gentle to moderate concave-up structures (Fig. 3.5J). Wispy laminations can be recognised as millimetric dark layers (approximately 0.5 mm to 1 cm), rich in mud, overlying centimetric light layers (0.5 cm to 2 cm) (Figs. 3.5G, 3.5H). Another example of convolute structures disturbing primary structures is visible on *Fig. 3.5H* where wispy laminations are truncated by a water escape structure. Vertical water escape conduits are 1 to 2 mm wide and commonly spaced at 1 mm up to 2 cm intervals (Fig. 3.5I). Flame structures can be observed in Sl1 facies (Fig. 3.5J). Sl1 facies is very common (157 times observed). The thickness of Sl1 ranges from 1 cm up to 4.25 m. This facies is largely observed in well 6407/7-1 (Fig. 3.9), and widely represented in the six other cored wells.

Facies Df1 (Table 3.2) consists of chaotic and structureless muddy sandstones to sandy mudstones containing mudstone clasts, sand injectites and pseudonodules (Figs. 3.5K, 3.5L, 3.5M, 3.5N). A normal grading is commonly observed between the base (usually composed of very-fine grained muddy sandstones with a high mud composition) and upper siltstones to sandy mudstones. Clasts are usually sub-rounded to rounded; elongated mudstone clasts are commonly found. Df1 facies is very commonly observed (118 times out of the 233 metres of studied cores). Df1 thickness usually measures between 1 cm and 2.12 m. Df1 facies was mainly observed in wells 6507/2-3 (Fig. 3.7) and 6507/3-9S (Fig. 3.10), and is also observed in the 5 other cored wells.

Facies Tu2 (Table 3.2) consists of alternating fine to very fine-grained sandstone laminae (<1 mm up to 2 cm) with fine siltstone to mudstone laminae (<1 mm up to 2 cm) (Figs. 3.5O, 3.5P, 3.5Q, 3.5R, 3.5S, 3.5T, 3.5U, 3.5V). Facies Tu2 also consists of well-structured very fine to fine-grained sandstones grading upwards into mudstone of facies O1. Laminations are parallel to sinusoidal (Figs. 3.5O, 3.5P, 3.5Q, 3.5R, 3.5S, 3.5T), and supercritical climbing-ripples (*sensu* Storms et al. (1999)) are commonly observed (Figs. 3.5R, 3.5S, 3.5T, 3.5U). Load structures and convolute laminations occur throughout the entire facies Tu2 (Fig. 3.5V). Thickness of Tu2 can measure between 1 cm up to 1.17 m. Facies Tu2 was mainly observed in cores of well 6507/2-2 (Fig. 3.6) and 6507/2-4 (Fig. 3.11).

Tu1 of type 2 consists of very fine- to fine-grained sandstones fining upwards to mudstones (Fig. 3.5W). The thin sandstone layers of Tu1 of type 2 are deposited on mudstones to siltstones of facies O1. Rounded mudstone clasts are rarely observed. Sedimentary structures

commonly recognised in Tu1 of type 2 are plane parallel laminations. Sinusoidal to wavy laminations, ripples, trough cross-beddings, subcritical climbing-ripples (*sensu* Jobe et al. (2012)) to supercritical climbing-ripples (*sensu* Storms et al. (1999)) can be identified but are not common in Tu1 of type 2. The base of Tu1 of type 2 is sharp (Fig. 3.5W), with a thickness ranging between 1 mm and 2 cm. Tu1 of type 2 was mainly observed in cores of wells 6507/2-2 (Fig. 3.6), 6507/2-3 (Fig. 3.7), 6507/3-9S (Fig. 3.10) and 6507/3-3 (Fig. 3.12).

Facies Un1 consists of siltstones to fine-grained sandstones (Table 3.2). This last facies is highly bioturbated and it is not possible to distinguish if they were originally Co1, Tu1, Sl1, Df1 and Tu2. Un1 can be dominated by fine-grained sandstones with some siltstones (Fig. 3.5X), or consist of a mixture of siltstones and fine-grained sandstones (Fig. 3.5Y), or even be made of siltstones including coarser grains up to fine sands (Fig. 3.5Z). Un1 thicknesses usually ranges between 1 cm up and 45 cm. Facies Un1 was only observed in the core of well 6507/2-2 (Fig. 3.6).

Table 3.2: Facies description summary. Columns from left to right: facies number, lithology, texture and average bed thickness, sedimentary structures, depositional mechanism, main sedimentary environment and associated sub-environments.

Facies #		Lithology	Texture and average bed thickness	Sedimentary structures	Depositional mechanism	Main depositional environment	Sub-environment
O1		Dark grey mudstones	Mud-supported and very well sorted.	Structureless and very commonly bioturbated.	Relatively calm zone (absence of wave energy) Transport by suspension below the storm wave-base.	**Offshore**	**Deep-water Offshore**
Hy1/2	Hy1	Grain-supported conglomerates	Grain-supported and mainly poorly to very poorly sorted. Clasts are usually sub-angular to rounded, polygenic in origin. Bed thickness: 23 cm up to 43 cm.	Erosional base and structureless.	Hyperconcentrated density flow *sensu stricto* (Hy1) is a non-cohesive flow part of the hyperconcentrated density flow *sensu lato* (Hy1/2). Frictional freezing process is dominating due to grain-to-grain interaction, such as hydroplaning process.	**Deep-water turbidite Lobe**	**Channel and/or Proximal Lobe (CPL)**
	Hy2	Coarse- to very coarse-grained sandstones			Grain-flow (Hy2) is a non-cohesive flow part of the hyperconcentrated density flow *sensu lato* (Hy1/2). Frictional freezing process is dominating due to grain-to-grain interaction, such as hydroplaning process.		**Channel and/or Proximal Lobe (CPL)**
Co1		Very coarse-grained sandstones fining upward to fine-grained sandstones	Grain-supported and commonly moderately to well sorted. Clasts are usually sub-angular to rounded. Bed thickness: 5 cm up to 1.24 m.	Lowe sequence (the ideal succession is uncommonly observed), from bottom to top: - strong erosional base; - massive sandstones (Ta term); - Ta thickness is much thicker than Tb, Tc, Td & Te; - Tb, Tc, Td and Te, if present, exhibit normal grading.	Concentrated density flow (Co1) is a non-cohesive flow. The base of the event bed is mainly controlled by frictional freezing, whereas the top is mostly controlled by partially turbulent flows.		**Commonly in:** **- Channel and/or Proximal Lobe (CPL)** **Less commonly in:** **- Mid to Distal Lobe (MDL)**
Tu1	Tu1 of type 1	Medium-grained sandstones fining upward to siltstones	Mainly grain-supported. The sequence is well sorted. Clasts are sub-rounded to rounded. Bed thickness: 2 cm up to 70 cm.	Bouma sequence (the ideal succession is uncommonly observed), commonly exhibiting from bottom to top: - erosional base; - Ta: normally graded to massive sandstones; - Tb: plane parallel laminations; And less commonly: - Tc: trough cross-beddings and ripples; - Td and Te: parallel laminations and suspension fallout.	Turbidity flow (Tu1) is a non-cohesive flow (turbidity currents). Tu1 of type 1 corresponds to the proximal deposits of a turbidity flow.		**Commonly in:** **- Mid to Distal Lobe (MDL)** **Less commonly in:** **- Channel and/or Proximal Lobe (CPL)** **- Frontal Lobe Fringe (FLF)**
	Tu1 of type 2	Very fine- to fine-grained sandstones fining upward to mudstones	Passing progressively from grain-supported to mud-supported. The sequence is well to very well sorted. Clasts are very well rounded. Bed thickness: 1 mm up to 2 cm.	Bouma sequence (the ideal succession is uncommonly observed), commonly exhibiting from bottom to top: - sharp base; - Td: parallel laminations; - Te: suspension fallout. And exhibiting less commonly: - Tc: trough cross-beddings and ripples; - Sinusoidal to wavy laminations, sub- to supercritical climbing-ripples	Turbidity flow (Tu1) is a non-cohesive flow (Turbidity currents). Tu1 of type 2 corresponds to the distal deposits of a turbidity flow.		**Commonly in:** **- Lateral Lobe Fringe (LLF)** **Less commonly in:** **- Mid to Distal Lobe (MDL)** **- Frontal Lobe Fringe (FLF)**
Tu2		Alternation of fine to very fine-grained sandstone laminae (<1 mm up to 2 cm) with fine siltstone to mudstone laminae (<1 mm up to 2 cm)	Alternatively grain-supported and mud-supported. The whole sequence is well sorted. Clasts are very well rounded. Bed thickness: 1 cm up to 1.17 m.	Plane parallel laminations; Sinusoidal laminations; Supercritical climbing-ripples; Subcritical climbing-ripples; Load structures; Convolute laminations.	Turbidity flow 2 (Tu2) generated during sub- to supercritical turbidity currents. Such as Tu1, Tu2 is a non-cohesive flow.		**Commonly in:** **- Frontal Lobe Fringe (FLF)** **Less commonly in:** **- Mid to Distal Lobe (MDL)** **- Lateral Lobe Fringe (LLF)**
Sl1		Very fine- to medium-grained sandstones	Grain-supported and commonly well to very well sorted. Clasts are commonly sub-rounded to rounded. Bed thickness: 1 cm up to 4.25 m.	Syn-depositional sedimentary structures (primary structures): - Banded sandstones; - Dish structures; - Wispy laminations; Post-depositional water escape and soft-sediment features: - Convolute laminations; - Vertical escape features.	Sl1 is interpreted as being deposited during slurry flow. Slurry-flow (Sl1) is a transitional flow between purely turbulent flow (Tu1 of type 1) and a full matrix-supported debris flow (Df1).		**Commonly in:** **- Mid to Distal Lobe (MDL)** **- Frontal Lobe Fringe (FLF)** **Less commonly in:** **- Lateral Lobe Fringe (LLF)**
Df1		Muddy sandstones to sandy mudstones	Mainly mud-supported, and rarely grain-supported. The entire sequence is unsorted. Clasts are commonly sub-rounded to rounded. Bed thickness: 1 cm up to 2.12 m.	Chaotic and structureless muddy sandstones to sandy mudstones containing: - Mudstone clasts; - Sand injectites; - Pseudonodules.	Debris flow (Df1) is interpreted as being deposited during a cohesive debris flow.		**Commonly in:** **- Frontal Lobe Fringe (FLF)** **- Mid to Distal Lobe (MDL)** **Less commonly in:** **- Lateral Lobe Fringe (LLF)**
Un1		Siltstones to fine-grained sandstones	Grain-supported and commonly well to very well sorted. Clasts are commonly sub-rounded to very well rounded. Bed thickness: 1 cm up to 45 cm.	This facies is highly bioturbated; hence it is not possible to discriminate the original facies (i.e., Co1, Tu1, Sl1, Df1 and Tu2).	Undefined (Un1) flow type. The deposit Un1 can not be attributed to any flow due to the absence of preserved primary structures.		**Commonly in:** **- Mid to Distal Lobe (MDL)** **- Frontal Lobe Fringe (FLF)** **Less commonly in:** **- Lateral Lobe Fringe (LLF)**

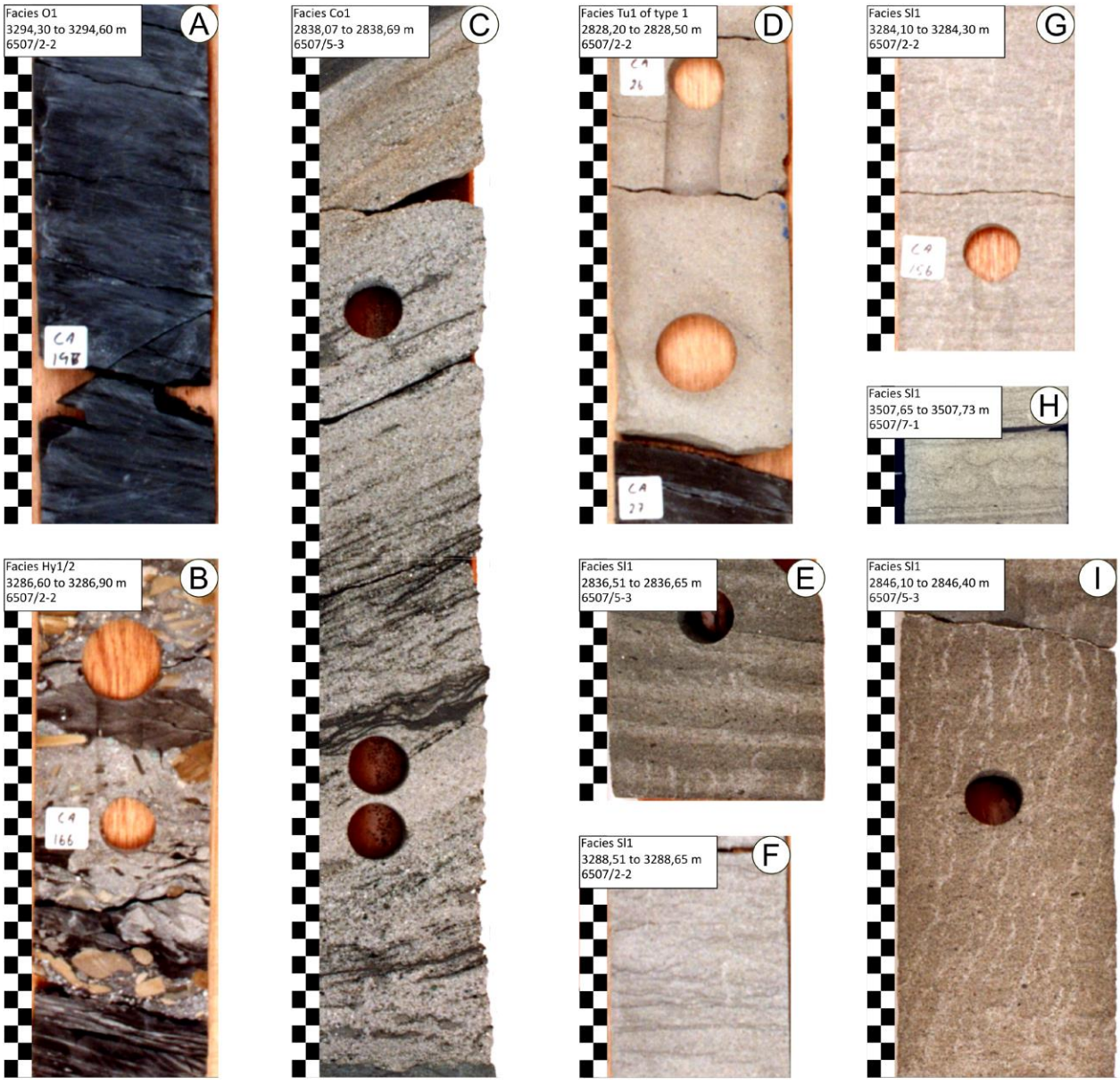

Fig. 3.5: Facies description summary related to deep-water turbidite lobe deposits. Facies O1 is characterised by (A) structureless mudstones. Facies Hy1/2 is characterised by (B) structureless conglomerates as well as coarse-grained sandstones. Facies Co1 (C) has a strong erosional base, followed by thick and massive coarse-grained sandstones rich in mudstone clasts. The upper part exhibits a fine-grained sandstone showing plane parallel laminations. Facies Tu1 of type 1 (D) is composed of a well-defined erosional to sharp base, followed by massive medium-grained sandstones and, in some cases, parallel laminations or trough cross-beddings and/or current ripples in very fine-grained sandstones. Facies Sl1 is composed of banded sandstones (E), dish structures (F) wispy lamination (G), convolute laminations (H), vertical escape features (I) ...

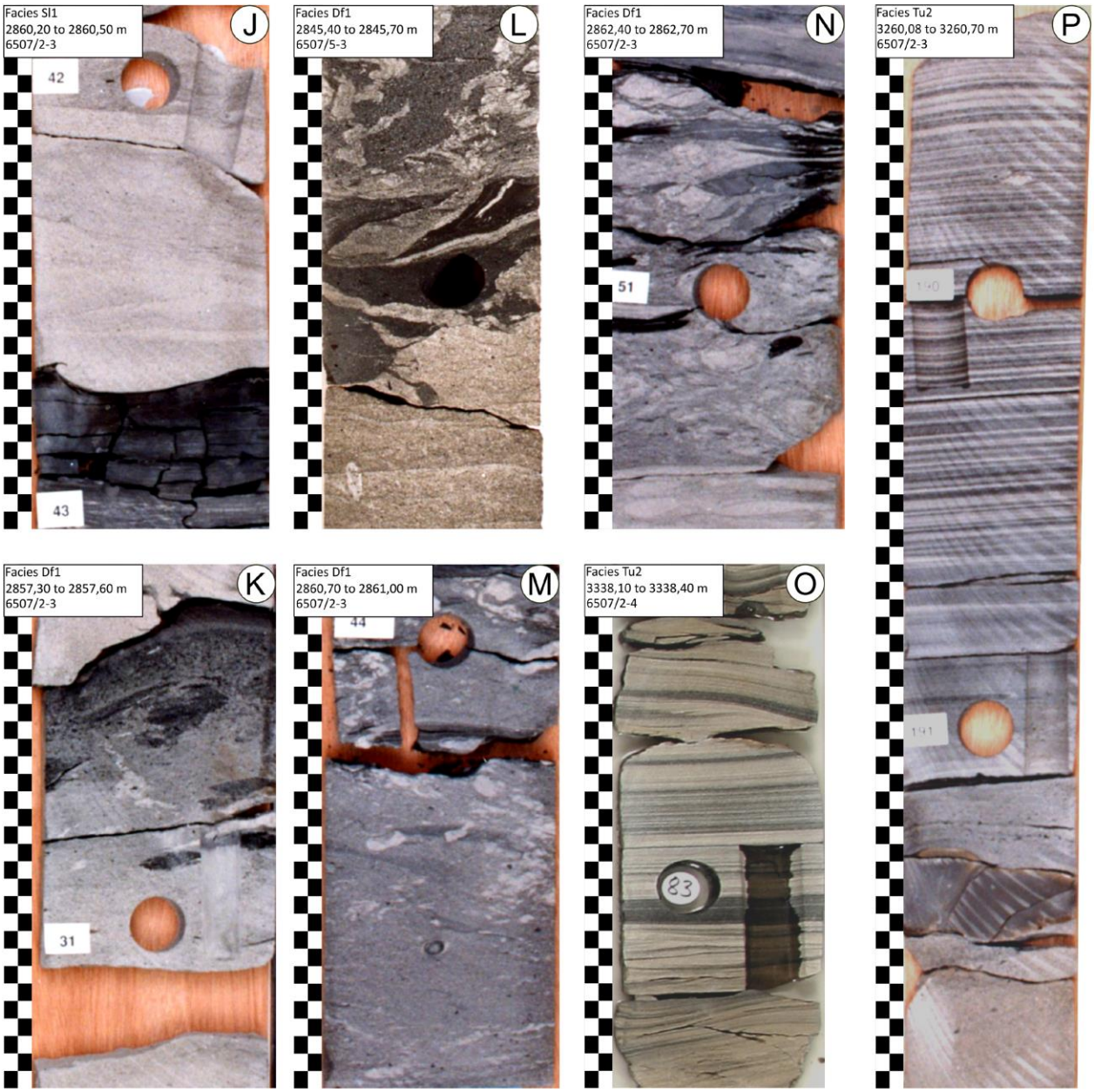

Fig. 3.5 (continued): ... and flame structures (J). Facies Df1 consists of muddy sandstones to sandy mudstones containing mudstone clasts, sand injectites and pseudonodules (K, L, M, N). Facies Tu2 consists of alternating fine to very fine-grained sandstone laminae (<1 mm up to 2 cm) with finer siltstone to mudstone laminae (<1 mm up to 2 cm). Tu2 is a well-structured very fine to fine-grained sandstone grading upwards into mudstones of facies O1. Laminations are parallel to sinusoidal (O, P, Q, R, S, T), and supercritical climbing-ripples (sensu **Storms et al. (1999)**) *are also commonly observed (R, S, T, U) ...*

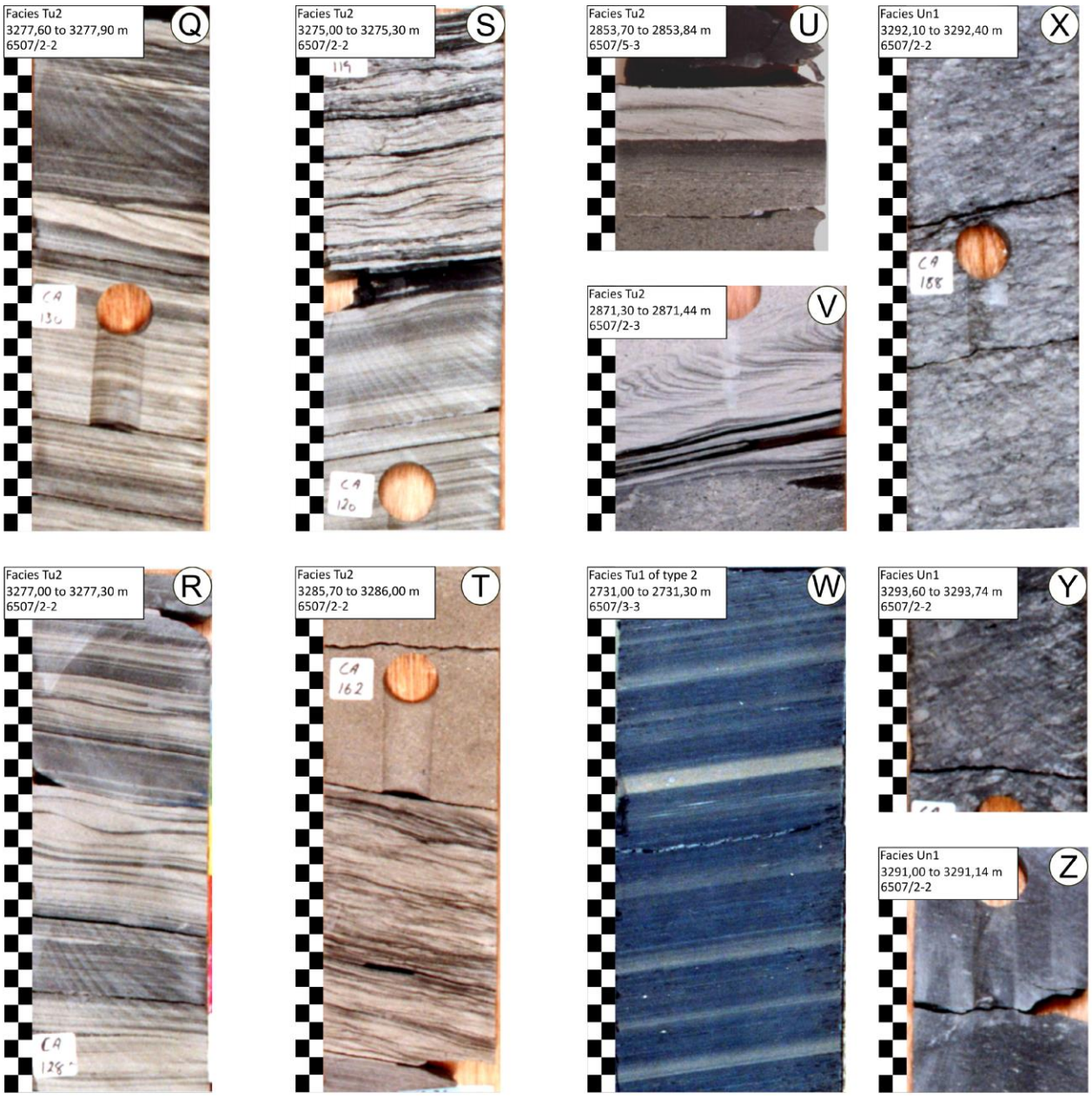

Fig. 3.5 (continued): ... Load structures and convolute laminations occur within Tu2 (V). Facies Tu1 of type 2 consists of very fine- to fine-grained sandstones with plane parallel laminations grading upwards into mudstone of facies O1 (W). Facies Un1 is highly bioturbated and it is not possible to distinguish any primary sedimentary structures (X, Y, Z). Black and white rectangles represent the vertical scale in centimetres.

5.2.2. Depositional model

Based on facies description, different subaqueous sedimentary density flow deposits (SSDF facies: Hy1/2, Co1, Tu1, Tu2, Sl1, Df1 and Un1) have been identified interbedded within mudstones of facies O1 and associated with a deep-water turbidite lobe sub-environment. O1 deposits most probably accumulated in a quiet environment below the storm wave base. Facies O1 is therefore considered as a deep-marine offshore environment (Evoy and Moslow, 1995; Reading, 2009). Nevertheless, the low resolution of core photographs hampers the identification of thin- to very thin-bedded mudstones that could have been deposited by low-density turbidity current (Boulesteix et al., 2020b).

5.2.2.1. Facies and flow regimes

Facies Hy1/2, Co1, Tu1, Tu2, Sl1, Df1 and Un1 are established based on different flow types and illustrate various subaqueous sedimentary density flow (SSDF) regimes.

Facies Hy1/2 (made of structureless coarse- to very coarse-grained sandstones up to grain-supported conglomerates) results from hyperconcentrated density flow *sensu lato* (Mulder and Alexander, 2001). Based on Mulder and Alexander (2001)'s classification, sub-facies Hy1 (consisting of grain-supported conglomerates) corresponds to hyperconcentrated density flow *sensu stricto* deposits, whereas sub-facies Hy2 (consisting of coarse- to very coarse-grained sandstones) is interpreted as grain-flow deposits.

Facies Co1 (made of structureless coarse-grained sandstones at the base, fining upwards to fine-grained sandstones) refers to the Lowe sequence (Lowe, 1982). Co1 density flow deposits are generated during concentrated flows (Mulder and Alexander, 2001).

Facies Tu1 of type 1 (composed at the base of massive medium-grained sandstones fining upward to siltstones) corresponds to incomplete Bouma sequences (Bouma, 1962), generated by turbulent flows, with Ta and Tb as the most represented horizons. Based on Mulder and Alexander (2001), turbidity currents can transport clasts smaller than coarse sand grains, while coarser clasts are usually transported by concentrated density flows. A threshold of coarse sand-grade clasts has been defined to differentiate turbidity flow deposits (Tu1 of type 1) from concentrated flow deposits (Co1).

Facies Sl1 (made of very fine- to medium-grained sandstones including both syn- and post-depositional disturbing sedimentary structures) deposited from slurry-flows (Lowe and Guy, 2000). This type of flow is a transitional flow between purely turbulent flows (Tu1 of type 1) and matrix-supported debris flows (Df1) (Lowe and Guy, 2000). Primary and secondary structures originate from disturbed water-loaded sediments (Haughton et al., 2003), such as flame structures caused by a simple loading process (Owen, 2003).

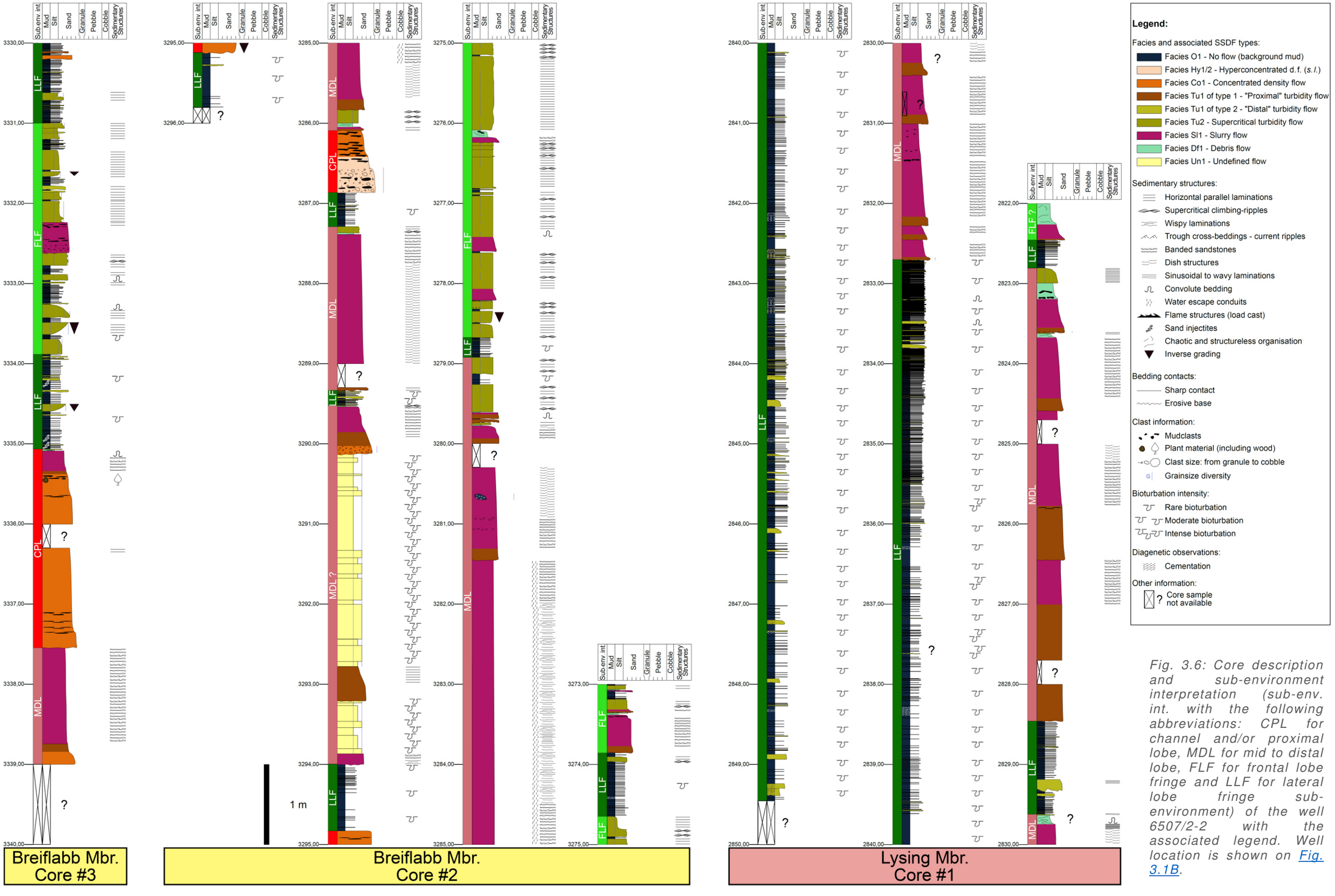

Fig. 3.6: Core description and sub-environment interpretation (sub-env. int. with the following abbreviations: CPL for channel and/or proximal lobe, MDL for mid to distal lobe, FLF for frontal lobe fringe and LLF for lateral lobe fringe sub-environment) of the well 6507/2-2 with the associated legend. Well location is shown on [Fig. 3.1B](#).

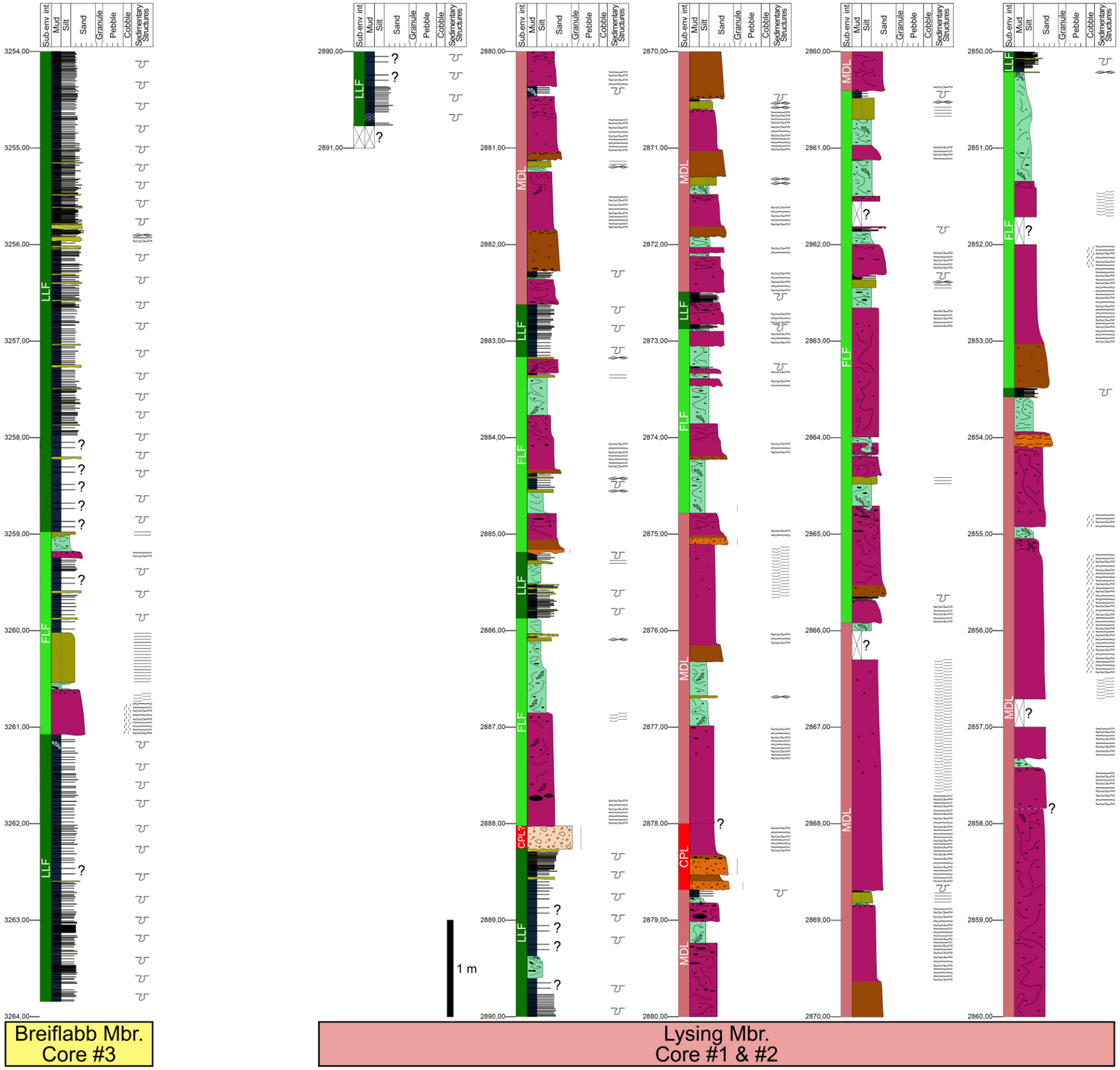

Fig. 3.7: Core description and sub-environment interpretation (sub-env. int. with the following abbreviations: CPL for channel and/or proximal lobe, MDL for mid to distal lobe, FLF for frontal lobe fringe and LLF for lateral lobe fringe sub-environment) of the well 6507/2-3. The corresponding legend is on Fig. 3.6, well location is shown on Fig. 3.1B.

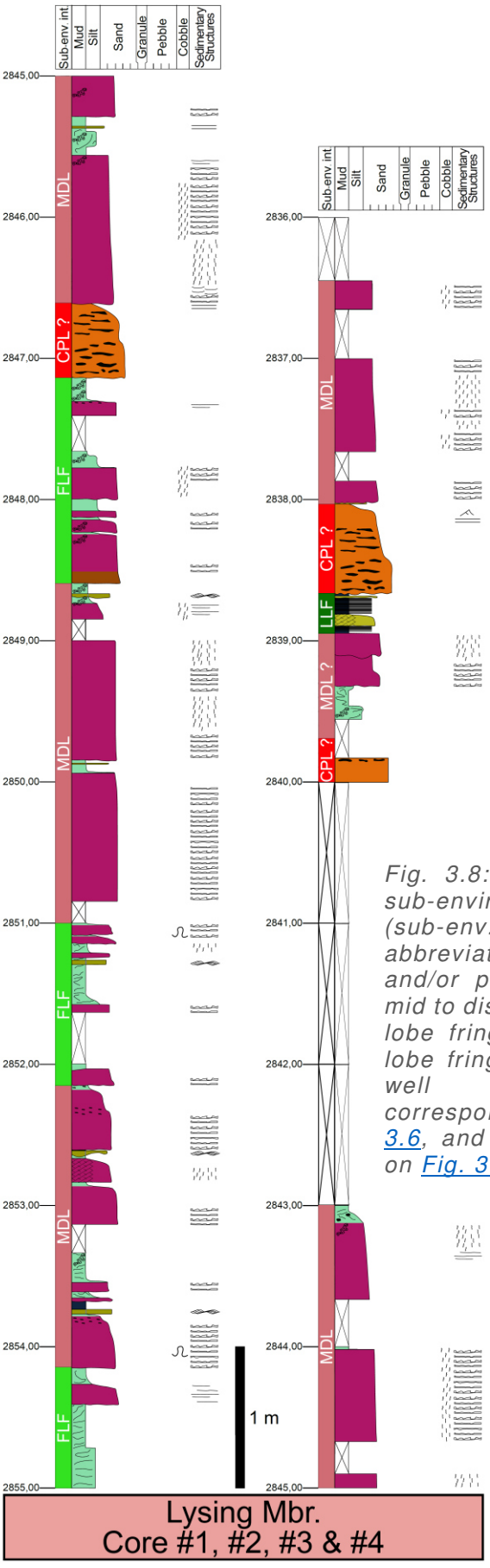

Fig. 3.8: Core description and sub-environment interpretation (sub-env. int. with the following abbreviations: CPL for channel and/or proximal lobe, MDL for mid to distal lobe, FLF for frontal lobe fringe and LLF for lateral lobe fringe sub-environment) of well 6507/5-3. The corresponding legend is on Fig. 3.6, and well location is shown on Fig. 3.1B.

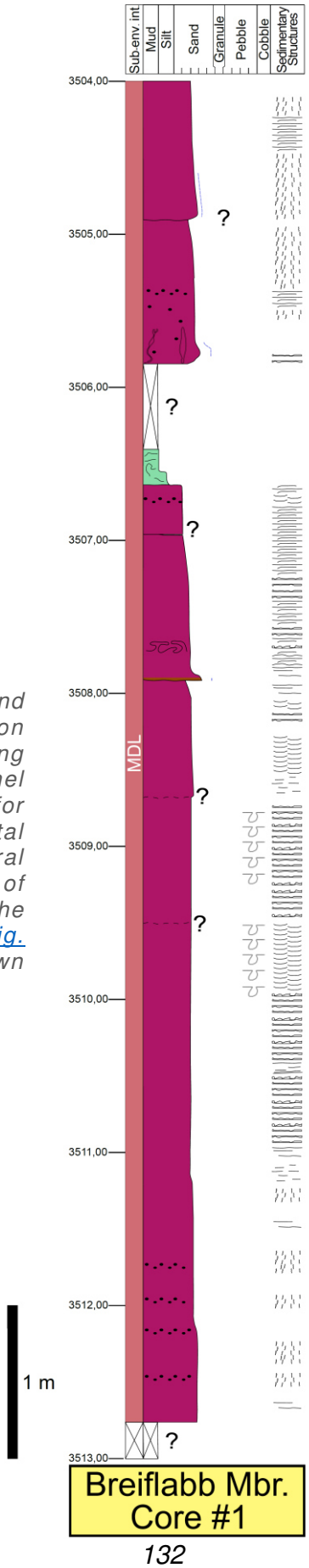

Fig. 3.9: Core description and sub-environment interpretation (sub-env. int. with the following abbreviations: CPL for channel and/or proximal lobe, MDL for mid to distal lobe, FLF for frontal lobe fringe and LLF for lateral lobe fringe sub-environment) of well 6507/7-1. The corresponding legend is on Fig. 3.6, and well location is shown on Fig. 3.1B.

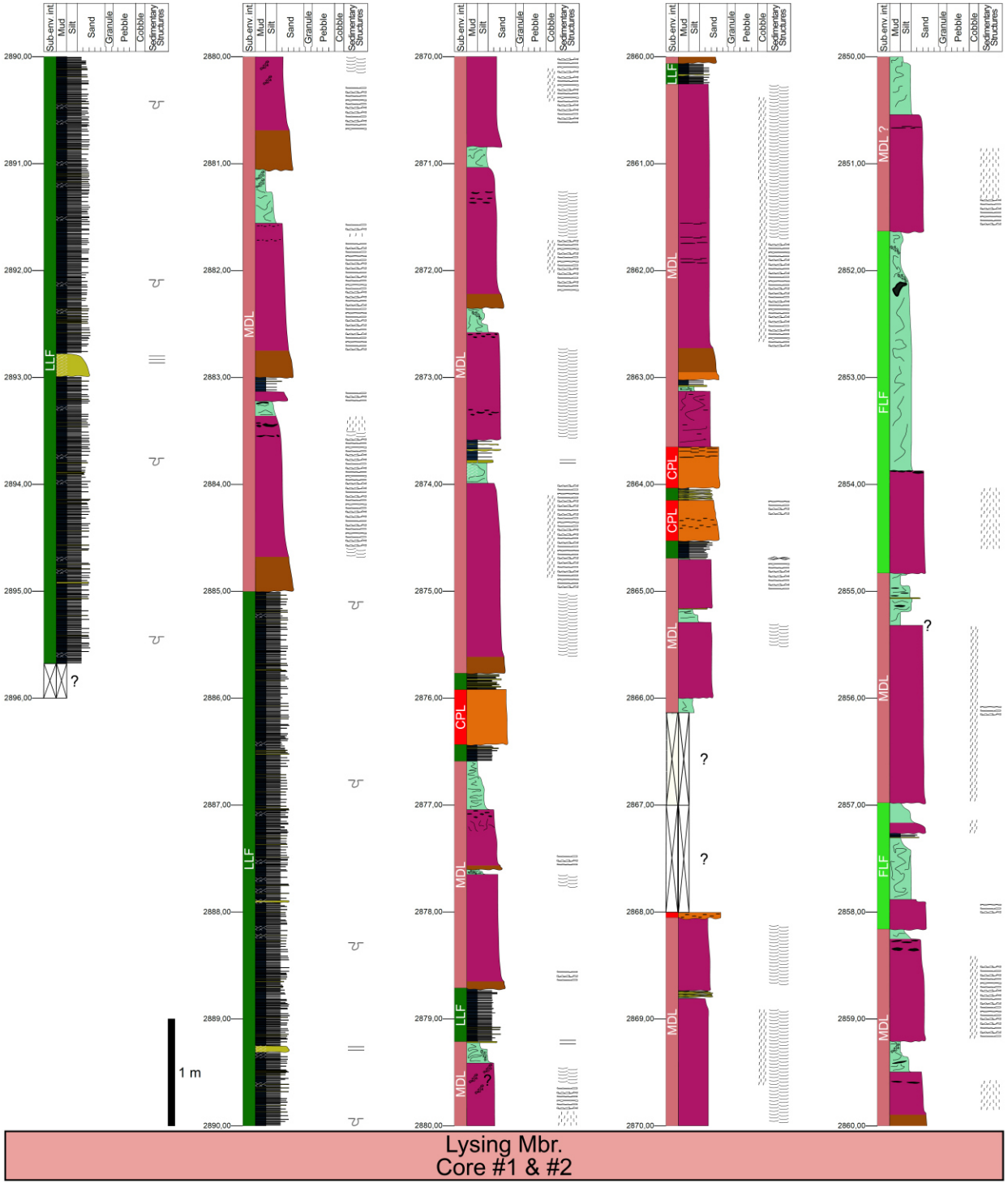

Fig. 3.10: Core description and sub-environment interpretation (sub-env. int. with the following abbreviations: CPL for channel and/or proximal lobe, MDL for mid to distal lobe, FLF for frontal lobe fringe and LLF for lateral lobe fringe sub-environment) of well 6507/3-9S. The corresponding legend is on Fig. 3.6, and well location is shown on Fig. 3.1B.

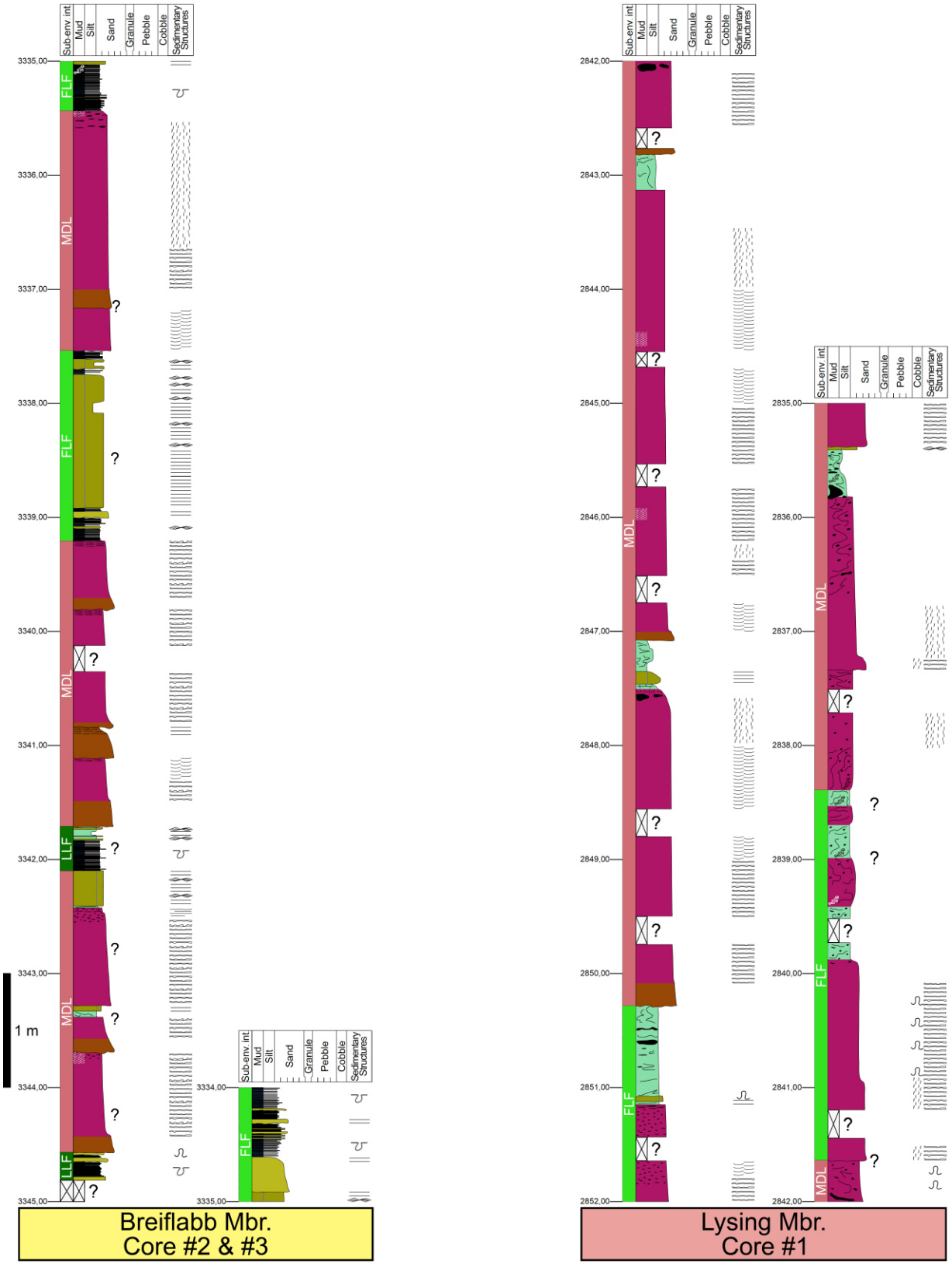

Fig. 3.11: Core description and sub-environment interpretation (sub-env. int. with the following abbreviations: CPL for channel and/or proximal lobe, MDL for mid to distal lobe, FLF for frontal lobe fringe and LLF for lateral lobe fringe sub-environment) of well 6507/2-4. The corresponding legend is on Fig. 3.6, and well location is shown on Fig. 3.1B.

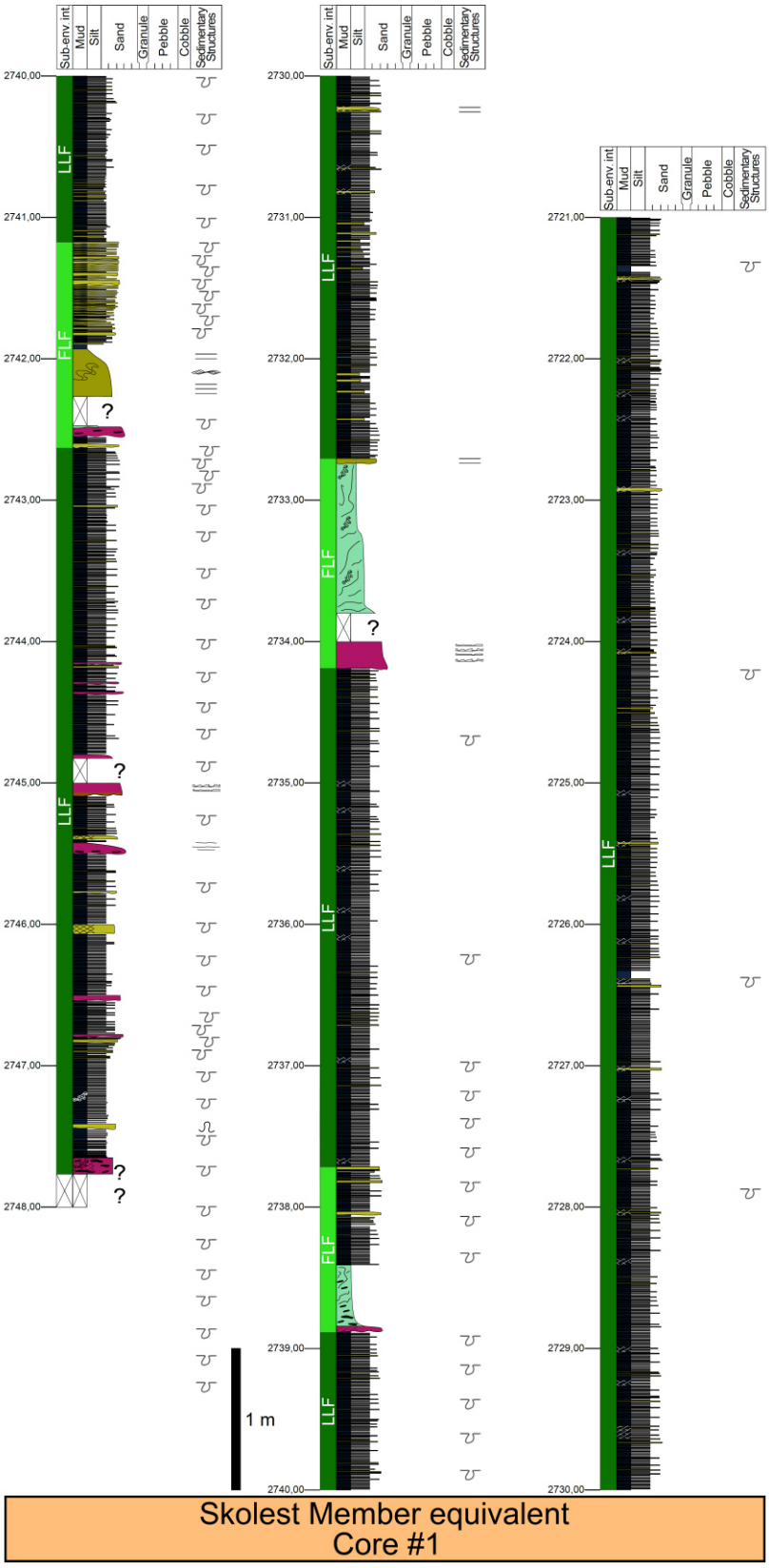

Fig. 3.12: Core description and sub-environment interpretation (sub-env. int. with the following abbreviations: CPL for channel and/or proximal lobe, MDL for mid to distal lobe, FLF for frontal lobe fringe and LLF for lateral lobe fringe sub-environment) of well 6507/3-3. The corresponding legend is on Fig. 3.6, and well location is shown on Fig. 3.1B.

Facies Df1 (composed of a structureless muddy sandstone fining up to sandy and silty mudstones) deposited from purely or partially cohesive debris flows (Mulder and Alexander, 2001). Pseudonodules occur as ball-and-pillow structures caused by a variety of liquidization processes (Owen, 2003).

Facies Tu2 includes subcritical climbing ripples (*sensu* Jobe et al. (2012)), supercritical climbing ripples (*sensu* Storms et al. (1999)), sinusoidal laminations (*sensu* Jobe et al. (2012)) and is composed of very fine to fine-grained sandstones (Jopling and Walker, 1968; Alexander et al., 2001; Jobe et al., 2012; Baas et al., 2021). Facies Tu2 results from sub- to supercritical turbidity flows (Postma and Cartigny, 2014).

Facies Tu1 of type 2 (consisting of siltstones to fine-grained sandstones) most likely corresponds to the last divisions of the Bouma sequence (Td, Te, and less commonly Tb and Tc horizons (Bouma, 1962)). Facies Tu1 of type 2, mainly deposited by low-density turbidity currents and occasionally during sub- to supercritical turbidity currents, displays similar sedimentary structures to Tu2.

Facies Un1 is composed partially or entirely of the same material as Co1, Tu1, Tu2, Sl1, and Df1 deposits but, due to strong bioturbation, lacks the original depositional structures.

5.2.2.2. Facies associations and lobe sub-environments

The seven facies (Hy1/2, Co1, Tu1, Tu2, Sl1, Df1 and Un1) identified in the studied successions are interpreted to have been deposited by various subaqueous sedimentary density flows (SSDF). From the 233 m of cores described, Tu1 of type 1, Sl1, Df1 and Tu2 are frequently observed together. Commonly at the base of SSDF deposits, the succession starts with Tu1 of type 1 with a well-marked erosive base, followed by Sl1, then Df1 and capped by a thin Tu2 facies. Haughton et al. (2003, 2009) named this facies succession linked debrites or hybrid event beds (HEBs). HEBs characterise deep-water turbidite lobe systems (Haughton et al., 2003, 2009; Kane and Pontén, 2012; Talling et al., 2012; Fonnesu et al., 2015, 2018; Kane et al., 2017; Spychala et al., 2017a, 2017b, 2021). HEBs composed of Tu1 of type 1, Sl1, Df1 and Tu2 facies are associated in different proportions based on specific turbidite lobe sub-environments.

A simplified model (Fig. 3.13) of turbidite lobe environment implies four sub-environmental settings relying on longitudinal (proximal, mid, distal) and lateral (axis, off-axis) sub-divisions (Prélat et al., 2009; Spychala et al., 2021) (Figs. 3.13A, 3.13B). These four lobe sub-environments are characterised by four common facies associations:

The channel and/or proximal lobe (CPL) facies association corresponds to the proximal and axial area of a turbidite lobe. This facies association consists of a stacked succession of conglomerates to medium-grained sandstones of facies Hy1/2, Co1 and less commonly Tu1 of type 1.

In terms of flow regime, CPL is dominated by hyperconcentrated to concentrated density flows and less commonly turbidity flows. No HEBs are observed in this facies association. The channel and/or proximal lobe (CPL) facies association, also named inner fan, is interpreted to be localised on the slope break zone, near the lobe apex (Fugelli and Olsen, 2007; Fonnesu et al., 2018; Fonnesu and Felletti, 2019). In some cases, this facies association occurs slightly upstream from the lobe apex and is therefore interpreted as a turbidite channel (Brooks et al., 2018a).

The mid to distal lobe (MDL) facies association corresponds to the mid and axial subdivision of a turbidite lobe. This facies association is commonly composed of a stacked succession of medium- to very fine-grained sandstones of facies Tu1 of type 1 and Sl1. Debris flow (Df1) deposits commonly cap the two previous facies. Coarse-grained sandstones (Co1) and very-fine to fine-grained sandstones (Tu1 of type 2, Tu2) also occur but are not often observed. Based on Haughton et al. (2003), turbidity flow deposits (Tu1 of type 1) correspond to the S1 subdivision, and slurry flow deposits (Sl1) correspond to the S2 and S3 subdivisions. These three sandstone members (S1, S2 and S3) correspond to the H1 and H2 members of the HEBs division of Haughton et al. (2009). MDL is referred to the mid- to outer-fan lobe and is located between the inner fan and the frontal lobe fringe (Haughton et al., 2003; Fonnesu et al., 2018).

The frontal lobe fringe (FLF) facies association corresponds to the distal axial part of the turbidite lobe. It is mainly characterised by HEB deposits made of Sl1, Df1 and Tu2 facies (Haughton et al., 2003; Spychala et al., 2017b), which illustrates a regime flow transition between slurry flows, debris flows and supercritical turbidity flows. Occasionally, the base of the FLF association exhibits pure turbulent flow deposits (Tu1 of type 1). Based on Haughton et al. (2003), when present, turbidity flow deposits (Tu1 of type 1) correspond to the S1 subdivision, slurry flow deposits (Sl1) to the S2 and S3 subdivisions, debris flow deposits (Df1) to the H1, H2 subdivisions and supercritical turbidity flow deposit (Tu2) to the S4 subdivision. In turn, based on Haughton et al. (2009), such a succession corresponds to the five members of HEBs (H1 to H5). The frontal lobe fringe (FLF) is characterised by beds thicker than 2 cm (Sl1, Df1 and Tu2), with the presence of numerous beds ranging between 1 mm up and 2 cm (Tu1 of type 2) (Spychala et al., 2017b).

Fig. 3.13: Depositional model and synthetic sedimentary logs of a turbidite lobe. (A) Longitudinal and lateral cross-section of a turbidite lobe with the channel and/or proximal lobe (CPL), the mid to distal lobe (MDL), the frontal lobe fringe (FLF) and the lateral lobe fringe (LLF) sub-environments, after Hodgson (2009). (B) Plan view of the lobe, after Hodgson (2009), defining longitudinal (proximal, intermediate and distal) and lateral subdivisions (axis and off-axis) of the lobe. (C) Synthetic sedimentary logs of the different lobe sub-environments (CPL, MDL, FLF and LLF) highlighting the different lobe elements defined by Prélat et al. (2009), which are the lobe bed, lobe element separated by interlobe elements, lobe separated by interlobes (note that the thicker element, i.e., the lobe complex, is not represented here). The corresponding legend regarding sedimentary structures is provided on Fig. 3.6.

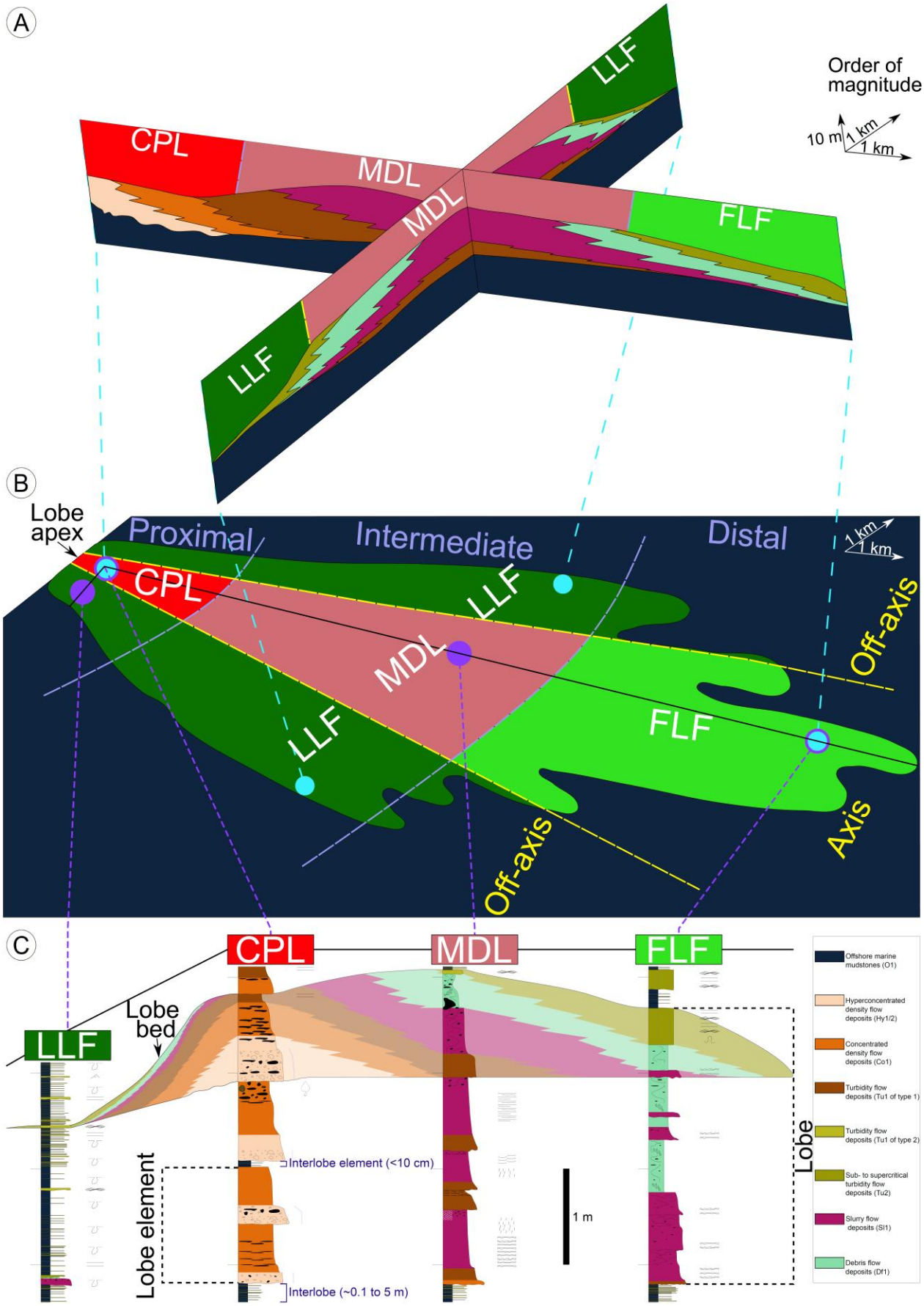
A
Order of magnitude
10 m
1 km
1 km
CPL
MDL
MDL
LLF
LLF
FLF
B
Lobe apex
Proximal
Intermediate
Distal
1 km
1 km
CPL
LLF
MDL
LLF
FLF
Off-axis
Off-axis
Axis
C
CPL
MDL
FLF
LLF
Lobe bed
Interlobe element (<10 cm)
Lobe element
Interlobe (~0.1 to 5 m)
1 m
Lobe
Offshore marine mudstones (O1)
Hyperconcentrated density flow deposits (Hy1/2)
Concentrated density flow deposits (Co1)
Turbidity flow deposits (Tu1 of type 1)
Turbidity flow deposits (Tu1 of type 2)
Sub- to supercritical turbidity flow deposits (Tu2)
Slurry flow deposits (Sl1)
Debris flow deposits (Df1)

The lateral lobe fringe (LLF) facies association corresponds to the proximal, mid, and distal off-axis lobe sub-environment. LLF is dominated by fine to very-fine grained sandstones deposited (facies Tu1 of type 2) onto O1 mudstones. Rare HEBs are observed in the lateral lobe fringe (Spychala et al., 2017b). LLF is dominated by turbidity flow deposits commonly composed of Td and Te horizons and less commonly Tb and Tc horizons (Bouma, 1962). The lateral lobe fringe (LLF) is commonly characterised by beds thinner than 2 cm and generally dominated by siltstones and mudstones. The differentiation between lateral lobe fringe (LLF) and frontal lobe fringe (FLF) in the distal part of the lobe may be difficult; it mainly depends on bed thickness, as well as the sand *vs* silt ratio (Spychala et al., 2017b), as sands are usually more abundant in frontal lobe settings.

A fifth facies association, corresponding to the distal lobe fringe (DLF), should be considered. According to Boulesteix et al. (2020b), the DLF is composed of thin- to very thin-bedded mudstones interpreted as low-density turbidity currents. However, based on low core picture resolution, it was not possible to discriminate between offshore marine mudstones (i.e., O1) of the LLF facies association and distal lobe fringe deposits (DLF deposits). In a way of simplification, the DLF facies association was grouped with the LLF facies association.

5.2.3. Lobe architecture

According to Prélat et al. (2009), four hierarchisation levels (Fig. 3.14) have been identified in the lobe architecture. The hierarchisation is established based on sediment core description and well-log analysis:

- The smallest element is the lobe bed, which represents a single depositional event (Prélat et al., 2009). Each bed is characterised based on its sedimentary facies (Fig. 3.13C). Facies (Hy1/2, Co1, Tu1, Tu2, Sl1, Df1 and Un1) are related to subaqueous sedimentary density flows (SSDF), which allow the identification of the prevailing flow regime at the scale of a single depositional event. Commonly lobe beds are composed of two to three of those facies, which are grouped into a facies association (CPL, MDL, FLF, and LLF);

Fig. 3.14: Lobe hierarchisation after Prélat et al. (2009). At the basin scale (A), several lobes are forming the turbidite lobe complex. The cross-section highlights that the basin infill can be composed of several lobe complexes. When zooming on lobe (B), each lobe is composed of several lobe elements (red corresponds to channel and/or proximal lobe (CPL), pink corresponds to mid to distal lobe (MDL), light green to frontal lobe fringe (FLF) and dark green to lateral lobe fringe (LLF) sub-environments). From well data (C), well-log data (Gamma Ray) outline the lobe complex, lobe and lobe element characteristics, whereas core data highlight lobe, lobe element and lobe beds signatures. The corresponding legend regarding core description is provided on Fig. 3.6. (D) The convention for lobe hierarchisation is defined after Prélat et al. (2009). A capital letter is assigned to the lobe complex, and the lobes constituting the lobe complex are labelled from the oldest to the youngest (1, 2, 3, etc.). Lobe elements are further named a, b, c, etc., whereas the lobe beds composing each lobe element have been numbered 1, 2, 3, etc. For instance, the lobe complex C is composed of 2 lobes (C1 and C2), with C2 composed of two lobe elements (C2a and C2b). C2a is composed itself of 3 lobe beds, respectively named C2a1, C2a2, C2a3.

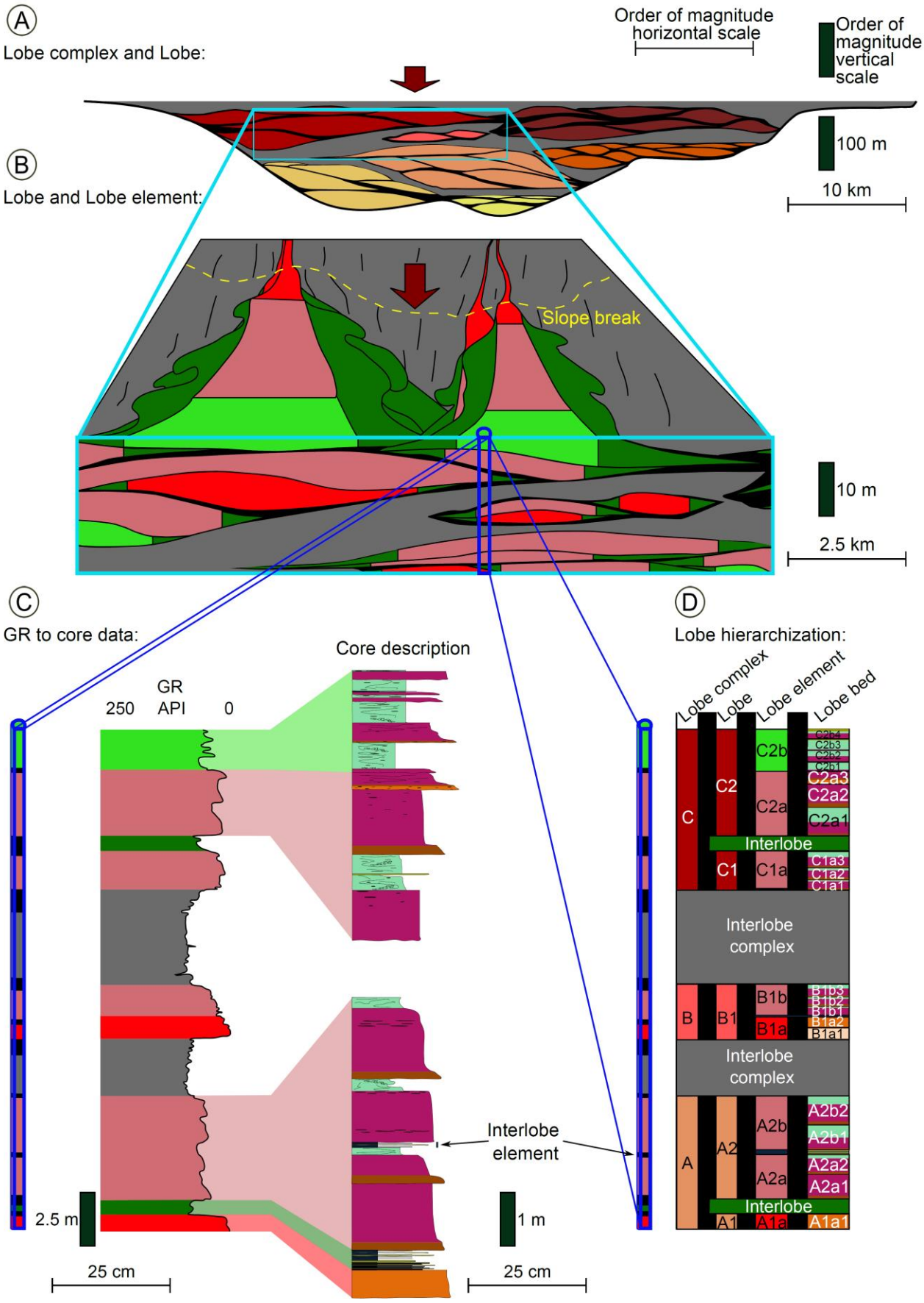
A
Lobe complex and Lobe:
Order of magnitude horizontal scale
Order of magnitude vertical scale
100 m
10 km
B
Lobe and Lobe element:
Slope break
10 m
2.5 km
C
GR to core data:
Core description
GR
250 API 0
2.5 m
25 cm
Interlobe element
1 m
25 cm
D
Lobe hierarchization:
Lobe complex
Lobe
Lobe element
Lobe bed
C
C2
C2b
C2a
C2b4
C2b3
C2b2
C2b1
C2a3
C2a2
C2a1
Interlobe
C1
C1a
C1a3
C1a2
C1a1
Interlobe complex
B
B1
B1b
B1a
B1b3
B1b2
B1b1
B1a2
B1a1
Interlobe complex
A
A2
A2b
A2a
A2b2
A2b1
A2a2
A2a1
Interlobe
A1
A1a
A1a1

- The lobe element is composed of stacked beds and is commonly represented by one facies association (Fig. 3.13C). Commonly lobe elements are interbedded with thin interlobe elements mainly composed of Tu1 of type 2 deposits above O1 mudstones (<10 cm). As suggested in the hierarchical scheme of Prélat et al. (2009), a single lobe bed (between 0.5 to 5 m) may itself represent a lobe element (Fig. 3.14);
- The lobe is commonly composed of one to three lobe elements. Interlobes correspond to thin-bedded Tu1 of type 2 siltstones overlying O1 mudstones (10 cm up to 5 m) interpreted as lateral lobe fringe (LLF) deposits. Deep-water turbidite lobe systems implies both axial and lateral displacements of the lobe (progradation, retrogradation, aggradation, and lateral motion). In a few cases, a lobe separated by two interlobes can be composed of a unique lobe element, itself composed of a single lobe bed (Fig. 3.14);
- Lobe complex is formed of several lobes that can reach up to 75 m in thickness, such as in well 6507/7-1 within the Lysing sandstone Member (Fig. 3.3). Two lobe complexes are separated by an interlobe complex that is composed of a mudstone unit commonly thicker than 5 m.

6. Discussion

6.1. Data exploitation

6.1.1. Lobe beds and their implication at lobe element scale

The identification of lobe bed type helps to decipher different depositional sub-environments. Beds dominated by Hy1/2, Co1 and less commonly by Tu1 of type 1 facies are dominant in the CPL sub-environment (Fig. 3.15A), and usually measure between 5 cm and 1.25 m. MDL is largely represented by beds dominated by Tu1 of type 1, Sl1, Df1 and less commonly by Co1 and Tu2 facies (Fig. 3.15B); MDL beds commonly range from 4 cm to 4.37m in thickness. In turn, the FLF sub-environment is composed of beds dominated by Sl1, Df1, Tu2 and Tu1 of type 1 and 2; FLF beds range from 1 cm and 3.28m. Tu1 of type 2 facies are the most abundant in the FLF sub-environment (Fig. 3.15C). LLF is almost always represented uniquely by millimetric (1 mm) to centimetric (up to 2 cm) Tu1 of type 2 beds deposited onto O1 facies (Supplementary data 3.A). The definition of depositional sub-environment based on lobe bed type and flow type after Mulder and Alexander (2001)'s classification resembles the lobe axial sub-environment described by Fonnesu et al. (2015) with the proximal, intermediate and distal lobe sub-environment, corresponding respectively in this study to the CPL, MDL and FLF. The main difference resides in the discrimination between axial and lateral fringe; in addition, very rare debris flow (Df1) deposits are observed in this study compared to the turbidite lobe observed in Spychala et al. (2017b)'s study.

Fig. 3.15: Statistical analysis based on the database used in this study. For the four first analysis (A, B, C, D), from left to right, the previous lobe sub-environment, the next lobe sub-environment and type and number of beds, for the channel and/or proximal lobe (A), mid to distal lobe (B), frontal lobe fringe (C), and lateral lobe fringe (D). At the bottom of the figure, the observed lobe composition (E), the observed mid to distal lobe thickness (F), and the observed lateral lobe fringe thickness (G).

A Channel and/or Proximal Lobe (CPL)

Previous lobe sub-environment (%):

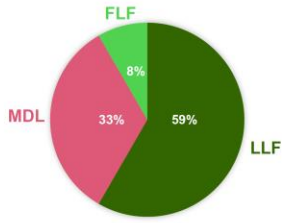

Next lobe sub-environment (%):

Type and number of beds (%):

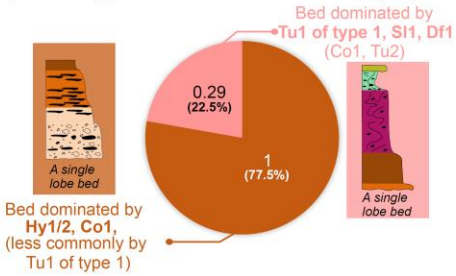

B Mid to Distal Lobe (MDL)

Previous lobe sub-environment (%):

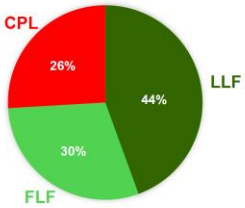

Next lobe sub-environment (%):

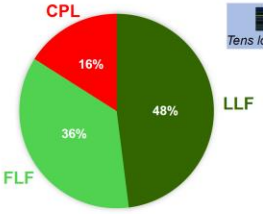

Type and number of beds (%):

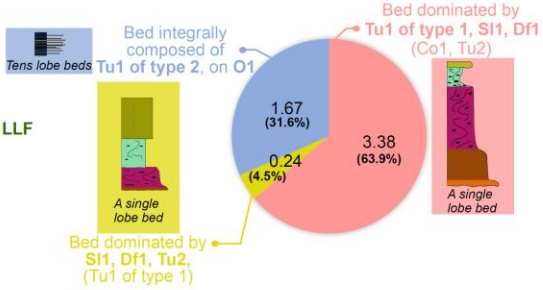

C Frontal Lobe Fringe (FLF)

Previous lobe sub-environment (%):

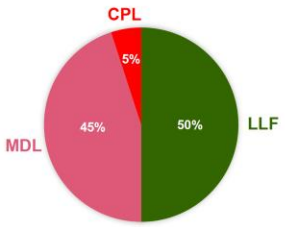

Next lobe sub-environment (%):

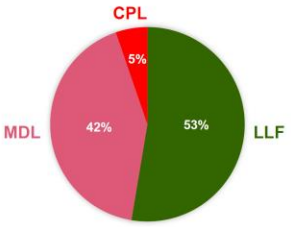

Type and number of beds (%):

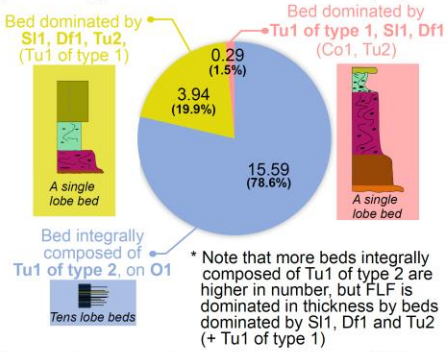

* Note that more beds integrally composed of Tu1 of type 2 are higher in number, but FLF is dominated in thickness by beds dominated by Sl1, Df1 and Tu2 (+ Tu1 of type 1)

D Lateral Lobe Fringe (LLF)

Previous lobe sub-environment (%):

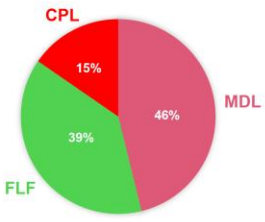

Next lobe sub-environment (%):

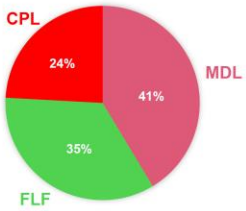

Type and number of beds (%):

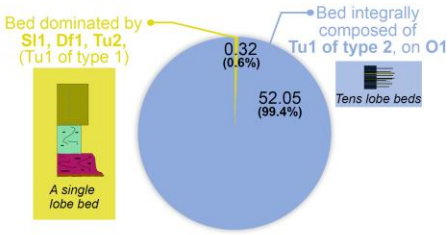

E Environment btw. 2 LLF

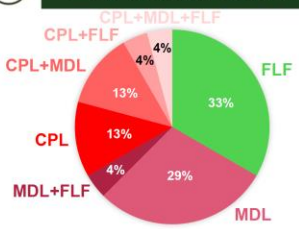

F Thickness of MDL

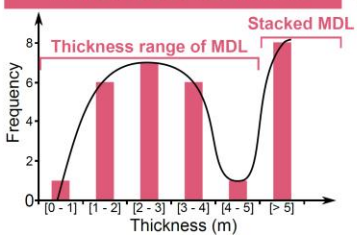

G Thickness of LLF

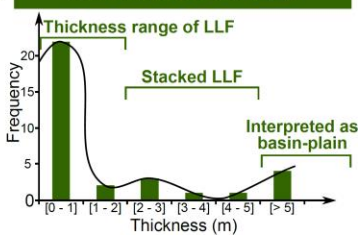

The CPL sub-environment is generally composed of one or two beds with at least one of the beds dominated by Hy1/2 and Co1 facies (Fig. 3.15A) and, less commonly, a second bed composed of Tu1 of type 1, Sl1 and Df1 facies. MDL has an average of ~5 beds with at least 3 beds dominated by Tu1 of type 1, Sl1 and Df1, and two beds composed of Tu1 of type 2 (on O1 facies) that is interpreted as a thin interlobe element (< 10 cm). The interlobe element observed in this study is similar to the one proposed by Prélat et al. (2009). FLF is composed of ~20 beds, 78.6% of which are composed of Tu1 of type 2 (on O1 facies), 19.9% are dominated by Sl1, Df1 and Tu2 facies, whereas rare beds (1.5%) dominated by Tu1 of type 1, Sl1 and Df1 facies also occur (Fig. 3.15C). LLF consists exclusively of Tu1 of type 2 (on O1 facies); it is averages about 52 beds composed of Tu1 of type 2 facies with the rare presence of beds dominated by Sl1, Df1 and Tu2 facies (Fig. 3.15D). The mean number of beds found in the different depositional sub-environment is 1 (CPL), 4 (MDL), 7 (FLF) and 21.5 (LLF) (Supplementary data 3.A).

A single bed can measure a few millimetres up to a few metres (amplitude of observed bed thickness: 1 mm to 4.37 m); it represents a single palaeo-gravity flow event. A CPL sub-environment that is composed of one bed corresponds to a single event that deposited instantaneously. Conversely, a LLF that is composed of tens of palaeo-gravity flow events likely accumulated over a protracted period. The high number of beds in LLF, which are mostly composed of Tu1 of type 2 facies (on O1 facies) most probably reflects numerous gravity flow events. Considering a constant sediment supply with time, the lobe apex is expected to shift laterally as most of the CPLs are composed of a single lobe bed. The increase of bed number towards the lobe front is related to the length and width of each depositional sub-environment. For instance, CPL has a small width and length and MDL a medium width and medium length, whereas the FLF has a large width and a medium to long length (Fig. 3.13B). Bed number and bed composition for each depositional sub-environment thus mainly reflects autocyclic processes regulating sediment dispersal through time and space.

6.1.2. Lobe elements and their implication at lobe scale

6.1.2.1. Lobe elements and their classification

At the lobe element scale, the succession of depositional sub-environments was classified into three distribution patterns: the simple pattern family (**S**) composed of only two sub-environments (for instance, CPL and MDL), the compound pattern family (**CP**) composed of a succession of 3 sub-environments (for instance, MDL, LLF and CPL), and the complex pattern family (**CPX**) composed of two to four lobe sub-environments (Table 3.3). In general, the simple pattern family (**S**) is very frequently observed, the compound pattern family (**CP**) is frequently observed, and the complex pattern family (**CPX**) is infrequently observed such as respectively illustrated by the colour code of *Table 3.3* in the “observed” column with green (very frequent), yellow (frequent) and orange (infrequent).

Each pattern family (**S**, **CP**, **CPX**) was subdivided into pattern groups. **S** is composed of 3 groups, these are the lateral shift pattern (Lsp), the axial pattern (Ap) and the stacked pattern (Sp). **CP** is composed of 4 groups, these are the lateral pattern (Lp), the proximal pattern (Pp),

the mid pattern (Mp) and the frontal pattern (Fp). **CPX** is composed of 3 groups, these are the axial jump pattern (Ajp), the lateral jump pattern (Ljp), and the axial straight pattern (Asp).

All these depositional sub-environment pattern groups were further subdivided into pattern classes. Pattern classes have a very simple naming convention, as it corresponds to the first letter of each lobe sub-environment. For instance, in the simple pattern family (**S**) and the lateral shift pattern group (Lsp), the most commonly observed pattern class is a lateral lobe fringe (LLF) preceding a mid to distal lobe (MDL) sub-environment; hence this class is named *LM* for LLF (L) and MDL (M). The second most commonly observed pattern exbibits the opposite association; this class is therefore named *ML* meaning that the first lobe sub-environment is a MDL, followed by a LLF sub-environment (Table 3.3).

The stacked pattern group (Sp) corresponds to the succession of the same lobe sub-environment. Four stacked classes have been observed, *MM, LL, FF* and *CC*. To identify a stacked succession, the following criteria must be considered: the thickness of a stacked succession is commonly at least twice the average thickness observed for a given depositional sub-environment. Moreover, if a thin mudstone to siltstone interval (< 10 cm) is regularly found over a succession, this interval is regarded as an interlobe element. However, the thickness of the interlobe element has been fixed to 10 cm (at maximum) in order to prevent any overestimation of sub-environment thicknesses.

A total of 42 classes have been identified. In this study, all data (AD) have been analysed, and then reassessed after exclusion of outliers (EO). Outliers are depositional sub-environments that have been only partially cored and/or are commonly found at the core extremities. Other depositional sub-environments have been considered as outliers because the interpretation was uncertain; in such a case, a “?” symbol was tagged in the core description. The full data base including outliers is available in the *Supplementary data 3.A*.

Pattern Family	Pattern Group	Pattern Class	Observed (n times)	Sorted by frequency*	Pattern (C for CPL: channel and/or proximal lobe sub-environment; M for MDL: mid to distal lobe sub-environment; F for FLF: frontal lobe fringe sub-environment; L for LLF: lateral lobe fringe sub-environment)			Displacement (A for Aggrading; P for Prograding; R for Retrograding; LS for Lateral Shift; RA: Retrograding to Aggrading; PA: Prograding to Aggrading; PLS for Prograding Lateral Shift; RLS for Retrograding Lateral Shift)		Interpreted dominating process	Controlling factors		
					First	Second	Third	First	Second	Allo. *vs* Auto.	Combination of controlling factors		
Simple (**S**)	Lateral shift pattern (Lsp)	*LM*	12	1	L	M		LS		Autocyclic	#2	#3	
		ML	12	1'	M	L		LS		Autocyclic	#2	#3	
		FL	10	3	F	L		LS		Autocyclic	#2		
		LF	10	3'	L	F		LS		Autocyclic	#2		
		LC	7	5	L	C		LS		Autocyclic	#2		
		CL	4	6	C	L		LS		Autocyclic	#2		
	Axial pattern (Ap)	*MF*	9	1	M	F		R		Autocyclic	#3	#4	
		FM	8	2	F	M		P		Autocyclic	#3	#4	
		CM	7	3	C	M		R		Autocyclic	#3	#4	
		MC	4	4	M	C		P		Autocyclic	#3	#4	
	Stacked pattern (Sp)	*MM*	8**	1	M	M		A		Autocyclic	#3	#4	
		LL	6**	2	L	L		A		Autocyclic	#4		
		FF	2**	3	F	F		A		Autocyclic	#4		
		CC	1**	4	C	C		A		Autocyclic	#4		
Compound (**CP**)	Lateral pattern (Lp)	*MLM*	5	1	M	L	M	LS	LS	Autocyclic	#2	#3	
		FLF	4	2	F	L	F	LS	LS	Autocyclic	#2		
		MLC	4	2'	M	L	C	PLS	PLS	Autocyclic	#2	#3	#4
		MLF	3	4	M	L	F	RLS	RLS	Autocyclic	#2	#3	#4
		FLM	2	5	F	L	M	PLS	PLS	Autocyclic	#2	#3	#4
		CLM	2	5'	C	L	M	RLS	RLS	Autocyclic	#2	#3	#4
		CLC	1	7	C	L	C	LS	LS	Autocyclic	#2		
	Proximal pattern (Pp)	*LCM*	3	1	L	C	M	LS	R	Autocyclic	#2	#3	#4
		LCL	3	1'	L	C	L	LS	LS	Autocyclic	#2		
		MCM	3	1''	M	C	M	P	R	Autocyclic	#3	#4	
		MCL	1	4	M	C	L	P	LS	Autocyclic	#2	#3	#4
	Mid pattern (Mp)	*LML*	7	1	L	M	L	LS	LS	Autocyclic	#2	#3	
		FMF	5	2	F	M	F	P	R	Autocyclic	#3	#4	
		CML	4	3	C	M	L	R	LS	Autocyclic	#2	#3	#4
		LMF	3	4	L	M	F	LS	R	Autocyclic	#2	#3	#4
		LMC	2	2	L	M	C	LS	P	Autocyclic	#2	#3	#4
		FML	1	6	F	M	L	P	LS	Autocyclic	#2	#3	#4
		CMC	1	6'	C	M	C	R	P	Autocyclic	#3	#4	
	Frontal pattern (Fp)	*LFL*	8	1	L	F	L	LS	LS	Autocyclic	#2		
		MFM	5	2	M	F	M	R	P	Autocyclic	#3	#4	
		MFL	1	3	M	F	L	R	LS	Autocyclic	#2	#3	#4
		LFM	0***	4	L	F	M	LS	P	Autocyclic	#2	#3	#4
Complex (**CPX**)	Axial jump pattern (Ajp)	*CF*	1	1	C	F		R		Allocyclic	#5		
		FC	1	1'	F	C		P		Allocyclic	#5		
	Lateral jump pattern (Ljp)	*CLF*	1	1	C	L	F	RLS	RLS	Allocyclic	#6		
		FLC	0***	2	F	L	C	PLS	PLS	Allocyclic	#6		
	Axial straight pattern (Asp)	*CMF*	1	1	C	M	F	R	R	Allocyclic	#5		
		FMC	0***	2	F	M	C	P	P	Allocyclic	#5		

* : Sorted by occurrence frequency inside pattern Group
** : Estimated number of occurences for stacked patterns (n= number of occurences of observed pattern seen out of 233 m of core described)
*** : Expected to exist

Table 3.3: Summary table highlighting, from left to right, the pattern family, pattern group, pattern class, the number of times a pattern has been observed, sorted by occurrence frequency, pattern type, displacement, interpreted processes, and controlling factors.

6.1.2.2. Autocyclic processes

a) Lobes

Autocyclic processes controlling lobe elements allow the self-regulation of sediment dispersion at the lobe scale. In this regard, the very common to common occurrence frequency of given depositional patterns is most likely controlled by autocyclic processes. For instance, the CPL sub-environment is very commonly to commonly succeeded or preceded by LLF or MDL (Table 3.3, Figs. 3.15A, 3.16A). Usually the channel and/or proximal lobe (CPL) is deposited on top of a lateral lobe fringe (LLF), and the opposite combination is less frequently observed. The higher occurrence frequency of the *LC* class compared to the *CL* class may be explained by the fact that the channel and/or proximal lobe sub-environment is forming a positive relief, forcing the subsequent lateral lobe fringe to develop on either side of the CPL sub-environment (thus laterally), i.e. in the areas of lower relief (Fig. 3.16A). A *CM* class is also more frequently observed than an *MC* class (Figs. 3.16B, 3.16C), as the first lobe element acts as a barrier constraining the subsequent channel and/or proximal lobe element to develop upstream, thus implying a retrogradation of the lobe (Table 3.3, Fig. 3.16B), such as observed in laboratory experiments by Hamilton et al. (2017) during the retrogradation phase. In turn, the *MC* class is less frequently observed due to the fact that the second lobe element requires a stronger sediment supply to prograde across the first channel and/or proximal lobe, which acts as a positive relief (Table 3.3, Fig. 3.16C).

The MDL sub-environment is very commonly preceded or succeeded by all other depositional sub-environments (including itself), thus highlighting its central position in the lobe (*LM, ML, MF, FM, CM, MC* and *MM* classes in *Table 3.3*). In terms of lobe dynamics, the lobe primarily migrates along the lobe axis by progradation (20%) or retrogradation (27%). Besides, there is a 40% probability that the lobe will shift laterally and 13% probability for lobe aggradation. These observations therefore outline that the MDL sub-environment is the centre of gravity of the lobe (Fig. 3.16D). In other words, the probability for any lobe sub-environment (LLF, CPL, FLF or MDL) to be proceeded or succeeded by a mid to distal lobe (MDL) sub-environment is equivalent, involving that the likelihood of lobe retrogradation, progradation, lateral shift or aggradation is practically equal. As comparison to laboratory experimentations, the centre of gravity of the lobe is indirectly evocated in the study of Hamilton et al. (2017) during the three steps, with first the progradation, then the aggradation and finally the retrogradation phases highlighting the central position of the equivalent “MDL” sub-environment. Hence the mid to distal lobe sub-environment is mainly controlled by autocyclic processes regulating sediment distribution by random migration of the lobe in any direction.

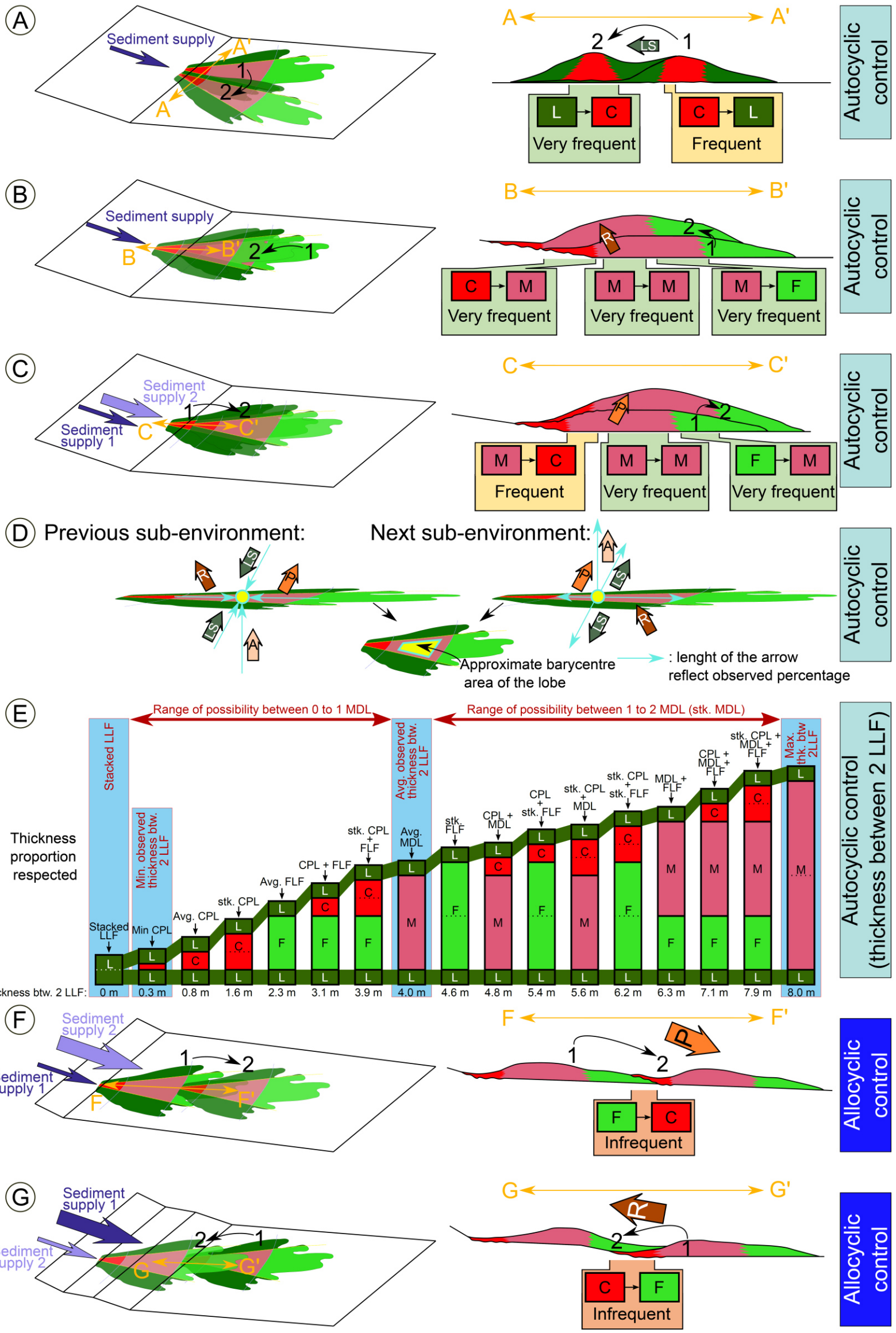

Fig. 3.16: Summary sketches for autocyclic and allocyclic controlling factors. (A) Lateral shift of the lobe in plan view (left) and cross-section (right) is interpreted as resulting from autocyclic processes. (B) Retrogradation of the lobe in plan view (left) and cross-section (right) is interpreted as resulting from autocyclic processes. (C) Progradation of the lobe in plan view (left) and cross-section (right) is interpreted as resulting from autocyclic processes. (D) Preceding and succeeding mid to distal lobe (MDL) is almost equal in all directions, reflecting that the MDL corresponds to the centre of gravity of the lobe. (E) Thickness variability between two lateral lobe fringe (LLFs) sub-environments is controlled by the thickness of the mid to distal lobe sub-environment. The thickness between 2 LLFs is regarded as resulting from autocyclic processes. (F) Progradation of the turbidite lobe entailing a lobe sub-environment gap in plan view (left) and cross-section (right), interpreted as resulting from allocyclic forcings. (G) Retrogradation of the turbidite lobe entailing a lobe sub-environment gap in plan view (left) and cross-section (right), interpreted as resulting from allocyclic forcings. The occurrence frequency (very frequent, frequent and infrequent) is documented in Table 3.3, with C: channel and/or proximal lobe, M: mid to distal lobe, F: frontal lobe fringe, and L: lateral lobe fringe. Avg., min., max., stk., thk., and btw. abbreviations correspond, respectively to, average, minimum, maximum, stacked, thickness, and between. Thicker arrows in C, F and G sketches correspond to enhanced sediment supply. Arrows with P, R, A and LS mean Progradation, Retrogradation, Aggradation and Lateral Shift, respectively.

b) Interlobes

Each depositional lobe sub-environment (CPL, MDL and FLF) is equivalently preceded or succeeded by a Lateral lobe fringe (LLF) sub-environment (Fig. 3.15D). The lateral shift pattern group (Lsp) is very commonly observed and implies a lateral shift of the lobe (Table 3.3). The mean thickness of the LLF sub-environment is 0.67 m with a median thickness of 0.39 m (Supplementary data 3.A). Interestingly, when a CPL is encased between 2 LLF sub-environments (LLFs), the LLF thickness is thin (ranging from approximately 10 to 40 cm), as illustrated between 2876.00 m and 2864.00 m in well 6407/3-9S (Fig. 3.10). Intermediate thicknesses of LLF (ranging between approximately 20 and 80 cm) are observed when a MDL sub-environment is encased between 2 LLFs. This configuration can be observed in well 6407/2-2 between 3294.00 m and 3287.00 m (Fig. 3.6). In turn, thick LLF deposits (ranging between approximately 40 cm and 3.50 m) are observed when a FLF sub-environment is encased between 2 LLFs. Thick LLFs can be observed at 2740.00 m and 2735.00 m in well 6407/3-3 (Fig. 3.12).

Thicknesses ranging from 10 cm up to 2 m are commonly found in LLF sub-environments (Fig. 3.15G), corresponding similarly to the interlobe interval defined by Prélat et al. (2009) which range from 20 cm to 2 m thick. Stacked LLF successions usually range between 2 and 5 metres, while LLF successions <10 cm are interpreted as interlobe elements. The class *LL (***S**, Sp) is very commonly observed (Table 3.3). A stacked LLF succession exceeding 5 metres reflects basin-plain deposits, as observed at the base of Core #1 of well 6507/2-2 (Fig. 3.6) between 2849.45 m and 2832.70 m in marine mudstones (Fig. 3.3).

The average thickness of each depositional sub-environments fluctuates across the turbidite lobe. The thinnest lobe sub-environment is the LLF, which corresponds to the interlobe. This is followed by the CPL, with a mean thickness of 0.78 m and a median thickness of 0.51 m. The FLF sub-environment has a mean thickness of 2.34 m and a median thickness of 2.02 m (Supplementary data 3.A). The thickest sub-environment is the MDL, with a mean thickness of 3.96 m and a median thickness of 3.08 m (Fig. 3.15F).

The mean lobe thickness, i.e., the thickness between 2 LLF sub-environments (interlobes) is 4.12 m. This thickness corresponds to approximately the average thickness of a mid to distal lobe (MDL) i.e., 3.96 m. The maximum thickness between 2 LLF sub-environments does not exceed 8 m, i.e., approximately the average thickness of 2 stacked MDL sub-environments. As a comparison, Prélat et al. (2009) reported that lobe thicknesses in the Permian Karoo Basin (South Africa) were typically ranging between 4 and 10 metres. These observations are valuable for any lobe element configurations observed within a lobe. Common configurations of lobe elements observed between 2 LLFs are as follows: FLF, MDL, CPL, 2 stacked FLF, 2 stacked MDL, 2 stacked CPL, MDL + FLF, CPL + MDL, CPL + FLF, CPL + MDL + FLF) (Figs. 3.15E, 3.16E).

In summary:

- The minimum sediment thickness between 2 LLFs is equal to the minimum thickness of the CPL;

- The average thickness of sediment between 2 LLFs is equal to the average thickness of the MDL;
- The maximum thickness of sediment between 2 LLF sub-environments is equal on average to 2 stacked MDL sub-environments.

The thickness between 2 LLFs is linked to the MDL thickness, as LLFs are indirectly linked to the gravity centre of the turbidite lobe that is located in the middle part of the MDL sub-environment. This could explain why there is an almost equal probability for the lobe to aggrade, retrograde, prograde or shift laterally (or develop) into an MDL sub-environment (Fig. 3.16D).

6.1.2.3. Allocyclic processes

Allocyclic processes are involved to account for the (rarely observed) depositional patterns of the Complex Pattern family (**CPX**) (Table 3.3). **CPX** groups imply a rapid retrogradation or progradation of the turbidite lobe under the influence of external controls such as eustatism, climate change and/or tectonics, which deeply impact on sediment supply and dispersal. For instance, the channel and/or proximal lobe (CPL) sub-environment in the *CF* and *FC* classes are abruptly preceded or succeeded by the frontal lobe fringe (FLF) sub-environment (Fig. 3.15C), thus involving a gap in the expected lobe succession. Besides, the “Axial jump pattern” group (Ajp) occurs when the lobe system undergoes a significant change in sediment supply. The *CF* class (**CPX**, Ajp) implies a considerable decrease of sediment supply or an upstream dipping slope break (or a combination of the two) to become retrogradational (Fig. 16-G). Conversely, the *FC* class (**CPX**, Ajp) implies an increase of the sediment supply or a downstream dipping slope break (or a combination of the two) to become progradational (Fig. 3.16F). In the *FC* class, for a similar sediment supply between lobe elements 1 and 2, a downstream dipping slope break is automatically generated by the tail of lobe element 1 (Fig. 3.16F).

6.1.3. Lobes and their significance at lobe complex scale

6.1.3.1. Autocyclic processes

Lobes can be composed of a single or multiple CPL, MDL and FLF sub-environments intercalated by interlobes (LLF lobe sub-environments). The lobe is recurrently composed of simple or compound (**S** and **CP**) depositional patterns within the lobe complex (Table 3.3), which defines the basic organisation of the lobe complex through time. For instance, the lobe complex of the Lysing Member cored in well 6407/2-3 (Fig. 3.7) is composed of lobes of variable thicknesses. Thin (2 m) to thick turbidite lobes (> 18 m) have been recognized, the latter being formed of several interlobe elements (0 to 10 cm). Both thick and thin lobes (Fig. 3.7) are composed of simple classes such as *MF* and *FM* (**S**, Ap) or compound classes such as *MLF* and *FLM* (**CP**, Lp). Classes *MF* and *MLF* imply a retrogradation of the lobe, whereas classes *FM* and *FLM* infer a lobe progradation. Hence sediment dispersal is regulated by alternating progradation and retrogradation of the lobe, between lateral shifts elements. Similar observations can be made for the Lysing Member in a more proximal lobe sub-environment (i.e., well 6407/3-9S; Fig. 3.10) where the succession of progradations and

retrogradations (*MLC*, *CLM* and *CM* classes) recall autocyclic avulsion cycles observed in laboratory experiments (Hamilton et al., 2015, 2017).

6.1.3.2. Allocyclic processes

Lobe complex evolution can be identified from cores but is more easily observed in well-log data (Fig. 3.3). In well 6507/2-2 (Fig. 3.6), the Breiflabb Member exhibits, from the bottom to the top, a general trend of alternating CPL to MDL sub-environments evolving to MDL and FLF sub-environments. The Breiflabb Member, at this well location, demonstrates the general retrograding trend of the entire lobe complex (Fig. 3.6) under the dominant influence of autocyclic processes. From the well-log correlation panel (Fig. 3.3), retrograding to prograding trends in lobe complexes are also observed and, when present, can be confirmed using core description. Retrograding to aggrading trends (blue arrows in *Fig. 3.3*) are detected in the Breiflabb Member and Skolest Member equivalent, whereas the Lysing Member is mainly progradational to aggradational (yellow arrows in *Fig. 3.3*). However, allocyclic processes may also be identified from core data; the Breiflabb lobe complex in core #3 of well 6507/2-2 (Fig. 3.6) is composed of a first lobe containing 2 lobe elements (MDL followed by CPL sub-environment), then an interlobe (LLF sub-environment), followed by a second lobe composed of a single lobe element, a FLF sub-environment. Such a succession follows the pattern class “CLF” (**CPX**, Lip) and implies an important retrograding lateral shift displacement of the lobe most probably caused by allocyclic forcings (Table 3.3).

6.1.4. Autocyclic and allocyclic forcings on lobe architecture

The analysis of depositional patterns undertaken in this study, at different scales, allows to define 4 autocyclic factors (#1, #2, #3, and #4) and 3 allocyclic forcings (#5, #6, and #7) (Fig. 3.17) controlling the development of the entire lobe complex (Fig. 3.18). Note that the autocyclic factor #1 and the allocyclic factor #7 are not mentioned in the depositional pattern table (Table 3.3), since the table focuses on the lobe element to lobe scales. The autocyclic factor #1 is interpreted at the lobe bed scale, whereas the allocyclic factor #7 is interpreted at the lobe complex scale (Fig. 3.17).

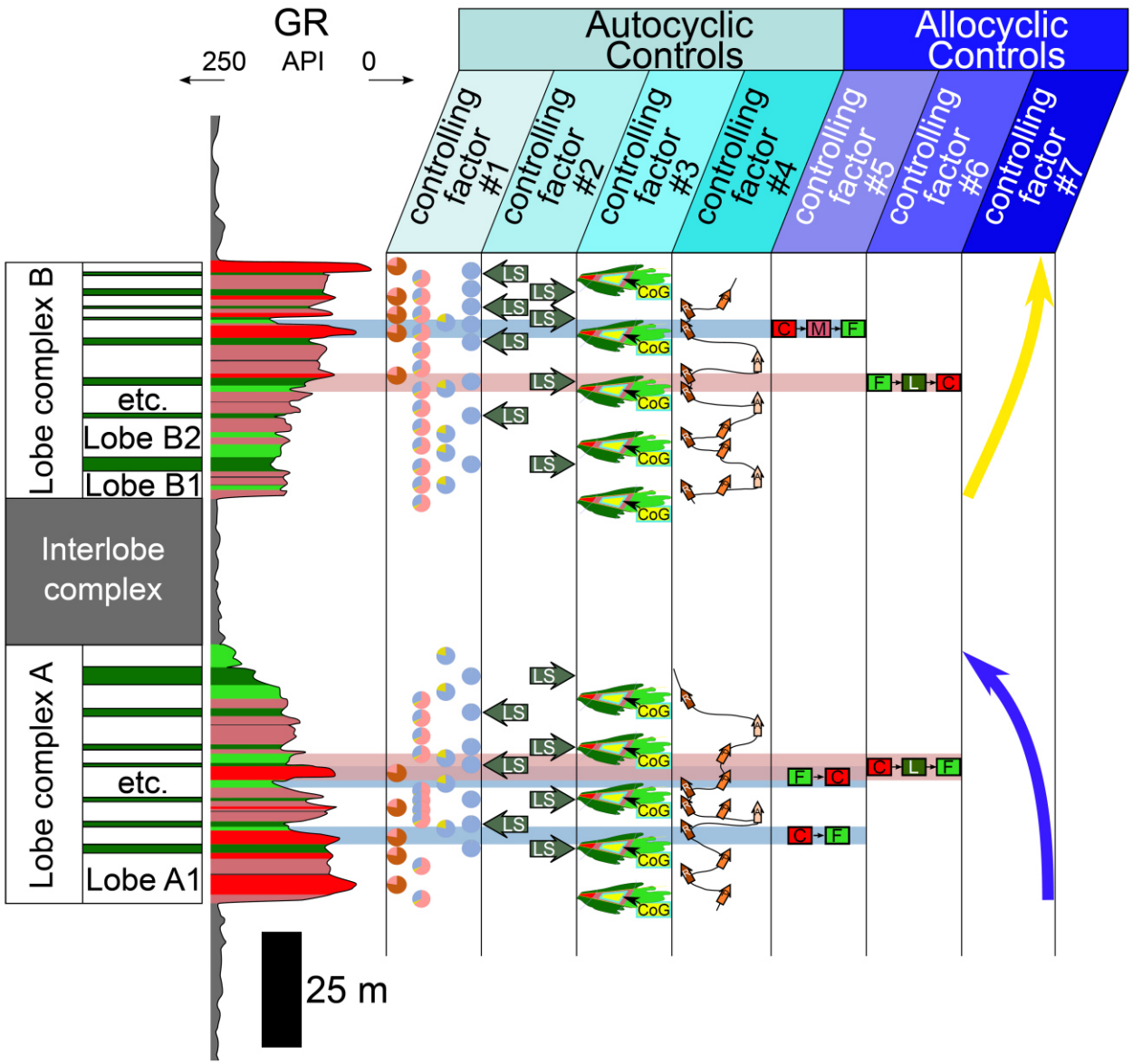

Fig. 3.17: Summary of the autocyclic and allocyclic forcings: the controlling factor #1 corresponds to the self-regulation of sediment dispersal by sorting of the type and number of beds over time; the controlling factor #2 forces the lobe to shift laterally; the controlling factor #3 corresponds to the centre of gravity of the lobe; the controlling factor #4 allows a lobe to migrate along its longitudinal axis by progradation, retrogradation or along its vertically axis by aggradation; the controlling factor #5 is considered as being allocyclic as it allows a turbidite lobe to migrate rapidly along its longitudinal axis by progradation or retrogradation (involving a depositional gap in the succession) at the intra-lobe scale; in turn, the controlling factor #6 is considered as being allocyclic as it allows a rapid progradation or retrogradation (with a depositional gap in the succession) at the extra-lobe scale; the controlling factor #7 regulates the evolution of sediment delivery over time. Two types of controlling factor #7 have been identified, the type A highlights a decrease of sediment input through time, whereas type B corresponds to an increase in sediment input caused by tectonics, eustatism and/or climate changes (or a combination of some of those factors). Arrows with P, R, A and LS mean Progradation, Retrogradation, Aggradation and Lateral Shift, respectively. Abbreviations are CoG for Centre of Gravity of the lobe, and letters in colored boxes are C, M, F and L meaning Channel and/or proximal lobe, Mid to distal lobe, Frontal lobe fringe and Lateral lobe fringe sub-environment, respectively.

6.1.4.1. Autocyclic factors

Autocyclic factors are mainly observed at the lobe bed to lobe scales, such as proposed by Piazza and Tinterri (2020). Self-organisation of the lobe regulates sediment distribution and delivery within the system. Autocyclic factors and inferred from a succession of simple (**S**) to compound (**CP**) depositional pattern families (Table 3.3). Note that the simple (**S**) pattern is composed of a combination of one or two autocyclic factors, whereas compound (**CP**) depositional patterns are composed of a combination of one to three autocyclic controls (Table 3.3).

The influence of the autocyclic factor #1 is observable at the lobe bed element scale. Autocyclic factor #1 regulates sediment dispersal by controlling the number of beds and bed type within each lobe element through time. It further highlights why a channel and/or proximal lobe sub-environment (CPL) is composed on average of a single palaeo-gravity event, whereas a lateral lobe fringe sub-environment (LLF) is composed of several thin (1 mm to 2 cm) palaeo-gravity events.

Autocyclic factor #2 involves a lateral shift of the lobe (Fig. 3.17), as also reported by Hamilton et al. (2015, 2017). Here, LLF thickness fluctuates as a function of the adjacent sub-environment following or preceding axial lobe sub-environments. LLF thickness is higher if laterally associated to a FLF and thinner close to a CPL. Moreover, the lobe thickness (i.e., the thickness between 2 interlobes) is controlled by lateral shift displacements of the lobe, which prevents the lobe to overpass the critical thickness of approximately 8 m (Fig. 3.16E).

The autocyclic factor #3 corresponds to the centre of gravity of the turbidite lobe (CoG in *Fig. 3.17*), as also reported from Hamilton et al. (2015, 2017). This factor regulates sediment distribution within the lobe through a constant return to its centre of gravity. As previously mentioned, the barycentre of the lobe is the MDL sub-environment (Fig. 3.16D), which can be equally preceded or succeeded by any of the other depositional sub-environment.

The autocyclic factor #4 is commonly observed at the lobe element to lobe scale, in the main lobe axis. It a gradual process determining whether the lobe progrades, retrogrades or aggrades (Fig. 3.17), as also observed by Hamilton et al. (2015, 2017). In other words, the CPL and FLF sub-environments can only be preceded, or succeeded, by a MDL sub-environment, or by another MDL in the case of an aggradation.

6.1.4.2. Allocyclic factors

Allocyclic controls are principally observed at the lobe element to lobe complex scales (Prélat et al., 2009). Allocyclic processes are governed by external factors such as tectonic, climate and/or sea level changes, which impact on the amount of sediment delivery and slope steepness. Allocyclic controls # 5 and #6 correspond to the complex (**CPX**) pattern family, whereas allocyclic control #7 drives the evolution of the entire lobe complex (Fig. 3.17).

Allocyclic control #5 corresponds to an intra-lobe shift of sedimentary dynamics (Fig. 3.17). In a turbiditic lobe, a direct progression from a CPL to a FLF sub-environment (omitting the MDL sub-environment) (**CPX**, Ajp, *CF* or *FC* in *Table 3.3*), or vice versa, implies a gap in the axial

depositional succession (Figs. 3.16F, 3.16G). Such migration (rapid retrogradation or progradation) implies an important change in sediment input which are related to allocyclic processes. Allocyclic control #6 corresponds to an extra-lobe shift of sedimentary dynamics (Fig. 3.17), occurring, for instance, when two turbidite lobes are separated by an interlobe undergoing a rapid progradation or retrogradation (Fig. 3.17). This factor also involves a gap in the axial depositional succession. *CLF* and *FLC* classes (**CPX**, Lip) thus imply significant changes in sediment delivery. Experimentally, Allocyclic controls #5 and #6 imply drastic changes in the amount of sediment delivery (Ferguson et al., 2020). The only difference between allocyclic controls #5 and #6 is the scale of observation (i.e., allocyclic controls #5 observed at the lobe element scale, while allocyclic controls #6 at the lobe scale).

Allocyclic control #7 corresponds to the impact of climate change, tectonic and/or sea-level changes on the lobe complex dynamics (Fig. 3.17). Such allocyclic controls are observed at lobe complex scale, such as proposed by Piazza and Tinterri (2020). These are easily observed based on GR-logs (Fig. 3.3) by steady increases or decreases in the log values (interpreted as grain size changes). Two trends can be interpreted from grain size changes: an aggrading to retrograding trend (Type A, blue arrows in *Figs. 3.3, 3.17*), or an aggrading to prograding trend (Type B, yellow arrows in *Figs. 3.3, 3.17*). Allocyclic control #7 governs lobe connectivity within the lobe complex (Fig. 3.18). The aggrading to prograding trend (Type B, yellow arrows in *Figs. 3.3, 3.17*) implies an increase of sediment delivery inducing a higher lobe connectivity. Conversely, the aggrading to retrograding trend (Type A, blue arrows in *Figs. 3.3, 3.17*) highlights a decrease of sediment delivery triggering a lower lobe connectivity. As to illustrate it, the Breiflabb sandstone Member is composed of lobes that are partially connected (sub-connected) and overlapping each other, whereas the Skolest equivalent sandstone Member contains lobes that are predominantly disconnected (Figs. 3.18A, 3.18B). In turn, the Lysing sandstone Member is composed of lobes that are well connected between them (Fig. 3.18C).

The degree of inter-lobe connectivity is indeed crucial from a petroleum production consideration. A petroleum discovery in the Lysing sandstone Member (exhibiting well-connected lobes) would produce the gas of several lobes in a single well such as in the Marulk field (Ormøy et al., 2011). In contrast, a discovery in the Skolest Member equivalent in the Dønna Terrace (exhibiting unconnected lobes with vertical and lateral shale barriers) would require several producer wells, therefore rendering the development uneconomic.

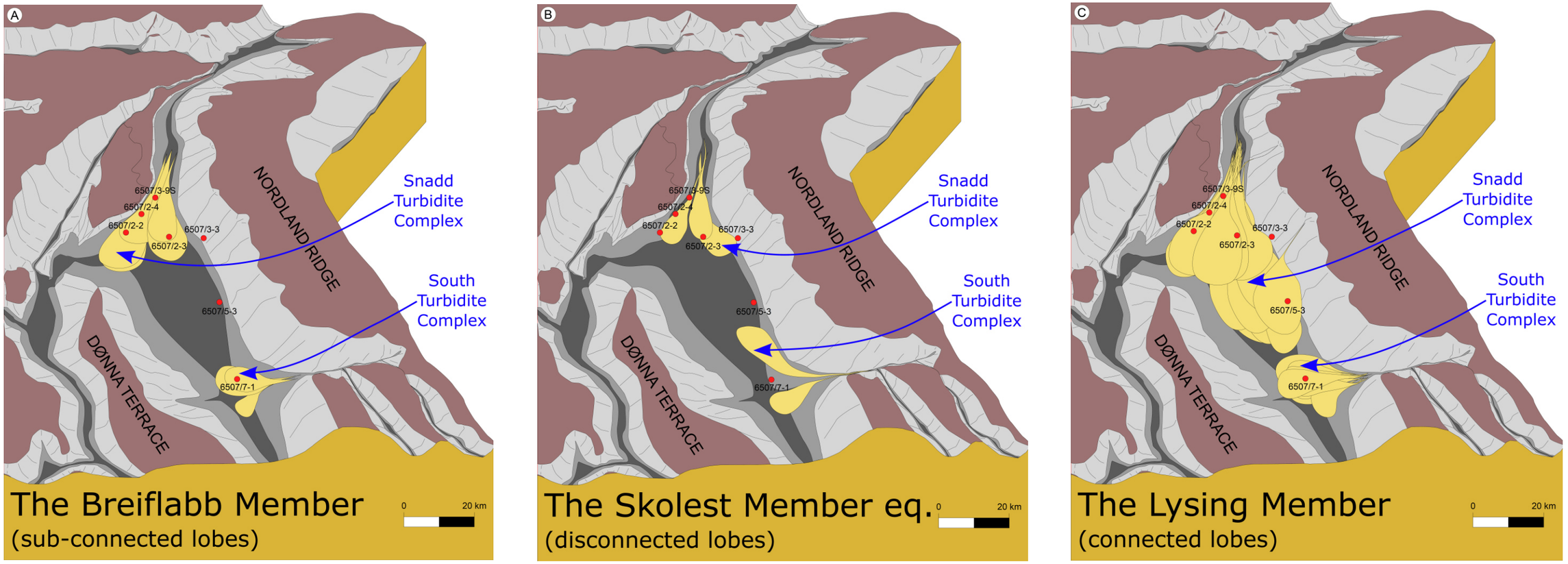

Fig. 3.18: 3D block diagrams of the three studied sandstone members: (A) The Breiflabb Member (sub-connected lobes); (B) The Skolest Member equivalent (disconnected lobes); (C) the Lysing Member (connected lobes). 3D background is modified after Fugelli and Olsen (2007).

6.2. Lobe sub-environment, lobe architecture and scale of observation

Four lobe sub-environments have been identified, providing an empirical basis for discussing lateral or axial lobe migration. From the lobe apex, the first depositional sub-environment encountered downstream is the channel and/or proximal lobe (CPL) also named inner fan (Fugelli and Olsen, 2007; Fonnesu et al., 2018). CPL is the least commonly observed depositional sub-environment in comparison to the other three lobe sub-environments (MDL, FLF and LLF). Compared to the two other axial lobe sub-environments (MDL and FLF), the channel and/or proximal lobe (CPL) sub-environment was observed only 12 times (~20% of instances). We believe that such a low occurrence (< 20%) reflects the restricted area of the slope break zone to which the CPL is confined, or in some cases, implies narrow turbidite channels located upstream of the lobe apex. In contrast, the MDL sub-environment is largely recognized in this study (50% of instances), and more commonly observed than axial deposits of the CPL and FLF sub-environments, thus reflecting a large depositional area for the MDL sub-environment. In the same way, FLF sub-environments represent >30% of the observed deposits, implying a large depositional area. Comparing the frequency of occurrence of axial (CPL + MDL + FLF) versus lateral (LLF) deposits, axial deposits were observed 63 times (66%), whereas lateral deposits were identified 33 times (34% of instances). This suggests that lateral lobe fringe deposits (LLF), i.e., interlobes, are generally deposited over two successive axial lobe deposits. In other words, a turbidite lobe is usually composed of two lobe elements (or sub-environments).

Various lobe architectures have been reported elsewhere, some with four lobe members (lobe bed, lobe element, lobe and lobe complex; Prélat et al., 2009), as in this study. Other works, instead, argued for five members in turbidite lobes (Mulder and Etienne, 2010). The fifth member is placed between the lobe and lobe complex and named the “lobe system”. The two hierarchisation models (Prélat et al., 2009; Mulder and Etienne, 2010) imply a different confinement setting of the basin. In this study, the Dønna Terrace consists of a high density of intraterrace highs and lows that result in extremely confined sub-basins. In such a confined setting, the lobe hierarchisation may rather be composed of four members (lobe bed, lobe element, lobe and lobe complex), as “lobe systems” are usually stacked and thus difficult to identify within the lobe complex. In an unconfined basin setting, however, Mulder and Etienne (2010)’s hierarchisation permits a 3D understanding of the lobe complex by the identification of “lobe systems”.

Piazza and Tinterri (2020) stated that autocyclic controls are mainly observed at the lobe bed to lobe scale, whereas allocyclic controls are dominantly observed at the lobe complex scale. Our study demonstrates that this affirmation is correct, but we believe that “minor” allocyclic processes (i.e., controlling factors #5 and #6) can also be identifiable at the lobe element to lobe scale. Conversely, autocyclic processes can also be involved at the lobe complex scale because autocyclic and allocyclic processes are obviously imbricated. In fact, lobe bed, lobe element, lobe and lobe complex are fractal geological objects, and are therefore most probably impacted by a combination of autocyclic and allocyclic processes at their respective scales. For instance, in a confined setting, at the lobe complex scale, a turbidite lobe complex can prograde, retrograde or aggrade, thus the migration is mainly related to allocyclic controls;

however, at intra-lobe scale, autocyclic controlling factor #4 allows a lobe to migrate along its longitudinal axis by progradation, retrogradation, or along its vertically axis by aggradation. The observation scale is thus fundamental in understanding sediment dispersal processes. Sediment delivery fluctuations (mainly controlled by allocyclic forcings) impact the lobe complex organisation; however, at a smaller scale (i.e., the lobe or lobe element scale), autocyclic sediment dispersal processes (such as controlling factor #4) allow sediment distribution where accommodation space is available. Experimental studies have highlighted the autoregulation of sediment distribution inside lobes (Hamilton et al., 2015, 2017; Ferguson et al., 2020). In this study, four main autocyclic factors regulating the internal organisation of a turbiditic lobe have been deciphered. Note that the lobe complex is formed of different combinations of simple pattern (**S**) and compound patterns (**CP**), interpreted as autocyclic controlling factors (cf. section 6.1. Data exploitation). We further scale the impact of each controlling factor (from lobe bed to lobe complex) on the lobe organisation. Note that the seven controlling factors are intimately linked together. For instance, in the case of increasing sediment delivery through time, a progradation of the lobe complex will be observed (allocyclic factor #7 of type B in *Fig. 3.17*), which will in turn enhance the probability of occurrence of allocyclic processes affecting the basin at an extra-lobe (controlling factor #6) to intra-lobe scale (controlling factor #5). In turn, the lobe will distribute the sediment over a wider area. This will cause the lobe to migrate along its own axis (controlling factor #4), by returning to its centre of gravity (controlling factor #3), by shifting laterally (controlling factor #2) and by regulating the type and number of beds at lobe bed scale (controlling factor #1). Conversely, the opposite chain of reactions is true with a controlling factor #7 of type A (Fig. 3.17) impacting on the effect of the six other controlling factors.

7. Conclusions

Most studies tackling the influence of allocyclic controls have focused on identifying whether sedimentary dynamics within turbidite systems was triggered by climate, eustatic or tectonic changes. In this study, we have deciphered whether the controlling factors are predominantly assignable to autocyclic or allocyclic forcings as it is known that internal and external processes are obviously imbricated. A detailed facies description was conducted in Turonian to Coniacian deep-water turbidite deposits of the Dønna Terrace, located offshore Mid-Norway, which allows the identification of various subaqueous sedimentary density flow (SSDF) deposits. SSDF deposits have been further grouped into facies associations, from which four depositional turbidite lobe sub-environments have been reconstructed. Three of those facies associations are axial lobe deposits: channel and/or proximal lobe (CPL), mid to distal lobe (MDL) and frontal lobe fringe (FLF), whereas one off-axis turbidite lobe element identified as a lateral lobe fringe sub-environment (LLF), corresponds to interlobe deposits. We further showed that each turbidite lobe complex is unique and related to various parameters such as slope angle, sediment grain-size, sand to mud ratio, water density, and basin setting configuration.

The analysis of lobe depositional sub-environments has revealed the following characteristics:

- The CPL sub-environment has an average thickness of 0.78 m and is generally composed of 1 to 2 beds, with at least one bed dominated by hyperconcentrated to concentrated flow deposits (Hy1/2 and Co1 facies);
- The MDL sub-environment has an average thickness of 3.96 m and is composed on average of 5 to 6 beds, with at least 3 beds dominated by turbidity, slurry and debris flow deposits (Tu1 of type 1, Sl1 and Df1 facies);
- The FLF sub-environment has an average thickness of 2.34 m and is composed of 19 to 20 beds, with thick beds dominated by slurry, debris flow and supercritical turbidity flow deposits (Sl1, Df1 and Tu2 facies);
- The LLF sub-environment has an average thickness of 0.67 m and contains on average of 52 to 53 beds, composed mainly of turbidity flow deposits accumulated in a deep-marine mudstone environment (Tu1 of type 2 onto O1 facies).

The depositional succession of lobe sub-environments reflects both autocyclic and allocyclic processes. Frequently observed depositional patterns (**S** and **CP** pattern family in *Table 3.3*) have been attributed to autocyclic sediment dispersal processes within the sedimentary system. The less common depositional patterns (i.e., **CPX** pattern family in *Table 3.3*) are in turn associated with a rapid axial migration of the lobe with or without a depositional sub-environment gap and have been thus attributed to dominant allocyclic controls.

Four closely related autocyclic and three allocyclic controlling factors have been identified:

- The 1st autocyclic factor, controlling factor #1, corresponds to the self-regulation of the sediment dispersal by sorting of the type and number of beds through time;
- The 2nd autocyclic factor, controlling factor #2, causes the lobe to shift laterally, thus deflecting the sedimentation away from the highest topography (of the lobe axis). This autocyclic process generates different thicknesses of LLF deposits (interlobes) based on the preceding or succeeding axial depositional sub-environments (CPL, MDL and FLF). Interlobe deposits are thinner when developing close to a CPL, and thicker when associated to a FLF. The critical heights of lobes observed in this study (i.e., 8 m) relies on the prevailing flow regimes at the locality of sedimentation, as well as flow parameters such as the average flow density and load volumes;
- The 3rd autocyclic factor, controlling factor #3, corresponds to the centre of gravity of the turbidite lobe. A mid to distal lobe sub-environment (MDL) is overlain, in almost equal proportions, by any other lobe depositional sub-environment (CPL, FLF, LLF and MDL);
- The 4th autocyclic factor, controlling factor #4, allows a lobe to migrate along its longitudinal axis by progradation, retrogradation, or along its vertically axis by aggradation. This intra-lobe migration is another way to regulate sediment dispersal over time. Intra-lobe dynamics along its longitudinal axis do not lead to depositional succession gaps;

- The 1st allocyclic factor, controlling factor #5, is observed at an intra-lobe scale and is associated with a depositional succession gap, or a rapid migration along its longitudinal axis by retrogradation or progradation. This controlling factor #5 forces a significant axial migration and accounts for allocyclic processes;
- The 2nd allocyclic factor, controlling factor #6, is also considered to be caused by allocyclic processes, but at the extra-lobe scale. This may be expressed by the development of two adjacent lobes separated by an interlobe (LLF). A rapid axial migration is mainly triggered by external processes causing an abrupt increase, or decrease, of sediment supply;
- The 3rd allocyclic factor, controlling factor #7, is the main external process. This controlling factor regulates the evolution of sediment delivery through time. A decrease of sedimentary inputs through time is illustrated by controlling factor #7 of type A, whereas an increase in sedimentary input (caused by tectonic, eustatic and/or climate changes) emphasizes a controlling factor #7 of type B.

8. Acknowledgements

This work corresponds to one section of Romain Grime's PhD thesis. The authors thank Edison Norge AS for funding RG's PhD. We sincerely thank Aker BP ASA for providing us core pictures for well 6507/3-9S, and Vår Energi AS for well 6507/2-4. We warmly thank Emerson E&P Software for providing excellent support and software solutions (https://www.pdgm.com/). We thank Jonathan Furic for his constructive and critical evaluation of the manuscript. Thanks to the three RG's PhD reviewers, David Hodgson, Thierry Mulder and Sylvie Bourquin who contribute to refine the interpretation of the proposed depositional model. Thanks to the rest of RG's PhD committee members composed of Emanuela Mattioli, Pascale Huyghe, Francesco Borraccini, Sten Rasmussen and Fernanda De Mesquita Lobo Veloso who contributed to propose the final version of this manuscript.

In the syn-rift (Chapter 2) and post-rift studies (Chapter 3), detailed sediment core descriptions coupled with well-log analyses dated biostratigraphically and properly calibrated to seismic data using checkshot data have constituted the main milestones to decipher depositional environments and their associated controlling mechanisms. The syn-rift (Chapter 2) and post-rift (Chapter 3) intervals in the terrace domain (Halten and Dønna terraces) of the Norwegian Sea are composed of proven sandy petroleum reservoirs (Supplementary data 4.A), the formation of which was shown to be predominantly controlled by external factors (e.g., tectonic activity, sea-level fluctuations and climatic changes) allowing to identify sub-stages (i.e., rift initiation, rift climax, final rift, early rift-sag, late rift-sag, early post-rift and late post-rift) (Supplementary data 4.A). In addition to the work presented in the syn-rift study (Chapter 2), additional seismic analyses were performed confirming the identification of the presented syn-rift sub-stages (i.e., rift initiation, rift climax, final rift) by identifying seismic pattern trends (Supplementary data 4.B). In the same way as in the syn-rift study (Chapter 2), seismic sequences (S8 to S15) were in turn identified for the post-rift interval by tying well to seismic data using checkshot data (Supplementary data 4.C, 4.D). Sedimentary facies observed in the syn-rift and post-rift stratigraphic intervals (Chapter 2 and Chapter 3) are summarized in *Supplementary data 4.E* and *Supplementary data 4.F* where flow transformations and flow gaps are described for the subaqueous sedimentary density flow deposits (SSDF deposits), thus recalling the main syn-rift and post-rift depositional environments (Supplementary data 4.E, 4.F). As presented in the syn-rift study (Chapter 2), two main depositional environments have been identified: (i) the wave-dominated coastal environment easily identified on GR-cut off values (Supplementary data 4.G) and (ii) the subaqueous deltaic environment that can also be interpreted based on GR-cut off values (Supplementary data 4.H). As further developed in the post-rift study (Chapter 3), two main depositional environments have been identified: (i) a deep-marine offshore mudstone environment and (ii) deep-water turbidite lobe complexes. Those two depositional environments can also be identified using GR-cut off values (Supplementary data 4.H). Seven 3rd-order sequences were identified for the syn-rift interval (Chapter 2, Supplementary data 4.I, 4.J) and eight sequences for the rift-sag and post-rift intervals (Supplementary data 4.K, 4.L) based on sequence stratigraphy. The syn-rift (Chapter 2), post rift study (Chapter 3) and supplementary materials (Supplementary data 4.A, 4.B, 4.C, 4.D, 4.E, 4.F, 4.G, 4.H, 4.I, 4.J) are thereafter integrated to tackle the tectonostratigraphic evolution of the entire Norwegian Sea (Chapter 4).

The discussion (Chapter 4) aims at discussing the following topics: (i) the tectonostratigraphic evolution of the Norwegian Sea, (ii) the Norwegian rift evolution in regards to other locations in the Atlantic rift system, (iii) the influence of autocyclic controls on deep-water turbidite lobe geometry, and (iv) the formation of sandstone reservoirs and the petroleum exploration potential of the Norwegian Sea. While the syn-rift (Chapter 2) and the post-rift studies (Chapter 3) were conducted in the greater Fenja area (Halten Terrace) and in the greater Marulk area (Dønna Terrace) at a local scale, Chapter 4 focuses on the entire Norwegian Sea including the platform domain, the terrace domain (formed of the Halten and Dønna terraces) and the deep domain, thus at a larger regional scale. In Chapter 4, the relationships between depositional environments (i.e., wave-dominated coastal environment, coarse-grained deltaic environment and deep-water turbidite complexes) and allocyclic processes (e.g., tectonic, climatic, eustatic) are discussed.

CHAPTER 4: Discussion

1. Tectonostratigraphic evolution of the Norwegian Sea

The tectonostratigraphic evolution of the entire Norwegian from the Middle Jurassic to the Late Cretaceous will be discussed using the following data: (i) well-log, sediment core, seismic and biostratigraphic analyses presented in *Chapter 2*, *Chapter 3* and *Supplementary data 4.A, 4.B, 4.C, 4.D, 4.E, 4.F, 4.G, 4.H, 4.I, 4.J, 4.K and 4.L*; (ii) public and available well-log, sediment core and biostratigraphic database for the exploration wells not presented in the 3 previous chapters (NPD, 2021); (iii) lithostratigraphic database for all the exploration wells drilled in the Norwegian Sea (NPD, 2021); (iv) former paleoenvironmental reconstructions (Koch and Heum, 1995; Swiecicki et al., 1998; Brekke et al., 1999, 2001; Roberts et al., 1999; Vergara et al., 2001; Surlyk, 2003; Fjellanger et al., 2005; Knaust, 2009; Elliott et al., 2015; Henstra et al., 2016a); (v) global sea level fluctuations after Haq (2014, 2017); (vi) climate changes after Price (1999); (vii) geomorphological domains after Peron-Pinvidic *et al.* (2013) and Peron-Pinvidic & Osmundsen (2018); and (viii) tectonic activity after the established "simplified tectonic curve" (Fig. 4.1, column #7) based on *Chapter 2*, *Supplementary data 4.A, 4.B, 4.C, 4.D, 4.E, 4.F, 4.G, 4.H, 4.I, 4.J, 4.K, 4.L*, *unpublished* regional seismic interpretation (Edison Norge AS, 2021) and former studies (Blystad *et al.*, 1995; Doré *et al.*, 1997b, 1999; Brekke, 2000; Færseth & Lien, 2002; Elliott *et al.*, 2015; Jones *et al.*, 2020).

The proposed "*simplified tectonic curve*" illustrates the tectonic evolution of the terrace domain during the Jurassic and the Cretaceous in the Norwegian Sea (Fig. 4.1, column #7). The rift initiation stage exhibits the progression from very low tectonic activity to very high tectonic activity (Fig. 4.1, columns #7, #8). The rift-climax stage is in turn marked by a single period of very high tectonic activity. Subsequently, the final rift stage corresponds to a period of high tectonic activity whereas the rift-sag is characterised by low tectonic activity, during which time the "Aptian sands" were deposited (well 6507/7-12 in Figs. 4.Cb, 4.Kb). The post-rift was a period of very low tectonic activity. However, there are still some uncertainties regarding the degree of tectonic activity during the Turonian and the Coniacian. As suggested by some authors, the Turonian to Coniacian deep-water turbidite lobe complexes were deposited during a period of tectonic quiescence (Lien, 2005; Lien et al., 2006), whereas other authors argue for a notable influence of tectonic activity (Doré et al., 1997b, 1999; Lundin and Doré, 1997) (Chapter 3). Based on our observations, the possible tectonic activity has potentially been generated by a combination of thermal subsidence episodes and uplift phases related to isostatic adjustments and elastic rebound as suggested by Færseth and Lien (2002).

We propose in this first section a method to identify which allocyclic parameters may predominate during the various syn-rift and post-rift sub-stages. We have attempted to correlate our results with the studies of Price (1999) and Haq (2014, 2017) in the aim to see which allocyclic parameters most probably prevailed during each sub-stage. The tectonostratigraphic evolution is illustrated in the final chart (Fig. 4.1), the simplified geological and tectonic sketches (Fig. 4.2) and the elaborated paleogeographic maps (Fig. 4.3). Those three figures (Figs. 4.1, 4.2, 4.3) are finally combined to propose a 4D tectonostratigraphic evolution of the entire Norwegian Sea.

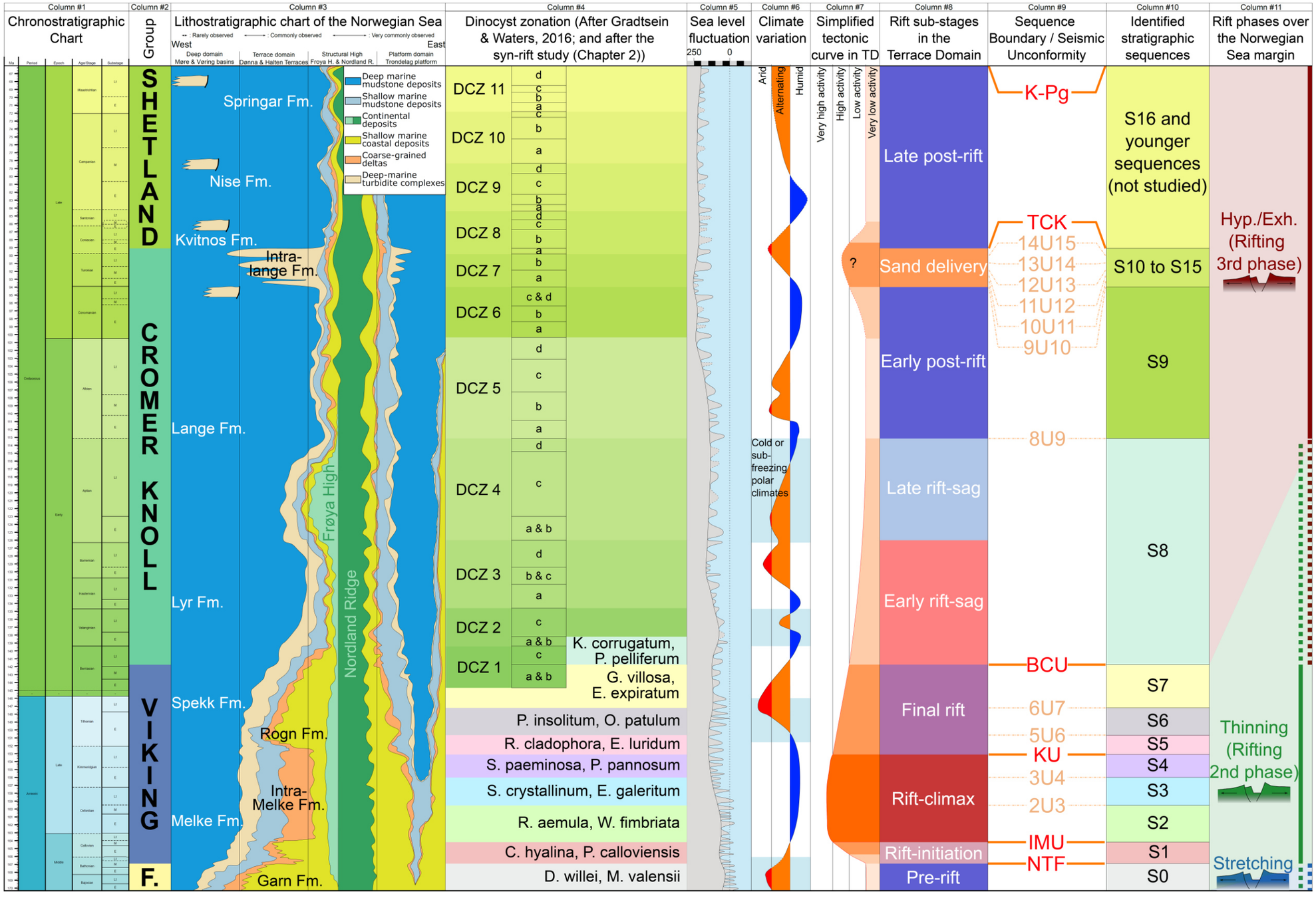

Fig. 4.1: The Norwegian Sea syn-rift to post-rift transition chart with the first column corresponding to the chronostratigraphic chart (imported from TS Creator and based on (Ogg et al., 2016)); the second column is the geological groups; the third column corresponds to the lithostratigraphic chart after Dalland et al. (1988), Gradstein and Waters (2016) and this PhD research; the fourth column corresponds to the dinoflagellate cyst zones with the Jurassic interval based on the work presented in Chapter 2 and the Cretaceous (after Gradstein et al., 2016); columns #5 and #6 correspond to sea level fluctuations (after Haq (2014, 2017)) and climate evolution after Price (1999). Column #7 corresponds to a proposed simplified tectonic curve based on seismic interpretation and literature (references are mentioned in Chapters 2, 3 and 4). Column #8, #9 and #10 highlight the rift sub-stages identified in this PhD research (Chapters 2, 3 and 4), the identified sequence boundaries and their associated seismic unconformities, and the identified sequences. The last column (column #11) corresponds to the rift phases (stretching, thinning and hyperextension/exhumation (hyp./exh.)) over the Norwegian Sea margin.

1.1. Pre-rift (S0) – Garn and Melke formations (Fangst Group)

Between the Bajocian and the Middle Bathonian (*"D. Willei, M. valensii"* dinoflagellate cyst zone), the sea level was stable (+50 m compared to today's level) (Haq (2017), Fig. 4.1). During S0, the climate was mainly arid (Price (1999), Fig. 4.1) and no clear tectonic activity has been observed. The Garn Formation represents a coastal environment dominated by the influence of wave- and fluvial- processes (Dalland et al., 1988). The palaeo-platform domain, formed at this stage of the today platform and terrace domains (Peron-Pinvidic *et al.*, 2013; Peron-Pinvidic & Osmundsen, 2018), is mainly dominated by shallow-marine coastal deposits; however, the northern part of the Nordland Ridge (structural high) was already subaerial. (S0 in *Fig. 4.2*, Map #1 in *Fig. 4.3*).

1.2. Syn-rift (S1 to S7) – Viking Group

1.2.1. Rift initiation (S1) – Intra-Melke & Melke formations (Viking Group)

Between the Middle Bathonian and the Middle Callovian ("*C. hyalina, P. calloviensis*" dinoflagellate cyst zone), the sea level was stable (+60 m compared to today's level) (Haq (2017), Fig. 4.1). During S1, the climate alternated between arid and humid periods (Price (1999), Fig. 4.1) and tectonic activity was initiated by the reactivation of pre-existing Caledonian structures (Phillips et al., 2016). S1 corresponds to the beginning of the formation of the terrace domain (S1 in *Fig. 4.2*) (Peron-Pinvidic *et al.*, 2013; Peron-Pinvidic & Osmundsen, 2018). The Intra-Melke sandstone Formation represents a wave-dominated coastal environment conjointly developed with shallow-marine coarse-grained deltas (Chapter 2). Such deposits are mainly observed on the terrace domain together with shallow-marine mudstones (Melke Formation) (S1 in *Fig. 4.2*). The Nordland Ridge and the Frøya High (structural highs) were emerged (S1 in *Fig. 4.2*).

1.2.2. Rift climax (S2 to S4) – Intra-Melke & Melke formations (Viking Group)

Between the Middle Callovian and the Late Kimmeridgian (three dinoflagellate cyst zones are identifiable, from the oldest to the youngest, "*R. aemula & W. fimbriata*", "*S. crystallinum & E. galeritum*", and "*S. paeminosa & P. pannosum*", respectively), global sea level rose from approximately +90 m between the Middle Callovian (+60 m compared to today's sea level) and the Late Kimmeridgian (+150 m) (Haq (2017), Fig. 4.1). During S2, S3 and S4, the climate was humid (Price (1999), Fig. 4.1) and tectonic activity was at its climax. The Intra-Melke sandstone Formation represents a coastal environment mainly dominated by shallow-marine coarse-grained deltas (Chapter 2). These shallow-marine subaqueous deltas are mainly observed on the terrace domain together with shallow-marine mudstones (Melke Formation) (S2, S3 and S4 in *Fig. 4.2*). The platform domain, when not emerged, e.g. the Nordland Ridge and the Frøya High, produced wave-dominated coastal environments due to weak activity of faults (Map #2 in *Fig. 4.3*).

1.2.3. Final rift (S5 to S7) – Rogn & Spekk formations (Viking Group)

Between the Late Kimmeridgian and the Middle Berriasian (three dinocyst zones are identifiable, from the oldest to the youngest, "*R. cladophora & E. luridum*", "*P. insolitum & O. patulum*", and "*G. villosa & E. expiratum*", respectively), global sea levels are high and remained constant (+150 m) until mid-S6, then dropped by 25 m to reach +125 m at the end of S7. Due to high sea levels and the initiation of thermal subsidence as a result of rifting, the terrace domain was the site of wave-dominated environments (the Rogn Formation) coevally developed with offshore organic-rich mudstones (the Spekk Fm) (S5 and S6 in *Fig. 4.2*). The total organic carbon (TOC) enrichment of the Spekk Formation is probably due to long-term eccentricity and a possible aridification of the climate (Price (1999), Fig. 4.1). During the final rift stage, fault activity gradually decreased. At the end of S7, a major period of erosion occurred eroding most of the evidence of the final rift stage across the terraces of the entire Norwegian Sea. Only few sandy coastal environments have been preserved on the terrace domain (BCU in *Fig. 4.2*). The platform domain, when not emerged (e.g. the Nordland Ridge and the Frøya High), developed widespread wave-dominated coasts such as in the Draugen field area. (Map #3 in *Fig. 4.3* and Supplementary data 4.F).

Fig. 4.2: Schematic geological cartoons of the syn-rift to post-rift transition evolution in the Norwegian Sea. First geological cartoon (S0) represents the initial palaeotopography exhibiting structural inherences which constrain rift structures; S1 corresponds to the rift initiation stage; S2, S3 and S4 corresponds to the rift-climax stage; S5, S6 and S7 are deposited during final rift stage; S7 is ended during intense erosion (Base Cretaceous Unconformity [BCU]) leaving sand relics; S8 (S8a and S8b) corresponds to the rift-sag, transitional period where major faults are active; S9 is characterised by a period of tectonic quiescence and corresponds to the early post-rift stage; during S10 to S15 which are part of the early post-rift; sand prone deep-water turbidite lobe complexes developed; the late rift stage started during S16 and ended approximately at the Cretaceous-Palaeogene (K–Pg) boundary; the last sketch (from K–Pg to seabed) outlines the present configuration. Today, three zones can be identified: (i) the light green zone where mainly post-rift reservoir can be encountered, (ii) the dark blue zone where syn-rift reservoir can be encountered (mainly on the Terrace domain) and (iii) the yellow zone located at the transition between the terrace and deep domains, and between the terrace and platform domain where both reservoirs can be encountered (sketch with no wells). The same cartoon (sketch with wells) outlines some key wells where siliciclastic reservoirs have been encountered in the Norwegian Sea. Legend is: light blue for shallow-marine mudstones, dark blue for deep-marine mudstones, yellow for shallow-marine coastal deposits, orange for subaqueous coarse-grained deltas; beige for deep-water turbidite lobe complexes, green for continental deposits, black faults for inactive faults; red faults for active faults and red dashed faults for fault reactivations.

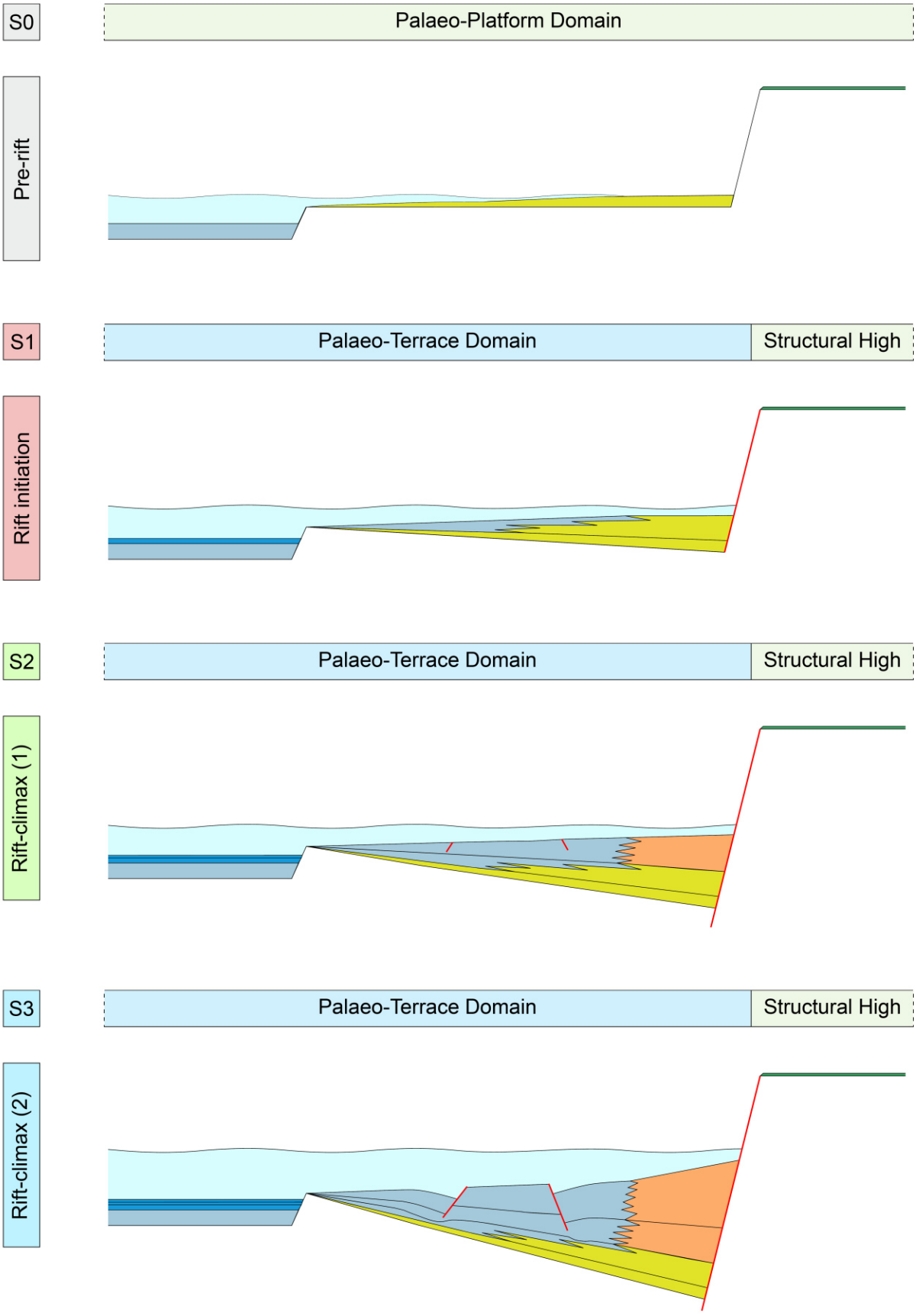
S0
Palaeo-Platform Domain
Pre-rift
S1
Palaeo-Terrace Domain
Structural High
Rift initiation
S2
Palaeo-Terrace Domain
Structural High
Rift-climax (1)
S3
Palaeo-Terrace Domain
Structural High
Rift-climax (2)

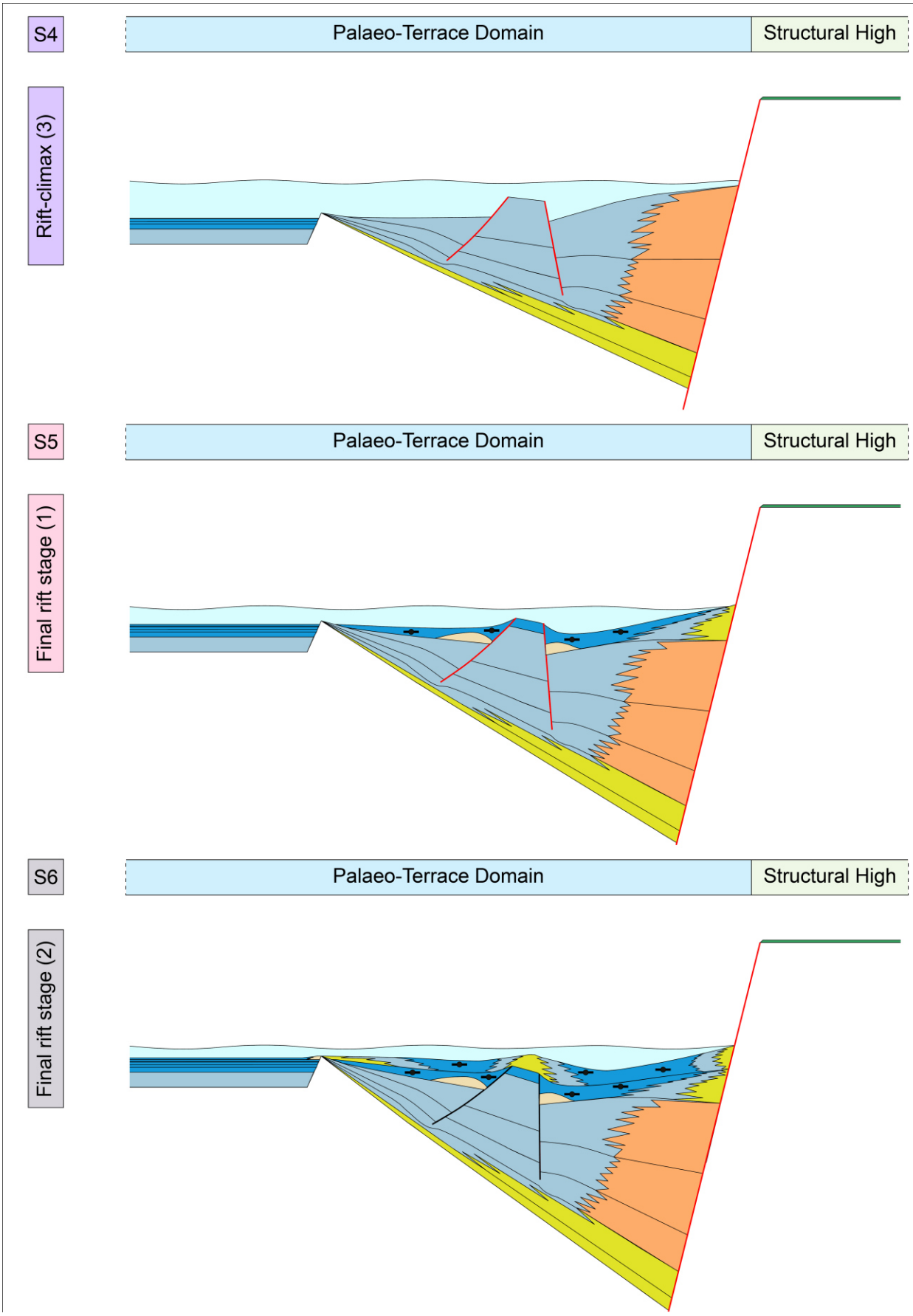
S4
Palaeo-Terrace Domain
Structural High
Rift-climax (3)
S5
Palaeo-Terrace Domain
Structural High
Final rift stage (1)
S6
Palaeo-Terrace Domain
Structural High
Final rift stage (2)

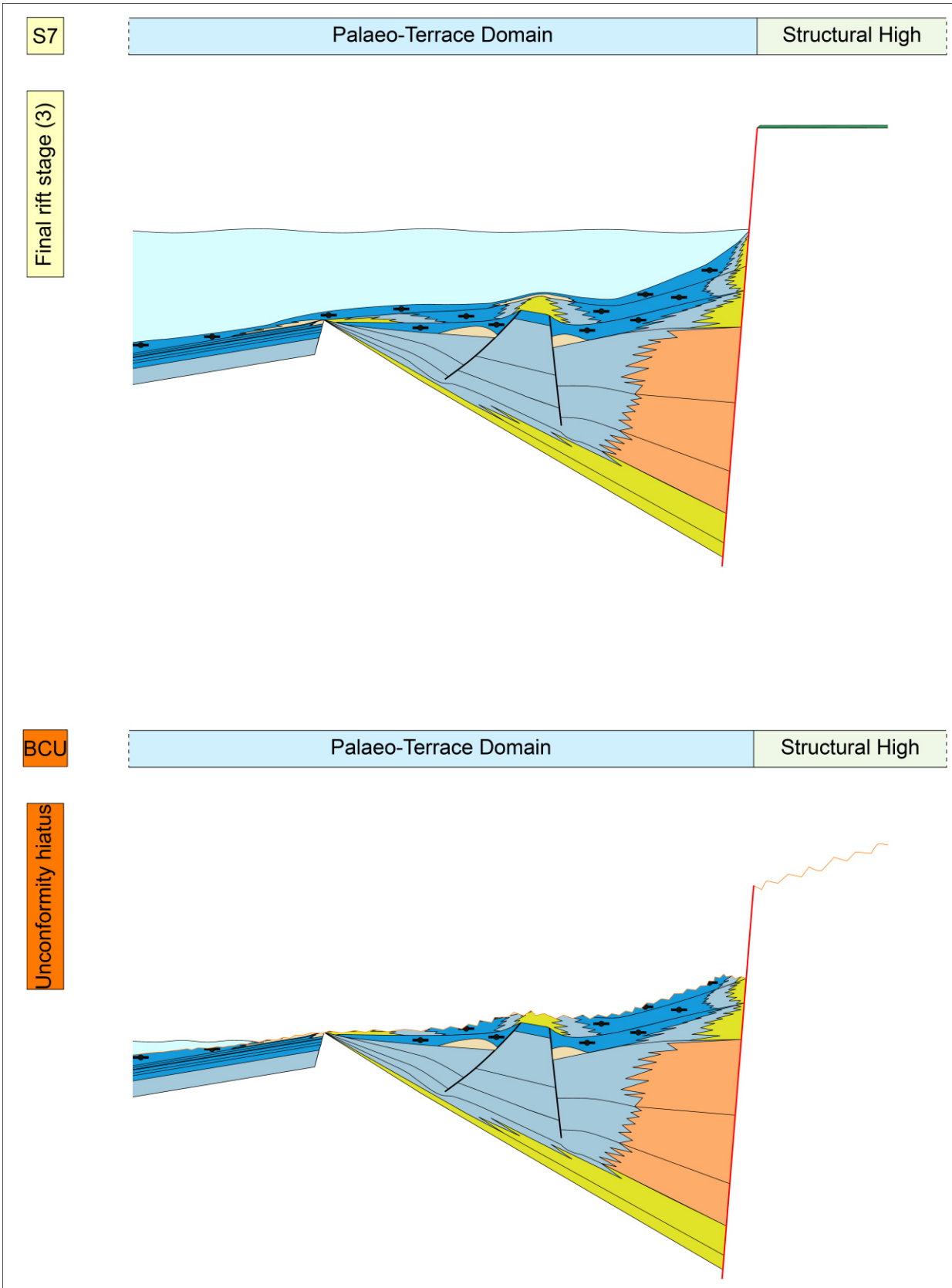
S7
Palaeo-Terrace Domain
Structural High
Final rift stage (3)
BCU
Palaeo-Terrace Domain
Structural High
Unconformity hiatus

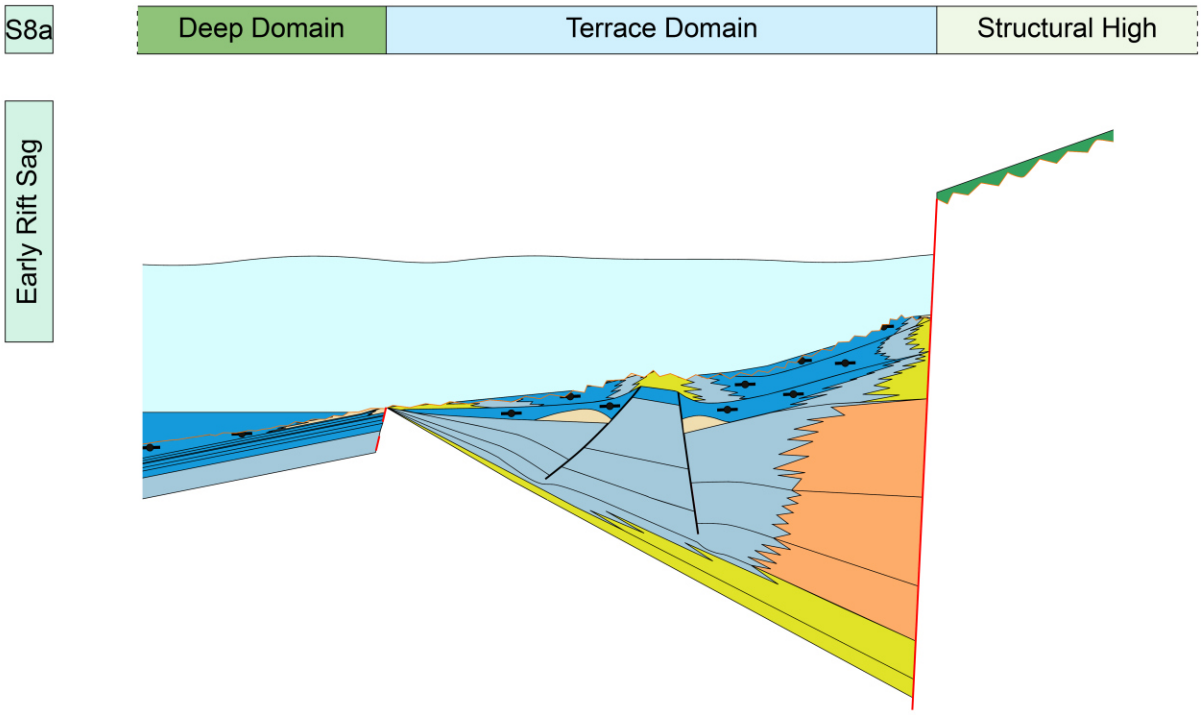
S8a
Deep Domain
Terrace Domain
Structural High
Early Rift Sag

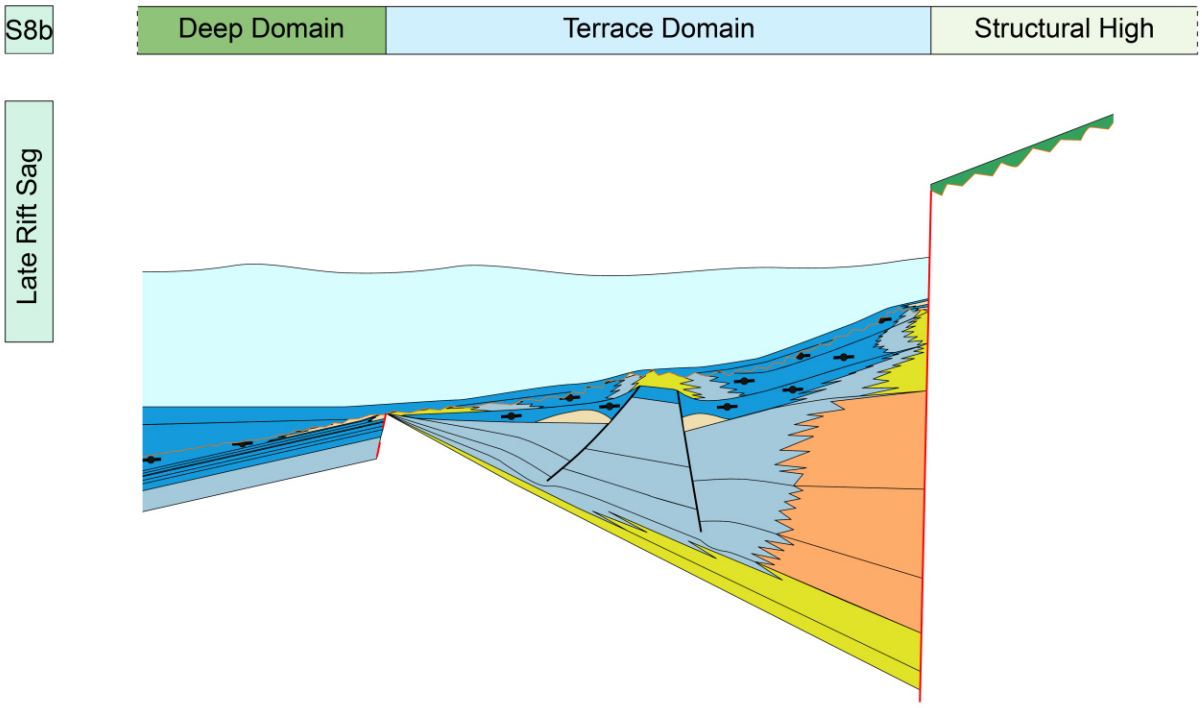
S8b
Deep Domain
Terrace Domain
Structural High
Late Rift Sag

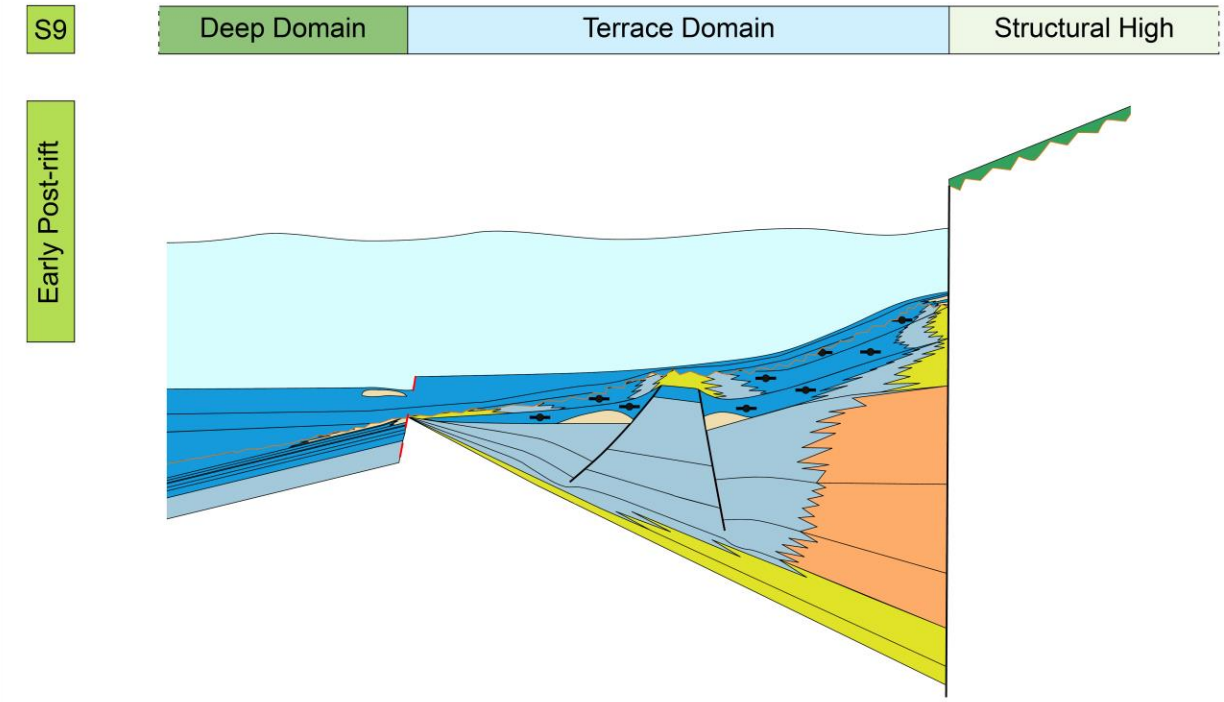
S9
Deep Domain
Terrace Domain
Structural High
Early Post-rift

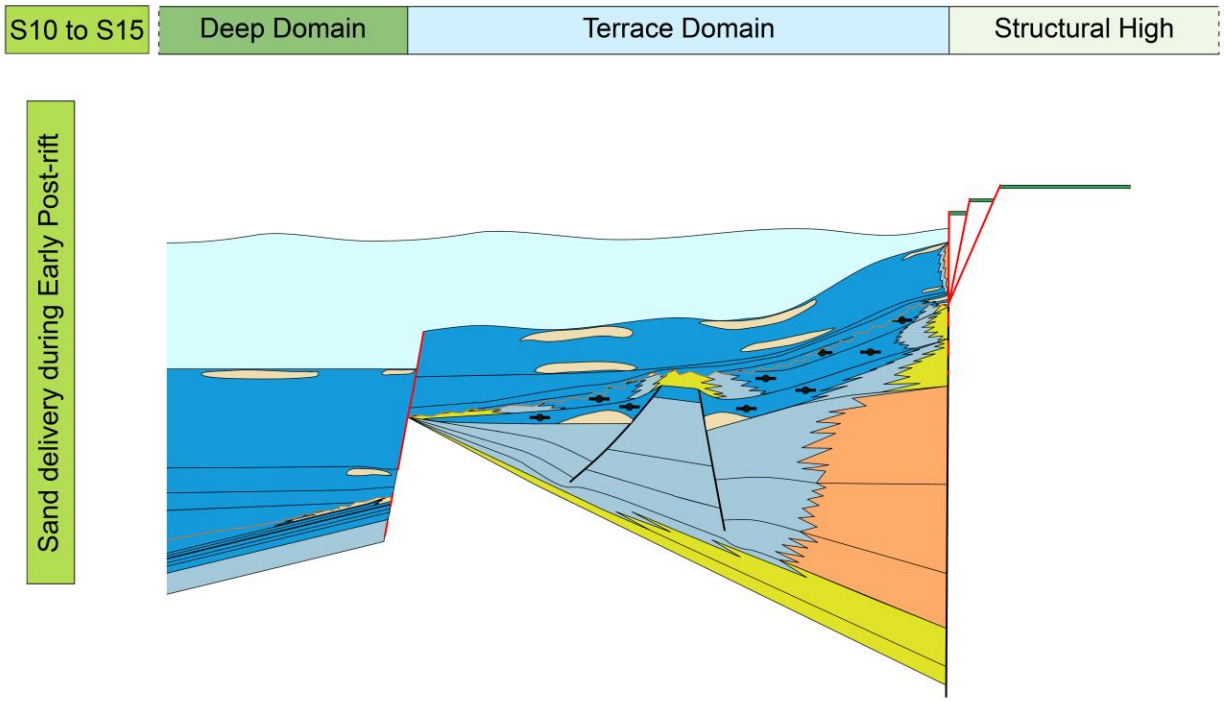
S10 to S15
Deep Domain
Terrace Domain
Structural High
Sand delivery during Early Post-rift

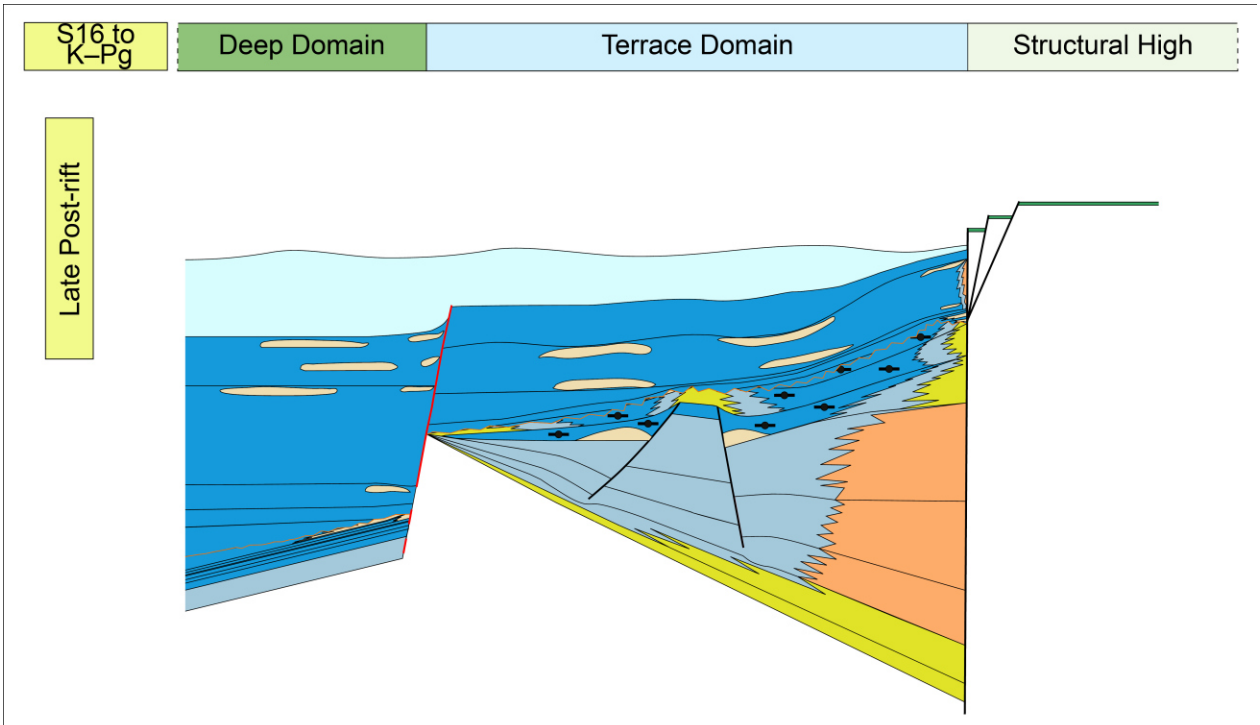
S16 to K–Pg
Deep Domain
Terrace Domain
Structural High
Late Post-rift

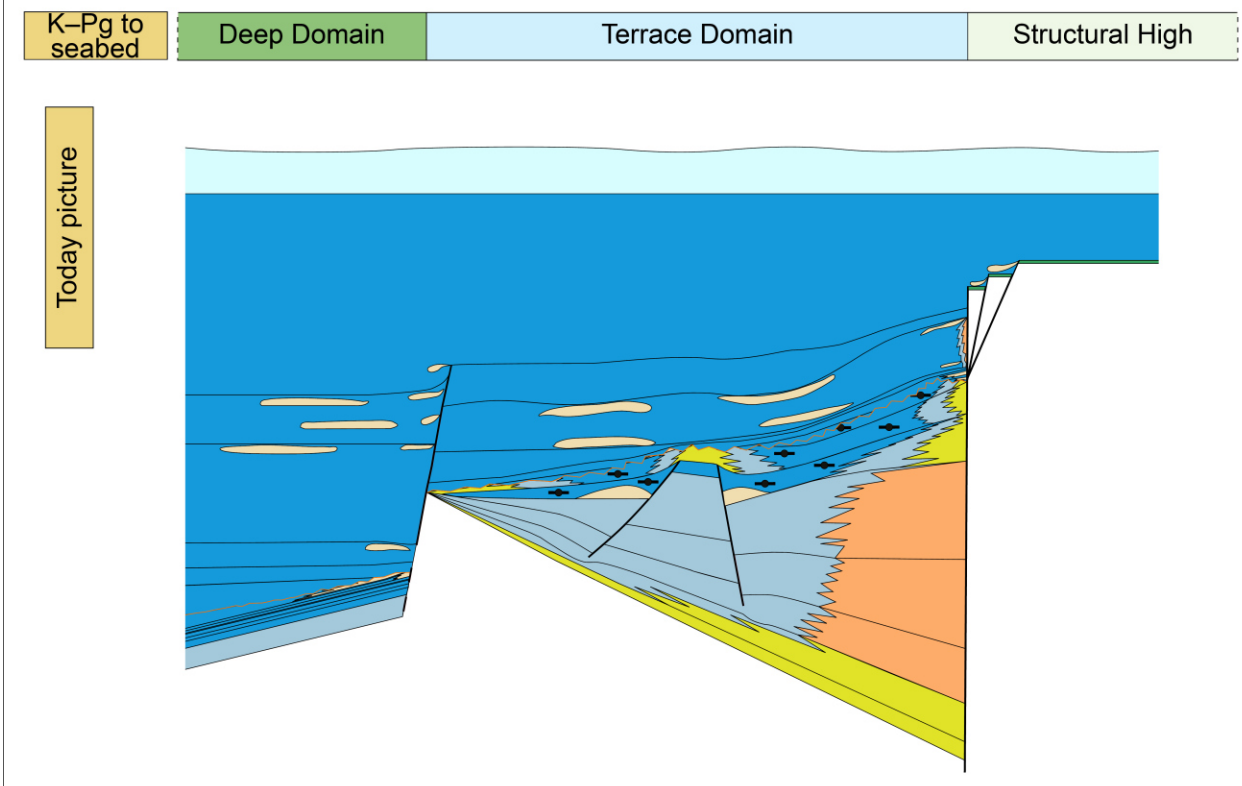
K–Pg to seabed
Deep Domain
Terrace Domain
Structural High
Today picture

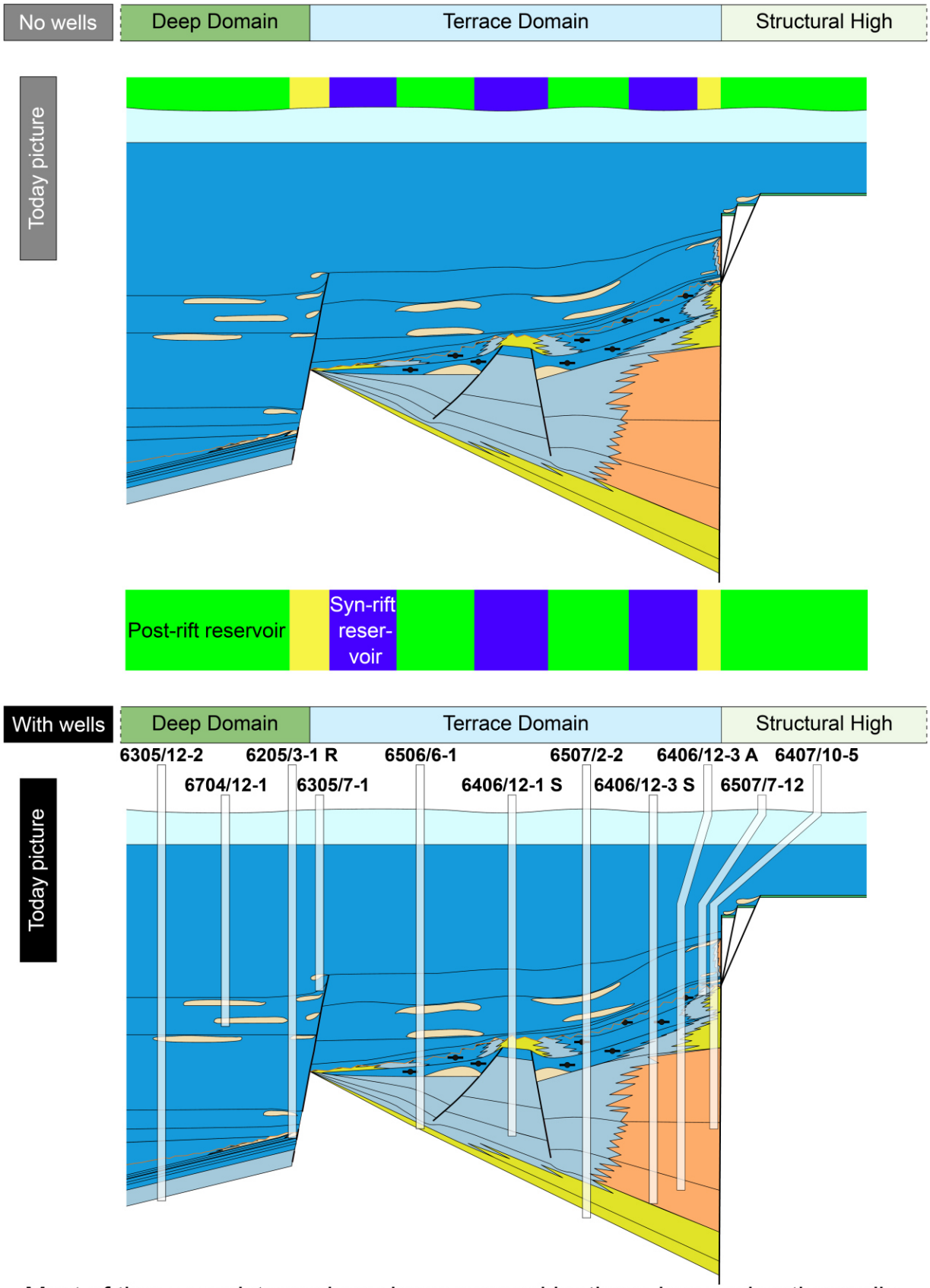

Most of these sandstones have been crossed by these key exploration wells.

1.3. Rift-sag (S8) – Lower Cromer Knoll Group

1.3.1. Early rift-sag (S8a) – Lyr Formation (Cromer Knoll Group)

Between the Middle Berriasian and the Barremian/Aptian boundary (three dinocyst zones are identifiable, from the oldest to the youngest, "*DCZ 1c*", "*DCZ 2*", and "*DCZ 3*", respectively), global sea levels dropped by 50 metres passing from +125 m at Middle Berriasian to + 75 m during the Early Valanginian, but rose again to peak at + 160 m at the end of the Berriasian (Haq, 2014) (Fig. 4.1). According to Price (1999), the early rift-sag is possibly dominated by a climate alternating between arid and humid periods or fully humid. During the early rift-sag, fault movement between the terrace and the platform domains had mostly ceased. Only rare activity occurred across master faults separating the terrace and the platform domains. Pre-existing Caledonian master faults separating the terrace domain and the deep domain may be reactivated by a new set of faults. S8 corresponds to the beginning of the formation of the deep domain (S8 in *Fig. 4.2*) (Peron-Pinvidic *et al.*, 2013; Peron-Pinvidic & Osmundsen, 2018). At that time the deep, the platform, and the terrace domains were mainly composed of calcareous mudstones to marlstones, namely the Lyr Formation (Map #4 and Map #5 in *Fig. 4.3*) which is mainly confined to the structural lows allowing the development of sag-type basins (S8a in *Fig. 4.2*). Along the Nordland Ridge, and some structural highs in the deep domains, deep marine SSDF deposits developed (NORLEX, 2021), coevally to the Rognkjeks Member observed in the North Sea (Ogg, 2012).

1.3.2. Late rift-sag (S8b) – Lange Formation (Cromer Knoll Group)

From the Barremian/Aptian boundary to the Aptian/Albian boundary ("*DCZ 4*" dinoflagellate cyst zone), global sea levels progressively dropped by 20 metres passing from +160 m to +140 m at the end of S8 (Haq, 2014) (Fig. 4.1). According to Price (1999), the late rift-sag period is marked by a climate alternating between arid and humid periods, possibly evolving towards moister climate conditions at the end of S8 (Price, 1999). During the late rift-sag, only very rare master faults separating the platform and the terrace domains were still active generating deep-marine SSDF deposits, such as the "Aptian sands", along the Nordland Ridge (Figs. 4.Cb, 4.Kb). The new set of faults generated during the early rift-sag continued to initiate between the deep and the terrace domains. However, the deep, platform, and terrace domains, were dominated by deep-marine mudstones of the Lange Formation (Map #6 in *Fig. 4.3*), which progressively sealed the remaining palaeo-highs (S8b in *Fig. 4.2*).

1.4. Post-rift (S9 to K–Pg) – Upper Cromer Knoll and Shetland groups

1.4.1. Early post-rift (S9) – Lange Formation (Cromer Knoll Group)

From the Aptian/Albian boundary to the Cenomanian/Turonian boundary (two dinoflagellate cyst zones are identifiable, from the oldest to the youngest, "DCZ 5", and "DCZ 6", respectively), the global sea levels dramatically rose passing from +140 m at the beginning of S9, to +250 m at the end of S9 (Haq, 2014) (Fig. 4.1). According to Price (1999), the early post-rift period is possibly marked by a humid climate, with a period alternating between arid and humid periods between the Middle and the Late Albian (DCZ 5b and DCZ 5c dinoflagellate cyst subzones) (Price, 1999; Gradstein and Waters, 2016). All the faults generated during the rifting phase (S1 to S7 + S8) ceased to be active. However, rare occurrences of deep-marine

SSDF deposits developed probably due to differential subsidence across newly generated faults linked to pre-existing basement structures (S9 in *Fig. 4.2*). S9 is regarded as a period of tectonic quiescence where deep marine mudstones (i.e., the Lange Formation) were deposited, finally filling up the basin and smoothing the relief (Map #7 in *Fig. 4.3*). As previously mentioned, occasional deep-marine SSDF deposits have been observed during S9 such as the Sandflyndre Member in the Vestfjorden Basin, or the Gapeflyndre Member in the Møre Basin (Gradstein and Waters, 2016) (Map #8 in *Fig. 4.3*).

1.4.2. Sand delivery during early post-rift (S10 to S15) – Breiflabb, Skolest, and Lysing members (Cromer Knoll Group)

From the Cenomanian/Turonian boundary to the Early Coniacian ("*DCZ 7*" dinoflagellate cyst zone and "*DCZ 8a*" dinoflagellate cyst subzone), sea levels dropped by 35 m, from +250 m at the beginning of S10, to + 215 m compared to present sea level, at the end of S15 (Haq (2014), Fig. 4.1). According to Price (1999), the climate potentially evolved from S10 to S15, between a purely humid climate to a purely arid climate (Fig. 4.1). All the three structural domains are characterized by the deposition of deep marine mudstones (Lange Formation) (Map #9 in *Fig. 4.3*). Deep marine SSDF deposits occurred mainly along the flanks of structural highs, in the terrace domain, as well as in the deep domain, but less commonly in the platform domain (S10 to S15 in *Fig. 4.2*). Shallow-marine SSDF deposits have been observed on the Nordland Ridge (Hansen et al., 2021).

1.4.3. Late post-rift (S16 to K–Pg) – Kvitnos, Nise and Springar formations (Shetland Group)

Between the Early Coniacian and the Cretaceous–Palaeogene (K–Pg) boundary ("*DCZ 8b*", "*DCZ 8c*", and "*DCZ 8d*" dinoflagellate cyst subzones, and "*DCZ 9*", "*DCZ 10*" and "*DCZ 11*" dinoflagellate cyst zones), sea levels are generally stable with a level above +200 m compared to today's sea level (Haq (2014), Fig. 4.1). Although the climate likely oscillated between arid and humid conditions, a humid period is reported between the Middle Santonian and the Early Middle Campanian (Price (1999), Fig. 4.1). No tectonic activity is inferred from seismic data in the platform and the terrace domains. However, in the outer domain, the breakup phase probably initiated during the Campanian, or later, in the Maastrichtian. The deep, the terrace and the platform domains are marked by the deposition of offshore mudstones (Map #10 in *Fig. 4.3*). In the deep domain, rare occurrences of deep-water SSDF deposits can be noted, most probably due to potential tectonic activity at the boundary between the deep domain and the oceanic domain (Map #11 in *Fig. 4.3*). The topography flattened due to the post-rift filling (S16 to K–Pg in *Fig. 4.2*), before eventually entirely flooding the Nordland Ridge with deep-marine mudstones, as observed nowadays (K–Pg to sea bed in *Fig. 4.2*).

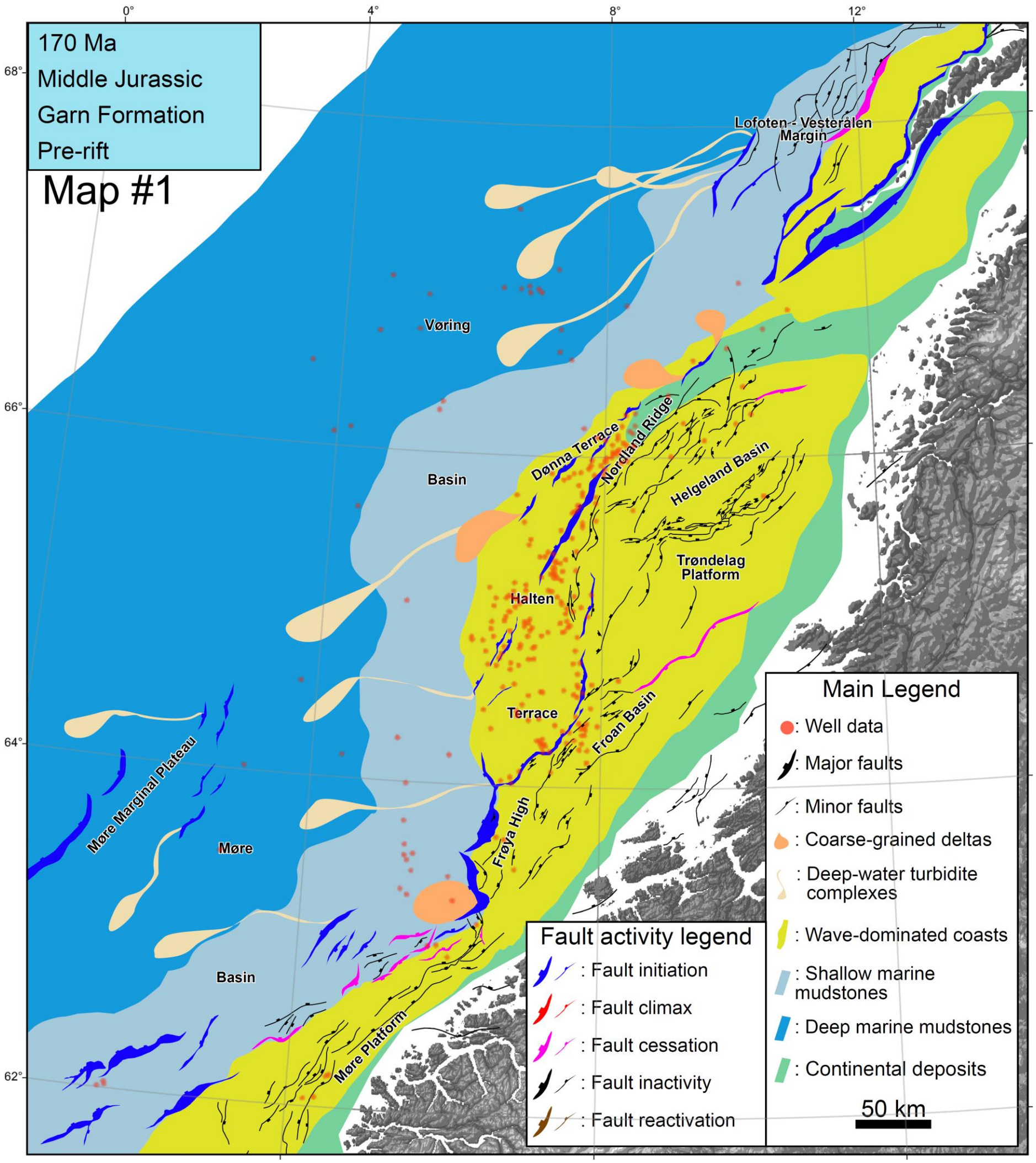

Fig. 4.3: Paleoenvironmental reconstructions of the Norwegian Sea between the Middle Jurassic to Upper Cretaceous. The map at 170 Ma (Map #1) represents the pre-rift period where wide shorefaces and beaches were simultaneously deposited on the terrace and platform domains. The map at 160 Ma (Map #2) represents the rift-climax stage where coarse-grained deltas are mainly observed on the terrace domain. The final rift stage (Map #3) is dominated by wave-dominated shorefaces and beaches (150 Ma). Between 140 (Map #4) and 130 Ma (Map #5), deep-marine mudstones are deposited on the terrace, deep and platform domains with some potential presence of deep-water turbidite lobe complexes along major faults (early rift-sag). The late rift-sag (120 Ma, (Map #6) is dominated by deep-marine mudstones and rare deep-water turbidite lobe complexes. The early post-rift is mainly represented by phase of tectonic quiescence (maps at 110 Ma (Map #7) and 100 Ma (Map #8)). A high density of deep deep-water turbidite lobe complexes were generated around 90 Ma (Map #9). This period is followed by the late post-rift marked by a tectonic quiescence and the deposition of deep-marine mudstones (maps at 80 Ma (Map #10) and 70 Ma (Map #11)). Chronostratigraphic ages are based on (Ogg et al., 2016). Formations and associated sub-rift phases are based on Fig. 4.Ab. Maps are based on well penetrations after (NPD, 2021). In undrilled zones maps are based on previous reconstructions (Koch and Heum, 1995; Swiecicki et al., 1998; Brekke et al., 1999, 2001; Roberts et al., 1999; Vergara et al., 2001; Surlyk, 2003; Fjellanger et al., 2005; Knaust, 2009; Elliott et al., 2015; Henstra et al., 2016a). Fault activity are based on seismic observation, and are model-driven when faults have not been observed (Peron-Pinvidic & Osmundsen, 2018; Whiting et al., 2021). Fault location are issued of Zastrozhnov et al. (2020)'s map; however major detachments are reactivated basement faults; they may have been reactivated during pre-, syn- and post-rift stages.

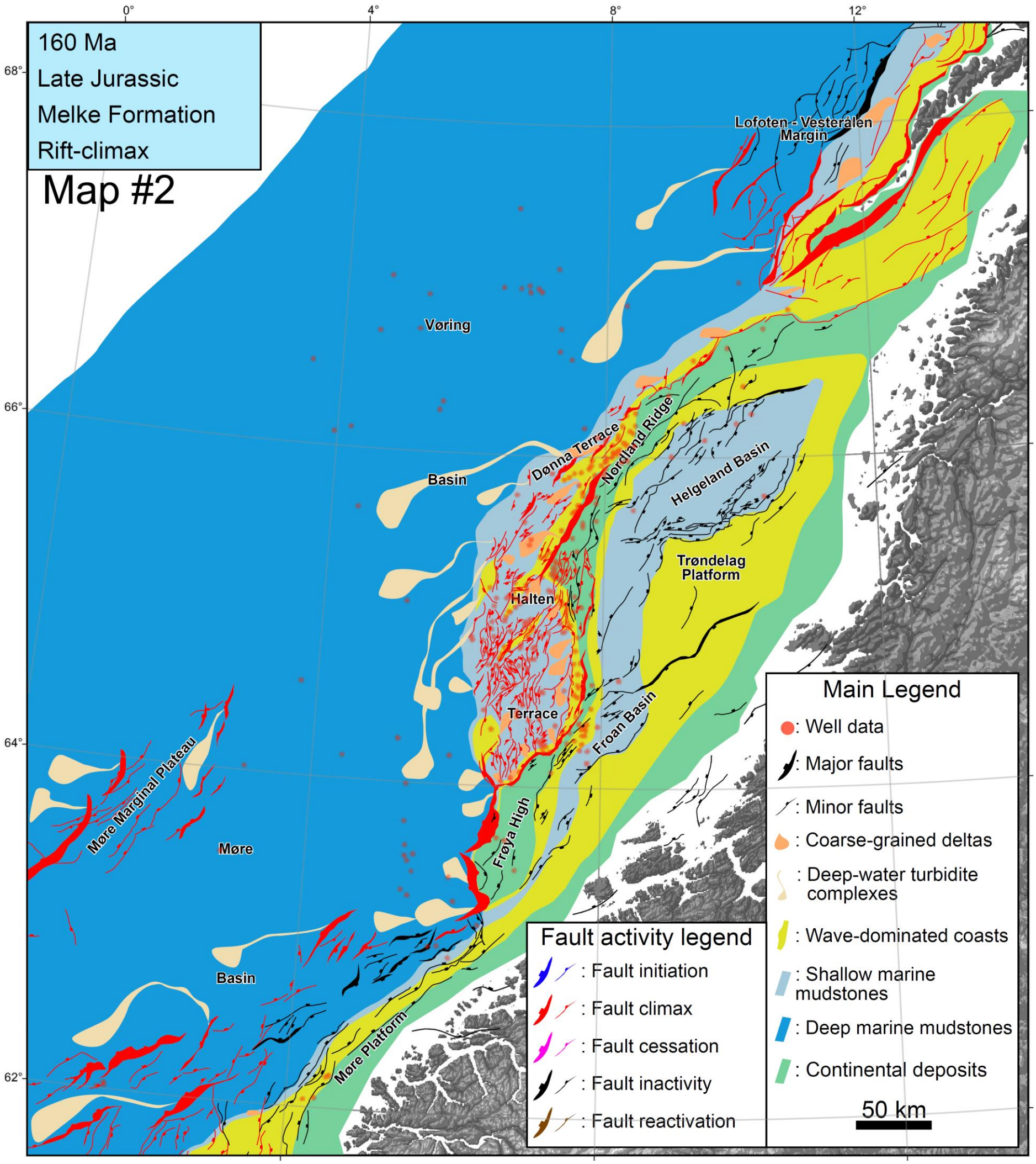
160 Ma
Late Jurassic
Melke Formation
Rift-climax
Map #2
0°
4°
8°
12°
68°
66°
64°
62°
Lofoten - Vesterålen Margin
Vøring
Basin
Dønna Terrace
Nordland Ridge
Helgeland Basin
Trøndelag Platform
Halten
Terrace
Froan Basin
Frøya High
Møre Marginal Plateau
Møre
Basin
Møre Platform
Main Legend
: Well data
: Major faults
: Minor faults
: Coarse-grained deltas
: Deep-water turbidite complexes
: Wave-dominated coasts
: Shallow marine mudstones
: Deep marine mudstones
: Continental deposits
50 km
Fault activity legend
: Fault initiation
: Fault climax
: Fault cessation
: Fault inactivity
: Fault reactivation

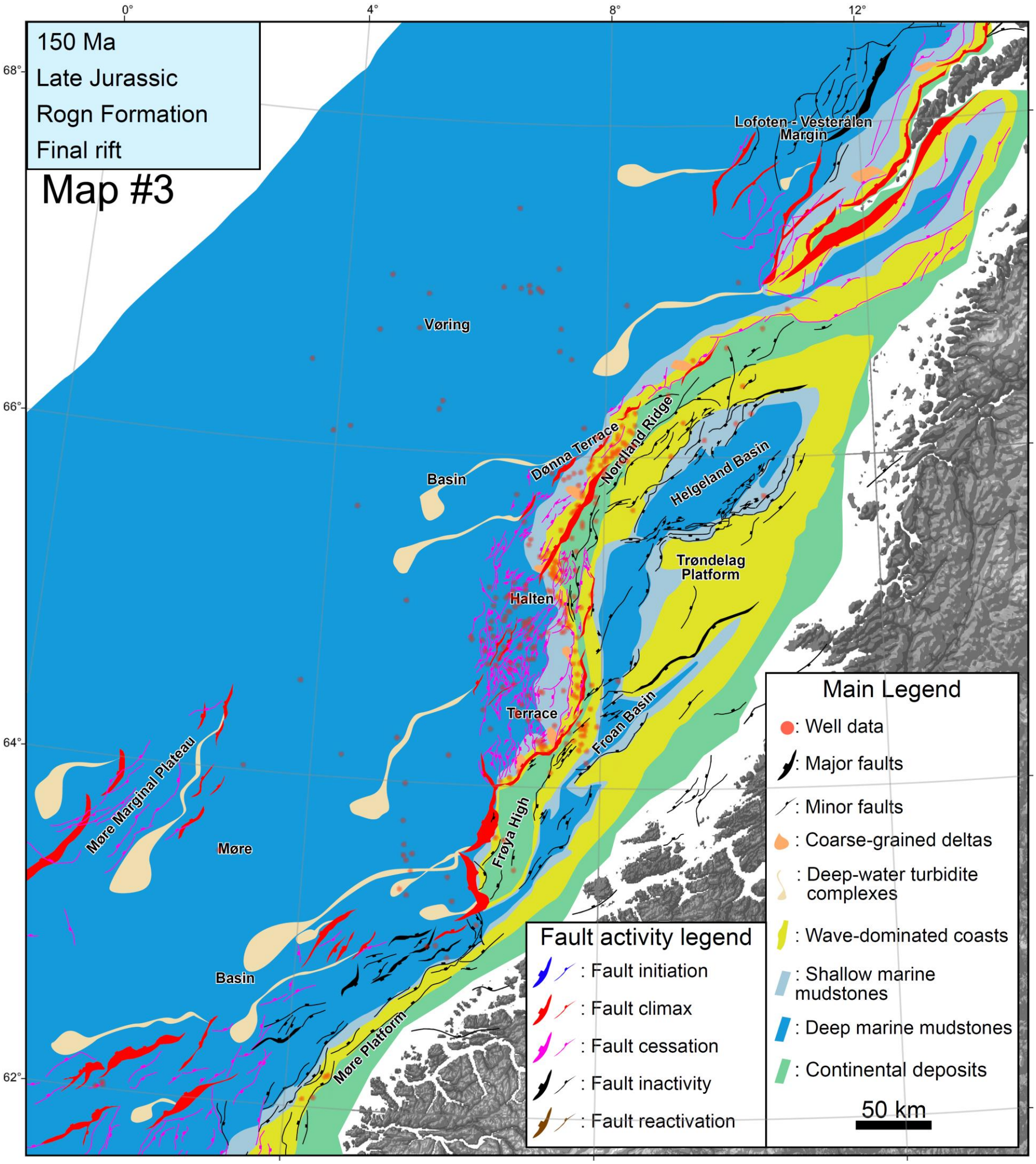
150 Ma
Late Jurassic
Rogn Formation
Final rift
Map #3
0°
4°
8°
12°
68°
66°
64°
62°
Lofoten - Vesterålen Margin
Vøring
Basin
Dønna Terrace
Nordland Ridge
Helgeland Basin
Trøndelag Platform
Halten
Terrace
Froan Basin
Frøya High
Møre Marginal Plateau
Møre
Basin
Møre Platfor
Main Legend
: Well data
: Major faults
: Minor faults
: Coarse-grained deltas
: Deep-water turbidite complexes
: Wave-dominated coasts
: Shallow marine mudstones
: Deep marine mudstones
: Continental deposits
50 km
Fault activity legend
: Fault initiation
: Fault climax
: Fault cessation
: Fault inactivity
: Fault reactivation

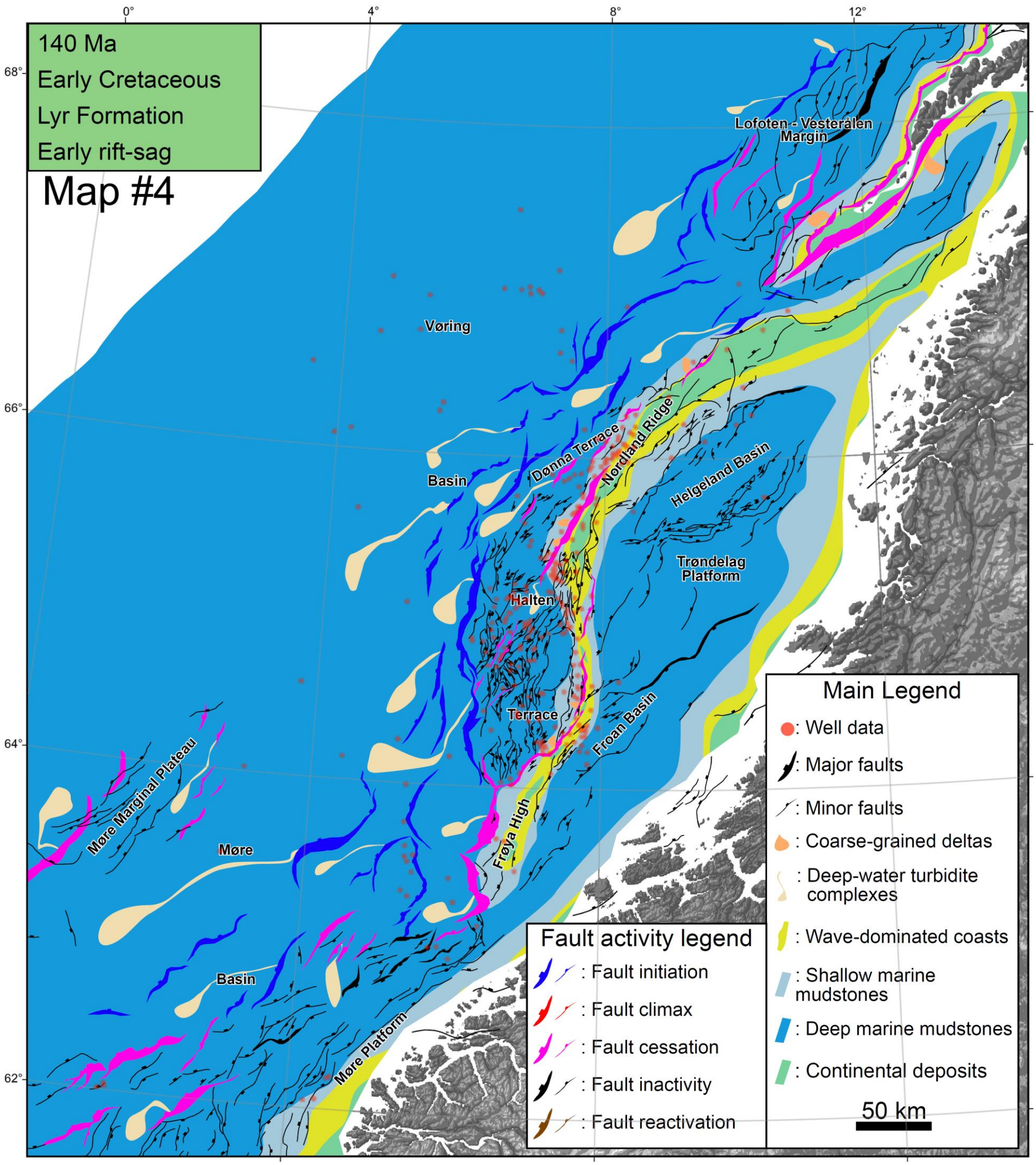
140 Ma
Early Cretaceous
Lyr Formation
Early rift-sag
Map #4
0°
4°
8°
12°
68°
66°
64°
62°
Lofoten - Vesterålen Margin
Vøring
Basin
Dønna Terrace
Nordland Ridge
Helgeland Basin
Trøndelag Platform
Halten
Terrace
Froan Basin
Frøya High
Møre Marginal Plateau
Møre
Basin
Møre Platform
Fault activity legend
: Fault initiation
: Fault climax
: Fault cessation
: Fault inactivity
: Fault reactivation
Main Legend
: Well data
: Major faults
: Minor faults
: Coarse-grained deltas
: Deep-water turbidite complexes
: Wave-dominated coasts
: Shallow marine mudstones
: Deep marine mudstones
: Continental deposits
50 km

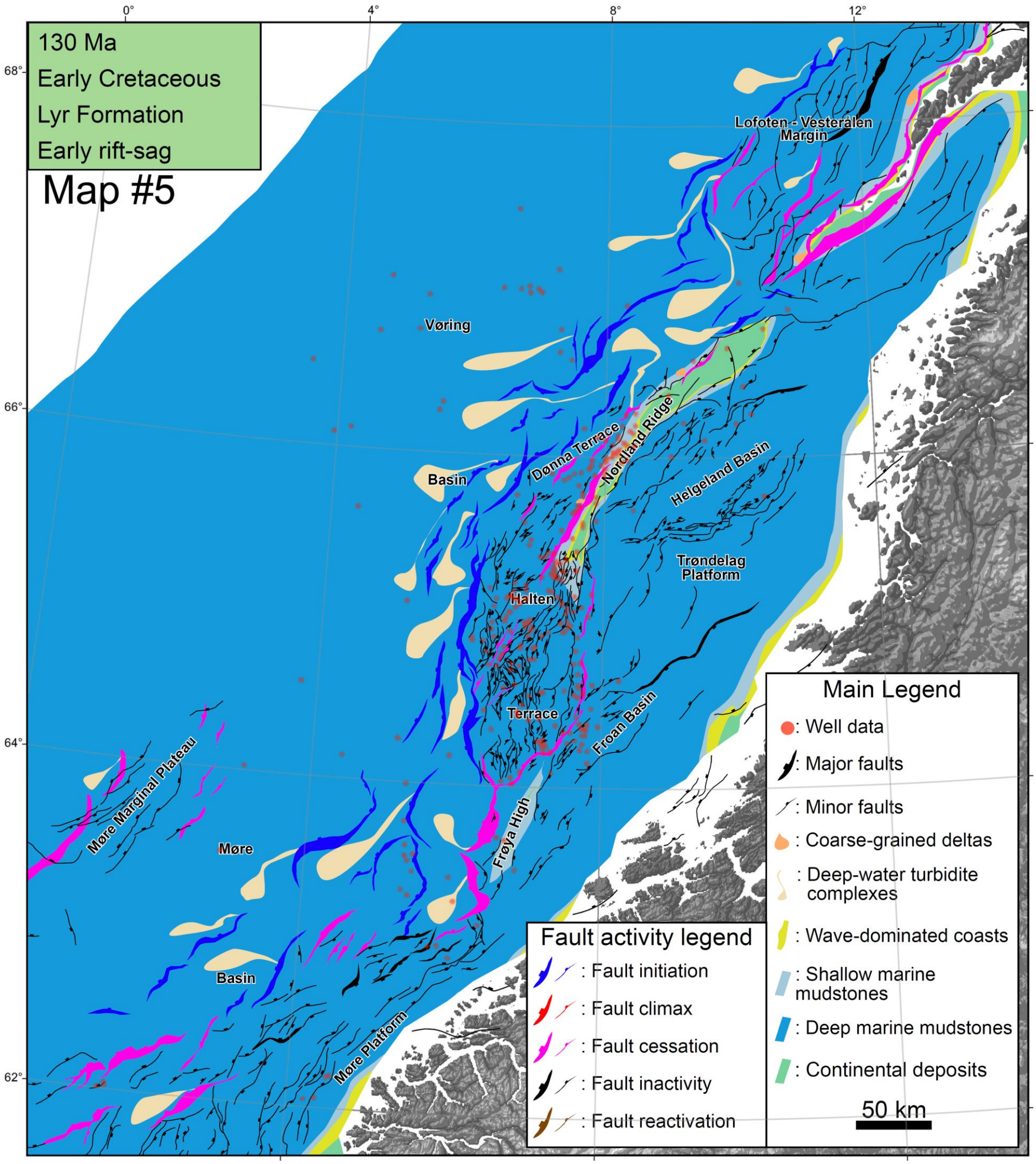
130 Ma
Early Cretaceous
Lyr Formation
Early rift-sag
Map #5
0°
4°
8°
12°
68°
66°
64°
62°
Lofoten - Vesterålen Margin
Vøring
Basin
Dønna Terrace
Nordland Ridge
Helgeland Basin
Trøndelag Platform
Halten
Terrace
Froan Basin
Frøya High
Møre Marginal Plateau
Møre
Basin
Møre Platform
Main Legend
: Well data
: Major faults
: Minor faults
: Coarse-grained deltas
: Deep-water turbidite complexes
: Wave-dominated coasts
: Shallow marine mudstones
: Deep marine mudstones
: Continental deposits
50 km
Fault activity legend
: Fault initiation
: Fault climax
: Fault cessation
: Fault inactivity
: Fault reactivation

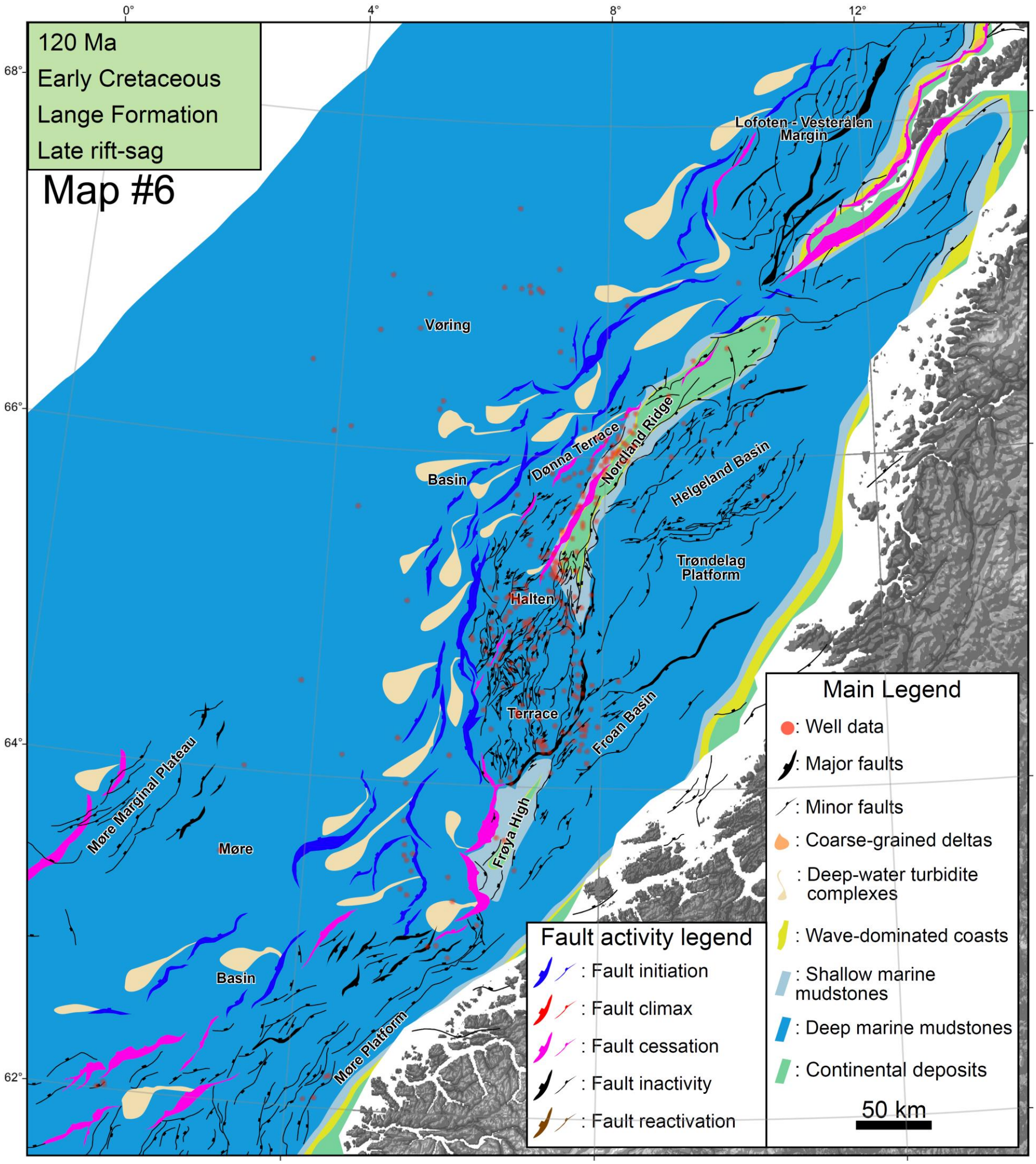
120 Ma
Early Cretaceous
Lange Formation
Late rift-sag
Map #6
0°
4°
8°
12°
68°
66°
64°
62°
Lofoten - Vesterålen Margin
Vøring
Basin
Dønna Terrace
Nordland Ridge
Helgeland Basin
Trøndelag Platform
Halten
Terrace
Froan Basin
Frøya High
Møre Marginal Plateau
Møre
Basin
Møre Platform
Fault activity legend
: Fault initiation
: Fault climax
: Fault cessation
: Fault inactivity
: Fault reactivation
Main Legend
: Well data
: Major faults
: Minor faults
: Coarse-grained deltas
: Deep-water turbidite complexes
: Wave-dominated coasts
: Shallow marine mudstones
: Deep marine mudstones
: Continental deposits
50 km

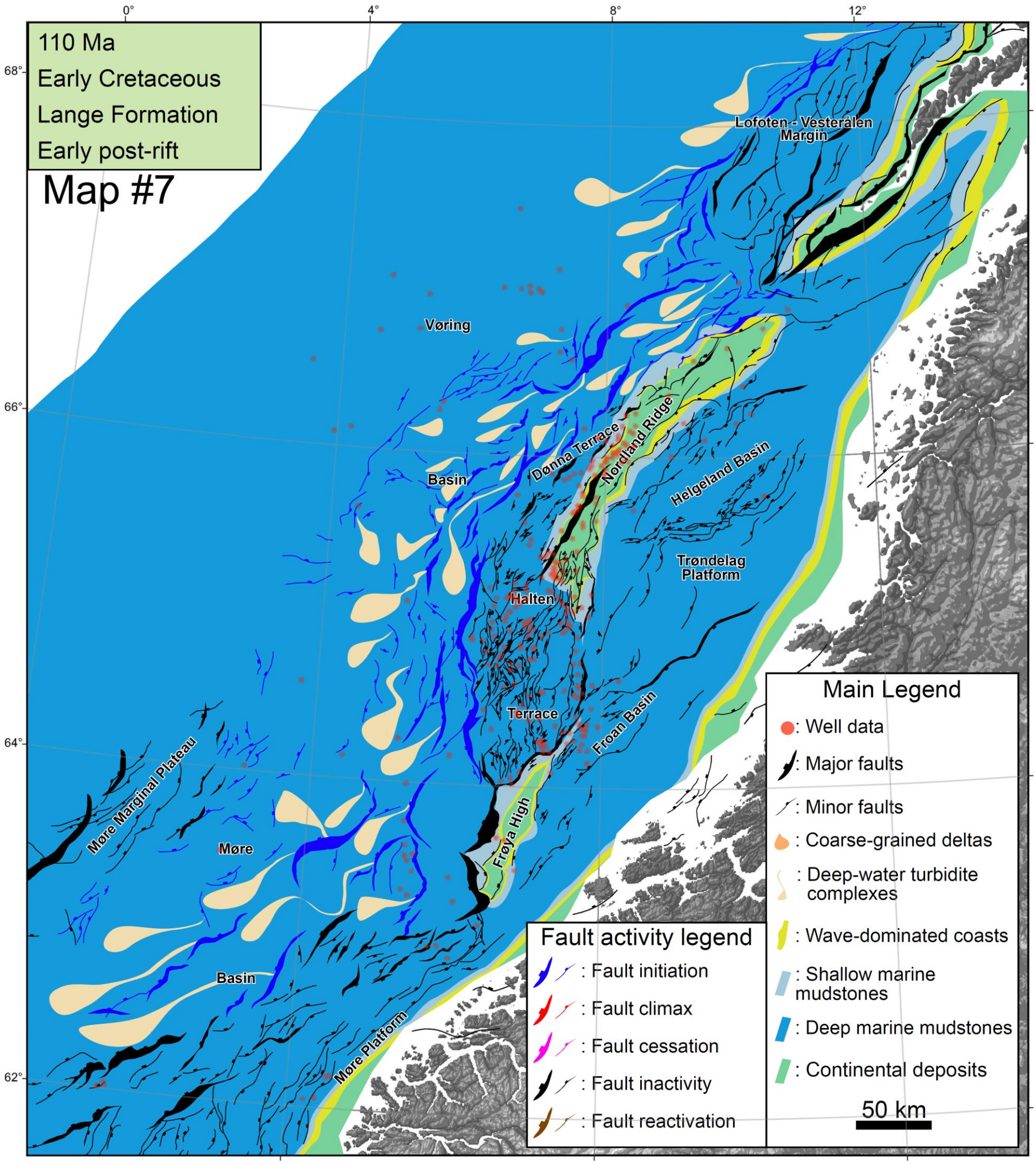
110 Ma
Early Cretaceous
Lange Formation
Early post-rift
Map #7
0°
4°
8°
12°
68°
66°
64°
62°
Lofoten - Vesterålen Margin
Vøring
Basin
Dønna Terrace
Nordland Ridge
Helgeland Basin
Trøndelag Platform
Halten
Terrace
Froan Basin
Frøya High
Møre Marginal Plateau
Møre
Basin
Møre Platform
Fault activity legend
: Fault initiation
: Fault climax
: Fault cessation
: Fault inactivity
: Fault reactivation
Main Legend
: Well data
: Major faults
: Minor faults
: Coarse-grained deltas
: Deep-water turbidite complexes
: Wave-dominated coasts
: Shallow marine mudstones
: Deep marine mudstones
: Continental deposits
50 km

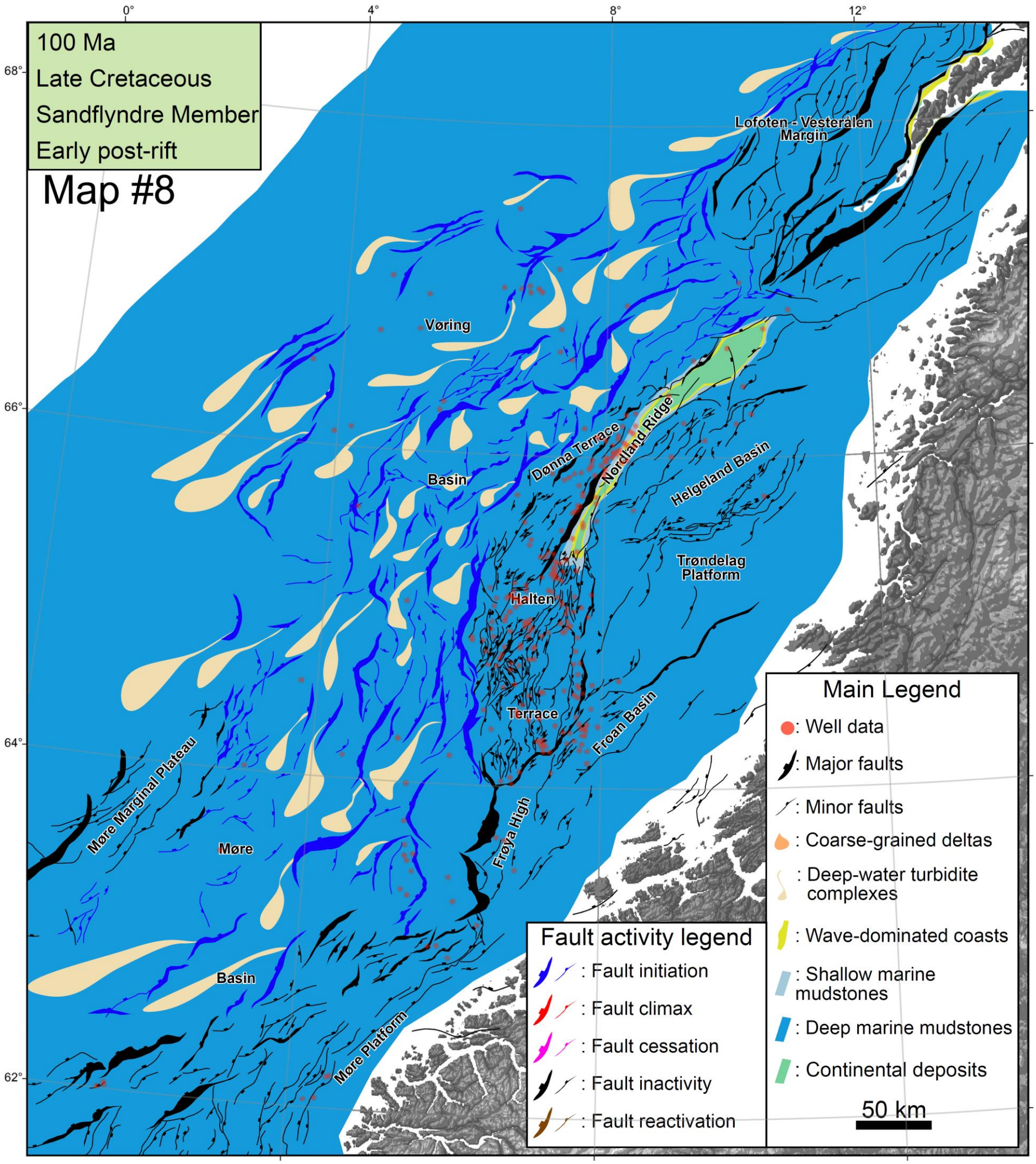
100 Ma
Late Cretaceous
Sandflyndre Member
Early post-rift
Map #8
0°
4°
8°
12°
68°
66°
64°
62°
Lofoten - Vesterålen Margin
Vøring
Basin
Dønna Terrace
Nordland Ridge
Helgeland Basin
Trøndelag Platform
Halten
Terrace
Froan Basin
Frøya High
Møre Marginal Plateau
Møre
Basin
Møre Platform
Main Legend
: Well data
: Major faults
: Minor faults
: Coarse-grained deltas
: Deep-water turbidite complexes
: Wave-dominated coasts
: Shallow marine mudstones
: Deep marine mudstones
: Continental deposits
50 km
Fault activity legend
: Fault initiation
: Fault climax
: Fault cessation
: Fault inactivity
: Fault reactivation

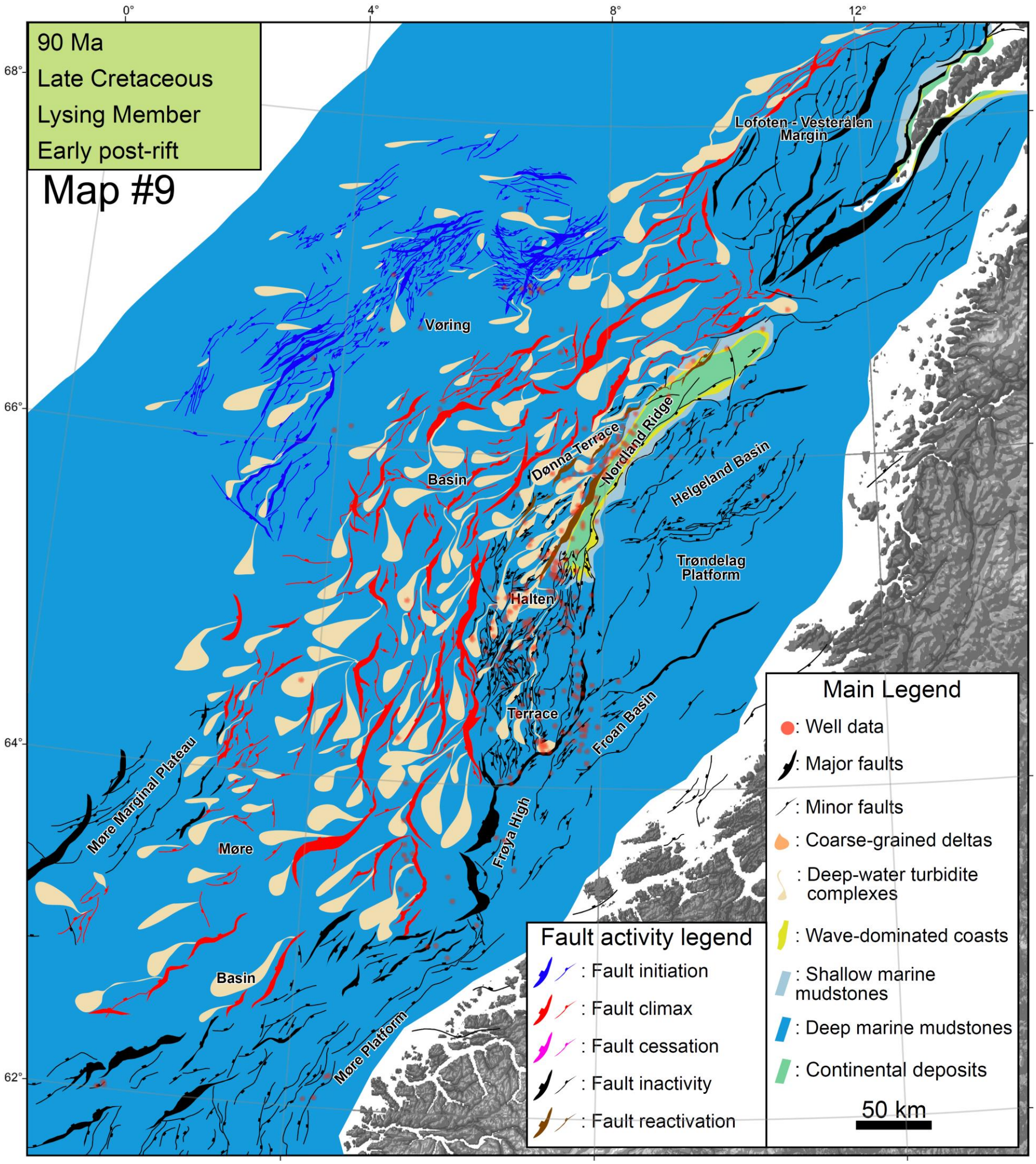
90 Ma
Late Cretaceous
Lysing Member
Early post-rift
Map #9
0°
4°
8°
12°
68°
66°
64°
62°
Lofoten - Vesterålen Margin
Vøring
Basin
Dønna Terrace
Nordland Ridge
Helgeland Basin
Trøndelag Platform
Halten
Terrace
Froan Basin
Frøya High
Møre Marginal Plateau
Møre
Basin
Møre Platform
Main Legend
: Well data
: Major faults
: Minor faults
: Coarse-grained deltas
: Deep-water turbidite complexes
: Wave-dominated coasts
: Shallow marine mudstones
: Deep marine mudstones
: Continental deposits
50 km
Fault activity legend
: Fault initiation
: Fault climax
: Fault cessation
: Fault inactivity
: Fault reactivation

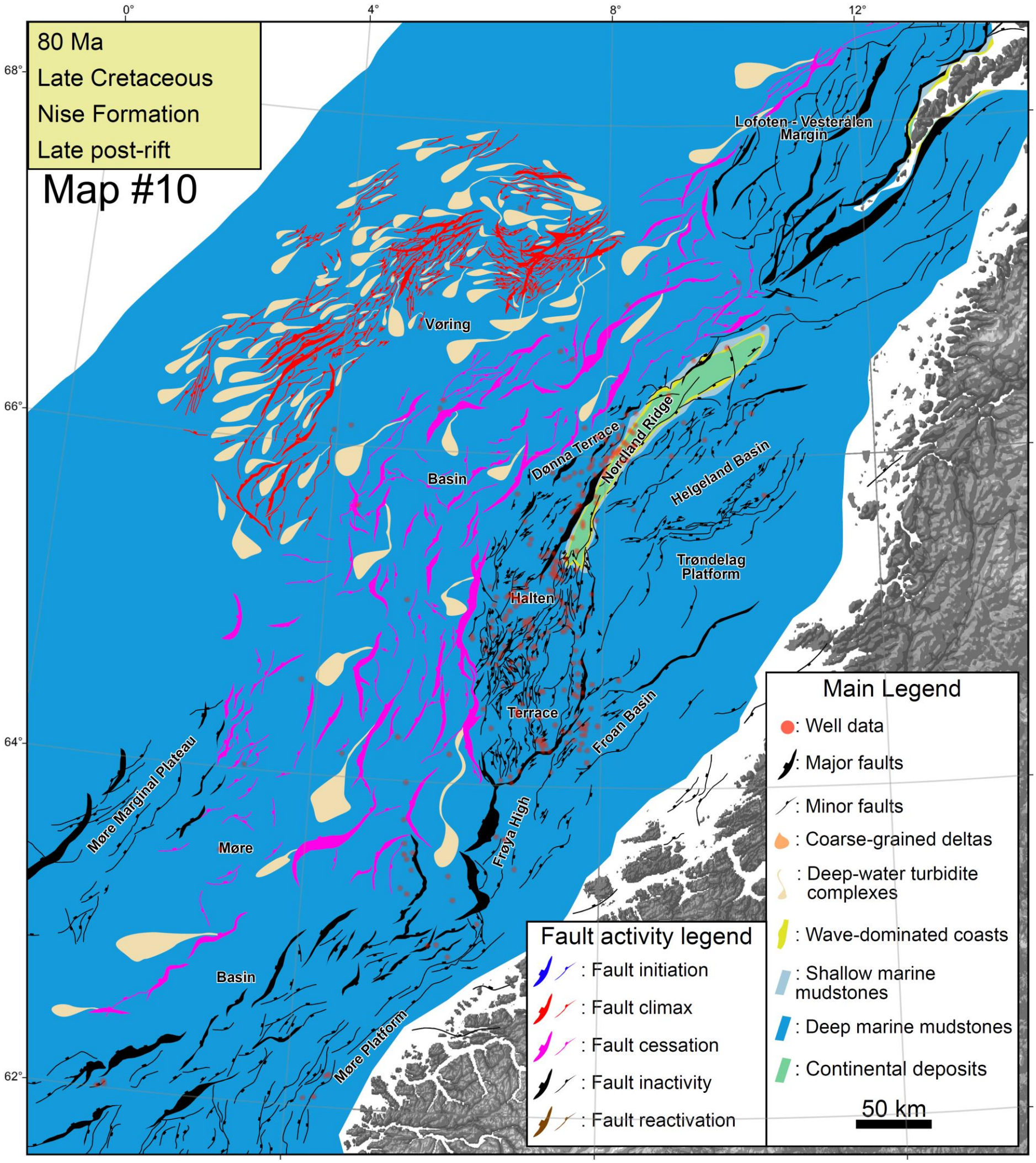
80 Ma
Late Cretaceous
Nise Formation
Late post-rift
Map #10
0°
4°
8°
12°
68°
66°
64°
62°
Lofoten - Vesterålen Margin
Vøring
Basin
Dønna Terrace
Nordland Ridge
Helgeland Basin
Trøndelag Platform
Halten
Terrace
Froan Basin
Frøya High
Møre Marginal Plateau
Møre
Basin
Møre Platform
Main Legend
: Well data
: Major faults
: Minor faults
: Coarse-grained deltas
: Deep-water turbidite complexes
: Wave-dominated coasts
: Shallow marine mudstones
: Deep marine mudstones
: Continental deposits
50 km
Fault activity legend
: Fault initiation
: Fault climax
: Fault cessation
: Fault inactivity
: Fault reactivation

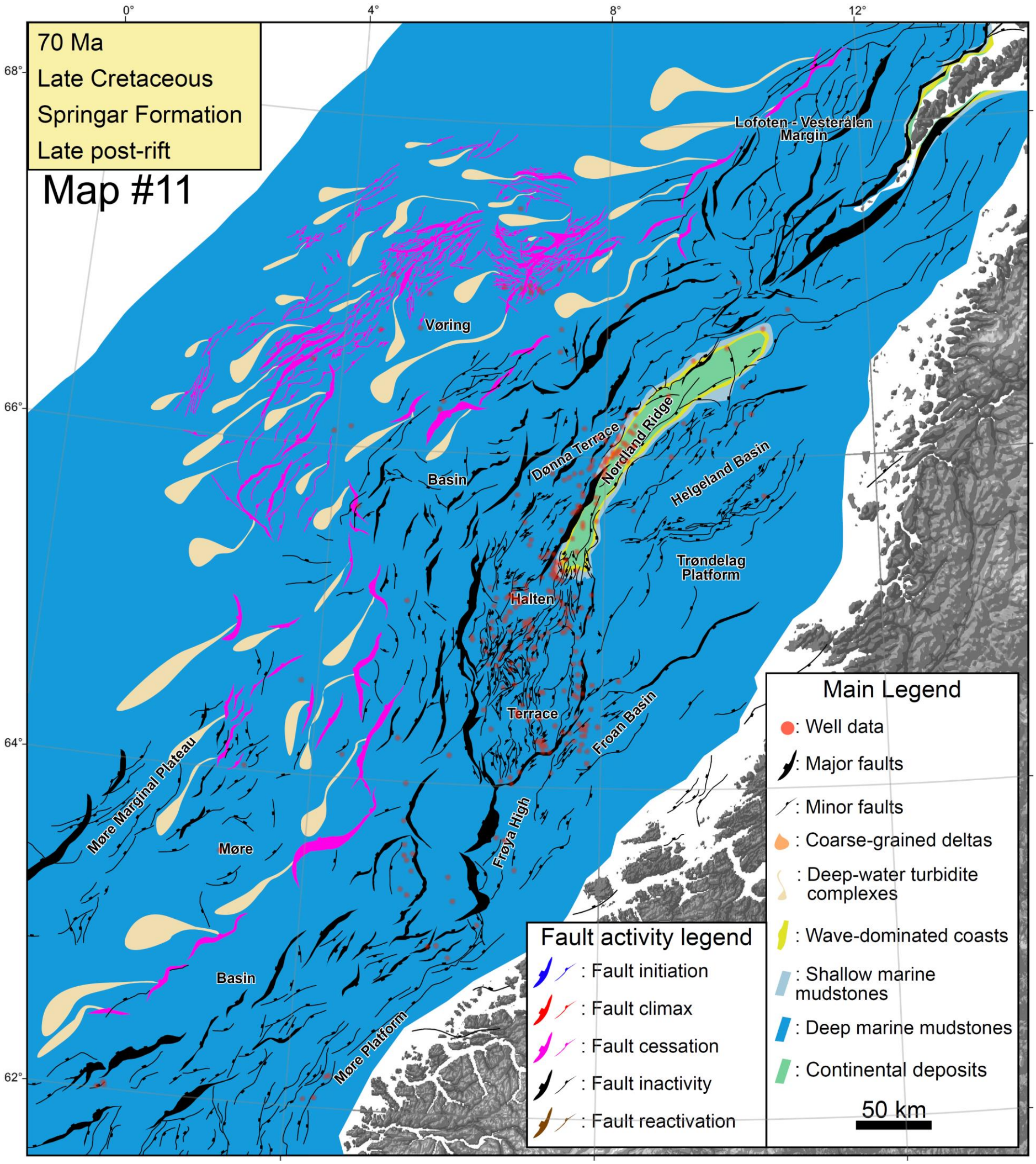
70 Ma
Late Cretaceous
Springar Formation
Late post-rift
Map #11
0°
4°
8°
12°
68°
66°
64°
62°
Lofoten - Vesterålen Margin
Vøring
Basin
Dønna Terrace
Nordland Ridge
Helgeland Basin
Trøndelag Platform
Halten
Terrace
Froan Basin
Frøya High
Møre Marginal Plateau
Møre
Basin
Møre Platform
Main Legend
: Well data
: Major faults
: Minor faults
: Coarse-grained deltas
: Deep-water turbidite complexes
: Wave-dominated coasts
: Shallow marine mudstones
: Deep marine mudstones
: Continental deposits
50 km
Fault activity legend
: Fault initiation
: Fault climax
: Fault cessation
: Fault inactivity
: Fault reactivation

2. Atlantic Rifting and associated depositional environments

2.1. Thinning phase: initiation, termination and duration

The thinning phase in the South Atlantic segment seems to have initiated during the Early Berriasian and ended during the Late Aptian (Heine et al., 2013; Ye et al., 2017). Based on the GTS2016 (Ogg et al., 2016), the rifting period in the South Atlantic segment lasted approximately 29 Ma. At the transition between the central segment and the north segment, the thinning period started during the Middle Oxfordian and probably ended during the Early Hauterivian, corresponding to a period of approximately 26 Ma (Péron-Pinvidic and Manatschal, 2009; Peron-Pinvidic et al., 2013). The Northern North Atlantic thinning stage was in turn initiated during the Middle Bathonian and ended during the Late Berriasian (Surlyk and Ineson, 2003; Verreussel et al., 2018), which corresponds to a duration of *circa* 27 Ma. This highlights the temporal variation in rifting episodes across the Atlantic. The duration of the thinning phase of the Atlantic rift ranges from 25 Ma to 30 Ma.

We propose for the Norwegian Sea, based on the reappraised dinoflagellate cyst zonation, a rifting episode (thinning stage) which lasted 25 Ma in *Chapter 2*, this could be extended a further 2.5 Ma toward the end due to a period of erosion or non-deposition (cf. section *6.2 Dating uncertainty* in *Chapter 2*). The Norwegian Sea which is part of the North Atlantic segment reflects similar initiation and duration of the rifting period to that of the Atlantic generally.

2.2. Rift-sag phase: a migration of the deformation

The Atlantic rifting has a multiphase history that is diachronous from the South Atlantic to the North Atlantic segments (Peron-Pinvidic et al., 2013). Those phases are: (i) the stretching which forms the proximal domain, then (ii) the thinning which models the terrace domain, and finally (iii) the hyperextension/exhumation stage which shapes the deep domain (Peron-Pinvidic and Osmundsen, 2020; Peron-Pinvidic et al., 2020). In this PhD study, we have focused on the 2nd and 3rd rift phases, where most of the syn-rift and post-rift sediments accumulated in the terrace domain (necking domain) and the deep domain (distal domain), respectively.

Based on our results, the transition between the 2nd and 3rd rift phases did apparently not correspond to an abrupt cessation of the fault activity as suggested by Færseth and Lien (2002). In the South Atlantic segment, the existence of a transitional phase (rift-sag) between the syn-rift and the post-rift periods has been reported by Jones et al. (2019). Our data here suggest, for the Northern Atlantic segment, that the rift-sag phase (*sensu* Jones et al. (2019)) most probably corresponds to a period of migration of the deformation from the necking domain (terrace domain) to the distal domain (deep domain) (Fig. 4.1, columns #8, #11). During the rift-sag period, master faults separating the terrace and the platform domains progressively ceased, while pre-existing basement faults separating the terrace and the deep domains were progressively reactivated by a new set of faults. In other words, during the rift-

sag stage, the terrace domain is bounded, on one hand, by the extinction of the faults along with the platform domain, on the other hand, by the initiation of faults along with the deep domain. The rift-sag period is commonly described as a period of tectonic quiescence which is part of the post-rift stage; nevertheless, a high-resolution sedimentological and tectonostratigraphic analysis provides therefore the possibility to identify the last tectonic activity between the platform and terrace domain and the first tectonic activity between the terrace and the deep domain.

2.3. Rift-related depositional environment: coexistence and proportion

Pre-, syn- and post-rift periods exhibit an evolution in depositional environments. In shallow-marine environments, coarse-grained deltas have been frequently encountered during the rift-climax e.g. in the Suez rift, Corinth rift, East Greenland rift, East Africa rift, North Sea rift, etc. (Gawthorpe et al., 1990; Scholz et al., 1990; Gupta et al., 1999; Colella and Prior, 2009; Turner and Cronin, 2018; Barrett et al., 2020). Tectonic activity becomes less influential during the final rift stage (Ravnås & Steel, 1998; Folkestad et al., 2014; Jones et al., 2020). In the North Atlantic segment, during the final rift stage, coastal shallow marine environments progressively developed at the expense of coarse-grained deltas, coevally with the deposition of organic-rich mudstones (Surlyk and Ineson, 2003; Armstrong et al., 2016; Verreussel et al., 2018; Atar et al., 2019; Jones et al., 2020).

In the Norwegian Sea, during the entire syn-rift period, subaqueous delta deposits and wave dominated shores are coexisting in various proportions. During the rift climax stage, the development of wave-dominated environments waned in favour to coarse-grained deltas due to important vertical displacements, the erosion of the footwall and subsidence in the hanging wall depocenter. Hence the rift climax stage is mainly represented by the coarse-grained deltaic sandstones of the Intra-Melke Fm. in the Norwegian Sea. During the final rift stage, widely distributed wave-dominated shore depositional environments are found whereas, conversely, coarse-grained deltas became rare thus reflecting the cessation of extensional fault activity. The final rift stage is predominantly represented by wave-dominated shore environments of the Rogn Fm. in offshore mid-Norway. Hence 4D analysis of siliciclastic shallow marine syn-rift systems enhances the prediction of new exploration targets by taking in account the sub-rift stages.

2.4. Depositional environments and rift geometry

The discrepancy between depositional environments from one to the other side of the rift conjugate margins must be investigated by considering the palaeotopography and geometry of the rift. The Mid Norwegian – NE Greenland conjugate margins reveal inherent basement structures (Elliott et al., 2012; Jones et al., 2020; Surlyk, 2003; Surlyk & Noe-Nygaard, 2005), which triggered different configurations for depositional environments. During the Tithonian to the Early Berriasian, coastal environments developed coevally in the terrace domain (Jameson, Liverpool Land Margin in NE Greenland and in the Halten and Dønna terraces in the Mid Norwegian conjugate margin) (Jones et al., 2020; Surlyk, 2003; Surlyk & Noe-Nygaard, 2005) (Fig. 2.2 in *Chapter 2*).

However, sedimentological data reveal some differences between the two rift margins (in terms of controlling mechanisms). In the Halten and Dønna terraces of the Mid Norwegian margin, the sandy coastal deposits of the Rogn Fm. were deposited in a wave-dominated environment (Elliott et al., 2015; Jones et al., 2020). Conversely, in the Jameson, Liverpool Land located in the NE Greenland conjugate margin, the coeval Raukelv Fm. is interpreted to develop in a tide-dominated setting (Surlyk & Noe-Nygaard, 2005). Looking at a regional sedimentological section stretching from NE Greenland to the Mid Norwegian margin, the Halten and Dønna terraces and the Jameson, Liverpool Land Margin (corresponding both to the terrace domain) exhibit a different topographical configuration (Fig. 4.4).

The influence of inherited palaeotopographies induced by differential tectonic activity or inherited basement structures can be discussed by means of rift geometry. In the NE Greenland Margin, the Jameson Land basin is confined between the Greenland continent and the Liverpool Land whereas, in the Mid Norwegian conjugate margin, the Halten and Dønna terraces are both exposed to the open sea (Fig. 4.4) (Peron-Pinvidic & Osmundsen, 2018). Furthermore, the Mid Norwegian – NE Greenland conjugate margins are asymmetric on either side of the central rift axis, which most likely had an influence on the dominant hydrodynamic process (tide *vs* wave) as recorded in sedimentary successions. In the case of the Mid Norwegian – NE Greenland conjugate margins, the Jameson Land basin recorded tide-dominated coastal environments due to the confined/restricted configuration where the Liverpool land is acting as a barrier. Conversely, in an unconfined setting such as in the Halten and Dønna terraces, the open configuration favoured the development of wave-dominated coastal environments (Fig. 4.4).

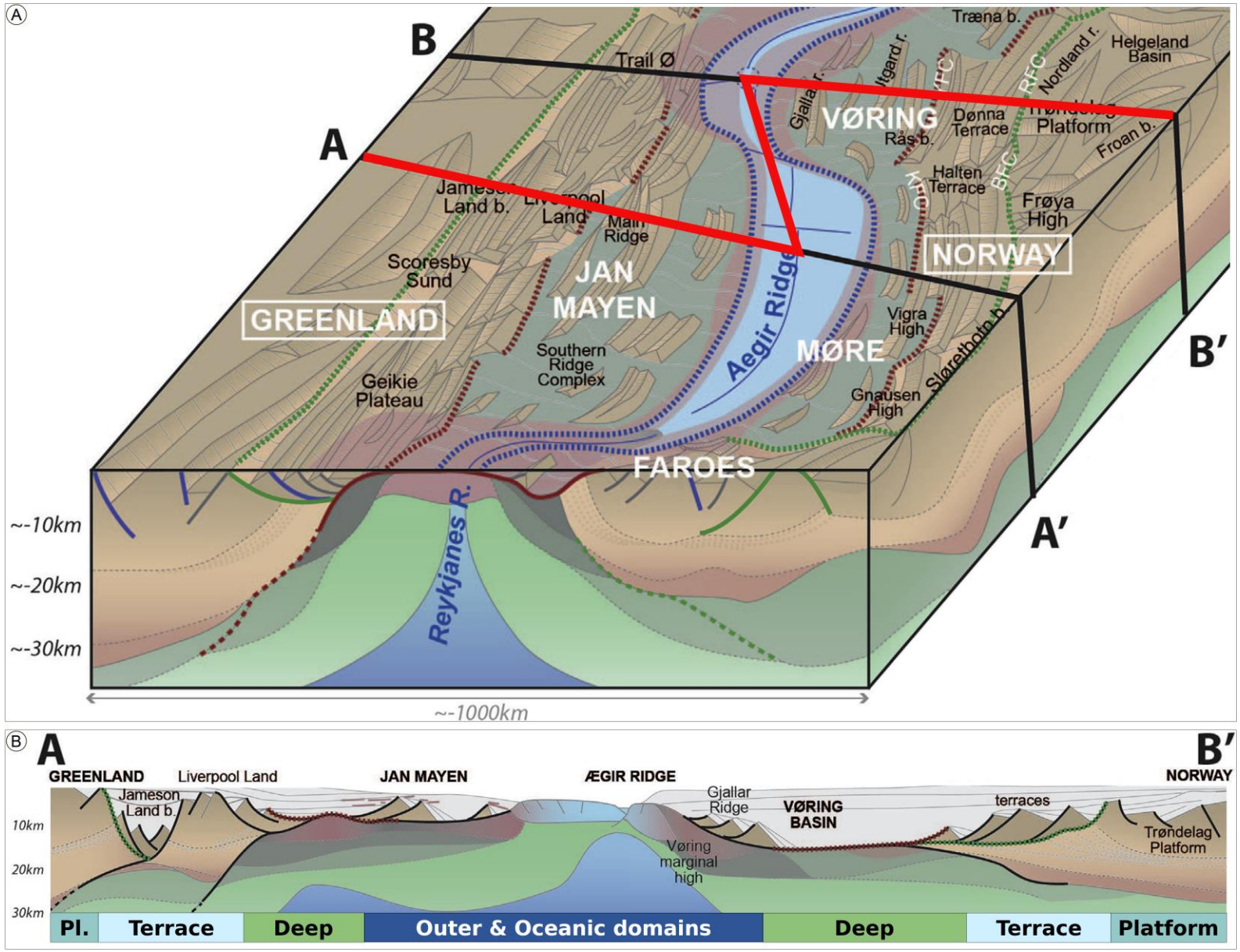

Fig. 4.4: Schematic first-order architecture of the Mid Norwegian / NE Greenland conjugate margins in plan view (A) and in cross-section (B) after Peron-Pinvidic & Osmundsen, (2018).

3. Autocyclic controls

3.1. Autocyclic controls on deep-water turbidites

Autocyclic processes imply cyclic depositional successions in the sense that they repeat themselves; however, they have an unpredictable frequency. Therefore, autocyclic processes are aperiodic because they do not have a predetermined frequency occurrence and imply local sedimentary responses (Cecil et al., 2011). Autocyclic controlling factors have been solely identified for deep-water turbidite lobe complex deposits (Chapter 3*).* Some of the internal controls that allow the effective dispersal of sediment inside turbidite lobes have been observed in laboratory experimentations. These processes include lateral lobe shifting or axial migration by progradation or retrogradation combined with aggradation (Hamilton et al., 2015, 2017; Ferguson et al., 2020). However, those observations are mainly done on aerial view.

Based on our data, and based on our proposed new subdivision of the lobe allowing to distinguish three axial lobe environments (channel and/or proximal lobe, mid to distal lobe and frontal lobe fringe) and one lateral lobe environment (lateral lobe fringe). This new segmentation of the lobe environments provides the possibility to discriminate whether the motion of the lobe is axial or lateral. In this study, our results allow to discriminate 4 autocyclic mechanisms controlling the spatial organisation of turbidite lobe environments, with 2 of them similarly to those reported from laboratory experimentations (Hamilton et al., 2015, 2017; Ferguson et al., 2020). However, in the fossil record, as opposed to laboratory experimentations, there is no constrain on accommodation space. For instance, a lobe complex on the fossil record can measure up to 100 m, whereas in a laboratory, the experimentation is limited commonly to 1 m tick. For this reason, fossil record can help to decipher unknown autocyclic controlling factors such as the centre of gravity of the lobe, or the self-regulation of the thickness of the lobe elements by controlling the type and the number of beds which play a role in sediment dispersal.

3.2. Autocyclic controls on coarse-grained deltas

Similar internal controls for the coarse-grained deltas should be expected such as autocyclic delta-lobe switching and channel avulsions (Dorsey *et al.*, 1997). Likely to the deep-water turbidite lobe complexes, based on fossil record, a detail sedimentological analysis combined with a statistical and numerical analysis can allow to subdivide axial depositional environment (delta front and prodelta) with lateral depositional environment (proposed name: “lateral delta” deposits).

Similarly, to the turbidite lobe environments, a well-defined difference between axial and lateral delta environments should be expect for 4 reasons: (i) the shape is ovoid, (ii) one main sediment entry point, (iii) abrupt change in slope (topset *vs.* foreset), (iv) composed of subaqueous sedimentary density flow (SSDF) deposits. Those 4 similitudes with the turbidite lobe deposits imply that a highly concentrated SSDF deposits arriving at the entrance of the delta, will progressively decrease in sediment concentration along the axis keeping a high-

density flow, whereas along the side will abruptly decrease in sediment concentration with a low-density flow.

As preliminarily observations (*Supplementary data 2.C* in *Chapter 2*), likely to the interlobe, we can easily identify some “interdelta” in the delta front and prodelta. Those “interdelta” which may correspond to lateral delta deposits (mudstone background with centimetric turbidity flow or concentrated density flow deposits) are thin in the delta front, and thicker in the prodelta. Similarly, the lateral lobe environment is thin when located adjacently to a channel and/or proximal lobe environment, and thick when juxtaposed to a frontal lobe fringe environment. All those similarities between coarse-grained deltas and deep-water turbidite lobe complexes, highlights that autocyclic processes in coarse-grained deltas can be further investigated.

4. Sandstone reservoirs and petroleum exploration potential

Coarse-grained deltas, wave-dominated shoreface to foreshore and deep-water turbidite lobe complexes are proven prolific petroleum reservoirs in the Norwegian Sea fields (Fugelli and Olsen, 2007; Jones et al., 2020; NPD, 2021). During the 1980s, petroleum exploration in the terrace domain from the Norwegian Sea mainly focused on Early to Middle Jurassic pre-rift sandstone reservoirs. However, over the following decades, as demonstrated in the syn-rift (Chapter 2) and post-rift (Chapter 3) studies, the Viking Group (Middle to Late Jurassic) and the Cromer Knoll Group (Early to Late Cretaceous) revealed good reservoir properties. The schematic cross-sections of the Norwegian Sea (sketch with no wells in *Fig. 4.2*) presents the reservoirs, seals and source rocks of the Viking and Cromer Knoll groups.

Commonly, in the terrace domain, a single vertical exploration well encounters both pre-rift and syn-rift sandstone reservoirs. In the same way, still in the terrace domain, a single vertical well often penetrates both pre-rift and post-rift sandstone reservoirs. Nonetheless, it is rare that a standard vertical exploration well encounters both syn-rift and post-rift sandstone reservoirs, as predicted. In most cases, when syn-rift coarse-grained deltas or wave-dominated shoreface to backshore environments and post-rift deep-water turbidite lobe complex sandstone reservoirs are targeted in a single vertical exploration well (within the terrace domain), one target will be sand-rich while the other one will have a poor reservoir quality (if any) (Fig. 4.5). Hence this study, from which outcomes a better understanding of the syn- to post-rift transition, enables for the first time a much better constrained of the stratigraphic succession, and thus prediction, of potential reservoirs. It appears, furthermore, that sedimentary successions are strongly controlled by the inherited topography (Fig. 4.5).

In the terrace domain, the sandy reservoirs of the syn-rift stage are mainly found along active syn-rift faults forming structural highs, whereas the sandy turbidite systems of the post-rift stage largely sealed the pre-existing structural lows. Grabens generated during syn-rift periods then acted as corridors for sedimentation during the post-rift stage. Post-rift deposits are therefore intimately linked to syn-rift deposits (Fig. 4.5). As a result, the terrace domain outlines distinct zones for syn-rift and post-rift reservoirs, which however rarely overlap (sketch with no wells in *Fig. 4.2*). The deep domain is, however, generally the best setting to

explore post-rift reservoirs. The structural highs of the platform domain represent, conversely, a privileged location for pre-rift and post-Cretaceous reservoirs (Fig. 4.5).

The most promising context where both syn-rift and post-rift reservoirs can simultaneously be discovered in a vertical succession is located at the boundary between different domains (Fig. 4.5). Syn-rift and post-rift reservoirs will be found directly on the hanging wall of faults where coastal (syn-rift), coarse-grained deltaic (syn-rift) and deep-water turbidite (rift-sag and post-rift) depositional environments have the most chance to develop. To this regard, the transition zone between the terrace and the deep domains, and the transition zone between the platform and the terrace domains, likely constitute the optimal places to simultaneously encounter syn-rift and post-rift sandstone reservoirs in the stratigraphic succession (yellow interval in the sketch with no wells in *Fig. 4.2*). This area is restricted to a narrow zone (only a few kilometres) and the viability of the exploration play can be highly dependent on sealing capacity (fault trap) and reservoir properties, which may be poor close to the fault damage zone (Fig. 4.5).

Interestingly, the narrow zone between the terrace and the deep domain has not been often explored. However, the few wells drilled (6205/3-1R; 6407/10-5) in this restricted area have encountered both syn-rift and post-rift reservoirs with good to moderate properties, although no hydrocarbon accumulation was found (sketch with wells in *Fig. 4.2*). Nevertheless, thick vertical successions in this area should be expected from syn-rift and post-rift successions (Fig. 4.5). A robust seal and trap study combing different approaches (e.g., seismic analysis, seal analysis, amplitude versus offset (AVO) study, petrophysical study, source-to-sink analysis, detailed core description, robust well correlation, spectral decomposition analysis and colour blending analysis) should then be undertaken to better evaluate and circumvent the risks inherent to such prospects, which are highly rewarding in the case of discovery.

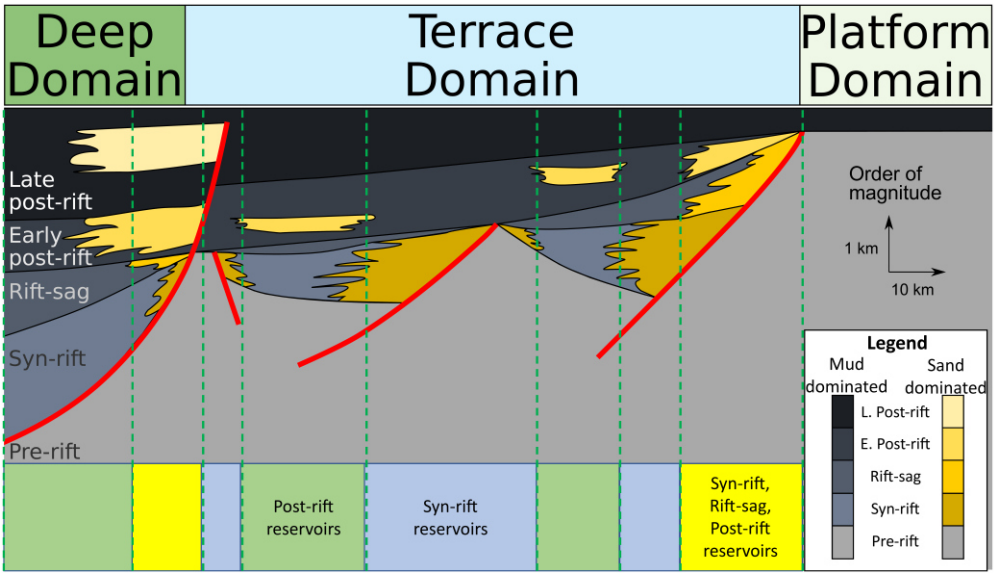

Fig. 4.5: Schematic illustration of the first-order architecture of the Mid Norwegian margin with focus on the most predictable locations for syn-rift reservoirs (blue squares), post-rift reservoirs (green squares) and a combination of syn-rift, rift-sag and post-rift reservoirs (yellow squares).

In the Conclusions (Chapter 5), a focus on the Norwegian Sea rift evolution outlines the links between depositional environment successions and tectonic activity; then, a short summarization of the main depositional environments (wave-dominated coastal environment, coarse-grained deltaic environment and deep-water turbidite complexes) observed within the syn-rift, rift-sag and post-rift periods is provided. Finally, some perspectives for future work are proposed. The two first parts of the conclusion (Chapter 5) tackle the main scientific issues raised in the Introduction (Chapter 1), i.e.: (i) how did tectonic activity evolve between syn-rift and post-rift phases?; (ii) is there any transitional rift period between syn-rift and post-rift phases? (iii) is it possible to discriminate between autocyclic and allocyclic forcings in sedimentary successions?

The last part entitled "*Perspectives for future work*" opens for further investigations on the following topics: (i) "*Tectonics and subsidence*", which include regional to semi-regional structural restoration; (ii) "*Palaeoclimate*" with a focus on spore and pollen grain analyses; (iii) "*Subaqueous sedimentary density flow*" (SSDF) deposits considered in a source-to-sink perspective, and (iv) the identification of "*autocyclic vs allocyclic factors*" for coarse-grained subaqueous deltaic systems by using the same approach as for deep-water turbidite lobe complexes (Chapter 3).

CHAPTER 5: Conclusions and perspectives

1. The Norwegian Sea rift evolution

The detailed sedimentological and tectonostratigraphic analysis of syn-rift and post-rift stages in the Norwegian Sea allows a refined reconstruction of depositional environments and palaeogeographical changes between the Middle to Upper Jurassic and Cretaceous. The syn-rift, rift-sag and post-rift periods fit well into the Atlantic multiphased rift evolution, where the rift-sag phase most probably corresponds to a period of migration of the deformation from the terrace domain to the deep domain. In this concluding chapter, an individual paragraph will be devoted to each substage (rift initiation, rift-climax, final rift, early rift-sag, late rift-sag, early post-rift and late post-rift), each of which recalling substage duration, the reconstructed depositional environment as well as petroleum exploration issues.

1.1. Rift initiation

The rift initiation corresponds to the first syn-rift substage. Chronostratigraphically, the rift initiation started during the Middle Bathonian and ended during the Middle Callovian. Based on absolute ages (Ogg *et al.*, 2016), the rift initiation substage in the Norwegian Sea lasted 2.7 Ma. The platform domain was principally emerged, coevally with the large development of shallow-marine coastal environments. Alternatively, the progressive increase in tectonic activity led to the development of subaqueous coarse-grained deltas and wave-dominated coasts in the terrace domain, where subaqueous coarse-grained deltas and wave-dominated coasts are the primary petroleum reservoirs. Seal rocks or poor reservoir properties are found in offshore deposits.

1.2. Rift-climax

The rift-climax corresponds to the second syn-rift substage. Chronostratigraphically, the rift-climax started during the Middle Callovian and ended during the Late Kimmeridgian. Based on absolute ages (Ogg *et al.*, 2016), the rift-climax substage in the Norwegian Sea lasted 11.1 Ma. This period is characterised by intense tectonic activity along syn-rift faults developed throughout the entire terrace domain. Master faults are commonly linked to pre-existing basement structures, but most syn-rift faults were newly generated. The platform domain was partially emerged, leading to widespread erosion of pre-rift deposits in this area. Conversely, in the terrace domain, subaqueous coarse-grained deltas mainly developed in the hanging wall of the master faults and constitute the main rift-climax deposits, although wave-dominated coastal deposits may also form good reservoirs. Poor reservoir properties (or seal rocks) are found distally and correspond to offshore sediments or distal prodeltaic deposits.

1.3. Final rift

The final rift corresponds to the last syn-rift substage. Chronostratigraphically, the final rift substage started during the Late Kimmeridgian and ended approximately during the Middle to Late Berriasian boundary. Based on absolute ages (Ogg *et al.*, 2016), the final rift in the Norwegian Sea lasted 11.4 Ma, corresponding approximately to the duration of the rift-climax substage. This period is characterised by a progressive decrease in tectonic activity leading to the gradual decline of subaqueous coarse-grained deltas in the terrace domain. The drowning of the terrace domain caused mainly by an important gobal sea level rose (Haq, 2017) favoured the development of widespread wave-dominated systems associated with offshore mudstones enriched in organic matter. During the final rift substage, good to excellent petroleum reservoir properties have been encountered predominantly in wave-dominated coastal deposits. Deep-water turbidite lobe complexes developed most probably at the transition between the terrace domain and the deep domain. Proven source rocks corresponding to offshore mudstones enriched in organic matter were deposited during this substage.

1.4. Early rift-sag

The early rift-sag corresponds to the first transitional period between the syn-rift and the post-rift stages. Chronostratigraphically, the early rift-sag started approximately across the Middle to Late Berriasian transition and ended at the Barremian/Aptian boundary. Based on absolute ages (Ogg *et al.*, 2016), the early rift-sag substage in the Norwegian Sea lasted 15.7 Ma. This period is characterised by a progressive decrease of tectonic activity, as fault offsets are limited to the master faults separating the platform and the terrace domains. A new set of faults seems to initiate along pre-existing Caledonian faults separating the terrace domain from the deep domain. The deep, terrace and platform domains were largely dominated by the deposition of deep-marine calcareous mudstones, with occasional occurrences of deep-water turbidite lobe complexes. During this substage, calcareous mudstones and marlstones are regarded as good seal rocks. No reservoir was encountered by exploration wells yet but deep-water turbidite lobe complexes are expected along marginal highs in the terrace and the deep domains.

1.5. Late rift-sag

The late rift-sag corresponds to the last transitional period between the syn-rift and the post-rift stages. Chronostratigraphically, the late rift-sag started approximately at the Barremian/Aptian boundary and ended at the Aptian/Albian boundary. Based on absolute ages (Ogg *et al.*, 2016), the late rift-sag substage in the Norwegian Sea lasted 12.9 Ma. This period is characterised by a progressive decrease in tectonic activity between the platform and the terrace domain where only rare master faults exhibit evidences of tectonic activity. However, the new set of faults separating the deep and the terrace domains which initiated during the early rift-sag substage continued to develop. During this substage, the deep, terrace and platform domains are characterised by the development of thick offshore

mudstones with very deep-water turbidite lobe complex deposits. Deep-water turbidite systems are considered as good petroleum reservoirs and are found in the deep and terrace domains along marginal highs. Some coastal deposits may have also developed along inherited marginal highs in the platform domain. Marine mudstones are regarded as good seal rocks.

1.6. Early post-rift

The early post-rift corresponds to the first post-rift substage. Chronostratigraphically, the early post-rift started at the Aptian/Albian boundary and ended during the Early Coniacian. Based on absolute ages (Ogg *et al.*, 2016), the early post-rift substage in the Norwegian Sea lasted 24.0 Ma. This period is characterised by a tectonic quiescence; however, tectonic activity was probably generated between the Turonian and the Early Coniacian since deep-water turbidite lobe complexes developed in the terrace domain and along marginal highs in the deep domain. Good to excellent petroleum reservoir properties are encountered in sandy deep-water turbidite lobe complexes. Seal rocks are found in offshore marine mudstone deposits.

1.7. Late post-rift

The late post-rift corresponds to the last post-rift substage. Chronostratigraphically, the late post-rift started during the Early Coniacian and ended at the Cretaceous–Paleogene (K–Pg) boundary. Based on absolute ages (Ogg *et al.*, 2016), the late post-rift substage in the Norwegian Sea lasted 23.1 Ma. This period is also characterised by a tectonic quiescence. The deep, terrace and platform domains were dominated by the deposition of deep-marine mudstones. Only rare deep-water turbidite lobe complexes are observed in the deep domain. The mudstones deposited during this substage are regarded as excellent seal rocks. However, rare deep-water turbidite lobe deposits having good quality petroleum reservoirs have been encountered in the deep domain. These sandy deposits are not expected to be found in the terrace and the platform domains.

2. Rift-related siliciclastic depositional environments

The rifting evolution in the Norwegian Sea generated three distinct siliciclastic depositional environments. Coarse-grained deltas and wave-dominated coastal environments were coevally observed during the syn-rift period. Conversely, deep-water turbidite lobe complexes mainly developed during the post-rift period *sensu lato* (including the rift-sag period).

2.1. Coarse-grained deltas

Coarse-grained deltas were mainly observed during the rift-climax substage on the hanging wall of normal faults. Subaqueous coarse-grained deltas are highly dependent on sediment source and fault linkage. Such deltas have a steep sedimentary profile and commonly exhibit wedge-shaped geometry along active faults. Coarse-grained deltas are subdivided into two sub-environments based on subaqueous sedimentary density flow types: (i) the delta front,

which corresponds to the proximal domain of the delta (steep slope) and is characterised by the amalgamation of hyperconcentrated density flow *sensu stricto* and grain-flow deposits; (ii) and the prodelta, which has a gentler slope implying the development of concentrated density flow and turbidity flow deposits.

2.2. Wave-dominated coastal environments

Wave-dominated coastal deposits were predominantly observed during the final rift substage. Wave-dominated coasts are commonly narrow (a few hundred metres to a few kilometres) but are laterally continuous over hundred to thousand kilometres. Wave-dominated coastal environments are characterised by a gentle slope of a few degrees as compared to the steeper coarse-grained deltaic systems. Wave-dominated coastal environments can be further subdivided into two main sub-environments with (i) the medium to coarse-grained foreshore/backshore (ii) and the sandy shoreface to the silty to muddy offshore transition. Those two main sub-environments can be further subdivided based on well-identified criteria such as the degree of bioturbation, wave-generated sedimentary structures, grain-size, etc.

2.3. Deep-water turbidite lobe complexes

Deep-water turbidite lobe complexes were mainly observed during the rift-sag and post-rift stages. The deep-water turbidite lobe complexes are generated downstream of the slope break. Lobe complexes usually measure between tens to one hundred kilometres in length and width, and between tens to hundred metres in thickness. The deep-water turbidite lobe complexes are composed of lobes that have been subdivided into five lobe environments: (i) the channel and/or proximal lobe, (ii) the mid to distal lobe, (iii) the frontal lobe fringe, (iv) the lateral lobe fringe and (v) the distal lobe fringe.

This proposed new subdivision offers the opportunity, within a stratigraphic succession, to interpret lobe dynamics (i.e., lateral motion *vs.* axial motion) as opposed to the commonly used “axial”, “off-axial” and “fringe” lobe environments. On the basis of the turbidite lobe successions studied here, the density of flow progressively decreases along the lobe axis, passing from hyperconcentrated density *flow sensu lato* in the channel and/or proximal lobe to supercritical turbidity flow (turbidity flow of type 2) in the frontal lobe fringe; in turn, the flow density abruptly decreases laterally, corresponding to the lateral lobe fringe environment mainly formed of turbidity flow of type 1.

Such a partitioning of the turbiditic lobe complex further allow to discriminate whether lobe dynamics are predominantly controlled by autocyclic or allocyclic processes. Aperiodic sub-environmental lobe successions with no depositional environment gap were attributed to autocyclic processes (controlling factors #1 to #4), whereas aperiodic lobe successions embedding depositional environment gaps (although rare) were attributed to allocyclic processes (allocyclic pulse controlling factors #5 and #6). However, at the basin-scale, the development of deep-water turbidite lobe complexes is mainly controlled by dominant allocyclic parameters (controlling factor #7of type A or type B).

3. Perspectives for future work

3.1. Tectonics and subsidence

Additional structural studies could be achieved to complete the present investigation and better constrain subsidence and tectonic activity: (i) detailed regional and semi-regional structural restorations, aiming at to deciphering the degree of erosion and the exact timing of fault activity during the different sub-stages; (ii) the construction of tectonic subsidence curves with the goal to highlight the impact of subsidence over the course of the rifting; (iii) detailed structural analyses on sediment cores combined with dip log analyses, which may provide additional information regarding deformation phases as well as strain, stress and kinematic patterns.

3.2. Palaeoclimate

The climate background considered in this PhD research mostly relies on the climate evolution reported by Price (1999) which is based on a multi-proxy analysis (e.g. clay mineral abundances, faunal and floral indicators, isotope analysis, sedimentary analysis, general circulation models, palaeotemperature proxy, etc.) and on a global compilation of existing paleoclimatic studies. The Mesozoic humidity-aridity curve of Price (1999) was drawn for the whole European continent. However, the European climate evolution may be different during the Mesozoic in the Norwegian Sea because this location corresponds to the northern part of Europe. Hence more studies conducted on spores and pollen grains, for instance, should be undertaken and would allow to decipher the genuine climatic variation throughout the syn- and post-rift periods.

3.3. Subaqueous sedimentary density flow

Subaqueous sedimentary density flow (SSDF) deposits, whether they occur in shallow-water (subaqueous coarse-grained deltas) or in deep-water (deep-water turbidite lobe complexes) environments could be investigated further through (i) a detailed sediment source-to-sink study to highlight sediment provenance and pathways, and/or (ii) a spectral decomposition analysis coupled with a colour blending analysis (as already started during this PhD) to identify geological features such as lobe shape, delta fans, etc. Unfortunately, due to the low quality of seismic data, this work could not document well-defined geological features. We are nevertheless confident that, with cutting-edge new seismic data, geometries within both deep-marine turbidite lobe complexes and delta fans (for the coarse-grained sandstones) could be identifiable.

3.4. Autocyclic and allocyclic factors

The identification of the main autocyclic factors controlling sedimentary dynamics within deep-marine turbidite lobe complexes allows the differentiation of axial and lateral motion of the lobe system. Such a study would be worth to be undertaken in shallow-marine subaqueous

coarse-grained deltas. Subaqueous coarse-grained deltaic environments include sub-depositional environments commonly described in the literature, such as the matryoshka doll (termed also Russian nested doll) corresponding to the centre of a turbidite lobe (or from a delta fan) (e.g. axial lobe) surrounded concentrically by more distal sub-environments (e.g. the off-axial lobe and the lobe fringe). We believe that SSDF deposits originating from one entry point will generate high density flows in the main axis of the flow, whereas the density flow may rapidly decelerate laterally. Hence, it is therefore important to identify axial and lateral displacement to discriminate between autocyclic and allocyclic factors on sediment dispersal. On the basis of the preliminary results obtained in this study (e.g., Chapter 2), we propose that subaqueous coarse-grained deltas could be subdivided in four axial sub-environments (proximal delta front, distal delta front, proximal prodelta, distal prodelta), including also one lateral sub-environment (lateral delta) which is comparable to the lateral lobe fringe environment described in *Chapter 3*. Therefore, a statistical and numerical analysis, such as presented in *Chapter 3*, tackling sedimentological successions in coarse-grained deltas may help discriminating dominant autocyclic from dominant allocyclic controlling factors of such proximal environments.

Bibliography

Ahmed, W., 2012. Structural analysis of the Troms-Finnmark fault complex, SW Barents Sea.

Ainsworth, R.B., Vakarelov, B.K., Nanson, R.A., 2011. Dynamic spatial and temporal prediction of changes in depositional processes on clastic shorelines: toward improved subsurface uncertainty reduction and management. AAPG bulletin 95, 267–297.

Alexander, J., Bridge, J.S., Cheel, R.J., Leclair, S.F., 2001. Bedforms and associated sedimentary structures formed under supercritical water flows over aggrading sand beds. Sedimentology 48, 133–152.

Alsen, P., Piasecki, S., 2018. Biostratigraphy of the Hareelv Formation (Upper Jurassic) in the Blokelv-1 core, Jameson Land, central East Greenland. Geological Survey of Denmark & Greenland Bulletin.

Alves, T.M., Moita, C., Cunha, T., Ullnaess, M., Myklebust, R., Monteiro, J.H., Manuppella, G., 2009. Diachronous evolution of Late Jurassic–Cretaceous continental rifting in the northeast Atlantic (west Iberian margin). Tectonics 28.

Andsbjerg, J., Nielsen, L.H., Johannessen, P.N., Dybkjær, K., 2001. Divergent development of two neighbouring basins following the Jurassic North Sea doming event: the Danish Central Graben and the Norwegian-Danish Basin, in: Norwegian Petroleum Society Special Publications. Elsevier, pp. 175–197.

Armstrong, H.A., Wagner, T., Herringshaw, L.G., Farnsworth, A.J., Lunt, D.J., Harland, M., Imber, J., Loptson, C., Atar, E.F.L., 2016. Hadley circulation and precipitation changes controlling black shale deposition in the Late Jurassic Boreal Seaway. Paleoceanography 31, 1041–1053.

Atar, E., März, C., Aplin, A.C., Dellwig, O., Herringshaw, L.G., Lamoureux-Var, V., Leng, M.J., Schnetger, B., Wagner, T., 2019. Dynamic climate-driven controls on the deposition of the Kimmeridge Clay Formation in the Cleveland Basin, Yorkshire, UK. Climate of the Past 15, 1581–1601.

Baas, J.H., Best, J., Peakall, J., 2021. Rapid gravity flow transformation revealed in a single climbing ripple. Geology 49, 493–497.

Bardaji, T., Dabrio, C.J., Goy, J.L., Somoza, L., Zazo, C., 1990. Pleistocene fan deltas in southeastern Iberian peninsula: sedimentary controls and sea-level changes. Coarse-grained deltas 10, 129–151.

Barrett, B.J., Gawthorpe, R.L., Collier, R.E.L., Hodgson, D.M., Cullen, T.M., 2020. Syn-rift delta interfan successions: Archives of sedimentation and basin evolution. The Depositional Record 6, 117–143.

Bartholomew, I.D., Peters, J.M., Powell, C.M., 1993. Regional structural evolution of the North Sea: oblique slip and the reactivation of basement lineaments, in: Geological Society, London, Petroleum Geology Conference Series. Geological Society of London, pp. 1109–1122.

Beerbower, J.R., 1964. Cyclothems and cyclic depositional mechanisms in alluvial plain sedimentation. Kansas Geological Survey Bulletin 169, 31–32.

Bellahsen, N., Fournier, M., d'Acremont, E., Leroy, S., Daniel, J.M., 2006. Fault reactivation and rift localization: Northeastern Gulf of Aden margin. Tectonics 25.

Beniest, A., 2017. From continental rifting to conjugate margins: insights from analogue and numerical modelling.

Berger, A., 1988. Milankovitch theory and climate. Reviews of geophysics 26, 624–657.

Biostrat, 1995. Well 6406/12-2, Biostratigraphic analysis prepared for Statoil AS. Internal report (unpublished).

Bjerager, M., Alsen, P., BOJESEN-KOEFOED, J., Fyhn, M.B.W., Hovikoski, J., Ineson, J.R., NØHR-HANSEN, H., Nielsen, L.H., Piasecki, S., Vosgerau, H., 2020. Cretaceous lithostratigraphy of North-East Greenland. Bulletin of the Geological Society of Denmark 68.

Blystad, P., Brekke, H., Færseth, R.B., Larsen, B.T., Skogseid, J., Tærudbakken, B., 1995. Structural elements of the Norwegian continental shelf. Part II. The Norwegian Sea Region. NPD, Norwegian Petroleum Directorate, Bulletin 8.

Bøe, R., Smelror, M., Fossen, H., 2010. Mesozoic sediments and structures onshore Norway and in the coastal zone.

Boulesteix, K., Poyatos-Moré, M., Flint, S.S., Hodgson, D.M., Taylor, K.G., Brunt, R.L., 2020a. Sedimentological and stratigraphic criteria to distinguish between basin-floor and slope mudstones: Implications for the delivery of mud to deep-water environments.

Boulesteix, K., Poyatos-Moré, M., Hodgson, D.M., Flint, S.S., Taylor, K.G., 2020b. Fringe or background: Characterizing deep-water mudstones beyond the basin-floor fan sandstone pinchout. Journal of Sedimentary Research 90, 1678–1705.

Bouma, A.H., 2004. Key controls on the characteristics of turbidite systems. Geological Society, London, Special Publications 222, 9–22.

Bouma, A.H., 1962. Sedimentology of some flysch deposits. A graphic approach to facies interpretation 168.

Brekke, H., 2000. The tectonic evolution of the Norwegian Sea Continental Margin with emphasis on the Vøring and Møre Basins. Geological Society, London, Special Publications 167, 327–378.

Brekke, H., Dahlgren, S., Nyland, B., Magnus, C., 1999. The prospectivity of the Vøring and Møre basins on the Norwegian Sea continental margin, in: Geological Society, London, Petroleum Geology Conference Series. Geological Society of London, pp. 261–274.

Brekke, H., Sjulstad, H.I., Magnus, C., Williams, R.W., 2001. Sedimentary environments offshore Norway—an overview. Norwegian Petroleum Society Special Publications 10, 7–37.

Brenninkmeyer, B., 1982. Major beach features, in: Beaches and Coastal Geology. Springer US, New York, NY, pp. 528–532. https://doi.org/10.1007/0-387-30843-1_268

Brooks, H.L., Hodgson, D.M., Brunt, R.L., Peakall, J., Hofstra, M., Flint, S.S., 2018a. Deep-water channel-lobe transition zone dynamics: Processes and depositional architecture, an example from the Karoo Basin, South Africa. GSA Bulletin 130, 1723–1746.

Brooks, H.L., Hodgson, D.M., Brunt, R.L., Peakall, J., Poyatos-Moré, M., Flint, S.S., 2018b. Disconnected submarine lobes as a record of stepped slope evolution over multiple sea-level cycles. Geosphere 14, 1753–1779.

Burk, C.A., Drake, C.L., 2013. The geology of continental margins. Springer.

Calabrese, M., Pirera, F., Rossi, M., Scaglioni, P., Tosoratti, F., 2011. Integration Of Seismic Lithology Data In The Reservoir Model, in: SPE EUROPEC/EAGE Annual Conference and Exhibition. OnePetro.

Cariou, E., Hantzpergue, P., 1997. Biostratigraphie du Jurassique ouest-européen et méditerranéen. Bulletin des Centres de recherches exploration-production Elf-Aquitaine. Mémoire 17.

Catuneanu, O., 2019. Model-independent sequence stratigraphy. Earth-Science Reviews 188, 312–388.

Cecil, C.B., DiMichele, W.A., Fedorko, N., Skema, V., 2011. Autocyclic and allocyclic controls on the origin of the Dunkard Group, in: Geology of the Pennsylvanian-Permian in the Dunkard Basin. Guidebook for the 76th Annual Field Conference of Pennsylvania Geologists. Field Conference of Pennsylvania Geologists, Inc.

Chiarella, D., Capella, W., Longhitano, S.G., Muto, F., 2021. Fault-controlled base-of-scarp deposits. Basin Research 33, 1056–1075.

Chiarella, D., Longhitano, S.G., Mosdell, W., Telesca, D., 2020. Sedimentology and facies analysis of ancient sand ridges: Jurassic Rogn Formation, Trøndelag Platform, offshore Norway. Marine and Petroleum Geology 112.

Clift, P.D., Tada, R., Zheng, H., 2010. Monsoon evolution and tectonics-climate linkage in Asia: an introduction. Geological Society, London, Special Publications 342, 1–4.

Clifton, H., 2005. Coastal sedimentary facies, in: Schwartz, M.L. (Ed.), Encyclopedia of Coastal Science. Springer-Verlag, Dordrecht, The Netherlands, pp. 270–278.

Clifton, H.E., 2003. Coastal sedimentary facies. Encyclopedia of Sediments and Sedimentary rocks 149–157.

Colella, A., Prior, D., 2009. Coarse-grained deltas. John Wiley & Sons.

Copestake, P., Sims, A.P., Crittenden, S., Hamar, G.P., Ineson, J.R., Rose, P.T., Tringham, M.E., Evans, D., Graham, C., Armour, A., 2003. The Millennium Atlas: petroleum geology of the central and northern North Sea. Geological Society, London.

Corfield, S., Sharp, I., Häger, K.-O., Dreyer, T., Underhill, J., 2001. An integrated study of the Garn and Melke formations (Middle to Upper Jurassic) of the Smørbukk area, Halten Terrace, mid-Norway, in: Norwegian Petroleum Society Special Publications. Elsevier, pp. 199–210.

Costa, L.I., 2000. BP Amoco Norway, 6507/5-3, Norwegian Sea Well - Biostratigraphy of the Interval 1380m-2999mTD.

Cowie, P.A., Gupta, S., Dawers, N.H., 2000. Implications of fault array evolution for synrift depocentre development: insights from a numerical fault growth model. Basin Research 12, 241–261.

Crawford, F.D., Szelewski, C.E., Alvey, G.D., 1984. Geology and exploration in the Takutu graben of Guyana. Oil & gas journal 82, 122–129.

Cumberpatch, Z.A., Soutter, E.L., Kane, I.A., Casson, M., Vincent, S.J., 2021. Evolution of a mixed siliciclastic-carbonate deep-marine system on an unstable margin: The Cretaceous of the Eastern Greater Caucasus, Azerbaijan. Basin Research 33, 612–647.

Dalland, A., 1981. Mesozoic sedimentary succession at Andoy, northern Norway, and relation to structural development of the North Atlantic area.

Dalland, A., Worsley, D., Ofstad, K., 1988. A lithostratigraphic scheme for the mesozoic and cenozoic and succession offshore mid-and northern norway. Norwegian Petroleum Directorate (NPD) Bulletin 4.

Dam, G., Sønderholm, M., 2021. Tectonostratigraphic evolution, palaeogeography and main petroleum plays of the Nuussuaq Basin: An outcrop analogue for the Cretaceous–Palaeogene rift basins offshore West Greenland. Marine and Petroleum Geology 129, 105047.

Dashtgard, S.E., Vaucher, R., Yang, B., Dalrymple, R.W., 2021. Hutchison Medallist 1. Wave-Dominated to Tide-Dominated Coastal Systems: A Unifying Model for Tidal Shorefaces and Refinement of the Coastal-Environments Classification Scheme. Geoscience Canada: Journal of the Geological Association of Canada/Geoscience Canada: journal de l'Association Géologique du Canada 48, 5–22.

Dauteuil, O., Brun, J.-P., 1993. Oblique rifting in a slow-spreading ridge. Nature 361, 145–148.

de Beaumont, E., 1830. Mémoires pour servir à une description géologique de la France. F.-G. Levrault.

de Beaumont, E., 1827. Observations géologiques. Ann. Mines 2, 5–82.

de Raaf, J.F.M., Boersma, J.R., van Gelder, S.A., 1977. Wave-generated structures and sequences from a shallow marine succession, Lower Carboniferous, County Cork, Ireland. Sedimentology 24, 451–483.

Doré, A.G., 1992. Synoptic palaeogeography of the northeast Atlantic seaway: Late Permian to Cretaceous. Geological Society, London, Special Publications 62, 421–446.

Doré, A.G., Lundin, E.R., Birkeland, O., Eliassen, P.E., Jensen, L.N., 1997a. The NE Atlantic margin; implications of late Mesozoic and Cenozoic events for hydrocarbon prospectivity. Petroleum Geoscience 3, 117–131.

Doré, A.G., Lundin, E.R., Fichler, C., Olesen, O., 1997b. Patterns of basement structure and reactivation along the NE Atlantic margin. Journal of the Geological Society 154, 85–92.

Doré, A.G., Lundin, E.R., Jensen, L.N., Birkeland, Ø., Eliassen, P.E., Fichler, C., 1999. Principal tectonic events in the evolution of the northwest European Atlantic margin, in: Geological Society, London, Petroleum Geology Conference Series. Geological Society of London, pp. 41–61.

Dorsey, R.J., Umhoefer, P.J. and Falk, P.D. (1997) Earthquake clustering inferred from Pliocene Gilbert-type fan deltas in the Loreto basin, Baja California Sur, Mexico. Geology, 25, 679–682.

Duxbury, S., Harpur, W., 1993. A Biostratigraphic Analysis of Cretaceous Sections in Four Mid Norwegian Shelf and Barents Sea Wells.

Edison Norge AS (2021) Mid-Norway - A regional seismic interpretation project.

Ehrlich, R., Gabrielsen, R.H., 2004. The complexity of a ramp–flat–ramp fault and its effect on hanging-wall structuring: an example from the Njord oil field, offshore mid-Norway. Petroleum Geoscience 10, 305–317.

Eide, C.H., Schofield, N., Jerram, D.A., Howell, J.A., 2017. Basin-scale architecture of deeply emplaced sill complexes: Jameson Land, East Greenland. Journal of the Geological Society 174, 23–40.

Elliott, G., Jackson, C.A.-L., Gawthorpe, R.L., Wilson, P., Sharp, I.R., Michelsen, L., 2020. Tectono-stratigraphic development of a salt-influenced rift margin; Halten Terrace, offshore Mid-Norway.

Elliott, G.M., Jackson, C.A.L., Gawthorpe, R.L., Wilson, P., Sharp, I.R., Michelsen, L., 2015. Late syn-rift evolution of the Vingleia Fault Complex, Halten Terrace, offshore Mid-Norway; a test of rift basin tectono-stratigraphic models. Basin Research 29, 465–487.

Elliott, G.M., Wilson, P., Jackson, C.A., Gawthorpe, R.L., Michelsen, L., Sharp, I.R., 2012. The linkage between fault throw and footwall scarp erosion patterns: an example from the Bremstein Fault Complex, offshore Mid-Norway. Basin Research 24, 180–197.

Embry, A.F. (1993) Transgressive–regressive (T–R) sequence analysis of the Jurassic succession of the Sverdrup Basin, Canadian Arctic Archipelago. Canadian Journal of Earth Sciences, 30, 301–320.

Embry, A.F. (1995) Sequence boundaries and sequence hierarchies: problems and proposals. In: Norwegian Petroleum Society Special Publications, Elsevier, 5, 1–11.

Engkilde, M., Surlyk, F., 2003. Shallow marine syn-rift sedimentation: Middle Jurassic Pelion Formation, Jameson Land, East Greenland. Geological Survey of Denmark and Greenland (GEUS) Bulletin 1, 813–863.

Evoy, R.W., Moslow, T.F., 1995. Lithofacies associations and depositional environments in the Middle Triassic Doig Formation, Buick Creek Field, northeastern British Columbia. Bulletin of Canadian Petroleum Geology 43, 461–475.

Exxon World Mapping Project, 1985. Tectonic Map of the World. Exxon Production Research Company, Houston, USA.

Færseth, R.B., Lien, T., 2002. Cretaceous evolution in the Norwegian Sea—a period characterized by tectonic quiescence. Marine and Petroleum Geology 19, 1005–1027.

Faleide, J.I., Bjørlykke, K., Gabrielsen, R.H., 2015. Geology of the Norwegian continental shelf, in: Petroleum Geoscience. Springer, pp. 603–637.

Faleide, J.I., Bjørlykke, K., Gabrielsen, R.H., 2010. Geology of the Norwegian continental shelf, in: Petroleum Geoscience. Springer, pp. 467–499.

Faleide, J.I., Tsikalas, F., Breivik, A.J., Mjelde, R., Ritzmann, O., Engen, O., Wilson, J., Eldholm, O., 2008. Structure and evolution of the continental margin off Norway and the Barents Sea. Episodes 31, 82–91.

Falk, P.D., Dorsey, R.J., 1998. Rapid development of gravelly high-density turbidity currents in marine Gilbert-type fan deltas, Loreto Basin, Baja California Sur, Mexico. Sedimentology 45, 331–349.

Ferguson, R.A., Kane, I.A., Eggenhuisen, J.T., Pohl, F., Tilston, M., Spychala, Y.T., Brunt, R.L., 2020. Entangled external and internal controls on submarine fan evolution: an experimental perspective. The Depositional Record 6, 605–624.

Fisher, R. V, 1983. Flow transformations in sediment gravity flows. Geology 11, 273–274.

Fisher, R. V, 1971. Features of coarse-grained, high-concentration fluids and their deposits. Journal of Sedimentary Research 41.

Fitzgerald, D.M., Baldwin, C.T., Ibrahim, N.A., Humphries, S.M., 1992. Sedimentologic and morphologic evolution of a beach-ridge barrier along an indented coast: Buzzards Bay, Massachusetts. Quaternary coasts of the United States 65–75.

Fjellanger, E., Surlyk, F., Wamsteeker, L.C., Midtun, T., 2005. Upper Cretaceous basin-floor fans in the Vøring Basin, Mid Norway shelf, in: Norwegian Petroleum Society Special Publications. Elsevier, pp. 135–164.

Folkestad, A., Odinsen, T., Fossen, H., Pearce, M.A., 2014. Tectonic influence on the Jurassic sedimentary architecture in the northern North Sea with focus on the Brent Group. Int. Assoc. Sedimentol. Spec. Publ 46, 389–416.

Fonnesu, M., Felletti, F., 2019. Facies and architecture of a sand-rich turbidite system in an evolving collisional-trench basin: a case history from the Upper Cretaceous-Palaeocene Gottero system (NW Apennines).

Fonnesu, M., Felletti, F., Haughton, P.D.W., Patacci, M., McCaffrey, W.D., 2018. Hybrid event bed character and distribution linked to turbidite system sub-environments: The North Apennine Gottero Sandstone (north-west Italy). Sedimentology 65, 151–190.

Fonnesu, M., Haughton, P., Felletti, F., McCaffrey, W., 2015. Short length-scale variability of hybrid event beds and its applied significance. Marine and Petroleum Geology 67, 583–603.

Fossen, H., Khani, H.F., Faleide, J.I., Ksienzyk, A.K., Dunlap, W.J., 2017. Post-Caledonian extension in the West Norway–northern North Sea region: the role of structural inheritance. Geological Society, London, Special Publications 439, 465–486.

Franke, D., 2013. Rifting, lithosphere breakup and volcanism: Comparison of magma-poor and volcanic rifted margins. Marine and Petroleum geology 43, 63–87.

Fraser, S.I., Robinson, A.M., Johnson, H.D., Underhill, J.R., Kadolsky, D.G.A., Connell, R., Johannessen, P., Ravnås, R., 2002. Upper Jurassic, in: The Millennium Atlas: Petroleum Geology of the Central and Northern North Sea. Geological Society, London. pp. 157–189.

Freer, G., Hurst, A., Middleton, P., 1996. Upper Jurassic sandstone reservoir quality and distribution on the Fladen Ground Spur. Geological Society, London, Special Publications 114, 235–249.

Fugelli, E.M.G., Olsen, T.R., 2007. Delineating confined slope turbidite systems offshore mid-Norway: The Cretaceous deep-marine Lysing Formation. AAPG bulletin 91, 1577–1601.

Gabrielsen, R.H., Faerseth, R.B., Jensen, L.N., 1990. Structural elements of the Norwegian continental shelf. Pt. 1. The Barents Sea region. Norwegian Petroleum Directorate.

Gaina, C., Gernigon, L., Ball, P., 2009. Palaeocene–Recent plate boundaries in the NE Atlantic and the formation of the Jan Mayen microcontinent. Journal of the Geological Society 166, 601–616.

Gallagher, E., Wadman, H., McNinch, J., Reniers, A., Koktas, M., 2016. A conceptual model for spatial grain size variability on the surface of and within beaches. Journal of Marine Science and Engineering 4, 38.

Gawthorpe, R.L., Colella, A., Prior, D.B., 1990. Tectonic controls on coarse-grained delta depositional systems in rift basins, in: Coarse-Grained Deltas. Blackwell Oxford, International, pp. 113–127.

Geostrat, 1999. Statoil Wells 6507/3-3A - Biostratigraphy of the interval 3,080m - 4,520m and 6507/3-3B - Biostratigraphy of the interval 3,980m - 4,275m.

Gernigon, L., Franke, D., Geoffroy, L., Schiffer, C., Foulger, G.R., Stoker, M., 2020. Crustal fragmentation, magmatism, and the diachronous opening of the Norwegian-Greenland Sea. Earth-Science Reviews 206, 102839.

Gilbert, G.K., 1885. The topographic features of lake shores. US Government Printing Office.

Gobo, K., Ghinassi, M., Nemec, W., 2015. Gilbert-type deltas recording short-term base-level changes: Delta-brink morphodynamics and related foreset facies. Sedimentology 62, 1923–1949.

Gobo, K., Ghinassi, M., Nemec, W., 2014. Reciprocal changes in foreset to bottomset facies in a Gilbert-type delta: response to short-term changes in base level. Journal of Sedimentary Research 84, 1079–1095.

Gradstein, F.M., Kaminski, M.A., Agterberg, F.P., 1999. Biostratigraphy and paleoceanography of the Cretaceous seaway between Norway and Greenland. Earth-Science Reviews 46, 27–98.

Gradstein, F.M., Waters, C.N., 2016. Stratigraphic guide to the Cromer Knoll, Shetland and Chalk Groups, North Sea and Norwegian Sea. Newsletters on Stratigraphy 71.

Gregory, J.W., 1896. The great rift valley. Routledge.

Gupta, S., Underhill, J.R., Sharp, I.R., Gawthorpe, R.L., 1999. Role of fault interactions in controlling synrift sediment dispersal patterns: Miocene, Abu Alaqa Group, Suez Rift, Sinai, Egypt. Basin Research 11, 167.

Guy, M., 1992. Facies analysis of the Kopervik sand interval, Kilda Field, Block 16/26, UK North Sea. Geological Society, London, Special Publications 67, 187–220.

Hamilton, P., Gaillot, G., Strom, K., Fedele, J., Hoyal, D., 2017. Linking hydraulic properties in supercritical submarine distributary channels to depositional-lobe geometry. Journal of Sedimentary Research 87, 935–950.

Hamilton, P.B., Strom, K.B., Hoyal, D.C.J.D., 2015. Hydraulic and sediment transport properties of autogenic avulsion cycles on submarine fans with supercritical distributaries. Journal of Geophysical Research: Earth Surface 120, 1369–1389.

Hampton, M.A., 1975. Competence of fine-grained debris flows. Journal of Sedimentary Research 45, 834–844.

Hampton, M.A., 1972. The role of subaqueous debris flow in generating turbidity currents. Journal of Sedimentary Research 42, 775–793.

Hansen, L.A.S., Hodgson, D.M., Pontén, A., Bell, D., Flint, S., 2019. Quantification of basin-floor fan pinchouts: examples from the Karoo Basin, South Africa. Frontiers in Earth Science 7, 12.

Hansen, L.A.S., Hodgson, D.M., Pontén, A., Thrana, C., Obradors Latre, A., 2021. Mixed axial and transverse deep-water systems: The Cretaceous post-rift Lysing Formation, offshore Norway. Basin Research.

Haq, B.U., 2017. Jurassic sea-level variations: a reappraisal. GSA Today 28, 4–10.

Haq, B.U., 2014. Cretaceous eustasy revisited. Global and Planetary change 113, 44–58.

Hardenbol, J.A.N., Thierry, J., Farley, M.B., Jacquin, T., De Graciansky, P.-C., Vail, P.R., 1998. Mesozoic and Cenozoic sequence chronostratigraphic framework of European basins.

Hastings, D.S., 1987. Sand-prone facies in the Cretaceous of Mid-Norway, in: Conference on Petroleum Geology of North West Europe. 3. pp. 1065–1078.

Haughton, P., Davis, C., McCaffrey, W., Barker, S., 2009. Hybrid sediment gravity flow deposits–classification, origin and significance. Marine and Petroleum Geology 26, 1900–1918.

Haughton, P.D.W., Barker, S.P., McCaffrey, W.D., 2003. 'Linked'debrites in sand-rich turbidite systems–origin and significance. Sedimentology 50, 459–482.

Hayes, M.O., Michel, J., Betenbaugh, D. V, 2010. The intermittently exposed, coarse-grained gravel beaches of Prince William Sound, Alaska: comparison with open-ocean gravel beaches. Journal of Coastal Research 26, 4–30.

Heine, C., Zoethout, J., Müller, R.D., 2013. Kinematics of the South Atlantic rift. Solid Earth 4, 215–253.

Hensen, C., Duarte, J.C., Vannucchi, P., Mazzini, A., Lever, M.A., Terrinha, P., Géli, L., Henry, P., Villinger, H., Morgan, J., 2019. Marine transform faults and fracture zones: a joint perspective integrating seismicity, fluid flow and life. Frontiers in Earth Science 7, 39.

Henstra, G.A., Gawthorpe, R.L., Helland-Hansen, W., Ravnås, R., Rotevatn, A., 2016a. Depositional systems in multiphase rifts: seismic case study from the Lofoten margin, Norway. Basin Research 29, 447–469.

Henstra, G.A., Grundvåg, S.-A., Johannessen, E.P., Kristensen, T.B., Midtkandal, I., Nystuen, J.P., Rotevatn, A., Surlyk, F., Sæther, T., Windelstad, J., 2016b. Depositional processes and stratigraphic architecture within a coarse-grained rift-margin turbidite system: The Wollaston Forland Group, east Greenland. Marine and Petroleum Geology 76, 187–209.

Higgs, K.E., Munday, S., Forbes, A., Crouch, E.M., Sagar, M.W., 2020. A geochemical and biostratigraphic approach to investigating regional changes in sandstone composition through time; an example from Paleocene–Eocene strata, Taranaki Basin, New Zealand. Geological Magazine 157, 1473–1498.

Hodgson, D.M., 2009. Distribution and origin of hybrid beds in sand-rich submarine fans of the Tanqua depocentre, Karoo Basin, South Africa. Marine and Petroleum Geology 26, 1940–1956.

Ichaso, A.A., Dalrymple, R.W., 2014. Eustatic, tectonic and climatic controls on an early syn-rift mixed-energy delta, Tilje Formation (Early Jurassic, Smørbukk field, offshore mid-Norway). From Depositional Systems to Sedimentary Successions on the Norwegian Continental Margin. International Association of Sedimentologists, Special Publication 46, 339–388.

Ichron Limited, 2015a. A Biostratigraphic Evaluation of Well 6406/12-3A (Bue), Norwegian Sea prepared for VNG Norge. Internal report (unpublished).

Ichron Limited, 2015b. A summary of wellsite biostratigraphy, Well 6406/12-4S, Boomerang Appraisal, Haltenbanken, NOCS prepared for VNG Norge. Internal report (unpublished).

Ichron Limited, 2014a. A Biostratigraphic Evaluation of Well 6406/12-3B (Pil), Norwegian Sea prepared for VNG Norge. Internal report (unpublished).

Ichron Limited, 2014b. A Biostratigraphic Evaluation of Well 6406/12-3S (Pil), Norwegian Sea prepared for VNG Norge. Internal report (unpublished).

Jaeger, H.M., Nagel, S.R., Behringer, R.P., 1996. The physics of granular materials. Physics today 49, 32–39.

Jobe, Z.R., Lowe, D.R., Morris, W.R., 2012. Climbing-ripple successions in turbidite systems: depositional environments, sedimentation rates and accumulation times. Sedimentology 59, 867–898.

Johannessen, P.N., Dybkjaer, K., Rasmussen, E.S., 1996. Sequence stratigraphy of Upper Jurassic reservoir sandstones in the northern part of the Danish Central Trough, North Sea. Marine and Petroleum Geology 13, 755–770.

Jones, D.J.R., McCarthy, D.J., Dodd, T.J.H., 2019. Tectonostratigraphy and the petroleum systems in the Northern sector of the North Falkland Basin, South Atlantic. Marine and Petroleum Geology 103, 150–162.

Jones, G.E.D., Welbon, A.I.F., Mohammadlou, H., Sakharov, A., Ford, J., Needham, T., Ottesen, C., 2020. Complex stratigraphic fill of a small, confined syn-rift basins: an Upper Jurassic example from offshore Mid-Norway. Geological Society, London, Special Publications 495.

Jongepier, K., Rui, J.C., Grue, K., 1996. Triassic to Early Cretaceous stratigraphic and structural development of the northeastern Møre Basin margin, off Mid-Norway. Norsk Geologisk Tidsskrift 76, 199.

Jopling, A. V, Walker, R.G., 1968. Morphology and origin of ripple-drift cross-lamination, with examples from the Pleistocene of Massachusetts. Journal of Sedimentary Research 38, 971–984.

Kalifi, A., Sorrel, P., Leloup, P., Spina, V., Huet, B., Galy, A., Rubino, J., Pittet, B., 2020. Changes in hydrodynamic process dominance (wave, tide or river) in foreland sequences: The subalpine Miocene Molasse revisited (France). Sedimentology 67, 2455–2501.

Kane, I.A., Pontén, A.S.M., 2012. Submarine transitional flow deposits in the Pal Schematic geological cartoons eogene Gulf of Mexico. Geology 40, 1119–1122.

Kane, I.A., Pontén, A.S.M., Vangdal, B., Eggenhuisen, J.T., Hodgson, D.M., Spychala, Y.T., 2017. The stratigraphic record and processes of turbidity current transformation across deep-marine lobes. Sedimentology 64, 1236–1273.

Karlsen, D.A., Skeie, J.E., Backer-Owe, K., Bjørlykke, K., Olstad, R., Berge, K., Cecchi, M., Vik, E., Schaefer, R.G., 2004. Petroleum migration, faults and overpressure. Part II. Case history:

the Haltenbanken Petroleum Province, offshore Norway. Geological Society, London, Special Publications 237, 305–372.

Keep, M., McClay, K.R., 1997. Analogue modelling of multiphase rift systems. Tectonophysics 273, 239–270.

Kelly, S., Gregory, F., Braham, W., Strogen, D., Whitham, A., 2015. Towards an integrated Jurassic biostratigraphy for eastern Greenland. Volumina Jurassica 13, 43–64.

Kingston, D.R., Dishroon, C.P., Williams, P.A., 1983. Global basin classification system. AAPG bulletin 67, 2175–2193.

Knaust, D., 2009. Characterisation of a Campanian deep-sea fan system in the Norwegian Sea by means of ichnofabrics. Marine and Petroleum Geology 26, 1199–1211.

Koch, J.O., Heum, O.R., 1995. Exploration trends of the Halten Terrace. Norwegian Petroleum Society Special Publications 4, 235–251. https://doi.org/10.1016/S0928-8937(06)80044-5

Koch, J.-O., Heum, O.R., 1995. Exploration trends of the Halten Terrace, in: Norwegian Petroleum Society Special Publications. Elsevier, pp. 235–251.

Kuenen, P.H., 1966. Matrix of turbidites: experimental approach. Sedimentology 7, 267–297.

Kyrkjebø, R., Gabrielsen, R.H., Faleide, J.I., 2004. Unconformities related to the Jurassic–Cretaceous synrift–post-rift transition of the northern North Sea. Journal of the Geological Society 161, 1–17.

Larsen, M., Surlyk, F., 2003. Shelf-edge delta and slope deposition in the upper Callovian–middle Oxfordian Olympen Formation, east Greenland. Geological Survey of Denmark and Greenland (GEUS) Bulletin 1, 931–948.

le Roy, P., Piqué, A., 2001. Triassic–Liassic Western Moroccan synrift basins in relation to the Central Atlantic opening. Marine Geology 172, 359–381.

Lien, T., 2005. From rifting to drifting: effects on the development of deep-water hydrocarbon reservoirs in a passive margin setting, Norwegian Sea. Norwegian Journal of Geology/Norsk Geologisk Forening 85.

Lien, T., Midtbø, R.E., Martinsen, O.J., 2006. Depositional facies and reservoir quality of deep-marine sandstones in the Norwegian Sea. Norwegian Journal of Geology/Norsk Geologisk Forening 86.

Lin, C., Zhang, Y., Li, S., Liu, J., Tong, Z., Ding, X., Li, X., 2002. Quantitative modelling of multiphase lithospheric stretching and deep thermal history of some Tertiary rift basins in eastern China. Acta Geologica Sinica-English Edition 76, 324–330.

Lister, G.S., Etheridge, M.A., Symonds, P.A., 1991. Detachment models for the formation of passive continental margins. Tectonics 10, 1038–1064.

Liu, X., Dong, B., Yin, Z., Smith, R., Guo, Q., 2019. Continental drift, plateau uplift, and the evolutions of monsoon and arid regions in Asia, Africa, and Australia during the Cenozoic. Science China Earth Sciences 62, 1053–1075.

Lohr, T., Underhill, J.R., 2015. Role of rift transection and punctuated subsidence in the development of the North Falkland Basin. Petroleum Geoscience 21, 85–110.

Lomas, S.A., Joseph, P., 2004. Confined turbidite systems. Geological Society, London, Special Publications 222, 1–7.

Longhitano, S.G., 2008. Sedimentary facies and sequence stratigraphy of coarse-grained Gilbert-type deltas within the Pliocene thrust-top Potenza Basin (Southern Apennines, Italy). Sedimentary Geology 210, 87–110.

Longhitano, S.G., Chiarella, D., Gugliotta, M., Ventra, D., 2021. Coarse-grained deltas approaching shallow-water canyon heads: A case study from the Lower Pleistocene Messina Strait, Southern Italy. Sedimentology.

Longhitano, S.G., Steel, R.J., 2016. Deflection of the progradational axis and asymmetry in tidal seaway and strait deltas: insights from two outcrop case studies. Geological Society, London, Special Publications 444, 141–172.

Loparev, A., Rouby, D., Chardon, D., Dall'Asta, M., Sapin, F., Bajolet, F., Ye, J., Paquet, F., 2021. Superimposed rifting at the junction of the Central and Equatorial Atlantic: Formation of the passive margin of the Guiana Shield. Tectonics e2020TC006159.

Lowe, D.R., 1982. Sediment gravity flows; II, Depositional models with special reference to the deposits of high-density turbidity currents. Journal of sedimentary research 52, 279–297.

Lowe, D.R., Guy, M., 2000. Slurry-flow deposits in the Britannia Formation (Lower Cretaceous), North Sea: a new perspective on the turbidity current and debris flow problem. Sedimentology 47, 31–70.

Lowe, D.R., Guy, M., Palfrey, A., 2003. Facies of slurry-flow deposits, Britannia Formation (Lower Cretaceous), North Sea: implications for flow evolution and deposit geometry. Sedimentology 50, 45–80.

Ludvigsen, R., Beard, G., 1997. West coast fossils: a guide to the ancient life of Vancouver Island. Harbour Publishing Company.

Lundin, E., Doré, A.G., 2002. Mid-Cenozoic post-breakup deformation in the 'passive'margins bordering the Norwegian–Greenland Sea. Marine and Petroleum Geology 19, 79–93.

Lundin, E.R., Doré, A.G., 1997. A tectonic model for the Norwegian passive margin with implications for the NE Atlantic: Early Cretaceous to break-up. Journal of the Geological Society 154, 545–550.

MacEachern, J.A., Bann, K.L., Hampson, G.J., Steel, R.J., Burgess, P.M., Dalrymple, R.W., 2008. The role of ichnology in refining shallow marine facies models. Recent advances in models of siliciclastic shallow-marine stratigraphy 90, 73–116.

Major, J.J., Iverson, R.M., 1999. Debris-flow deposition: Effects of pore-fluid pressure and friction concentrated at flow margins. Geological Society of America Bulletin 111, 1424–1434.

Mann, U., Zweigel, J., 2008. Modelling source-rock distribution and quality variations: the organic facies modelling approach. Analogue and Numerical Modelling of Sedimentary Systems: From Understanding to Prediction 239–274.

Marsh, N., Imber, J., Holdsworth, R.E., Brockbank, P., Ringrose, P., 2010. The structural evolution of the Halten Terrace, offshore Mid-Norway: extensional fault growth and strain localisation in a multi-layer brittle–ductile system. Basin Research 22, 195–214.

Martinius, A.W., 2017. Multiscale Gilbert-type delta lobe architecture and heterogeneities: The case of the Roda Sandstone Member. AAPG Bulletin 101, 453–463.

Martinsen, O.J., Lien, T., Jackson, C., 2005. Cretaceous and Palaeogene turbidite systems in the North Sea and Norwegian Sea Basins: source, staging area and basin physiography controls on reservoir development, in: Geological Society, London, Petroleum Geology Conference Series. Geological Society of London, pp. 1147–1164.

Masiero, I., Burgess, P., Hollis, C., Manifold, L., Gawthorpe, R., Lecomte, I., Marshall, J., Rotevatn, A., 2021. Syn-rift carbonate platforms in space and time: testing and refining conceptual models using stratigraphic and seismic numerical forward modelling. Geological Society, London, Special Publications 509, 179–203.

Matthews, K.J., Müller, R.D., Wessel, P., Whittaker, J.M., 2011. The tectonic fabric of the ocean basins. Journal of Geophysical Research: Solid Earth 116.

McKenzie, D., 1978. Some remarks on the development of sedimentary basins. Earth and Planetary science letters 40, 25–32.

McLaughlin, P.P., 2005. Sequence stratigraphy.

Mercier de Lépinay, M., Loncke, L., Basile, C., Roest, W.R., Patriat, M., Maillard, A., de Clarens, P., 2016. Transform continental margins–Part 2: A worldwide review. Tectonophysics 693, 96–115.

Middleton, M.F., 1989. A model for the formation of intracratonic sag basins. Geophysical Journal International 99, 665–676.

Middleton, G. V, 1967. Experiments on density and turbidity currents: III. Deposition of sediment. Canadian Journal of Earth Sciences 4, 475–505.

Mikkelsen, P.L., Guderian, K., du Plessis, G., 2008. Improved reservoir management through integration of 4D-seismic interpretation, Draugen Field, Norway. SPE Reservoir Evaluation & Engineering 11, 9–17.

Mosar, J., Eide, E.A., Osmundsen, P.T., Sommaruga, A., Torsvik, T.H., 2002. Greenland–Norway separation: a geodynamic model for the North Atlantic, in: Norwegian Journal of Geology. p. 282.

Mouslopoulou, V., Begg, J., Fülling, A., Moraetis, D., Partsinevelos, P., Oncken, O., 2016. Distinct phases of eustatism and tectonics control the late Quaternary landscape evolution at the southern coastline of Crete. Earth Surf. Dyn. Discuss.

Mulder, T., Alexander, J., 2001. The physical character of subaqueous sedimentary density flows and their deposits. Sedimentology 48, 269–299.

Mulder, T., Etienne, S., 2010. Lobes in deep-sea turbidite systems: state of the art. Sedimentary Geology 3, 75–80.

Mulder, T., Hüneke, H., 2014. Turbidite, in: Harff, J., Meschede, M., Petersen, S., Thiede, J. (Eds.), Encyclopedia of Marine Geosciences. Springer Netherlands, Dordrecht, pp. 1–7.

Müller, R.D., Sdrolias, M., Gaina, C., Roest, W.R., 2008. Age, spreading rates, and spreading asymmetry of the world's ocean crust. Geochemistry, Geophysics, Geosystems 9.

Mutti, E., 1985. Turbidite systems and their relations to depositional sequences, in: Provenance of Arenites. Springer, pp. 65–93.

Mutti, E., Tinterri, R., Benevelli, G., di Biase, D., Cavanna, G., 2003. Deltaic, mixed and turbidite sedimentation of ancient foreland basins. Marine and Petroleum Geology 20, 733–755.

Naliboff, J.B., Buiter, S.J.H., Péron-Pinvidic, G., Osmundsen, P.T., Tetreault, J., 2017. Complex fault interaction controls continental rifting. Nature communications 8, 1–9.

Nemec, W., 1990a. Aspects of Sediment Movement on Steep Delta Slopes. Coarse-Grained Deltas 29–73.

Nemec, W., 1990b. Deltas—remarks on terminology and classification, in: Coarse-Grained Deltas. International Association of Sedimentologists Special Publication 10, pp. 3–12.

Nirrengarten, M., Manatschal, G., Tugend, J., Kusznir, N., Sauter, D., 2017. Kinematic evolution of the southern North Atlantic: Implications for the formation of hyperextended rift systems. Tectonics 37, 89–118.

NORLEX, 2021. Lyr Formation [WWW Document]. URL https://nhm2.uio.no/norges/litho/lyr.php

Normark, W.R., 1970. Growth patterns of deep-sea fans. AAPG bulletin 54, 2170–2195.

Norsk Hydro AS, 1992. Final Well Report Well: 6507/2-2.

NPD, 2021. Norwegian Petroleum Directorate - NPD Factpages [WWW Document]. URL https://factpages.npd.no/

Nyberg, B., Howell, J.A., 2016. Global distribution of modern shallow marine shorelines. Implications for exploration and reservoir analogue studies. Marine and Petroleum Geology 71, 83–104.

Ogg, G.M., 2012. Standard Lithostratigraphy of Offshore Norway - Norlex Project.

Ogg, J.G., Ogg, G.M., Gradstein, F.M., 2016. A concise geologic time scale: 2016. Elsevier.

Olsen, K.H., 1995. Continental rifts: evolution, structure, tectonics. Elsevier.

Olsen, T.M., 2019. Provenance on the Lysing-Lange megasequences on the Dønna Terrace: focus on stratigraphic variability and lateral sandbody connectivity.

Ormøy, J., Rossi, M., Pirera, F., Tosoratti, F., Berto, R., Scaglioni, P., Bersezio, R., Fellett, F., 2011. Integrated Characterization of Intra-Slope Reservoirs: Transferring Facies and Log Imaging Data to Seismic Inversion Constrained by Outcrop Analogues (Marulk Field, Offshore Norway), in: AAPG.

Osmundsen, P.T., Ebbing, J., 2008. Styles of extension offshore mid-Norway and implications for mechanisms of crustal thinning at passive margins. Tectonics 27.

Osmundsen, P.T., Sommaruga, A., Skilbrei, J.R., Olesen, O., 2002. Deep structure of the Mid Norway rifted margin. Norwegian Journal of Geology/Norsk Geologisk Forening 82.

Otvos, E.G., 2000. Beach ridges—definitions and significance. Geomorphology 32, 83–108.

Oudmayer, B.C., de Jager, J., 1993. Fault reactivation and oblique-slip in the Southern North Sea, in: Geological Society, London, Petroleum Geology Conference Series. Geological Society of London, pp. 1281–1290.

Owen, G., 2003. Load structures: gravity-driven sediment mobilization in the shallow subsurface. Geological Society, London, Special Publications 216, 21–34.

Palcon, W.E.-W., 1985. Biostratigraphic reevaluation and regional correlation study of wells: 6406/3-1, 6407/1-3, 6407/2-1, 6507/11-1, 6507/11-2, 6507/7-1, 6609/7-1, 6609/10-1, 6610/7-1.

Partington, M.A., Copestake, P., Mitchener, B.C. and, Underhill, J.R., 1993. Biostratigraphic calibration of genetic stratigraphic sequences in the Jurassic–lowermost Cretaceous (Hettangian to Ryazanian) of the North Sea and adjacent areas, in: Geological Society, London, Petroleum Geology Conference Series. Geological Society of London, pp. 371–386.

Patruno, S., Helland-Hansen, W., 2018. Clinoforms and clinoform systems: Review and dynamic classification scheme for shorelines, subaqueous deltas, shelf edges and continental margins. Earth-Science Reviews 185, 202–233.

Pemberton, S.G., MacEachern, J.A., Dashtgard, S.E., Bann, K.L., Gingras, M.K., Zonneveld, J.-P., 2012. Shorefaces, in: Developments in Sedimentology. Elsevier, pp. 563–603.

Peron-Pinvidic, G., Gernigon, L., Gaina, C., Ball, P., 2012. Insights from the Jan Mayen system in the Norwegian–Greenland sea—I. Mapping of a microcontinent. Geophysical Journal International 191, 385–412.

Peron-Pinvidic, G., Manatschal, G., 2019. Rifted margins: state of the art and future challenges. Frontiers in Earth Science 7, 218.

Péron-Pinvidic, G., Manatschal, G., 2009. The final rifting evolution at deep magma-poor passive margins from Iberia-Newfoundland: a new point of view. International Journal of Earth Sciences 98, 1581–1597.

Peron-Pinvidic, G., Manatschal, G., Osmundsen, P.T., 2013. Structural comparison of archetypal Atlantic rifted margins: A review of observations and concepts. Marine and Petroleum Geology 43, 21–47.

Peron-Pinvidic, G., Osmundsen, P.T., 2020. From orogeny to rifting: insights from the Norwegian 'reactivation phase.' Scientific Reports 10, 14860. https://doi.org/10.1038/s41598-020-71893-z

Peron-Pinvidic, G., Osmundsen, P.T., 2018. The Mid Norwegian-NE Greenland conjugate margins: Rifting evolution, margin segmentation, and breakup. Marine and Petroleum Geology 98, 162–184.

Peron-Pinvidic, G., Osmundsen, P.T., 2016. Architecture of the distal and outer domains of the Mid-Norwegian rifted margin: Insights from the Rån-Gjallar ridges system. Marine and Petroleum Geology 77, 280–299.

Peron-Pinvidic, G., Osmundsen, P.T., Bunkholt, H., 2020. The proximal domain of the Mid-Norwegian rifted margin: The Trøndelag Platform revisited. Tectonophysics 790, 1–15.

Phillips, T.B., Fazlikhani, H., Gawthorpe, R.L., Fossen, H., Jackson, C.A., Bell, R.E., Faleide, J.I., Rotevatn, A., 2019. The Influence of Structural Inheritance and Multiphase Extension on Rift Development, the Northern North Sea. Tectonics 38, 4099–4126.

Phillips, T.B., Jackson, C.A.-L., Bell, R.E., Duffy, O.B., Fossen, H., 2016. Reactivation of intrabasement structures during rifting : a case study from offshore southern Norway. Journal of Structural Geology 91, 54–73.

Piazza, A., Tinterri, R., 2020. Cyclic stacking pattern, architecture and facies of the turbidite lobes in the Macigno Sandstones Formation (Chattian-Aquitanian, northern Apennines, Italy). Marine and Petroleum Geology 122, 104704.

Picot, M., 2015. Cycles sédimentaires dans le système turbiditique du Congo: nature et origine.

Piqué, A., Laville, E., 1996. The central Atlantic rifting: Reactivation of Palaeozoic structures? Journal of Geodynamics 21, 235–255.

Planke, S., Eldholm, O., 1994. Seismic response and construction of seaward dipping wedges of flood basalts: Vøring volcanic margin. Journal of Geophysical Research: Solid Earth 99, 9263–9278.

Pohl, F., Eggenhuisen, J.T., Cartigny, M.J.B., Tilston, M.C., de Leeuw, J., Hermidas, N., 2020. The influence of a slope break on turbidite deposits: an experimental investigation. Marine Geology 424, 106160.

Pollitz, F.F., 1999. From rifting to drifting. Nature 398, 21–22.

Poprawski, Y., Jacquin, T., Basile, C., Rossi, M., Gaudin, M., 2010. Albian depositional systems along the faulted Basque-Cantabrian northern margin as an analogue to slope-apron fan systems occurring on the western side of the Klakk Fault complex, in: From Depositional Systems to Sedimentary Successions on the Norwegian Continental Shelf. Stavanger, Norway.

Posamentier, H.W., Allen, G.P., James, D.P., Tesson, M., 1992. Forced regressions in a sequence stratigraphic framework: concepts, examples, and exploration significance. AAPG bulletin 76, 1687–1709.

Posamentier, H.W., Jervey, M.T., Vail, P.R., 1988. Eustatic controls on clastic deposition I—conceptual framework.

Postma, G., 1995. Sea-level-related architectural trends in coarse-grained delta complexes. Sedimentary Geology 98, 3–12.

Postma, G., Cartigny, M.J.B., 2014. Supercritical and subcritical turbidity currents and their deposits - A synthesis. Geology 42, 987–990. https://doi.org/10.1130/G35957.1

Postma, G., Kleverlaan, K., 2018. Supercritical flows and their control on the architecture and facies of small-radius sand-rich fan lobes. Sedimentary Geology 364, 53–70.

Poulsen, N.E., Riding, J.B., 2003. The Jurassic dinoflagellate cyst zonation of subboreal Northwest Europe. Geological Survey of Denmark and Greenland (GEUS) Bulletin 1, 115–144.

Prélat, A., Hodgson, D.M., Flint, S.S., 2009. Evolution, architecture and hierarchy of distributary deep-water deposits: a high-resolution outcrop investigation from the Permian Karoo Basin, South Africa. Sedimentology 56, 2132–2154.

Price, G.D., 1999. The evidence and implications of polar ice during the Mesozoic. Earth-Science Reviews 48, 183–210.

Privat, A.M., Hodgson, D.M., Jackson, C.A., Schwarz, E., Peakall, J., 2021. Evolution from syn-rift carbonates to early post-rift deep-marine intraslope lobes: The role of rift basin physiography on sedimentation patterns. Sedimentology.

Prosser, S., 1993. Rift-related linked depositional systems and their seismic expression. Geological Society, London, Special Publications 71, 35–66.

Provan, D.M.J., 1992. Draugen Oil Field, Haltenbanken Province, Offshore Norway: Chapter 23.

Rattey, R.P., Hayward, A.B., 1993. Sequence stratigraphy of a failed rift system: the Middle Jurassic to Early Cretaceous basin evolution of the Central and Northern North Sea, in: Geological Society, London, Petroleum Geology Conference Series. Geological Society of London, pp. 215–249.

Ravnås, R., Steel, R.J., 1998. Architecture of marine rift-basin successions. AAPG bulletin 82, 110–146.

Reading, H.G., 2009. Sedimentary environments: processes, facies and stratigraphy. John Wiley & Sons.

Rees, C., Palmer, J., Palmer, A., 2017. Gilbert-style Pleistocene fan delta reveals tectonic development of North Island axial ranges, New Zealand. New Zealand journal of geology and geophysics 61, 64–78.

Reineck, H.-E., Singh, I.B., 2012. Depositional sedimentary environments: with reference to terrigenous clastics. Springer Science & Business Media.

Riis, F., Fjeldskaar, W., 1992. On the magnitude of the Late Tertiary and Quaternary erosion and its significance for the uplift of Scandinavia and the Barents Sea, in: Structural and Tectonic Modelling and Its Application to Petroleum Geology. Elsevier, pp. 163–185.

Riley, L.A., Roberts, M.J., Connell, E.R., 1989. The application of palynology in the interpretation of Brae Formation stratigraphy and reservoir geology in the South Brae Field area, British North Sea, in: Correlation in Hydrocarbon Exploration. Springer, pp. 339–356.

Roberts, A.M., Yielding, G., 1991. Deformation around basin-margin faults in the North Sea/mid-Norway rift. Geological Society, London, Special Publications 56, 61–78.

Roberts, D.G., Thompson, M., Mitchener, B., Hossack, J., Carmichael, S., Bjørnseth, H.-M., 1999. Palaeozoic to Tertiary rift and basin dynamics: mid-Norway to the Bay of Biscay–a new context for hydrocarbon prospectivity in the deep water frontier, in: Geological Society, London, Petroleum Geology Conference Series. Geological Society of London, pp. 7–40.

Roberts, T.M., Wang, P., Puleo, J.A., 2013. Storm-driven cyclic beach morphodynamics of a mixed sand and gravel beach along the Mid-Atlantic Coast, USA. Marine Geology 346, 403–421.

Rousse, S., Duringer, P., Stapf, K.R.G., 2012. An exceptional rocky shore preserved during Oligocene (late Rupelian) transgression in the Upper Rhine Graben (Mainz Basin, Germany). Geol. J. 47, 388–408.

RPS Ichron, 2016. Biostratigraphic Evaluation of Well 6406/12-4A (Boomerang), NOCS prepared for VNG Norge. Internal report (unpublished).

Salomon, E., Rotevatn, A., Kristensen, T.B., Grundvåg, S.-A., Henstra, G.A., 2021. Microstructure and fluid flow in rift border fault-bounded basins–insights from the Dombjerg Fault, NE Greenland.

Schiffer, C., Doré, A.G., Foulger, G.R., Franke, D., Geoffroy, L., Gernigon, L., Holdsworth, B., Kusznir, N., Lundin, E., McCaffrey, K., 2020. Structural inheritance in the North Atlantic. Earth-Science Reviews 206, 102975.

Schiffer, C., Doré, A.G., Foulger, G.R., Franke, D., Geoffroy, L., Gernigon, L., Holdsworth, B., Kusznir, N., Lundin, E., McCaffrey, K., 2019. Structural inheritance in the North Atlantic. Earth-Science Reviews 102975.

Scholz, C.A., Rosendahl, B.R., Scott, D.L., 1990. Development of coarse-grained facies in lacustrine rift basins: Examples from East Africa. Geology 18, 140–144.

Seilacher, A., 1967. Bathymetry of trace fossils. Marine geology 5, 413–428.

Serra, O., Serra, L., 2004. Well Logging. Data Acquisitions and Applications.

Serra, O., Serra, L., 2001. Well logging. Acquisition and applications; Diagraphies. Acquisition et applications.

Shanmugam, G., Lehtonen, L.R., Straume, T., Syvertsen, S.E., Hodgkinson, R.J., Skibeli, M., 1994. Slump and debris-flow dominated upper slope facies in the Cretaceous of the Norwegian and Northern North Seas (61–67 N): implications for sand distribution. AAPG bulletin 78, 910–937.

Short, A.D., 1984. Beach and nearshore facies: southeast Australia. Marine Geology 60, 261–282.

Smith, R., 2004. Turbidite systems influenced by structurally induced topography in the multi-sourced Welsh Basin. Geological Society, London, Special Publications 222, 209–228.

Snedden, J.W., Liu, C., 2010. A compilation of Phanerozoic sea-level change, coastal onlaps and recommended sequence designations. Search and discovery article 40594.

Sømme, T.O., Jackson, C.A., 2013. Source-to-sink analysis of ancient sedimentary systems using a subsurface case study from the Møre-Trøndelag area of southern Norway: Part 2–sediment dispersal and forcing mechanisms. Basin Research 25, 512–531.

Soutter, E.L., Bell, D., Cumberpatch, Z.A., Ferguson, R.A., Spychala, Y.T., Kane, I.A., Eggenhuisen, J.T., 2021. The Influence of Confining Topography Orientation on Experimental Turbidity Currents and Geological Implications. Front. Earth Sci 8, 540633.

Spychala, Y.T., Hodgson, D.M., Lee, D.R., 2017a. Autogenic controls on hybrid bed distribution in submarine lobe complexes. Marine and Petroleum Geology 88, 1078–1093.

Spychala, Y.T., Hodgson, D.M., Prélat, A., Kane, I.A., Flint, S.S., Mountney, N.P., 2017b. Frontal and lateral submarine lobe fringes: comparing sedimentary facies, architecture and flow processes. Journal of Sedimentary Research 87, 75–96.

Spychala, Y.T., Ramaaker, T.A.B., Eggenhuisen, J.T., Grundvåg, S.-A., Pohl, F., Wroblewska, S., 2021. Proximal to distal grain-size distribution of basin-floor lobes: A study from the Battfjellet Formation, Central Tertiary Basin, Svalbard.

Stauble, A.J., Milius, G., 1968. Geology of Groningen gas field, Netherlands. AAPG Bulletin 52, 550.

Stoker, M.S., Stewart, M.A., Shannon, P.M., Bjerager, M., Nielsen, T., Blischke, A., Hjelstuen, B.O., Gaina, C., McDermott, K., Ólavsdóttir, J., 2016. An overview of the Upper Palaeozoic–Mesozoic stratigraphy of the NE Atlantic region. Geological Society, London, Special Publications 447, 11–68.

Storms, J.E.A., Dam, R.L. Van, Leclair, S.F., 1999. Preservation of cross-sets due to migration of current ripples over aggrading and non-aggrading beds: comparison of experimental data with theory. Sedimentology 46, 189–200.

Stratlab AS, 1994. Well 6507/2-3 - Biostratigraphy, Kerogen analysis.

Stratlab AS, 1991a. Well 6406/12-1S, Biostratigtaphy, Kerogen analysis prepared for Statoil AS. Internal report (unpublished).

Stratlab AS, 1991b. Well 6406/11-1S, Biostratigtaphy, Kerogen analysis prepared for Saga Petroleum AS. Internal report (unpublished).

Surlyk, F., 2003. The Jurassic of Denmark and Greenland: The Jurassic of East Greenland: a sedimentary record of thermal subsidence, onset and culmination of rifting. Geological Survey of Denmark and Greenland (GEUS) Bulletin 1, 657–722.

Surlyk, F., Bjerager, M., Piasecki, S., Stemmerik, L., 2017. Stratigraphy of the marine Lower Triassic succession at Kap Stosch, Hold with Hope, North-East Greenland. Bulletin of the Geological Society of Denmark 65, 87–123.

Surlyk, F., Bruhn, R., 2020. Flood-generated hyperpycnal delta front sands of the Brora Arenaceous Formation (upper Callovian–middle Oxfordian), of the Inner Moray Firth, Scotland, record the onset of rifting. Scottish Journal of Geology.

Surlyk, F., Ineson, J.R., 2003. The Jurassic of Denmark and Greenland: key elements in the reconstruction of the North Atlantic Jurassic rift system. Geological Survey of Denmark and Greenland (GEUS) Bulletin 1, 9–20.

Surlyk, F., Noe-Nygaard, N., 1992. Sand bank and dune facies architecture of a wide intracratonic seaway: late Jurassic-early Cretaceous Raukelv Formation, Jameson Land, east Greenland.

Surlyk, F., Noe-Nygaard, N., 2005. A forced regressive shelf-margin wedge formed by transition-slope progradation: lowermost Cretaceous Rauk Plateau Member, Jameson Land, East Greenland. Bulletin of the Geological Society of Denmark 52, 227–243.

Swiecicki, T., Gibbs, P.B., Farrow, G.E., Coward, M.P., 1998. A tectonostratigraphic framework for the Mid-Norway region. Marine and Petroleum Geology 15, 245–276.

Talling, P.J., Masson, D.G., Sumner, E.J., Malgesini, G., 2012. Subaqueous sediment density flows: Depositional processes and deposit types. Sedimentology 59, 1937–2003.

Talling, P.J., Wynn, R.B., Masson, D.G., Frenz, M., Cronin, B.T., Schiebel, R., Akhmetzhanov, A.M., Dallmeier-Tiessen, S., Benetti, S., Weaver, P.P.E., 2007. Onset of submarine debris flow deposition far from original giant landslide. Nature 450, 541–544.

Tegle, K.W., 2017. Provenance of the Upper Cretaceous Lange-Lysing deep-marine sandstone in the Norwegian Sea: with implication for reservoir quality.

Thiede, J., Dinkelman, M.G., 1977. Occurrence of Inoceramus remains in Late Mesozoic pelagic and hemipelagic sediments.

Tsikalas, F., Faleide, J.I., Eldholm, O., Blaich, O.A., 2012. The NE Atlantic conjugate margins. Regional geology and tectonics: Phanerozoic passive margins, cratonic basins and global tectonic maps 1, 140–201.

Turner, C.C., Cronin, B.T., 2018. Rift-related Coarse-grained Submarine Fan Reservoirs: The Brae Play, South Viking Graben, North Sea. American Association of Petroleum Geologists.

Turner, C.C., Cronin, B.T., Riley, L.A., Patruno, S., Reid, W.T.L.R., Hoth, S., Knaust, D., Allerton, S., Jones, M.A., Jackson, C.A.L., 2018. The South Viking Graben: Overview of Upper Jurassic rift geometry, biostratigraphy, and extent of Brae Play submarine fan systems. AAPG Memoir 115, 9–38.

Unternehr, P., Péron-Pinvidic, G., Manatschal, G., Sutra, E., 2010. Hyper-extended crust in the South Atlantic: in search of a model. Petroleum Geoscience 16, 207–215.

USGS, 2013. Worldwide map of the tectonic plates, earthquakes (between 1900 and 2013) and volcanoes [WWW Document]. URL https://www.usgs.gov/

van Bemmelen, R.W., 1961. The scientific character of geology. The Journal of Geology 69, 453–463.

Van der Zwan, C.J., 1990. Palynostratigraphy and palynofacies reconstruction of the Upper Jurassic to lowermost Cretaceous of the Draugen Field, offshore Mid Norway. Review of palaeobotany and palynology 62, 157–186.

Vergara, L., Wreglesworth, I., Trayfoot, M., Richardsen, G., 2001. The distribution of Cretaceous and Paleocene deep-water reservoirs in the Norwegian Sea basins. Petroleum Geoscience 7, 395–408.

Verreussel, R., Bouroullec, R., Munsterman, D.K., Dybkjær, K., Geel, C.R., Houben, A.J.P., Johannessen, P.N., Kerstholt-Boegehold, S.J., 2018. Stepwise basin evolution of the Middle Jurassic–Early Cretaceous rift phase in the Central Graben area of Denmark, Germany and The Netherlands. Geological Society, London, Special Publications 469, 305–340.

Vosgerau, H., Alsen, P., Carr, I.D., Therkelsen, J., Stemmerik, L., Surlyk, F., 2004. Jurassic syn-rift sedimentation on a seawards-tilted fault block, Traill Ø, North-East Greenland. Geological Survey of Denmark and Greenland (GEUS) Bulletin 5, 9–18.

Walker, R.G., 1992. Wave-and storm-dominated shallow marine systems., Facies Models - Response to sea level change. Geol Assoc Canada.

Wegener, A., 1920. Die entstehung der kontinente und ozeane. F. Vicweg & Sohn.

Weirich, F.H., 1988. Field evidence for hydraulic jumps in subaqueous sediment gravity flows. Nature 332, 626–629.

Whiting, L., Haughton, P. D. W., & Shannon, P. M., 2021. From rifting to hyperextension: Upper Jurassic–Lower Cretaceous tectono-stratigraphy of the Porcupine Basin, Irish Atlantic Margin. Basin Research 33(2), 1662–1696.

Wright, L.D., Chappell, J., Thom, B.G., Bradshaw, M.P., Cowell, P., 1979. Morphodynamics of reflective and dissipative beach and inshore systems: Southeastern Australia. Marine Geology 32, 105–140.

Wright, L.D., May, S.K., Short, A.D., Green, M.O., 1985. Beach and surf zone equilibria and response times, in: Coastal Engineering 1984. pp. 2150–2164.

Wright, L.D., Short, A.D., 1984. Morphodynamic variability of surf zones and beaches: a synthesis. Marine geology 56, 93–118.

Würtzen, C., Osmond, J.L., Faleide, J.I., Nystuen, J.P., Anell, I.M., Midtkandal, I., 2021. Syn-to post-rift alluvial basin fill: seismic stratigraphic analysis of Permian-Triassic deposition in the Horda Platform, Norway.

Ye, J., Chardon, D., Rouby, D., Guillocheau, F., Dall'asta, M., Ferry, J.-N., Broucke, O., 2017. Paleogeographic and structural evolution of northwestern Africa and its Atlantic margins since the early Mesozoic. Geosphere 13, 1254–1284.

Yu, X., Li, Shengli, Li, Shunli, 2018. Sandy Coast (Shore) and Neritic Depositional System, in: Clastic Hydrocarbon Reservoir Sedimentology. Springer, pp. 573–632.

Zastrozhnov, D., Gernigon, L., Gogin, I., Planke, S., Abdelmalak, M.M., Polteau, S., Faleide, J.I., Manton, B., Myklebust, R., 2020. Regional structure and polyphased Cretaceous-Paleocene rift and basin development of the mid-Norwegian volcanic passive margin. Marine and Petroleum Geology 115.

Ziegler, P.A., 1988. Evolution of the Arctic-North Atlantic and the Western Tethys: A visual presentation of a series of Paleogeographic-Paleotectonic maps. AAPG memoir 43, 164–196.

Supplementary data

1. Supplementary data 2.A: Stratigraphy of North East Greenland and the Mid-Norwegian conjugate margins

In the Greenland conjugate margin, onshore reservoir analogues of the Intra-Melke Formation sandstone and of the Rogn Formation have been observed at Jameson Land (Figs. 2.1A, 2.2). The lower Intra-Melke Formation (Sequence 1, Fig. 2.2) is time equivalent to the Parnas Member, which corresponds to the upper part of the Pelion Formation, and correspond to near-shore to shoreface environments (Engkilde and Surlyk, 2003; Surlyk, 2003; Vosgerau et al., 2004). This sandy member is covered by mudstones of the Fossilbjerget Formation (Fig. 2.2). The upper Intra-Melke Formation sandstone and the associated Melke Formation in the Norwegian Sea (Sequence 2 and 3, Fig. 2.2) are time equivalent to the Hades, Athene and Zeus Members of the Olympen Formation, described as subaqueous sedimentary density flow (SSDF) deposits occurring in basin floor, slope apron and delta top environments, respectively (Larsen and Surlyk, 2003; Surlyk, 2003).

The Rogn Formation in the Halten Terrace is time equivalent to the Raukelv Formation and the Sjaellandselv Member in Jameson Land (Fig. 2.2). The Raukelv Formation exhibits evidence of tidal activity (Surlyk and Noe-Nygaard, 1992; Surlyk, 2003). The Sjaellandselv Member, which belongs to the Hareelv Formation, contain SSDF that likely deposited between the upper slope and the basin floor. In the basin, the sandy Sjaellandselv Member is interbedded with the Katedralen Member, described as black mudstones, which is a part of the Hareelv Formation. The Spekk Formation and the Katedralen Member are time equivalent to the Kimmeridge Clay Formation in the North Sea (UK); they are regarded as prolific Upper Jurassic source rocks for hydrocarbons in the Norwegian-Greenland Seaway. They are enriched in total organic carbon (TOC) and were deposited under anoxic bottom-water conditions (Dalland et al., 1988; Karlsen et al., 2004; Mann and Zweigel, 2008; Alsen and Piasecki, 2018), during periods of climatic changes and sea-level variations (Armstrong et al., 2016; Atar et al., 2019).

During the Kimmeridgian, sea-level rise resulted in a regional backstepping of the shorelines (Freer et al., 1996; Johannessen et al., 1996; Andsbjerg et al., 2001). Causes for the sea-level rise are still debated, i.e., whether it was (i) initiated by regional thermal subsidence, (ii) purely eustatic in origin, (iii) resulted from the rifting or (iv) a combination of all three mechanisms (Rattey and Hayward, 1993). Indeed, the backstepping of the shorelines was diachronous and associated with sandy and silty coastal facies along the main rift axes, the configuration of which was predominantly controlled by palaeo-structural highs (Fraser et al., 2002). Both the conjugate margin in East Greenland and the mid-Norwegian continental shelf experienced the deposition of organic-rich mudstones and associated shallow-marine sandstones during the Upper Oxfordian / Lower Kimmeridgian to Upper Volgian / Lower Berriasian on both margins (Surlyk, 2003; Surlyk and Ineson, 2003; Kelly et al., 2015; Stoker et al., 2016).

2. Supplementary data 2.B: Additional information regarding material and methods

A routine method was developed to establish a robust sedimentological and stratigraphic model. It consists of a workflow that is composed of three main steps: sequence stratigraphy, chronostratigraphy, and finally, a sedimentological and stratigraphic evolution analysis. Seismic data coupled with sediment core analysis provided the three-dimensional geometry of the studied geological units. The vertical resolution is defined by well-log data and sedimentary core data when available (centimetres to tens of centimetre scale), whereas the lateral resolution relies on seismic data (metres to tens of metre scale). This method supports multi-disciplinary and multi-scale approaches helping to improve sedimentological and stratigraphic models through an iterative process between horizontal and vertical directions. The three main steps can be further subdivided into sub-steps that are based on the concepts of sequence stratigraphy as defined by Embry (1993, 1995):

- Sequence stratigraphic analysis:

This first step provides the identification of stratigraphic sequences from different databases. Sequence stratigraphy is performed, firstly on seismic data, secondly on core data and thirdly on well-log data. Well-log data associated with core data provide the possibility of defining well-log signatures. The fourth step is the validation step, which links all the interpretations from each dataset. This first analysis may be conducted as an iterative process, starting from major sequences to high-resolution sequence stratigraphy.

(i) Identification of sequences from seismic data:
- Seismic sequence surfaces can be identified looking at the relationships between seismic terminations. For instance, from land to basin, a sequence boundary (SB) *sensu* Embry (1993, 1995) is identifiable landwards by a subaerial unconformity exhibiting onlaps above an erosional truncation, whereas basinwards, the SB corresponds to a transgressive surface. Note that, the maximum flooding surface (MFS) is a conformable surface.
- Internal relationships between seismic reflectors (toplaps, onlaps, downlaps, offlaps) inside seismic T-R sequences *sensu* Embry (1993, 1995) supports the identification of parasequences;
- Faults are interpreted in parallel to seismic reflectors at different scales, starting with regional faults and progressively towards local faults. Fault orientations, and fault assemblages also need to be identified;
- To establish the links between T-R sequences and seismic sequences, it is mandatory to tie wells to seismic data.

(ii) Identification of sequences from core data:
- Core description allows us to observe conformable (normal bedding) and unconformable surfaces (reactivation and erosional surfaces). Moreover, core analysis establishes sedimentary facies and facies associations;
- Facies help to determine parasequences (thickness varying from few to tens of meters). The stacking pattern of parasequences is identified (progradational, aggradational, retrogradational or degradational),

highlighting the degree and direction of the progression of the shoreline (landwards or basinwards);
- Sedimentary facies are grouped into facies associations based on their vertical succession to establish depositional models (application of the Walther's law);
- In parallel, faults and fractures observed on cores can be characterised and correlated to the core location using seismic data. These structural observations help to determine the impact of syn-sedimentary faults on the associated deposits.

(iii) Identification of sequences from well-log data:
- Core description is mandatory to correlate well-log signatures with the associated sedimentary facies classification. Such correlation help to generate well-log cut-off, such as GR cut-off values that are fundamental for describing uncored intervals;
- Facies and facies associations observed from core data are used to establish the T-R sequences on well logs;
- In addition to core analyses, well log analyses enable the discrimination of stratigraphic sequences based on the stacking patterns of parasequences;
- Structural features identified on well logs help to outline recurrent sequences across faults that can be confirmed by core and seismic analyses.

(iv) Dataset consistency:
- Sequence boundaries (SBs) delimiting a T-R sequence must be precisely correlated across the entire database (seismic, core and well log data);
- In addition, the presence of faults close to (or even crossing) a well bore should be confirmed in the three datasets;
- Finally, seismic interpretation enable the identification of timelines (isochrones) that constrain temporally each T-R sequence, for the whole database. Isochrones allow the construction of well log correlation panels and the correlation of genetic units.

- Chronostratigraphy:

This second step aims at assigning a chronostratigraphic age to the identified stratigraphic sequences. Based on existing biostratigraphic reports (Stratlab AS, 1991a, 1991b; Biostrat, 1995; Ichron Limited, 2014a, 2014b, 2015a, 2015b; RPS Ichron, 2016), the observed dinoflagellate cysts identified in the stratigraphic interval of interest have been compiled. Dinoflagellate cyst compilation was reported in a biostratigraphic scheme combining several dinoflagellate cyst zonations. From this scheme, the observed dinoflagellate cyst species have been synthetised and grouped into zones to obtain the proposed (reconstructed) dinoflagellate cyst zonation. The proposed scheme, for the study area, provides a chronostratigraphic age (stage and sub-stage) to the observed stratigraphic sequences. The sequences are then compared to existing sequences in the North Sea, i.e., the J sequences (Partington et al., 1993). The discrimination of reworked fossils was a challenging task but necessary to avoid misdating the observed sequences. The syn-rift period, and more precisely the rift-climax stage, was a period during which sediments originated from the erosion of local highs (in our case the Frøya High). The utilisation of a biostratigraphic scheme that combined

several dinoflagellate cyst zonation schemes facilitated the identification of older reworked fossil assemblages. Time range uncertainty at the boundary between two dinoflagellate cyst zones has been addressed based on the time span of common assemblages occurring along the two juxtaposed biozones.

(i) Biostratigraphic compilation work:
- This 1st step aims to identify in the literature if biostratigraphic charts have already been established for the study area. If there is no existing chart for the area of interest, regional or adjacent charts are sought and compiled as to establish the biostratigraphic framework. In this study, the chronological framework is based on the compilation of existing biostratigraphic schemes mainly relying on ammonite zonation (Riley et al., 1989; Van der Zwan, 1990; Partington et al., 1993; Hardenbol et al., 1998; Poulsen and Riding, 2003; Kelly et al., 2015; Turner et al., 2018; Verreussel et al., 2018) and calibrated on sub-boreal ammonite zones (Cariou and Hantzpergue, 1997; Hardenbol et al., 1998; Ogg et al., 2016).

(ii) Attribution of a chronostratigraphic age to the biostratigraphic compilation:
- Once the biostratigraphic compilation is established and calibrated to ammonite zonation (for instance), the next step is to attribute a chronostratigraphic age to the biostratigraphic compilation using the most recent Geologic Time Scale (GTS). The international chronostratigraphic chart is basically calibrated on ammonite zones, helping us to easily calibrate the previously established biostratigraphic compilation.

(iii) Reporting biostratigraphy data on a well correlation panel for the studied wells:
- Biostratigraphic data for the study area can be derived from the present case study, or other studies. If obtained from other studies, a quick validation step should be performed;
- On the previously established well log correlation panels, all the observed fossils (from macro- to nannofossils) must be reported. Once all the recognized fossils have been reported at the appropriate well depth, the establishment of fossil zonations (next sub-step) can be undertaken in order to constrain chronostratigraphically the observed stratigraphic sequences.

(iv) Establishment of the zonation based on the observed fossil assemblages within the study area:
- Based on the compilated chart (sub-steps (i) and (ii)) and biostratigraphic data for each well location (sub-step (iii)), the fossil zonation can be established. Endemic species for the study area can be added to the compilation chart. In this study, the specimens with long time ranges as well as reworked micro-fossils are discarded. This zonation is based on “acme”, “top occurrence” and “base occurrence” of marker species (i.e., species having a short time-life range). Boundaries between dinoflagellate cyst zones were addressed based on common assemblages, thus providing time uncertainty range (Fig. 2.5). Marker species, along with the most observed species within a given interval, are used to name the zone. The obtained zones are then compared to existing sequences in the North Sea, i.e., the J sequences (Partington et al., 1993).

- Sedimentological and stratigraphic evolution analysis:

The final step consisted of combining chronostratigraphic data with the sequence stratigraphic interpretations in order to describe the 4-dimensional sedimentological and stratigraphic evolution of the study area. The first step was the construction of 2D palaeo-environmental maps. The last step aims to create 3D sedimentological and stratigraphic block-diagrams based on the previously constructed 2D palaeo-environmental maps.

(i) 2D evolutive palaeo-environmental maps:
The depositional environments observed for each well location on well-log and core data allow the creation of palaeo-environmental maps for each stratigraphic sequence. The establishment of these maps outlines the evolution of depositional environments through time;

(ii) 3D sedimentological and stratigraphic block-diagram:
The 3D block diagrams emphasise the 2D maps obtained previously (sub-step (i)). Block diagrams can be highly detailed, and can document the evolution of two different depositional environment at different locations.

3. Supplementary data 2.C: Core description

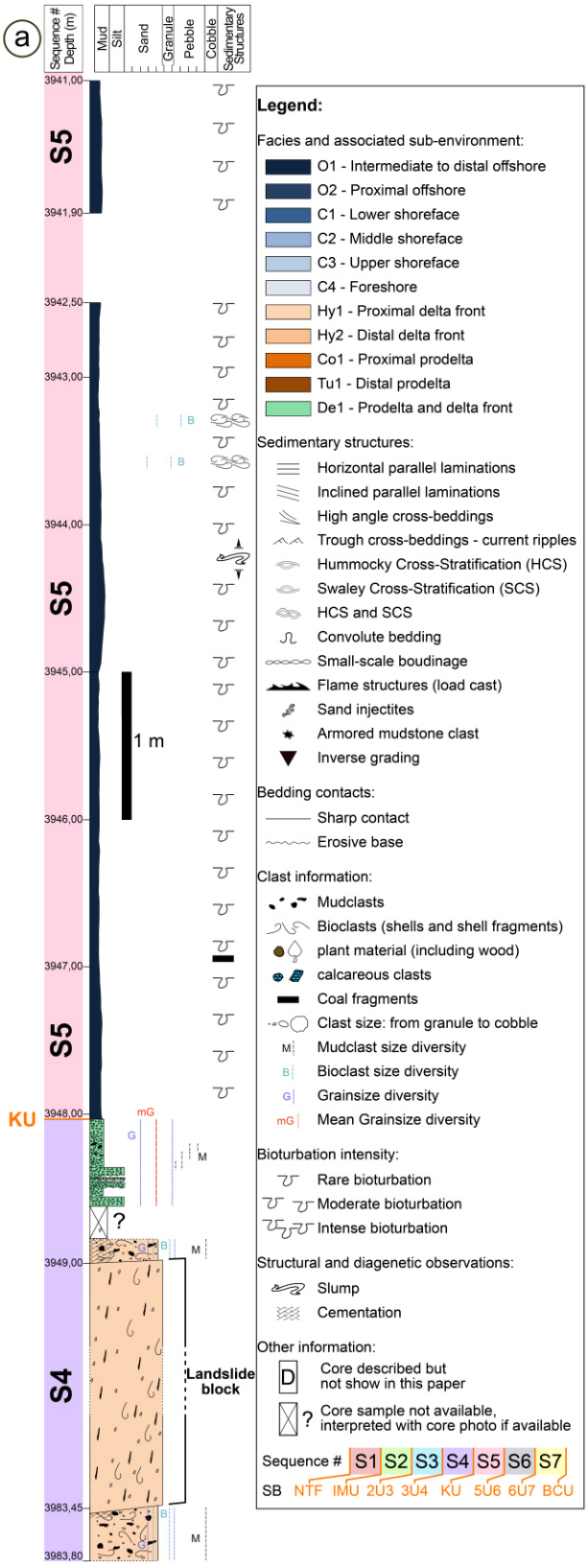

Fig. 2.Ca: Core description of well 6406/12-4S with the associated legend. The landslide block corresponds to a highly cemented interval with vertical orientation of the clasts (e.g. mudstone clasts elongated vertically). This landslide block has been generated along the fault segment 3 (FS3) which has been observed on seismic data. 6406/12-4S and FS3 location are displayed on Fig. 2.1D.

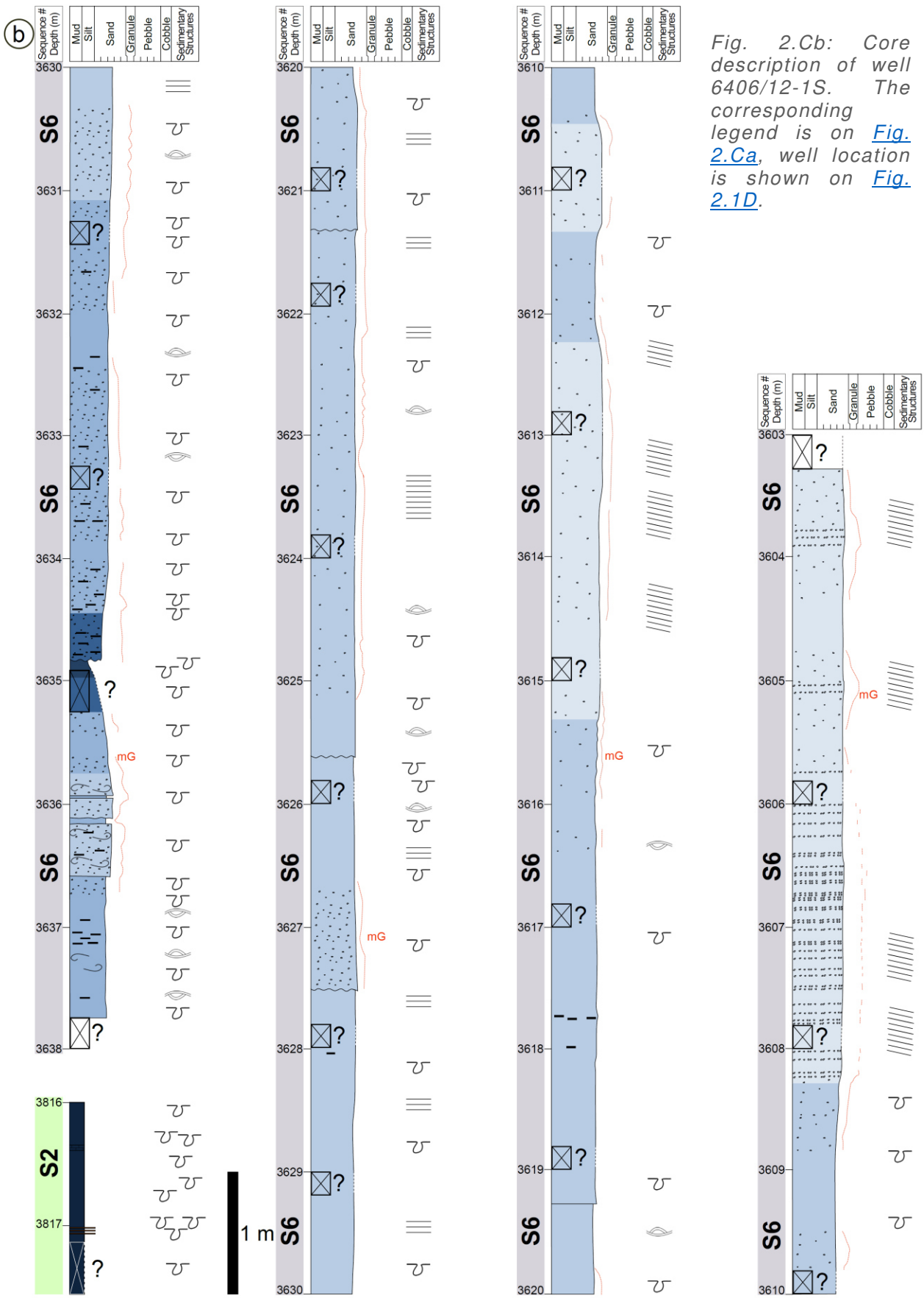

Fig. 2.Cb: Core description of well 6406/12-1S. The corresponding legend is on Fig. 2.Ca, well location is shown on Fig. 2.1D.

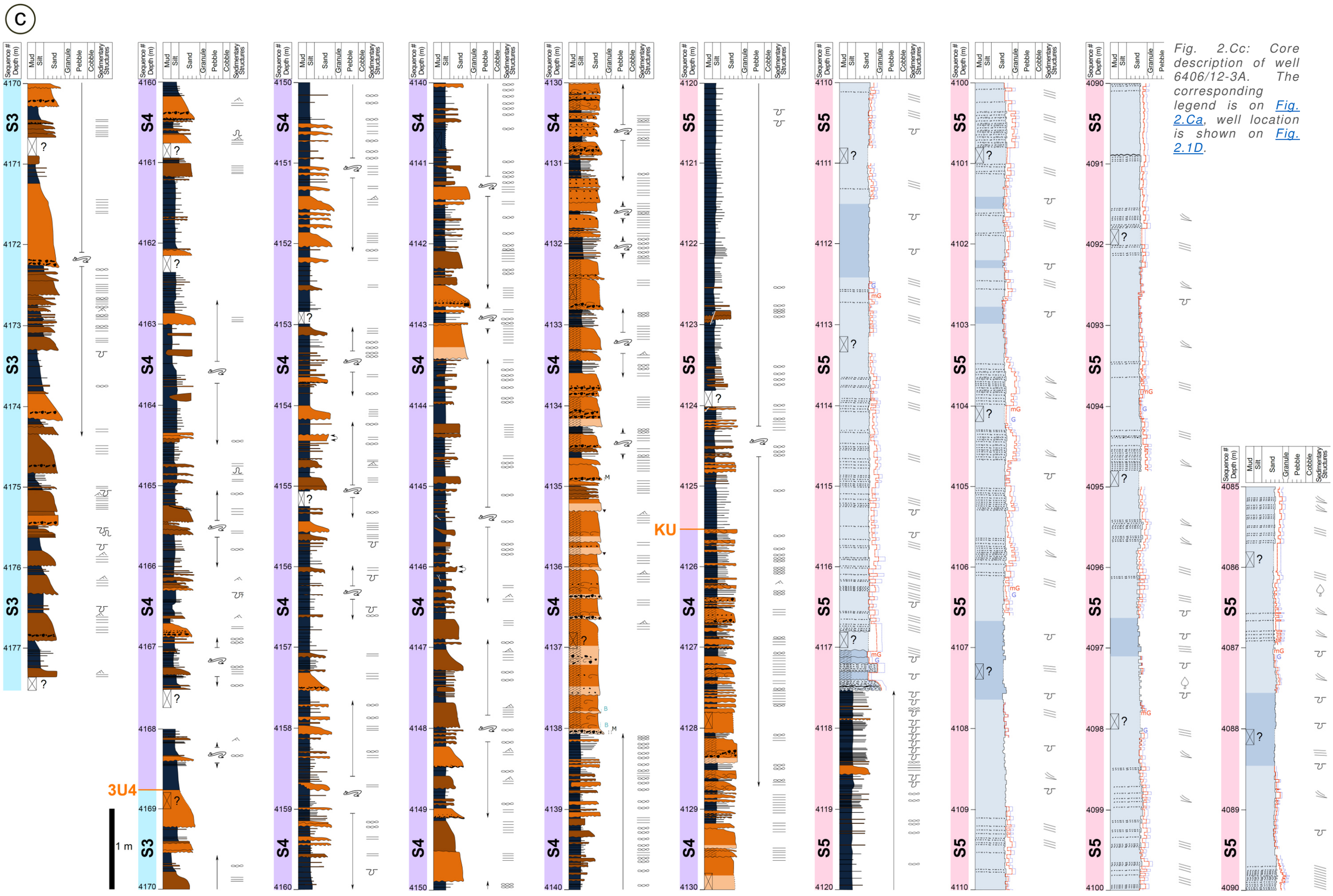

Fig. 2.Cc: Core description of well 6406/12-3A. The corresponding legend is on Fig. 2.Ca, well location is shown on Fig. 2.1D.

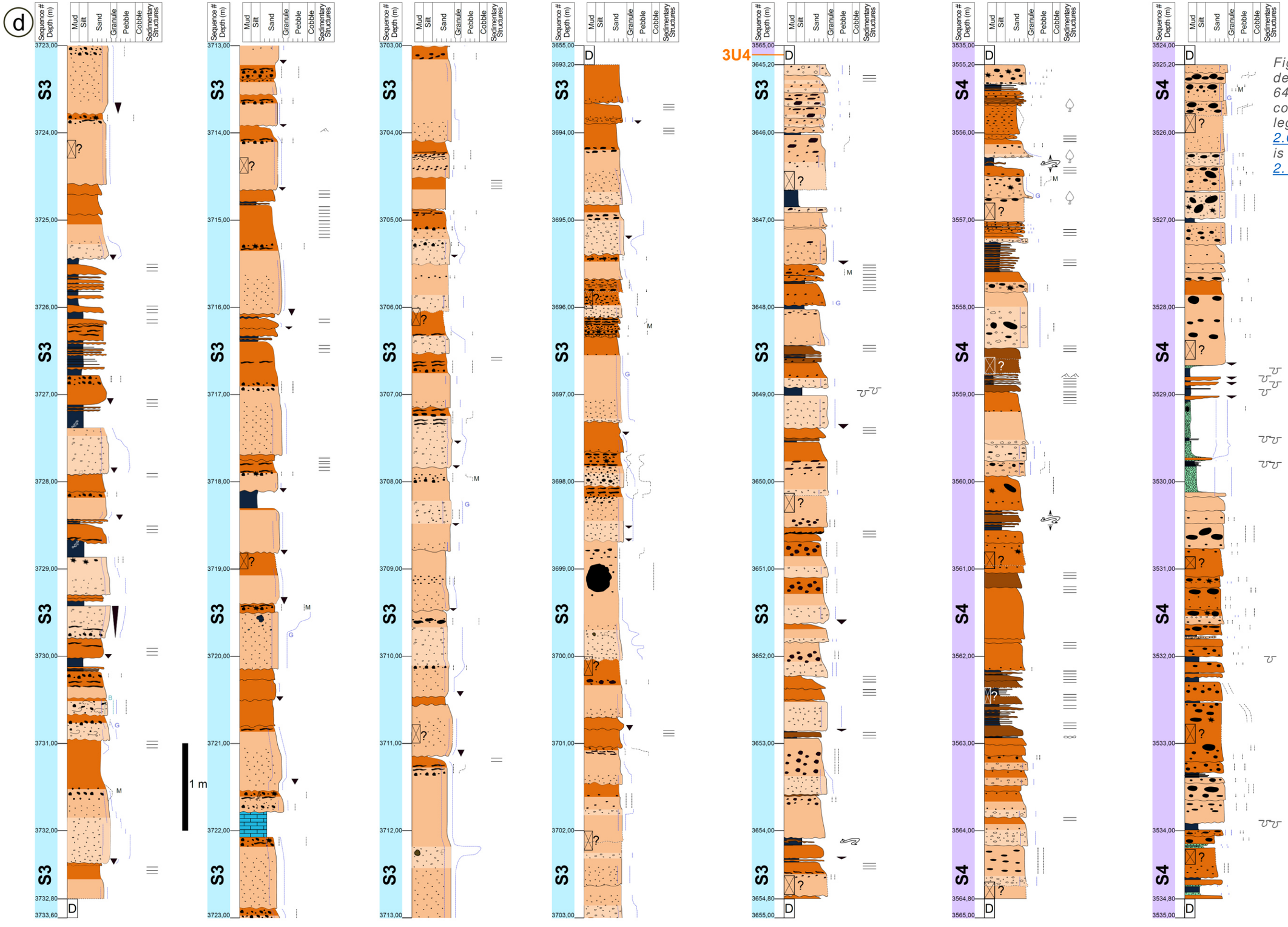

Fig. 2.Cd: Core description of well 6406/12-3S. The corresponding legend is on Fig. 2.Ca, well location is shown on Fig. 2.1D.

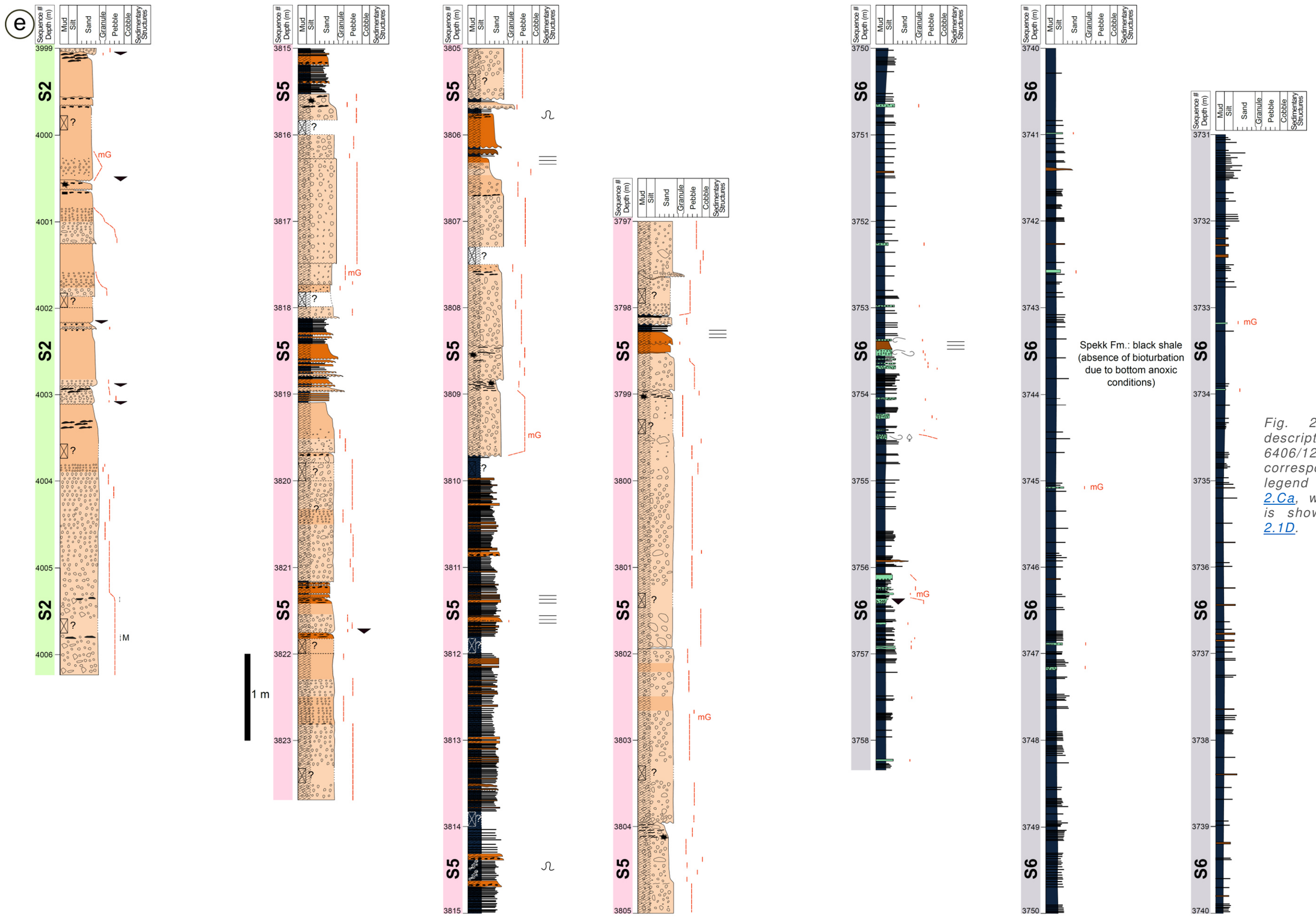

Fig. 2.Ce: Core description of well 6406/12-2. The corresponding legend is on Fig. 2.Ca, well location is shown on Fig. 2.1D.

4. Supplementary data 2.D: Detailed description of the dinoflagellate cyst assemblages

1. Zone "*D. willei & M. valensii*" (pre-rift assemblage)

This assemblage (Fig. 2.5) is characterised by the top occurrence of *Dissilodinium willei* and *Meiourogonaulax valensii* and by the base occurrence of *Atopodinium prostatum.*

This zone is dated pre-middle Bathonian.

2. Zone "*C. hyalina & P. calloviensis*" (Assemblage that approximately dates Sequence 1)

This assemblage (Fig. 2.5) can be easily identified by the simultaneous presence of the top and base occurrences of *Paragonyaulacysta calloviensis* and *Chytroeisphaeridia hyalina*.

This assemblage can also be identified by the acme of *Chytroeisphaeridia hyalina and Nannoceratopsis pellucida* and *the base occurrence of Gonyaulacysta jurassica, Pareodinia prolongata, Compositosphaeridium? polonicum, Stephanelytron spp., Rhynchodiniopsis cladophora and Mendicodinium groenlandicum.*

This dinoflagellate cyst zone starts during the middle Bathonian and ends during the middle Callovian (166.9 to 164.2 Ma).

3. Zone "*R. aemula & W. fimbriata*" (Assemblage that approximately dates Sequence 2)

This assemblage (Fig. 2.5) is identifiable with the acme of *Rigaudella aemula*, *Wanaea fimbriata*, *Mendicodinium groenlandicum* and *Trichodinium scarburghensis*.

This assemblage is marked by the first occurrence of *Wanaea fimbriata*, *Wanaea thysanota*, Scriniodinium crystallinum, *Systematophora areolate and Trichodinium scarburghensis*.

The dinoflagellate cyst assemblage of Sequence 2 is recognised by the last occurrence of *Rigaudella aemula*, *Pareodinia prolongata*, *Ctenidodinium continuum*, *Ctenidodinium thulium*, *Lithodinia jurassica*, *Trichodinium scarburghensis*, *Wanaea acollaris*, *Wanaea thysanota* and more generally by the last occurrence of *Wanaea spp.*

This assemblage starts during the middle Callovian and ends at the beginning of the late Oxfordian (164.2 to 159.5 Ma).

4. Zone "*S. crystallinum & E. galeritum*" (Assemblage that approximately dates Sequence 3):

This assemblage (Fig. 2.5) can be identified by the acme of *Scriniodinium crystallinum* and *Endoscrinium galeritum*.

The dinoflagellate cyst assemblage of Sequence 3 is recognised by the top occurrence of *Scriniodinium crystallinum*, *Endoscrinium galeritum*, *Nannoceratopsis pellucida, Gonyaulacysta eisenackii and Stephanelytron redcliffense.*

This zone is dated from the late Oxfordian to the early Kimmeridgian (159.5 to 156.0 Ma).

5. Zone "*S. paeminosa & P. pannosum*" (Assemblage that approximately dates Sequence 4)

This assemblage (Fig. 2.5) can be identified by the first occurrence of *Subtilisphaera? paeminosa* and *Perisseiasphaeridium pannosum*.

The last occurrence of *Endoscrinium galeritum* and *Stephanelytron spp.* enables the identification of dinoflagellate cyst assemblage of Sequence 4. In addition, this assemblage is marked by the acme of *Perisseiasphaeridium pannosum*.

This assemblage starts during the early Kimmeridgian and ends during the late Kimmeridgian (156.0 to 153.1 Ma).

6. Zone "*R. cladophora & E. luridum*" (Assemblage that approximately dates Sequence 5)

This assemblage (Fig. 2.5) is marked by the top occurrence of *Rhynchodiniopsis cladophora*, *Endoscrinium luridum*, *Gonyaulacysta jurassica* and by the base occurrence of *Systematophora daveyi*. As the previous assemblage, this one is also marked by the acme of *Perisseiasphaeridium pannosum and cannot be used as a single criterion of recognition.*

This dinoflagellate cyst zone starts during the late Kimmeridgian and ends during the early Tithonian (153.1 to 150.7 Ma).

7. Zone "*P. insolitum & O. patulum*" (Assemblage that approximately dates Sequence 6)

This assemblage (Fig. 2.5) can be identified by the first occurrence of *Perisseiasphaeridium insolitum* and *Muderongia sp. A.* This assemblage is also marked by the last occurrence of *Oligosphaeridium patulum*, *Perisseiasphaeridium pannosum*, *Cribroperidinium longicorne* and *Egmontodinium ovatum*. The acme of *Muderongia sp. A* in this assemblage is an obvious criterion of recognition.

This assemblage starts during the early Tithonian and ends during the late Tithonian (150.7 to 147.2 Ma).

8. Zone "*G. villosa & E. expiratum*" (Assemblage that approximately dates Sequence 7)

This assemblage (Fig. 2.5) can be identified by the first occurrence of *Gochteodinia villosa, Scriniodinium pharo* and the last occurrence of *Egmontodinium expiratum*, *Muderongia sp. A* and *Senoniasphaera jurassica*.

This dinoflagellate cyst zone starts during the late Tithonian and approximately ends at the end of the middle Berriasian (Fig. 2.5) taking in account the uncertainty range (147.2 to 141.7 Ma).

9. Zone "*K. corrugatum & P. pelliferum*" (post-rift Assemblage)

This assemblage (Fig. 2.5) is characterised by the base occurrence of *Kleithriasphaeridium corrugatum*, *Pseudoceratium pelliferum*, *Daveya boresphaera*, *Kleithriasphaeridium fasciatum*, *Gochteodinia villosa multifurcata*, *Ctenidodinium elegantulum* and by the top occurrence of *Scriniodinium pharo*, *Systematophora palmula* and *Daveya boresphaera*.

This zone is dated post-middle Berriasian.

5. Supplementary data 2.E: Sequence boundaries and well correlations

This *supplementary data 2.E* contains 2 well correlations (Figs. 2.Ea, 2.Eb).

Seven T-R sequences (S1 to S7) *sensu* Embry (1993, 1995) were identified within the Viking Group based on 8 sequence boundaries (i.e., NTF, IMU, 2U3, 3U4, KU, 5U6, 6U7, and BCU). The integration of seismic data (Figs. 2.3, 2.4), sediment core data (Figs. 2.6, 2.7, 2.9, 2.Ca, 2.Cb, 2.Cc, 2.Cd, 2.Ce), well log data (Figs. 2.9, 2.10, 2.Ea, 2.Eb), and checkshot data enables the calibration of SUs to SBs.

Starting with the oldest SU/SB, the NTF was previously described as a conformable to unconformable surface (Figs. 2.3, 2.4). The NTF has not been cored but was logged in a single well, 6406/11-1S (Fig. 2.Eb). In this well, the GR log highlights a transition from pre-rift deposits (interpreted as shoreface deposits) to syn-rift deposits (interpreted as offshore deposits). A study on the Halten Terrace reveals that the Garn Formation (youngest Formation of the Fangst Group) exhibits a transgressive pattern coevally with the development of retrogradational shoreface deposits (Corfield et al., 2001). Similar observations were reported from the contemporaneous Pelion and Fossilbjerget formations (Fig. 2.2) in East Greenland (Engkilde and Surlyk, 2003).

Subsequently, the IMU that is also marked by a well-defined erosional surface (Figs. 2.3, 2.4), has not been cored but was logged in four wells, 6406/12-1S, 6406/12-2, 6406/12-3A, and 6406/12-3B. GR log data from well 6406/12-3A highlight a transition from delta front to offshore environments, whereas a shift from prodelta to offshore mudstones is observed in well 6406/12-1S (Fig. 2.Ea). The IMU highlights a transgressive pattern between S1 and S2, as reported elsewhere in the Norwegian Sea (Corfield et al., 2001; Ichaso and Dalrymple, 2014).

The 2U3 was penetrated in most of the wells. The 2U3 has not been cored in a single well but is easily identifiable based on GR log data with; for instance in well 6406/12-3S, a coarsening-upward succession is documented in a coarse-grained deltaic environment reflecting a shift from a delta front environment to a prodelta above 2U3 (Fig. 2.Ea). It is noteworthy that, in well 6406/12-1S and 6406/12-3A, the SB is almost merged with the following MFS (Fig. 2.Ea).

The 3U4 was cored in two wells only (6406/12-3A and 6406/12-3S) allowing the precise observation of this SB in cores (Figs. 2.9A, 2.9D, 2.9E, 2.Cc, 2.Cd). The 3U4 in core 6406/12-3A is observed at -4168.75 m (Fig. 2.Cc) and at -3634.95 m in core 6406/12-3S. This SB is also well-defined on GR log data, for instance in well 6406/12-4S, judging from a shift from delta front to prodelta depositional environments (Fig. 2.Ea). In most wells located close to the land, the 3U4 is regarded as a merged surface combining the subaerial unconformity and the transgressive surface, thus highlighting a well-defined transgressive pattern between S3 and S4.

The KU was cored in two wells 6406/12-3A and 6406/12-4S (Figs. 2.9A, 2.9B, 2.9C, 2.Ca, 2.Cc). In core 6406/12-4S, this SB is extremely well-pronounced at the depth of -3948.05 m (Figs. 2.9B, 2.Ca), where the upper part of S4 is described as a proximal delta front (presence of Hy1 and De1 facies). Conversely, the bottom part of S5 corresponds to deep offshore mudstones (O1). Such a basinward facies shift is marked in well 6406/12-4S by an increase in GR values of 80 API (Fig. 2.Ea). In well 6406/12-4S, the KU is directly overlain by the following MFS (J63 MFS) found a few meters above (Fig. 2.Ea), exactly at 3945.00 m in the core (Fig. 2.Ca). For well 6406/12-3A, the KU is observed at -4125.55 m (Figs. 2.9C, 2.Cc). GR log data in this well document a drastic increase around the KU reflecting a basinward facies shift between delta front/prodelta and prodelta/basin plain (Fig. 2.Ea). In all well locations, the KU highlights a clear transgressive pattern between S4 and S5.

The 5U6 is uncored but, however, logged in several wells. This SB is well-developed in well 6406/12-3A and reflect an environmental shift between a foreshore environment in the upper part of S5 to a middle to lower shoreface environment at the base of S6 (Fig. 2.Ea). Similar observations outcome from the GR log curve in well 6406/12-4S, exhibiting a basinward shift of sedimentary facies from foreshore to lower shoreface environments (Fig. 2.Ea).

The 6U7 was not cored but penetrated by a single well, 6406/12-2 (Fig. 2.Eb). This SB exhibits a drastic increase in GR values, interpreted as a shift from prodelta to offshore environments.

The last and most conspicuous SU/SB is the BCU. The BCU, which merges several younger erosional surfaces, is found in each of the 10 studied wells. In most of the wells (6406/11-1S, 6406/12-2, 6406/12-3A, 6406/12-4S, 6407/10-4), the GR values abruptly decrease with, in some cases, a drop of ca. 100 API (Figs. 2.Ea, 2.Eb). This is explained by the presence of the Lyr Formation above the BCU, which mostly consists of marls with interbedded carbonate stringers (Dalland et al., 1988).

The coherency between well log, sediment core, and seismic data enables the observation of the sequence geometries in 3D. A chronostratigraphic age was further assigned to those seven T-R sequences using the established dinoflagellate cyst zonation (Fig. 2.5). For comparison purposes, S1 approximately corresponds to the J34-42 sequence (Partington et al., 1993), S2 to the J44-52 sequences (Fig. 2.5) and S3 to the J54-56 sequences. S4 is bounded by the J62 MFS and the J63 MFS and corresponds to the sequence J62. S5, S6 and S7 can be correlated to sequences J63-64, J66-71 and J72-74, respectively (Fig. 2.5).

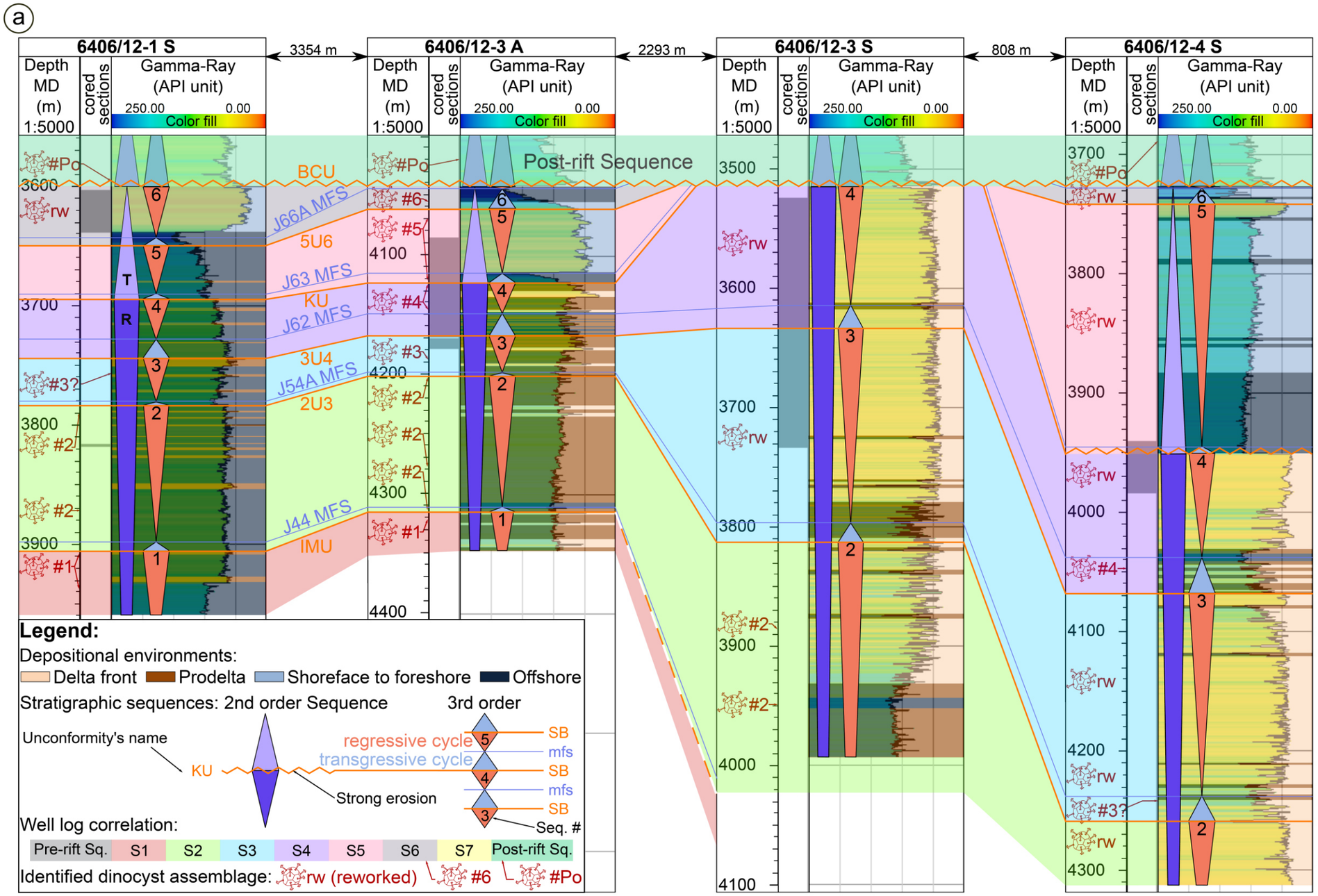

Fig. 2.Ea: Gamma-Ray (GR) log correlation showing the 2nd to 3rd order stratigraphic sequences in the greater Fenja area. The GR-log correlation is orientated approximately N-S, the exact well location is shown on Fig. 2.1D. Dinoflagellate cyst assemblages and major depositional environments are outlined in this panel. Sequence boundaries are identified within the correlation, with the Near Top Fangst (NTF), Intra-Melke Unconformity (IMU), Kimmeridgian Unconformity (KU), Base Cretaceous Unconformity (BCU), 2U3 (Unconformity between sequence 2 and 3), 3U4, 5U6 and 6U7 highlighting the 7 seismic sequences (S1, S2, S3, S4, S5, S6 and S7). Checkshot data allows the seismic unconformities (SUs) observed on Figs. 2.3 and 2.4 to be calibrated to the presented SBs. MFS are identified and named after Partington et al. (1993): J34 MFS, J44 MFS, J54A MFS, J62 MFS, J63 MFS, J66A MFS, J72 MFS and J76 MFS.

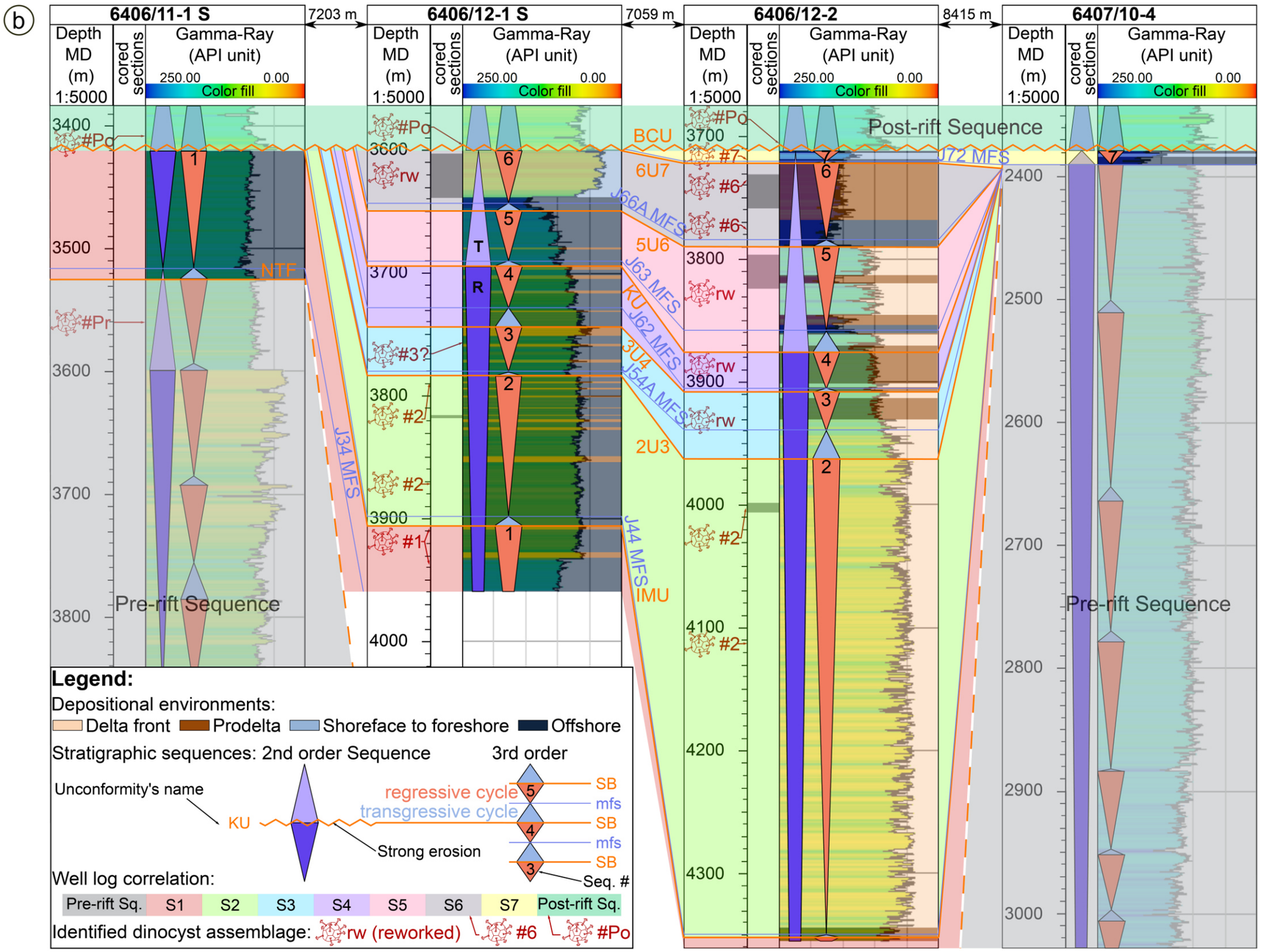

Fig. 2.Eb: GR-log correlation showing 2nd to 3rd order stratigraphic sequences in the greater Fenja area. The orientation of this GR-log correlation is SW-NE, the exact well location is shown on Fig. 2.1D. Dinoflagellate cyst assemblages and major depositional environments are outlined in this panel. Sequence boundaries (SBs) are identified within the correlation, with the Near Top Fangst (NTF), Intra-Melke Unconformity (IMU), Kimmeridgian Unconformity (KU), Base Cretaceous Unconformity (BCU), 2U3 (Unconformity between sequence 2 and 3), 3U4, 5U6 and 6U7 highlighting the 7 seismic sequences (S1, S2, S3, S4, S5, S6 and S7). Checkshot data allows the seismic unconformities (SUs) observed on Figs. 2.3 and 2.4 to be calibrated to the presented SBs. MFS are identified and named after Partington et al. (1993): J34 MFS, J44 MFS, J54A MFS, J62 MFS, J63 MFS, J66A MFS, J72 MFS and J76.

6. Supplementary data 3.A: Supplementary table regarding database

Abbreviations are CPL for channel and/or proximal lobe, MDL for mid to distal lobe, FLF for frontal lobe fringe and LLF for lateral lobe fringe sub-environment. O1, Hy1/2, Co1, Tu1 of type 1 and type 2, Sl1, Df1, and Tu2 correspond to the facies presented on Fig. 3.5.

Well name	Lobe sub-environment	Lobe sub-environment #	Depth base (m)	Depth top (m)	Thickness (m)	Previous lobe sub-environment	Next lobe sub-environment	Not sure?	Entire event?	Bed dominated by **Hy1/2**, **Co1**, (less commonly Tu1 of type 1)	Bed dominated by **Tu1 of type 1**, **Sl1**, **Df1** (Co1, Tu2)	Bed dominated by **Sl1**, **Df1**, **Tu2** (Tu1 of type 1)	Bed integrally composed of **Tu1 of type 2**, on a **O1** facies	Total number of beds
6507_2-2	MDL	A01	3339	3337,56	1,44	/	CPL	NO	NO	0	1	0	0	1
6507_2-2	CPL	A02	3337,56	3335,09	2,47	MDL	LLF	NO	YES	1	1	0	0	2
6507_2-2	LLF	A03	3335,09	3333,88	1,21	CPL	FLF	NO	YES	0	0	1	49	50
6507_2-2	FLF	A04	3333,88	3331	2,88	LLF	LLF	NO	YES	0	0	13	55	68
6507_2-2	LLF	A05	3331	3330	1	FLF	/	NO	NO	1	1	3	65	70
6507_2-2	LLF	B01	3295,8	3295,12	0,68	/	CPL	NO	NO	0	0	0	6	6
6507_2-2	CPL	B02	3295,12	3294,83	0,29	LLF	LLF	NO	YES	1	0	0	0	1
6507_2-2	LLF	B03	3294,83	3294	0,83	CPL	MDL	NO	YES	0	0	0	22	22
6507_2-2	MDL	B04	3294	3289,54	4,46	LLF	LLF	YES	YES	0	3	0	0	3
6507_2-2	LLF	B05	3289,54	3289,33	0,21	MDL	MDL	NO	YES	0	0	0	13	13
6507_2-2	MDL	B06	3289,33	3287,29	2,04	LLF	LLF	NO	YES	0	1	0	0	1
6507_2-2	LLF	B07	3287,29	3286,87	0,42	MDL	CPL	NO	YES	0	0	0	21	21
6507_2-2	CPL	B08	3286,87	3286,09	0,78	LLF	MDL	NO	YES	1	0	0	0	1
6507_2-2	MDL	B09	3286,09	3278,93	7,16	CPL	LLF	NO	YES	0	5	3	2	10
6507_2-2	LLF	B10	3278,93	3278,67	0,26	MDL	FLF	NO	YES	0	0	0	14	14
6507_2-2	FLF	B11	3278,67	3274,65	4,02	LLF	LLF	NO	YES	0	0	14	2	16
6507_2-2	LLF	B12	3274,65	3273,86	0,79	FLF	FLF	NO	YES	0	0	1	41	42
6507_2-2	FLF	B13	3273,86	3273	0,86	LLF	/	NO	NO	0	1	2	5	8
6507_2-2	LLF	C01	2849,45	2832,7	16,75	/	MDL	NO	NO	0	0	0	846	846
6507_2-2	MDL	C02	2832,7	2829,62	3,08	LLF	LLF	NO	YES	0	5	0	0	5
6507_2-2	LLF	C03	2829,62	2828,46	1,16	MDL	MDL	NO	YES	0	0	0	58	58
6507_2-2	MDL	C04	2828,46	2822,81	5,65	LLF	LLF	NO	YES	0	4	0	0	4
6507_2-2	LLF	C05	2822,81	2822,45	0,36	MDL	FLF	NO	YES	0	0	0	19	19
6507_2-2	FLF	C06	2822,45	2822	0,45	LLF	/	YES	NO	0	0	1	0	1
6507_2-3	LLF	D01	3263,84	3261,07	2,77	/	FLF	NO	NO	0	0	0	125	125
6507_2-3	FLF	D02	3261,07	3258,98	2,09	LLF	LLF	NO	YES	0	0	2	21	23
6507_2-3	LLF	D03	3258,98	3254	4,98	FLF	/	NO	NO	0	0	0	285	285
6507_2-3	LLF	E01	2890,77	2888,25	2,52	/	CPL	NO	NO	0	0	1	74	75
6507_2-3	CPL	E02	2888,25	2888,02	0,23	LLF	FLF	YES	YES	1	0	0	0	1
6507_2-3	FLF	E03	2888,02	2885,87	2,15	CPL	LLF	NO	YES	0	0	2	0	2
6507_2-3	LLF	E04	2885,87	2885,19	0,68	FLF	FLF	NO	YES	0	0	1	30	31
6507_2-3	FLF	E05	2885,19	2883,17	2,02	LLF	LLF	NO	YES	0	0	3	7	10
6507_2-3	LLF	E06	2883,17	2882,62	0,55	FLF	MDL	NO	YES	0	0	0	30	30
6507_2-3	MDL	E07	2882,62	2878,68	3,94	LLF	CPL	NO	YES	0	5	0	11	16
6507_2-3	CPL	E08	2878,68	2878	0,68	MDL	MDL	NO	YES	1	1	0	0	2
6507_2-3	MDL	E09	2878	2874,78	3,22	CPL	FLF	NO	YES	0	3	0	0	3
6507_2-3	FLF	E10	2874,78	2872,88	1,9	MDL	LLF	NO	YES	0	0	6	1	7
6507_2-3	LLF	E11	2872,88	2872,49	0,39	FLF	MDL	NO	YES	0	0	1	14	15
6507_2-3	MDL	E12	2872,49	2865,92	6,57	LLF	FLF	NO	YES	0	4	2	2	8
6507_2-3	FLF	E13	2865,92	2860,41	5,51	MDL	MDL	NO	YES	0	0	8	8	16

Well name	Lobe sub-environment	Lobe sub-environment #	Depth base (m)	Depth top (m)	Thickness (m)	Previous lobe sub-environment	Next lobe sub-environment	Not sure?	Entire event?	Bed dominated by **Hy1/2**, **Co1**, (less commonly Tu1 of type 1)	Bed dominated by **Tu1 of type 1**, **Sl1**, **Df1** (Co1, Tu2)	Bed dominated by **Sl1**, **Df1**, **Tu2** (Tu1 of type 1)	Bed integrally composed of **Tu1 of type 2**, on a **O1** facies	Total number of beds
6507_2-3	MDL	E14	2860,41	2853,59	6,82	FLF	LLF	NO	YES	0	5	0	0	5
6507_2-3	LLF	E15	2853,59	2853,49	0,1	MDL	FLF	NO	YES	0	0	0	10	10
6507_2-3	FLF	E16	2853,49	2850,21	3,28	LLF	LLF	NO	YES	0	0	1	0	1
6507_2-3	LLF	E17	2850,21	2850	0,21	FLF	/	NO	NO	0	0	0	19	19
6507_2-4	LLF	F01	3344,81	3344,57	0,24	/	MDL	NO	NO	0	0	0	23	23
6507_2-4	MDL	F02	3344,57	3342,1	2,47	LLF	LLF	NO	YES	0	3	0	0	3
6507_2-4	LLF	F03	3342,1	3341,71	0,39	MDL	MDL	NO	YES	0	0	3	35	38
6507_2-4	MDL	F04	3341,71	3339,21	2,5	LLF	FLF	NO	YES	0	4	0	0	4
6507_2-4	FLF	F05	3339,21	3337,54	1,67	MDL	MDL	NO	YES	0	0	4	34	38
6507_2-4	MDL	F06	3337,54	3335,44	2,1	FLF	FLF	NO	YES	0	2	0	0	2
6507_2-4	FLF	F07	3335,44	3334	1,44	MDL	/	NO	NO	0	0	0	103	103
6507_2-4	FLF	G01	2852	2850,28	1,72	/	MDL	NO	NO	0	0	1	0	1
6507_2-4	MDL	G02	2850,28	2841,64	8,64	FLF	FLF	NO	YES	0	3	0	0	3
6507_2-4	FLF	G03	2841,64	2838,39	3,25	MDL	MDL	NO	YES	0	1	2	0	3
6507_2-4	MDL	G04	2838,39	2835	3,39	FLF	/	NO	NO	0	3	0	0	3
6507_3-3	LLF	H01	2747,77	2742,63	5,14	/	FLF	NO	NO	0	1	6	484	491
6507_3-3	FLF	H02	2742,63	2741,18	1,45	LLF	LLF	NO	YES	0	0	1	66	67
6507_3-3	LLF	H03	2741,18	2738,89	2,29	FLF	FLF	NO	YES	0	0	0	255	255
6507_3-3	FLF	H04	2738,89	2737,72	1,17	LLF	LLF	NO	YES	0	0	1	69	70
6507_3-3	LLF	H05	2737,72	2734,19	3,53	FLF	FLF	NO	YES	0	0	0	386	386
6507_3-3	FLF	H06	2734,19	2732,71	1,48	LLF	LLF	NO	YES	0	0	1	0	1
6507_3-3	LLF	H07	2732,71	2721	11,71	FLF	/	NO	NO	0	0	0	1297	1297
6507_3-9S	LLF	I01	2895,68	2885	10,68	/	MDL	NO	NO	0	0	0	1167	1167
6507_3-9S	MDL	I02	2885	2879,22	5,78	LLF	LLF	NO	YES	0	4	0	5	9
6507_3-9S	LLF	I03	2879,22	2878,71	0,51	MDL	MDL	NO	YES	0	0	0	51	51
6507_3-9S	MDL	I04	2878,71	2876,59	2,12	LLF	LLF	NO	YES	0	2	0	0	2
6507_3-9S	LLF	I05	2876,59	2876,43	0,16	MDL	CPL	NO	YES	0	0	0	15	15
6507_3-9S	CPL	I06	2876,43	2875,92	0,51	LLF	LLF	NO	YES	1	0	0	0	1
6507_3-9S	LLF	I07	2875,92	2875,76	0,16	CPL	MDL	NO	YES	0	0	0	14	14
6507_3-9S	MDL	I08	2875,76	2868,05	7,71	LLF	CPL	NO	YES	0	5	0	12	17
6507_3-9S	CPL	I09	2868,05	2868	0,05	MDL	MDL	YES	NO	1	0	0	0	1
6507_3-9S	MDL	I10	2866,14	2864,7	1,44	CPL	LLF	NO	YES	0	3	0	0	3
6507_3-9S	LLF	I11	2864,7	2864,53	0,17	MDL	CPL	NO	YES	0	0	0	14	14
6507_3-9S	CPL	I12	2864,53	2864,15	0,38	LLF	LLF	NO	YES	1	0	0	0	1
6507_3-9S	LLF	I13	2864,15	2864,03	0,12	CPL	CPL	NO	YES	0	0	0	8	8
6507_3-9S	CPL	I14	2864,03	2863,65	0,38	LLF	MDL	NO	YES	1	0	0	0	1
6507_3-9S	MDL	I15	2863,65	2860,26	3,39	CPL	LLF	NO	YES	0	2	0	3	5
6507_3-9S	LLF	I16	2860,26	2860,06	0,2	MDL	MDL	NO	YES	0	0	0	21	21
6507_3-9S	MDL	I17	2860,06	2858,16	1,9	LLF	FLF	NO	YES	0	2	0	0	2
6507_3-9S	FLF	I18	2858,16	2856,98	1,18	MDL	MDL	NO	YES	0	0	2	2	4
6507_3-9S	MDL	I19	2856,98	2854,83	2,15	FLF	FLF	NO	YES	0	1	0	0	1
6507_3-9S	FLF	I20	2854,83	2851,63	3,2	MDL	MDL	NO	YES	0	0	1	0	1
6507_3-9S	MDL	I21	2851,63	2850	1,63	FLF	/	YES	NO	0	1	0	0	1

Well name	Lobe sub-environment	Lobe sub-environment #	Depth base (m)	Depth top (m)	Thickness (m)	Previous lobe sub-environment	Next lobe sub-environment	Not sure?	Entire event?	Bed dominated by **Hy1/2**, **Co1**, (less commonly Tu1 of type 1)	Bed dominated by **Tu1 of type 1**, **Sl1**, **Df1** (Co1, Tu2)	Bed dominated by **Sl1**, **Df1**, **Tu2** (Tu1 of type 1)	Bed integrally composed of **Tu1 of type 2**, on a **O1** facies	Total number of beds
6507_5-3	FLF	J01	2855	2854,14	0,86	/	MDL	NO	NO	0	0	2	0	2
6507_5-3	MDL	J02	2854,14	2852,15	1,99	FLF	FLF	NO	YES	0	6	0	0	6
6507_5-3	FLF	J03	2852,15	2851	1,15	MDL	MDL	NO	YES	0	2	3	0	5
6507_5-3	MDL	J04	2851	2848,6	2,4	FLF	FLF	NO	YES	0	2	0	0	2
6507_5-3	FLF	J05	2848,6	2847,14	1,46	MDL	CPL	NO	YES	0	2	3	0	5
6507_5-3	CPL	J06	2847,14	2846,61	0,53	FLF	MDL	YES	YES	1	0	0	0	1
6507_5-3	MDL	J07	2846,61	2843	3,61	CPL	CPL	NO	NO	0	3	0	0	3
6507_5-3	CPL	J08	2840	2839,69	0,31	MDL	MDL	YES	NO	1	0	0	0	1
6507_5-3	MDL	J09	2839,69	2838,95	0,74	CPL	LLF	YES	YES	0	2	1	0	3
6507_5-3	LLF	J10	2838,95	2838,66	0,29	MDL	CPL	NO	YES	0	0	0	25	25
6507_5-3	CPL	J11	2838,66	2838,03	0,63	LLF	MDL	YES	YES	1	0	0	0	1
6507_5-3	MDL	J12	2838,03	2836,45	1,58	CPL	/	NO	NO	0	1	0	1	2
6507_7-1	MDL	K01	3512,76	3504,02	8,74	/	/	NO	NO	0	6	0	0	6

	CPL		MDL		FLF		LLF		Thicknesss between 2 LLF
Data types (all data [AD] *vs* Outliers excluded[OE])	AD	OE	AD	OE	AD	OE	AD	OE	AD no OE
Minimum thickness (m)	0,05	0,29	0,74	1,44	0,45	1,15	0,10	0,10	0,29
Maximum thickness (m)	2,47	2,47	8,74	8,64	5,51	5,51	16,75	3,53	18,90
Average thickness (m)	0,60	0,78	3,75	3,96	2,05	2,34	2,17	0,67	4,12
Mean thickness (m)	0,44	0,51	3,08	3,08	1,69	2,02	0,55	0,39	2,68
standard deviation (Population)	0,60	0,71	2,31	2,23	1,17	1,16	3,76	0,79	4,13
Variance (Population)	0,36	0,50	5,31	4,96	1,37	1,35	14,17	0,63	17,02
Number of sub-environment counted (n)	12	7	29	21	22	17	33	22	24

	Bed dominated by **Hy1/2**, **Co1**, (less commonly by Tu1 of type 1)	Bed dominated by **Tu1 of type 1**, **Sl1**, **Df1** (Co1, Tu2)	Bed dominated by **Sl1**, **Df1**, **Tu2** (Tu1 of type 1)	Bed integrally composed of **Tu1 of type 2**, on a **O1** facies
Minimum observed thickness (m)	0,05	0,04	0,01	0,001
Maximum observed thickness (m)	1,25	4,37	3,28	0,02

	Number of beds in CPL									
	Bed dominated by **Hy1/2**, **Co1**, (less commonly by Tu1 of type 1)		Bed dominated by **Tu1 of type 1**, **Sl1**, **Df1** (Co1, Tu2)		Bed dominated by **Sl1**, **Df1**, **Tu2** (Tu1 of type 1)		Bed integrally composed of **Tu1 of type 2**, on a **O1** facies		Total number of beds	
Data types (all data [AD] *vs* Outliers excluded[OE])	AD	OE	AD	OE	AD	OE	AD	OE	AD	OE
Minimum number of bed	1	1	0	0	0	0	0	0	1	1
Maximum number of bed	1	1	1	1	0	0	0	0	2	2
Average number of bed	1	1	0,17	0,29	0	0	0	0	1,17	1,29
Mean number of bed	1	1	0	0	0	0	0	0	1	1
standard deviation (Population)	0	0	0,37	0,45	0	0	0	0	0,37	0,45
Variance (Population)	0	0	0,14	0,2	0	0	0	0	0,14	0,2
Number of sub-environment counted (n)	12	7	12	7	12	7	12	7	12	7

	Number of beds in MDL									
	Bed dominated by **Hy1/2**, **Co1**, (less commonly by Tu1 of type 1)		Bed dominated by **Tu1 of type 1**, **Sl1**, **Df1** (Co1, Tu2)		Bed dominated by **Sl1**, **Df1**, **Tu2** (Tu1 of type 1)		Bed integrally composed of **Tu1 of type 2**, on a **O1** facies		Total number of beds	
Data types (all data [AD] *vs* Outliers excluded[OE])	AD	OE	AD	OE	AD	OE	AD	OE	AD	OE
Minimum number of bed	0	0	1	1	0	0	0	0	1	1
Maximum number of bed	0	0	6	6	3	3	12	12	17	17
Average number of bed	0	0	3,14	3,38	0,21	0,24	1,24	1,67	4,59	5,29
Mean number of bed	0	0	3	3	0	0	0	0	3	4
standard deviation (Population)	0	0	1,52	1,43	0,66	0,75	3,01	3,44	3,96	4,37
Variance (Population)	0	0	2,35	2,05	0,44	0,56	9,08	11,84	15,69	19,06
Number of sub-environment counted (n)	29	21	29	21	29	21	29	21	29	21

	Number of beds in FLF									
	Bed dominated by **Hy1/2**, **Co1**, (less commonly by Tu1 of type 1)		Bed dominated by **Tu1 of type 1**, **Sl1**, **Df1** (Co1, Tu2)		Bed dominated by **Sl1**, **Df1**, **Tu2** (Tu1 of type 1)		Bed integrally composed of **Tu1 of type 2**, on a **O1** facies		Total number of beds	
Data types (all data [AD] *vs* Outliers excluded [OE])	AD	OE	AD	OE	AD	OE	AD	OE	AD	OE
Minimum number of bed	0	0	0	0	1	1	0	0	1	1
Maximum number of bed	0	0	2	2	14	14	103	69	108	70
Average number of bed	0	0	0,27	0,29	3,55	3,94	16,95	15,59	20,77	19,82
Mean number of bed	0	0	0	0	2	2	1,5	2	6	7
Standard deviation (Population)	0	0	0,62	0,67	3,61	3,95	28,74	23,92	29,36	24,31
Variance (Population)	0	0	0,38	0,44	13,07	15,58	825,95	572,36	862,27	591,09
Number of sub-environments counted (n)	22	17	22	17	22	17	22	17	22	17

	Number of beds in LLF									
	Bed dominated by **Hy1/2**, **Co1**, (less commonly by Tu1 of type 1)		Bed dominated by **Tu1 of type 1**, **Sl1**, **Df1** (Co1, Tu2)		Bed dominated by **Sl1**, **Df1**, **Tu2** (Tu1 of type 1)		Bed integrally composed of **Tu1 of type 2**, on a **O1** facies		Total number of beds	
Data types (all data [AD] *vs* Outliers excluded [OE])	AD	OE	AD	OE	AD	OE	AD	OE	AD	OE
Minimum number of bed	0	0	0	0	0	0	6	8	6	8
Maximum number of bed	1	0	1	0	6	3	1297	386	1297	386
Average number of bed	0,03	0	0,06	0	0,52	0,32	167,76	52,05	168,36	52,36
Mean number of bed	0	0	0	0	0	0	30	21,5	30	21,5
Standard deviation (Population)	0,17	0	0,24	0	1,23	0,70	321,15	88,21	321,22	88,15
Variance (Population)	0,03	0	0,06	0	1,52	0,49	103140,2	7781,59	103183,2	7770,69
Number of sub-environments counted (n)	33	22	33	22	33	22	33	22	33	22

7. Supplementary data 4.A: Stratigraphy, structural geology and prolific petroleum areas

- Introduction
  - Syn-rift and post-rift studies

The syn-rift study (Chapter 2) of the southern part of the Halten Terrace (greater Fenja area) examined the syn-rift evolution based on a tremendous dataset (i.e., almost half a kilometre of core, seven wells out of ten drilled after 2014 with last generation well-logging tools, and a good 3D seismic coverage). The integration of the different datasets (well-log data, core data, seismic data and biostratigraphic data) supports a robust 4D tectonostratigraphic evolution of the syn-rift stage by the accurate identification of sub-rift stages (rift initiation, rift-climax and final rift stages).

The post-rift study (Chapter 3) of the Dønna Terrace (greater Marulk area) detailed the internal organisation of sand-prone Turonian to Coniacian deep-marine turbidite lobe complexes during the post-rift stage. This stratigraphic interval is rich in data in the Dønna Terrace (i.e., high-quality sediment core photo data, an already established biostratigraphic chart, well data, 3D seismic coverage), thus allowing to decipher the dominant autocyclic and allocyclic controlling factors. These factors control the distribution of the sediment inside the lobe. The incorporation of the whole dataset further helped to define sub-stages (early and late rift-sag, and early and late post-rift) that will be discussed in *Chapter 5*.

  - Exploring the Norwegian Sea

The Norwegian Sea is composed of three structural domains (Fig. 4.Aa). The deep domain corresponds to the Vøring and the Møre basins. The terrace domain consists of the Halten Terrace (Chapter 2) and the Dønna Terrace (Chapter 3). The platform domain is formed by the Trøndelag Platform and the Møre Platform, including the Frøya High. The Trøndelag Platform, the Halten and Dønna terraces are separated by the Nordland Ridge that is a structural high (Fig. 4.Aa).

Since the early 1980s, the Norwegian Sea has been intensively drilled, as 395 exploration wells have been drilled over the past 40 years (NPD, 2021). Exploration well locations are intimately linked to structural domains. Wells drilled in the deep domain target Cretaceous-Palaeocene highs with the aim to discover petroleum reservoirs in post-rift deep-water turbidite systems. These wells represent 10% of the exploration targets. A further 10% of total exploration targets have been drilled in the platform domain. These wells have predominately targeted pre-rift Jurassic coastal deposits. The remaining 80% of the wells have been drilled in the terrace domain focusing on pre-, syn- and post-rift exploration targets.

The terrace domain is a prolific petroleum area for several reasons:

- Source rocks are not too deeply buried (remaining in the oil window) as compared to the deep domain, and not too shallow as in the platform domain;
- Gas from deeper source rocks can migrate from the deep domain to the terrace domain. Source rocks in the platform domain are also commonly immature;

- The terrace domain is not affected by intense erosion during its geological history, unlike the platform domain;
- The Cretaceous deep-marine offshore succession is commonly less than one kilometre thick in the terrace domain, although it can extend several kilometres in the deep domain and may be absent in the platform domain;
- Pre-, syn- and post-rift reservoirs are commonly found at 2.5 to 4.5 km MD (Measured depth) corresponding to a standard depth in the Oil & Gas Industry;
- Multi-targets (pre- and syn-rift targets or pre- and post-rift targets) can be planned for a single vertical exploration well in the terrace domain. This is not the case in the other structural domains. Note, however, that sandy syn-rift and post-rift reservoirs are commonly not compatible (cf. section *4. Sandstone reservoirs and petroleum exploration potential* in *Chapter 5*);
- The terrace domain (such as the platform) is located near the Norwegian continental shelf, thus simplifying development and exploration options.
    - Syn-rift and post-rift petroleum reservoirs

The syn-rift period is composed of two prolific proven reservoirs, the Intra-Melke Formation and the Rogn Formation. The Intra-Melke Formation was encountered in well 6406/12-3S and 6406/12-3A, whereas the Rogn Formation was identified in well 6406/12-1S (Chapter 2). The Draugen field, which was discovered within the Rogn Formation (wave-dominated shoreface to foreshore), is oil-bearing, has a porosity ranging from 28 to 32 % and an average permeability of 5 Darcies (Mikkelsen et al., 2008). The Fenja field (Chapter 2) produces hydrocarbons within both the Intra-Melke Formation sandstones (coarse-grained deltas) and the Rogn Formation. In turn, the Spekk Formation is recognized as a prolific source rock with high total organic carbon (TOC) in most of the wells drilled within the terrace and deep domains. Note that well 6205/3-1R revealed deep marine SSDF deposits intertwined with organic-rich mudstones. Two seals have been identified in this period, the muddy Melke and Spekk formations.

The post-rift period consists of two recognized prolific reservoirs, the Intra-Lange sandstone members within the Cromer Knoll Group, and the sandstone members observed in the Shetland Group. The “Aptian Sands” were found at the boundary between the platform and the terrace domain in well 6507/7-12. The Breiflabb Member has been solely encountered in the terrace domain, whereas the Lysing Member was recognized in the terrace domain, as well as in the deep domain (Gradstein and Waters, 2016). The Marulk field (Chapter 3) extracts condensate and gas from the Breiflabb and Lysing members (deep-water turbidite lobe complexes), in which porosity ranges from 10 to 32 % and permeability averages ca. 1 Darcie (Calabrese et al., 2011). Sandstone members such as the Hvithval and Spekkhogger members of the Shetland Group have only been observed in the deep domain, such as in well 6704/12-1 (Gradstein and Waters, 2016). Other members that are post-Shetland Group, such as the Egga sandstone Member, were mainly observed in the deep domain (Gradstein and Waters, 2016). Note that Cretaceous or post-Cretaceous mudstones are good seal rocks.

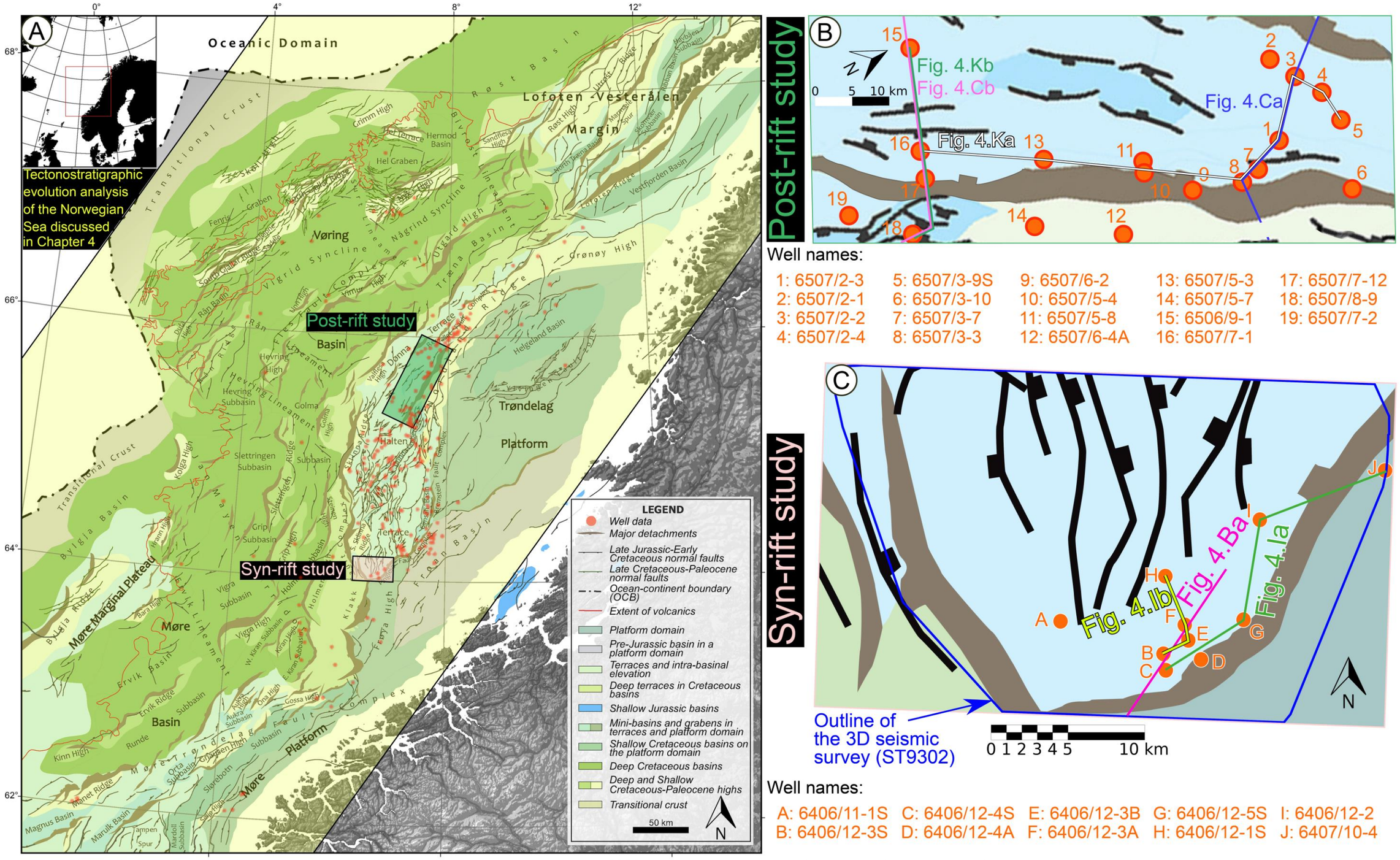

Fig. 4.Aa: Structural maps of the: A) Norwegian Sea map after Zastrozhnov et al. (2020) showing the location of the post-rift study, syn-rift study and the area for the paleoenvironment reconstructions presented in Fig. 4.3 (yellow polygon); B) Dønna Terrace modified after Zastrozhnov et al. (2020) showing the location of the presented seismic lines (Figs. 4.Ca, 4.Cb) and well correlations (Figs. 4.Ka, 4.Kb); C) Southern part of the Halten Terrace modified after Zastrozhnov et al. (2020) showing the location of the presented seismic lines (Fig. 4.Ba) and well correlations (Figs. 4.Ia, 4.Ib).

- Stratigraphy and structural geology of the Norwegian Sea

The Fangst Group (Fig. 4.Ab) dated from the Late Toarcian to the Middle Bathonian is formed of three geological formations (Dalland et al., 1988): the Ile, Not and Garn formations, from the oldest to the youngest, respectively (Figure 1.16 in *Chapter 1*). The Fangst Group is equivalent to the prolific petroleum Brent Group in the North Sea (Copestake et al., 2003).

The Viking Group dated from the Middle Bathonian to the Late Berriasian is formed of three formations and one informal formation (Dalland et al., 1988; NPD, 2021). Listed chronologically, these are the Melke Formation, the Intra-Melke informal Formation, the Rogn Formation and the Spekk Formation. (Fig. 4.Ab). The Spekk Formation is equivalent to the well-known source rock, i.e., the Kimmeridge Clay, of the North Sea (Copestake et al., 2003).

The Cromer Knoll Group dated from the Late Berriasian to the Earliest Coniacian, is composed of two formal formations and one informal formation. At the base, the Lyr Formation consists of calcareous mudstones, grading to marlstones with occasional limestone stringers (Gradstein and Waters, 2016). The Lange Formation consists of deep-marine mudstones. The Intra-Lange informal Formation is composed of several sandstone members with the most regional extension, the Lysing Member, then the Breiflabb Member, and other members deposited as sand intervals during the Aptian and the Early Coniacian.

The Shetland Group is composed of three geological formations, named (from the oldest to the youngest) the Kvitnos Formation, the Nise Formation and the Springar Formation (Fig. 4.Ab). The Shetland Group is dated from the Earliest Coniacian to the Late Maastrichtian. The three formations consist predominantly of deep-marine mudstones and/or calcareous mudstones. These three formations contain sandstone members described as deep-water turbidite lobe complexes similarly to the sandy deep-water turbidite members observed in the Cromer Knoll Group.

In term of tectonic activity, the Norwegian Sea and principally the terrace domain was subjected to an extensional phase (rifting episode) between the Middle Bathonian and the Late Berriasian (Viking Group) (Chapter 2). The pre-rift (Fangst Group) and the post-rift periods (Cromer Knoll and Shetland groups) are generally linked to a period of tectonic quiescence and regional subsidence (Brekke, 2000; Færseth and Lien, 2002; Tsikalas et al., 2012; Peron-Pinvidic and Osmundsen, 2018). The rift-sag phase is a transitional period where only master faults will observe fault displacements. However, during this phase, sag-type basins will develop. The aforementioned sub-stages in Fig. 4.Ab (i.e., Rift-initiation; Rift-climax; Final rift stage; Early rift-sag; Late rift-sag; Early post-rift and late post-rift) have been identified based on seismic, well-log, biostratigraphy and core data.

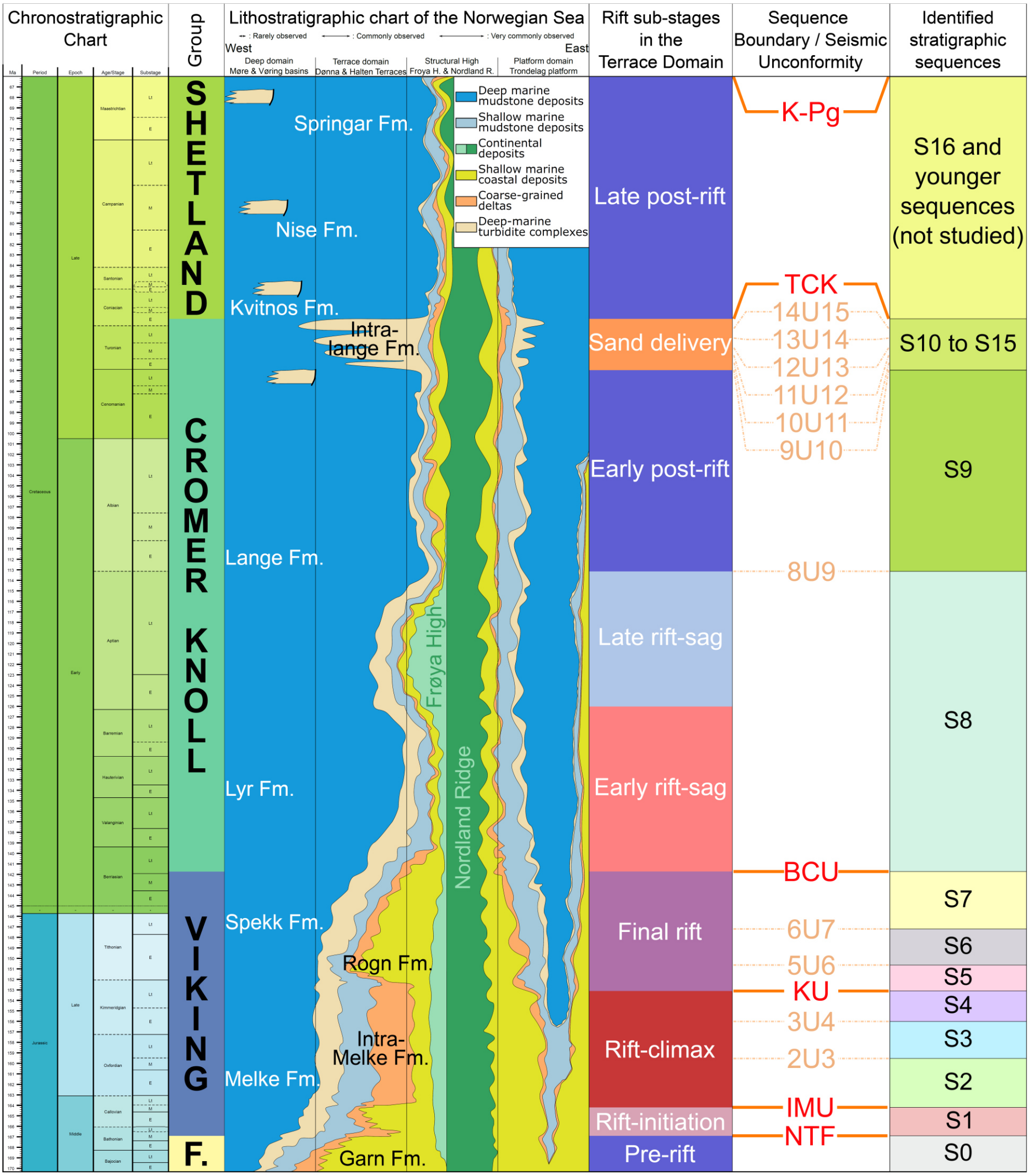

Fig. 4.Ab: The Norwegian Sea syn-rift to post-rift transition chart with the first column corresponding to the chronostratigraphic chart (imported from TS Creator and based on (Ogg et al., 2016)); the second column is the geological groups; the third column corresponds to the lithostratigraphic chart after Dalland et al. (1988), Gradstein and Waters (2016) and this PhD research; the fourth, fifth and last columns highlight the rift sub-stages identified in this PhD research (Chapters 2, 3 and 4), the identified sequence boundaries and their associated seismic unconformities, and the identified stratigraphic sequences.

8. Supplementary data 4.B: Syn-rift seismic patterns

- Syn-rift seismic patterns

The seven Middle Jurassic to lowermost Cretaceous stratigraphic sequences (S1 to S7 in Fig. 4.Ab), identified within the Viking Group in the southern Halten Terrace (Chapter 2), have been grouped based on their stacking pattern trends (progradational, aggradational and retrogradational) as observed on seismic data (Fig. 4.Ba). The following description presents the seismic pattern trend of the entire syn-rift episode from the oldest seismic pattern trend group to the youngest.

- Predominately prograding seismic pattern trend (Sequence 1: Rift initiation)

Seismic Sequence 1 (Fig. 4.Ba-A) is bounded by two major discontinuities: at the base, the "Near Top Fangst" (NTF); and, at the top, the Intra-Melke Unconformity (IMU) (Fig. 4.Ab). Seismic Sequence 1 is heavily eroded, erasing the upper parasequence sets. A total of 6 parasequence-set seismic pattern trends have been observed (Fig. 4.Ba-B). From the seismic line (Fig. 4.Ba-A), the main seismic pattern of the rift initiation stage (Sequence 1) is a progradational trend (Figs. 4.Ba-C, 4.Ba-D).

- Predominately aggrading seismic pattern trend (Sequence 2, 3 & 4: Rift-climax)

The rift-climax stage is defined by Sequences 2, 3 and 4 (Chapter 2). Sequence 2 is bounded at the base by the Intra-Melke Unconformity (IMU), and Sequence 4 is bounded at the top by the Kimmeridgian Unconformity (KU) (Fig. 4.Ab). The rift-climax highlights a seismic pattern trend that is mostly aggrading (Fig. 4.Ba).

- Predominately retrograding seismic pattern trend (Sequence 5, 6 & 7: Final rift stage)

The final rift stage presented in *Chapter 2*, is composed of Sequences 5, 6 and 7 (Fig. 4.Ab). The final rift stage is bounded at the base by the Kimmeridgian Unconformity (KU), and at the top by the Base Cretaceous Unconformity (BCU). From the seismic line (Fig. 4.Ba-A), the main seismic pattern of the final rift stage (Sequences 5, 6 and 7) has a retrogradational trend (Figs. 4.Ba-C, 4.Ba-D).

Fig. 4.Ba: Seismic pattern trend analysis: (A) Seismic line with observed seismic pattern trends for each identified seismic sequence, question marks highlight the uncertainty of the interpretation, the location of the line is shown in Fig. 4.Aa-C. (B) Example of the calculation of the mean seismic pattern trend for sequence S1 that is highly eroded. (C) Seismic pattern trend diagram and the mean seismic pattern trend for the 7 sequences. (D) Seismic pattern trend evolution of the 7 sequences and the associated seismic pattern trend group associated with sequence number and to the chronostratigraphic chart imported from TS Creator and based on (Ogg et al., 2016).

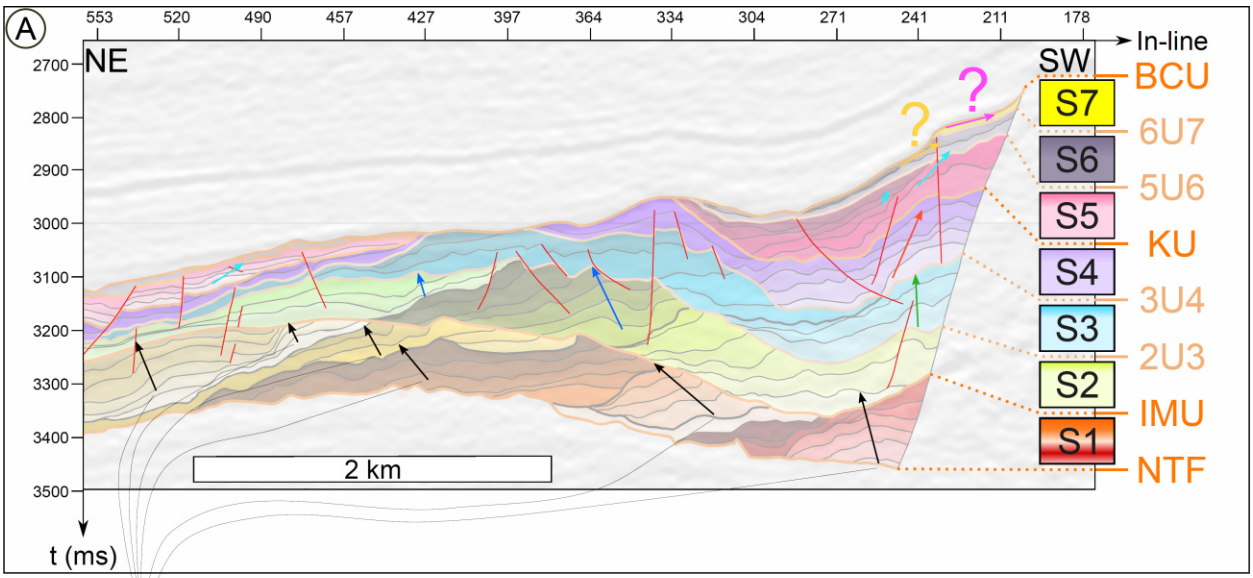
A
553 520 490 457 427 397 364 334 304 271 241 211 178
In-line
NE
SW
2700
2800
2900
3000
3100
3200
3300
3400
3500
2 km
t (ms)
S7
S6
S5
S4
S3
S2
S1
BCU
6U7
5U6
KU
3U4
2U3
IMU
NTF

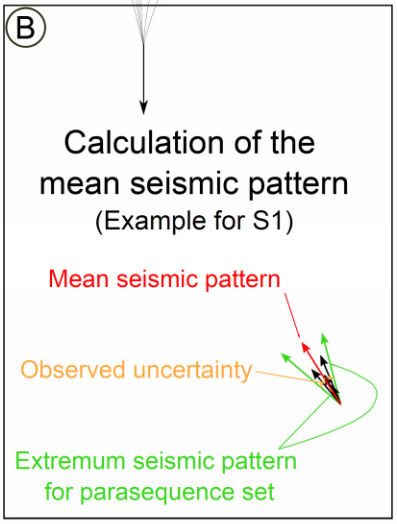
B
Calculation of the mean seismic pattern
(Example for S1)
Mean seismic pattern
Observed uncertainty
Extremum seismic pattern for parasequence set

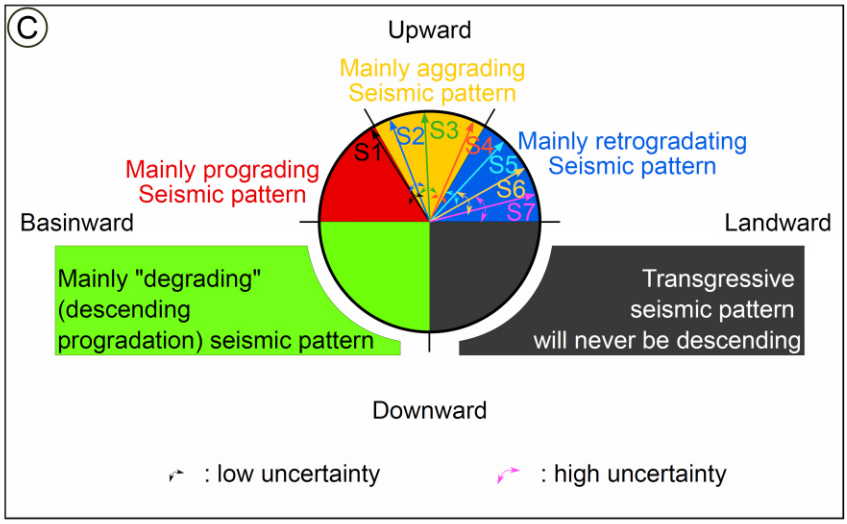
C
Upward
Mainly aggrading Seismic pattern
Mainly retrogradating Seismic pattern
Mainly prograding Seismic pattern
Basinward
Landward
Mainly "degrading" (descending progradation) seismic pattern
Transgressive seismic pattern will never be descending
Downward
: low uncertainty
: high uncertainty

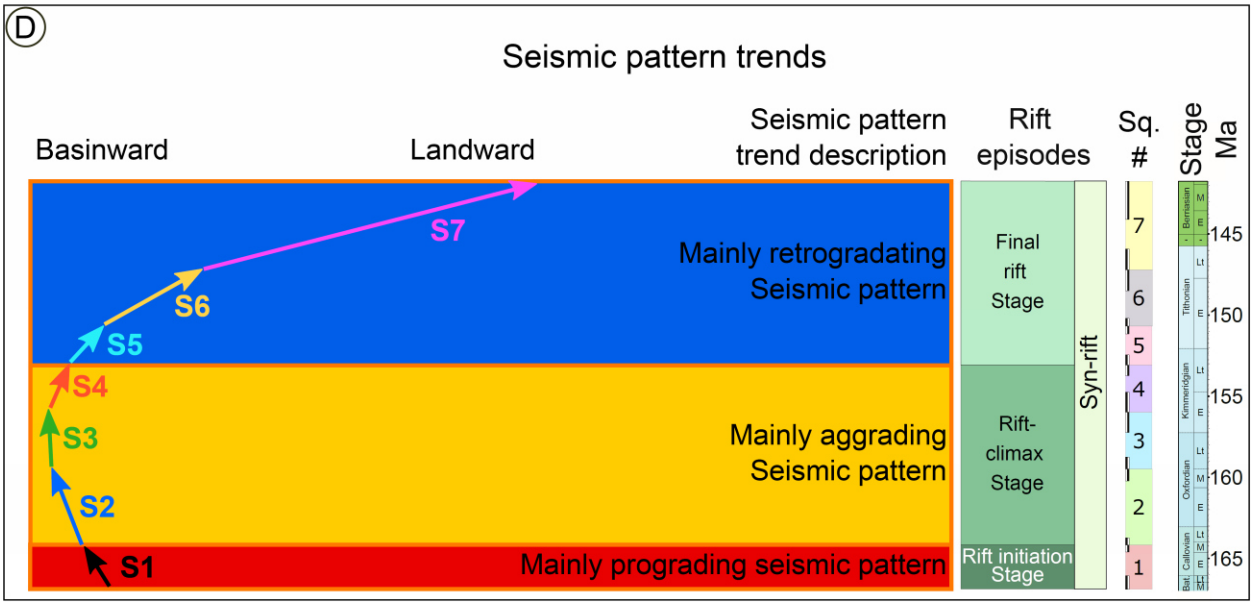
D
Seismic pattern trends
Basinward
Landward
Seismic pattern trend description
Rift episodes
Sq. #
Stage
Ma
Mainly retrogradating Seismic pattern
Mainly aggrading Seismic pattern
Mainly prograding seismic pattern
Final rift Stage
Rift-climax Stage
Rift initiation Stage
Syn-rift
145
150
155
160
165

9. Supplementary data 4.C: Post-rift seismic sequences – Part A

- Post-rift seismic sequences

In the post-rift study, the line presented in *Chapter 3* highlights the development of major sandy deep-water turbidite deposits (Fig. 4.Ca-A). Based on seismic data tied to the well and core data, 8 sequences have been identified in the Cromer Knoll Group (S8 to S15) (Figs. 4.Ab, 4.Ca, 4.Cb and Supplementary data 4.D).

The pre-existing Jurassic syn-rift palaeotopography plays a major role, with tilted fault blocks formed during the syn-rift period controlling the deposition of Cretaceous sequences. Sequence 8 fills pre-existing structural lows. Note that S8 has not been observed on the structural highs implying a structural control during the deposition (Figs. 4.Ca, 4.Cb). Sequences 9 to 15 correspond to a passive infill of the Norwegian Sea. It is important to note that the Nordland Ridge was subaerially exposed during the entire Cromer Knoll period (Figs. 4.Ca-A, 4.Cb). The majority of faults in the area appear to be inactive post SB #7 (Figs. 4.Ca-A, 4.Cb) corresponding to the Base Cretaceous Unconformity (BCU). However, some master faults such as the one located SE of well 6507/7-12 (Fig. 4.Cb) seem to be active during the deposition of S8. The westernmost fault in *Fig. 4.Ca-A* can be interpreted to have been active between S8 and S15, but it is most probably the result of differential subsidence mainly caused by pre-existing syn-rift structures. The seismic line A in *Supplementary data 4.D* suggests that major faults are still active during the deposition of S8. The first seismic line presented in *Supplementary data 4.D* highlights some extensional activity during S13 to early S16 (Figs. 4.Da, 4.Db, 4.Dc in *Supplementary data 4.D*) in the western area. The second seismic line presented in *Supplementary data 4.D* (Figs. 4.Dd, 4.De, 4.Df in *Supplementary data 4.D)* exhibits a differential filling of S8 in structural lows such as between lines 21350 and 21500 (a set of several seismic reflectors onlapping the BCU (SB #7)), whereas S9 to S15 exhibit a passive filling of the basin.

In conclusion, tectonic activity is weak during the Cretaceous (sequences S8 to S16). Some extensional activity localised along major syn-rift faults appears to operate until the end of Sequence 8. The deposition of Sequence 8 smooths up the palaeotopography by infilling structural lows while no deposition occurred on structural highs. Sequences 9 to 15 mainly exhibit a passive infill with rare tectonic activity. Observed tectonic activity can be related to differential subsidence between intraterrace highs and intraterrace lows.

Fig. 4.Ca: Semi-regional seismic line taken from the 3D seismic "Spectrum mega merge" survey (A) Uninterpreted line; (B) Interpreted line, highlighting the different geological groups (Viking Group or older in blue, in green the Cromer Knoll Group with the studied sandstones and the Sheltland and younger groups in light grey); (C) Interpreted line showing the stratigraphic sequences identified within the Cromer Knoll Group. The 3 wells (6507/2-2, 6507/2-3 and 6507/3-3) have been tied to the seismic using checkshot data. Fault sticks are in white colour. Structural elements (SF, SL and SH) defining a basin or sub-basin have been highlighted. See Fig. 4.Aa-B for location.

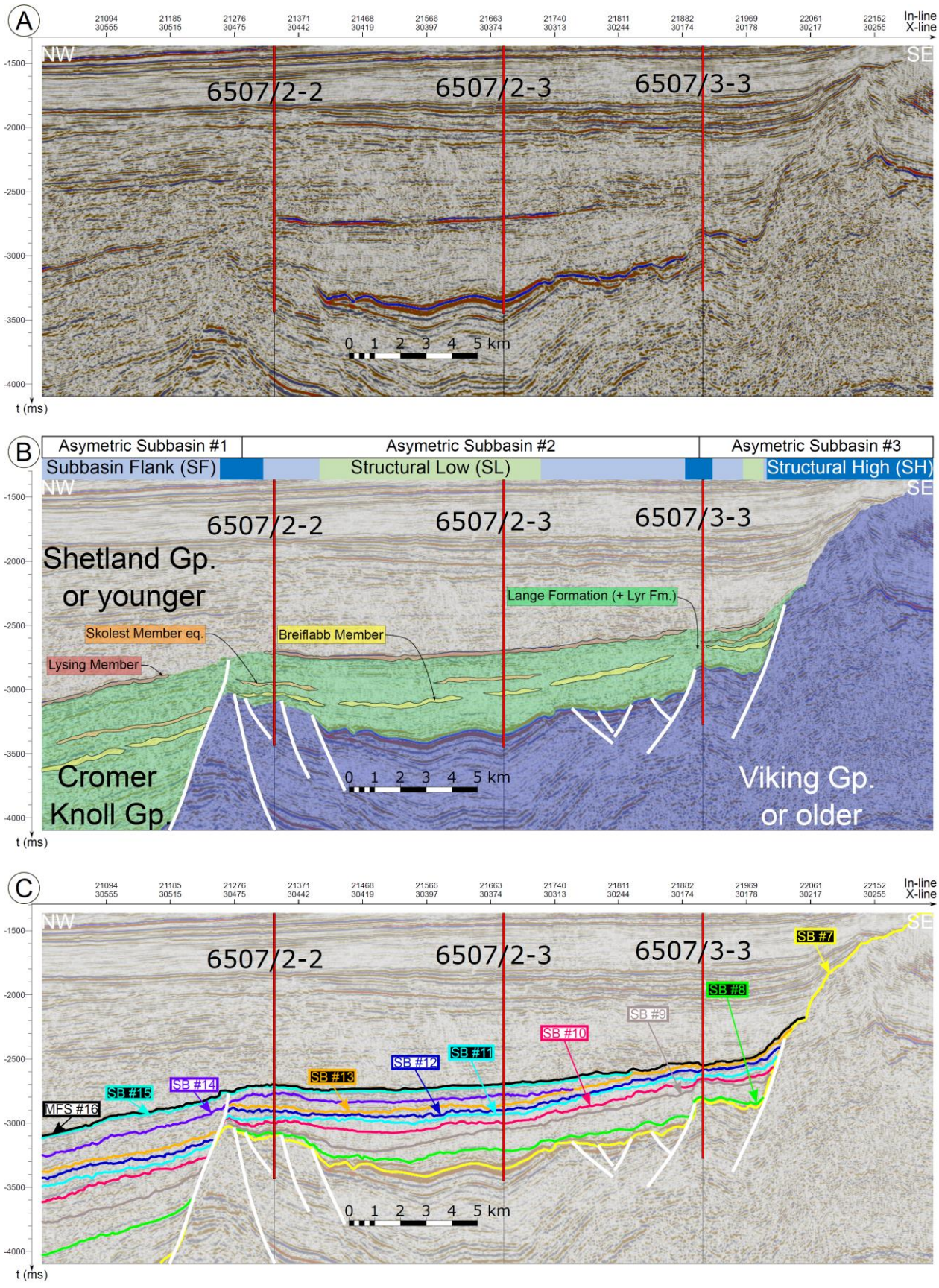
A
In-line
X-line
NW
SE
6507/2-2
6507/2-3
6507/3-3
0 1 2 3 4 5 km
t (ms)
B
Asymetric Subbasin #1
Asymetric Subbasin #2
Asymetric Subbasin #3
Subbasin Flank (SF)
Structural Low (SL)
Structural High (SH)
Shetland Gp.
or younger
Lange Formation (+ Lyr Fm.)
Skolest Member eq.
Breiflabb Member
Lysing Member
Cromer
Knoll Gp.
Viking Gp.
or older
C
SB #7
SB #8
SB #9
SB #10
SB #11
SB #12
SB #13
SB #14
SB #15
MFS #16

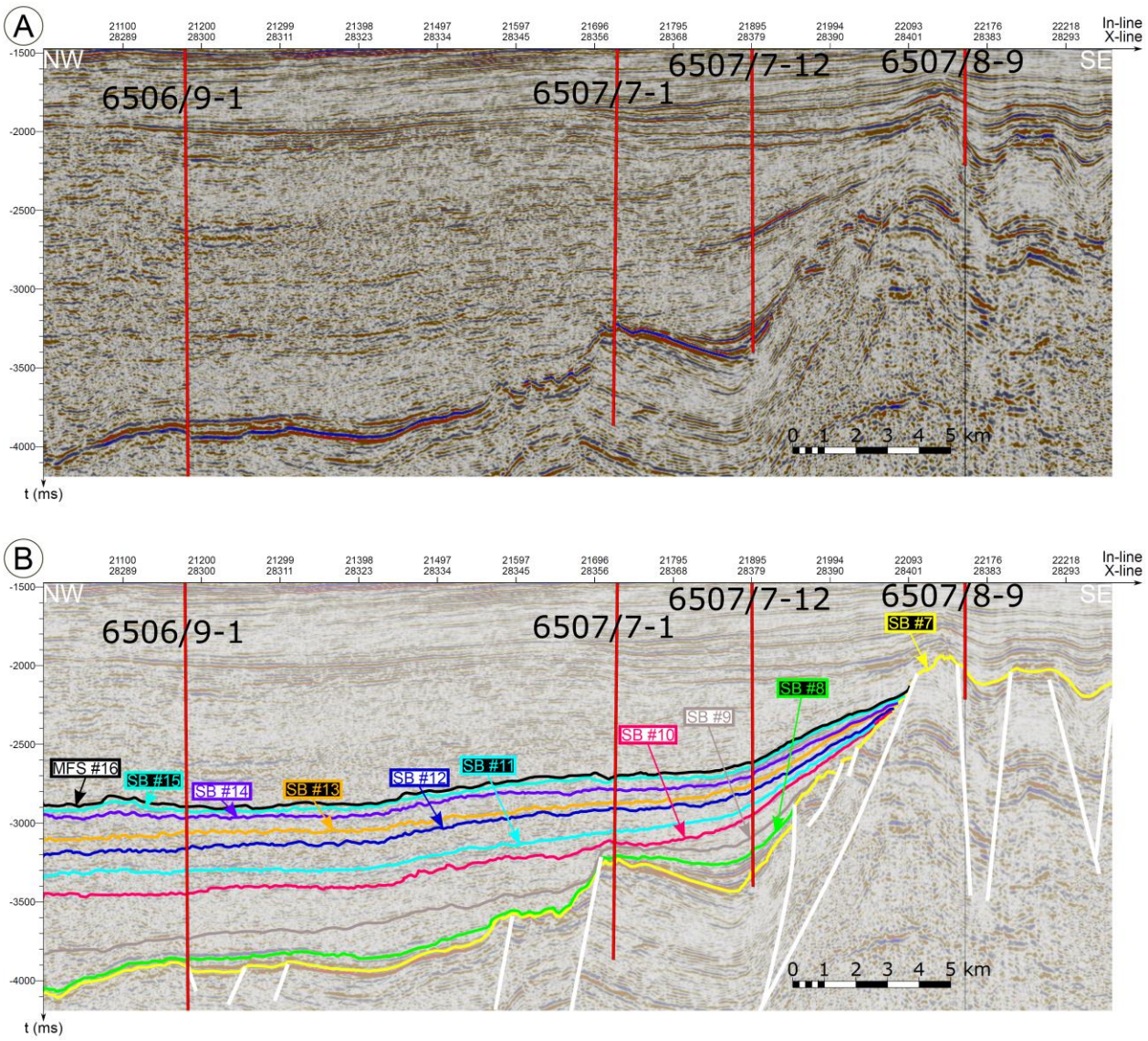

Fig. 4.Cb: Semi-regional seismic line taken from the 3D seismic "Spectrum mega merge" survey (A) Uninterpreted line; (B) Interpreted line, showing the stratigraphic sequences identified within the Cromer Knoll Group. The 4 wells (6506/9-1, 6507/7-1, 6507/7-12 and 6507/8-9) have been tied to the seismic using checkshot data. Fault sticks are in white colour. See Fig. 4.Aa-B for location.

10. Supplementary data 4.D: Post-rift seismic sequences – Part B

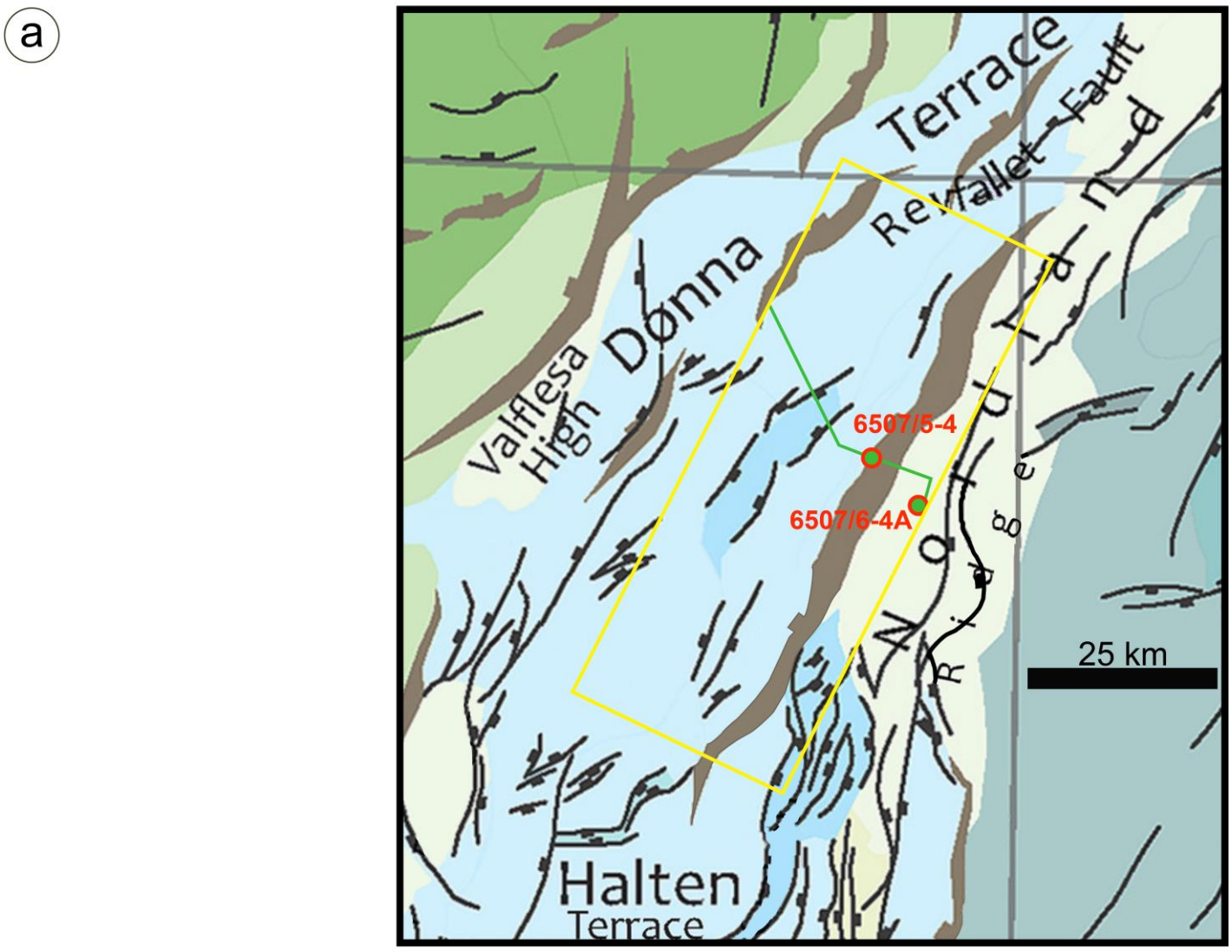

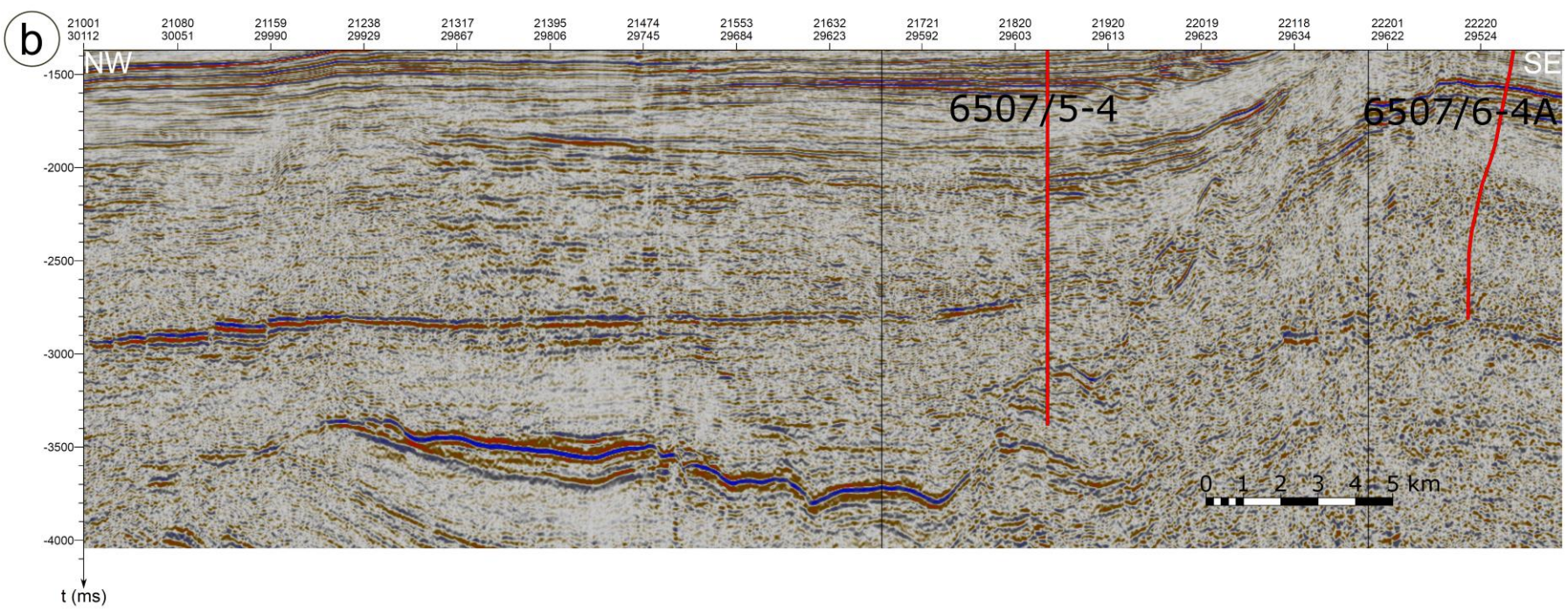

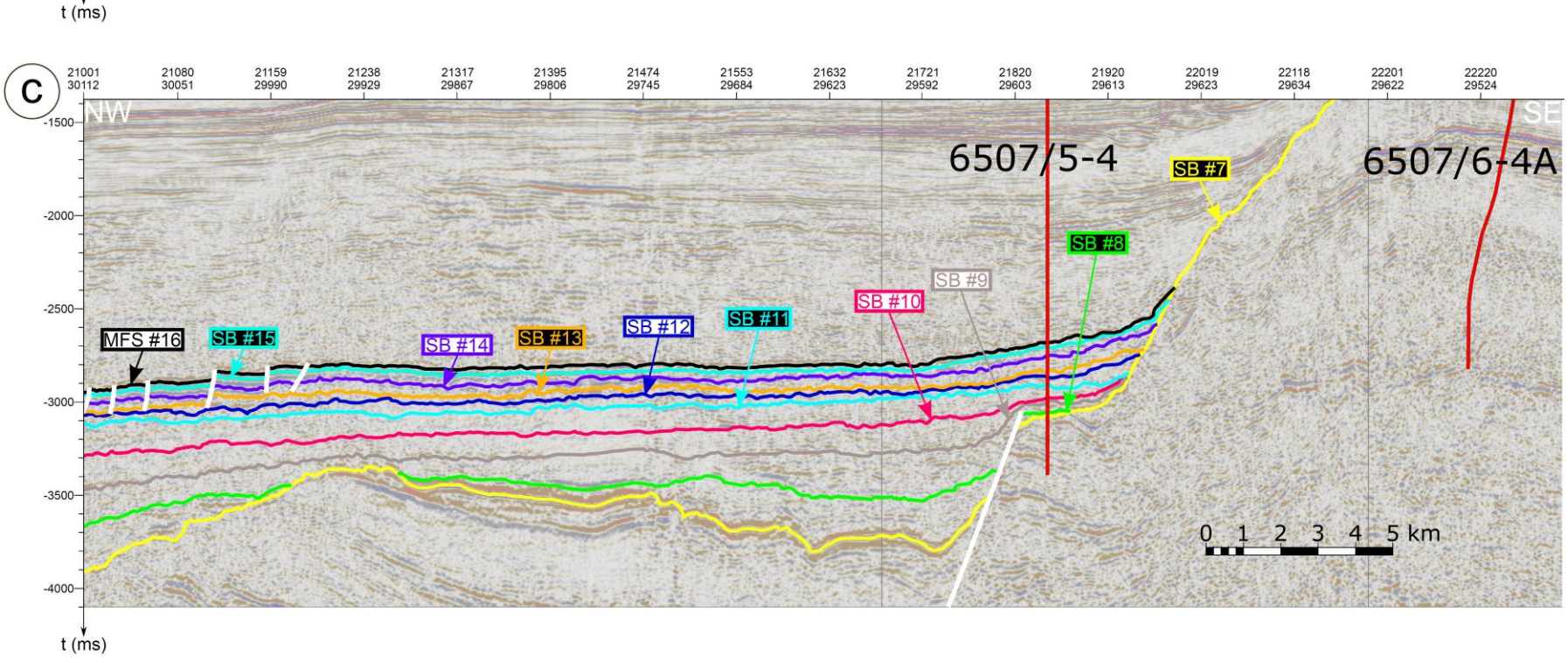

Fig. 4.D: Semi-regional seismic line taken from the 3D seismic "Spectrum mega merge" survey (a) line location; (b) uninterpreted line; (c) interpreted line, showing the stratigraphic sequences identified within the Cromer Knoll Group. The 2 wells (6507/5-4 and 6507/6-4A) have been tied to the seismic using checkshot data. Fault sticks are in white colour…

d

Fig. 4.D (continued): ... Semi-regional seismic line taken from the 3D seismic "Spectrum mega merge" survey (d) line location; (e) uninterpreted line; (f) interpreted line, showing the stratigraphic sequences identified within the Cromer Knoll Group. The 2 wells (6507/5-3 and 6507/5-7) have been tied to the seismic using checkshot data. Fault sticks are in white colour.

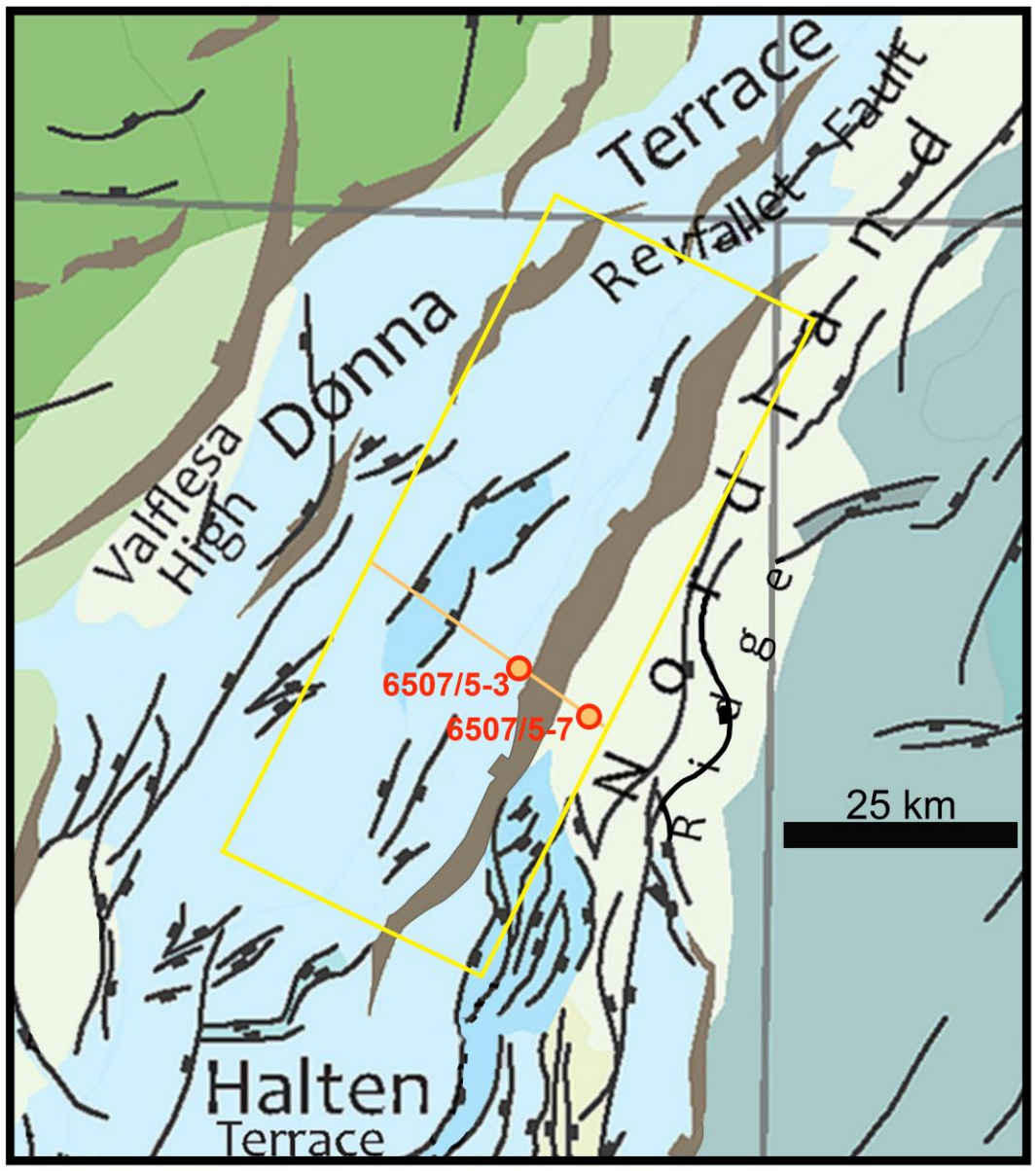

e

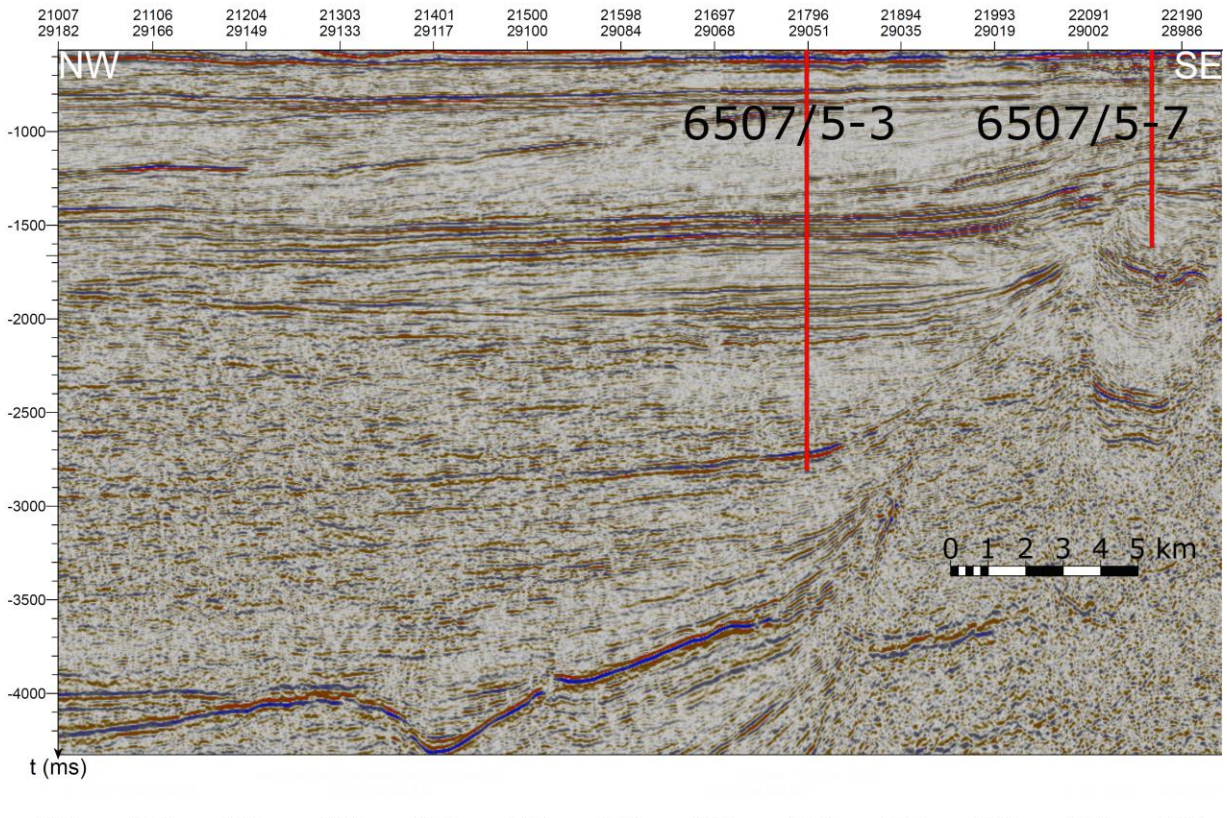

f

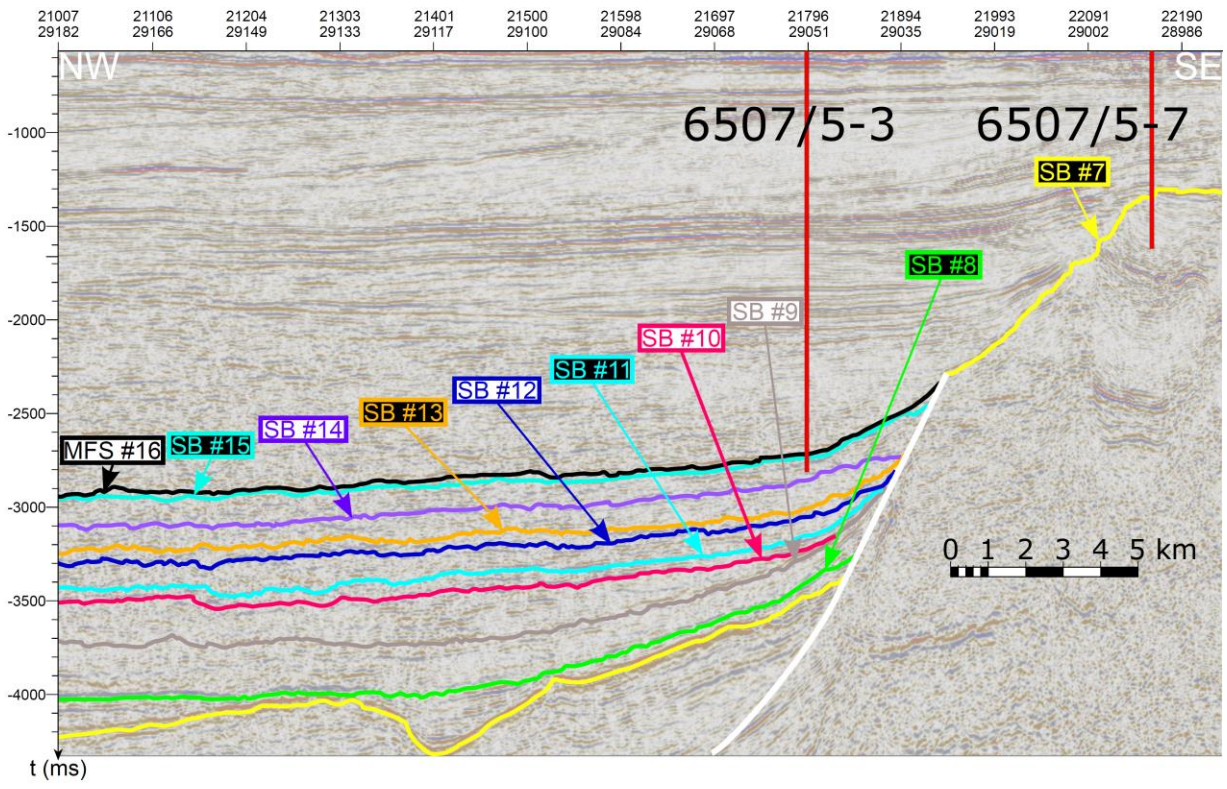

11. Supplementary data 4.E: Sedimentary facies and associated depositional environments – Part A

- Sedimentary facies

In the two previous chapters (Chapter 2 and Chapter 3), facies description and depositional models have been presented in detail. In this section, based on the description of more than 1.5 km of sediment core including the cores described in *Chapter 2* and *Chapter 3*, a summary of the facies observed in the Norwegian Sea for the Viking Group and the Cromer Knoll Group is provided, along with a summary of the interpreted depositional environments. Then a summary of the interpreted deposition environments. This section is further complemented by the *Supplementary data 4.F* where a detailed core description and a detailed depositional model analysis is presented. Moreover the *Table 4.Fa* in *Supplementary data 4.F* outlines raw core descriptions studied during this PhD research.

This detailed core description at 1:100 to 1:1000 scale for the Viking and Cromer Knoll groups throughout the entire Norwegian Sea enabled the identification of 16 sedimentary facies with C1 to C5 corresponding to coastal deposits, with O1 to O2 corresponding to offshore deposits, and nine other facies (Hy1, Hy2, Co1, Tu1, Tu2, Sl1; De1, Df1 and Un1) corresponding to subaqueous sedimentary density flow (SSDF) facies (Table 4.Ea). Facies described in the 2 previous chapters are summarised on *Table 4.Ea*. For more detail regarding facies description, *Chapter 2*, *Chapter 3* and *Supplementary data 4.F* can be used as complementary materials.

Facies O1 consists predominantly of a structureless dark grey mudstone (Table 4.Ea, Fig. 4.Ea-I). O1 commonly exhibits intense bioturbation.

Facies O2 is formed from an alternation of millimetric siltstone laminae to fine-grained sandstone laminae with muddy to silty intervals (Table 4.Ea, Fig. 4.Ea-H). The silty to sandy laminae can exhibit parallel-laminations and cross-laminations. Bioturbation is highly present.

Facies C1 consists of a very fine- to fine-grained sandstone with the sporadic presence of angular coarse sand clasts (Table 4.Ea, Fig. 4.Ea-G). Small-scale cross-laminations, undulating to curved laminations, angular to horizontal planar laminations are present. C1 is characterised by intense bioturbation.

Facies C2 consists of fine- to medium-grained sandstones with the sporadic presence of angular coarse sand clasts (Table 4.Ea, Fig. 4.Ea-F). Sub-horizontal to horizontal plane-parallel laminations with some small- to large-scale SCS and HCS structures are present (Fig. 4.Ea-F). C2 has a moderate degree of bioturbation.

Facies C3 consists of a medium-grained sandstone with the sporadic presence of angular granules (Table 4.Ea, Fig. 4.Ea-E). Sub-horizontal to horizontal plane-parallel laminations and SCS (swaley cross-stratification) are commonly observed. Coal fragments can be present, and the degree of bioturbation is relatively low.

Facies C4 consists of a medium to coarse-grained sandstone with the presence of polygenic granules and pebbles (Table 4.Ea, Fig. 4.Ea-D). Parallel laminations of high-angle cross bedding are commonly observed. Bioturbation is absent and plant debris is noted in C4.

Facies C5 is the only facies which has not been observed in any of the previous chapters. Facies C5 consists of a light beige, yellowish to light orange fine to medium-grained sandstone (Table 4.Ea, Figs. 4.Ea-A, 4.Ea-B, 4.Ea-C). C5 commonly contains very coarse to fine pebbles with a sub-angular to rounded shape. Roots, belemnites and plant debris are commonly present in C5 (Fig. 4.Ea-A). Large foreset beds can be observed but are not frequently preserved (Fig. 4.Ea-B). C5 sandstone can be unconsolidated and composed of intervals rich in vegetal materials (Fig. 4.Ea-C).

Facies Hy1 consists of a structureless and very poorly sorted grain-supported conglomerate with angular clasts (Table 4.Ea, Fig. 4.Ea-J). Hy1 commonly exhibits inverse grading and a slightly erosional base. Hy1 can measure from 20 cm up to 3 m.

Facies Hy2 consists of a massive and structureless coarse- to very coarse-grained sandstone (Table 4.Ea, Fig. 4.Ea-K). The base of Hy2 is frequently erosional. Hy2 commonly presents inverse grading and can measure from 10 cm up to 1.05 m. A continuum flow transformation from Hy1 facies to Hy2 facies is frequently observed (Fig. 4.Eb – column #2).

Facies Co1 consists of very coarse-grained sandstone fining upward to fine-grained sandstone and exhibits normal grading (Table 4.Ea, Fig. 4.Ea-L). The base of Co1 is strongly erosional (Fig. 4.Ea-L). Upper sedimentary structures are commonly plane parallel laminations. Co1 can measure from 1 cm up to 0.95 m. A continuum flow transformation from Hy2 facies to Co1 facies is commonly observed (Fig. 4.Eb – column #4).

Facies Tu1 consists of medium-grained sandstones fining upward to siltstones (Table 4.Ea, Fig. 4.Ea-O). Tu1 has a sharp to erosional base. Tu1 facies commonly exhibits normal grading, plane-parallel laminations, current ripples, trough cross-beddings and sinusoidal to wavy laminations (Fig. 4.Ea-O). Tu1 can measure from 1 mm up to 30 cm. The most common observed flow transformation is between Co1 and Tu1 facies (Fig. 4.Eb – column #8).

Facies Tu2 alternates between fine to very fine-grained sandstone laminae (<1 mm up to 2 cm) and finer siltstone to mudstone laminae (<1 mm up to 2 cm) (Table 4.Ea, Figs. 4.Ea-P, 4.Ea-R, 4.Ea-S). Tu2 commonly exhibits parallel laminations, sinusoidal laminations and supercritical climbing-ripples (*sensu* Storms et al. (1999)) (Figs. 4.Ea-P, 4.Ea-R, 4.Ea-S). Tu2 can measure from 1 cm up to 1.17 m. Df1 frequently transforms to Tu2 facies (Fig. 4.Eb – column #14).

Facies Sl1 consists of very fine- to medium-grained sandstones (Table 4.Ea, Fig. 4.Ea-P). The base of Sl1 is commonly erosional. Sl1 exhibits dish structures, banded sandstones, wispy lamination (*sensu* Lowe and Guy (2000)), vertical escape features and convolute laminations. Sl1 can measure from 1 cm up to 4.25 m. Tu1 commonly transforms to Sl1 facies (Fig. 4.Eb – column #10).

Facies De1 consists of conglomeratic mudstones (Table 4.Ea, Figs. 4.Ea-M, 4.Ea-N). De1 can measure from 1 cm up to 70 cm. The most common observed flow transformation is

between Co1 and the first type of De1 facies (Fig. 4.Eb – column #6). However, flow transformation between Hy1 to De1 (first type) and between Hy2 to De1 (first type) have also been observed.

Facies Df1 consists of structureless and chaotic sandy mudstones to muddy sandstones (Table 4.Ea, Fig. 4.Ea-Q). Df1 contains sand injectites, pseudonodules and elongated mudstone clasts. Df1 can measure from 1 cm up to 2.12 m. Sl1 commonly evolves to Df1 facies (Fig. 4.Eb – column #12).

Facies Un1 consists of a highly bioturbated siltstone to fine-grained sandstone with no visible sedimentary structures (Table 4.Ea, Fig. 4.Ea-T).

	Offshore facies		Coastal sedimentary facies					Gravity-driven facies								
Facies name	**O1**	**O2**	**C1**	**C2**	**C3**	**C4**	**C5**	**Hy1**	**Hy2**	**Co1**	**De1**	**Tu1**	**Sl1**	**Df1**	**Tu2**	**Un1**
Interpreted deposit or flow type	Distal offshore	Proximal offshore	Lower shoreface	Middle shoreface	Upper shoreface	Foreshore	Backshore	Hyper-concentrated density flow *sensu stricto*	Grain-flow	Concentrated density flow	Debris flow type 1	Turbidity flow type 1	Slurry flow	Debris flow type 2	Turbidity flow type 2	Undefined flow type
Shallow marine sedimentary succession		Proximal offshore	Wave-dominated shorefaces and beaches					Subaqueous delta-scale clinoforms								
Deep marine sedimentary succession	Distal offshore							Rarely observed in Deep-water turbidite complexes (< 5%)				Deep-water turbidite complexes (> 95%)				

Table 4.Ea: Facies summary table highlighting the sixteen facies which contribute to interpret depositional environments. This facies summary table can be used as a correspondent table between the syn-rift and post-rift studies (Chapter 2 and Chapter 3).

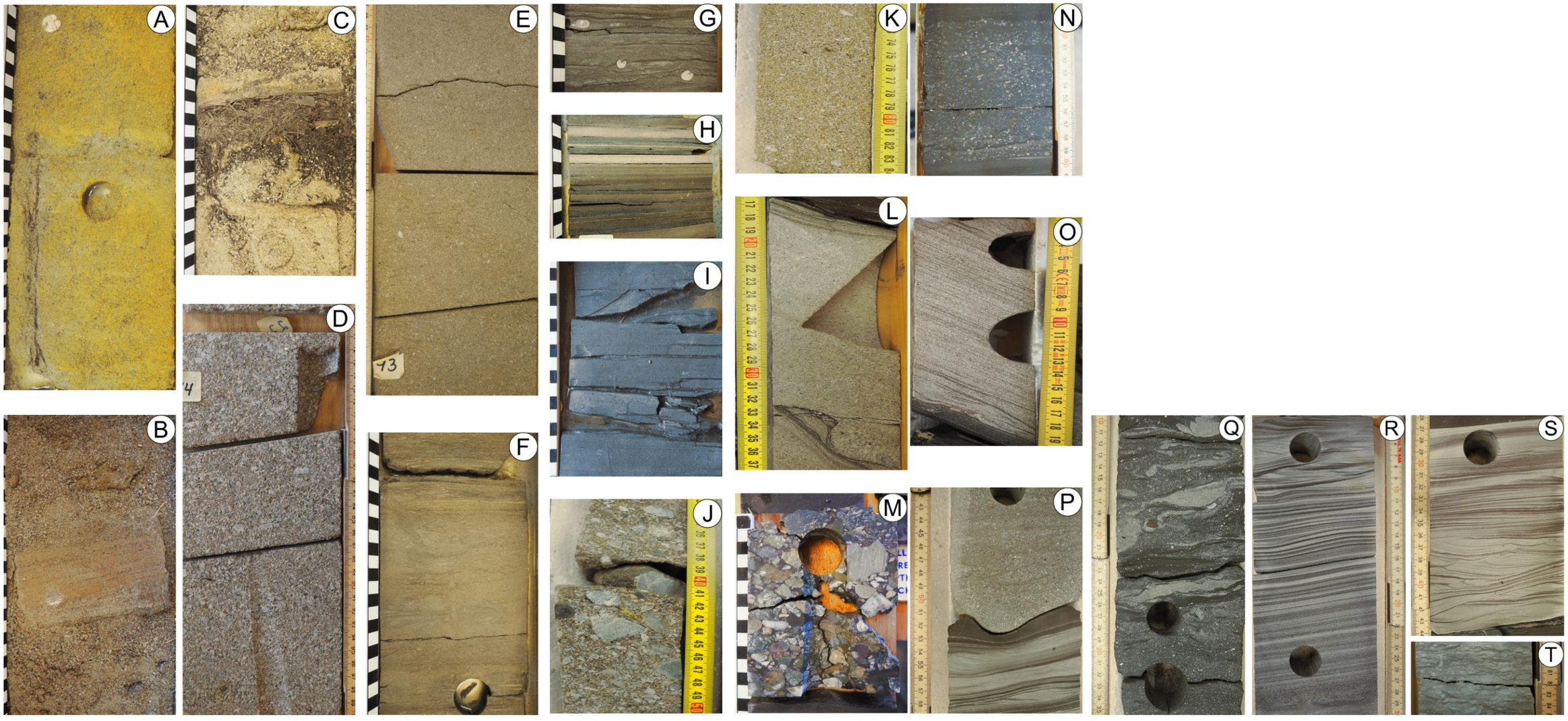

Fig. 4.Ea: Facies description summary. Facies C5 is characterised by roots, belemnites (A), large foreset beds (B) and composed of intervals rich in vegetal material (C). Facies C4 consists of medium to coarse-grained sandstone with intervals rich in angular to very angular polygenic granules to pebbles (D). Facies C3 is characterised by a medium-grained sandstone with a relatively low degree of bioturbation (E), whereas C2 is characterised by a fine- to medium-grained sandstone with a moderate degree of bioturbation (F). C1 consists of a very fine- to fine-grained sandstone with a high degree of bioturbation and the presence of belemnites (G). Conversely, O2 is formed from an alternation of millimetric siltstone laminae to very fine- to fine-grained sandstone laminae with muddy to silty intervals (H). O1 corresponds to a structureless dark grey mudstone (I). Hy1 consists of a structureless and very poorly sorted grain-supported conglomerate (J), whereas Hy2 is characterised by a massive and structureless coarse- to very coarse-grained sandstone (K). Co1 is formed of a very coarse-grained sandstone fining upward to fine-grained sandstone and exhibits normal grading (L). De1 is characterised by a conglomeratic mudstone which can be unsorted and structureless (M), or composed of clasts not larger than a granule and can present a normal grading (N). Facies Tu1 consists of medium-grained sandstone fining upward to siltstone and commonly exhibits plane-parallel laminations, current ripples, trough cross-beddings and sinusoidal to wavy laminations (O). Facies Sl1 is characterised by very fine- to medium-grained sandstone exhibiting primary structures such as dish structures, banded sandstones and wispy lamination (P). Facies Df1 consists of structureless and chaotic sandy mudstones to muddy sandstones (Q). Facies Tu2 is characterised by fine- to very fine-grained sandstone alternating between fine to very fine-grained sandstone laminae and finer siltstone to mudstone laminae exhibiting parallel laminations, sinusoidal laminations and supercritical climbing-ripples (P, R and S). Facies Un1 consists of a highly bioturbated siltstone to fine-grained sandstone with no identifiable sedimentary structures (T). Black and white rectangles represent the vertical scale in centimetres.

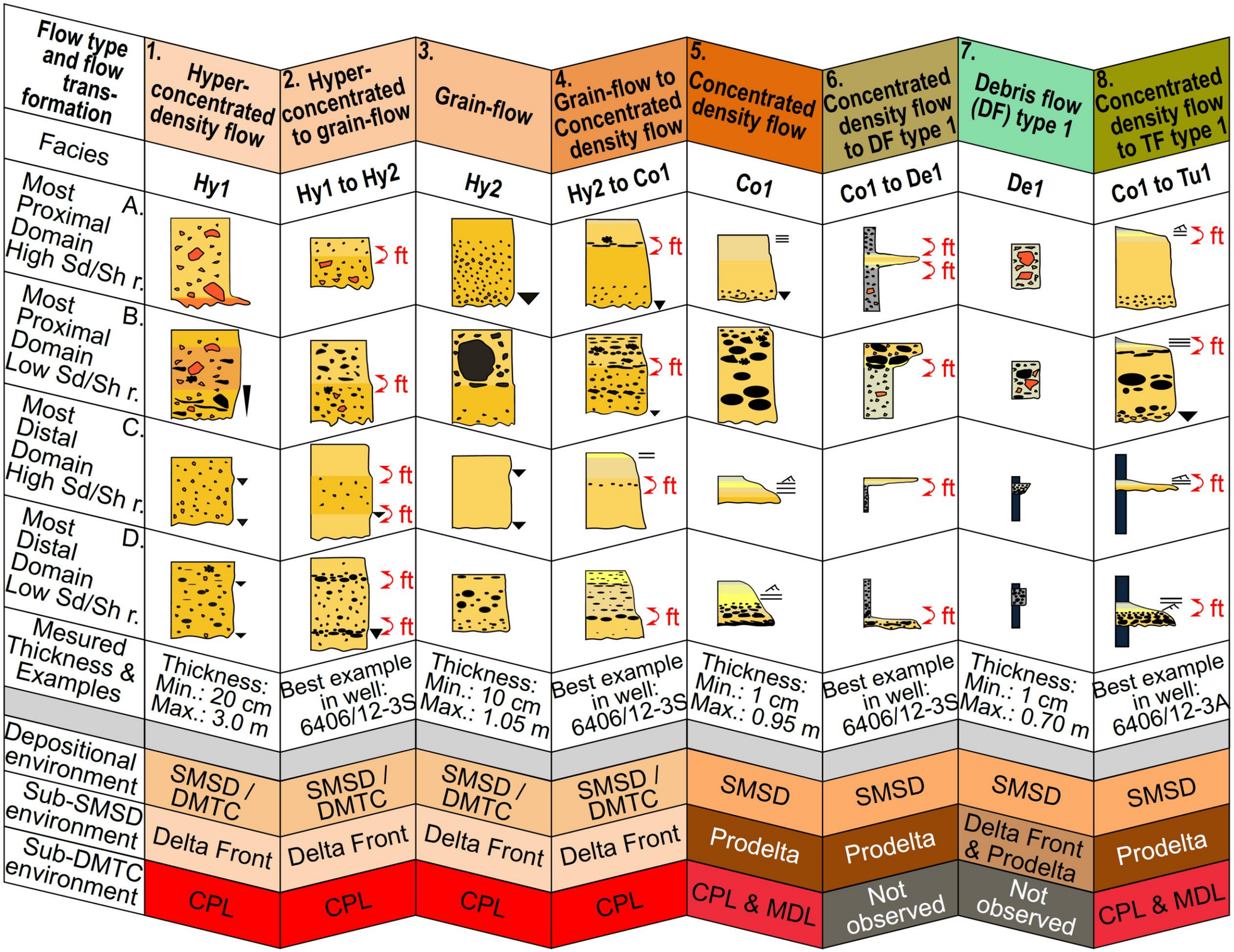

Fig. 4.Eb: Flow transformation diagram highlighting the most observed flow transformations (ft) in this PhD research. Abbreviations in the row "Flow type and flow transformation" are DF for "Debris Flow" and TF for "Turbidity Flow". The second row "Facies" corresponds to the facies presented in Fig. 4.Ea. The rows #3, #4, #5 and #6 correspond to some synthetic logs in a proximal or distal domain with a high or low sand- shale ratio (Sd/Sh r.). The row "Measured thickness & examples" highlights the minimum (min.) and maximum (max.) observed thickness for each flow facies column; whereas, this row shows, for the flow transformation columns where this kind of flow transformation is commonly observed on core…

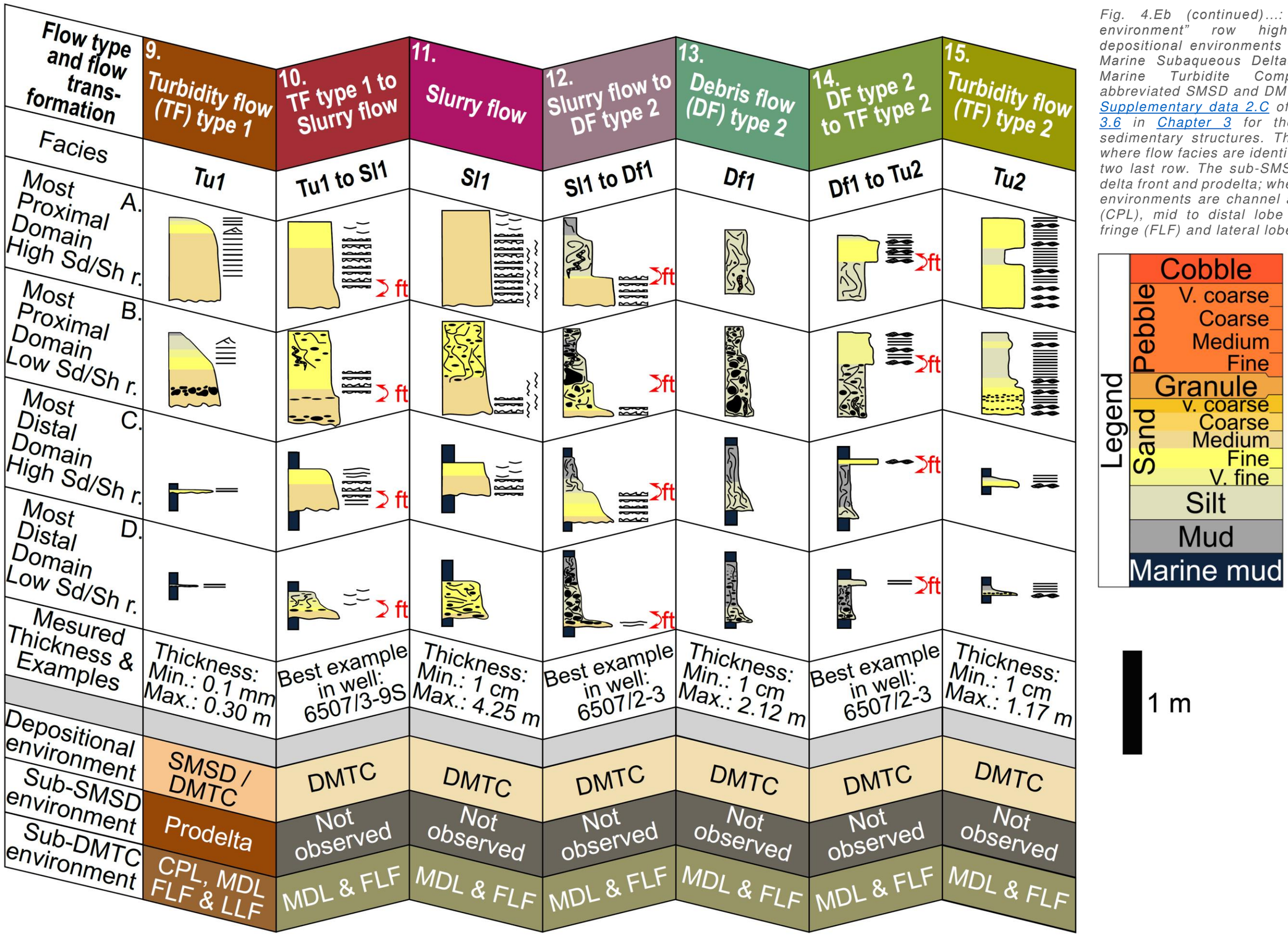

Fig. 4.Eb (continued)…: The "Depositional environment" row highlights the major depositional environments which are "Shallow-Marine Subaqueous Deltas", and the "Deep-Marine Turbidite Complex", respectively abbreviated SMSD and DMTC. See Fig. 2.Ca in Supplementary data 2.C of Chapter 2 and Fig. 3.6 in Chapter 3 for the legend regarding sedimentary structures. The sub-environments where flow facies are identified, are found in the two last row. The sub-SMSD environments are delta front and prodelta; whereas, the sub-DMTC environments are channel and/or proximal lobe (CPL), mid to distal lobe (MDL), frontal lobe fringe (FLF) and lateral lobe fringe (LLF).

- SSDF facies, flow transformations and flow gaps
  - SSDF facies

The Norwegian Sea is an exceptional fossil laboratory for investigating gravity-driven deposits. The subaqueous sedimentary density flow (SSDF) facies have been interpreted in detail by describing more than 1.5 km of sediment core.

Clay content is one of the factors that can vary the sediment concentration which affects the nature of the flow. According to Mulder and Alexander (2001), particle concentration is commonly high (40-70%) for the hyperconcentrated density flow *sensu lato* this includes hyperconcentrated density flows *sensu stricto* (Hy1), grain-flows (Hy2) and slurry flows (Sl1). The concentrated density flow deposits (Co1) commonly have a medium sediment concentration (10-25%), whereas the turbidity flow deposits (Tu1 and Tu2) frequently have a low concentration of sediment (0- 10%). The cohesive flows (De1 and Df1) commonly have a wide range in sediment concentration (35 to 85%). This classification inside the non-cohesive flow (Mulder and Alexander, 2001) highlights, in the case of a decrease in sediment concentration, a continuum from a hyperconcentrated density flow *sensu lato* into a concentrated density flow, and then into a turbidity flow. Cohesive flows, have a wide range in sediment concentrations which reveal a progression to any of the non-cohesive flows, or vice-versa.

Starting with the non-cohesive flow deposits, Hy1 and Hy2 correspond to deposits from hyperconcentrated density flows *sensu lato*, with Hy2 interpreted being a grain-flow deposit and Hy1 a hyperconcentrated density flow deposit *sensu stricto* (Mulder and Alexander, 2001). Co1 corresponds to the Lowe sequence and is interpreted as deposition from a concentrated density flow. Tu1 consists of the Bouma sequence and is interpreted as a turbidity flow deposit (*sensu* Bouma (1962)) defined as “Turbidity flow type 1”. Sl1 is described as slurry flow deposit (*sensu* Lowe and Guy (2000)). Tu2 is described as sub- to super-critical turbidity flow deposit (*sensu* Alexander et al. (2001)) and named “turbidity flow type 2” (Table 4.Ea, Fig. 4.Eb).

Continuing with the cohesive flow deposits, two cohesive flows deposits have been identified, the “debris flow of type 1” (De1) and the “debris flow of type 2” (Df1). According to Mulder and Alexander (2001)‘s classification the “debris flow of type 1” (De1) corresponds to debris flow (*sensu stricto*) and the “debris flow of type 2” (Df1) corresponds to mud-flows. “Debris flow of type 2” is however defined by Lowe and Guy (2000) and Haughton et al. (2003, 2009) simply as a “debris flow”. To clarify these classifications, we define the two debris flow types as “debris flow of type 1” (De1) *sensu* Mulder and Alexander (2001) and “debris flow of type 2” (Df1) *sensu* Lowe and Guy (2000). As stated by Mulder and Alexander (2001), cohesive flows that include “debris flow of type 1” (De1) and “debris flow of type 2” (Df1) have boundary conditions ranging from 30 % to 90% of sediment concentration.

The slurry flow (Sl1) initially described as a turbidity flow deposit (Guy, 1992) is, in fact, a transitional flow between “turbidity flow of type 1” (Tu1) and “debris flow of type 2” (Df1) (Lowe and Guy, 2000; Haughton et al., 2003, 2009; Lowe et al., 2003) Lowe & Guy (2000) interpreted the sand content of the slurry flow to be between 65% to 90%. In the same way, Haughton et

al. (2003) proposed an overall sand content ranging from 70% to 90-95%. In those studies, slurry flow deposits have been observed with a high concentration of sandy sediment fluctuating between 65 to 90-95%. Based on this high concentration of sediment, slurry flows (Sl1) can be considered as a hyperconcentrated density flow sensu lato (ranging from 25% to 90-95%), as defined by Mulder and Alexander (2001). This can also explain some flow transformation passing from hyperconcentrated density flow *sensu stricto* (Hy1) or grain-flow (Hy2) into slurry flow (Sl1).

According to Mulder and Alexander (2001), the concentrated density flow (Co1), and the turbidity flow *sensu lato* (including turbidity flow of type 1 and 2 (Tu1 and Tu2)), have a sediment concentration of 10-40% and 0-10%, respectively. “Turbidity flow of type 1” (Tu1) and “turbidity flow of type 2” (Tu2) have similar sediment concentrations but have been disassociated in terms of flow behaviour. “Turbidity flow of type 1” (Tu1) is generated by a “normal” turbidity current whereas “turbidity flow of type 2” (Tu2) is caused by a sub- to supercritical turbidity current. “Turbidity flow of type 1” (Tu1) will correspond to the Bouma sequence (Bouma, 1962) whereas “Turbidity flow of type 2” (Tu2) will be composed of subcritical climbing ripples (Jobe et al., 2012), supercritical climbing-ripples (Storms et al., 1999) and sinusoidal lamination (Jobe et al., 2012) that are generally associated to non-uniformity in the flow that can occur due to loss in confinement, hydraulic jump and/or abrupt decrease in slope gradient (Jobe et al., 2012).

- Flow transformations
  - Main transformations

Between each SSDF facies (Hy1, Hy2, Co1, Tu1, Tu2, Sl1; De1 and Df1) excluding the highly bioturbated Un1 facies (that can be initially correspond as different SSDF types (Co1, Tu1, Tu2, Sl1 or Df1)), a clear continuum between deposits from different flow types was observed. Since we have distinguished two types of debris flows deposits (De1 and Df1) and two types of turbidity flow deposits (Tu1 and Tu2), it is now possible to observe a continuum between deposits of non-cohesive flows (Hy1, Hy2, Co1, Tu1, Tu2, Sl1) and cohesive flows (De1 and Df1). The most commonly observed flow transformations have been described in the flow transformation diagram (Fig. 4.Eb). However, the predicted SSDF facies succession allows us to decipher flow gaps due to the absence of some SSDF facies.

Inside the hyperconcentrated density flow *sensu lato* group (Hy1 and Hy2), a continuum has been clearly identified between hyperconcentrated density flow *sensu stricto* (Hy1) and grain-flow deposits (Hy2). Density flow concentration commonly tends to decrease, passing from hyperconcentrated density flow *sensu stricto* (Hy1) to grain-flow (Hy2), but we have observed the opposite in a more distal domain (Fig. 4.Eb – column #2-C, 2-D) where density flow concentrations appear to have increased. Density flow concentration increase are relatively rare and short-lived phenomena judging from deposit thicknesses ranging from a few centimetres to a few decimetres; hence they can be considered as density flow concentration pulses. Grain-flow deposits (Hy2) can evolve into concentrated density flow deposits (Co1) through a decrease in density flow concentration (Fig. 4.Eb – column #4). This last SSDF (Co1) commonly originates from a non-cohesive flow (Tu1), or from a cohesive flow deposit

(De1) (Fig. 4.Eb – column #6, 8). In turn, concentrated density flows deposits (Co1) form the flow type that most commonly evolves into to debris flows of type 1 deposit (De1). Commonly a thick debris flow deposits of type 1 (De1) will evolve for a few centimetres (< 10 cm) in a concentrated density flow (facies Co1 deposits) with very coarse to medium grains passing again to a debris flow of type 1 (De1) deposits (Fig. 4.Eb – column #6-A). However, debris flows of type 1 (De1) can evolve from hyperconcentrated density flows (facies Hy1 deposits), or grain-flows (facies Hy2 deposits), or concentrated density flows (facies Co1 deposits), as well as from turbidity flows of type 1 (facies Tu1 deposits).

Concentrated density flows (facies Co1 deposits) evolve commonly to turbidity flows of type 1 (facies Tu1 deposits). However, based on core descriptions of *Chapter 2* and *Chapter 3*, turbidity flow (facies Tu1 deposits) and concentrated density flow deposits (Co1) are easily distinguishable by the threshold of coarse sand that can be transported by a turbidity current *sensu stricto*. The Bouma term Ta is relatively thick in concentrated density flow (facies Co1 deposits) in comparison to turbidity flows (facies Tu1 deposits) (Mulder and Alexander, 2001). Based on the Mulder and Alexander (2001)'s classification, the upper part of the concentrated density flow deposits (Co1) is fully turbulent allowing a differentiation between grain-flow deposits (Hy2) and those of concentrated density flow deposits (Co1). As proposed in the flow transformation diagram (Fig. 4.Eb), concentrated flow (facies Co1 deposits) evolves into turbidity flow deposits (Tu1) with a rapid decrease in grain-size, ending with the particle suspension fall-out deposits (Fig. 4.Eb – column #8).

Turbidity flow of type 1 (facies Tu1 deposits) commonly evolves into slurry flow (facies Sl1 deposits), and then commonly into debris flow of type 2 (Df1) which itself may turn back into a turbidity flow of type 2 (facies Tu2 deposits). "Linked debrites", also named "hybrid event beds" or HEBs are composed at the base of Tu1, then Sl1, then Df1 and are capped by Tu2 illustrating a clear continuum between each flow type (Haughton et al., 2003, 2009) (Fig. 4.Eb – column #10, 12, 14). The sedimentary succession described by Haughton et al. (2003, 2009) is however, not always complete. Some core sections will be dominated by turbidity flow deposits (Tu1) evolving into slurry flow (facies Sl1 deposits), others by slurry flow (facies Sl1 deposits) evolving into debris flow of type 2 (facies Df1 deposits), and some others dominated by debris flow (facies Df1 deposits) evolving into turbidity flow of type 2 (facies Tu2 deposits).

- Flow transformation successions and depositional environments

Our descriptions and observations highlight two main idealised flow transformation successions. The thickness of these idealised flow transformation successions ranges from 15 m to 35 m. Those successions are composed of tens to hundreds palaeo-gravity flow events. Each event bed are commonly composed of one to two flow transformations. However, the idealised flow transformation succession, show step by step the following described flow transformation evolution:

The first idealised flow transformation successions, has been observed in the syn-rift study (Chapter 2), where we regularly observed an evolution from hyperconcentrated density flows to grain-flows, then to concentrated density flow and finally to turbidity flow (type 1). The

concentrated density flow progressed in some cases to debris flow (type 1). This first flow transformation indicates a decrease in sediment concentration that reflects, in terms of depositional environment, the continuity between the proximal delta front to the distal toe of the prodelta environments.

The second idealised flow transformation successions, has been observed in the post-rift study (Chapter 3), where we mainly observed at the base hyperconcentrated density flow (*sensu lato*) deposits transforming into concentrated density flow deposits, evolving then to turbidity flow (type 1) deposits. The turbidity flow of type 1 may then transform into a slurry flow, then into a debris flow type 2, and then back into a turbidity flow of type 2. In this case, the sediment concentration is decreasing from hyperconcentrated density flow to turbidity flow (type 1), then increasing between turbidity flows of type 1 to slurry flow, and then decreases again into debris flow of type 2 and finally to turbidity flow of type 2. In terms of depositional environments, we explained this succession of flow transformations generated by the slope break, where acceleration causes water to become entrained causing an abrupt decrease in sediment concentration (e.g. passing from hyperconcentrated density flow *sensu lato* into concentrated density flow, and then into turbidity flow of type 1). This zone corresponds to the channel and/or proximal lobe (CPL) environment. The concentration of sediment will then, rapidly increase after the slope break (rebound) evolving from turbidity flow (type 1) to slurry flow, this area corresponds to the mid to distal lobe (MDL) environment. The “rebound” mechanism will increase the sediment concentration and the water and mud content will be pushed toward the front of the flow head, laterally and at the top of the flow. The water and mud content will increase, passing from slurry flow to debris flow (type 2) and finally to supercritical turbidity flow (turbidity flow of type 2) caused by an abrupt decrease in slope gradient, a hydraulic jump and/or a loss in confinement. This last decrease of sediment concentration operates in the frontal lobe fringe (FLF) environment generally found on the basin plain.

- Flow gaps

Flow gaps, based on the most observed density flow transformation (Fig. 4.Eb), have been identified. Inside the well-defined sedimentary succession of (Haughton et al., 2003, 2009), flow gaps have been observed. For example, in well 6507/2-2 (Fig. 3.6 in *Chapter 3*), 5 metres of core (from -3280,00 to -3275,00 m) demonstrates an evolution from slurry flow deposits (Sl1) to turbidity flow of type 2 deposits (Tu2) where the debris flow of type 2 deposits (Df1) are missing. We can interpret the absence of debris flow of type 2 deposits (Df1) from the low occurrence or an absence of mud content (the slurry flow deposits in this interval are barren of mud clasts). Other flow gaps have been observed such as hyperconcentrated density flow *sensu stricto* (facies Hy1 deposits) evolving directly into concentrated density flow (facies Co1 deposits) with the absence of grain-flow (facies Hy2 deposits). This type of gap can be observed in well 6406/12-3S (Fig. 2.Cd in *Supplementary data 2.C* of *Chapter 2*). The absence of grain-flow deposits (Hy2) between hyperconcentrated density flow *sensu stricto* (Hy1) and concentrated density flow (Co1) deposits can be interpreted as a rapid decrease of the density flow concentration leading to an abrupt grain-size reduction in the depositional record.

- Depositional models

Three depositional environments characterise the Viking and Cromer Knoll groups in the Norwegian Sea. Two depositional environments develop in a shallow-marine environment, whereas one depositional environment refers to a deep-marine environment. During the syn-rift period, the two shallow-marine depositional environments will be conjointly deposited in the terrace domain; these are the wave-dominated coastal environment and subaqueous coarse-grained deltas (Chapter 2). During the post-rift period, deep-water turbidite lobe complexes will mainly develop in the deep and terrace domains (Chapter 3). For more detail regarding depositional models, *Chapter 2*, *Chapter 3* and *Supplementary data 4.F* can be used as complementary materials.

The first shallow-marine depositional environment is characterised by a progressive increase of the intensity of bioturbation from C5 to O1 with non-bioturbated facies (C5) to extremely bioturbated facies (O1). With respect to grain-size, these progressively evolve from medium-grained sandstones (C5) to mudstones (O1). All these observations, along with the observed sedimentary structures, suggest that the succession of C5 to O1 facies corresponds to a wave-dominated coastal environment (Table 4.Ea, Fig. 4.Ec), with C5 interpreted as backshore, C4 as foreshore, C3 as upper shoreface, C2 as middle shoreface, C1 as lower shoreface, O2 as proximal offshore, and O1 as distal offshore (de Raaf et al., 1977; Wright et al., 1979, 1985; Short, 1984; Wright and Short, 1984; Walker, 1992; Clifton, 2003, 2005; Reading, 2009; Reineck and Singh, 2012; Yu et al., 2018). Both coarsening-upward and fining-upward sequences have been observed for wave-dominated coastal environments (Fig. 4.Ec, A1 & A2).

The second shallow-marine depositional environment is defined by the association of flow-facies Hy1, Hy2, Co1, Tu1 and De1. Based on Mulder and Alexander (2001)'s classification, Hy1 corresponds to hyperconcentrated density flow *sensu stricto* deposits, Hy2 to grain-flow deposits, Co1 to concentrated density flow deposits, De1 to debris flow deposits and Tu1 to turbidity flow deposits. Based on the association and the sedimentary succession of the subaqueous sedimentary density flow (SSDF) facies (Hy1, Hy2, Co1, Tu1 and De1), the depositional environment is interpreted to be subaqueous coarse-grained deltas (Gilbert, 1885; Falk and Dorsey, 1998; Longhitano, 2008; Gobo et al., 2014; Elliott et al., 2015; Henstra et al., 2016b). Hy1 and Hy2 will be observed in the delta front (foreset), whereas Co1 and Tu1 will be found in the prodelta (bottomset). In turn, De1 could be found both in the prodelta and delta front. Both coarsening-upward and fining-upward sequences have been observed for coarse-grained deltaic environments (Fig. 4.Ec, B1 & B2).

The third depositional environment, corresponding to a deep-marine environment, is defined by the association of facies Hy1, Hy2, Co1, Tu1, Tu2, Sl1; De1, Df1 and Un1, in which De1 has been very rarely observed. Most observed SSDF facies are Tu1, Tu2, Sl1, Df1, and Un1 corresponding to the sedimentary succession of Haughton et al. (2003, 2009), named "hybrid event beds" or "linked debrites". Based on the association and the sedimentary succession of the SSDF facies (Tu1, Tu2, Sl1 and Df1), the depositional environment is interpreted as deep-

water turbidite lobe complexes (Haughton et al., 2003, 2009; Kane and Pontén, 2012; Talling et al., 2012; Fonnesu et al., 2015, 2018; Kane et al., 2017; Spychala et al., 2017b, 2021).

This broad deep-water turbidite lobe complex environment can be subdivided into five lobe environments. The channel and/or proximal lobe (CPL) is characterised by a sedimentary succession dominated by Hy1, Hy2 and Co1. The mid to distal lobe (MDL) is dominated by facies Tu1, Sl1 and Df1. Frontal lobe fringe (FLF) is characterised by lobe beds dominated Sl1, Df1 and Tu2. The lateral lobe fringe (LLF) is the only off-axial deposit in contrast to the 3 axial lobe environments (CPL, MDL and FLF). The LLF is dominated by mm- to cm-beds of Tu1 facies. Un1 can be identified in any of the lobe environments (CPL, MDL, FLF and LLF). A fifth depositional environment identified as the distal lobe fringe (DLF) has not been identified on core pictures due to their low resolution. The DLF is characterised by a part of facies O1. Note that any LLF or FLF can evolve laterally or axially into DLF. Coarsening-upward and fining-upward sequences have been observed for the deep-water turbidite lobe complex environment (Fig. 4.Ec, C1 & C2).

.

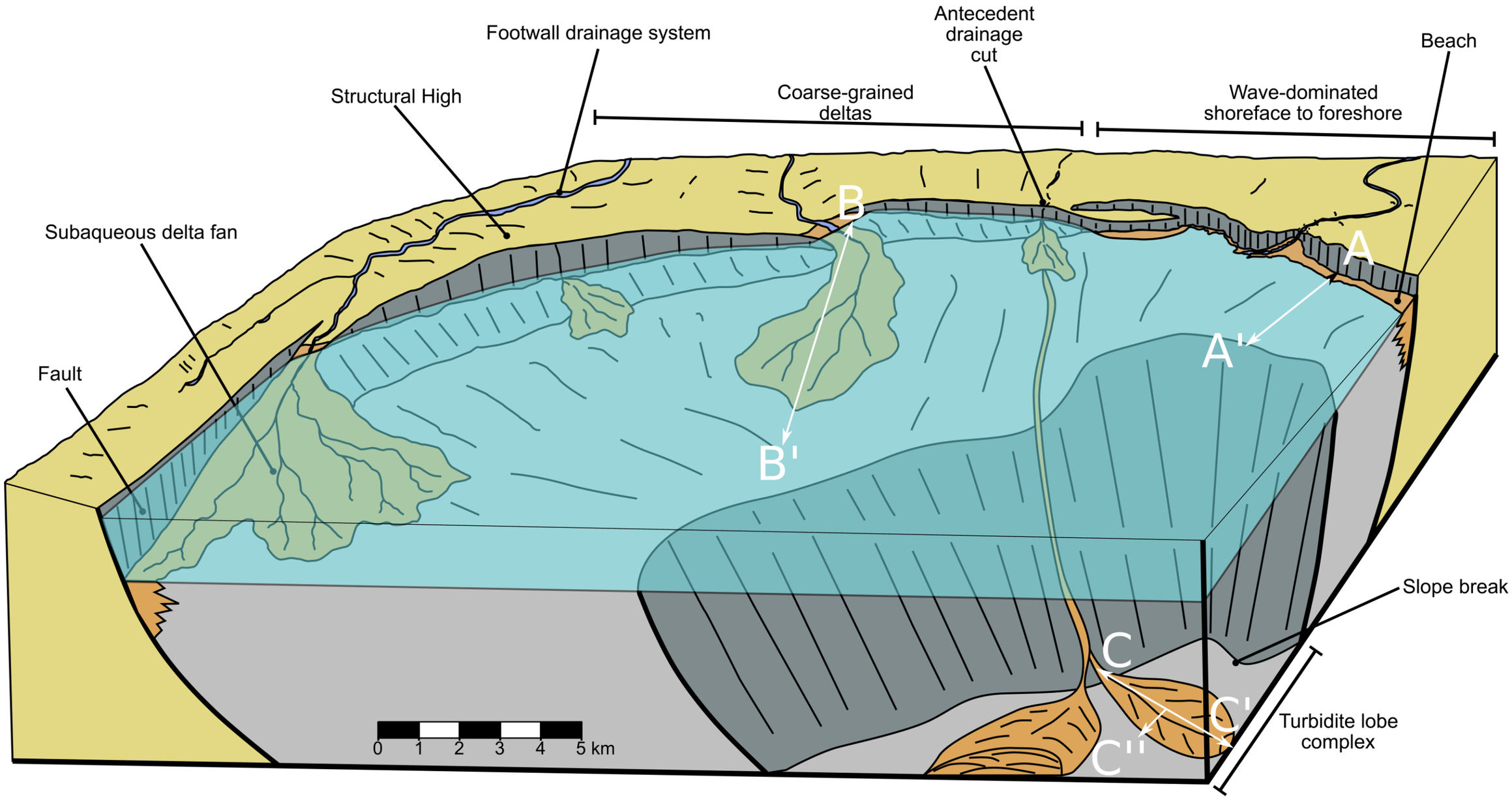

Fig. 4.Ec: Depositional models, synthetic sedimentary logs and synthetic Gamma Ray (GR) logs for (A) wave-dominated coastal environment, (B) coarse-grained delta environment, and (C) deep-water turbidite environment; with facies colour shown in Table 4.Ea. The GR logs A1, B1 and C1 correspond to coarsening-upward sequences; conversely, the GR logs A2, B2 and C2 correspond to fining-upward sequences. The legend regarding clast composition and sedimentary structures of the synthetic sedimentary logs is shown on Fig. 2.Ca in Supplementary data 2.C of Chapter 2 and Fig. 3.6 in Chapter 3. "CPL" signifies channel and/or proximal lobe, "MDL" means mid to distal lobe, "FLF" signifies frontal lobe fringe and "LLF" means lateral lobe fringe

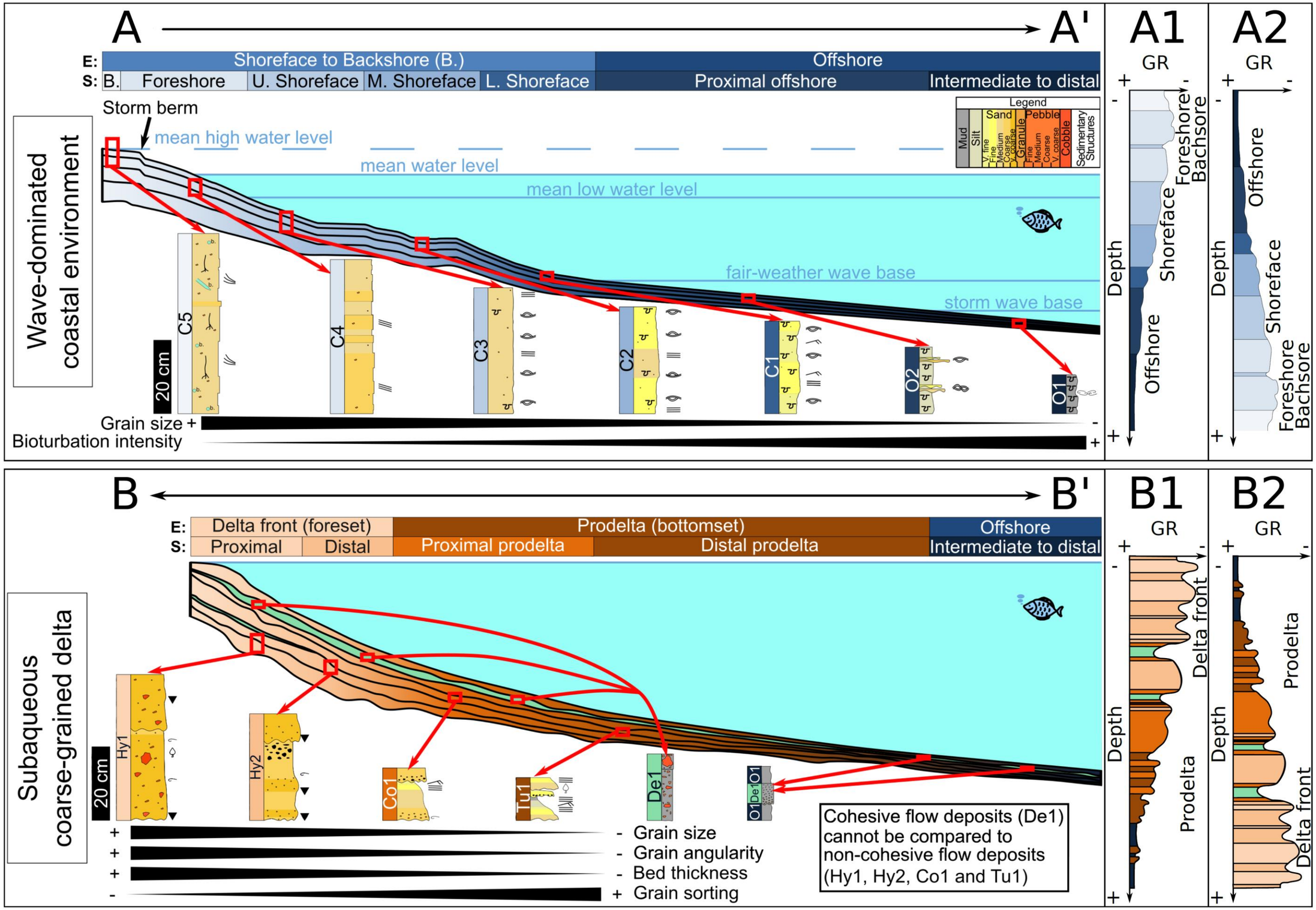
A
A'
E:
S:
Shoreface to Backshore (B.)
Offshore
B.
Foreshore
U. Shoreface
M. Shoreface
L. Shoreface
Proximal offshore
Intermediate to distal
Storm berm
mean high water level
mean water level
mean low water level
fair-weather wave base
storm wave base
Wave-dominated coastal environment
Legend
Mud
Silt
Sand
Pebble
Granule
Sedimentary Structures
C5
C4
C3
C2
C1
O2
O1
20 cm
Grain size
Bioturbation intensity
A1
A2
GR
Depth
Foreshore
Backshore
Shoreface
Offshore
B
B'
Delta front (foreset)
Prodelta (bottomset)
Offshore
Proximal
Distal
Proximal prodelta
Distal prodelta
Intermediate to distal
Subaqueous coarse-grained delta
Hy1
Hy2
Co1
Tu1
De1
O1
20 cm
Grain size
Grain angularity
Bed thickness
Grain sorting
Cohesive flow deposits (De1) cannot be compared to non-cohesive flow deposits (Hy1, Hy2, Co1 and Tu1)
B1
B2
Delta front
Prodelta

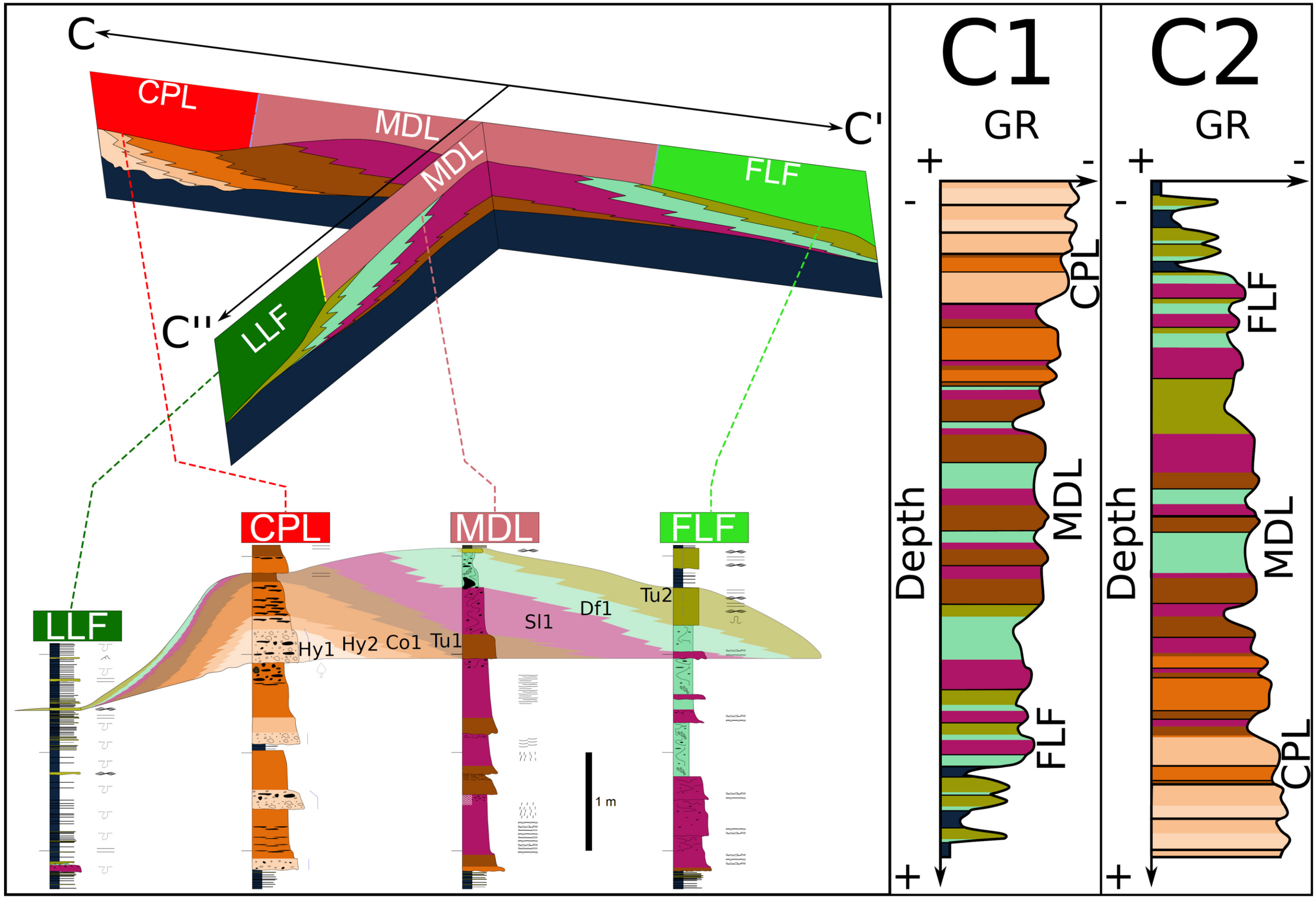
C
C'
C''
CPL
MDL
MDL
FLF
LLF
CPL
MDL
FLF
LLF
Hy1
Hy2
Co1
Tu1
Sl1
Df1
Tu2
1 m
C1
GR
+
-
-
Depth
+
CPL
MDL
FLF
C2
GR
+
-
-
Depth
+
FLF
MDL
CPL

12. Supplementary data 4.F: Sedimentary facies and associated depositional environments – Part B

- **Facies description**

More than 1.5 km of core was described at 1:100 to 1:1000 scale for the Viking and Cromer Knoll groups throughout the entire Norwegian Sea. This detailed core description permits the identification of 16 sedimentary facies with C1 to C5 corresponding to coastal deposits, with O1 to O2 corresponding to offshore deposits, and nine other facies (Hy1, Hy2, Co1, Tu1, Tu2, Sl1; De1, Df1 and Un1) corresponding to subaqueous sedimentary density flow (SSDF) facies (Table 4.Ea). Facies described in the 2 previous chapters are summarised on *Table 4.Ea*. Previously described facies in those chapters will be briefly reviewed. A more detailed description will be provided for the remaining undescribed facies C5 and to distinguish between the two debris flow facies described in the syn-rift study (De1) and the debris flow facies described in the post rift study (Df1).

- Coastal to deep offshore sedimentary facies

Facies O1 consists predominantly of a structureless dark grey mudstone (Table 4.Ea, Fig. 4.Ea-I). O1 can grade up to a light to dark grey siltstone. The mudstone can be calcareous grading up, in some cases, to marlstone. This facies can exhibit intense bioturbation with the presence of J-shaped burrows, or in some cases, be barren of bioturbation. O1 can be composed of centimetric intervals rich in bivalves provisionally attributed to the genus *Inoceramus.*

Facies O2 is formed from an alternation of millimetric siltstone laminae to very fine- to fine-grained sandstone laminae with muddy to silty intervals (Table 4.Ea, Fig. 4.Ea-H). The silty to sandy laminae can exhibit parallel-laminations and cross-laminations. The base is commonly a sharp contact with the muddy/silty background (Fig. 4.Ea-H). Bioturbation is present, and ichnotaxon such as Chondrites are easily identifiable.

Facies C1 consists of a very fine- to fine-grained sandstone (Table 4.Ea, Fig. 4.Ea-G). The sporadic presence of belemnites and sub-angular to very angular coarse sand clasts are noted (Fig. 4.Ea-G). Small-scale cross-laminations, undulating to curved laminations, angular to horizontal planar laminations are the main observed sedimentary structures. Sandy lenses and thin muddy to silty laminae are frequently observed in C1 (Fig. 4.Ea-G). This facies is characterised by intense bioturbation and several ichnotaxa can be identified such as Phycosiphon, Palaeophycus and Skolithos.

Facies C2 consists of fine- to medium-grained sandstones (Table 4.Ea, Fig. 4.Ea-F). In some cases, the sporadic presence of angular coarse sand clasts is observed. Sub-horizontal to horizontal plan-parallel laminations with some small- to large-scale SCS and HCS structures are present (Fig. 4.Ea-F). C2 has a moderate degree of bioturbation. Ophiomorpha ichnotaxon is (provisionally) observed, in addition to the properly-identified Skolithos ichnotaxon.

Facies C3 consists of a medium-grained sandstone (Table 4.Ea, Fig. 4.Ea-E). Sporadic presence of sub-angular to very-angular granules can be observed in C3. Sub-horizontal to

horizontal plane-parallel laminations and SCS (swaley cross-stratification) are commonly observed, whereas HCS (hummocky cross-stratification) is less frequently found (Fig. 4.Ea-E). Coal fragments can be present. Note a relatively low degree of bioturbation with Skolithos ichnotaxon identified.

Facies C4 consists of a medium to coarse-grained sandstone (Table 4.Ea, Fig. 4.Ea-D). Some intervals are rich in angular to very angular polygenic granules to pebbles. Commonly when granules and pebbles are present, they form layers (1 to 8 cm) that alternate with intervals barren of granules and pebbles (Fig. 4.Ea-D). Parallel laminations of high-angle cross bedding are frequently observed when these layers are present. Bioturbation is not present in this facies, however, debris of plants is noted.

Facies C5 consists of a light beige, yellowish to light orange fine to medium-grained sandstone (Table 4.Ea, Figs. 4.Ea-A, 4.Ea-B, 4.Ea-C). C5 commonly contains very coarse to fine pebbles with a sub-angular to rounded shape. Roots, belemnites and plant debris are commonly present in C5 (Fig. 4.Ea-A). Large foreset beds can be observed but are not frequently preserved (Fig. 4.Ea-B). C5 sandstone can be unconsolidated and composed of intervals rich in vegetal materials (Fig. 4.Ea-C). This facies has frequently been observed in wells 6407/9-5 and 6407/9-6 (Table 4.Fa).

- Subaqueous Sedimentary density flow (SSDF) facies

Facies Hy1 consists of a structureless and very poorly sorted grain-supported conglomerate (Table 4.Ea, Fig. 4.Ea-J). Hy1 is commonly composed of a large range of clasts (silt to boulder) having a polygenic origin (Fig. 4.Ea-J). Clasts are sub-rounded to very angular. Elongated mudstone clasts are commonly observed. Co1 is frequently composed of armored mudstone clasts. Hy1 commonly exhibits inverse grading and a slightly erosional base. Hy1 can be composed of a variety of clasts such as carbonate rock fragments, plant materials, coal and piece of shells. This facies can measure from 20 cm up to 3 m.

Facies Hy2 consists of a massive and structureless coarse- to very coarse-grained sandstone (Table 4.Ea, Fig. 4.Ea-K). Hy2 is commonly composed of mudstone clasts that can have elongated shapes. Sporadic presence of polygenic sub-rounded to very angular clasts up to granule size is observed in this facies. The base of Hy2 is frequently erosional. This facies commonly presents inverse grading. Hy2 can measure from 10 cm up to 1.05 m. A continuum flow transformation from Hy1 facies to Hy2 facies is commonly observed (Fig. 4.Eb – column #2).

Facies Co1 consists of very coarse-grained sandstone fining upward to fine-grained sandstone and exhibits normal grading (Table 4.Ea, Fig. 4.Ea-L). Clasts up to gravel size, are frequently sub-angular to rounded. Co1 is commonly formed of mudstone clasts, some of which have elongated shapes. The base of Co1 is strongly erosional (Fig. 4.Ea-L). This base is overlain by a structureless and massive coarse to very coarse-grained sandstone fining upward to fine-grained sandstone, commonly composed of plane parallel laminations and occasionally topped by trough cross-bedding and current ripples. Co1 can measure from 1 cm up to 0.95 m. A continuum flow transformation from Hy2 facies to Co1 facies is commonly observed (Fig. 4.Eb – column #4).

Facies Tu1 consists of medium-grained sandstone fining upward to siltstone (Table 4.Ea, Fig. 4.Ea-O). Tu1 has a sharp to erosional base. Tu1 has been subdivided into three sub-facies in Chapter 2: the millimetric, centimetric and decimetric deposits whereas in *Chapter 3*, Tu1 has been subdivided into two types: Tu1 of type 1 corresponds to the centimetric (> 2 cm) to decimetric deposits and Tu1 of type 2 corresponds to the centimetric (< 2 cm) to millimetric deposits. Tu1 has been subdivided into two sub-facies. The first type of Tu1 is thicker than 2 cm and composed of a massive medium-grained sandstone (Tu1 of type 1 in *Chapter 3*, and centimetric to decimetric Tu1 deposit in *Chapter 2*). This first type of Tu1 facies exhibits a normal grading passing from medium-grained sandstone fining upward to siltstone or mudstone. This first type commonly exhibits parallel laminations in a fine-grained sandstone (Fig. 4.Ea-O). Less commonly trough cross-beddings and current ripples are observed in a very fine-grained sandstone. The base of this first type of Tu1 facies is commonly erosional with a thickness ranging from 2 cm up to 30 cm. The second type of Tu1 ranges from few millimetres up to 2 cm in thickness, and is composed of very fine- to fine-grained sandstone (Tu1 of type 2 in *Chapter 3*, and millimetric to centimetric Tu1 deposit in *Chapter 2*). This second type of Tu1 facies exhibits a normal grading passing from fine-grained sandstone fining upward to mudstone. These thin sandstone layers of facies Tu1 are deposited on a mudstone to siltstone of facies O1. The sedimentary structures that are commonly observed in this second type of Tu1 are plane-parallel laminations, current ripples, trough cross-beddings and sinusoidal to wavy laminations (Fig. 4.Ea-O). Subcritical climbing-ripples (sensu jobe2011) to supercritical climbing-ripples (sensu storms1999) can be identified but are very uncommon. The base of this second type of Tu1 facies is commonly sharp with a thickness ranging from 1 mm to 2 cm. The most common observed flow transformation is between Co1 and Tu1 facies (Fig. 4.Eb – column #8).

Facies Tu2 consists of fine- to very fine-grained sandstone grading up into siltstone and/or mudstone of facies O1 (Table 4.Ea, Figs. 4.Ea-P, 4.Ea-R, 4.Ea-S). This facies alternates between fine to very fine-grained sandstone laminae (<1 mm up to 2 cm) and finer siltstone to mudstone laminae (<1 mm up to 2 cm). The following sedimentary structures are commonly observed in Tu2: parallel laminations, sinusoidal laminations and supercritical climbing-ripples (sensu storms1999) (Figs. 4.Ea-P, 4.Ea-R, 4.Ea-S). Load structures and convolute laminations are frequently observed in Tu2. This facies can measure from 1 cm up to 1.17 m. Tu2 commonly transforms to Tu2 facies (Fig. 4.Eb – column #14).

Facies Sl1 consists of very fine- to medium-grained sandstones (Table 4.Ea, Fig. 4.Ea-P). The base of Sl1 is commonly erosional. At the base, a medium-grained sandstone grading normally to very fine-grained sandstone and less commonly to siltstone is observed. Clasts are commonly well- to very well-rounded. Mudstone clasts are commonly present with an elongate shape. Sl1 exhibits post-depositional water escape and soft-sediment features and/or syn-depositional sedimentary structures. Identified primary structures are dish structures, banded sandstones and wispy lamination (sensu Lowe & Guy, 2000). Post-depositional structures such as vertical escape features and convolute laminations can be identified (Fig. 4.Eb – column #11-A, B). Loading processes have been rarely observed but can be present as flame structures. Sl1 can be extremely rich in mud content exhibiting multi-directional water escape structures (Fig. 4.Eb – column #11-B, D). Sl1 can

measure from 1 cm up to 4.25 m. Tu1 commonly transforms to Sl1 facies (Fig. 4.Eb – column #10).

Facies De1 consists of conglomeratic mudstones (Table 4.Ea, Figs. 4.Ea-M, 4.Ea-N). The size of the clasts composing this conglomeratic mudstone can vary from silt- to boulder-size. De1 is infrequently composed of mudstone clasts. Some plant remains and shell fragments can be found. De1 can be subdivided into two types. The first type is unsorted and structureless. The clasts are commonly sub-rounded to very angular. The thickness of this first De1 sub-facies type commonly ranges from one to several decimetres (Fig. 4.Ea-M). The second De1 sub-facies type is better sorted and the clasts can present a normal grading in the muddy matrix. The clasts are commonly not larger than a granule with the sporadic presence of pebbles that are commonly sub-rounded to very rounded (Fig. 4.Ea-N). This second type of conglomeratic mudstone is commonly associated with O1 facies and measures from 1 to 10 centimetres in thickness. The most common observed flow transformation is between Co1 and the first type of De1 facies (Fig. 4.Eb – column #6). However, flow transformation between Hy1 to De1 (first type) and between Hy2 to De1 (first type) have also been observed.

Facies Df1 consists of structureless and chaotic sandy mudstones to muddy sandstones (Table 4.Ea, Fig. 4.Ea-Q). Df1 contains sand injectites, pseudonodules and a significant quantity of elongated mudstone clasts. Clasts are on average less than pebble sized and are commonly well- to very well-rounded. Multi-directional water escape structures and the high number of mudstone clasts are the key characteristics of Df1 facies as compared to De1 facies. De1 is barren of multi-directional water escape structures and contains rare presence of mudstone clasts (Fig. 4.Eb – column #7 and #13). Df1 can measure from 1 cm up to 2.12 m. Sl1 commonly evolves to Df1 facies (Fig. 4.Eb – column #12).

Facies Un1 consists of siltstone to fine-grained sandstone (Table 4.Ea, Fig. 4.Ea-T). This facies is highly bioturbated and it is not possible to distinguish if it was originally Co1, Tu1, Sl1, Df1 or Tu2. Un1 can be dominated by fine-grained sandstone, with some siltstone, or can consist of a mix of siltstone and fine-grained sandstone, or can be dominantly siltstone with coarser grains up to fine-sized sands present. Un1 is a highly bioturbated facies and there is no trace of primary structures (Fig. 4.Ea-T). In most of the wells where the Un1 facies was encountered, three sub-facies are observed, the first sub-facies of Un1 is dominated by siltstone with the presence of coarser grains up to fine-sized sands. The second sub-facies is a mix of siltstone and fine-grained sandstone, and the third sub-facies is dominated by fine-grained sandstone, with the presence of siltstone (Fig. 4.Ea-T). The well 6405/7-1 has 31.10 metres of core composed solely of Un1 facies (Table 4.Fa). The three sub-facies provide a good way to highlight the sandier intervals *versus* the siltier intervals.

- **Depositional models**

In the Norwegian Sea, three depositional environments characterise the Viking and Cromer Knoll groups. Two depositional environments are shallow-marine environments and the other is a deep-marine environment. In the terrace domain, during the syn-rift period, the two shallow-marine depositional environments will be conjointly deposited, these are the wave-

dominated coastal environment and subaqueous coarse-grained deltas (Chapter 2). During the post-rift period, deep-water turbidite lobe complexes will develop (Chapter 3).

- Shallow-marine depositional environments
  - *Wave-dominated coastal environment*

This depositional environment is defined by a progressive increase of the intensity of bioturbation from C5 to O1, from non-bioturbated facies (C5) to extremely bioturbated facies (O1). With respect to grain-size, these progressively evolve from medium-grained sandstone (C5) to mudstone (O1). The grain-size, C5 is a medium-grained sandstone with very-coarse sand to fine pebbles commonly present. C4 is a medium- to coarse-grained sandstone; C3 is a medium-grained sandstone; C2 fine- to medium-grained sandstone; C1 is a fine- to very fine-grained sandstone; O2 is a siltstone to mudstone with thin laminae of very fine- to fine-sandstone; O1 is mainly mudstone grading up to siltstone. Sedimentary structures such as large- and small-scale HCS and SCS imply a shallow water setting affected by wave action (de Raaf et al., 1977). C5 is the only facies where roots are found. The other facies when ichnotaxa are recognisable, illustrate that C3 formed in a shallower environment than C2, C1, O2 and O1. O1 is considered to have been deposited in a deep-marine environment (Walker, 1992; Pemberton et al., 2012). All these observations suggest that the succession of C5 to O1 facies correspond to a wave-dominated coastal environment (Table 4.Ea, Fig. 4.Ec). With C5 interpreted as backshore, C4 as foreshore, C3 as upper shoreface, C2 as middle shoreface, C1 as lower shoreface, O2 as proximal offshore, and O1 as distal offshore (de Raaf et al., 1977; Wright et al., 1979, 1985; Short, 1984; Wright and Short, 1984; Walker, 1992; Clifton, 2003, 2005; Reading, 2009; Reineck and Singh, 2012; Yu et al., 2018). Both coarsening-upward and fining-upward sequences have been observed for wave-dominated coastal environments (Fig. 4.Ec, A1 & A2).

  - *Subaqueous coarse-grained deltas*

This depositional environment is defined by the association of facies Hy1, Hy2, Co1, Tu1 and De1. Based on the association and the sedimentary succession of the SSDF facies (Hy1, Hy2, Co1, Tu1 and De1), the depositional environment is interpreted to be subaqueous coarse-grained deltas as previously demonstrated in *Chapter 2* (Gilbert, 1885; Falk and Dorsey, 1998; Longhitano, 2008; Gobo et al., 2014; Elliott et al., 2015; Henstra et al., 2016b). The sub-environments that can be identified in the subaqueous coarse-grained delta environment are as follows: the delta front (foreset) where unsorted, structureless and thick deposits accumulate commonly showing inverse grading. The delta front is typically composed of a succession of hyperconcentrated density flow deposits sensu lato (Hy1 and Hy2) with some presence of cohesive flow deposits (De1-1st type). Conversely, the prodelta (bottomset) is composed of sorted, structured and thin deposits commonly normally graded. The prodelta contains concentrated density flow (Co1) and turbidity flow (Tu1) deposits in addition to debris flow (De1) deposits. In the proximal prodelta, concentrated density flow (Co1) combined with unsorted debris flow (De1-1st type) deposits; whereas in distal prodelta to offshore mudstones, the sedimentary succession will be dominated by turbidity flow (Tu1) and well-sorted debris flow (De1-2nd type) deposits. Coarsening-upward and fining-upward sequences have been observed for the subaqueous coarse-grained delta environment (Fig. 4.Ec, B1 & B2).

- Deep-marine depositional environment
  - *Deep-water turbidite lobe complexes*

This deep-marine depositional environment is defined by the association of facies Hy1, Hy2, Co1, Tu1, Tu2, Sl1; De1, Df1 and Un1. De1 (Debris flow of type 1) has been very rarely observed whereas hyperconcentrated density flow sensu lato (Hy1 and Hy2) and concentrated density flow (Co1) deposits have been rarely but more commonly observed than De1. Most observed SSDF facies are Tu1, Tu2, Sl1, Df1 and Un1 corresponding to the sedimentary succession of Haughton et al. (2003, 2009), named “hybrid event beds” or “linked debrites”. Based on the association and the sedimentary succession of the SSDF facies (Tu1, Tu2, Sl1 and Df1), the depositional environment is interpreted to be deep-water turbidite lobe complex as previously demonstrated in Chapter 3 (Haughton et al. 2003, 2009; Fonnesu et al. 2015, 2017; Talling et al. 2012, Kane et al. 2012, 2017; Spychala et al. 2017, 2021). Nevertheless, this broad environment can be subdivided into five lobe environments. The channel and/or proximal lobe (CPL) is characterised by a sedimentary succession dominated by hyperconcentrated density flow sensu lato (Hy1 and Hy2) to concentrated density flow (Co1) deposit. The mid to distal lobe (MDL) is defined by lobe beds composed mainly of turbidity flow of type 1 (Tu1-2nd type), slurry flow (Sl1) and debris flow of type 2 (Df1) deposits. Frontal lobe fringe (FLF) is characterised by lobe beds dominated by slurry flow (Sl1), debris flow of type 2 (Df1) and turbidity flow of type 2 (Tu2) deposits. The lateral lobe fringe (LLF) is the only off-axial deposit in contrast to the 3 axial lobe environments (CPL, MDL and FLF). The LLF is dominated by turbidity flow of type 1 deposits with beds less than 2 cm thick (Tu1-1st type). Un1 can be identified in any of the lobe environments (CPL, MDL, FLF and LLF), but due to the high degree of bioturbation, it is not possible to identify the primary origin of these SSDF deposits. A fifth depositional environment identified as the distal lobe fringe (DLF) has not been identified on core pictures due to their low resolution. The DLF is characterised by a part of facies O1. Note that any LLF or FLF can evolve laterally or axially into DLF. Coarsening-upward and fining-upward sequences have been observed for the deep-water turbidite lobe complex environment (Fig. 4.Ec, C1 & C2). Note that the coarsening-upward sequence (Fig. 4.Ec, C1) can be referred to type B, and fining-upward sequence (Fig. 4.Ec, C2) can be referred to type A in *Chapter 3*.

Well #	Well name	Core length described	Link
1	6406/12-3 A	[92.2 m]	click here
2	6406/12-3 S	[209.8 m]	click here
3	6406/12-4 S	[42.0 m]	click here
4	6405/7-1	[31.1 m]	click here
5	6406/12-1 S	[36.6 m]	click here
6	6406/12-2	[61.3 m]	click here
7	6406/2-3	[45.0 m]	click here
8	6406/3-3	[14.5 m]	click here
9	6406/3-4	[10.0 m]	click here
10	6406/3-5	[10.0 m]	click here
11	6406/3-9	[50.5 m]	click here
12	6407/10-1	[28.0 m]	click here
13	6407/1-7	[8.5 m]	click here
14	6407/1-7 A	[18.4 m]	click here
15	6407/2-5 S	[44.5 m]	click here
16	6407/4-1	[7.0 m]	click here
17	6407/5-1	[9.1 m]	click here
18	6407/5-2 S	[27.8 m]	click here
19	6407/6-1	[17.4 m]	click here
20	6407/6-6	[9.0 m]	click here
21	6407/6-7 S	[22.3 m]	click here
22	6407/7-1 S	[13.1 m]	click here
23	6407/7-5	[8.7 m]	click here
24	6408/4-1	[1.4 m]	click here
25	6407/9-1	[39.5 m]	click here
26	6407/9-2	[40.7 m]	click here
27	6407/9-3	[46.4 m]	click here
28	6407/9-5	[42.4 m]	click here
29	6407/9-6	[16.8 m]	click here
30	6407/9-8	[82.7 m]	click here
31	6204/10-2 R	[10.1 m]	click here
32	6204/11-1	[100.3 m]	click here
33	6201/11-2	[13.9 m]	click here
34	6205/3-1	[7.3 m]	click here
35	6205/3-1 R	[47.5 m]	click here
36	6305/1-1	[20.0 m]	click here
37	6305/12-1	[7.0 m]	click here
38	6305/12-2	[33.9 m]	click here
39	6306/10-1	[11.3 m]	click here
40	6306/6-1	[18.8 m]	click here
All	**40 wells**	**[1356.8 m]**	**https://drive.google.com/drive/folders/1hPprh0g6QtspHj6VfuqzZHAKjpi9D-04**

Table 4.Fa: List of wells with raw core description done at the Weatherford core store, and the hyperlink with access to the raw core description.

13. Supplementary data 4.G: GR cut-off for wave-dominated coastal environments

- Gamma-Ray log

The gamma-ray log (GR-log) is a powerful tool that records the natural radioactivity of the penetrated geological formations. The three radioactive elements measured are Potassium (^{40}K), Thorium (^{232}Th) and Uranium (^{238}U). The measurement of those 3 elements provides the “total gamma-ray” curve, which is used to describe changes in lithology. Claystone contains clay minerals which preferentially trap those 3 radioactive elements (^{40}K, ^{232}Th, ^{238}U). In addition, when mudstones are rich in organic matter (OM), radioactivity increases because OM is commonly enriched in uranium. Sandstones however, are not commonly enriched in radioactive elements. However, sandstones or conglomerates rich in potassic feldspars, zircons, allanite, monazite, titanite, xenotime, micas, uranium minerals or phosphates can present high radioactive values (Serra and Serra, 2001, 2004). Factors that control the GR-log response are the speed of the logging (generally fixed at 1800 ft/h equivalent to approximately to 550 m/h), the drilling hole characteristics (tubing, cement, casing, hole fluid attenuating the GR radiation), bed thickness (GR curve will not display a correct value if the bed thickness is less than the diameter of the investigated sphere) and the statistical models employed (most commonly a Gaussian or a Poisson distribution is used to get a reasonable estimation of the mean radioactivity). In the syn-rift study (Fig. 4.Aa, *Chapter 2*), all the wells display GR values enriched in radioactive elements originating from the nearby Frøya High formed of basement rocks.

GR log is a robust tool to determine lithological change when core data are not available. Core descriptions can be tied to the GR-log curve. When the calibration is established, it reflects reliably the type of lithology described in the core. A GR cut-off corresponds to a defined threshold value for the GR. Those threshold GR values are thereby used for core description, with the aim to associate one facies described on core data to a range of GR values. Once a GR cut-off has been determined in parallel to the core description, GR-log intervals can be interpreted in terms of lithology without core description. Thus, trends in the GR-log curve reflect changes in lithology that can in turn be indirectly interpreted in terms of sub-environments. For instance, in a coastal environment, the highest GR value will be interpreted as an offshore mudstone, whereas the lowest GR value will be interpreted as sand-rich foreshore to backshore sub-environments. Once GR values are calibrated with core descriptions, intermediate sub-environments can be interpreted as the proximal offshore, or the lower, middle and upper shoreface.

- GR cut-off for wave-dominated coastal environments

For the coastal environment, it is common to use a GR cut-off to interpret sub-environments when only GR-log data are available. A coarsening-upward sequence passing from offshore mudstones to foreshore coarse-grained sandstones is represented on *Fig. 4.Ga-A*. When GR-log data are tied to the core description, the GR-log cut-off provides a good sub-environment prediction for the uncored intervals. A fining-upward sequence passing from foreshore/backshore medium- to coarse-grained sandstones and offshore mudstones exhibits the progressive decrease in grain-size reflecting a progressive flooding event of the area (Fig. 4.Ga-B). The increase of water column thus reflects a progressive evolution from proximal to distal sub-environments, passing from foreshore to shoreface and finally to deep offshore environments. Note that the GR cut-off between 6406/12-1S (Fig. 4.Ga-A) and 6406/12-3A (Fig. 4.Ga-B) exhibits a shift of 20 API, although variations within the different intervals are similar. One hypothesis to account for this shift of 20 API is the time lag (23 years) between the acquisition of those two wells, with slightly different acquisition speeds of the logging, tubing, cement, casing, hole fluid and statistical models, thus implying slight a shift in the GR values.

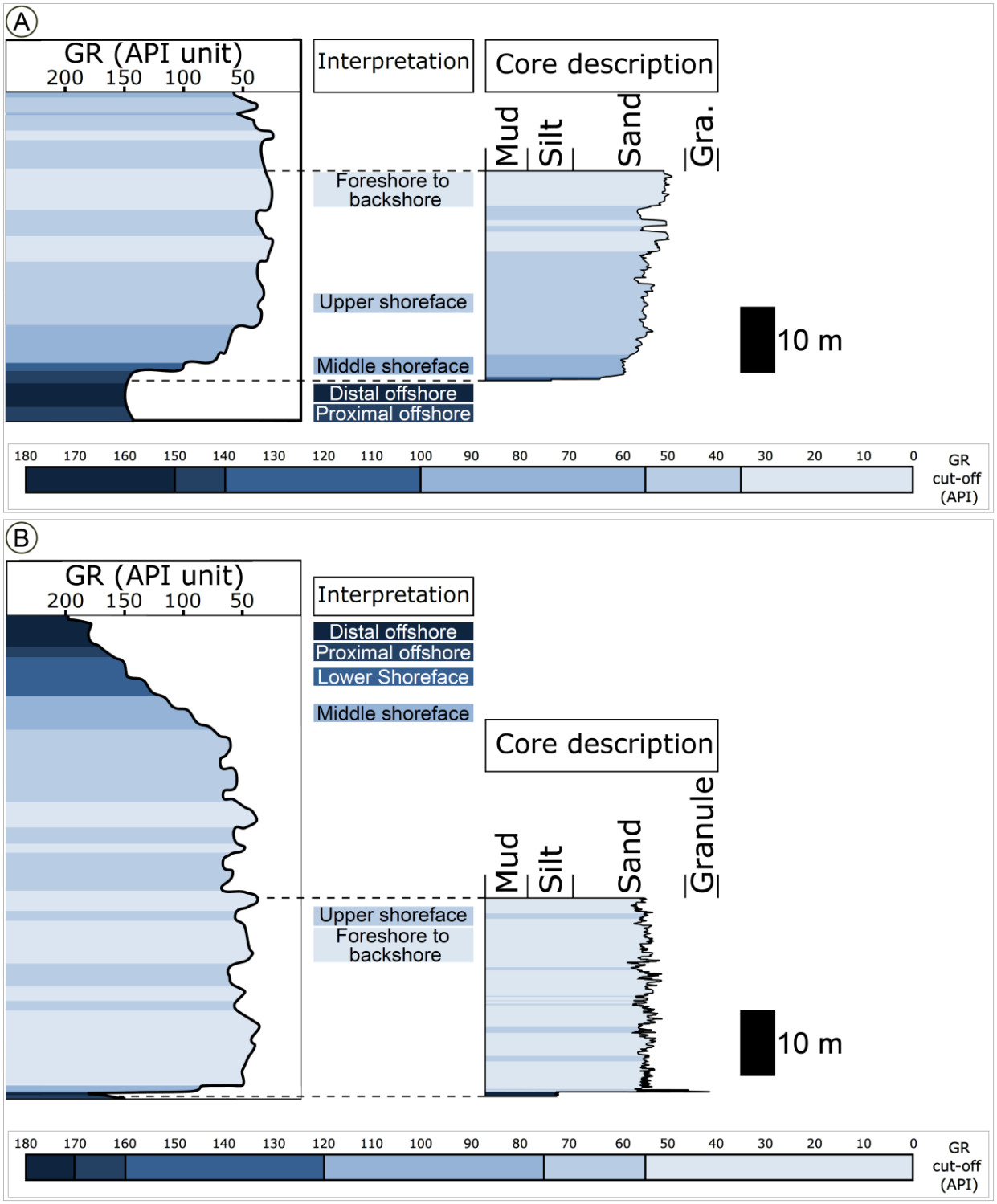

Fig. 4.Ga: Gamma Ray (GR) cut-off and associated core description for wave-dominated coastal environment with (A) corresponding to a coarsening-upward sequence (from well 6406/12-1S), and (B) corresponding to a fining-upward sequence (from well 6406/12-3A). Vertical scale bar represents 10 meters for GR log and core description.

14. Supplementary data 4.H: GR cut-off for SSDF deposits

- SSDF facies

Subaqueous sedimentary density flow deposits can be deposited in subaqueous coarse-grained deltas or deep-marine turbidite lobe complexes. Assuming that we are dealing with shallow-marine coarse-grain deltas or deep-marine turbidites, it is possible to make a GR cut-off with the goal of interpreting SSDF facies (Hy1, Hy2, Co1, Tu1, Tu2, Sl1; De1, Df1 and Un1) based on GR-log data. Note, however, that it is uncommon to interpret SSDF facies based solely on GR-log data, unlike for coastal facies.

Within the 9 gravity-driven flow facies (Hy1, Hy2, Co1, Tu1, Tu2, Sl1; De1, Df1 and Un1), two have been excluded (De1 and Un1) and two other facies have been grouped together (Df1+Tu2) to establish the GR cut-off. The highly bioturbated facies (Un1) where primary flow structures are not visible, has not been used in the GR-cut off. Indeed, Un1 is frequently identical to Tu2 (Turbidity flow of type 2) and Df1 (Debris flow of type 2) based solely on GR values. Note that Df1 and Tu2 have been grouped together because the turbidity flow of type 2 (Tu2) is composed of fine to very fine-grained sandstone with a significant quantity of siltstone and mudstone content. Conversely, the debris flow of type 2 (Df1) is composed of a muddy sandstone to sandy mudstone including sand injectites, which are composed of very fine- to fine-grained sandstones. Hence, the similarity of lithologies for Df1 and Tu2 do not support a differentiation based solely on GR-log data.

Regarding cohesive flow deposits in subaqueous deltaic environments, the debris flow of type 1 (De1) may be found both in the delta front and the prodelta, rendering its interpretation based solely on GR-log data difficult. In addition, the average thickness of De1 (1 cm to 70 cm) is frequently below the resolution of GR-log data. Moreover, when De1 facies occurs in a proximal setting, clasts can be of a boulder size. For instance, when crossing a 1 m carbonate boulder clast, the debris flow will be observed on GR-log with a low GR-value that does not reflect the high GR value of the muddy matrix. Hence, after excluding debris flow of type 1 (De1), undefined SSDF (Un1) and merging deposits from debris flow of type 2 and turbidity flow of type 2 (Df1 and Tu2), it becomes possible to interpret SSDF facies based solely on GR-log data. All the other facies (Hy1, Hy2, Co1, Tu1, Sl1 and Df1-Tu2) are associated with a well-defined lithology, allowing to interpret SSDF facies directly on the GR-log curves.

- Subaqueous coarse-grained deltas

The wells 6406/12-3S (Fig. 4.Ha-A) and 6406/12-3A (Fig. 4.Ha-B) were drilled in 2014 (during the same drilling campaign) in a nearby location, and with the same well-logging tools. As a result, the GR-value cut-offs used for these two wells are identical. Note that there is a clear continuation between each flow type as indicated by the figure caption. For instance, the GR value corresponding to 60 API could correspond to a hyperconcentrated density flow or a concentrated density flow but is most likely a grain-flow. Note that these two wells are located near the Frøya High which is the main sediment source for this area; hence, these sediments are consequently enriched in radioactive elements. The 40 metres interpreted using only the GR-log data correlate well to the SSDF facies described in the detailed core description.

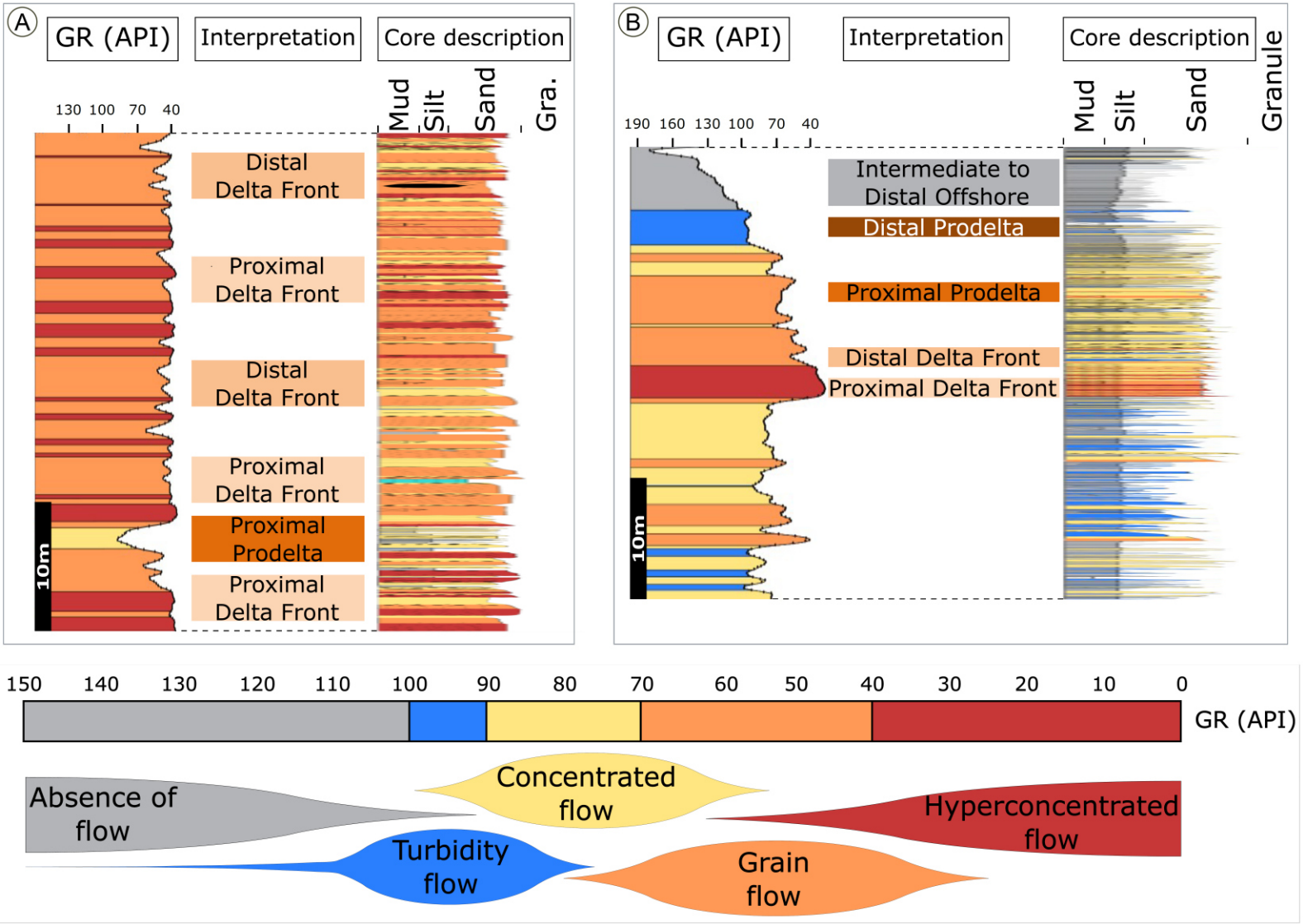

Fig. 4.Ha: Gamma Ray (GR) cut-off and associated core description for subaqueous coarse-grained delta with (A) corresponding to an abrupt and quick coarsening-upward sequence passing from proximal prodelta to proximal delta front (from well 6406/12-3S), and (B) corresponding to a fining-upward sequence passing from proximal delta front to intermediate to distal offshore (from well 6406/12-3A). Vertical scale bar represents 10 meters for GR log and core description.

- Deep-water turbidite lobe complexes

The GR cut-off has been shifted 35 API between the two studied wells (Fig. 4.Hb); however, the interval ranges have been preserved. Here also, such a shift of GR-log values is attributable to the fact that well 6507/2-3 (Fig. 4.Hb-A) was drilled 18 years before well 6507/3-9S (Fig. 4.Hb-B) and thus that numerous factors may have affected the GR values. Moreover, those 2 wells are located 9 km away from each other, possibly reflecting different sediment source with an enriched source of coarse material for well 6507/2-3 (Fig. 4.Hb-A) may be located closer to a fault than well 6507/3-9S (Fig. 4.Hb-B). GR-log data and core descriptions for well 6507/2-3 can be easily correlated and exhibit one interval dominated by slurry flow (Sl1) and another interval dominated by debris flow of type 2 (Df1) deposits (Fig. 4.Hb-A).

In well 6507/3-9S, SSDF facies interpreted from GR-log cut-offs generally reflect core observations, with the presence of turbidity flow of type 1 deposits (Tu1), concentrated density flow deposits (Co1), debris flow of type 2 and turbidity flow of type 2 (Df1-Tu2) and slurry flow (Sl1) deposits. The GR log cut-off provides a reliable overview of SSDF facies in the deep-water turbidite environments when core data are partial or missing. When no core data is available, the GR cut-off can be calibrated from other data sets. For instance, this issue can be solved out by identifying seismic facies that can be tied to the GR-log cut-off, with the aim of predicting lithology in undrilled areas (cf. section *3. Perspectives for future work* in *Chapter 5*).

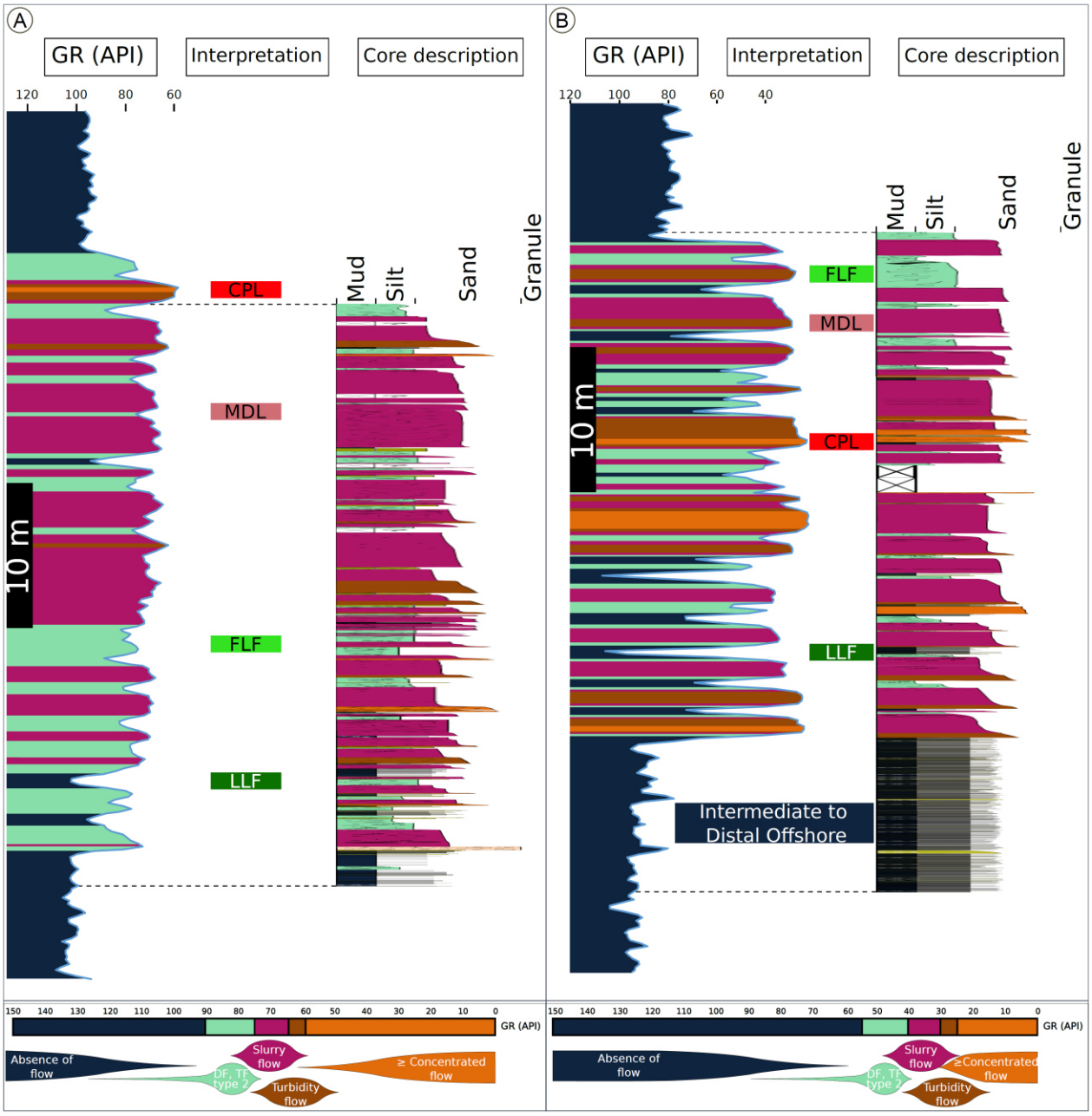

Fig. 4.Hb: Gamma Ray (GR) cut-off and associated core description for deep-water turbidite lobe complex with (A) corresponding to a coarsening-upward sequence (from well 6507/2-3), and (B) corresponding to a fining-upward sequence passing progressively from channel and/or proximal lobe (CPL), to mid to distal lobe (MDL), then to frontal lobe fringe (FLF) and finally to intermediate to distal offshore (from well 6507/3-9S). Lateral lobe fringe (LLF) environments are commonly present through coarsening- and fining-upward sequences. Vertical scale bar represents 10 meters for GR log and core description.

15. Supplementary data 4.I: Syn-rift stratigraphic sequences – Part A

- Syn-rift sequences (S1 to S7)

According to Catuneanu (2019), five orders of sequence can be identified based on the scale of observation, the sequence duration (in years (yrs)) and the vertical thickness (m): (i) the megasequence (1st order) is observable at the basin-scale, lasts commonly between 10^6 and 10^8 yrs and have a thickness of approximately 10^3 m; (ii) the supersequence (2nd order) is observable at the continental scale, lasts commonly between 10^5 and 10^7 yrs and have a thickness between 10^2 and 10^3 m; (iii) the sequence (3rd order) is observable at the scale of seismic profiles, lasts commonly between 10^4 and 10^6 yrs and have a thickness between 10^1 and 10^2 m; (iv) the parasequence (4th order) is observable at the sub-seismic scale, lasts commonly between 10^3 and 10^5 yrs and commonly have a thickness between 10^0 and 10^1 m; (v) the high-resolution parasequence (5th order and lower ranks) is observable at the core and well-log scale, lasts commonly between 10^2 and 10^4 yrs and commonly have a thickness of approximately plus or minus 10^0 m (Catuneanu, 2019).

Stratigraphic sequences in the syn-rift study have been described at different orders. The sequences identified in the syn-rift study (Chapter 2) are of 2nd and 3rd order. For the sake of completion, we also identified here 4th to 5th order syn-rift sequences (Figs. 4.Ga, 4.Ha, 4.Ia, 4.Ib, 4.Ic and Supplementary data 4.J). 4th to 5th order sequences have been established from well log and core data, although the dinoflagellate cyst zonation (Chapter 2) has only been tied to 3rd order sequences (S1 to S7). The 4th to 5th order sequences are named, “a”, “b”, “c”, etc. from the oldest to the youngest sequence. For instance, five 4th to 5th order sequences have been identified in sequence 4 (S4) and are named from the oldest to the youngest, S4a, S4b, S4c, S4d and S4e (Fig. 4.Ic). The 3rd order sequences presented in *Chapter 2*, as well as the newly identified 4th to 5th order sequences, are bounded by SBs *sensu* Embry (1993, 1995). Such 4th to 5th order sequences based on GR-log data have further been tied to core data when available (Fig. 4.Ic). In core data of well 6406/12-3A, Sequence 4 (S4) is dominated by subaqueous coarse-grained delta deposits, whereas Sequence 5 (S5) is dominated by wave-dominated coastal environments (Fig. 4.Ic). 4th to 5th order sequences of, S4a, S4b, S4c, S4d and S4e have thicknesses varying from *circa* 3.50 to 20.50 m, whereas S5a, S5b, S5c, S5d and S5e have thicknesses of *circa* 10 metres (+/- 3 m).

4th to 5th order sequences in S4 are composed of subaqueous coarse-grained delta deposits, thus suggesting variations in sediment delivery related to fault activity (as S4 is the last sequence of the rift-climax period). Alternatively, S5 (corresponding to the first sequence of the final rift period) with a thickness of 61 m (Fig. 4.Ib) is composed of 6 sequences each of which measuring *circa* 10 metres, mostly composed of wave-dominated shoreface to foreshore deposits.

Zone “R. cladophora & E. luridum” (Fig. 2.5 in *Chapter 2*) provides an approximate dating control for S5 between the Late Kimmeridgian and the Early Tithonian (153.1 to 150.7 Ma). In terms of absolute age, assuming that the sedimentation rate was constant throughout the

entire sequence, the deposition of S5 lasted 2.4 Ma (+/-500 kyr). The six 4th to 5th order sequences composing S5 (S5a, S5b, S5c, S5d, S5e and S5f) having a similar thickness (i.e. ~ 10 m) most likely represent, for each sequence, the same time span. Based on this assumption which can be done because no major hiatus is observed and no major lithological change is notable, the 4th to 5th order sequences of S5 had an approximate duration of 400 kyr (2.4 Ma/6 Sequences = 400 kyr/Sq.). During S5, as discussed in *Chapter 2*, the Spekk Formation (offshore mudstones) corresponds to the distal deposits of the Rogn Formation (wave-dominated coastal sandstones). The enrichment of the Spekk Formation in organic matter has been attributed to the long eccentricity cycles (Atar et al., 2019). It may thus be possible that these 400 kyr long eccentricity cycles are also recorded in the sandy coastal deposits of the Rogn Formation in S5 (Figs. 4.Ib, 4.Ic).

Fig. 4.Ia: Gamma-Ray (GR) log correlation showing the 3rd to 5th order stratigraphic sequences in the greater Fenja area. The GR-log correlation is orientated approximately NE-SW, the exact location is shown on Fig. 4.Aa-C. Sequence boundaries are identified within the correlation, with the Near Top Fangst (NTF), Intra-Melke Unconformity (IMU), Kimmeridgian Unconformity (KU), Base Cretaceous Unconformity (BCU), 2U3 (Unconformity between sequence 2 and 3), 3U4, 5U6 and 6U7 highlighting the seven 3rd order stratigraphic sequences (S1, S2, S3, S4, S5, S6 and S7). Checkshot data allows the seismic unconformities (SUs) to be calibrated to the presented SBs. MFS are identified and named after Partington et al. (1993): J34 MFS, J44 MFS, J54A MFS, J62 MFS, J63 MFS, J66A MFS, J72 MFS and J76 MFS.

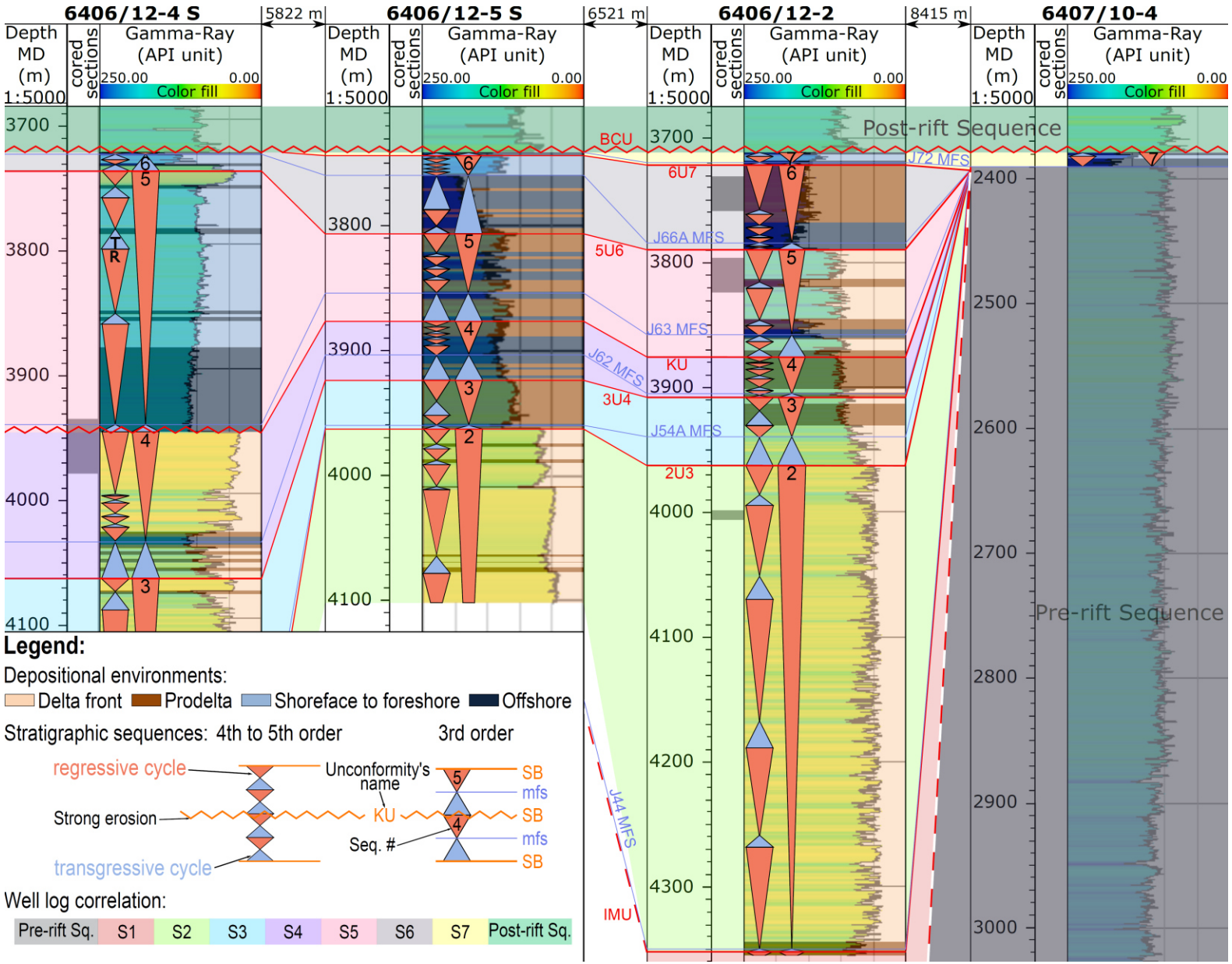
6406/12-4 S
5822 m
6406/12-5 S
6521 m
6406/12-2
8415 m
6407/10-4
Depth MD (m) 1:5000
cored sections
Gamma-Ray (API unit)
250.00
0.00
Color fill
BCU
6U7
5U6
J66A MFS
J63 MFS
J62 MFS
KU
3U4
J54A MFS
2U3
J44 MFS
IMU
J72 MFS
Post-rift Sequence
Pre-rift Sequence
Legend:
Depositional environments:
Delta front
Prodelta
Shoreface to foreshore
Offshore
Stratigraphic sequences: 4th to 5th order
3rd order
regressive cycle
Strong erosion
transgressive cycle
Unconformity's name
Seq. #
SB
mfs
Well log correlation:
Pre-rift Sq.
S1
S2
S3
S4
S5
S6
S7
Post-rift Sq.

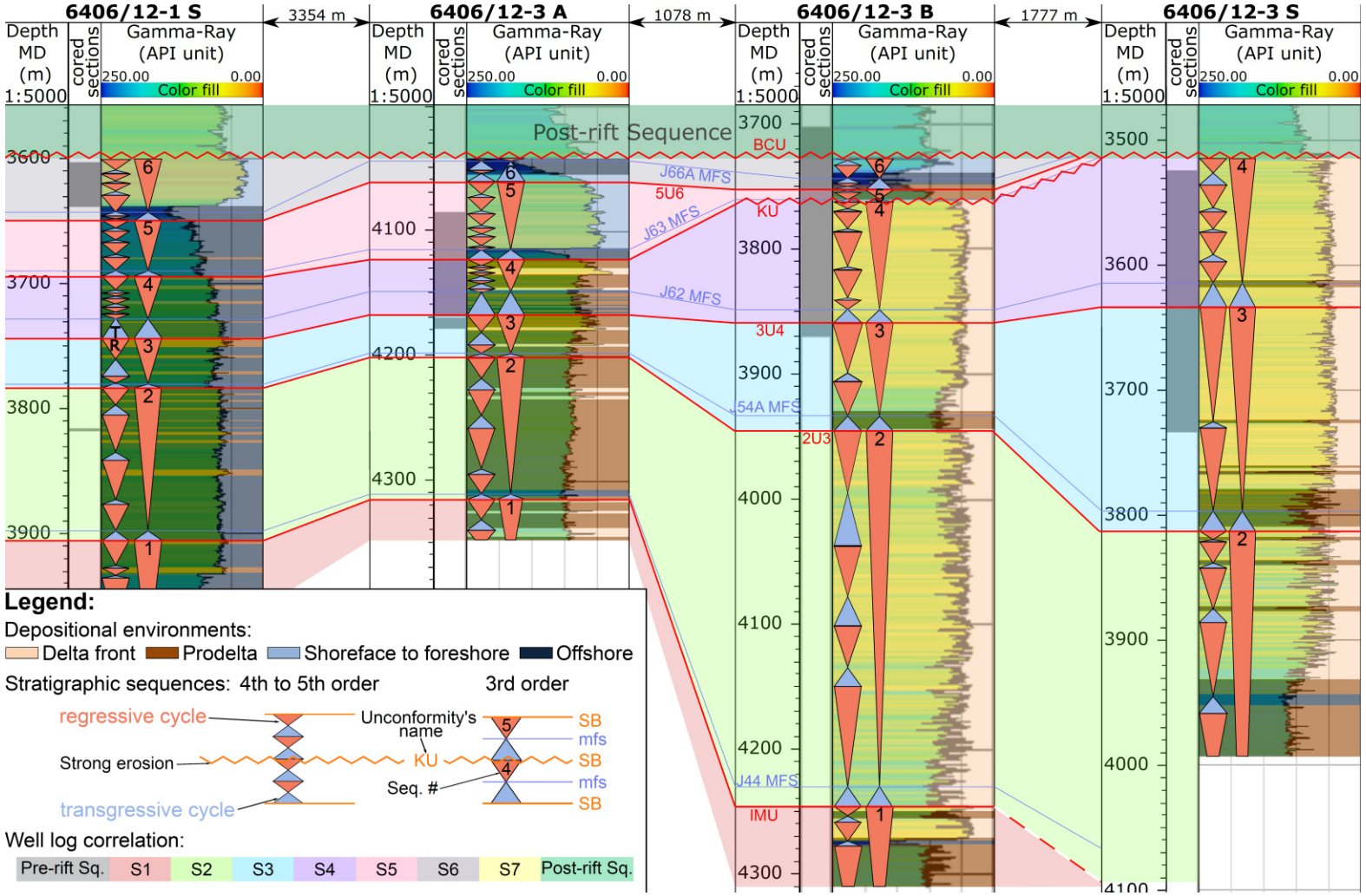

Fig. 4.Ib: Gamma-Ray (GR) log correlation showing the 3rd to 5th order stratigraphic sequences in the greater Fenja area. The GR-log correlation is orientated approximately N-S, the exact location is shown on Fig. 4.Aa-C. Sequence boundaries are identified within the correlation, with the Near Top Fangst (NTF), Intra-Melke Unconformity (IMU), Kimmeridgian Unconformity (KU), Base Cretaceous Unconformity (BCU), 2U3 (Unconformity between sequence 2 and 3), 3U4, 5U6 and 6U7 bringing to light the seven 3rd order stratigraphic sequences (S1, S2, S3, S4, S5, S6 and S7). Checkshot data allows the seismic unconformities (SUs) to be calibrated to the presented SBs. MFS are identified and named after Partington et al. (1993): J34 MFS, J44 MFS, J54A MFS, J62 MFS, J63 MFS, J66A MFS, J72 MFS and J76 MFS.

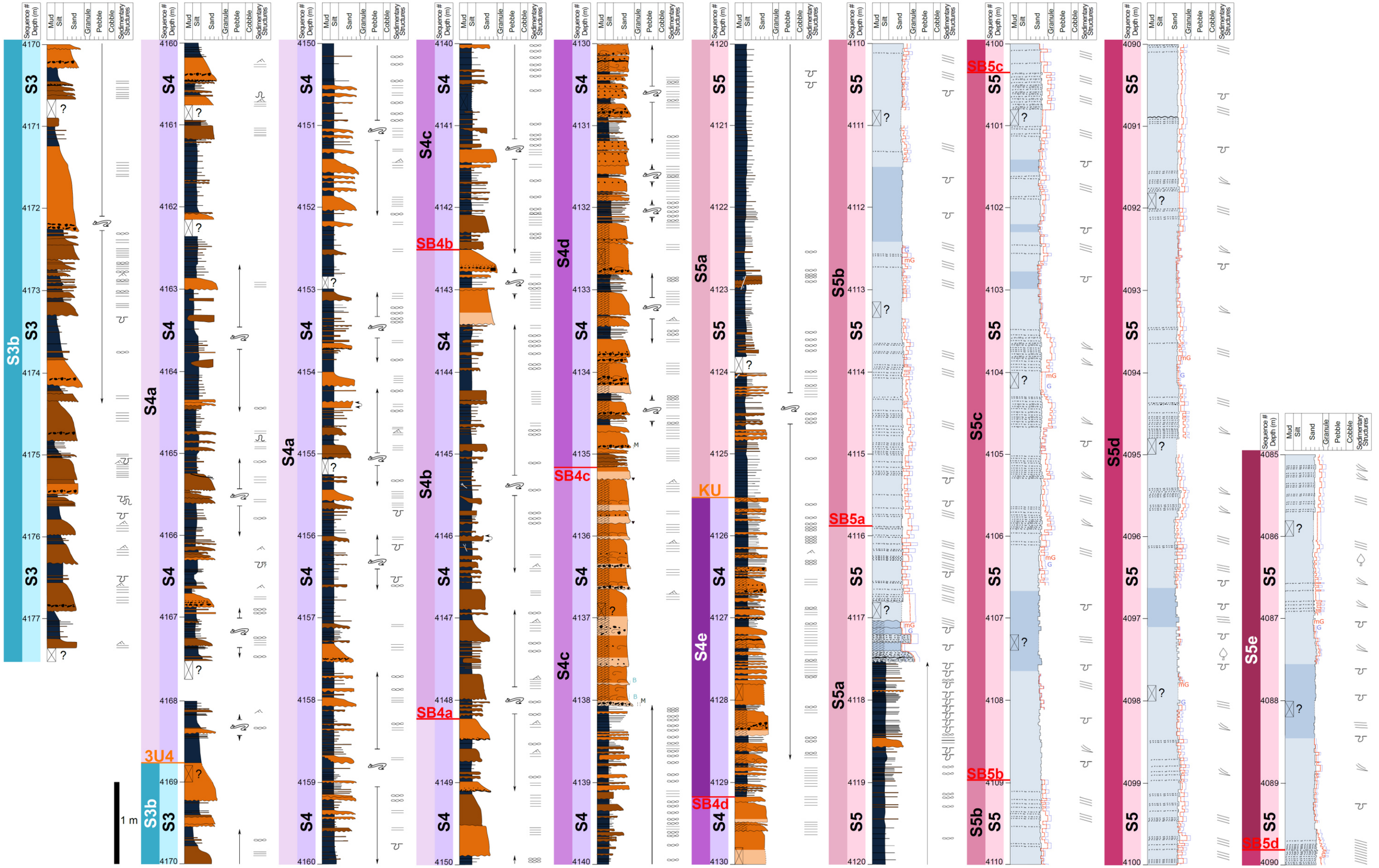

Fig. 4.Ic: Core description of well 6406/12-3A. The corresponding legend is on Fig. 2.Ca, well location is shown on Fig. 4.Aa-C. The core description highlights 3rd order sequences (S3, S4 and S5), and 4th to 5th order sequences (e.g., S4a, S4b and S4c).

16. Supplementary data 4.J: Syn-rift stratigraphic sequences – Part B

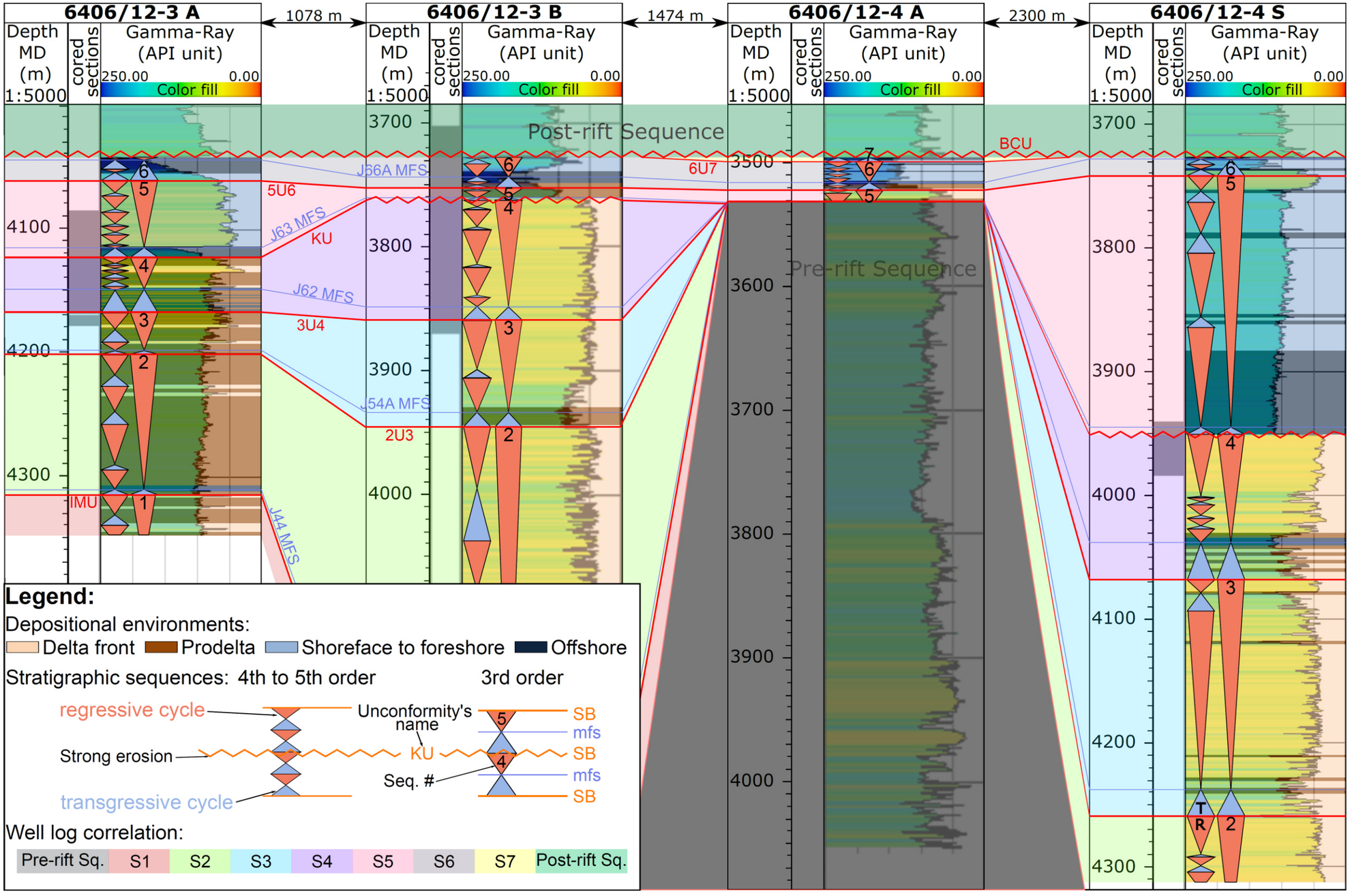

Gamma-Ray (GR) log correlation showing the 3rd to 5th order stratigraphic sequences in the greater Fenja area. The GR-log correlation is orientated approximately N-S. Sequence boundaries are identified within the correlation, with the Near Top Fangst (NTF), Intra-Melke Unconformity (IMU), Kimmeridgian Unconformity (KU), Base Cretaceous Unconformity (BCU), 2U3 (Unconformity between sequence 2 and 3), 3U4, 5U6 and 6U7 showing the seven 3rd order stratigraphic sequences (S1, S2, S3, S4, S5, S6 and S7). Checkshot data allows the seismic unconformities (SUs) to be calibrated to the presented SBs. MFS are identified and named after Partington et al. (1993): J34 MFS, J44 MFS, J54A MFS, J62 MFS, J63 MFS, J66A MFS, J72 MFS and J76 MFS.

17. Supplementary data 4.K: Post-rift stratigraphic sequences – Part A

- Post-rift sequences (S8 to S15)

T-R sequences have been identified after the interpretation of SBs *sensu* Embry (1993, 1995). 2nd to 3rd order sequences have been identified within the Cromer Knoll Group from well-log data, then tied to seismic using checkshot data (Figs. 4.Ca, 4.Cb, 4.Ka, 4.Kb, Supplementary data 4.D and Supplementary data 4.L). On seismic profiles, the Cromer Knoll Group is bounded at the base by the Base Cretaceous Unconformity (SB7 = BCU), and at the top by the Top Cromer Knoll (SB15). Note that SB #15 is almost merged with the following MFS of sequence S16. Post-rift sequences have been dated using the proposed dinoflagellate cyst zonation of Gradstein and Waters (2016). From well-log data (Figs. 4.Ka, 4.Kb and Supplementary data 4.L), the Cromer Knoll Group is mainly composed of deep-marine mudstones in which SB and MFS surfaces may be difficult to decipher where few biostratigraphic markers are observed. From *Figs. 4.Ka, 4.Kb* and *Supplementary data 4.L*, we have thus proposed the most likely scenario that can be tied to seismic data.

S8 & S9 are 2nd order sequences, whereas S10, S11, S12, S13, S14 and S15 are all 3rd to 4th order sequences. Indeed, based on seismic and well-log data (Figs. 4.Ca, 4.Cb, 4.Ka, 4.Kb, Supplementary data 4.D and Supplementary data 4.L), S8 and S9 were deposited mainly in the deep (Cretaceous) domains (Møre and Vøring Basins in Fig. 4.Aa), whereas thicknesses are reduced in the terrace domains (Halten and Dønna terraces in Fig. 4.Aa) where accommodation space is constantly available, whereas sediment thicknesses are reduced in the terrace domains (Halten and Dønna terraces in Fig. 4.Aa). Nevertheless, S10 to S15 are well-developed in the terrace domains and can be easily correlated (Figs. 4.Ka, 4.Kb and Supplementary data 4.L). To this regard, the turbidite sandstone members described in *Chapter 3* were deposited during S10 to S15. The Breiflabb Member was deposited during S10, whereas the Skolest Member equivalent was deposited during S11 and the Lysing Member during S15 (Fig. 4.Ka).

As described by Gradstein and Waters (2016), the “Aptian sands” observed only in well 6507/7-12 (Fig. 4.Kb) exhibits well developed deep-water turbidite deposits in S8 (S8). From a seismic viewpoint, it seems that the “Aptian sands were controlled by fault activity as they reveal wedge-shaped geometries in S8 (Fig. 4.Cb) The fault related to these “Aptian sands” is a 100 km long, SW-NE oriented master fault separating the Dønna Terrace and the Nordland Ridge (Fig. 4.Aa). Rare sandstone stringers, commonly less than one metre thick, have been observed in the other sequences. Note that the Skolest Member equivalent is considered as corresponding to sandstone stringers compared to the well-developed turbidite sandstones of the Breiflabb and Lysing members described in the greater Marulk area in *Chapter 3*.

Looking in detail at the seismic line of *Figs. 4.Dd, 4.De, 4.Df* in *Supplementary data 4.D*, S15 (bounded at the base by SB #14 and at the top by SB #15) has a wedge-shaped geometry, which can be related to the presence of a master fault (Fig. 4.Cb). Intra-S15 seismic markers exhibit high and low seismic amplitudes that are interpreted as alternations between

sandstones and mudstones as further confirmed by well-log data of well 6507/7-12 (Figs. 4.Cb, 4.Kb). Extensional fault motions are also observed between S12 and S15 (*Figs. 4.Da, 4.Db, 4.Dc* in *Supplementary data 4.D*), resulting either from tectonic activity or to differential compaction between intraterrace lows and intraterrace highs. It is not possible, however, to conclude if the Lysing Member was generated by extensional tectonic activity, since no clear evidence arises from the entire 3D seismic survey.

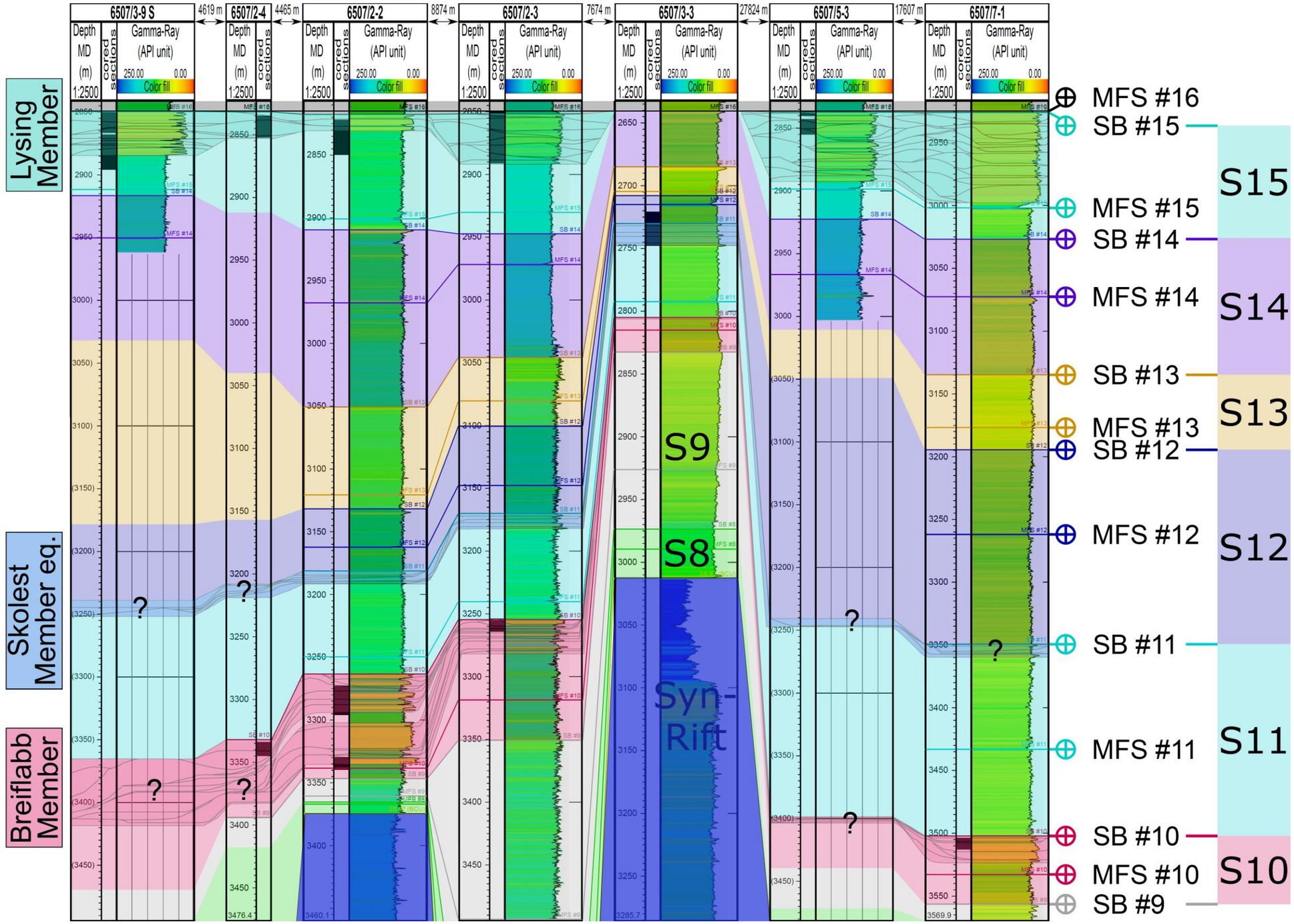

Fig. 4.Ka: Gamma-Ray (GR) log correlation showing the 2nd to 3rd order stratigraphic sequences in the greater Marulk area. The GR-log correlation is orientated approximately NE-SW, the exact location is shown on Fig. 4.Aa-B. Sequence boundaries are identified within the correlation, with the SB #7 corresponding to the BCU, SB #8, SB #9, SB #10, SB #11, SB #12, SB #13, SB #14 and SB #15, this latter one corresponding to the top of the Cromer Knoll Group. These SBs show the eight 2nd to 3rd order stratigraphic sequences within the Cromer Knoll Group (S8, S9, S10, S11, S12, S13, S14 and S15). Checkshot data allows the seismic unconformities (SUs) to be calibrated to the presented SBs. Maximum flooding surfaces (MFS) are identified and named from the oldest to the youngest, MFS #8, MFS #9, MFS #10, MFS #11, MFS #12, MFS #13, MFS #14, MFS #15 and MFS #16, respectively.

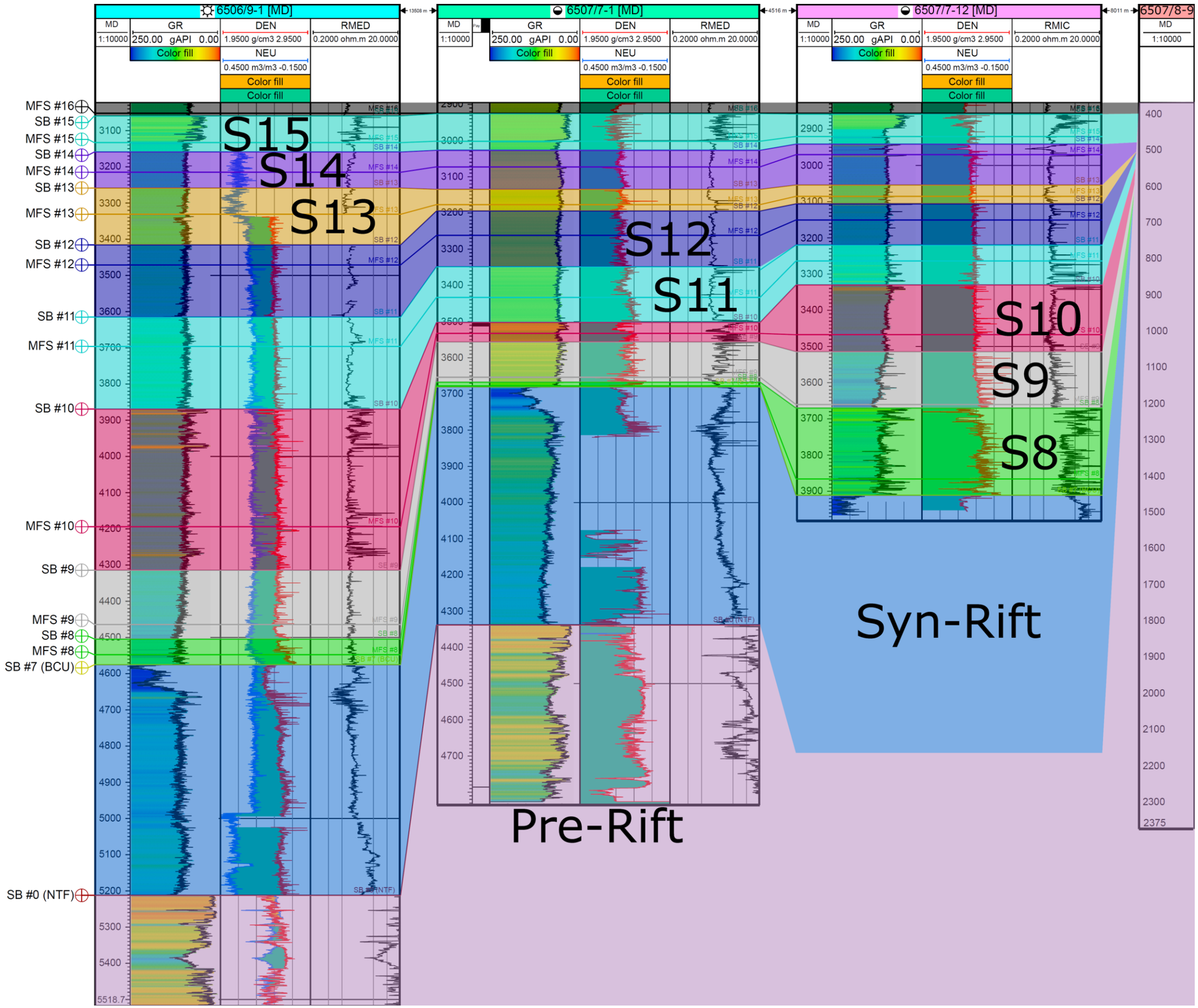

Fig. 4.Kb: Gamma-Ray (GR), Density/Neutron and Resistivity log correlation showing the 2nd to 3rd order stratigraphic sequences in the greater Marulk area. The GR-log correlation is orientated approximately WNW-ESE, the exact location is shown on Fig. 4.Aa-B. Sequence boundaries are identified within the correlation, with the SB #0, SB #7 corresponding respectively to the NTF (Near top Fangst) BCU (Base Cretaceous Unconformity), SB #8, SB #9, SB #10, SB #11, SB #12, SB #13, SB #14 and SB #15, this latter one corresponding to the top of the Cromer Knoll Group. These SBs show the eight 2nd to 3rd order stratigraphic sequences within the Cromer Knoll Group (S8, S9, S10, S11, S12, S13, S14 and S15). Checkshot data allows the seismic unconformities (SUs) to be calibrated to the presented SBs. Maximum flooding surfaces (MFS) are identified and named from the oldest to the youngest, MFS #8, MFS #9, MFS #10, MFS #11, MFS #12, MFS #13, MFS #14, MFS #15 and MFS #16, respectively.

18. Supplementary data 4.L: Post-rift stratigraphic sequences – Part B

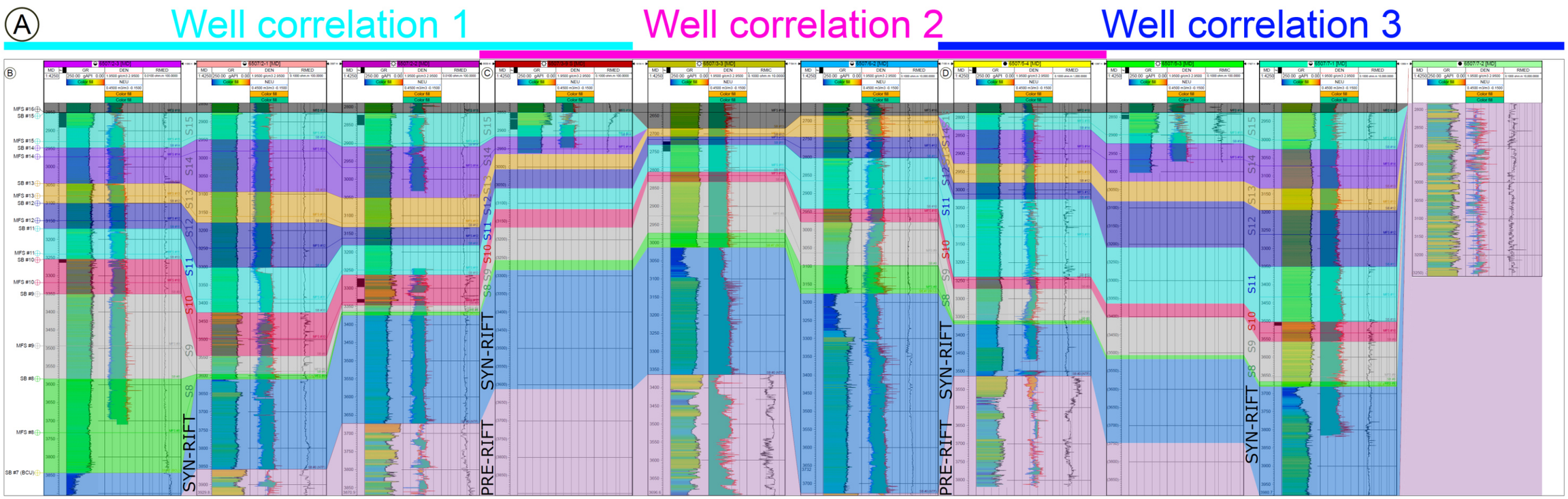

Gamma-Ray (GR), Density/Neutron and Resistivity log correlation showing the 2nd to 3rd order stratigraphic sequences in the greater Marulk area. The GR-log correlation is orientated approximately NE-SW, the exact well location is shown on Fig. 4.Aa-B. Sequence boundaries are identified within the correlation, with the SB #0, SB #7 corresponding respectively to the NTF (Near top Fangst) BCU (Base Cretaceous Unconformity), SB #8, SB #9, SB #10, SB #11, SB #12, SB #13, SB #14 and SB #15, this latter one corresponding to the top of the Cromer Knoll Group. These SBs show the eight 2nd to 3rd order stratigraphic sequences within the Cromer Knoll Group (S8, S9, S10, S11, S12, S13, S14 and S15). Checkshot data allows the seismic unconformities (SUs) to be calibrated to the presented SBs. Maximum flooding surfaces (MFS) are identified and named from the oldest to the youngest, MFS #8, MFS #9, MFS #10, MFS #11, MFS #12, MFS #13, MFS #14, MFS #15 and MFS #16, respectively. Regional well-log correlation (A) with an approximate length of 100 km, with semi-regional well-log correlation zooms (B), (C) and (D) named well correlation 1, 2 and 3, respectively.

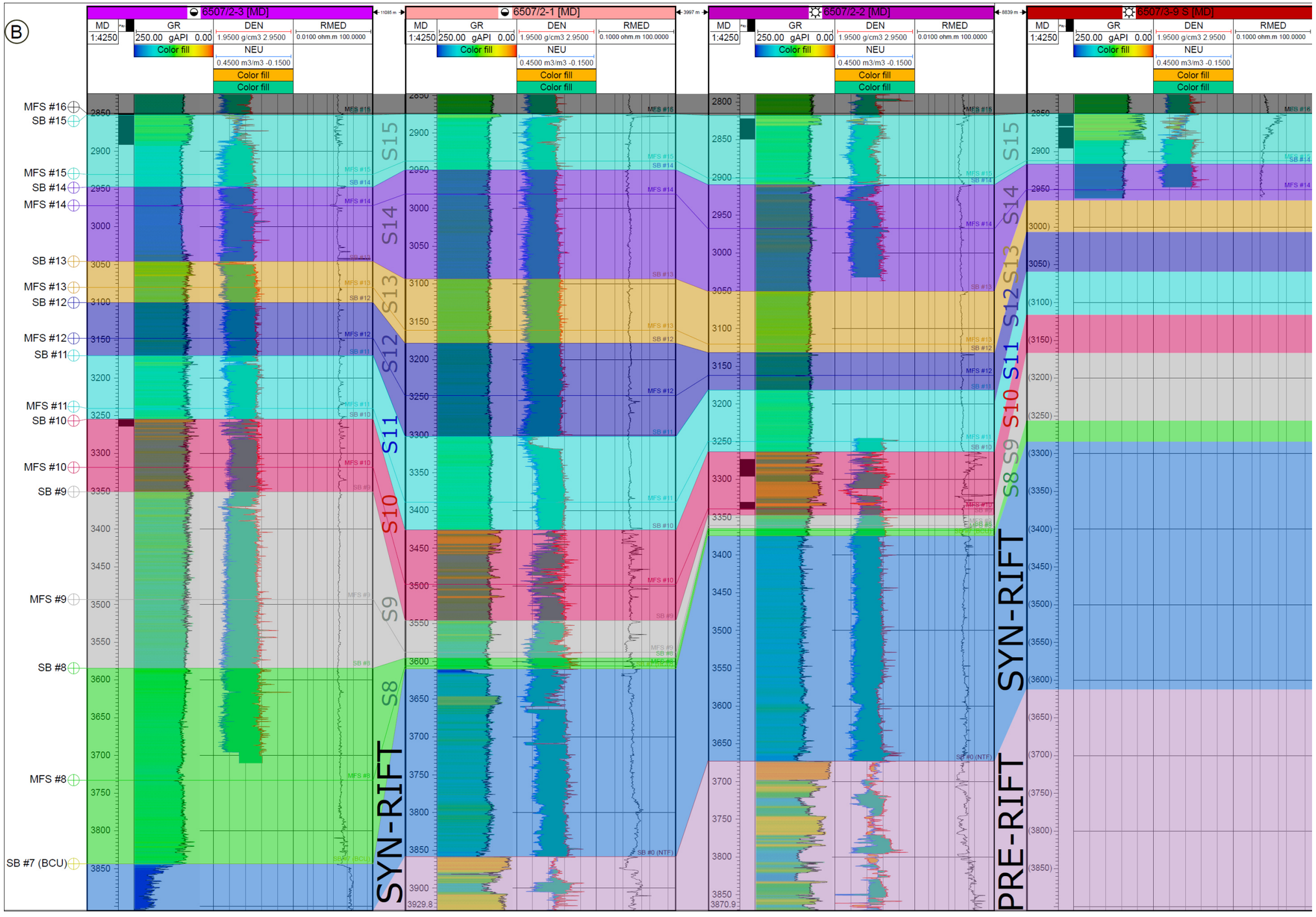

(B) Semi-regional well correlation 1: From left to right, well 6507/2-3, well 6507/2-1, well 6507/2-2, and well 6507/3-9S;

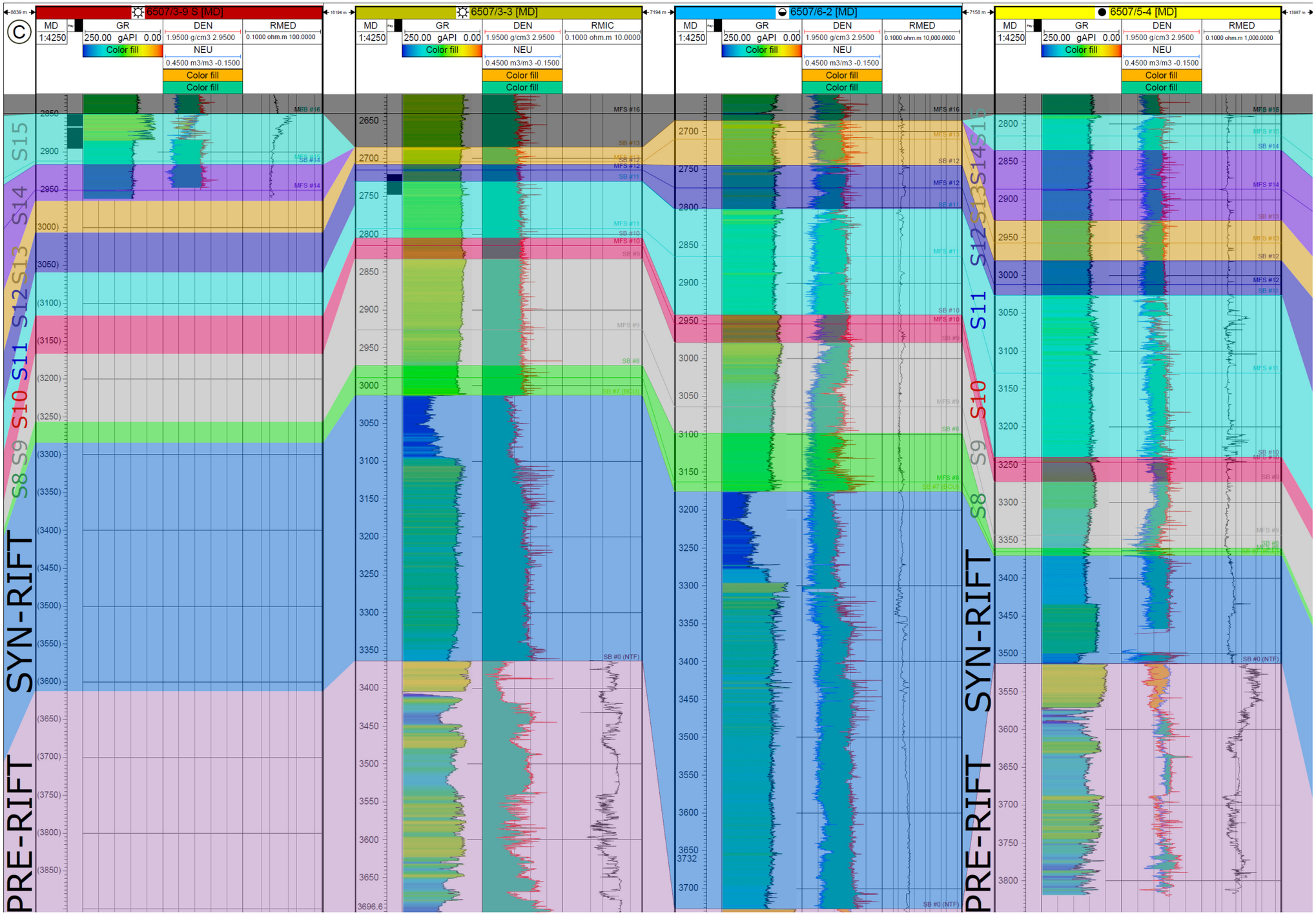

(C) Semi-regional well correlation 2: From left to right, well 6507/3-9S, well 6507/3-3, well 6507/6-2, and well 6507/5-4;

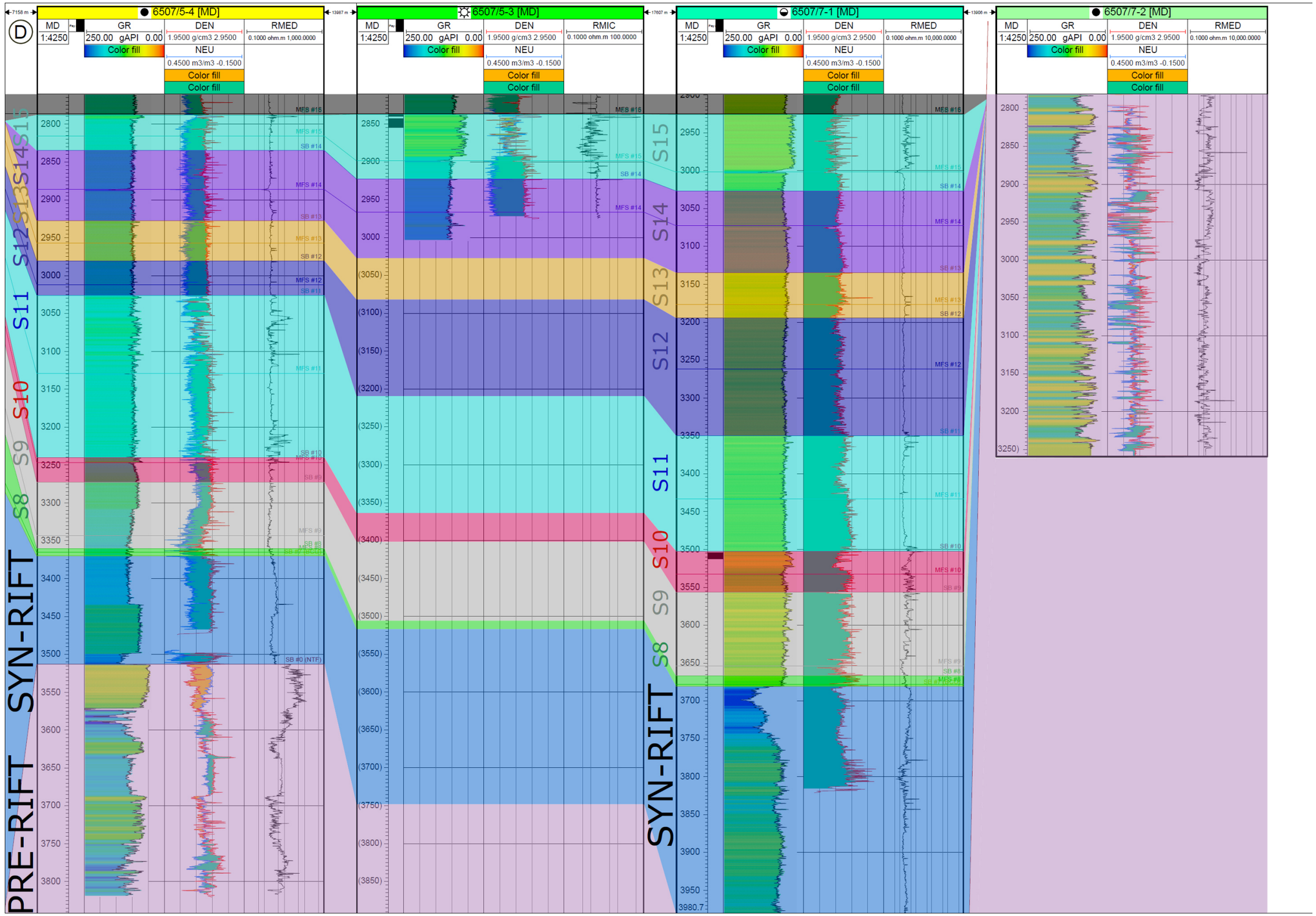

(D) Semi-regional well correlation 3: From left to right, well 6507/5-4, well 6507/5-3, well 6507/7-1, and well 6507/7-2.